

P-1

THE INTERNATIONAL HYDROGRAPHIC REVIEW

VOL. 31 · Nº 2
NOVEMBER 2025

IHO
International Hydrographic Organization

P-1

THE INTERNATIONAL HYDROGRAPHIC REVIEW

VOL. 31 · Nº 2
NOVEMBER 2025

IHO
International Hydrographic Organization

International Hydrographic Organization
Vol. 31 · Nº 2 — November 2025

© Copyright International Hydrographic Organization [2025]

This work is copyright. Apart from any use permitted in accordance with the Berne Convention for the Protection of Literary and Artistic Works (1886), and except in the circumstances described below, no part may be translated, reproduced by any process, adapted, communicated or commercially exploited without prior written permission from the Secretariat of the International Hydrographic Organization (IHO). Copyright in some of the material in this publication may be owned by another party and permission for the translation and/or reproduction of that material must be obtained from the owner.

This document or partial material from this document may be translated, reproduced or distributed for general information, on no more than a cost recovery basis. Copies may not be sold or distributed for profit or gain without prior written agreement of the IHO Secretariat and any other copyright holders.

In the event that this document or partial material from this document is reproduced, translated or distributed under the terms described above, the following statements are to be included:

"Material from IHO publication [reference to extract: Title, Edition] is reproduced with the permission of the IHO Secretariat (Permission No ……./…) acting for the International Hydrographic Organization (IHO), which does not accept responsibility for the correctness of the material as reproduced: in case of doubt, the IHO's authentic text shall prevail. The incorporation of material sourced from IHO shall not be construed as constituting an endorsement by IHO of this product." "This [document/publication] is a translation of IHO [document/publication] [name]. The IHO has not checked this translation and therefore takes no responsibility for its accuracy. In case of doubt the source version of [name] in [language] should be consulted."

The IHO Logo or other identifiers shall not be used in any derived product without prior written permission from the IHO Secretariat.

Cover image

Lago Cachet II in the Northern Patagonian Icefield after a glacier lake outburst flood event. The photo (© H.-G. Maas) shows the flank of Glaciar Colonia, which dammed a river and formed Lago Cachet II during its advance approximately 15,000 years ago. Due to recent glacier retreat and changes in hydrostatic balance, the lake water carved a subglacial pathway, creating a wide tunnel through melting and erosion. The corresponding article by Hans-Gerd Maas et al. introduces an early warning system for glacier lake outburst floods based on monoscopic image sequences and explores additional photogrammetric techniques for hydrographic environmental monitoring (pp. 12–29).

Open Access Policy

This journal provides immediate open access to its content on the principle that making research freely available to the public supports a greater global exchange of knowledge.

About the Journal

The International Hydrographic Review (IHR) is an international scientific journal publishing peer-reviewed papers on all aspects of hydrography and associated subjects, ranging from the latest technical developments and significant events to book reviews and historical recollections. The IHR was first published in 1923 and since then has been published regularly.

Editorial



Patrick Westfeld

Welcome to the second issue of the 31st volume of The International Hydrographic Review (IHR).

Hydrography is a decisive enabler for the sustainable use of our oceans while ensuring their protection for future generations. In a year when global attention is focused on climate resilience and integrated ocean governance, notably during UN Climate Change Conference in Belém (Brazil), the discipline of hydrography has assumed a central role in shaping strategies that balance economic development with ecological responsibility. Far beyond its traditional remit of charting and navigation, hydrography now underpins critical decisions in coastal zone management, marine spatial planning, and environmental monitoring. Rising sea levels, intensifying storm patterns, and accelerating sediment dynamics demand precise and timely hydrographic data to safeguard infrastructure and ecosystems alike. At the same time, the hydrographic community is increasingly called upon to contribute to global sustainability goals, ensuring that marine operations align with climate adaptation measures and biodiversity conservation. This issue reflects these imperatives by presenting research that not only advances technical capabilities but also addresses the broader challenge of reconciling efficiency, safety, and environmental stewardship. Through innovative methodologies, data-driven risk assessments, and collaborative frameworks, the contributions herein demonstrate how hydrography provides the foundation for resilience and sustainable ocean use in an era of unprecedented environmental change.

The invited article by Hans-Gerd Maas and colleagues offers a detailed review of photogrammetric techniques in hydrographic environmental monitoring (pp. 12–29). By integrating camera and LiDAR systems with advanced image analysis and AI-driven algorithms, the authors present solutions that enable high-resolution, accurate measurements for monitoring dynamic coastal and estuarine environments. These innovations not only enhance hydrographic precision but also provide essential tools for environmental stewardship, supporting long-term strategies to protect vulnerable ecosystems.

The peer-reviewed section begins with Anders Knudby's study on satellite imagery for hazard detection in the Canadian Arctic (pp. 30–43). By applying Sentinel-2 data and satellite-derived bathymetry, this research illustrates how proactive use of remote sensing can prevent groundings and reduce environmental risks in poorly surveyed waters. Lucas Dammert and co-authors advance multibeam bathymetry by integrating robotic total stations with multi-sensor adjustment (pp. 44–62), delivering sub-centimetre accuracy and robust solutions for GNSS-challenged environments – an essential capability for precise data acquisition in inland waters, harbours, and complex coastal zones. Shivani Seepersad & Dexter Davis introduce an economic risk assessment framework for Small Island Developing States (pp. 64–79), addressing the socio-economic and environmental consequences of maritime incidents. Alberto Costa Neves and colleagues tackle the complex issue of nautical depth in fluid mud environments (pp. 80–100), proposing conservative definitions that reconcile port efficiency with environmental safety. A series of papers by Amrika Maharaj and collaborators (pp. 102–121, 122–139 and 140–150) employ geostatistical and AI-driven models to analyse maritime accidents and predict risks in the Caribbean Sea, offering strategies that strengthen resilience and reduce the likelihood of environmentally damaging incidents. Collectively, these contributions underscore the growing importance of data-driven approaches in safeguarding both navigation and marine ecosystems.

ISSN print: 0020-6946
DOI prefix: 10.58440
URL: https://ihr.iho.int/

Publisher:
International Hydrographic Organisation
4b Quai Albert 1er
98011 Monaco

Printing/Binding: German Federal Maritime and Hydrographic Agency (BSH)
Editorial Board:
https://ihr.iho.int/editorial-team/

The notes and technical reports not only offer practical insights into specialized hydrographic applications but also highlights initiatives by Member States that strengthen capacity and promote sustainable ocean use. Several contributions emphasize environmental aspects, demonstrating how hydrography supports ecosystem protection alongside technical innovation. Guy Van Rentergem & Sofie de Volder describe innovative methods for conducting bathymetric surveys in caves (pp. 152–156), demonstrating adaptability to extreme environments where groundwater systems play a vital role in global water cycles. Chandana Rathnayake & Huibert-Jan Lekkerkerk present a structured framework for survey system calibration and verification (pp. 158–172), reinforcing professional standards that underpin reliable data for navigation and environmental monitoring. Jacob Inostroza Torres reviews Chile's recent achievements in naming submarine features (pp. 174–180), a contribution that enriches global ocean knowledge and supports the objectives of the UN Decade of Ocean Science for Sustainable Development. Additional notes include Nickolás Roscher and colleagues reporting on the inauguration of the LA-RENC Training Center (pp. 182–185), Mohammad Musa examining Bangladesh's role in hydrography and sustainable blue economy initiatives (pp. 186–197), and Varun Jai evaluating satellite-derived bathymetry for nearshore mapping around Agatti Island, India (pp. 198–208). Each of these contributions reflects the interconnectedness of technology, governance, and environmental responsibility in modern hydrography.

Finally, we extend our sincere gratitude to the peer reviewers whose expertise and dedication ensure the scientific quality of The International Hydrographic Review (p. 210). Their invaluable contributions uphold the standards of excellence that define this publication.

We trust that this issue will inform and inspire your work, and we invite you to share your insights and research with the IHR as we collectively advance the science and practice of hydrography for the benefit of navigation safety, environmental protection, ocean sustainability, and beyond.

On behalf of the Editorial Board, I hope that you will enjoy reading this new issue of the IHR!



Dr Patrick Westfeld
Chief Editor, IHR

https://doi.org/10.58440/ihr-31-2-e02

Content

Invited article

12 **Photogrammetric techniques in hydrographic environmental monitoring**
Hans-Gerd Maas, Robert Blaskow, Melanie Elias, David Mader, Christian Mulsow, Katja Richter, Hannes Sardemann, Ellen Schwalbe and Anette Eltner

Peer-reviewed articles

30 **Satellite imagery for hazard detection: better use of satellite imagery could help prevent groundings in the Canadian Arctic**
Anders Knudby

44 **Leveraging robotic total stations and multi-sensor adjustement for accurate multibeam bathymetry**
Lucas Dammert, Florian Pöppl, Jan Rhomberg-Kauert, Tomas Thalmann, David Monetti, Hans-Berndt Neuner and Gottfried Mandlburger

64 **Quantifying economic consequences of maritime incidents: a framework for Small Island Developing States**
Shivani Seepersad and Dexter Davis

80 **Nautical depth investigation in fluid mud environment at Santa Catarina Terminal (Port of São Francisco do Sul, Brazil)**
Alberto Pedrassani Costa Neves, Augusto Dantas Sampaio and Reginaldo Gonçalves Abreu

102 **Geostatistical analysis of maritime accidents: identifying contributory factors and risk patterns in maritime navigation**
Amrika Maharaj, Keith Miller, Dexter Davis and Michael Sutherland

122 **Risk assessment and mitigation measures of maritime navigation in the Caribbean Sea**
Amrika Maharaj, Keith Miller, Dexter Davis and Michael Sutherland

140 **A comparative assessment of spatial regression methods for predicting maritime events in the Caribbean Sea**
Amrika Maharaj, Keith Miller, Dexter Davis and Michael Sutherland

Notes / Technical reports

152 **Bathymetry in caves**
Guy Van Rentergem and Sofie de Volder

158 **Survey system verification and calibration in the hydrospatial domain**
Chandana Rathnayake and Huibert-Jan Lekkerkerk

174 **Submarine geographical names – a review of the recent incorporation of seabed features submitted by Chile to the GEBCO gazetteer**
Jacob Inostroza Torres

182 **The Directorate of Hydrography and Navigation inaugurates the new LA-RENC training center of IC-ENC in favor of navigation safety**
Nickolás Roscher, Ana Mileze, Isaias Brito, Bruna Pinheiro and Igor Justin

186 **Leadership in regional hydrography: vision, capacity building and integration**
Mohammad Musa

198 **Evaluation of SDB data for near shore mapping around Agatti Island, India: a comparative study with echo sounder survey**
Varun Jai

INVITED ARTICLE

Photogrammetric techniques in hydrographic environmental monitoring

Authors

Hans-Gerd Maas[1], Robert Blaskow[1], Melanie Elias[2], David Mader[1], Christian Mulsow[1], Katja Richter[1], Hannes Sardemann[1], Ellen Schwalbe[1] and Anette Eltner[1]

Abstract

The article gives an overview on photogrammetric techniques in hydrographic environmental monitoring by presenting a collection of recent research projects and pilot studies, based both on cameras and LiDAR systems. Both techniques offer a very large spatial resolution and a high accuracy potential. In addition, stationary cameras also offer an almost arbitrarily high spatial resolution for spatio-temporal measurements. Subpixel accuracy image analysis techniques, combined with thorough geometric sensor modelling and calibration strategies, offer a very high accuracy potential, making even low-cost cameras a powerful measurement tool. The integration of imaging sensors and dedicated processing algorithms allows for the development of efficient solutions to novel challenging measurement tasks, which could not be solved at reasonable effort beforehand, and AI techniques increasingly facilitate the solution of complex image analysis tasks.

Keywords

photogrammetry · LiDAR · environmental monitoring · image sequence analysis · sensor fusion · sensor modelling · spatio-temporal data

Resumé

Cet article donne un aperçu des techniques photogrammétriques utilisées pour suivre l'environnement hydrographique en présentant une série de projets de recherche et d'études pilotes récents, qui se basent à la fois sur des caméras et des systèmes lidar. Ces deux techniques offrent une très grande résolution spatiale et un potentiel de précision élevé. En outre, les caméras fixes offrent également une résolution spatiale pratiquement illimitée pour les mesures spatio-temporelles. Les techniques d'analyse d'images à précision subpixel, combinées à une modélisation géométrique rigoureuse des capteurs et à des stratégies de calibration approfondies, permettent d'atteindre un très haut niveau de de précision, faisant même des caméras à faible coût des outils de mesure performants. L'intégration de capteurs d'imagerie et d'algorithmes de traitement dédiés permet de développer des solutions efficaces pour des tâches de mesure nouvelles et complexes, qui ne pouvaient auparavant être résolues sans efforts considérables, et les techniques d'IA facilitent de plus en plus la résolution de tâches complexes d'analyse d'images.

Resumen

El artículo ofrece una visión general de las técnicas fotogramétricas en el seguimiento medioambiental hidrográfico, presentando una colección de proyectos de investigación y estudios piloto recientes, basados tanto en cámaras como en sistemas lidar. Ambas técnicas ofrecen una resolución espacial muy amplia y un alto potencial de precisión. Además, las cámaras fijas también ofrecen una resolución espacial casi arbitrariamente alta para mediciones espacio-temporales. Las técnicas de análisis de imágenes con precisión de subpíxel, combinadas con estrategias detalladas de modelado y calibración de sensores geométricos, ofrecen un potencial de precisión muy alto, convirtiendo incluso a las cámaras de bajo coste en una potente herramienta de medición. La integración de sensores de imagen y algoritmos de procesamiento específicos permite el desarrollo de soluciones eficientes para tareas novedosas de mediciones difíciles, que antes no podían resolverse con un esfuerzo razonable, y las técnicas de IA facilitan cada vez más la resolución de tareas de análisis de imágenes complejas.

✉ Hans-Gerd Maas · hans-gerd.maas@tu-dresden.de

[1] Dresden University of Technology, Institute of Photogrammetry and Remote Sensing, 01062 Dresden, Germany

[2] Dresden University of Applied Sciences, Faculty of Spatial Information, 01069 Dresden, Germany

https://doi.org/10.58440/ihr-31-2-a18

1 Introduction

Photogrammetry is the technology for extracting precise and reliable 3D information from image data. Photogrammetry uses image analysis techniques for the automation of image measurement tasks, combined with strict geometric and stochastic modelling for optimizing solutions, both in precision and reliability. Besides image data, photogrammetry also works with 3D point clouds and full-waveform data obtained from light detection and ranging (LiDAR; or laser scanning) techniques. The research in photogrammetry at TU Dresden is focused on the integration of sensors and processing algorithms for the development of efficient solutions to novel challenging measurement tasks.

In general, cameras as sensors offer the inherent advantage of acquiring highly resolved spatio-temporal data, allowing for measurements simultaneously at many locations in an image at an almost arbitrary temporal resolution. The amount of spatio-temporal data generated by a photogrammetric sensor system in environmental monitoring tasks will usually necessitate the development of task-specific fully automatic data processing schemes, which may – depending on the needs of the application at hand – run online in real-time or offline in a batch process. Photogrammetry has developed a wide range of image analysis techniques over the past decades, with artificial intelligence (AI) techniques recently playing a rapidly increasing role especially in tasks such as image segmentation.

Besides their advantage of providing spatio-temporally resolved data, digital cameras also offer themselves as environmental monitoring sensors as they have become rather inexpensive over the past decades, with a wide choice of outdoor-suited peripheral devices being available as well. Increasingly, this also holds for LiDAR sensors, where solid state LiDAR systems for instance find lucrative markets in automotive autonomous driving, thus also creating mass markets. Using state-of-the-art subpixel accuracy image measurement techniques, combined with photogrammetric techniques for thorough geometric sensor modelling and camera calibration (Luhmann et al., 2016), even simple cameras may show a surprisingly high measurement accuracy potential.

In this paper, we give a tour through some recent research and development projects at our institute, showing the potential of photogrammetric techniques in hydrographic environmental monitoring. The application fields include river monitoring (Sections 2–5), photo- and LiDAR-based bathymetry (Sections 6 and 8), uncrewed aerial vehicle (UAV)-based turbidity analyses (Section 9) as well as a glacier lake outburst flood early warning system (Section 7). All projects briefly shown in the following have in common, that they use stationary or moving cameras or LiDAR sensors, which acquire time sequences of images or 3D point cloud data to monitor slow or fast environmental processes related to hydrography. Automation in precise and reliable data processing is a further commonality. Obviously, such a paper can only give a glimpse into the research and application field, without any claim of completeness or representativeness.

2 Automated hydrological monitoring using computer vision and photogrammetry

A primary application of modern technologies in hydrology is the detailed monitoring of riverine systems. This involves the acquisition of water levels, flow velocities, and discharge rates to enable rapid and effective disaster response and improve flash flood forecasting. Traditional gauging stations are often cost-prohibitive and labour-intensive, leaving smaller catchments unmonitored. This has made the development of cost-effective, camera-based solutions particularly attractive (Krüger et al., 2024).

2.1 Machine learning and data augmentation

Central to automated water level determination is the use of artificial intelligence (AI), specifically convolutional neural networks (CNNs). Models such as UPerNet, STCN, and the Segment Anything Model (SAM) are employed for the automated detection and semantic segmentation of water surfaces from camera imagery (Blanch et al., 2025a, Zamboni et al., 2025). These networks are trained to differentiate between water and non-water regions. AI models are trained using diverse datasets, such as the RIWA (River Water Segmentation) dataset (Wagner et al., 2023). These datasets comprise images of various water bodies, captured with different cameras, and under varying resolutions, qualities, times of day, and seasons. This diversity is crucial for ensuring the models' robustness and transferability to novel, unobserved rivers and locations, thereby preventing overfitting.

To enhance the models' resilience to diverse environmental conditions, including varying lighting, shadows, reflections, fog, rain, or snow, data augmentation strategies are applied. These include geometric transformations (e.g., rotation, scaling, distortion) and radiometric transformations (e.g., brightness, contrast, artificial fog or snow). A distinction is made between offline and online augmentation strategies (Wagner et al., 2023). Offline augmentation involves pre-manipulating and storing images before training, which can be advantageous for small datasets. Online augmentation occurs "on the fly" during training, and is especially beneficial for larger datasets as it can theoretically generate a much greater volume of data without a significant increase in storage requirements.

2.2 Photogrammetric reconstruction and georeferencing

The accurate transformation of image-based measurements into object-space requires geo-referenced, high-precision 3D models of the monitoring site and

https://doi.org/10.58440/ihr-31-2-a18

the riverbed (Eltner et al., 2021). Furthermore, for georeferencing the hydrological models, ground control points (GCPs) are usually installed and surveyed using total stations or global navigation satellite system (GNSS) as these points serve to orient the camera system within a global coordinate system and transform image measurements into the object space. A significant advancement is a new AI-based algorithm for the automated detection of GCPs in camera imagery (Blanch et al., 2025b). This algorithm, which leverages bounding box and keypoint detection, allows for the automated re-identification of marked points. This enables the re-determination of the camera's position for each frame using a spatial resection, thereby reducing measurement inaccuracies caused by camera instability (e.g., from wind). The method exhibits high robustness to variations in camera properties, GCP geometry, and environmental conditions, achieving sub-pixel accuracy across various tested datasets. This development minimizes manual effort and accelerates the processing of large image time series. Note that temperature variations can influence a camera's internal geometry, leading to measurement inaccuracies (Elias et al., 2019), necessitating regular on-site calibration or self-calibration. Recent advances in image-to-geometry registration potentially enable the usage of the 3D model only for image pose estimation, even allowing for interior camera calibration if sufficient matches are found well-distributed throughout the image (Elias et al., 2023), making the camera-based water level observation very flexible and robust. Camera-gauges can now be run across several years with cm-accurate water surface height measurements (Blanch et al., 2025a).

2.3 Flow velocity and discharge rate determination

In addition to water level, the acquisition of flow velocities and resulting discharge rates is critical for hydrological monitoring. For surface flow velocity determination from short video sequences, e.g., the Particle Tracking Velocimetry (PTV) method can be used (Eltner et al., 2021a). PTV's accuracy depends on the presence of traceable particles and prevailing lighting and visibility conditions. To obtain continuous discharge hydrographs under challenging conditions, the novel statistical model "OptiQ" was developed (Grundmann et al., 2024). This method learns from past measurements to fill data gaps in the surface velocity distribution, which may arise from a lack of particles. Discharge is estimated by multiplying the wetted cross-sectional area (derived from the optically determined water level and the terrain model) by the surface velocity. However, accurate discharge determination requires a correction factor to convert from the mean surface velocity to a depth-averaged velocity, which is ideally determined through comparative measurements, e.g., from acoustic doppler current profilers (ADCPs). Furthermore, minor errors in water level measurement can lead to significant deviations in discharge.

The developed methods demonstrate compelling accuracies: water level measurements are within the centimetre range, with root mean squared errors (RMSEs) of 1.3 cm to 3.0 cm for daily values over two years (Blanch et al., 2025a). Surface flow velocity measurements often exceed 90 % accuracy (Eltner et al., 2020). Discharge estimations for regular cross-sections show maximum errors of 4 % to 5 %, and the OptiQ approach achieved a RMSE of 0.045 m³/s (Grundmann et al., 2024).

3 Long-term monitoring of riverbank dynamics using low-cost stereo cameras

Riverbanks are inherently dynamic landscapes, shaped continuously by hydrological and geomorphological processes. Understanding these changes

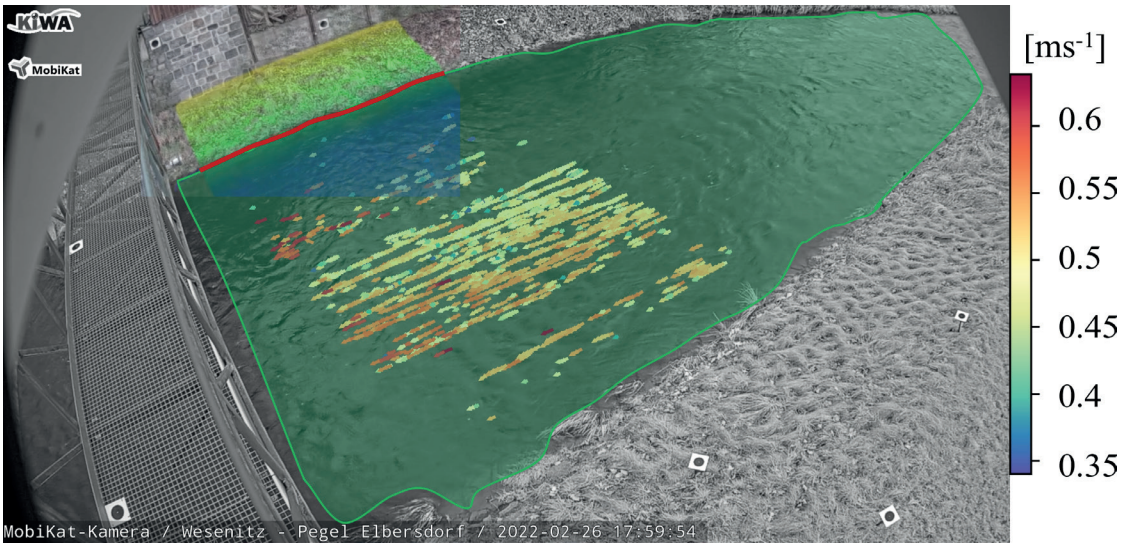


Fig. 1 Illustration of a prototype-camera gauge measuring water level and river surface flow velocities. Green polygon indicates with CNN automatically segmented water area. Coloured shore line in the back illustrates the projected 3D point cloud for the water level retrieval. Coloured tracks on the river show the scaled flow velocities derived from video measurements.

https://doi.org/10.58440/ihr-31-2-a18

is critical, as riverbank erosion can have significant ecological, social, and economic consequences. Conventional monitoring approaches, however, are often resource-intensive and limited in duration, restricting the ability to capture long-term dynamics. To address these limitations, we explore a low-cost, automated approach for sustained, high-resolution observation.

Over a five-year period, a system of four stereo cameras was deployed at the Pulmanki River in Lapland, Finland, capturing images at two-hour intervals (Lotsari et al., 2020). While the hardware setup is relatively simple, the resulting image datasets serve as a foundation for sophisticated photogrammetric processing. Through Structure-from-Motion and Multi-View-Stereo techniques, the imagery is transformed into 4D point clouds, providing a continuous representation of the riverbank in both space and time.

3.1 Capturing change in four dimensions

The transformation of raw images into actionable data relies on the 4D Objects-by-Change (4D-OBC) framework (Anders et al., 2021). This methodology enables the identification and characterization of morphological changes by integrating temporal and spatial information. The workflow includes multi-temporal point cloud reconstruction with AI-assisted georeferencing (Blanch et al., 2025), precise co-registration through ICP alignment, and computation of surface differences using M3C2 distances (Lague et al., 2013). Temporal smoothing reduces stochastic variability (Eltner et al., 2017), and trend analysis identifies areas of significant morphological evolution (Fig. 2; Ulm et al., 2025). Finally, fusion of 4D-OBC results consolidates spatial and temporal information, improving the resolution and reliability of detected changes.

This approach allows the riverbank's morphology to be tracked continuously, revealing patterns of erosion, deposition, and structural transformation. By generating detailed 4D point clouds, the system facilitates quantitative analyses of volumetric change, spatial extent, and temporal progression of landscape evolution. Moreover, visualizations such as color-coded 4D-OBCs and time series of high-amplitude change points provide intuitive yet rigorous depictions of morphological dynamics.

3.2 Capabilities and applications

The system offers a robust platform for long-term environmental monitoring. It enables continuous, high-frequency observation of riverbanks without extensive fieldwork, making it suitable for remote or inaccessible locations. By combining low-cost hardware with advanced 4D analysis, it supports scalable and repeatable monitoring of landscape dynamics. Beyond riverine environments, this approach holds potential for applications across geomorphology, environmental change studies, and habitat monitoring, wherever detailed spatiotemporal analysis of morphological evolution is required.

In essence, the integration of low-cost stereo cameras with 4D change detection transforms simple image acquisition into a comprehensive, long-term monitoring capability, allowing researchers to observe, quantify, and interpret landscape evolution with unprecedented temporal resolution.

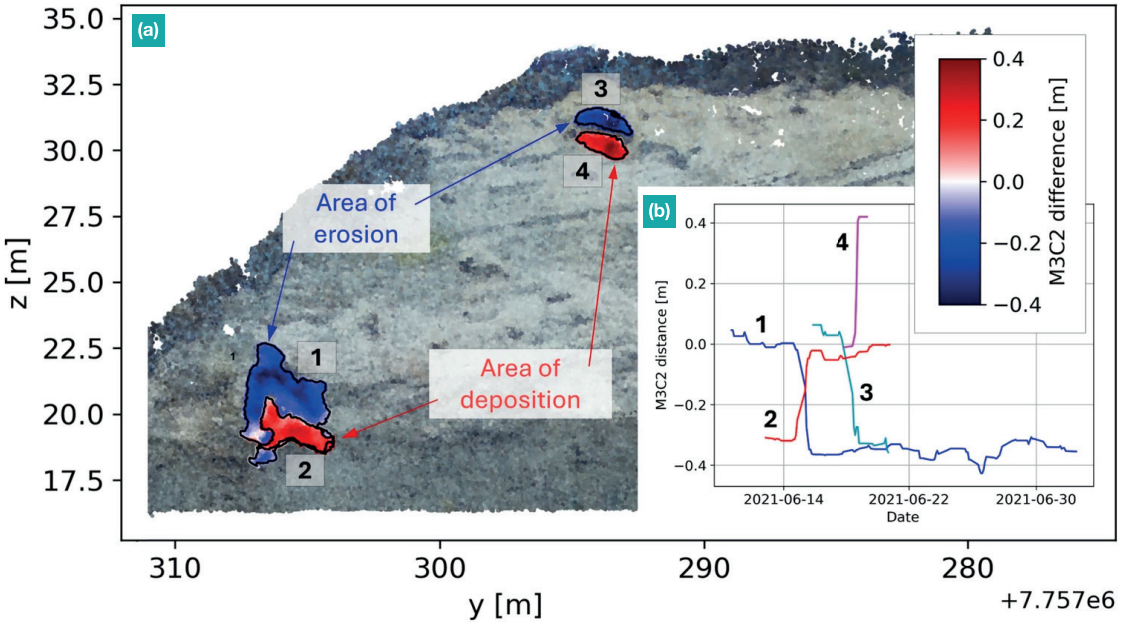


Fig. 2 (a) Example of fused 4D Objects-by-Change (4D-OBCs), with coloration representing M3C2-derived surface differences between the initial and final epochs. (b) Temporal evolution of core points exhibiting the highest change amplitude within each 4D-OBC, shown over the duration of the detected morphological changes (from Ulm et al., 2025).

4 River monitoring by an uncrewed water vehicle

When it comes to the monitoring of water bodies that are surrounded by vegetation, optical airborne systems are often limited in their vision. This can be overcome by using a multi-sensory uncrewed water vehicle (UWV; Fig. 3) that operates underneath the vegetation.

UWVs are autonomous or remote-controlled sensor platforms, that are especially useful in small, hazardous or remote water bodies, where crewed vessels cannot be utilized. Castano-Londono et al. (2024) give a systematic review on existing platforms and evaluation algorithms. The following paragraphs will present our UWV and the type of data that can be recorded with it.

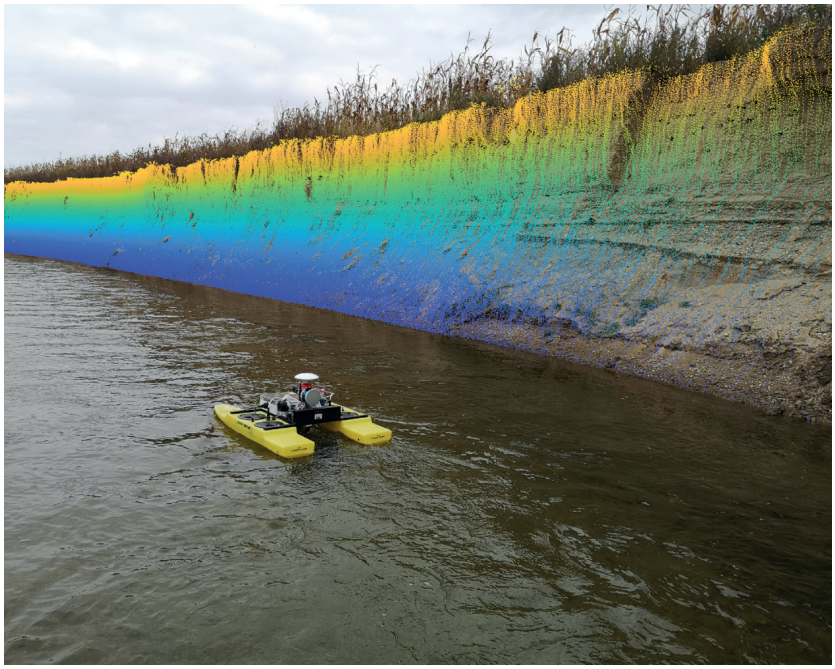


Fig. 3 Uncrewed water vehicle on a small river with LiDAR point cloud overlay on the river bank.

4.1 Navigation

Positioning of the UWV in world coordinates is solved with a multi-band-multi-constellation GNSS receiver. Orientation is determined by an IMU, which is also (single-band) GNSS-aided. Since the intended application fields are water bodies, often surrounded by vegetation, occlusion and multipath form a demanding challenge for satellite-based positioning. It may therefore be beneficial to use the camera images for positioning (Sardemann et al., 2023).

The UWV is built as a modular system with a Raspberry-Pi computer based on-board recording system. The central control unit serves mainly the tasks of starting the recording with dedicated commands to the respective sensor and to receive and log the sensor data. It also ensures the synchronisation of most of the sensors (see below). However, evaluation of the data is done in post processing.

4.2 Above water

Recording of the bank or shore areas is done by LiDAR and camera. The UWV can be equipped either with a panoramic dual-fisheye camera, that observes both riverbanks simultaneously when steered on a river (Sardemann et al., 2018). Using a panoramic view has the advantage that high overlap is achieved between the images, while its drawback is the limited image quality. Alternatively, the UWV can be equipped with one or multiple central-projection cameras with better optical quality (Sardemann et al., 2023). The active LiDAR generates detailed 3D point clouds of the river bank areas (Sardemann et al., 2023).

4.3 Under water

The UWV is equipped with a single-beam echo sounder, enabling the bathymetric measurement of a river (Sardemann et al., 2018) or a lake (Mader et al., 2024) applying adopted navigation and interpolation strategies. However, echo sounders are limited especially in very shallow waters. We therefore developed an optical measurement system, that delivers sub-mm accurate depths in the range of a few decimetres. The sensor system follows the principle of laser triangulation, but considers the influence of refraction to depth calculation (Sardemann et al., 2022). The system has so far thoroughly been tested in laboratory environments, and its suitability on the UWV was also proven (Fig. 4).

4.4 Calibration strategy

One central goal of the UWV is to combine the above-mentioned sensors to generate a geo-referenced point cloud of the water bottom and the adjacent bank areas (Fig. 5). It therefore is mandatory to calibrate the relative positions and orientations of all sensors and their coordinate systems. We developed a calibration strategy that can be applied in the field, directly before each measurement with the according sensor configuration and their final orientations (Sardemann et al., 2023).

5 High-resolution acquisition of hydro-morphological parameters of small watercourses to support flood risk management and the achievement of good ecological status

The development of small streams and drainage ditches in order to achieve a good ecological status of water bodies, as required by the European Water Framework Directive, poses a particular challenge for municipalities. For the planning of integrated measures for the protection and management of these water bodies, geodetic documentation and hydro-morphological classification are fundamental. Since data collection, especially for small second- and third-order watercourses, is highly time-consuming and cost-intensive, the project developed a combined surveying and evaluation

https://doi.org/10.58440/ihr-31-2-a18

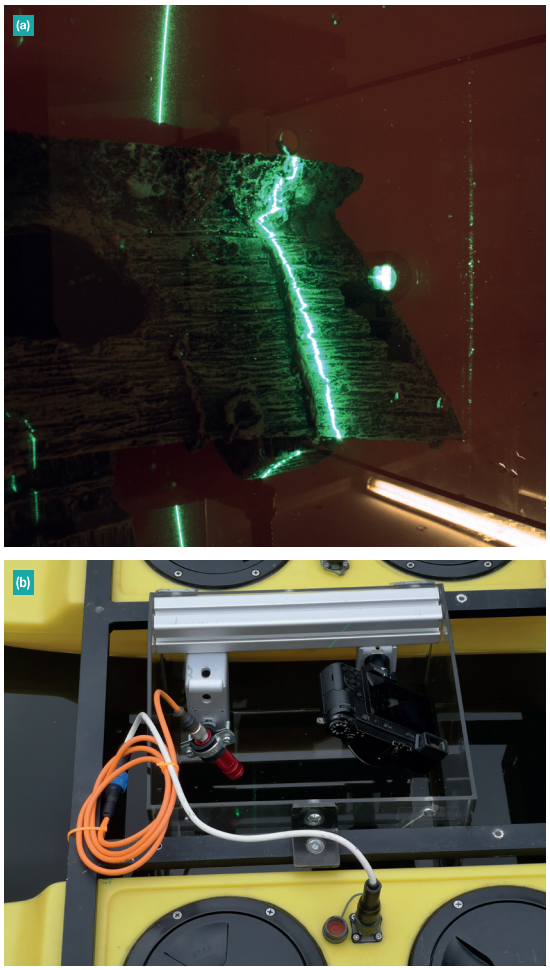


Fig. 4 Underwater laser light sheet triangulation system: (a) Laser line on a wreck model in a laboratory environment. (b) Sensor system mounted on the UWV.

methodology that enables efficient mapping of small water bodies using mobile handheld laser scanners, as well as the derivation of water-specific parameters from the acquired measurement data. Consequently, the project was structured around three main tasks: data acquisition, data analysis, and validation of results.

5.1 Data acquisition

The work on data acquisition initially focused on the development of a mobile low-cost multi-sensor platform, which was used for testing and development purposes (Blaskow & Schwalbe 2021). For the actual survey of stream morphology, the mobile laser scanning system *GeoSlam ZEB* Horizon equipped with an RGB camera was employed. Owing to its 360° × 270° field of view, even narrow and overgrown stream sections could be fully captured. A key area of work was the calibration of the relative orientation between scanner and camera in order to improve the transfer of RGB colour information onto the 3D point clouds. To this end, a procedure (including an appropriate calibration environment) was developed that allows for precise determination of both temporal offsets between the trajectories of the camera and scanner as well as deviations in the positioning of the lever arm. Stream surveys were conducted using a stop-and-go method supported by RTK-GNSS control points and loop closures. For geo-referencing, control points were defined along the stream and directly integrated into the trajectory during scanning by briefly positioning the scanner on the control points while passing. Depending on the measurement conditions, the surveying of control points was carried out either prior to or simultaneously with the scanning process.

5.2 Data analysis

A main objective was the development of a freely available prototype software package[1] capable of deriving hydro-morphologically relevant parameters from image and laser scanner data (Fig. 6).

A graphical user interface allows the visualization of input data, intermediate results, and final outputs in both 2D and 3D, as well as the control of analysis algorithms. For areal features, a method was implemented to separate terrain and vegetation points within the point cloud, classify them, and subsequently convert them into raster and vector data. This,

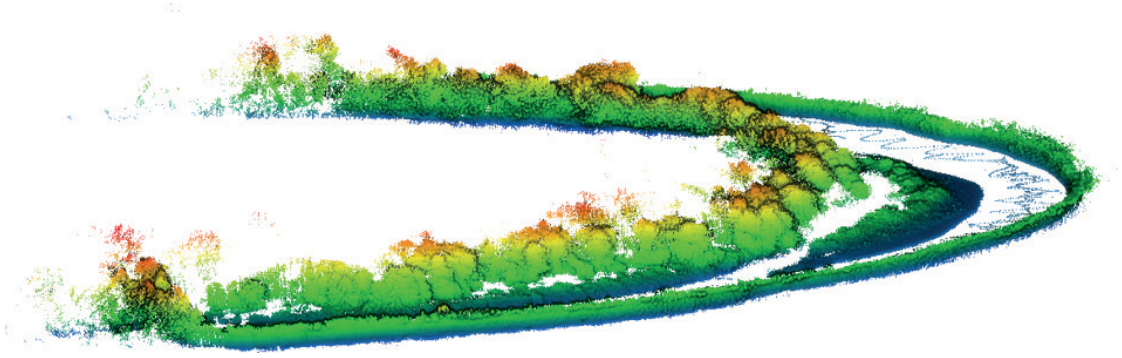


Fig. 5 UWV-based point cloud of a small river with river banks recorded by LiDAR and bathymetry by single-beam echo sounder.

[1] Download *Creek4D Mapping-Software* (C4D) following https://tud.link/eglx (last accessed 4 October 2025).

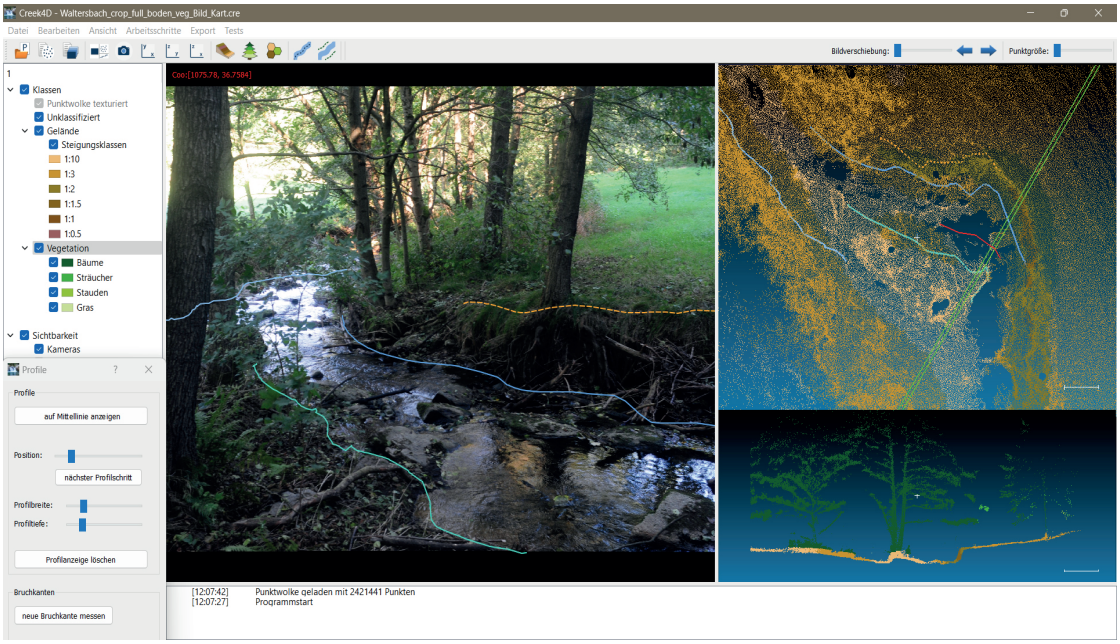


Fig. 6 Open-source research software C4D for deriving waterbody-specific parameters from point clouds and image sequences. It includes methods for terrain and vegetation classification within point clouds, subsequent approaches for generating and mapping areal features, techniques for 3D mapping of linear and point features in image data and point clouds, as well as methods for extracting geometric and semantic attributes of the mapped objects.

for example, enables the mapping of slope areas or vegetation zones. Linear features such as shorelines or embankment edges are extracted through a combined analysis of point cloud and image data. In this process, lines can be measured manually or semi-automatically within the images and then projected directly into 3D space. This allows the precise derivation of creek centre-lines, riparian strips, and break lines. Point features, such as small structures or special objects, are directly marked within the point cloud and assigned with attributes. A superimposed visualization of image and laser scanning data facilitates unambiguous identification. In addition, initial tests with AI-supported segmentation were conducted, indicating potential for future automation of shoreline mapping. All detected objects can be transformed into a reference coordinate system and exported as shape-files for subsequent integration into geographic information systems. Separate files with associated attribute tables are generated for areal, linear, and point features. Key parameters, such as slope classes or vegetation height for surface features, are automatically derived and included in the corresponding attribute tables.

5.3 Validation

To assess the accuracy of the entire acquisition and evaluation process, reference and repeat measurements were carried out, particularly along shorelines. Comparisons with RTK-GNSS reference data resulted in mean deviations of approximately 0.12 m (spring survey) and 0.15 m (summer survey). Seasonal effects such as water level and vegetation density influence the interpretability of the survey data and contribute significantly to the overall accuracy. In general, the achievable positional accuracy is on the order of one to two decimetres. To evaluate efficiency, the time required for data acquisition and analysis was also documented. Compared to conventional tacheometric methods, time savings of approximately one order of magnitude were achieved.

6 Compensation of wave effects in through-water photogrammetry by processing short image sequences

The key problem when mapping and monitoring of water bodies with photogrammetric methods is the modelling or compensation of refraction effects when imaging through water. While the modelling of the refraction is clearly defined for still water surfaces, as here the water surface can be considered as a horizontal plane, the problem becomes much more complex when the water surface has waves – as actually in many cases. Several approaches, such as the one described by Sardemann et al. (2024), attempt to address this issue by mathematically modelling the water in object space using spline or Fourier parametrizations and simultaneously determining the water parameters together with the object point coordinates. However, some aspects limit this this method to rather simple wave patterns only. Firstly, a decent imaging quality of submerged features is essential for proper detection and measurement. This is seldom the case for water bodies with small crippling waves which cause irregular image distortions. Furthermore, the complexity of water modelling cannot be driven too far, otherwise the reliability and accuracy of the determination of the parameter drops dramatically. Lastly, the submerged scene must be captured simultaneously from different directions (e.g. cameras) which means a high effort in synchronisation and costs for equipment.

An alternative approach to solving the problem of wavy water surfaces is to transfer it to image space. The

https://doi.org/10.58440/ihr-31-2-a18

pixel-wise analysis of the variation of grey values within a short image sequence taken by a stationary camera is one way to reduce the disturbing effects down to an acceptable level. We assume, that the water surface moves randomly around its idle state, so moments with horizontally oriented water surface elements should occur more frequently than others. Through simple pixel-wise Median-filtering on the time axis, the 'right' grey value, which would ideally be captured through a horizontal water element, can be identified. The result is an image, which almost corresponds to one taken through a flat water surface. Several lab experiments provided proof of concept (Mulsow et al., 2024).

To test the method in a real-world scenario, several data sets were acquired during a measurement campaign at the pre-alpine Pielach River in October 2024 following a major flood event in September of that year (Mandlburger et al., 2025). The image sequences were captured using a DJI M350 RTK multicopter with a Zenmuse P1 45 MP RGB camera, flying at an altitude of 30 m, which means a ground sample distance of 3 mm. Operating the UAV in hovering mode, around 100 images per sequence were taken with a frequency of 0.7 Hz from defined positions. However, even with the use of a gimbal, the images showed motion effects of up to 30 pixels in every direction within a sequence. However, any remaining small movements could be compensated for by co-registering all images to a reference image (e.g. a frame in the middle of the sequence), based on least-squares matching applied to stable tie points on dry land. The RMSE of this co-registration was in the order of 0.1 pixels.

The stack of co-registered images can then be forwarded to the pixel-wise analysis of grey values within the image sequence. Finally, a corrected image with a geometry almost as if it would have been captured through a flat horizontal water surface can be forwarded to the standard multi-media photogrammetry pipeline for forward intersection of homologous image points. Fig. 7 shows the results of image sequence processing, Fig. 8 shows a comparison of Structure from Motion (SfM) results using original and sequence-processed image data. Besides the improvement in geometric accuracy for the underwater terrain points, the number of feature points could be increased significantly due to compensated local image distortions.

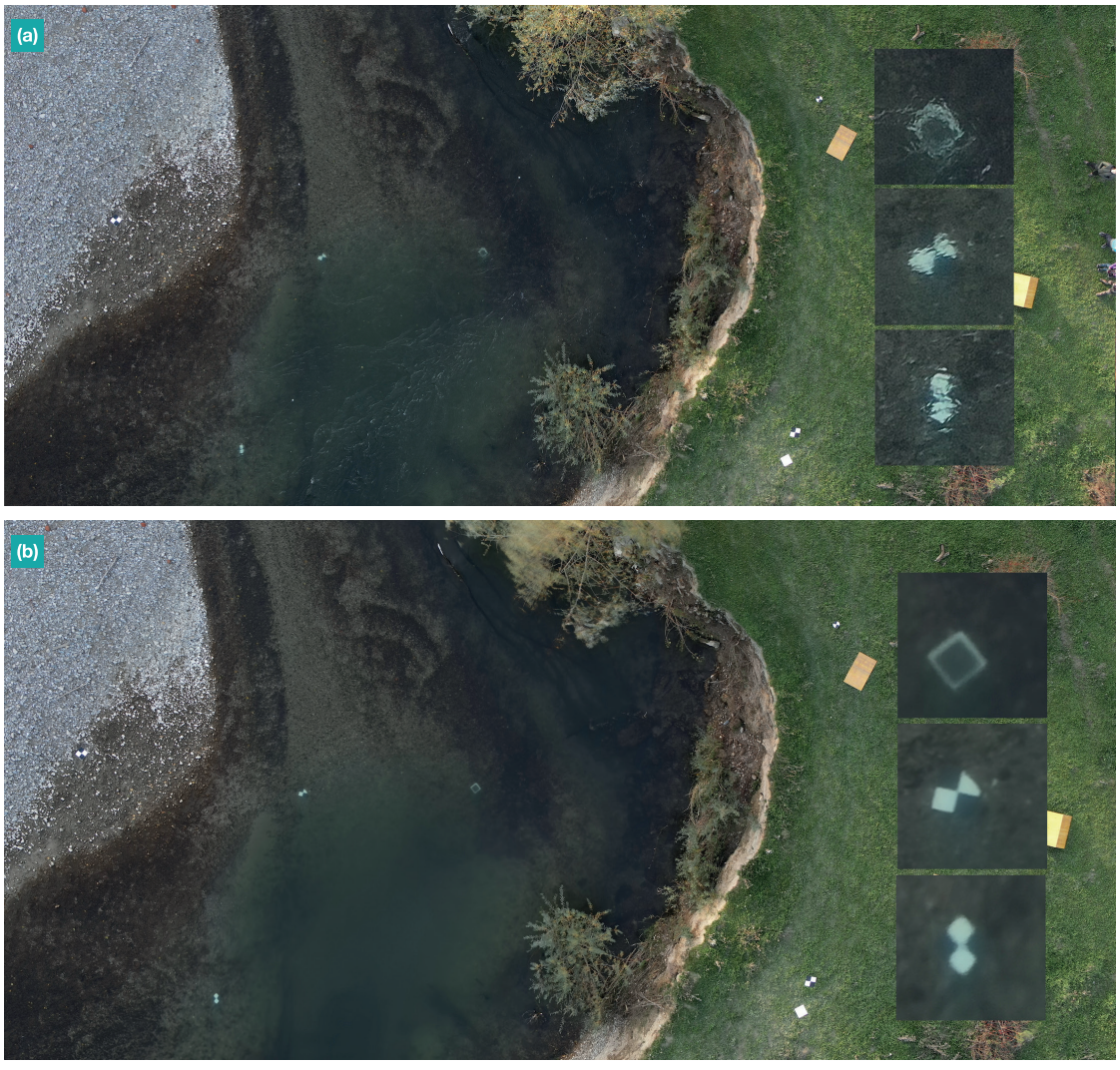


Fig. 7 (a) Original image with wave effects. Small inlets illustrate the-blurring effect at the submerged checkerboard targets. (b) Corrected image (processed from~100 images) with the geometry of an image which would have been taken through a calm flat water surface. The shape of the targets could be successfully restored.

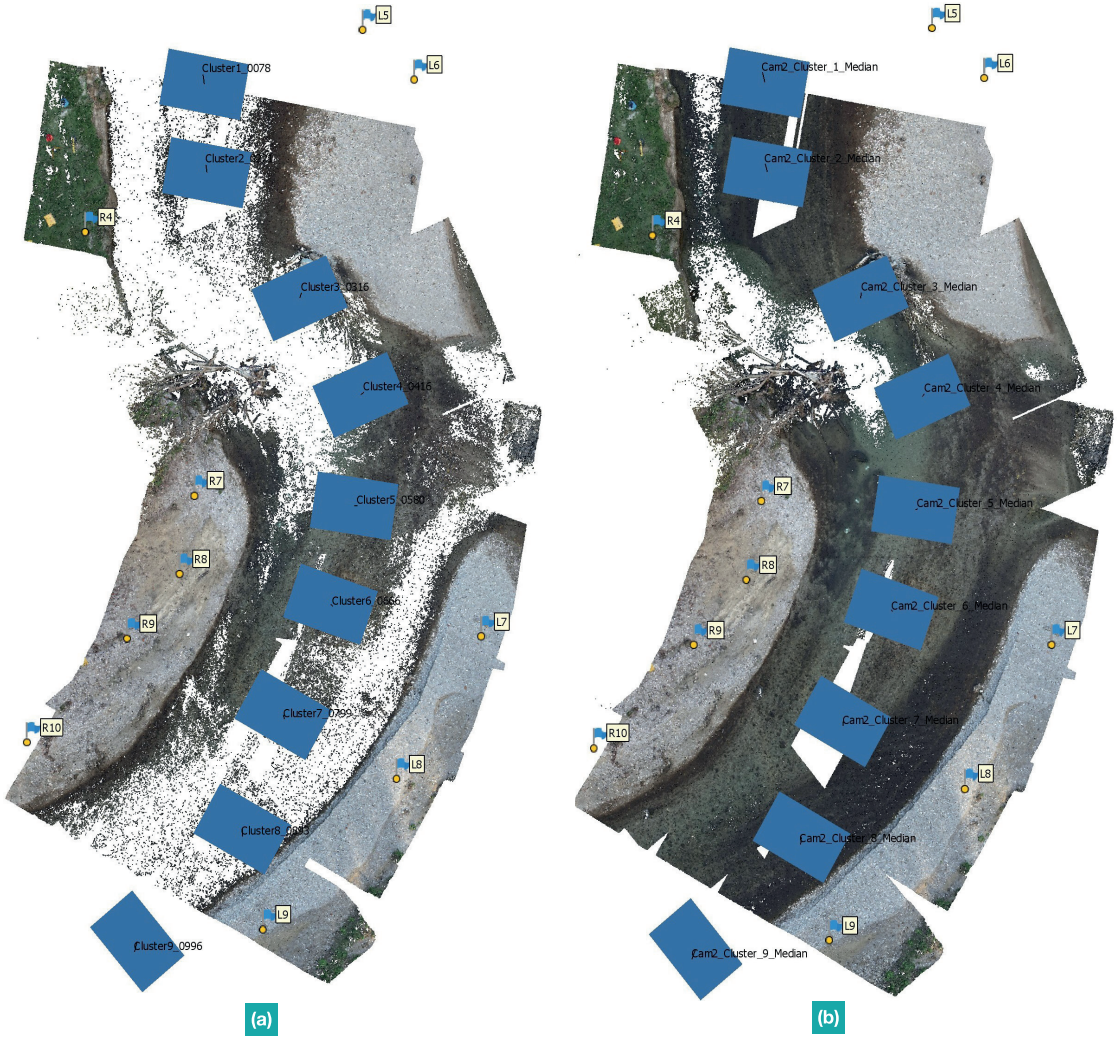


Fig. 8 (a) Point clouds extracted from uncorrected image material and (b) from processed mage sequences. The improvement in quality and coverage is quite obvious.

7 Pilot study on a photogrammetric glacier lake outburst flood early warning system

Glacier Lake Outburst Floods (GLOFs) depict an environmental risk with an increasing damage potential in many regions of the world. GLOFs are often caused by glacier margin lakes, which suddenly find a drainage path underneath the bottom of a glacier, which is retreating and destabilized as a consequence of local or global climate changes. In a typical GLOF event, a glacier margin lake may drain completely in 24 hours, causing a large flood wave in the area downstream the glacier.

A pilot study has been conducted on the configuration of a terrestrial photogrammetric glacier margin lake monitoring system observing some recent GLOF events in the Northern Patagonian Icefield in Chile (Fig. 9; Maas et al., 2012). The monitoring system is based on a camera taking images at regular time intervals. In these images, variations of the water level can be detected by tracking the water-land interface at pre-defined image spots. Due to the drainage mechanism, which is characterized by erosion and melting at the bottom of the glacier, GLOFs are indicated by a progressive water level drop in the lake. Water level changes may be detected with subpixel accuracy by image sequence processing methods. If a 3D model of the lake bottom topography (or at least one height profile into the lake) exists, water level changes in monoscopic image sequences may be transformed into volume loss. The basic idea herein is the intersection of a terrain profile with a water level detected in the image and projected into object space (Fig. 10).

The camera orientation can be determined via a GNSS-supported photogrammetric network. Camera orientation changes, which may for instance be induced by wind, can be compensated by tracking some fiducial marks at suitable positions in the image (Schwalbe & Maas, 2017). The system has been used in a pilot study at two glacier margin lakes in the Northern Patagonian Icefield. These lakes have a depth of about 80–100 meters. The larger one (Lago Cachet II) has a length of 5 km and a maximum volume of about 200,000,000 m3. During the pilot study, several GLOF events could be recorded and processed (one of them shown in Fig. 11). Water level changes can be determined a precision of less than one decimetre. The results prove the feasibility of the concept, which has to be completed by a data telemetry and alarm system.

https://doi.org/10.58440/ihr-31-2-a18



Fig. 9 (a) Camera installation at Lago Nef Norte and (b) empty lake after GLOF event.

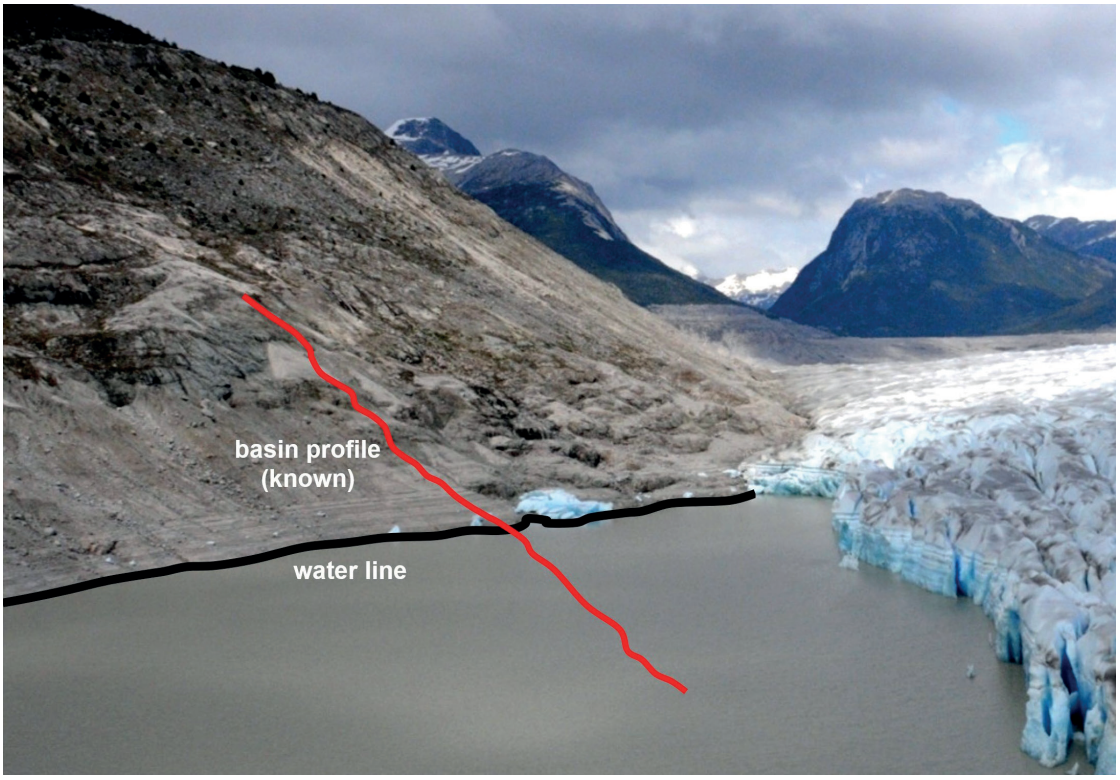


Fig. 10 Principle of monoscopic camera-based water level determination.

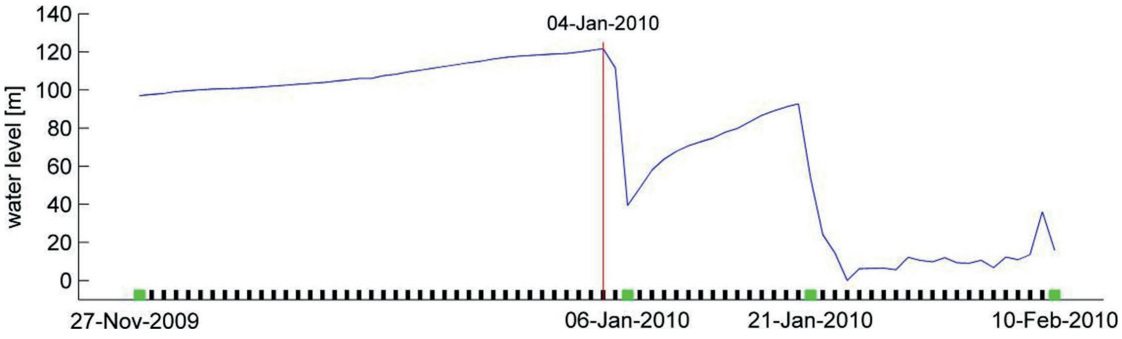


Fig. 11 Water level at Lago Cachet II over a two months period (Maas et al, 2012).

8 Improved LiDAR bathymetry water bottom topography acquisition by non-linear waveform stacking techniques

Coastal marine areas are subject to dynamic natural processes such as currents, tides, storm events as well as human impact, which significantly influence the topography of the seabed (Wright & Thom 2023; Hendriks et al., 2020; Kubicki et al., 2007). Continuous monitoring of seabed topography enables morphological changes to be detected at an early stage and appropriate measures to be taken to ensure safe navigation, infrastructure planning, and coastal protection. This requires high-resolution, reliable, regularly updated bathymetry data.

Ship-based hydro-acoustic methods are considered a proven method for the accurate and reliable acquisition of water bottom information. However, these methods reach their limits in shallow waters, as they are logistically complex and their efficiency decreases with decreasing water depth. Airborne LiDAR bathymetry (ALB) is a promising alternative for these areas and a useful addition in general. Bathymetric laser scanners use green laser pulses (mostly 532 nm) to acquire information about the water body (surface, column/volume, bottom) (Guenther et al., 2000). The sensors record the backscattered laser signal parts at high temporal resolution as full-waveform (FWF) signal, which provides detailed insights into the characteristics of the water body.

The underwater range of the laser signal is reduced by absorption and scattering effects in the water, especially at high turbidity levels, which often makes it difficult to detect water bottom echoes and limits the measurement process significantly (Guenther, 1985; Guenther & Goodman, 1978). While measurement depths of ~50 meter can be reached in very clear water, these may be reduced to less than two meter under turbid water conditions. This leads to data gaps and limited measurement coverage of the bottom.

Depending on the water properties, suitable processing methods for ALB data, in particular FWF data, can significantly improve penetration depth and thus the acquisition of water bottom information. Two such processing methods are the signal-based full-waveform stacking (sigFWFS; Fig. 12; Mader et al., 2021) and the volumetric full-waveform stacking (volFWFS; Fig. 13; Mader et al., 2023a). Both approaches combine multiple adjacent FWF into a pseudo-waveform signal, assuming that closely spaced measurement signals have very similar characteristics in terms of water depth and FWF shape. The pseudo waveforms have a significantly improved signal-to-noise ratio, in consequence even weak water bottom echoes can be detected. Instead of simple averaging to avoid low pass filtering induced smoothing effects, a non-linear majority voting-based filtering techniques has been introduced (Mader et al., 2021). While sigFWFS focuses on the stacking of the FWFs themselves, volFWFS is based on the projection of the measured FWF data into a voxel space representation. Additional filtering methods increase the reliability of both methods significantly.

Both methods have been validated using ALB data from a part of an inland waterway, the Elbe River, and an area in the German North Sea (Fig. 14; Mader et al., 2021, 2023a, 2023b). The results show a significant improvement: Compared to standard data processing, the average penetration depth was increased by up to 33 % (from 1.65 m to 2.20 m) in inland waters and by 26 % (from 2.87 m to 3.62 m) in marine waters. This results in the coverage of a significantly larger area of the water bottom with measurement points. In the case of the Elbe River, the information on the riverbed was doubled. In the North Sea area, the value was lower at +14.6 %, but still represents a significant gain in water bottom information solely through enhanced data processing. Of course, the metrics of the information gained about the water bottom are dependent on the characteristics of the water, such as turbidity, and the nature of the bottom topography and can vary from water to water.

Hydroacoustic measurements were used for a

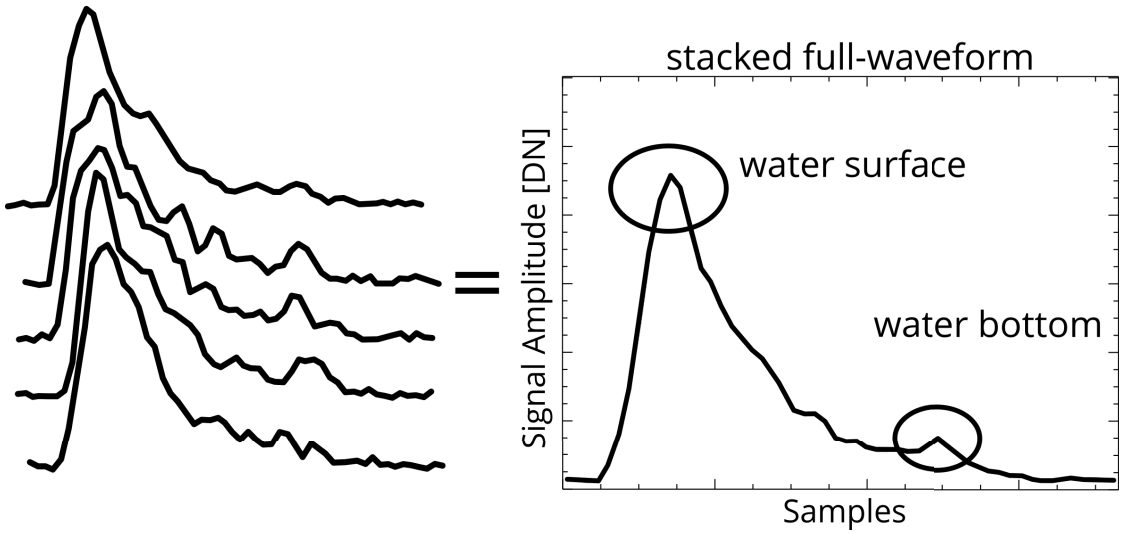


Fig. 12 Principle of the generation of a stacked FWF. On the left side are the individual full-waveforms and on the right side is the stacked full-waveform resulting from the stacking of the individual full-waveforms.

https://doi.org/10.58440/ihr-31-2-a18

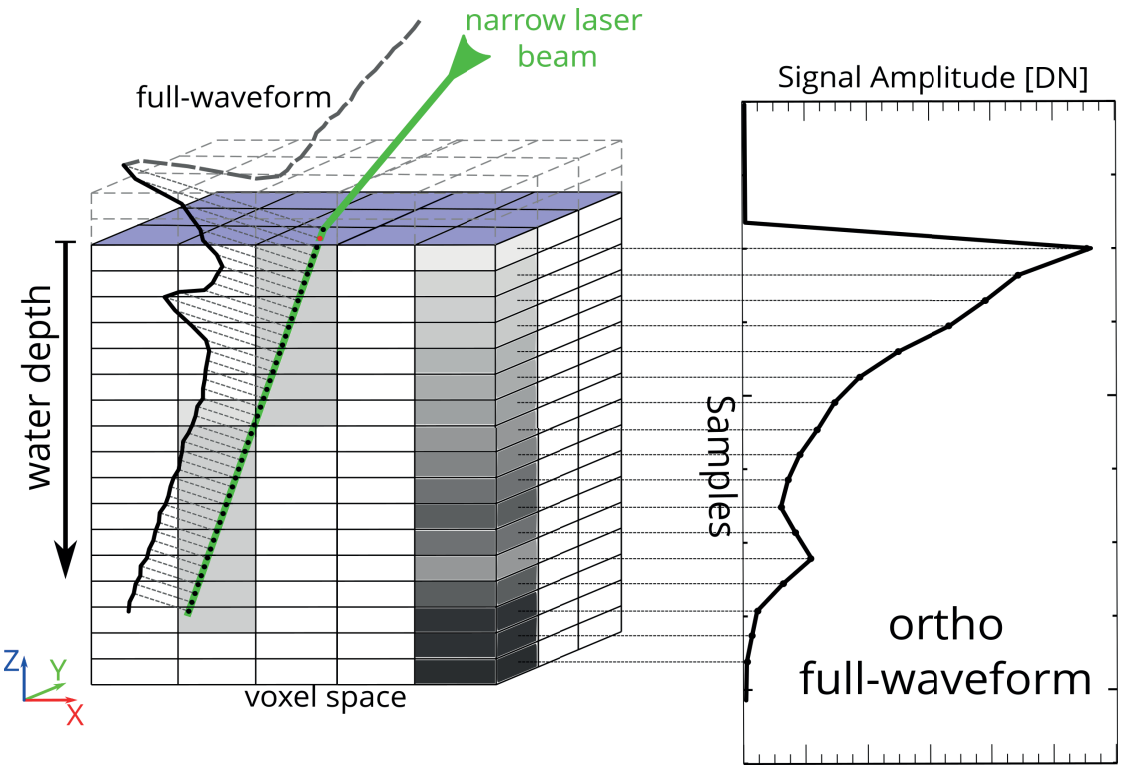


Fig. 13 Principle of the generation of an ortho FWF. On the left there is a voxel space representation including intensity information of individual FWF, on the right the derived ortho FWF based on intensity information of a voxel column.

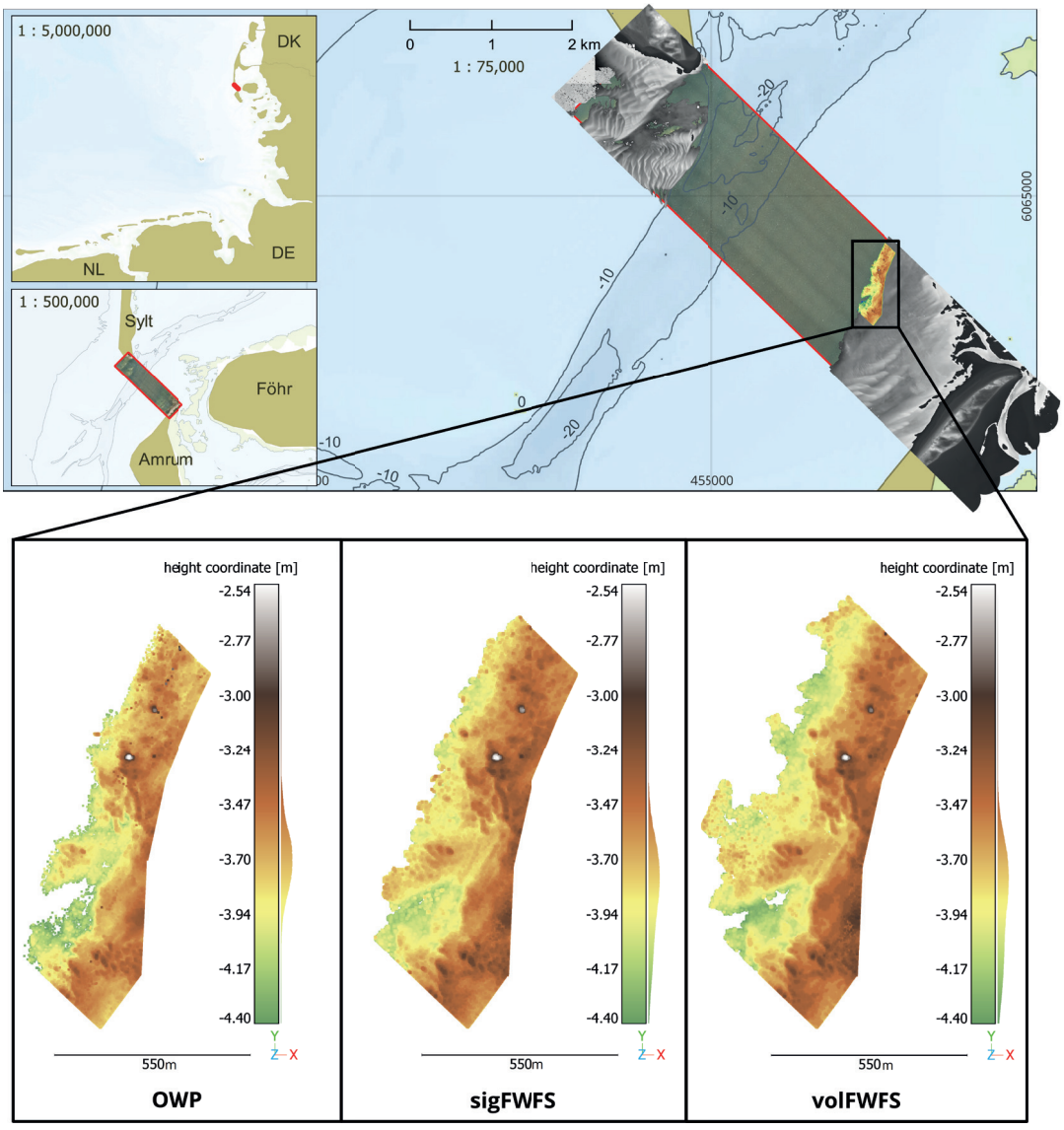


Fig. 14 ALB in the German Wadden Sea National Park. Top: Location of the study area (left) and the investigated subarea (right). Bottom: Seabed point clouds resulting from standard processing (OWP), the sigFWFS processing and the volFWFS processing. The point clouds are color coded by their height coordinate.

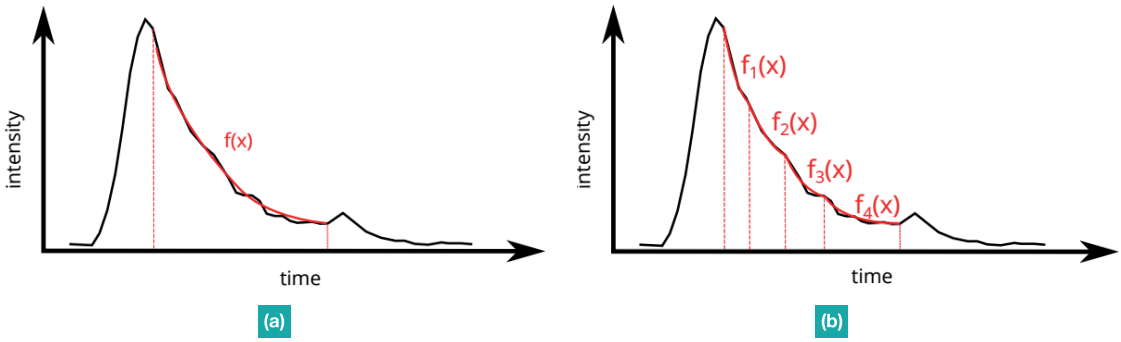


Fig. 15 Schematic representation of the methodology for analysing the decay in ALB full-waveforms: (a) Integral Turbidity Mapping and (b) Depth-Resolved Turbidity Mapping.

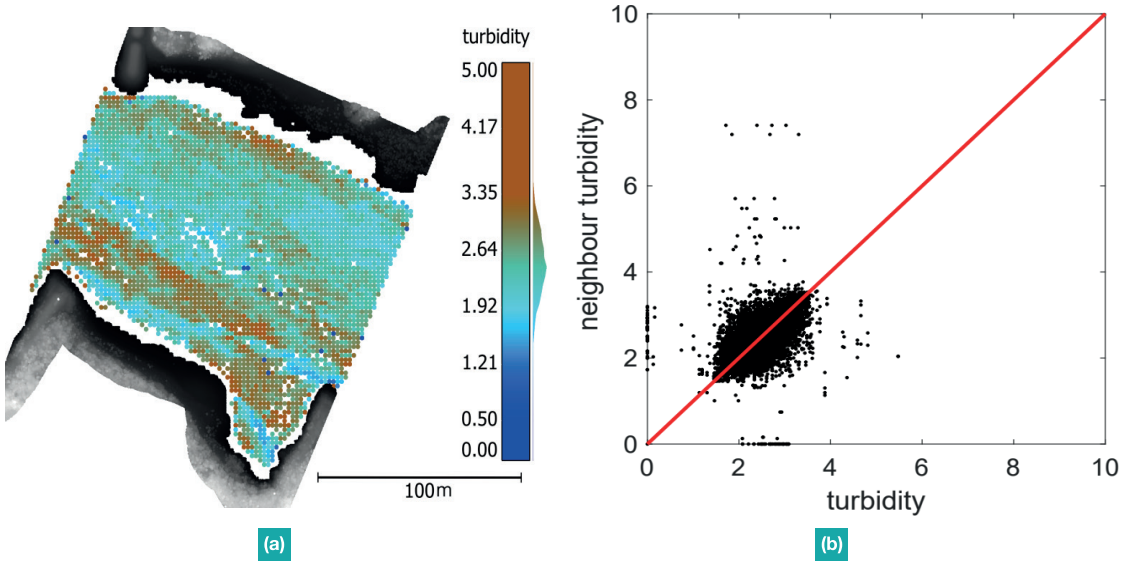


Fig. 16 Example for the Integral Turbidity Mapping approach: (a) 2D turbidity parameter field of a shallow inland water body, (b) results of quantitative evaluation.

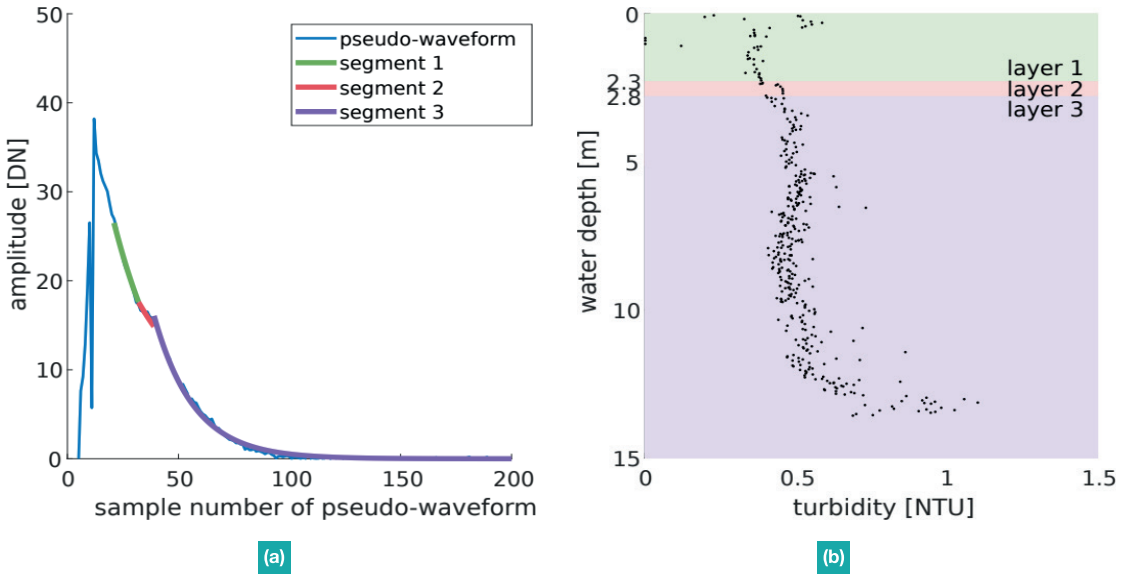


Fig. 17 Example for the Depth-Resolved Turbidity Mapping approach: (a) vertical turbidity layers detect-ed in ortho full-waveform, (b) vertical turbidity layers measured with turbidimeter at CTD probe.

https://doi.org/10.58440/ihr-31-2-a18

quantitative validation of the FWF stacking results, confirming high accuracy and reliability achieved with the new methods for both the Elbe study area and the North Sea. The calculated RMS values are around 0.10 m for sigFWFS and volFWFS. Over 98% of the newly acquired points had an absolute height deviation of less than 0.25 m. These results demonstrate the good plausibility and reliability of the water bottom information gained through FWF stacking methods.

9 Quantification of water turbidity by volumetric analysis of LiDAR bathymetry data

Turbidity, an optical measure of water clarity, is a key water quality metric. It results from suspended inorganic and organic particles, as well as coloured dissolved materials that absorb and scatter light, reducing transparency. Turbidity levels can greatly vary within a water body, indicating factors like algae growth from fertilizers or sediment from erosion. These changes affect light transmission, impacting photosynthesis and predator visibility, making turbidity a vital environmental indicator.

Conventional in-situ turbidity measurements are time-consuming and often only represent small areas. ALB offers a promising alternative since the measurement data not only provide detailed information about water depth but also capture valuable insights into water turbidity. Dissolved organic and inorganic particles influence the amount of laser energy that is backscattered, which in turn affects the shape of the recorded LiDAR full-waveform signal. By analysing the decay of the full-waveform signal, it is possible to comprehensively evaluate water turbidity. For this purpose, we have developed two methods: The Integral Turbidity Mapping (2D) and the Depth-Resolved Turbidity Mapping (3D). Both methods are applied to ortho full-waveforms, which are derived from volumetric reconstructions of the measurement data (Section 8).

In the Integral Turbidity Mapping approach (Richter et al., 2017, 2021), an exponential function is fitted into the water column part of the ortho full-waveform (Fig. 15a). The resulting exponential decay coefficient serves as a quantitative, integral, and non-metric indicator of water turbidity. This approach enables the extraction of 2D turbidity parameter fields from ALB data. Fig. 16a shows such a 2D turbidity parameter field in a study area of a shallow river. It can be seen that small-scale differences in flow velocity caused by the groynes lead to locally varying turbidity values. The results of the quantitative evaluation indicate that neighbouring full-waveforms yield similar turbidity values (Fig. 16b).

The Depth-Resolved Turbidity Mapping approach (Richter et al., 2022, 2024) enables the derivation of 3D turbidity parameter fields from small-footprint LiDAR bathymetry data. For this purpose, depth-resolved turbidity values are extracted for each water column segment of the ortho full-waveforms by fitting multiple exponential segments to the volume backscatter signal (Fig. 15b). Both the number of segments and the transition points between them are automatically determined from the dataset itself. The methodology was evaluated on a clear-water lake using UAV-based LiDAR bathymetry data. Fig. 3a shows an example of an ortho full-waveform in which three layers of varying turbidity were detected. For validation, an extensive set of conventional in-situ turbidity measurements was collected concurrently with the LiDAR survey (Fig. 17b). The comparison demonstrates strong agreement between the turbidity layers derived from the LiDAR data and those obtained from the reference measurements, confirming the reliability of the approach.

In summary, volumetric analysis of LiDAR bathymetry data enables detailed and spatially resolved turbidity quantification. Using both Integral and Depth-Resolved Turbidity Mapping, 2D and 3D turbidity fields can be generated, capturing lateral and vertical water quality variations. The strong correspondence with conventional measurements demonstrates the potential of these methods for efficient, large-scale aquatic monitoring.

10 Conclusion

The goal of the paper was to give a brief overview on some recent application of photogrammetric techniques in hydrographic environmental monitoring. Obviously, the list of applications shown in the paper is incomplete and does not claim to be representative. But the applications may give a glimpse into the large potential and the very wide range of applications of photogrammetric techniques in hydrographic measurement and monitoring tasks. Cameras and their periphery have become ubiquitous and ever cheaper, and so do small solid state LiDAR sensors, thus forming a basis for the configuration of manifold task-specific 2D or 3D spatio-temporal data acquisition systems. Subpixel accuracy image analysis techniques, combined with photogrammetric sensor modelling and calibration strategies, offer a very high accuracy potential, making even low-cost cameras a serious measurement tool. The use of such sensors for hydrographic monitoring tasks is further boosted by AI techniques increasingly facilitating the solution of complex image measurement tasks.

https://doi.org/10.58440/ihr-31-2-a18

References

Anders, K., Winiwarter, L. and Höfle, B. (2021). Fully automatic spatiotemporal segmentation of 3D LiDAR time series for the extraction of natural surface changes. I*SPRS Journal of Photogrammetry and Remote Sensing, 173,* 297–308. https://doi.org/10.1016/j.isprsjprs.2021.01.015

Blanch, X., Grundmann, J., Hedel, R. and Eltner A. (2025): AI Image-based method for a robust automatic real-time water level monitoring: A long-term application case. *Hydrology and Earth System Sciences – EGUSphere* [preprint], https://doi.org/10.5194/egusphere-2025-724

Blanch, X., Jäschke, A., Elias, M. and Eltner, A. (2025). Subpixel automatic detection of GCP coordinates in time-lapse images using a deep learning keypoint network. *IEEE Transactions on Geoscience and Remote Sensing, 63*, 1–14. https://doi.org/10.1109/TGRS.2024.3514854

Blaskow, R. and Schwalbe, E. (2021). Development of a low-cost, hand-held Multi-Sensor System for the Monitoring of small Water Bodies. *The International Archives of Photogrammetry, Remote Sensing and Spatial Information Sciences, 43*, 93–96. https://doi.org/10.5194/isprs-archives-XLIII-B1-2021-93-2021

Castano-Londono, L., Marrugo Llorente, S. D. P., Paipa-Sanabria, E., Orozco-Lopez, M. B., Fuentes Montaña, D. I. and Gonzalez Montoya, D. (2024). Evolution of Algorithms and Applications for Unmanned Surface Vehicles in the Context of Small Craft: A Systematic Review. *Applied Sciences (2076-3417), 14*(21). https://doi.org/10.3390/app14219693

Eltner, A., Kaiser, A., Abellan, A. and Schindewolf, M. (2017). Time lapse structure-from-motion photogrammetry for continuous geomorphic monitoring. *Earth Surface Processes and Landforms, 42*, 2240–2253. https://doi.org/10.1002/esp.4178

Elias, M., Eltner, A., Liebold, F. and Maas, H.-G. (2020). Assessing the influence of temperature changes at the geometric stability of low-cost chip cameras. *Sensors, 20*(3), 643. https://doi.org/10.3390/s20030643

Elias, M., Weitkamp, A. and Eltner, A. (2023). Multi-modal image matching to colorize a SLAM based point cloud with arbitrary data from a thermal camera. *ISPRS Open Journal of Photogrammetry and Remote Sensing, 9*, 100041, https://doi.org/10.1016/j.ophoto.2023.100041

Eltner, A., Sardemann, H. and Grundmann, J. (2020). Technical Note: Flow velocity and discharge measurement in rivers using terrestrial and UAV imagery. *Hydrology and Earth System Sciences, 24*, 1429–1445, https://doi.org/10.5194/hess-24-1429-2020

Eltner, A., Bressan, P., Goncalves, W., Akiyama, T. and Marcato Junior, J. (2021). Using deep learning for automatic water level measurement. *Water Resources Research, 55*(3), e2020WR027608, https://doi.org/10.1029/2020WR027608

Grundmann, J., Eltner, A., Blanch, X., Kutscher, A. and Hedel, R. (2024). Zum Einsatz künstlicher Intelligenz für die optische Bestimmung von Wasserstand und Durchfluss in natürlichen Fließgewässern. *Von der Technischen Hydromechanik zu Environmental Fluid Dynamics – Dresdner Wasserbauliche Mitteilungen, 72,* 11–18. https://hdl.handle.net/20.500.11970/113728

Guenther, G. C. and Goodman, L. R. (1978). Laser Applications for Near-Shore Nautical Charting. Proceedings of SPIE, The International Society for Optical Engineering/*Proceedings Of SPIE, 0160*, 174–183. https://doi.org/10.1117/12.956863

Guenther, G. C. (1985). *Airborne laser hydrography: system design and performance factors* [Technical Report, National Oceanic and Atmospheric Administration Rockville MD].

Guenther, G. C., Cunningham, A. G., LaRocque, P. E. and Reid, D. J. (2000). *Meeting the accuracy challenge in airborne bathymetry* [Technical Report, National Oceanic Atmospheric Administration / NESDIS Silver Spring, MD].

Hendriks, H., Van Prooijen, B., Aarninkhof, S. and Winterwerp, J. (2020). How human activities affect the fine sediment distribution in the Dutch Coastal Zone seabed. *Geomorphology, 367*, 107314. https://doi.org/10.1016/j.geomorph.2020.107314

Kirillov, A., Mintun, E., Ravi, N., Mao, H., Rolland, C., Gustafson, L. and Xiao, T. (2023). *Segment Anything.* https://arxiv.org/abs/2304.02643 (last accessed 4 October 2025).

Krüger, R., Blanch, X., Grundmann, J., Al-Rawas, G. and Eltner, A. (2024). Low-Cost sensors for measuring wadi discharge – a Raspberry Pi based seismometer and time-lapse camera setup. *ISPRS Archives, XLVIII-2/W8-2024,* 243–250, https://doi.org/10.5194/isprs-archives-XLVIII-2-W8-2024-243-2024

Kubicki, A., Manso, F. and Diesing, M. (2006). Morphological evolution of gravel and sand extraction pits, Tromper Wiek, Baltic Sea. *Estuarine Coastal and Shelf Science, 71*(3–4), 647–656. https://doi.org/10.1016/j.ecss.2006.09.011

Lague, D., Brodu, N. and Leroux, J. (2013). Accurate 3D comparison of complex topography with terrestrial laser scanner: Application to the Rangitikei canyon (New Zealand). *ISPRS Journal of Photogrammetry and Remote Sensing, 82,* 10–26. https://doi.org/10.1016/j.isprsjprs.2013.04.009

Lotsari, E., Hackney, C., Salmela, J., Kasvi, E., Kemp, J., Alho, P. and Darby, S. E. (2020). Sub-arctic river bank dynamics and driving processes during the open-channel flow period. *Earth Surface Processes and Landforms, 45*(5), 1198–1216. https://doi.org/10.1002/esp.4793

Luhmann, T., Fraser, C. and Maas, H.-G. (2016). Sensor modelling and camera calibration for close-range photogrammetry. *ISPRS Journal of Photogrammetry and Remote Sensing, 115,* 37–46, https://doi.org/10.1016/j.isprsjprs.2015.10.006

Maas, H.-G., Mulsow, C., Wendt, A., and Casassa, G (2012). Pilot Studies with a Photogrammetric Glacier Lake Outburst Flood Early Warning System. *Int. Arch. Photogramm. Remote Sens. Spatial Inf. Sci., XXXIX-B5*, 523–527. https://doi.org/10.5194/isprsarchives-XXXIX-B5-523-2012

Mandlburger, G., Rhomberg-Kauert, J., Gueguen, L.-A., Mulsow, C., Brezovsky, M., Dammert, L., Haines, J., Himmelsbach, T., Schulte, F., Amon, P., Winiwarter, L., Jutzi, B. and Maas, H.-G. (2025). Mapping shallow inland running waters with UAV-borne photo and laser bathymetry. The Pielach River showcase. *Journal of Applied Hydrography, 130*(3), 42–54, https://doi.org/10.23784/HN130-06

Mader, D., Richter, K., Westfeld, P. and Maas, H.-G. (2021). Potential of a non-linear Full-Waveform stacking technique in airborne LiDAR bathymetry. *PFG – Journal of Photogrammetry, Remote Sensing and Geoinformation Science, 89*(2), 139–158. https://doi.org/10.1007/s41064-021-00147-y

Mader, D., Richter, K., Westfeld, P. and Maas, H.-G. (2023a). Volumetric Nonlinear Ortho Full-Waveform Stacking in Airborne LiDAR Bathymetry for Reliable Water Bottom Point Detection in Shallow Waters. *ISPRS Journal of Photogrammetry and Remote Sensing, 204*, 145–162. https://doi.org/10.1016/j.isprsjprs.2023.08.014

https://doi.org/10.58440/ihr-31-2-a18

Mader, D., Richter, K., Westfeld, P., Nistad, J.-G. and Maas, H. (2023b). Analysis of the potential of full-waveform stacking techniques applied to coastal airborne LiDAR bathymetry data of the German Wadden Sea National Park. *The International Hydrographic Review, 29*(2), 46–64. https://doi.org/10.58440/ihr-29-2-a31

Mader, D., Richter, K., Sardemann, H. and Maas, H.-G. (2024). Erprobung von UAV-basierter Laserbathymetrie an einem alpinen Bergsee. *DGPF-Jahrestagung 2024 (44. Wissenschaftlich-Technische Jahrestagung der DGPF)*, 295–309.

Mulsow, C., Mandlburger, G. and Maas, H.-G. (2020). Comparison of Subaquatic Digital Elevation Models from Airborne Laser Scanning and Imagery. *ISPRS Ann. Photogramm. Remote Sens. Spatial Inf. Sci., V-2–2020*, 671–677.

Mulsow, C., Sardemann, H., Gueguen, L.-A., Mandlburger, G. and Maas, H.-G. (2024). Concepts for compensation of wave effects when measuring through water surfacesin photogrammetric applications. T*he International Archives of the Photogrammetry, Remote Sensing and Spatial Information Sciences, XLVIII-2-2024*, 289–295, https://doi.org/10.5194/isprs-archives-XLVIII-2-2024-289-2024

Richter, K., Maas, H.-G., Westfeld, P. and Weiß, R. (2017). An approach to determining turbidity and correcting for signal attenuation in airborne lidar bathymetry. *PFG–Journal of Photogrammetry, Remote Sensing and Geoinformation Science, 85*(1), 31–40. https://doi.org/10.1007/s41064-016-0001-0

Richter, K., Mader, D., Westfeld, P. and Maas, H.-G. (2021). Water turbidity estimation from lidar bathymetry data by full-waveform analysis–comparison of two approaches. *The International Archives of the Photogrammetry, Remote Sensing and Spatial Information Sciences, 43,* 681–688. https://doi.org/10.5194/isprs-archives-XLIII-B2-2021-681-2021

Richter, K., Mader, D., Westfeld, P. and Maas, H.-G. (2022). Determination of 3D Water turbidity parameter fields from LiDAR bathymetry data by volumetric data analysis. *The International Archives of the Photogrammetry, Remote Sensing and Spatial Information Sciences, 43*, 945–951. https://doi.org/10.5194/isprs-archives-XLIII-B2-2022-945-2022

Richter, K., Mader, D., Sardemann, H. and Maas, H.-G. (2024). UAV-based LiDAR Bathymetry at an Alpine Mountain Lake. *The International Archives of the Photogrammetry, Remote Sensing and Spatial Information Sciences, 48*, 341–348. https://doi.org/10.5194/isprs-archives-XLVIII-2-2024-341-2024

Sardemann, H., Eltner, A. and Maas, H.-G. (2018). Acquisition of Geometrical Data of Small Rivers with an Unmanned Water Vehicle. *Int. Arch. Photogramm. Remote Sens. Spatial Inf. Sci., XLII–2,* 1023–1027. https://doi.org/10.5194/isprs-archives-XLII-2-1023-2018

Sardemann, H., Mulsow, C. and Maas, H.-G. (2022). Accuracy Analysis of an Oblique Underwater Laser Lightsheet Triangulation System. PFG 90, 3–18. https://doi.org/10.1007/s41064-022-00196-x

Sardemann, H., Blaskow, R. and Maas, H.-G. (2023). Camera-aided Orientation of Mobile Lidar Point Clouds Acquired from an Uncrewed Water Vehicle. *Sensors, 23*(13), 6009. https://doi.org/10.3390/s23136009

Sardemann, H., Mulsow, C., Gueguen, L.-A., Mandlburger, G. and Maas, H.-G. (2024). Multimedia Photogrammetry with non-planar Water Surfaces – accuracy analysis on simulation basis. *Int. Arch. Photogramm. Remote Sens. Spatial Inf. Sci., XLVIII-2-2024*. https://doi.org/10.5194/isprs-archives-XLVIII-2-2024-363-2024

Schwalbe, E. and Maas, H.-G. (2017). The determination of high-resolution spatio-temporal glacier motion fields from time-lapse sequences. *Earth Surf. Dynam., 5*, 861–879. https://doi.org/10.5194/esurf-5-861-2017

Ulm, M., Elias, M., Eltner, A., Lotsari, E. and Anders, K. (2025). Automated change detection in photogrammetric 4D point clouds: Transferability and extension of 4D objects-by-change for monitoring riverbank dynamics using low-cost cameras. *Applied Geomatics.* https://doi.org/10.1007/s12518-025-00623-9

Wagner, F., Eltner, A. and Maas, H.-G. (2023). River Water Segmentation in Surveillance Camera Images: A Comparative Study of Offline and Online Augmentation using 32 CNNs. *International Journal of Applied Earth Observation and Geoinformation, 119,* 103305. https://doi.org/10.1016/j.jag.2023.103305

Wright, L. D. and Thom, B. G. (2023). Coastal Morphodynamics and Climate Change: A Review of Recent Advances. *Journal Of Marine Science and Engineering, 11*(10), 1997. https://doi.org/10.3390/jmse11101997

Zamboni, P., Blanch, X., Marcato Jr., J., Goncalves, W. and Eltner, A. (2025). Do we need to label large datasets for river water segmentation? Benchmark and stage estimation with minimum to non-labeled image time series. *International Journal of Remote Sensing, 46*(7). https://doi.org/10.1080/01431161.2025.2457131

Authors' biographies

Prof. Dr. sc. techn. habil. Hans-Gerd Maas is professor of Photogrammetry at TU Dresden, involved both in research and teaching. His research focus is on the integration of imaging sensors (both cameras and lidar) and processing algorithms for the development of efficient solutions for new challenging measuring tasks in high-resolution spatio-temporally resolved 3D data acquisition, combined with strict geometric and stochastic sensor modelling and calibration for optimizing solutions. He has been involved in several collaborative research centers and research training groups and was former president of ISPRS Technical Commission V.



Hans-Gerd Maas



Robert Blaskow

Robert Blaskow is a research associate at the Institute of Photogrammetry and Remote Sensing at the TU Dresden. His research interests include the development of efficient monitoring methods for water bodies and water-related infrastructure using mobile laser scanning and unmanned aerial vehicles (UAVs). He is currently working on a project focusing on optical 3D measurement methods for generating, updating and acquiring condition data for digital twin models of bridges.



Melanie Elias

Prof. Dr.-Ing. Melanie Elias is professor of Geovisualisation at HTW Dresden since August 2025. From 2014–2025 she was research associate at TU Dresden, contributing to projects on intelligent patient positioning, glacier monitoring, river-change detection, crowdsourced hydrology networks. She earned her Ph.D. in 2021 on smartphone-based photogrammetric water-level measurement via crowdsourcing. Her work focuses on multiscale 3D/4D reconstruction from terrestrial, UAV, aerial and satellite data, advanced spatiotemporal visualisation, and low-cost AR-enabled environmental monitoring tools.



David Mader

Dr.-Ing. David Mader is a PostDoc at the Institute of Photogrammetry and Remote Sensing at the TU Dresden. In 2022, he received his Ph.D. on novel methods for the analysis of airborne LiDAR bathymetry data. In this context, he developed full-waveform stacking techniques for the detection of weak water-bottom echoes in airborne LiDAR bathymetry. His research focuses on improved derivation of water bottom topography from airborne LiDAR bathymetry data, enabling an efficient monitoring of shallow water areas of rivers, lakes and oceans.



Christian Mulsow

Christian Mulsow began his career as a surveying technician at a private company in Rostock. After completing his degree in Geodesy in 2003, he joined the Institute of Photogrammetry and Remote Sensing at TU Dresden as a technical assistant. His research interests include developing methods for compensation and modelling of refraction in close-range applications. In recent years, he has focused his research on optical bathymetry of inland waters, particularly from UAVs.



Katja Richter

Dr.-Ing. Katja Richter is a research associate at the Institute of Photogrammetry and Remote Sensing at the TU Dresden. In 2018, she received her Ph.D. on the topic "Analysis of full-waveform airborne laser scanner data for volumetric representation in environmental applications". Her research interests include the development of novel data analysis techniques in airborne LiDAR bathymetry with a particular focus on deriving high spatial resolution water turbidity parameters and increasing the accuracy potential of the measuring method.

https://doi.org/10.58440/ihr-31-2-a18

Hannes Sardemann, Ph.D. has a B.Sc. in Geodesy and Geoinformation from the University of Bonn and a M.Sc. in Geodesy from TU Dresden. In 2023 he finished his Dr.-Ing. on photogrammetry from an uncrewed water vehicle. His current research focuses on through-water-photogrammetry with wavy water surfaces.



Hannes Sardemann

Dr.-Ing. Ellen Schwalbe studied Geodesy at TU Dresden from 1998 to 2003. Since 2004, she has been a research associate at the Institute of Photogrammetry and Remote Sensing at TU Dresden. In 2013, she received her PhD with a dissertation on the development of methods for deriving high spatio-temporal resolution motion vector fields of glaciers from monoscopic image sequences. Since then, she has been involved as a postdoctoral researcher in several projects, with a particular focus on environmental monitoring.



Ellen Schwalbe

Jun.-Prof. Dr.-Ing. Anette Eltner is Junior Professor for Geosensor Systems at TU Dresden. She studied Geography at TU Dresden and obtained her PhD on photogrammetric methods for soil erosion assessment. Her research focuses on high-resolution sensing and photogrammetric techniques for geomorphology, hydrology, and environmental monitoring. She has authored 94 scientific publications (59 peer-reviewed journal papers) and serves as Chief Editor of Geoscientific Instrumentation, Methods and Data Systems.



Anette Eltner

https://doi.org/10.58440/ihr-31-2-a18

PEER-REVIEWED ARTICLE

Satellite imagery for hazard detection: better use of satellite imagery could help prevent groundings in the Canadian Arctic

Author
Anders Knudby[1,2]

Abstract
This study demonstrates how satellite imagery can reduce the risk of grounding in poorly surveyed waters. Automated shoal detection and satellite-derived bathymetry (SDB) were applied to Sentinel-2 imagery for seven grounding sites in the Canadian Arctic. Shoal detection was successful for all sites, and SDB showed depths as shallow as 0.3 m. Proactive use of satellite imagery, even without advanced image processing, could have provided mariners with vital information on the location of uncharted shoals and prevented costly and dangerous accidents. The hydrographic community should accelerate the inclusion of satellite-derived products into the information provided to mariners for safety of navigation.

Keywords
satellite imagery · satellite-derived bathymetry · shoal detection · groundings · Canadian Arctic

Resumé
Cette étude démontre comment l'imagerie satellitaire peut contribuer à réduire le risque d'échouement dans les eaux faiblement hydrographiées. La détection automatisée des hauts-fonds et la bathymétrie dérivée par satellite (SDB) ont été appliquées à l'imagerie Sentinel-2 pour sept sites d'échouement dans l'Arctique canadien. La détection des hauts-fonds a été couronnée de succès pour tous les sites, et la SDB a montré des profondeurs aussi faibles que 0,3 m. L'utilisation proactive de l'imagerie satellite, même sans traitement d'image avancé, aurait pu fournir aux navigateurs des informations vitales sur l'emplacement des hauts-fonds non cartographiés et éviter des accidents coûteux et dangereux. La communauté hydrographique devrait accélérer l'intégration des produits dérivés des satellites dans les informations fournies aux navigateurs pour la sécurité de la navigation.

✉ Anders Knudby · aknudby@uottawa.ca
[1] University of Ottawa, Department of Geography, Environment and Geomatics, Ottawa, ON K1N 6N5, Canada
[2] Liquid Geomatics Ltd., Ottawa, ON, K1S 0T3, Canada

https://doi.org/10.58440/ihr-31-2-a13

Resumen

Este estudio demuestra cómo las imágenes por satélite pueden reducir el riesgo de tocar fondo en aguas con levantamientos hidrográficos pobres. Se aplicó la detección automatizada de bajos y la batimetría derivada por satélite (SDB) a las imágenes de Sentinel-2 para siete lugares donde se había tocado fondo en el Ártico canadiense. La detección de bajos fue satisfactoria en todos los casos, y SDB mostró profundidades tan someras como 0,3 m. El uso proactivo de imágenes por satélite, incluso sin un procesamiento avanzado de las imágenes, podría haber proporcionado a los navegantes información vital sobre la ubicación de bajos no cartografiados y haber evitado accidentes costosos y peligrosos. La comunidad hidrográfica debería acelerar la inclusión de productos derivados de satélite en la información que se proporciona a los navegantes para la seguridad de la navegación.

1 Introduction

The Arctic Ocean is experiencing profound and rapid climatic changes, with significant implications for sea ice, navigability and maritime transportation. Human-induced warming has accelerated the decline in sea ice extent and thickness (Yadav et al., 2020), lengthening the ice-free season, and projections suggest that the Arctic could experience nearly ice-free summers as early as 2030 (Kim et al., 2023). These changes allow the opening of new shipping routes into and across the Canadian Arctic, routes that are becoming more accessible for longer periods each year (Liu et al., 2024). Recent years have seen an increase in maritime transportation in the Canadian Arctic Ocean (Dawson et al., 2018). In 2024, 466 ship voyages were recorded in Canadian Arctic waters, compared to 301 in 2014, a 55 % increase over the last decade, despite excluding data from November and December 2024 (Lasserre & Baudu, 2024).

However, the Canadian Arctic Ocean remains poorly surveyed and charted. The Canadian Hydrographic Service (CHS) estimates that only 15.8 % of Canadian Arctic waters have been adequately surveyed, including only 44.7 % of key navigational routes, and many charts contain minimal or insufficient information to support safe and efficient navigation (CHS, 2023). Many areas outside shipping corridors contain only outdated survey data, or no data at all, leading charts to be sparsely populated with soundings or simply contain white space with no information. The soundings that do exist can be over 100 years old, created from lead line measurements with positioning based on triangulation to points on land, the locations of which are themselves of unknown accuracy (Government of Canada, 2014). Even the distinction between land and water is sometimes incorrect on older CHS charts. For example, while supporting recent updates to CHS charts 7185 and 7193, the author identified the correct location of an island charted almost 2 km from its actual location, in addition to numerous previously uncharted shoals. An island >500 m across, which had been charted as a shoal, was also identified (Fig. 1). Such incomplete and erroneous charts, combined with increasing production and mobility of icebergs in the Arctic Ocean (Dalton, 2023) and increasing maritime traffic, inevitably create a substantial risk to the safety of navigation in Canada's Arctic (Howell et al., 2024; Nicoll et al., 2024; TSB, 2010).

While groundings are relatively infrequent in the Canadian Arctic due to the small total number of voyages, compared to other marine regions the Arctic has the highest accident rate at ~10 accidents per 1000 commercial ship movements (Council of Canadian Academies, 2016). Approximately 16 % of these are groundings (TSB, 2025). From 2000 to 2018, the Transportation Safety Board of Canada (TSB) received reports of 74 instances of vessel



Fig. 1 During work to update CHS chart 7185, a shoal indicated in the chart from 2016 (A) was found in satellite imagery to be an island larger than 500 m across (B), allowing it to be positioned and outlined correctly in the updated chart (C).

https://doi.org/10.58440/ihr-31-2-a13

grounding or bottom contact in the Canadian Arctic. The severity of these occurrences varies; some vessels sustain little to no damage and simply refloat at high tide, while others result in hull damage and breached fuel tanks, pollution, evacuation of crew and passengers, and high costs for search and rescue, cleanup, and repairs (TSB, 2021). A substantial number of these groundings occur on uncharted shoals; some of these shoals are known to the CHS but not included on charts and instead communicated to mariners through the use of Notices to Shipping (NOTSHIP; TSB, 2010). Others only become known after a grounding has occurred.

Satellite imagery remains underutilized in Canada's Arctic, especially for identifying hazards not included on official charts. While most shoals are not known to CHS in advance of a vessel grounding, many of them are nonetheless easily detectable using satellite imagery. Water is typically clear throughout much of the Arctic Ocean and shoals are often easily visible in optical satellite imagery. This includes free and publicly available imagery such as that provided by the Sentinel-2 MultiSpectral Instrument (MSI), for which imagery has been available for most of the Arctic Ocean since 2015 (Trémas et al., 2015). These shoals can be identified either using automated image processing algorithms (Richardson et al., 2024) or simply by visually inspecting the imagery and delineating the areas where the seafloor is visible. In areas of high turbidity, as is typical in glacial fjords or near river outlets, or under other unsuitable environmental conditions (e.g. in the presence of ice cover, cloud shadowing, whitecaps, or excessive sunglint), detection and delineation of shoals from optical satellite imagery is not always possible. But for large parts of the Arctic Ocean shoals are clearly visible to depths of at least ~10 m.

In addition to delineation of the locations and extents of shoals, a variety of algorithms exist to estimate the depth of water from the colour of the area as observed in a satellite image. These algorithms are collectively known as satellite-derived bathymetry (SDB) and can be used to approximate the depth of shoals. Most SDB algorithms employ one of two approaches. In empirical SDB, trusted geolocated water depth measurements, typically obtained with acoustic or lidar instruments, are used to establish an empirical relationship between pixel colour and water depth. That relationship is then extrapolated to the parts of the image for which water depths are to be estimated (Caballero & Stumpf, 2023; Ilori et al., 2019; Knudby & Richardson, 2023; Lyzenga, 1985, 1978; Stumpf et al., 2003). An alternative approach, often termed physics-based SDB, inverts a radiative transfer model by matching the color observed in each pixel to a set of realistic environmental parameters, including water depth, that it most closely matches (Dekker et al., 2011; Hedley et al., 2012; Knudby et al., 2016; Lee et al., 1999). This approach eliminates the need for trusted geolocated water depths measurements, which often do not exist in the Canadian Arctic, but instead relies on the ability to accurately account for all environmental factors that influence how water depth influences pixel color. Less-used alternative approaches to SDB also exist, including the use of photogrammetry (Hodúl et al., 2020, 2018) and wave-based kinematics (Daly et al., 2022). SDB is increasingly used in production of nautical charts, including by the United Kingdom, France, the United States (Mavraeidopoulos et al., 2017), and more recently Canada (Ahola et al., 2020; Chénier et al., 2018). However, despite the availability of satellite imagery for the entire Canadian Arctic, operational application of SDB has been limited.

The limited bathymetric information displayed on many charts of the Canadian Arctic, contrasted with the wealth of such information available in satellite imagery, suggests that an expanded use of satellite imagery for providing bathymetric information to mariners would be beneficial and could help reduce the frequency of groundings in Canada's increasingly busy Arctic Ocean. In this study, satellite imagery is used for i) shoal detection and ii) SDB, to illustrate the potential for satellite imagery to provide information that could reduce the risk of navigation in poorly charted waters. The study is based on seven cases from the Canadian Arctic Ocean, each featuring a vessel grounding on a shoal that a) is clearly visible in satellite imagery but b) was uncharted at the time of grounding.

2 Data and methods

2.1 Groundings

Relevant case studies were identified using the TSB's publicly available marine transportation occurrences database (TSB, 2025). As of February 2025, the database contained 86124 occurrences from 1975 to 2025 (many entries were duplicates, so the actual number of occurrences is smaller). Occurrences were first filtered to include only those classified as bottom contact or grounding under power, outside a harbor area, and located north of 65 °N, leaving 760 occurrences. Of those, seven were chosen for inclusion in this study based on i) their location in the Canadian Arctic Ocean, ii) the visibility of shoals in satellite imagery, iii) a desire to achieve a geographically distributed set of cases, and iv) other factors, such as weather, that indicate that the groundings could have been avoided if the shoals had been included on CHS charts, and v) the need to focus on a subset of occurrences for investigation. The resulting set of selected groundings is outlined in Table 1 and shown on Fig. 2. As per the criteria listed above, this is not intended to be an exhaustive or representative list of groundings in the Canadian Arctic Ocean. Interested readers are referred to the TSB's official list of occurrences for more examples.

2.2 Satellite imagery and CHS charts

For each grounding site, all Sentinel-2 images

https://doi.org/10.58440/ihr-31-2-a13

available from July to October for the years 2023 and 2024 were accessed, imagery with >50 % cloud cover was removed, and the remaining images were visually assessed to remove those with substantial ice cover, haze, or other environmental conditions rendering them unsuitable for SDB. As a result, between nine and thirteen images were available for each grounding site. The location, date and year of each grounding was used to identify the CHS chart that was current, i.e. the chart that the vessel crew would have had access to, at the time of grounding. These charts were located and accessed from Libraries and Archives Canada and scanned on a large-format scanner. A section of the relevant chart surrounding each grounding site was then manually georeferenced based on distinctive coastline features, using the Sentinel-2 satellite imagery for reference.

2.3 Shoal detection

For shoal detection, a global model for delineation of optically shallow water (Richardson et al., 2024) was applied to the Sentinel-2 images available for each site. For each image, this model produces a per-pixel probability of water being optically shallow, i.e. the probability that the seafloor is visually detectable in the imagery, after applying a mask to exclude non-water pixels. To identify shoals, the mean unmasked value of these per-image probabilities was then calculated, and pixels with a resulting value greater than 50 % were labeled as shoals. Visual examination of the results suggested that this 50 % threshold achieved a good trade-off between limiting false positives (image noise labeled as shoals) and limiting false negatives (undetected shoals).

2.4 Satellite-derived bathymetry

For SDB production, the Fully Automated Bathymetry (FAB) workflow, developed by Liquid Geomatics Ltd. was employed. FAB processing is based on 100 km × 100 km Sentinel-2 image tiles; products for smaller areas such as those surrounding each of the grounding sites illustrated in this paper can be extracted from the larger tiles. FAB processes Sentinel-2A and -2B images end-to-end, including image download from Copernicus Dataspace, land and cloud masking, deglinting (optional), atmospheric correction (Hedley, 2018), bathymetry estimation based on radiative transfer model (RTM) inversion (Hedley et al., 2009), correction for tide level at image acquisition (Lyard et al., 2021), and ensemble predictions based on multiple images for each site (Ilori & Knudby, 2020). FAB is implemented in Python 3.11, with calls to the IDA software (Hedley, 2019) for deglinting, atmospheric correction and RTM inversion (Hedley et al. 2018; Casal et al., 2020). Detailed information on data processing in the FAB workflow is provided in Appendix A.

2.5 SDB accuracy assessment

For most of the grounding sites, no or insufficient acoustic data was available to assess the accuracy of the SDB bathymetry maps produced with FAB. For the two sites where data was available, namely the grounding sites of the *Clipper Adventurer* and *V/L Camsell*, NONNA10 data was downloaded from CHS (CHS, 2024) and reprojected to match the spatial reference system of the relevant Sentinel-2 imagery. Sentinel-2 imagery is distributed projected to WGS-based UTM zones based on the Military Grid Reference System (MGRS). CHS's NONNA data is a set of non-navigational bathymetric survey data, compiled from individual surveys and made publicly available in raster format. For the *Clipper Adventurer* site, most of the NONNA data came

Table 1 List of the seven groundings included in this study, in chronological order.

Vessel name	Date	Location (lat / lon)	Notes	TSB report
Unknown	31 Aug. 1980	77.51 N, 85.48 W	Hull damage sustained, grounding during clear weather and smooth seas.	4287
V/L Camsell	25 Aug. 1984	68.57 N, 99.65 W	Grounding happened in an area of incomplete soundings, during clear weather and smooth seas. Hull damage sustained.	9351
Unknown	24 Aug. 1990	68.13 N, 99.08 W	Grounding happened during search and rescue, clear weather, light ice cover.	18332
Clipper Adventurer	27 Aug. 2010	67.97 N, 112.67 W	128 passengers evacuated. Extensive hull damage, minor fuel oil spill.	M10H0006
Martin Bergmann	03 Sept. 2014	68.40 N, 99.21 W	Grounding happened during search for the lost Franklin ships.	M14C0182
Akademik Ioffe	24 Aug. 2018	69.72 N, 91.35 W	163 passengers and crew evacuated, hull damage and minor fuel oil spill.	M18C0225
Hanse Explorer	23 Aug. 2019	72.58 N, 85.66 W	Passengers onboard, grounding in far northern location.	M19C0276

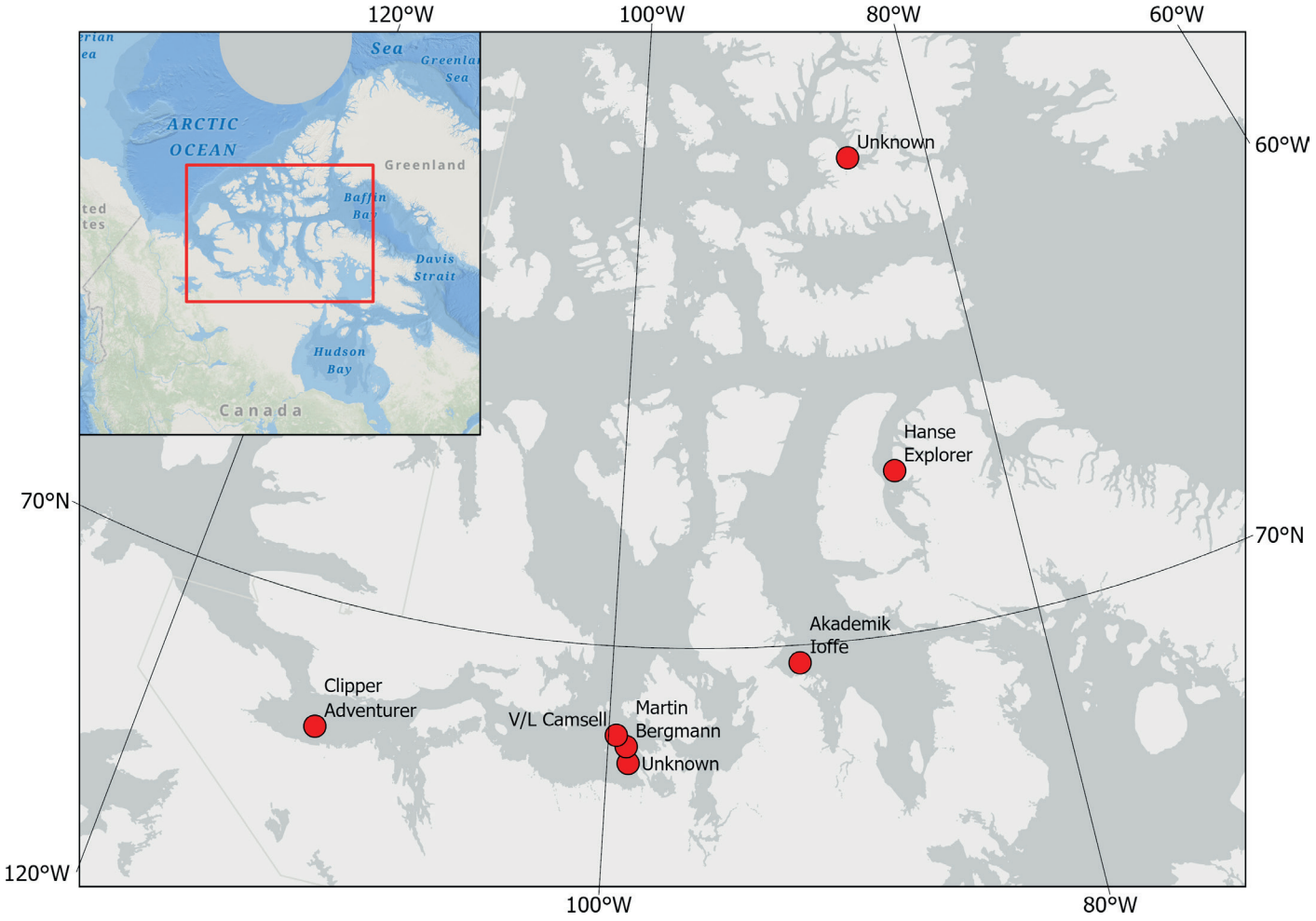


Fig. 2 The locations of the seven groundings used in this study, within the Canadian Arctic Archipelago.

from a 2010 multi-beam survey conducted following the grounding. This survey covered the entire shoal and the immediate surroundings and is categorized as Zone of Confidence (CATZOC) A2. For the *V/L Camsell* site, ~95 % of the NONNA data came from an Airborne Lidar Bathymetry (ALB) survey from 1986 categorized as CATZOC B; a few additional data points came from a single-beam survey conducted sometime between 1955 and 1964, categorized as CATZOC C. Bathymetry was extracted from overlapping SDB and NONNA10 pixels for comparison and calculation of the coefficient of determination (R^2) and the mean absolute difference (MAD) between the two data sets. This comparison was limited to SDB depths <= 10 m, beyond which the accuracy of SDB estimates in this region rapidly degrades due to the decreasing magnitude of the bottom-reflected optical signal recorded in the satellite imagery.

3 Results

3.1 The groundings

Below, a review of i) the CHS chart at the time of grounding, ii) satellite imagery of the grounding site, and iii) the shoal detection and FAB SDB products, is provided for the most recent four groundings listed in Table 1. Similar reviews for the remaining three groundings are provided in Appendix B.

3.1.1 Clipper Adventurer grounding

On 27 August 2010, the *Clipper Adventurer* ran aground on a known but uncharted shoal in Coronation Gulf, Nunavut, during calm seas and with clear visibility. All passengers were uninjured but evacuated from the vessel, and minor pollution was reported. The vessel was successfully refloated after multiple attempts conducted over a ~2-week period (TSB, 2010). Fig. 3 shows a comparison between the relevant subset of the 1990 version of CHS chart 7777, current at the time of the grounding (A), satellite imagery of the area (B, C), the shoal detection product (D), and the FAB SDB product (E). Soundings on the chart appear in a single line passing closely to the northeast of the shoal on which the *Clipper Adventurer* grounded. The shoal is clearly visible in the satellite imagery, identified in the shoal detection product, and the FAB SDB product indicates that it has a minimum depth of 4.0 m. For comparison, the draught of the *Clipper Adventurer* is 4.5 m (forward) and 4.6 m (aft) (TSB, 2010), making prior knowledge of a shoal at 4.0 m depth critically important to navigational decision-making. This particular shoal had actually already been reported in 2007 by

https://doi.org/10.58440/ihr-31-2-a13

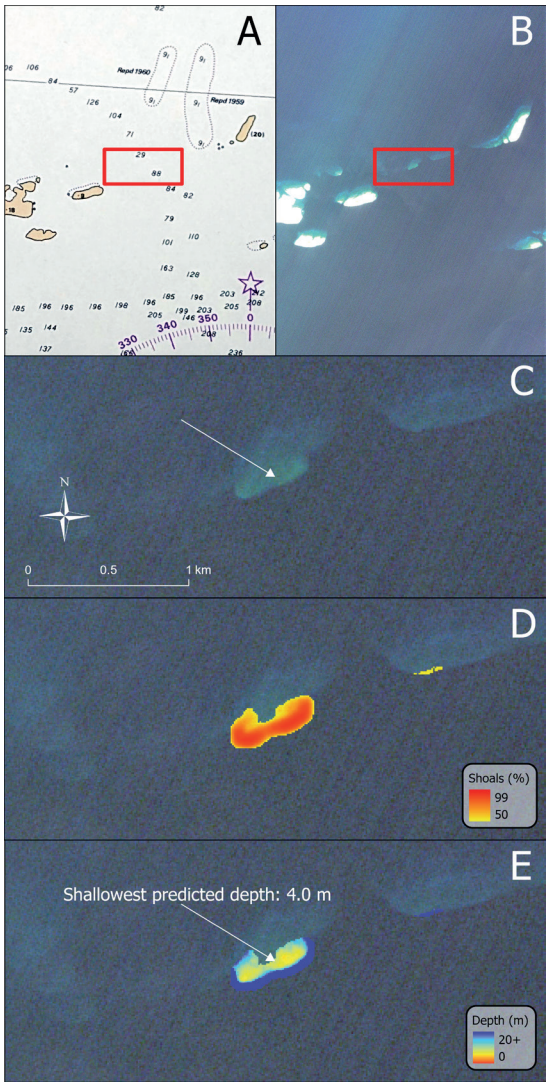


Fig. 3 Comparison of a subset of CHS chart 7777 from 1990, current at the time of grounding (A), a Sentinel-2 satellite image covering the same area (B), a section of the satellite image showing the shoal on which the grounding happened in greater detail (C), the same satellite image with the shoal detection product overlaid (D), and the same satellite image with the FAB SDB product overlaid (E). The extent of the areas shown in (C-E) is indicated by the red rectangles in (A) and (B). Note that the location of the grounding reported by TSB is approximately 500 m SE of the shoal shown here, which was correctly identified on the basis of the CHS survey that followed the grounding.

the Canadian Coast Guard Ship (CCGS) *Sir Wilfrid Laurier*, leading to the publication of a Notice to Shipping (NOTSHIP) that indicated a minimum depth of 3.3 m. However, CHS determined that the information provided from *Sir Wilfrid Laurier* did not meet the requirements for a permanent chart update and instead planned a detailed survey for 2009 to produce data of sufficient quality. Ultimately this did not happen until after the *Clipper Adventurer* grounding in 2010. In the meantime, in 2008, another passenger vessel, the *Akademik Ioffe*, passed near the same shoal. The crews of both vessels were unaware of the NOTSHIP that reported the shoal's existence (TSB, 2010).

3.1.2 Akademik Ioffe grounding

On 24 August 2018, the passenger vessel *Akademik Ioffe* ran aground 78 nautical miles north-northwest of Kugaaruk, Nunavut, in an area almost entirely without charted bathymetric information. The vessel was refloated the same night, and the passengers, all uninjured, were evacuated the next morning. Minor pollution was reported (TSB, 2021). Fig. 4 shows a comparison between the relevant subset of the 1998 version of CHS chart 7502, current at the time of the grounding (A), satellite imagery of the area (B, C), the shoal detection product (D), and the FAB SDB product (E). Two soundings appear on the subset of the chart shown in Fig. 4, indicating depths of 71 and 92 meters respectively, both over 2 km from the shoal on which the *Akademik Ioffe* ran aground. This corresponds to the note on the chart that the charted information is "of a reconnaissance nature collected from CHS spot sounding surveys". The shoal appears faint but is clearly visible in the satellite image, correctly detected by the shoal product, and the FAB SDB product indicates a minimum depth of 4.5 m. The draught of the *Akademik Ioffe* is 5.9 m.

3.1.3 Hanse Explorer grounding

On 23 August 2019, the yacht *Hanse Explorer* ran aground in Admiralty Inlet, Nunavut. No pollution or injuries were reported, and the vessel sustained only minor damage. Approaching Levasseur Inlet, "the under-keel water depth abruptly diminished from 44 m to 0 m and the vessel ran aground" (TSB, 2021). Fig. 5 shows a comparison between the relevant subset of the 1985 version of CHS chart 7568, current at the time of the grounding (A), satellite imagery of the area (B, C), the shoal detection product (D), and the FAB SDB product (E). No soundings are charted in or near Levasseur Inlet; a single line of soundings are charted for Admiralty Inlet (west of the area shown in Fig. 5). A shoal dominating the entrance to Levasseur Inlet is clearly visible in the satellite imagery (C), and is correctly detected by the shoal product, though with central parts of the shoal missing (not indicated as shoal). FAB SDM estimates a minimum depth of 0.3 m for the part of the shoal where the grounding occurred. The draught of the *Hanse Explorer* is 4.3 m.

3.1.4 Martin Bergmann grounding

On 03 September 2014, the *Martin Bergmann* ran aground in largely uncharted waters near Gjoa Haven, eastern Queen Maud Gulf, Nunavut, while searching for Sir John Franklin's lost ships, *HMS Erebus* and *HMS Terror*. Weather conditions during the grounding were not reported. Fig. 6 shows that the chart contains two soundings just west of the shoal that caused the grounding, but very sparse bathymetric data are charted in the area near the grounding, which contains many shoals. The shoal that caused the grounding is clearly visible in the satellite image, correctly detected in the shoal product, and the FAB SDB indicates its minimum depth as 0.3 m. With a draught of 3.43 m (Arctic Focus, 2025), knowledge of this shoal and its minimum depth would have had obvious implications for navigation of the *Martin Bergmann*.

https://doi.org/10.58440/ihr-31-2-a13

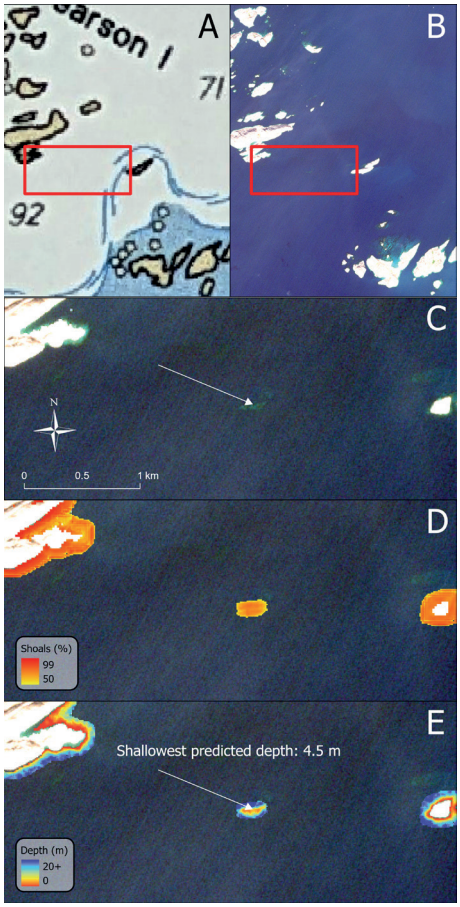


Fig. 4 Comparison of a subset of CHS chart 7502 from 1998, current at the time of grounding (A), a Sentinel-2 satellite image covering the same area (B), a section of the satellite image showing the shoal on which the grounding happened in greater detail (C), the same satellite image with the shoal detection product overlaid (D), and the same satellite image with the FAB SDB product overlaid (E). The extent of the areas shown in (C-E) is indicated by the red rectangles in (A) and (B).

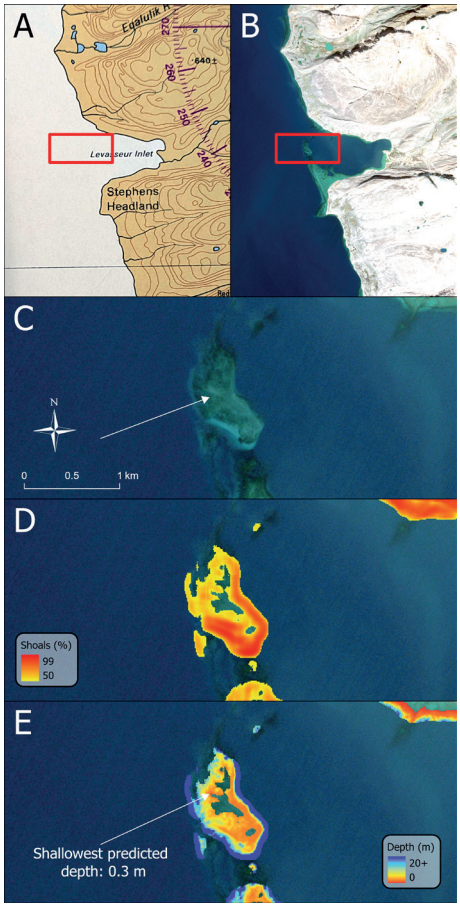


Fig. 5 Comparison of a subset of CHS chart 7568 from 1985, current at the time of grounding (A), a Sentinel-2 satellite image covering the same area (B), a section of the satellite image showing the shoal on which the grounding happened in greater detail (C), the same satellite image with the shoal detection product overlaid (D), and the same satellite image with the FAB SDB product overlaid (E). The extent of the areas shown in (C-E) is indicated by the red rectangles in (A) and (B).

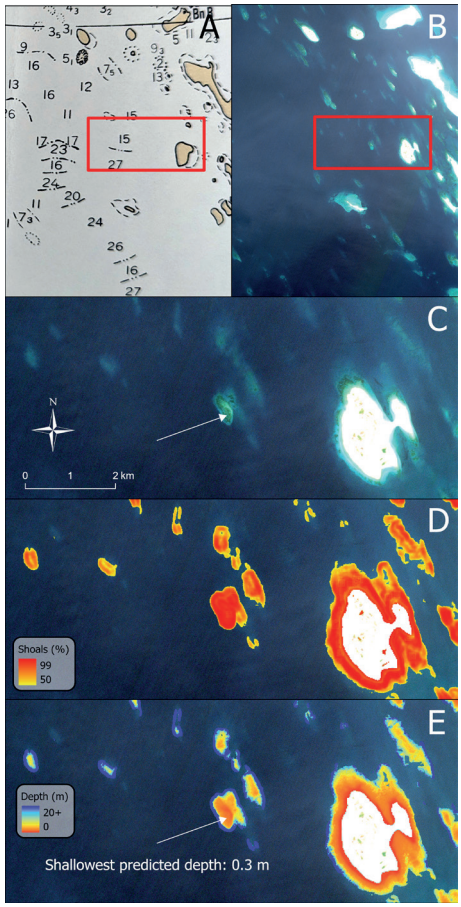


Fig. 6 Comparison of a subset of CHS chart 7083 from 1980, current at the time of grounding (A), a Sentinel-2 satellite image covering the same area (B), a section of the satellite image showing the shoal on which the grounding happened in greater detail (C), the same satellite image with the shoal detection product overlaid (D), and the same satellite image with the FAB SDB product overlaid (E). The extent of the areas shown in (C-E) is indicated by the red rectangles in (A) and (B).

3.2 SDB accuracy

Comparison between the FAB SDB estimates and survey data provided by CHS in the form of NONNA10 rasters was limited to depths up to 10 m due to the rapid degradation of SDB performance at deeper depths. This comparison, possible only for the shoals on which the *Clipper Adventurer* and *V/L Camsell* ran aground due to the limited coverage of CHS data, shows that FAB SDB performs similarly to what is reported for SDB products elsewhere in the Arctic (Ahola et al., 2020; Chénier et al., 2018). The comparison for the *Clipper Adventurer* (Fig. 7A; n = 380, R^2 = 0.58), shows a slight bias toward depth overestimation, with depths overestimated by an average of 0.71 m, and a mean absolute difference between SDB and survey data of 1.04 m. The comparison for *V/L Camsell* (Fig. 7B; n = 78, R^2 = 0.45) instead shows a slight bias toward depth underestimation, with depths underestimated by an average of 0.89 m, and a mean absolute difference between SDB and survey data of 1.35 m. Given these error statistics, the FAB SDB product would not meet International Hydrographic Organization (IHO) Order 2 specifications for vertical accuracy and would be categorized as CATZOC D data. In consequence, and as has been the practice at CHS, the FAB SDB product should not be directly used for charting. However, it is important to note that especially the comparison of FAB SDB to the CATZOC B and C survey data available for the *V/L Camsell* grounding site, and the resulting error statistics, should be interpreted considering the quality of the CHS data available for that comparison. It is possible that the relatively lower R^2 and larger MAD of the FAB SDB product at the *V/L Camsell* grounding site is due to the lower quality of the data used for comparison at this site.

4 Discussion

This study presented a review of seven groundings that occurred on shoals in the Canadian Arctic. All these shoals are clearly visible and easily detectable in satellite imagery but were not indicated on the CHS charts current at the time of each grounding. SDB applied to the satellite imagery suggests that the shallowest depths of these shoals ranged from 0.3 m to 5.1 m. In comparison, the draughts of the four vessels whose groundings were described above range

https://doi.org/10.58440/ihr-31-2-a13

between 3.43 m (*Martin Bergmann*) and 5.9 m (*Akademik Ioffe*). The first three of the groundings listed in Table 1, reported in Appendix B, occurred in 1980, 1984, and 1990, before the near-global coverage of free and publicly available satellite imagery that exists today. As a result, at the time of these groundings no satellite imagery of the shoals was publicly available. However, the shoals responsible for the remaining four groundings are clearly visible in both Landsat imagery, which has been available at 30-m spatial resolution for many areas since 1984 and has been free and publicly available since 2008 (Wulder et al., 2012), as well as in the Sentinel-2 imagery used in this study, which has been free and publicly available since 2015. It is therefore reasonable to suggest that at least the four groundings that took place since 2010 could have been avoided if the information contained in free and publicly available satellite imagery had been used to better inform mariners of the existence of these shoals. It is notable that following several of the reviewed groundings, CHS conducted detailed multi-beam surveys of the shoals and nearby areas. Although such post-incident surveys are undoubtedly beneficial for refining the relevant charts, this reactive approach misses the critical opportunity to avoid incidents entirely through proactive identification of hazards.

It is important to note that providing image-derived information to mariners does not necessarily require sophisticated image processing methods to be applied to the imagery. It should be clear to anyone looking at Figs. 3–6, as well as the figures in Appendix B, that satellite imagery inherently contains valuable information on water depth because variations in color and texture provide direct visual cues indicating the locations of shoals. Most simply, supplying mariners with satellite imagery in a format that allows it to be accessed and visualized, including while on the water, would in many cases be sufficient for route planning and hazard avoidance. Additional products, such as the ones shown in this study, should ideally accompany the imagery. In addition to the shoal detection product used in this study, examples of similar products include EOMAP's shoals database (EOMAP, 2023) and the StayAway product (ChartWorld, 2025). Several SDB products are also available, including Liquid Geomatics's FAB SDB used here, and similar products provided either commercially or by hydrographic offices. It is clear that products derived from satellite imagery cannot and should not replace the charts and other documents that are legally required for vessels operating in Canadian waters (DFO, 2020) or elsewhere; rather, satellite imagery and products derived from it can provide additional information on hazards that are not shown on those charts.

The continued occurrence of groundings in uncharted or poorly surveyed waters underscores the need to make better use of satellite-derived information in some form. The question is how best to make use of the information contained in the imagery. In

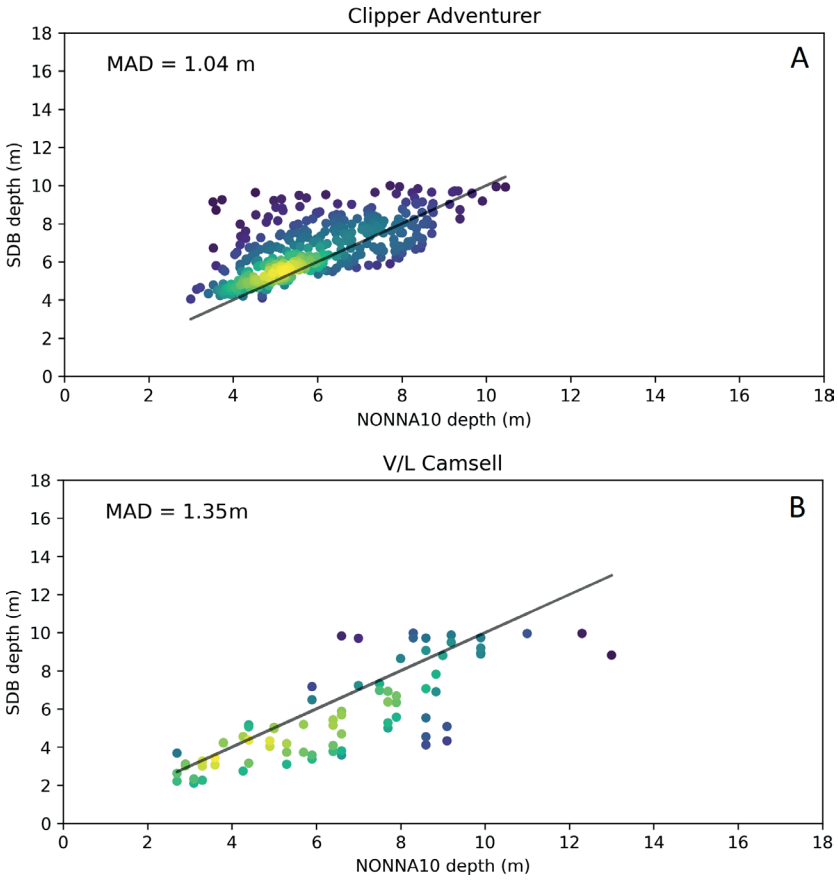


Fig. 7 Scatter plots comparing bathymetry estimates from FAB SDB (y-axes) to NONNA10 bathymetry data from CHS (x-axes) for the two groundings sites for which data were available: the site of the *Clipper Adventurer* (A) and *V/L Camsell* (B).

2021 IHO established an SDB project team that has produced a guidance document (IHO, 2024) providing "technical best practices and guidelines" for SDB. This may help guide the use of satellite imagery for SDB and facilitate international discussions of its appropriate use. SDB is gradually finding its way onto charts, including in France, the United Kingdom, the United States, and Canada (Chénier et al., 2018), where the CHS has established a Remote Sensing Centre of Excellence (RSCoE) to accelerate the use satellite imagery in hydrography, including for SDB purposes (Chénier et al., 2020). Where SDB products are of sufficient quality integration on charts is often the best solution, but SDB products are limited in coverage to relatively shallow depths, and their errors increase with the depth of water (Duan et al., 2022; Knudby & Richardson, 2023) until the seafloor becomes undetectable, at which point SDB estimates are no longer meaningful. SDB products should thus not blindly be included on charts; indeed, the SDB errors reported here for the two shoals for which reference data were available for comparison may be deemed unacceptable for inclusion on charts.

Yet there is no doubt that the imagery contains real and valuable information on the location of shoals. As of April 2025, CHS is exploring the use of automated shoal detection with an approach similar to the one used in this study, testing its ability to

both validate SDB results and delineate hazards to navigation for production of navigational warnings (NAVWARNs) and notices to mariners (NOTMARs). Where the quality of SDB products is deemed insufficient for direct inclusion on charts, the IHO's S-100 universal hydrographic data model may also provide other avenues for inclusion of information derived from satellite imagery. SDB data products could be included under S-102 (Bathymetric Surface), a raster product designed to represent bathymetric depths, and identified shoals could be included under S-124 (Navigational Warnings), a vector product intended to provide information on the nature and extent of navigational warnings. No S-100 data product seems suitable to hold the imagery itself; development of such a product could be beneficial and should be considered. In summary, despite useful satellite imagery having been freely available since 2008, many nautical charts continue to contain nothing but white space in areas where shoals are clearly visible in the imagery. This results in needless groundings, including the four reviewed in this study that occurred since 2010. This situation highlights the need for a paradigm shift in the utilization of satellite imagery within the hydrographic community. Such a shift is already under way, but with a rapidly warming Arctic and its associated increase in vessel traffic, it is imperative to further accelerate the use of satellite imagery to extract information on the location of shoals and, where possible, their approximate depth, and to provide such information to mariners in the form that is most useful to them.

5 Conclusion

This study has demonstrated that several recent vessel groundings in the Canadian Arctic might have been prevented if mariners had been provided with satellite-derived information on the locations of shoals that were not indicated on the official charts at the time. It is the responsibility of the hydrographic community to produce data products that improve the safety of navigation for mariners. Satellite imagery contains valuable information that can be used for this purpose; specifically, it contains clear visual cues that enable identification of shoal locations and estimation of water depth. In unsurveyed or poorly surveyed regions of the world, such information may be the best that is available. Given the rapidly warming Arctic Ocean and the corresponding increase in vessel traffic, proactive use of satellite imagery in this inadequately surveyed region, rather than reactive multi-beam surveys conducted after groundings have already occurred, would significantly improve the safety of navigation. Vessel groundings have serious financial, environmental, and safety consequences, including potential loss of life. It is imperative for the hydrographic community to incorporate satellite imagery proactively to improve navigational safety in poorly surveyed waters.

Acknowledgements

Development of the FAB SDB workflow began in 2018 after discussions with Dr. John Hedley about the possibility of fully automating physics-based SDB. Since then, it has been continuously refined with input and inspiration from numerous people. Funding for its development has been provided by the Canadian Space Agency (22AO2-LIQU). The model that differentiates optically shallow and optically deep water, which is the basis for the shoal detection product, was developed mostly by a group of students at the University of Ottawa: Galen Richardson, Neve Foreman, Yulun Wu, and Yiwen Lin. The idea for the present paper was inspired by discussion with several other colleagues who prefer to remain anonymous. The initial manuscript was improved on the basis of very constructive comments from three anonymous reviewers

References

Ahola, R., Chénier, R., Sagram, M. and Horner, B. (2020). The impact of sensors for satellite derived bathymetry within the Canadian Arctic. *Geomatica, 74*, pp. 46–64.

Arctic Focus (2025). *R/V Martin Bergmann*. Arctic Focus. https://www.arcticfocus.org/about/vessels-and-labs/rv-martin-bergmann/ (last accessed 27 July 2025).

Caballero, I. and Stumpf, R. P. (2023). Confronting turbidity, the major challenge for satellite-derived coastal bathymetry. *Science of the Total Environment, 870*, 161898.

Carrere, L., Lyard, F., Cancet, M. and Guillot, A. (2015). FES 2014, a new tidal model on the global ocean with enhanced accuracy in shallow seas and in the Arctic region. *Geophysical Research Abstracts, 17*, 5481.

Casal, G., Hedley, J. D., Monteys, X., Harris, P., Cahalane, C. and McCarthy, T. (2020). Satellite-derived bathymetry in optically complex waters using a model inversion approach and Sentinel-2 data. *Estuarine and Coastal Shelf Science, 241*, 106814.

ChartWorld (2025). *StayAway service complements ENC Depth Information*. ChartWorld. https://www.chartworld.com/web/news/stayaway-service-complements-enc-depth-information/ (last accessed 19 March 2025).

Chénier, R., Faucher, M.-A. and Ahola, R. (2018). Satellite-Derived Bathymetry for Improving Canadian Hydrographic Service Charts. *ISPRS International Journal of Geo-Information, 7*, 306.

Chénier, R., Omari, K., Blondel, E., Sagram, M. and Jirovec, A. (2020). Accelerating the usage of earth and oceans observation data in hydrographic applications. *The International Hydrographic Review, 30*, pp. 103–127. CHS (2024). *Canadian Hydrographic Service Non-Navigational (NONNA) Bathymetric Data*. Open Government Portal. https://open.canada.ca/data/en/dataset/d3881c4c-650d-4070-bf9b-1e00aabf0a1d (last accessed 6 March 2025).

CHS (2023). *Arctic charting*. Canadian Hydrographic Service. https://www.charts.gc.ca/arctic-arctique/index-eng.html (last accessed 25 February 2025).

https://doi.org/10.58440/ihr-31-2-a13

Council of Canadian Academies (2016). *Commercial Marine Shipping Accidents: Understanding the Risks in Canada*. Council of Canadian Academies. Ottawa, Canada.

Dalton, A. (2023). *Identifying Iceberg Production Processes, Drift Patterns and Coexistence with Ships in the Eastern Canadian Arctic* [PhD thesis, Université d'Ottawa / University of Ottawa].

Daly, C., Baba, W., Bergsma, E., Thoumyre, G., Almar, R. and Garlan, T. (2022). The new era of regional coastal bathymetry from space: A showcase for West Africa using optical Sentinel-2 imagery. *Remote Sensing of Environment, 278*, 113084.

Dawson, J., Pizzolato, L., Howell, S. E. L., Copland, L. and Johnston, M. E. (2018). Temporal and Spatial Patterns of Ship Traffic in the Canadian Arctic from 1990 to 2015. *ARCTIC, 71*, pp. 15–26.

Dekker, A. G., Phinn, S. R., Anstee, J., Bissett, P., Brando, V. E., Casey, B., Fearns, P., Hedley, J., Klonowski, W., Lee, Z. P., Lynch, M., Lyons, M., Mobley, C. and Roelfsema, C. (2011). Intercomparison of shallow water bathymetry, hydro-optics and benthos mapping techniques in Australian and Caribbean coastal environments. *Limnology & Oceanography Methods, 9*, pp. 396–425.

DFO (2020). *Navigation Safety Regulations. Government of Canada*. https://lois.justice.gc.ca/eng/regulations/SOR-2020-216/index.html (last accessed 19 March 2025).

Duan, Z., Chu, S., Cheng, L., Ji, C., Li, M. and Shen, W. (2022). Satellite-derived bathymetry using Landsat-8 and Sentinel-2A images: assessment of atmospheric correction algorithms and depth derivation models in shallow waters. *Optics Express, 30*, pp. 3238–3261.

Emde, C., Buras-Schnell, R., Kylling, A., Mayer, B., Gasteiger, J., Hamann, U., Kylling, J., Richter, B., Pause, C., Dowling, T. and Bugliaro, L. (2016). The libRadtran software package for radiative transfer calculations (version 2.0.1). *Geoscientific Model Development, 9*, pp. pp. 1647–1672.

EOMAP (2023). Shoals Database. EOMAP. https://www.eomap.com/*shoals-database/* (last accessed 19 March 2025).

Government of Canada (2014). *Fall Report of the Commissioner of the Environment and Sustainable Development*. Office of the Auditor General of Canada. Ottawa, Canada.

Hedley, J., Roelfsema, C., Koetz, B. and Phinn, S. (2012). Capability of the Sentinel 2 mission for tropical coral reef mapping and coral bleaching detection. *Remote Sensing of Environment, 120*, pp. 145–155.

Hedley, J., Roelfsema, C. and Phinn, S. R. (2009). Efficient radiative transfer model inversion for remote sensing applications. *Remote Sensing of Environment, 113,* pp. 2527–2532.

Hedley, J. D. (2019). *Image Data Analysis (IDA) software*. Numerical Optics, Tiverton, UK.

Hedley, J. D. (2018). Atmospheric correction of Sentinel-2 and Landsat 8 for satellite derived bathymetry. *Ocean Optics XXIV, Dubrovnik, Croatia.*

Hedley, J. D., Roelfsema, C. and Phinn, S.R. (2010). Propagating uncertainty through a shallow water mapping algorithm based on radiative transfer model inversion. *Ocean Optics XX, Anchorage, USA.*

Hodúl, M., Bird, S., Knudby, A. and Chénier, R. (2018). Satellite derived photogrammetric bathymetry. *ISPRS Journal of Photogrammetry and Remote Sensing, 142*, pp. 268–277.

Hodúl, M., Chénier, R., Faucher, M.-A., Ahola, R., Knudby, A. and Bird, S. (2020). Photogrammetric Bathymetry for the Canadian Arctic. *Marine Geodesy, 43*, pp. 23–43.

Howell, S. E. L., Babb, D. G., Landy, J. C., Glissenaar, I. A., McNeil, K., Montpetit, B. and Brady, M. (2024). Sea ice transport and replenishment across and within the Canadian Arctic Archipelago, 2016–2022. *The Cryosphere, 18,* pp. 2321–2333.

IHO (2024). *B-13 Satellite-Derived Bathymetry Best Practice Guide*. International Hydrographic Organization (IHO), Monaco.

Ilori, C. O. and Knudby, A. (2020). An Approach to Minimize Atmospheric Correction Error and Improve Physics-Based Satellite-Derived Bathymetry in a Coastal Environment. *Remote Sensing, 12*, 2752.

Ilori, C. O., Pahlevan, N. and Knudby, A. (2019). Analyzing Performances of Different Atmospheric Correction Techniques for Landsat 8: Application for Coastal Remote Sensing. *Remote Sensing, 11*, 469.

Kim, Y.-H., Min, S.-K., Gillett, N. P., Notz, D. and Malinina, E. (2023). Observationally-constrained projections of an ice-free Arctic even under a low emission scenario. *Nature Communications, 14*, 3139.

Knudby, A., Ahmad, S. K. and Ilori, C. (2016). The potential for Landsat-based bathymetry in Canada. *Canadian Journal of Remote Sensing, 42*, pp. 367–378.

Knudby, A. and Richardson, G. (2023). Incorporation of neighborhood information improves performance of SDB models. *Remote Sensing Applications: Society and Environment, 32*, 101033.

Lasserre, F. and Baudu, H. (2024). *Navigation in the Arctic in 2024, The Arctic Review.* Observatoire de la politique et la sécurité de l'arctique (OPSA), Québec, Canada.

Lee, Z., Carder, K. L., Mobley, C. D., Steward, R. G. and Patch, J. S. (1999). Hyperspectral remote sensing for shallow waters: 2. Deriving bottom depths and water properties by optimization. *Applied Optics, 38*, pp. 3831–3843.

Lee, Z., Carder, K. L., Mobley, C. D., Steward, R. G., Patch, J. S., 1998. Hyperspectral remote sensing for shallow waters. I. A semianalytical model. *Applied Optics, 37*, pp. 6329–6338.

Liu, Y., Luo, H., Min, C., Chen, Q. and Yang, Q., (2024). Changes in the Arctic Traffic Occupancy and Their Connection to Sea Ice Conditions from 2015 to 2020. *Remote Sensing, 16*, 1157.

Lyard, F. H., Allain, D.J., Cancet, M., Carrère, L. and Picot, N. (2021). FES2014 global ocean tide atlas: design and performance. *Ocean Science, 17*, pp. 615–649.

Lyzenga, D. R. (1985). Shallow-water bathymetry using combined lidar and passive multispectral scanner data. *International Journal of Remote Sensing, 6*, pp. 115–125.

Lyzenga, D. R. (1978). Passive remote sensing techniques for mapping water depth and bottom features. *Applied Optics, 17*, pp. 379–383.

Mavraeidopoulos, A., Pallikaris, A. and Oikonomou, E. (2017). Satellite Derived Bathymetry (SDB) and safety of navigation. *The International Hydrographic Review, 17*.

Nicoll, A., Dawson, J., Marty, J., Copland, L. and Sawada, M. (2024). Analysis of shipping accident patterns among commercial and non-commercial vessels operating in ice-infested waters in Arctic Canada from 1990 to 2022. *Journal of Transportation Geography, 121*, 104046.

NOAA, NASA and USAF (1976). *U.S. Standard Atmosphere, 1976*. National Oceanic and Atmospheric Administration, National Aeronautics and Space Administration, United States Air Force, Washington, USA.

Richardson, G., Foreman, N., Knudby, A., Wu, Y. and Lin, Y. (2024). Global deep learning model for delineation of optically shallow and optically deep water in Sentinel-2 imagery. *Remote Sensing of Environment, 311*, 114302.

Robin, C., Nudds, S., MacAulay, P., Godin, A., De Lange Boom, B. and Bartlett, J. (2016). Hydrographic Vertical Separation Surfaces (HyVSEPs) for the Tidal Waters of Canada. *Marine Geodesy, 39*, pp. 195–222.

Stumpf, R. P., Holderied, K. and Sinclair, M. (2003). Determination of water depth with high-resolution satellite imagery over variable bottom types. *Limnology and Oceanography, 48*, pp. 547–556.

Trémas, T. L., Déchoz, C., Lacherade, S., Nosavan, J. and Petrucci, B. (2015). Sentinel-2: presentation of the CAL/VAL commissioning phase. Proceedings of the Image and Signal *Processing for Remote Sensing XXI conference, SPIE*, pp. 94–106.

TSB (2010). *Marine Investigation Report M10H0006*. Transportation Safety Board of Canada, Ottawa, Canada.

TSB (2021). *Marine transportation safety investigation report M18C0225*. Transportation Safety Board of Canada, Ottawa, Canada.

TSB (2025). *Data and statistics on marine transportation occurrences*. Transportation Safety Board of Canada. https://www.tsb.gc.ca/eng/stats/marine/index.html (last accessed 25 February 2025).

Wulder, M. A., Masek, J. G., Cohen, W. B., Loveland, T. R. and Woodcock, C. E. (2012). Opening the archive: How free data has enabled the science and monitoring promise of Landsat. *Remote Sensing of Environment, 122*, pp. 2–10.

Yadav, J., Kumar, A. and Mohan, R. (2020). Dramatic decline of Arctic Sea ice linked to global warming. *Natural Hazards, 103*, pp. 2617–2621.

Zhu, Z., Wang, S. and Woodcock, C. E. (2015). Improvement and expansion of the Fmask algorithm: cloud, cloud shadow and snow detection for Landsats 4–7, 8 and Sentinel 2 images. *Remote Sensing of Environment, 159*, pp. 269–277.

Appendix A: Additional details on the FAB SDB workflow

A.1 Masking

After downloading all Sentinel-2 images, all pixels with top-of-atmosphere (TOA) reflectance >1.5 % in the shortwave infrared (SWIR; band 12) are masked out; this threshold has been determined from testing on >100 images globally. Initially the internal cloud flags for each sensor were tested for this purpose, as was the Fmask algorithm (Zhu et al., 2015), but both produced generally poor results over coastal areas. In addition to masking out clouds, a simple SWIR-based threshold also serves to mask out land, sea ice, vessels, white caps and pixels with excessive sunglint, all of which are undesirable for SDB and detectable by increased SWIR reflectance. In addition to these masks developed for each image, a land mask is created by masking out all pixels with less than three unmasked observations across all images for the area. This is done to ensure that pixels that were masked out in most images, but remained unmasked once or twice, were excluded from further processing (Fig. 8).

A.2 Deep-water detection and atmospheric correction

Atmospheric correction in FAB is based on deep-water reference polygons, 24 of which are identified for each tile. To do so, all available images are combined to calculate the per-pixel median unmasked TOA reflectance in the 490-nm band. A 1000 m × 1000 m mean filter is applied

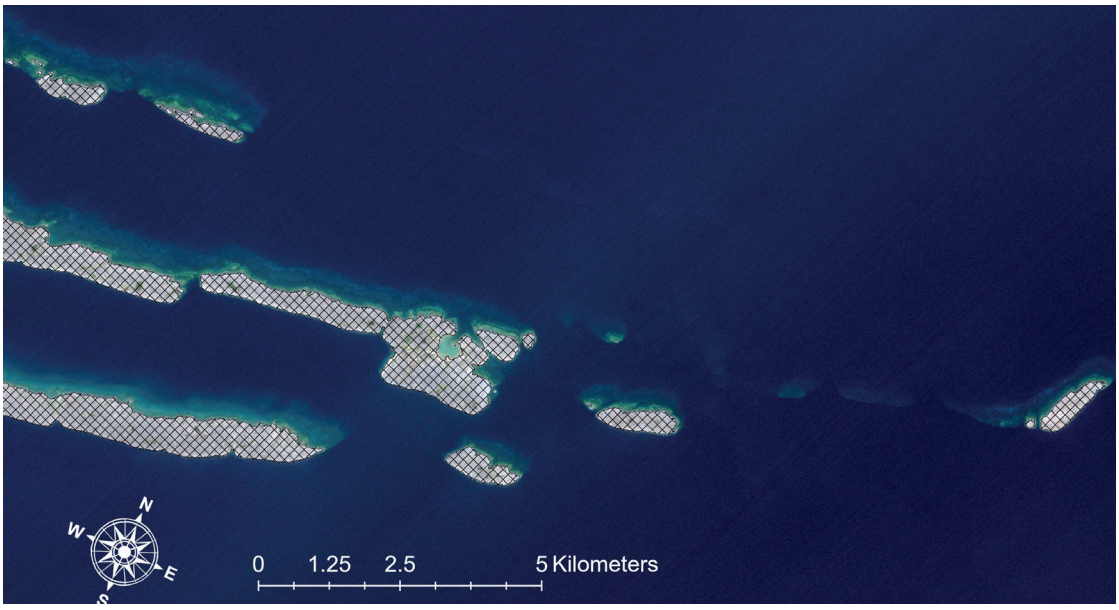


Fig. 8 An example of the land mask applied to satellite imagery covering the area surrounding the 2010 grounding of the Clipper Adventurer. Masked-out pixels are shown with cross-hatching.

https://doi.org/10.58440/ihr-31-2-a13

to the result to reduce noise; this also serves to make pixels close to land less likely to be identified as deep water. Pixels that are unmasked in less than three images, or located within 500 m of the tile edge, as well as pixels that do not connect through other valid pixels to the tile edge (i.e. lakes) are then removed. The resulting data layer is divided into four quadrats, and within each quadrat six random pixels, selected among those with values less than or equal to 1.5 times the darkest unmasked pixel, are randomly selected as the centers of 1000 m × 1000 m deep-water areas.

Atmospheric correction is then performed with the deep-water calibration (DWC) method implemented in the IDA software (Casal et al., 2020; Hedley, 2019, 2018). The DWC method is based on look-up tables of atmospheric reflectance and transmission calculated with libRadtran (Emde et al., 2016) using the US standard atmosphere model (NOAA et al., 1976) and a maritime 99 % relative humidity aerosol model (MAR99) parameterized with scene-averaged sun and view angles. The atmospheric correction requires specifying aerosol optical thickness at 550 nm (τ550), and wind speed (u10). The wind speed term is effectively a proxy for the spatially averaged residual sun glint, dependent on the solar-view geometry. While the values of these two parameters can be estimated with auxiliary data, the DWC method instead utilizes the deep-water areas identified above, in combination with the bathymetry model described below, to estimate the values of τ550 and u10 that will lead to water depth estimates of at least 15 m for the deep-water areas. In consequence, the estimated τ550 and u10 values may not be correct for each image, but they ensure that deep water will be correctly identified as deep in the bathymetry estimation.

A.3 Bathymetry estimation

Per-pixel water depth is estimated for all atmospherically corrected images using the RTM inversion implemented in IDA. This approach is based on least-squares matching between the above-water remote sensing reflectance (R_{rs}) observed in each pixel and a look-up table containing R_{rs} values forward-modeled for a range of water depth, water quality and seafloor reflectance parameters. This forward modeling is based on the semi-analytical model developed by Lee et al. (1999, 1998), which takes the general form:

$$R_{rs}(\lambda) = f(P, G, X, H, e, \Theta_s, \Theta_v, \lambda) \quad (1)$$

In Eq. 1, *P*, *G*, and *X* are proxies for the amount of phytoplankton (mg m^{-3}), absorption at 440 nm due to coloured dissolved organic matter (CDOM; m^{-1}), and backscattering at 440 nm due to suspended sediment (m^{-1}), respectively, *H* is the water depth (m), *e* is the seafloor reflectance (unitless), Θ_s is the solar zenith angle, and Θ_v is the viewing zenith angle. λ (henceforth omitted for simplicity) is the wavelength. This forward model is specified for each image, using default value ranges for *P*, *G*, *X*, and *H* (Table 2), linear mixes of two default seafloor reflectance spectra as *e*, and image-specific values of Θs and Θv.

Table 2 Default value ranges for forward modeling of R_{rs}.

Variable	*P*	*G*	*X*	*H*
Minimum	0	0	0	0
Maximum	2	0.2	0.1	30

FAB processes an image by inverting this forward model: an Adaptive Look-Up Table (ALUT; Hedley et al., 2009) with approximately 10^6 entries is built and then searched using the Binary Space Partitioning approach (BSP; Hedley et al., 2009) to estimate H for a given R_{rs}. This ALUT search is not applied directly to the R_{rs} values; rather an uncertainty propagation is performed by inverting each R_{rs} spectrum 20 times, each time after adding a random spectrally correlated noise term derived from the covariance matrix of pixels from the deep-water areas (Hedley et al., 2010; Knudby et al., 2016). Water depth at the time of image acquisition is then estimated for each pixel as the mean water depth value from those 20 inversions.

A.4 Vertical referencing and post-processing

The estimated depths for each image are vertically referenced to mean sea level (MSL) by correcting for tidal level at the time of image acquisition using the FES2014 global tide model (Carrere et al., 2015; Lyard et al., 2021) and then referenced to chart datum using a vertical separation model provided by CHS (Robin et al., 2016). CHS uses Lower Low Water, Large Tide (LLWLT), as the vertical datum for most of its coastal charts. An ensemble bathymetry estimate is produced by calculating the median unmasked per-pixel water depth from all images (Ilori & Knudby, 2020) and applying a 3 × 3 mean filter to the result. Finally deep water is masked out from this bathymetry estimate by applying the FAB SDB estimates only to pixels deemed optically shallow (see Section 2.3).

Appendix B: Additional groundings

This appendix contains the case studies for the groundings that occurred prior to 2010, before the availability of Sentinel-2 satellite imagery, and before the availability of free and publicly available Landsat imagery. A review of the Landsat image archives did not yield any satellite imagery in which these shoals were visible prior to the time of each grounding.

https://doi.org/10.58440/ihr-31-2-a13

B.1 TSB Occurrence ID 4287

In the morning of 31 August 1980, a vessel (name unknown) ran aground under power and sustained damage near Gunnar's Island in Baumann Fiord, Nunavut, during clear weather, low wind and smooth sea state. Fig. 9 shows that the chart indicated a sounding of 24 m depth nearby, but did not indicate the presence of the shoal that caused the grounding. The shoal is clearly visible in the satellite image, correctly detected by the shoal product, and FAB SDB indicated its minimum depth as 5.1 m.

B.2 TSB Occurrence ID 9351

On 25 August 1984, *V/L Camsell* ran aground under power and sustained damage near Wiik Island in Storis Passage, eastern Queen Maud Gulf, Nunavut, during clear weather, low wind and smooth sea state. The TSB report indicates that the vessel "proceeded slowly in area of incomplete soundings". Fig. 10 shows that the chart contains several soundings near the shoal that caused the grounding, the nearest of which indicates a depth of 5.2 m. The shoal is clearly visible in the satellite image, correctly detected by the shoal product, and FAB SDB indicated its minimum depth as 1.9 m.

B.3 TSB Occurrence ID 18332

On 24 August 1990, a vessel (name unknown) reported bottom contact while on a Search and Rescue (SAR) in largely uncharted waters near O'Reilly Island south of Storis Passage, eastern Queen Maud Gulf, Nunavut, during clear weather and with light ice cover. Fig. 11 shows that the chart contains a line of soundings just west of the shoal that caused the grounding, but very sparse bathymetric data are charted in the general area of the grounding, which contains many shoals. The shoal that caused the grounding is clearly visible in the satellite image, correctly detected by the shoal product, and FAB SDB indicated its minimum depth as 1.3 m. Note that the TSB reports the grounding location in between several shoals visible in the satellite imagery (Fig. 11); the 1.3 m depth estimated by FAB SDB refers to the shoal located northwest of the reported grounding location.

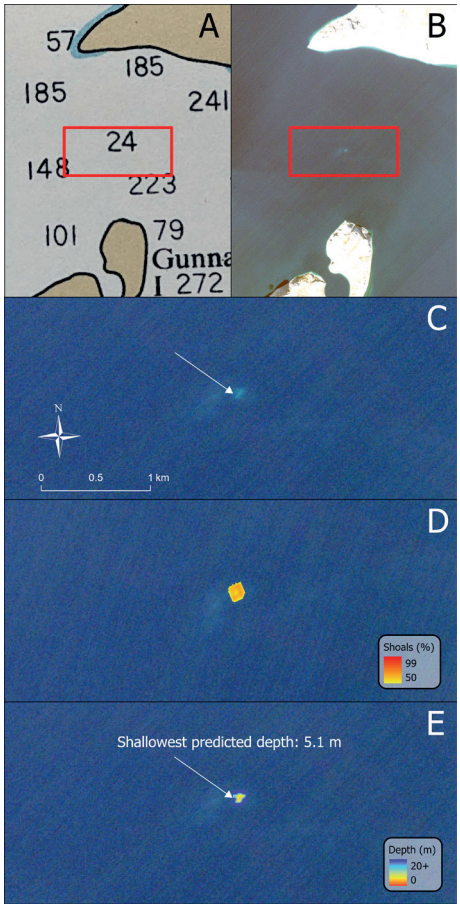


Fig. 9 Comparison of a subset of CHS chart 7590 from 1974, current at the time of grounding (A), a Sentinel-2 satellite image covering the same area (B), a section of the satellite image showing the shoal on which the grounding happened in greater detail (C), the same satellite image with the shoal detection product overlaid (D), and the same satellite image with the FAB SDB product overlaid (E). The extent of the areas shown in (C-E) is indicated by the red rectangles in (A) and (B).

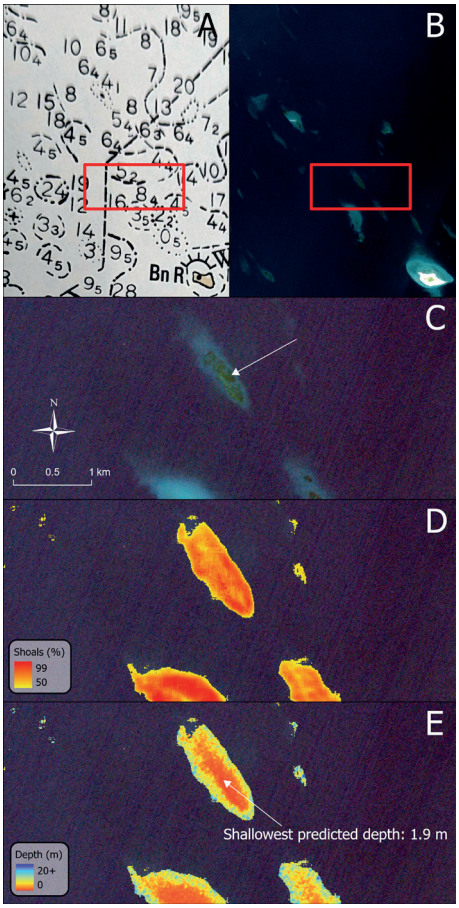


Fig. 10 Comparison of a subset of CHS chart 7083 from 1980, current at the time of grounding (A), a Sentinel-2 satellite image covering the same area (B), a section of the satellite image showing the shoal on which the grounding happened in greater detail (C), the same satellite image with the shoal detection product overlaid (D), and the same satellite image with the FAB SDB product overlaid (E). The extent of the areas shown in (C-E) is indicated by the red rectangles in (A) and (B).

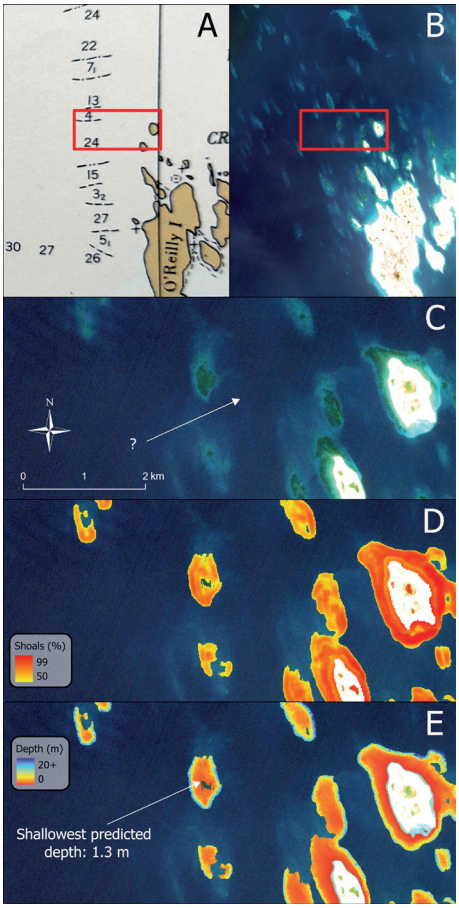


Fig. 11 Comparison of a subset of CHS chart 7083 from 1980, current at the time of grounding (A), a Sentinel-2 satellite image covering the same area (B), a section of the satellite image showing the shoal on which the grounding happened in greater detail (C), the same satellite image with the shoal detection product overlaid (D), and the same satellite image with the FAB SDB product overlaid (E). The extent of the areas shown in (C-E) is indicated by the red rectangles in (A) and (B).

https://doi.org/10.58440/ihr-31-2-a13

Author's biography

Dr. Anders Knudby is a Professor at the University of Ottawa, where he directs the Shallow-Water Earth Observation Laboratory (https://www.shallowwaterlab.com/). He is also the Principal Scientist at Liquid Geomatics Ltd. (https://www.liquidgeomatics.ca/). Having worked with satellite remote sensing for over 25 years, he has broad experience with optical satellite image processing and applied earth observation, and has specific expertise in aquatic remote sensing. He has worked with satellite-derived bathymetry for over a decade. Dr. Knudby is the University of Ottawa's representative with the Canada Ocean Mapping Research and Education Network (COMREN; https://oceanmapping.ca/), and on the steering committee of NetCOLOR, the network of Canadian experts and end-users in the field of aquatic color remote sensing (https://www.netcolor.ca/).



Anders Knudby

https://doi.org/10.58440/ihr-31-2-a13

PEER-REVIEWED ARTICLE

Leveraging robotic total stations and multi-sensor adjustment for accurate multibeam bathymetry

Authors

Lucas Dammert[1], Florian Pöppl[2], Jan Rhomberg-Kauert[1], Tomas Thalmann[1], David Monetti[3], Hans-Berndt Neuner[1] and Gottfried Mandlburger[1]

Abstract

In our study we geo-reference a multibeam echosounder (MBES) data set with a robotic total station (RTS). We use this data to perform a multi-sensor least-squares adjustment that leverages planar correspondences within the MBES data to estimate the trajectory. We compare this to GNSS-based processing and conventional direct geo-referencing. Our results show that the adjustment improves the precision from an interquartile range of 8 cm to 4 cm. Also, the height residuals of the trajectory adjustment can be reduced to 1 mm with RTS-based positioning versus 12 mm with GNSS. When the RTS-based MBES dataset is compared with bathymetric LiDAR, the standard deviation is 4 cm, and the median difference is -1 cm. Our approach offers improved accuracy and precision compared to GNSS-based systems and can also be used in GNSS-challenged environments such as mountainous regions or next to quay walls.

Keywords

bathymetric LiDAR · hydrography · MBES · RTS · trajectory

Resumé

Dans notre étude, nous géoréférençons un ensemble de données provenant d'un sondeur multifaisceaux (MBES) à l'aide d'une station totale robotisée (RTS). Nous utilisons ces données pour effectuer un ajustement multicapteur par la méthode des moindres carrés qui exploite les correspondances planes dans les données MBES afin d'estimer la trajectoire. Nous comparons cette méthode à un traitement se basant sur le GNSS et au géoréférencement direct conventionnel. Nos résultats montrent que l'ajustement améliore la précision, passant d'un intervalle interquartile de 8 cm à 4 cm. De plus, les résidus de hauteur de l'ajustement de la trajectoire peuvent être réduits à 1 mm avec le positionnement basé sur le RTS, contre 12 mm avec le GNSS. Lorsque le jeu de données MBES basé sur le RTS est comparé au LiDAR bathymétrique, l'écart type est de 4 cm et la différence médiane est de -1 cm. Notre approche offre une précision et une exactitude améliorées par rapport aux systèmes qui se basent sur le GNSS et peut également être utilisée dans des environnements difficiles pour le GNSS, tels que les régions montagneuses ou à proximité des murs de quai.

Resumen

En nuestro estudio georreferenciamos un conjunto de datos de una ecosonda multihaz (MBES) con una estación total robótica (RTS). Usamos estos datos para realizar un ajuste multisensor por mínimos cuadrados que aprovecha las correspondencias planares dentro de los datos MBES para estimar la trayectoria. Lo comparamos con el procesamiento basado en GNSS y la georreferenciación directa convencional. Nuestros resultados muestran que el ajuste mejora la precisión desde un rango intercuartil de 8 cm a uno de 4 cm. Además, se pueden reducir los residuos de altura del ajuste de trayectoria a 1 mm con el posicionamiento basado en RTS, frente a los 12 mm con GNSS. Cuando se compara el conjunto de datos MBES basado en RTS con el LiDAR batimétrico, la desviación estándar es de 4 cm, y la mediana de la diferencia es de -1 cm. Nuestro enfoque ofrece una mayor exactitud y precisión en comparación con los sistemas basados en GNSS, y también se puede utilizar en entornos difíciles para GNSS, como regiones montañosas o junto a muros de contención.

✉ Lucas Dammert · lucas.dammert@geo.tuwien.ac.at

[1] TU Wien, Department of Geodesy and Geoinformation, 1040 Vienna, Austria

[2] *RIEGL* Laser Measurement Systems GmbH, 3580 Horn, Austria

[3] Skyability GmbH, GZO-Dienstleistungszentrum 5, 7011 Siegendorf, Austria

https://doi.org/10.58440/ihr-31-2-a14

1 Introduction

Bathymetric mapping of water bodies is a topic that becomes increasingly relevant, e.g. in the context of climate change and environmental research (Mandlburger et al., 2025; Mokhtar et al., 2023). The development of uncrewed surface vehicles (USVs) facilitates the surveying of inland water bodies with Sound Navigation and Ranging (SONAR). Meanwhile, the ranging accuracy of SONAR reaches the cm-level for shallow water depths (Ernstsen et al., 2006; Norbit Subsea, 2021), comparable to bathymetric LiDAR (Light Detection and Ranging) sensors (Mandlburger et al., 2025; RIEGL, 2021). Similar to topographic LiDAR (Dammert et al., 2025b), the geo-referencing of the SONAR data with Real-Time Kinematic (RTK) GNSS accounts for a large part of the error budget of the resulting point cloud. Thus, the GNSS-RTK trajectory can limit the overall accuracy of multi-sensor systems consisting of SONAR, GNSS, and Inertial Measurement Unit (IMU) (Skaloud & Lichti, 2006; Dammert et al., 2025a, 2025b). Consequently, a more accurate trajectory can directly improve the overall accuracy of the multi-sensor system. Especially GNSS-derived heights exhibit low accuracy (Möser et al., 2012; Krzyzek and Kudrys, 2022), while quality standards, such as the International Hydrographic Office's IHO S-44, emphasize vertical accuracy requirements over horizontal accuracy requirements (IHO, 2022). For example, the IHO S-44 Special Order and Exclusive Order require Total Horizontal Uncertainty (THU) values of 2 m and 1 m respectively, while the required Total Vertical Uncertainty (TVU) value is, e.g. at a water depth of 20 m, 0.29 m and 0.17 m respectively. While the magnitude of these values varies depending on the Order and water depth, the general relationship between THU and TVU is apparent: The vertical uncertainty requirement is more strict than the horizontal uncertainty requirement.

This motivates two research questions, which we address in our publication: (i) Can Robotic Total Stations (RTS) improve the geo-referencing accuracy, in particular the height, of bathymetric point clouds compared to GNSS, and what impact does the trajectory estimation strategy have on the precision of our data set? (ii) how consistent is our RTS-based data with Airborne Laser Bathymetry (ALB) data?

Modern RTS allow reliable position measurements of kinematic platforms, with measurement rates of up to 20 Hz and uncertainties below 1 cm (Dammert et al., 2025a). Thus, RTS outperform GNSS-based positioning systems in accuracy (Dammert et al., 2025b) and often also in sampling rate. Measurements of RTS are initially obtained in a local coordinate frame. This usually requires an additional transformation of the measured positions in a global coordinate frame based on reference points which are known in this global coordinate frame. However, the accuracy of transformed RTS measurements is generally higher than that of kinematic GNSS-RTK measurements, as the transformation parameters can be estimated based on more accurate, static GNSS observations (millimetre level with sufficient observation time) compared to kinematic GNSS measurements (low centimetre level) onboard the survey vehicle (Möser et al., 2012). In addition, the RTS allows a higher accuracy of the data set's inner geometry as any transformation uncertainties affect the complete data set in the same way. In general, the application of RTS offers the possibility of reducing the influence of inaccurate trajectory information and results in an improved (bathymetric) point cloud. Although most publications focus on terrestrial platforms (Vaidis et al., 2023; Kälin et al., 2023; Kerekes & Schwieger, 2018) or airborne platforms (Dammert et al., 2025b; Maxim et al., 2017), RTS-based positioning of water surface vehicles has also been subject to discussion (Hesse et al., 2021; Popielarczyk, 2016) but lacks a detailed investigation of its achievable uncertainties and advantages. However, RTS can only measure the position of the multi-sensor system and require IMU data for additionally obtaining the platform's orientation (roll, pitch, and yaw) and, thus, a full 6-Degree-of-Freedom (DoF) trajectory estimation, which consists of three translation and three rotation elements.

In this study, we present a hardware-based approach using RTS measurements to geo-reference a multibeam echosounder (MBES) multi-sensor system. The general idea, already described in Hesse et al. (2021) and in Popielarczyk (2016), is motivated by the high measurement accuracy of RTS and their independence from GNSS multipath effects and signal obstructions, e.g., by quay walls, trees, and mountains or, more recently, signal jamming. Recent studies show that, in particular, the height accuracy of RTS offers superior accuracy compared to GNSS (Dammert et al., 2025b; Popielarczyk, 2016).
The integration of time-synchronized RTS data with the onboard data of the survey vessel, namely IMU and MBES, to obtain 6-DoF trajectories is also a topic of recent research. Classic sensor integration for hydrographic multi-sensor systems employs real-time Kalman Filtering based on position information measured by GNSS and the attitude data of an IMU to estimate the trajectory of the system (Groves, 2013). In post-processing, these trajectories are usually refined by employing Post-Processed Kinematic (PPK) GNSS and replacing the sequential filter by a forward-backward smoother (Gong et al., 2013). The data of the mapping sensor, e.g. MBES, is directly geo-referenced with this trajectory, leading to a geo-referenced 3D point cloud. Recent work on Kalman Filtering for RTS data makes direct use of the polar elements observed by the RTS enabling tight coupling with IMU data and allowing separate evaluation of distance and angle measurements (Thalmann & Neuner, 2024). Although they present the example of a tilt compensating prism pole in their work, the concept can easily be transferred to multi-sensor systems in general.

https://doi.org/10.58440/ihr-31-2-a14

To fully leverage the potential of highly accurate trajectory information by RTS, we use a state-of-the-art software-based approach originating from airborne laser scanning (ALS) which leverages correspondences in the point cloud to optimize the trajectory estimation. For this, we make use of the multi-sensor trajectory estimation approach described by Pöppl et al. (2024) integrating GNSS, IMU, and LiDAR measurements, and adapt it by replacing GNSS with RTS positions and LiDAR data with MBES data.

This multi-sensor adjustment enables, in addition to the estimation of the 6-DoF trajectory and the IMU errors, the reliable estimation of boresight and lever arm parameters based on the complete data set. Therefore, the traditional misalignment calibration using a Patch Test (Gueriot et al., 2000), which usually focusses on (manually) aligning only a small part of the survey data to estimate the angular offsets of the MBES sensor head, is here replaced by a numerical approach that considers the complete available data set. This shift toward numerical, algorithmic methods which make use of the complete data set is further supported by the advantages outlined in Le Deunf et al. (2020) and Skaloud & Lichti (2006). Among the most important advantages are the increased objectivity and repeatability of this automated calibration. In addition, the least-squares-based approach has, due to the use of the complete data set, redundancy and can thus provide a measure of precision.

The resulting highly accurate RTS-based MBES data set allows a reliable comparison of the MBES data to ALB data. When using GNSS-based geo-referencing for both, MBES and ALB, the precise registration of both data sets is only possible when using submerged geometric features. For bathymetric data sets the ground is one such feature and structures with diverse orientations as are e.g. available in airborne laser scans of urban scenarios are lacking. The ground is usually nearly horizontal and thus offers little information for the horizontal registration of the point clouds. With our RTS-based MBES data set, we can register the ALB data without relying on submerged geometric features. To minimize the impact of geo-referencing uncertainties on the ALB data, they are indirectly geo-referenced using reference planes in the study area, from which the plane parameters are known based on RTS measurements.

In our contribution, we present a decentralized multi-sensor system consisting of an RTS and an MBES equipped with an IMU together with an integrated geo-referencing approach and thorough evaluation thereof. The three main contributions are: (i) the integration of MBES and RTS with tight IMU coupling, (ii) the assessment of the resulting geo-referenced point cloud compared to an analogously processed GNSS-based data set, and (iii) the comparison of the former data set to an ALB data set.

Our article is structured as follows: Section 2 focuses on the available data sets and the sensors used for data acquisition. In Section 3, we first describe our approach to sensor fusion of RTS and IMU, and GNSS and IMU, respectively (Section 3.1) and then describe the additional integration of MBES data (Section 3.2). We also elaborate on the error exhibited by not adapting the sound velocity correction when optimizing the trajectory. In Section 4, we evaluate the precision of the resulting point clouds and analyse the impact of different swath widths on the precision. We also compare our RTS-based data set with the GNSS-based data set and compare our RTS-based MBES data set with ALB data. We end with a discussion of our results in Section 5.

2 Data set and study area

Our study is based on a data set acquired at Lake Erlauf (Fig. 1) in Austria. The data set consists of data acquired by MBES and ALB. The MBES data used in our study employ a Norbit Winghead i77h MBES (Norbit Subsea, 2021) and are geo-referenced once with RTS and once with GNSS measurements. The setup used is shown in Fig. 2. In addition to the MBES survey, an ALB survey was conducted, where a topo-bathymetric *RIEGL* VQ-840-G sensor was operated from a helicopter platform.

2.1 Robotic total station

In our study, a Leica GRZ-122 360° prism mounted on the boat is used as a target for a Leica MS60 RTS (Zogg & Maar, 2020), which continuously measures the position of the prism. The Leica MS60 RTS is one of the newest RTS from the manufacturer Leica. It features very reliable target tracking, that can track the prism even during fast movement, e.g., in Dammert et al. 2025 this instrument is used to track an airborne platform at speeds of 10 m/s. Our test showed that the tracking of fast targets is reliably possible until about 800 m, depending on the atmospheric conditions. The target tracking requires an unobscured line-of-sight between RTS and target.

In our study, the boat was moving quite slowly and the only observable reason for failure of the target tracking is the appearance of specular reflection of sunlight at the water surface in the image sensor that guides the target tracking. In those situations, the image sensor cannot distinguish the reflection of its emitted laser signal from the prism from the ambient sunlight. If those interruptions remain reasonably short, they can later be bridged by using the IMU data, similar to handling short GNSS outages. However, if the platform, i.e. USV, moves beyond a threshold (depending on the settings of the RTS) during these interruptions, and without real-time communication between the RTS and the platform, the RTS needs to be manually guided to re-establish the target tracking.

To allow for time-synchronized measurements of the RTS, we employ the approach described in Thalmann & Neuner (2021) and Dammert et al. (2025b). It incorporates a controller unit that requests and receives the measurements of the RTS using

https://doi.org/10.58440/ihr-31-2-a14

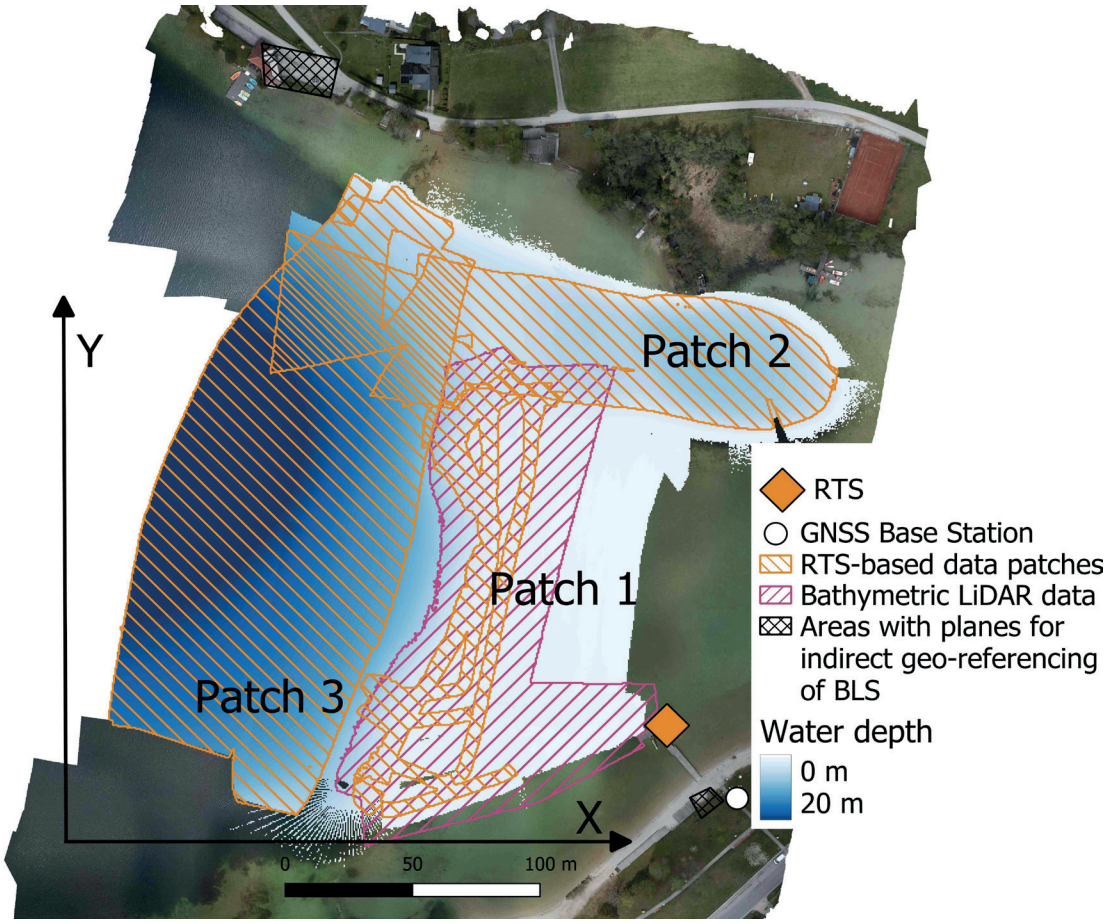


Fig. 1 Map for better spatial orientation within the entire study area, with colour coded water depths from GNSS-based MBES data, extent of MBES data, and ALB data.

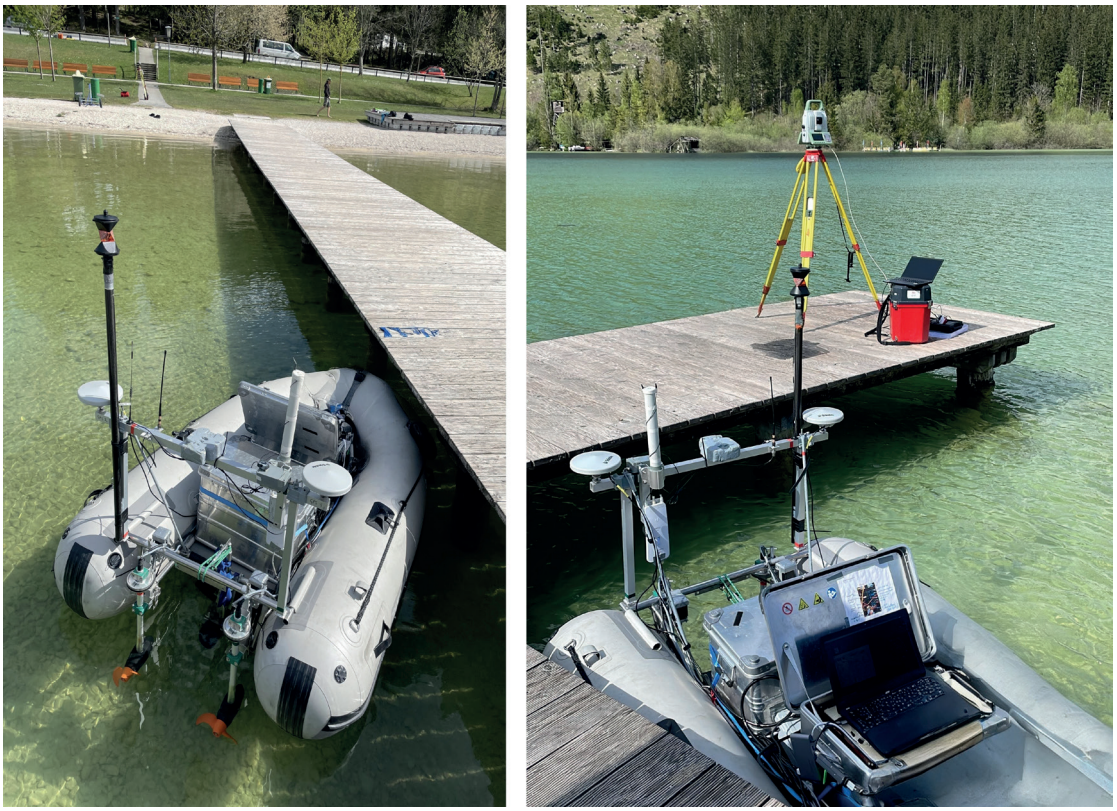


Fig. 2 Setup of the multi-sensor system with RTS, prism, GNSS antennas, and MBES (submerged).

the communication interface of the RTS. For Leica RTS, this interface is called GeoCom. The controller is synchronized with GPS time using a uBlox GNSS receiver that transmits the received NMEA string and the PPS (pulse-per-second) signal to the controller. The temporal offset and drift of the RTS with regard to the synchronized controller are measured in the field, and the exhibited latencies of the setup are calibrated in our laboratory (Thalmann & Neuner, 2021). In general, the RTS has no absolute time information but a relative time system which starts when the instrument is powered on. Thus, the temporal offset yields no meaningful value. However, the drift of this time system, which we identified and corrected for, is about 40 ppm. After application of these parameters, we consider an additional (extrinsic) latency of about 61 ms for the measurements of the Leica MS60.

Our RTS data set is divided into three approximately 10 min to 15 min long patches (Fig. 1). We used the three patches, Patches 1–3, for the evaluation of our data, but due to the limited water depth penetration of the ALB, only one of these patches, Patch 1, is used in Section 4.3 for the comparison between MBES and ALB.

2.2 GNSS

We process the kinematic GNSS data of our hydrographic multi-sensor system in addition to the RTS data and evaluate them in Section 4.2. All GNSS data were acquired in ITRF2020 (Epoch 2015.0), and all heights refer to ellipsoidal heights of the GRS80 ellipsoid. In contrast to the RTS data, the GNSS data was recorded consecutively without interruption, leading to slightly larger coverage. In addition, to transform all data sets into a common coordinate frame, we performed four static GNSS observations of at least 1.5 hours as part of a geodetic network at the study site. During the entire data acquisition, we used the same local base station for all GNSS-related measurements (i.e. MBES and ALB).

2.3 Multibeam echosounder

MBES allow the efficient acquisition of bathymetric data by sending out multiple acoustic beams at different angles. In our study, a NORBIT Winghead i77h is used, allowing the acquisition of 1024 simultaneous beams or measurements in a swath perpendicular to the forward direction of the vessel. The Winghead i77h uses an Applanix Oceanmaster IMU mounted directly on the sensor head of the MBES to record inertial data. In our survey, the beam divergence of the MBES was 0.5° × 0.9° with a point spacing of 2–10 cm across, depending on the water depth, and 12 cm along the trajectory. The range resolution of the sensor is given by the manufacturer with < 10 mm (Norbit Subsea, 2021). We acquired data with a swath width of 180° and limited the swath width to 90° during data processing. In Section 4.1.2 we investigate the effect of different swath widths on the height precision of our data. We use MBES data acquired with QPS Qinsy and pre-processed with QPS Qimera. We rely on the QPS software suite for the sound velocity correction (Section 2.4) and export the initially geo-referenced MBES data together with the used trajectory from the software. From this we transform the data back into the sensor coordinate frame using the OPALS software (Pfeifer et al., 2014) and the transformation parameters used for the initial data acquisition with QPS Qinsy. This data is then used for our processing, e.g. geo-referencing using RTS position information (Section 3).

2.4 Sound velocity data

For processing of the MBES data, we recorded a sound velocity profile (SVP) with a sound velocity profiler in the centre of our study area. The water depth covered by this profile was 14 m and this profile was used for the sound speed correction of the complete data set in the QPS software (Section 2.3). However, we encountered large geometric discrepancies in our data set and found that the surface-near sound velocity, logged by the MBES, varied between 1,444 ms^{-1} to 1,451 ms^{-1} for the surveyed part of Lake Erlauf (Fig. 3). These measurements are taken by a sound velocity profiler, mounted in the MBES sensor head, during the survey which took about two hours. While the surface sound velocity logged by the MBES for the location of our SVP matches the value recorded in our SVP, the surface sound velocities are very heterogeneous. Thus, the measured SVP does not give a good representation of the study area, and the depth measurements at outer beam angles, e.g. greater than 45°, are severely affected by this incorrect modelling of the sound velocity profile. The acquired sound velocity data are visualized in Fig. 3 for better understanding. We see a correlation of the sound velocity with the extent of the underlying water column as the survey took place in the evening, where the shallow parts of the lake were already heated by the sun. In addition, the Lake drains into a small river on the northeastern part, causing potential differences in the water column due to the flow of fresh water. We find that this variation in the surface sound velocity can, when assuming a constant temperature gradient, impact our depth measurements by up to 2 cm. In Section 4.1 we also elaborate on the effect of different swath widths on the quality of the data set.

2.5 Bathymetric LiDAR

For the acquisition of bathymetric LiDAR data, a *RIEGL* VQ840-G was used in our field campaign. The sensor was mounted on a helicopter with a flying altitude of 100 m. For the initial processing of the bathymetric LiDAR data, the manufacturer's processing software, *RIEGL* RiPROCESS, was used. For the refraction correction of the LiDAR data, the OPALS module Snellius was used with 1.3355 as the refractive index of water (Parrish, 2020; Mobley, 2010; Austin & Halikas, 1976).

A local GNSS base station was set up in the study area to allow preliminary geo-referencing of the ALB data. However, to provide the best possible transformation between the ALB data and the RTS, and

https://doi.org/10.58440/ihr-31-2-a14

thus MBES, data we used reference planes to indirectly geo-reference the ALB data by aligning the ALB data with the RTS-measured planes and eliminating the remaining datum shift. The workflow for indirect geo-referencing of the ALB data is illustrated in Fig. 4. In addition to planar features available in the study area, six reference planes were set up in our study area, i.e. wooden saddle roofs of 80 cm by 60 cm. For each of these planes at least eight points were measured with RTS. The estimated accuracy of each point, in our local network, is better than 5 mm and each plane is estimated based on a least-squares plane-fit. By performing point sampling on the estimated plane, we obtain a point cloud representation of the RTS-measured planes. In the ALB data, the points which correspond to the planes were manually selected based on the preliminary geo-referencing of the ALB data. Then, the shift relative to the RTS-measured planes is calculated using an Iterative-Closest-Point algorithm which only estimates a translation vector. Thus, the ALB point cloud can be transformed into the local coordinate frame by applying this translation vector. We refer to this as indirect geo-referencing with RTS. The estimated shift is $(-3.7,0.4,-5.7)^T$ cm, which meets the accuracy expectations of GNSS in mountainous environments. We use the ALB data in Section 4.3 to show that we achieve bias-free data sets by using RTS-based (indirect) geo-referencing for ALB and MBES.

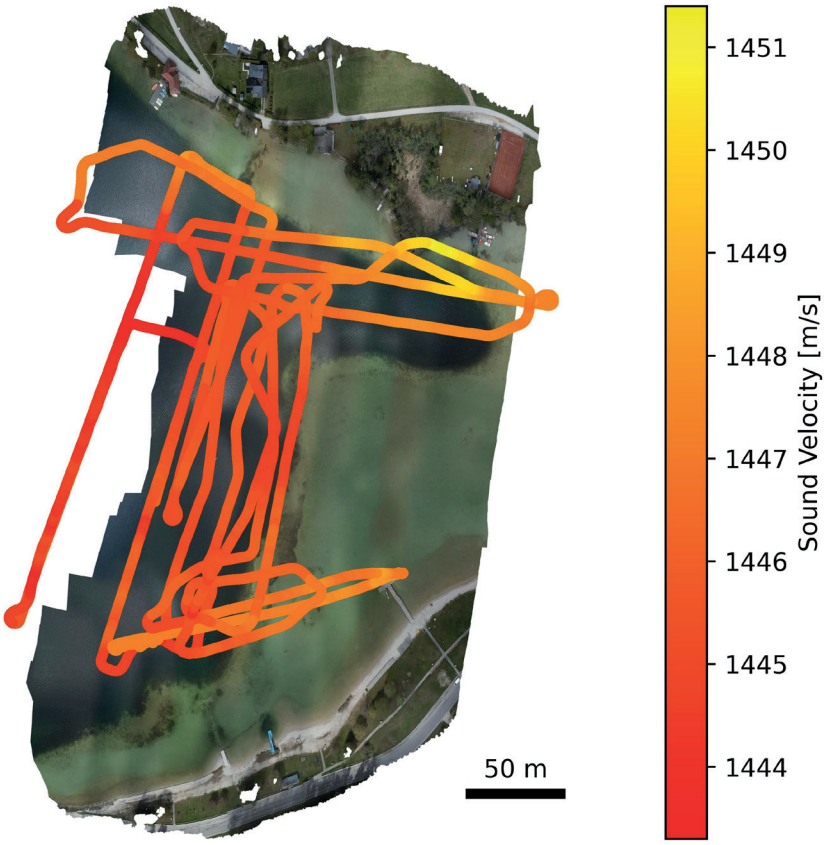


Fig. 3 Map of the measured sound velocities near the water surface by the MBES.

3 Method

In this section, we first describe our two sensor integration approaches for the multi-sensor system consisting of RTS, MBES, and IMU. The first approach uses only the RTS and IMU data for the trajectory estimation, while the second approach additionally leverages planar-correspondences of the MBES data for the trajectory estimation. Afterwards, we investigate the impact of adjustment-based improvements of the trajectory with regard to incorrect sound velocity correction of the MBES data.

In Fig. 5, we show our workflow, together with the software used, to produce the geo-referenced MBES data set. The ALB data are processed entirely in proprietary software and thus omitted from our flowchart.

3.1 Trajectory estimation with RTS/IMU or GNSS/IMU

The determination of platform position and orientation, i.e. trajectory estimation, is framed as a probabilistic parameter estimation problem, where trajectory parameters and mounting calibration are estimated from noisy measurements stemming from the inertial sensors, a positioning sensor (GNSS or RTS), and optionally a mapping sensor (LiDAR or MBES). The use of full-rate IMU measurements and high-fidelity modelling of the trajectory at the same rate leads to a large number of observations and parameters in the adjustment. A recent extension, also employed here, addresses this by introducing an iterated down and upsampling scheme that reduces the number

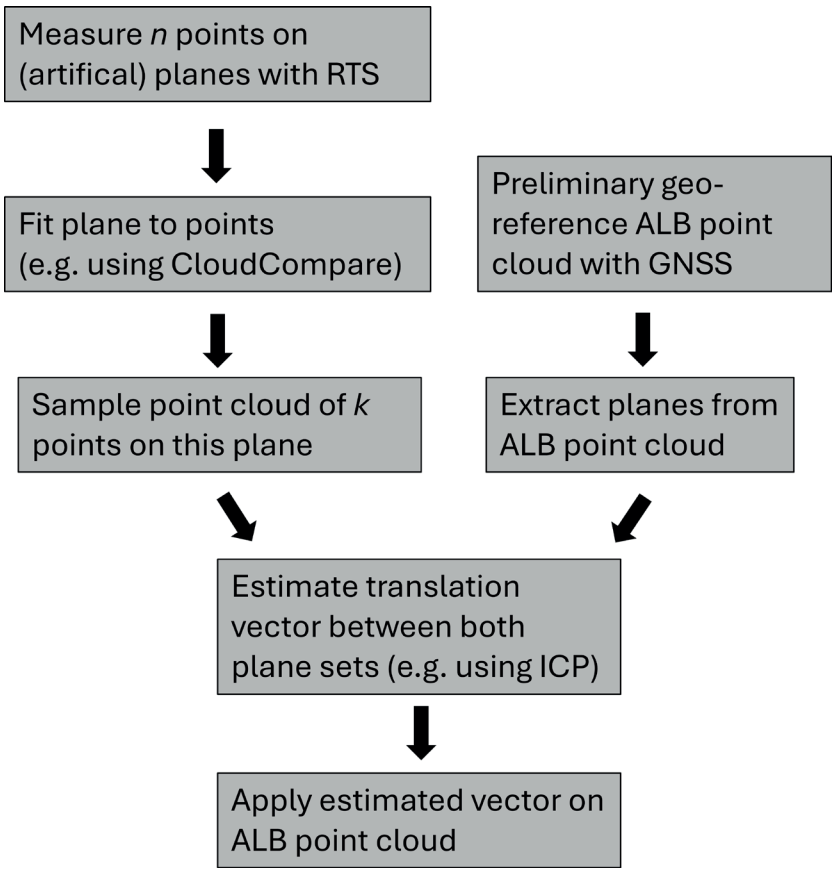


Fig. 4 Flowchart of indirect geo-referencing of ALB data based on RTS measurements.

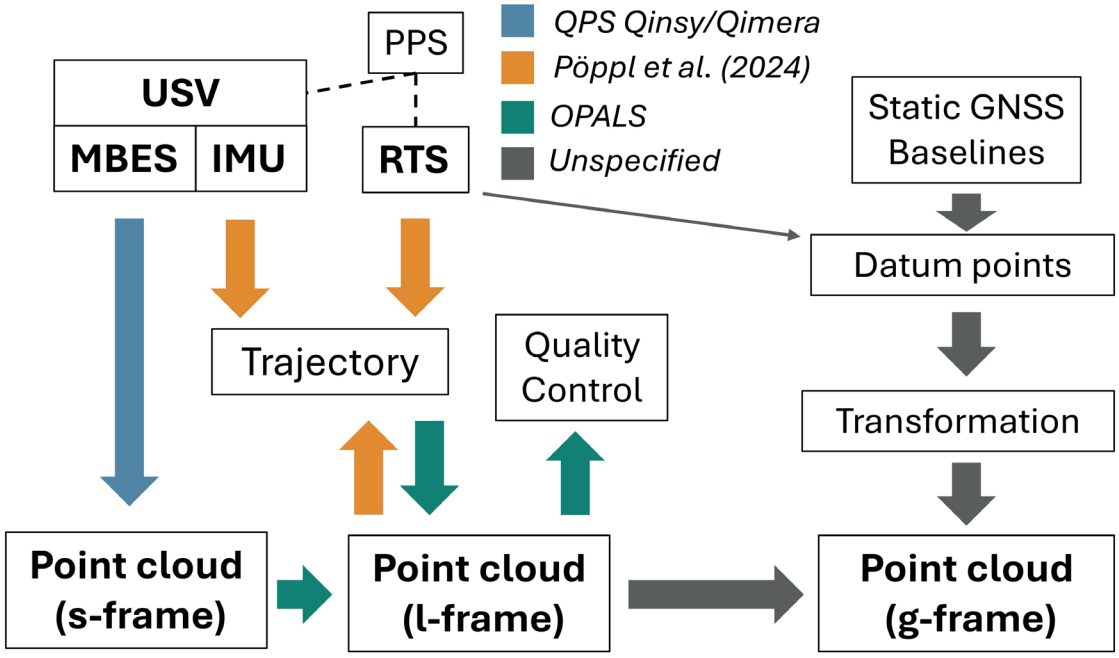


Fig. 5 Flowchart of data processing. Dashed lines represent GNSS timing information (Pulse-Per-Second). S-frame denotes the sensor frame, l-frame the local navigation frame, and g-frame the global frame.

of parameters and measurements in the adjustment while retaining the full frequency spectrum in the trajectory (Pöppl et al., 2025).

The original methodology was designed for ALS applications with GNSS positioning and is here adapted by substituting GNSS with RTS and LiDAR with MBES. Each measurement type is explicitly modelled by Eqs. 1–3. The difference between model and measurement is then minimized in a non-linear least-squares adjustment. All noise is assumed Gaussian with zero-mean, i.e. free from systematic influences, and known covariance. The functional and stochastic models for the inertial measurements remain the same as in previous works (Dammert et al., 2025b; Pöppl et al., 2024). For the GNSS-based direct geo-referencing of the MBES data an adjustment independent from RTS is performed which uses the inertial measurements and GNSS positions. The stochastic model of the GNSS positions is defined by the covariance information derived from the GNSS processing. For our study the GNSS processing yielded estimated standard deviations between 5–15 mm per coordinate component.

Eq. 1 gives the observation equation for the position, where $\tilde{p}$ is the measured position at time t, either from the RTS or from GNSS, $p(t)$ the modelled platform position, $R(t)$ the orientation, and l_a the lever arm of the prism or GNSS antenna respectively. The parameter ϵ_p denotes the gaussian, zero-mean, noise component

$$\tilde{p} = p(t) + R(t) \cdot l_a + \epsilon_p \tag{1}$$

The model of the inertial measurements (Eq. 2) considers the biases $b_f(t)$ and $b_\omega(t)$, the scale factors S_f and S_ω of accelerometers and gyroscopes respectively, which are made up as diag(s_{xf},s_{yf},s_{zf}) and diag($s_{x\omega}$,$s_{y\omega}$,$s_{z\omega}$) respectively, as well as additive white noise ϵ_f and ϵ_ω of the three-axis accelerometer and gyroscope. The obtained measures are the specific force $\tilde{f}$ and the angular velocity $\tilde{\omega}$.

$$\begin{aligned} \tilde{f} &= (I + S_f) \cdot f(t) + b_f(t) + \epsilon_f \\ \tilde{\omega} &= (I + S_\omega) \cdot \omega(t) + b_\omega(t) + \epsilon_\omega \end{aligned} \tag{2}$$

For the trajectory estimation, we use a local north-east-down coordinate system (l-frame), which originates at an arbitrary selected point of our study area. The transformation between this local coordinate system and the global coordinate frame (g-frame), i.e. the reference frame of the GNSS measurements, is estimated from our static GNSS baseline observations. For the RTS-based direct geo-referencing of the MBES data, inertial measurements and RTS positions are included in the adjustment. For simplicity, the measurement equation for RTS is the same as for GNSS, and the integration is done on the coordinate level and not based on polar measurements. For the position measurements derived from the RTS, available as Cartesian coordinates, the covariance information of the RTS is estimated using a Monte-Carlo simulation (Dammert et al., 2025a).

The Euclidean norm of the standard deviation of the horizontal coordinates and the standard deviation of the vertical coordinates based on the simulated distributions of the USV trajectory, derived from RTS measurements, are shown in Fig. 6. Both components show a small variation over the trajectory, ranging less than 1 mm with a median value of 5.6 mm for the Euclidean norm of the horizontal position and 3.7 mm for the vertical position. For the trajectory estimation, we introduce a full covariance

https://doi.org/10.58440/ihr-31-2-a14

matrix extracted from our simulation. Geo-referencing of MBES data is handled using the OPALS software (Pfeifer et al., 2014).

3.2 Trajectory estimation with RTS/IMU/MBES or GNSS/IMU/MBES

In Fig. 7, the general workflow of the multi-sensor adjustment is visualized. A first MBES point cloud is obtained by using a preliminary RTS/IMU trajectory for the geo-referencing. The introduction of MBES data in the adjustment is performed functionally in the same way as for LiDAR data (Pöppl et al., 2024).

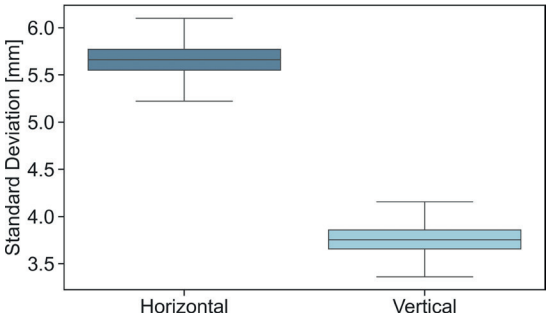


Fig. 6 Simulated standard deviation of all trajectory points measured by RTS. Horizontal refers to the Euclidean norm of the x and y component.

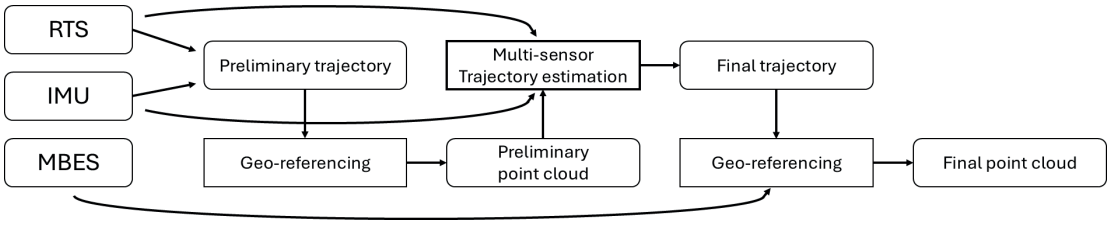


Fig. 7 Trajectory estimation workflow in the multi-sensor trajectory estimation based on RTS, IMU, and MBES.

Based on the preliminary point cloud, the points are sorted in a time-segmented voxel structure (Fig. 8), and a principal component analysis (PCA) is computed for each time segment within each voxel (Fig. 9).

The PCA results are filtered on the basis of planarity conditions, and a best-fit plane, a planar feature or feature plane, is obtained for all remaining voxels.

The corresponding observation Eq. 3 describes the planar features, derived from the MBES point cloud, using the plane centre $\tilde{c}$ and plane normal $\tilde{n}$. Planar features in the same voxel and with similar plane orientation are assumed to correspond to the same planar object. The planar object is then defined by its plane centre c and its plane normal n. Using these definitions, three constraints are defined which describe the normal distance between the planes and the slopes of the object plane with reference to the feature plane axes $\tilde{k}_1$ and $\tilde{k}_2$, which are orthonormal to each other as well as the plane normal n. Here, ϵ_{n,k_1,k_2} denotes again the noise components.

$$
\begin{aligned}
0 &= (c - \tilde{c}) \cdot \tilde{n} + \epsilon_n \\
0 &= \frac{\tilde{n} \cdot \tilde{k}_1}{n \cdot \tilde{n}} + \epsilon_{k_1} \\
0 &= \frac{\tilde{n} \cdot \tilde{k}_2}{n \cdot \tilde{n}} + \epsilon_{k_2}
\end{aligned}
\tag{3}
$$

Planes within the same voxel but different time segments are matched and merged into one object plane (Fig. 9). Correspondences between feature planes and object planes are formed, which in turn are introduced in the adjustment as three observations (Eq. 3): the normal distance and the slope with respect to both plane axes. The object planes are modelled explicitly, with

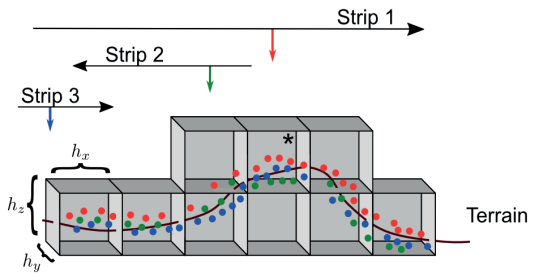


Fig. 8 Points are voxelized and clustered by time (Pöppl et al., 2024).

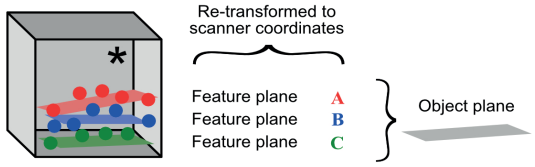


Fig. 9 For each voxel and time-cluster, a PCA is computed. All feature planes belonging to a single cell are combined into a corresponding object plane (Pöppl et al., 2024).

three parameters per plane. Note that the core adjustment is the same as in the previous section, with the only difference that a new class of observations is added: the MBES-derived plane observations. Thus, the multi-sensor adjustment yields an improved trajectory estimate by minimizing discrepancies in the point cloud data. For the stochastic model of the MBES measurements, we rely on the manufacturer's data sheet, which states a range resolution of about 10 mm (Norbit Subsea, 2021). In the absence of any uncertainty specifications, we treat the range solution as standard deviation of the distance

measurement. However, we tested different values for this distance uncertainty and found the effect on the estimated trajectory to be smaller than 2–3 mm and thus neglectable.

Although the measurement equations and the feature extraction and matching process are the same as for the LiDAR case, the extraction parameters have to be adapted to account for the different point density, error characteristics, and environment geometry in MBES data. Voxel size and time segment length must be chosen so that sufficient points are available for a plane-fit within each voxel and time segment. A large voxel size is generally more robust as more points are available for the PCA within each cell but may result in decreased precision as the fidelity of the plane model decreases because the assumption of planarity is generally violated at larger scales. On the other hand, a small voxel size enables better plane approximations for smaller features in the environment geometry but may result in a large amount of spurious correspondences. Additionally, a small voxel size results in a large number of observations in the adjustment and thus require computational effort to solve the adjustment problem or additional filtering of planes. Thus, the choice of voxel size is generally a trade-off between precision of the plane model, robustness of correspondences and computational effort. Here, a voxel size of 1 m and a maximum time segment length of 3 s are used. The time segment was selected to allow the separation of different survey strips, while, as stated in Pöppl et al. (2024), including at least two voxels even for the slower parts of our survey. In the final step of the multi-sensor adjustment, the original MBES data, in the s-frame, is geo-referenced using the final trajectory (Fig. 7).

3.3 Impact of small orientation changes on sound velocity correction

The optimization of bathymetric MBES data holds a key challenge. The range and refraction correction, necessary to compensate for the transition between different layers of the water column, is usually applied to the initial geo-referenced data. After estimation of an improved trajectory, ideally the uncorrected measurements would be used and the sound velocity correction re-computed based on the new trajectory. However, for our study, the uncorrected measurements are not available, therefore, we estimate the error exhibited by not re-computing the sound velocity correction. For our data set, our pre-investigation reveals that the resulting error caused by neglecting this re-application of the refraction correction is smaller than our expected measurement noise. To demonstrate this, we assume a sound velocity profile with constant gradient g, and use the corresponding equation to calculate the measured depth z given in (IHO, 2005):

$$z = \int_0^{\frac{\Delta t}{2}} (c_0 + g \cdot z) \cdot \cos(\theta)\, dt \tag{4}$$

We use the measured surface sound velocity c_0 of 1445 ms^{-1}, and the measured sound velocity gradient g of about 1 s^{-1}. We perform our calculation for beam angles θ between 0° and 75°, and a signal one-way run time $\Delta t/2$ between 4 ms and 16 ms, depending on the beam angle, which corresponds to a constant water depth of approximately 6 m, which is the average water depth of our study area. To assess the impact of an improved boresight misalignment or vessel orientation on the calculated depth value, we vary the beam emission angles by steps of 0.1° between 0° and 0.5°. Improvements of the vessel position do not have a significant impact on the necessary correction of sound velocity. Horizontal shifts of the position have no effect, if we can assume practically identical sound velocity profiles in the range of the position shift, which is usually in the range of a few cm. A vertical shift of the platform would also shift the application point of the sound velocity profile and thus shift the vertical coordinate of the water bottom measurement itself but not affect the applied correction which is relative to the MBES. The estimation of varied beam emission angles is shown in Fig. 10.

We can conclude that, for near-nadir soundings, the effect on the depth measurement is negligible, independent of the variation of the beam angle. However, for soundings with larger beam angles, e.g. a beam angle of 45°, a change in MBES orientation of 0.5° leads to a 6 cm different depth. For small changes of less than 0.1°, the deviation of about 1 cm is smaller and below the measurement uncertainty of the MBES. Thus, the error introduced by relying on the initial sound velocity correction of the acquisition software increases with the beam angle and the variation of the sensor orientation. In general, this means that we need to include the sound velocity correction in the multi-sensor adjustment when processing acoustic data. However, for the study at hand, we see that the rotation deviations between the initial trajectory and the trajectory estimated in the multi-sensor adjustment are below 0.06°. When separating the different angles, the yaw angle shows the largest differences, while the pitch and roll differences are smaller than 0.01°. In addition, the estimated improvement of the boresight misalignment shows values below 0.05°. Consequently, the change of rotations is smaller than 0.11°. Thus, with reference to Fig. 10, we conclude that the error introduced due to not re-applying the sound velocity corrections is smaller than 1 cm, for soundings with beam angles less than 45°, and therefore acceptable.

4 Results

In this Section, we first analyse our RTS-based MBES data set, resulting from the multi-sensor adjustment. In Section 4.1 we analyse the height discrepancies, i.e. precision, in the overlap areas of the MBES data. For this we compare the precision values from direct geo-referencing and after the multi-sensor adjustment and show the improvement achieved through

https://doi.org/10.58440/ihr-31-2-a14

the multi-sensor adjustment. We also focus on the effect of different swath widths on the precision.

Afterwards, in Section 4.2, we compare the RTS-based data set to the GNSS-based data set using the trajectory residuals of the adjustment, the final trajectory differences, and the resulting precision of the RTS- and GNSS-based data sets after direct geo-referencing and after multi-sensor adjustment. These comparisons show the improvement that the RTS-based data set allows compared to the GNSS-based data set. Finally, in Section 4.3, we compare the MBES data, geo-referenced by RTS, to the ALB data, indirectly geo-referenced by RTS with the reference planes. The comparison is performed first in a quantitative comparison that shows the height differences between both data sets. This is followed by a qualitative comparison that focuses on the characteristics of both data sets.

While we can conduct the latter comparison in the l-frame, the comparison of the RTS-based data set to the GNSS-based data set is done in the g-frame. This introduces the transformation uncertainty, based on the static GNSS baselines, in our results.

For all point cloud processing and raster operations described in this Section we use the scientific point cloud processing software OPALS (Pfeifer et al., 2014).

4.1 RTS-based MBES data

For the relative evaluation of the geo-referencing quality of our data sets, we rely on the Quality package of OPALS described in Ressl et al. (2008). We focus on the precision of the directly geo-referenced data set and the data set resulting from the multi-sensor adjustment. For quality evaluation, each strip is converted into a digital elevation model (DEM) using a grid size of 20 cm and moving planes interpolation. The overlaps of all strips, using a swath width of 90°, are determined. Especially in the shallower part of Lake Erlauf we have very little overlap between the different strips in our data set (Fig. 1). Thus, the precision can mostly be calculated for the deeper sections of the study area. After matching the strips into pairs, the DEM of Difference (DoD) model is calculated for each overlapping strip pair.

4.1.1 Precision of RTS-based MBES data

Fig. 11 shows the aggregated differences of the DoDs of all 84 strip pairs after direct geo-referencing using the RTS/IMU integration (left) and after multi-sensor adjustment (right). It shows that the change in the mean value is negligible and that both distributions are roughly cantered around 7 mm to 8 mm. However, the standard deviation of the differences is reduced by 33 % after multi-sensor adjustment. Most importantly, the number of values that exceed the range from -10 cm to 10 cm (orange overflow bins) reduces from 6 % to 2 %. Consequently, the multi-sensor adjusted data set shows the expected outcome of increased precision of the data due to the consideration of the MBES information.

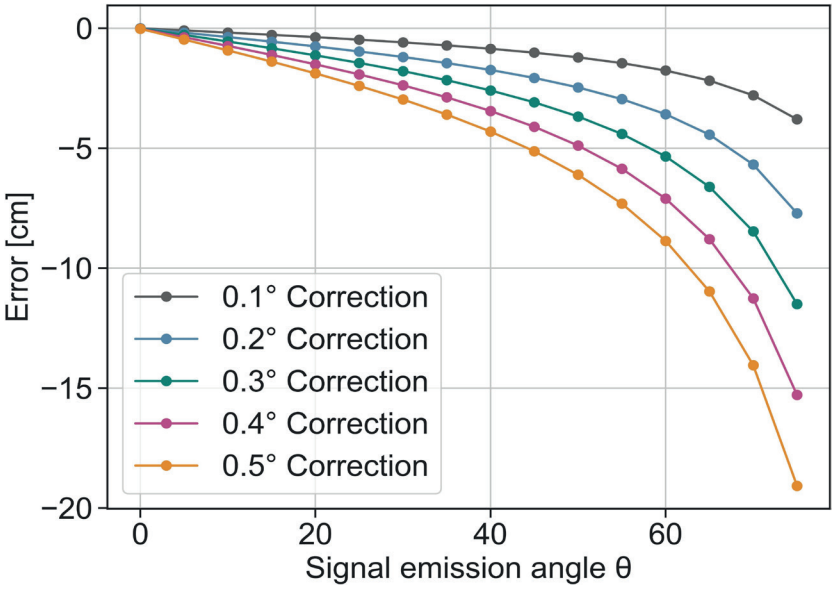


Fig. 10 Effect of varying orientation or beam emission angles on the sound velocity correction.

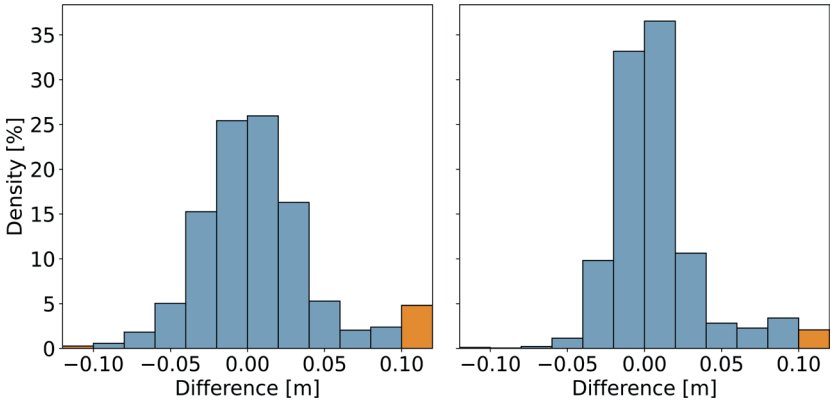


Fig. 11 Histogram of the height precision of RTS/IMU integration (left) and multi-sensor adjustment (right). Orange bins sum up all values that exceed -0.1 or 0.1 m respectively.

4.1.2 Effect of swath width

Due to the larger impacts of orientation uncertainties, sound correction uncertainties and, in general, a longer interaction with the water column, the outer beams of a swath are less accurate than the inner beams. In Lucieer et al. (2016), the increasing uncertainty of multibeam systems with increasing distance to the nadir beam is investigated on the basis of simulations. In (Grzadziel & Waz, 2016), experiments are carried out and a swath width of 90° is recommended as the most effective swath width. Thus, we focus on data with a swath width of 90° but also investigate the effect of different swath widths on the resulting precision. However, we only limit the swath width in post-processing. Fig. 12 shows the distribution of the precision of all strip pairs after the multi-sensor adjustment for increasing swath widths ranging from 30° to 180°. The figure shows the mean and median values, as well as the 60th, 70th, 80th, and 90th percentiles.

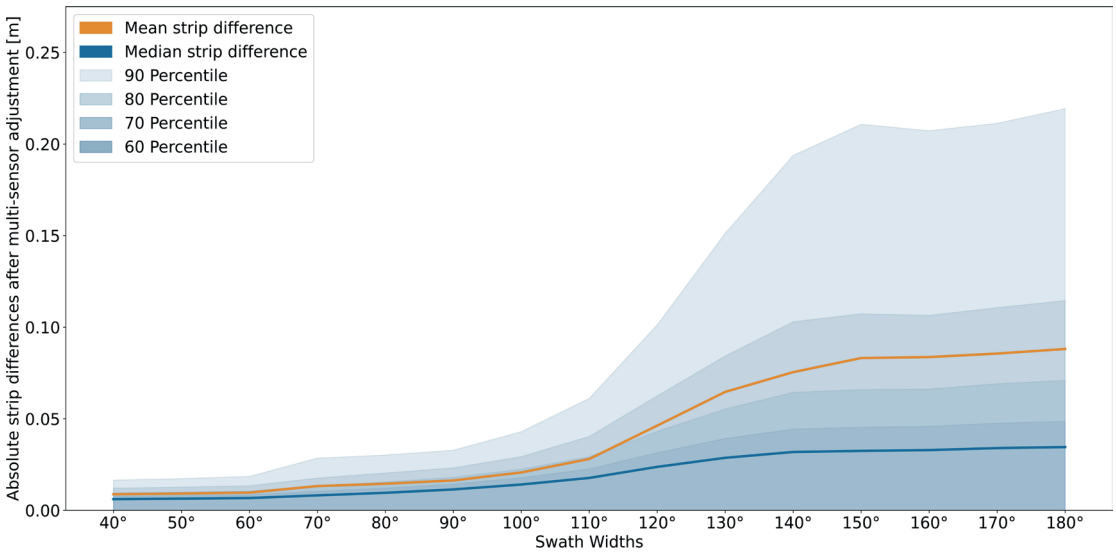


Fig. 12 Distribution of the precision (i.e. height differences) over all strip pairs for increasing swath widths after multi-sensor adjustment.

In general, we see a decrease in the exhibited precision with increasing swath widths. Regarding the best possible precision, we can conclude that a swath width smaller than 60° provides the best results, as the narrow beams of an MBES are generally more accurate than the outer beams. While many factors contribute to the lower accuracy of the outer beams, e.g., footprint size, signal attenuation and incidence angle, the inaccurate SVP used in our study also has, due to the longer interaction time of the signal with the water column, a large effect on the precision for larger swath widths. Consequently, a narrow swath width of 60° might be most useful when performing multibeam surveys aiming at highest accuracy. At a swath width larger than 100° we see an amplification of the increase of the point cloud discrepancies. However, it is worth noting that these particular values depend on the specific data set, e.g., water body, availability of sound velocity data, and MBES system. For our data set it is reasonable to use a swath width of 90° as compromise between accuracy and efficiency / strip overlap as a swath width of 60° would lead to an insufficient overlap for our investigation. These results should be especially interpreted in the context of the different sound velocities shown in Fig. 3, as our imprecise sound velocity profile leads to these large discrepancies in the outer swath areas.

4.2 Comparison of RTS- and GNSS-based data set

In this subsection, we compare our RTS-based data set with the GNSS-based data set for the areas where both are available (Patches 1–3). Both data sets follow the same processing workflow (Sections 3.1 and 3.2) and are thus comparable. We first focus on the exhibited residuals of the (multi-sensor) trajectory estimation process and then compare the resulting trajectories directly. Afterwards, we compare the precision exhibited by both data sets.

4.2.1 Residuals of trajectory estimation

Fig. 13 shows the residuals of the trajectory estimation as part of the multi-sensor adjustment. When analysing those residuals, we see that the Euclidean norm of the horizontal trajectory component of the RTS- and GNSS-based data is quite similar with median values of 2 mm and 4 mm, respectively. The interquartile range (IQR) shows a spread of 2 mm (RTS) and 3 mm (GNSS). As the horizontal component is given as the Euclidean norm of the along- and across-trajectory component, a median value of zero is not expected. The vertical component exhibits a strong difference for both data sets. While the RTS data show a median of 0 mm with an IQR of less than 1 mm, the GNSS data show a median of 0 mm with an IQR of 12 mm. Thus, while the horizontal residuals are quite similar with the RTS showing slightly smaller residuals than the GNSS, the vertical residuals are more than ten times smaller for the RTS data set. It should be noted that, while the residuals show the agreement between the three subsystems (RTS or GNSS, IMU, and MBES) considered in the multi-sensor adjustment, they do not reflect the absolute accuracy of the trajectory, because the absolute positioning system (RTS or GNSS) has no redundancy.

4.2.2 Trajectory comparison of RTS- and GNSS-based trajectory estimation

Fig. 14 shows the horizontal (Euclidean distance) and vertical discrepancies of the trajectory estimates based on RTS and GNSS of the position part of the trajectory for the data Patch 3. For the calculation of the absolute trajectory errors, we use the trajectory evaluation package *trajectopy* (Tombrink et al., 2024). The horizontal differences (Euclidean distance) show strongly varying values that range up to 8 cm with a mean value of about 3 cm. However, the average deviations of x and y are close to zero. The vertical

https://doi.org/10.58440/ihr-31-2-a14

component shows a similar strong variation with an overall upward trend but has a mean value close to zero. Based on the adjustment residuals and theoretical knowledge of the height accuracy of both RTS and GNSS measurements, we can allocate the vertical discrepancies largely to the accuracy of the GNSS measurement.

4.2.3 Comparison of precision

We also compare the precision for the RTS-based data (Section 4.1.1) with the differences obtained from the analogue GNSS processing. These results are shown in Fig. 15 for both steps, RTS/IMU-based direct geo-referencing and multi-sensor adjustment. There, the precision over all 84 evaluated strip pairs is aggregated and shown as box plots. First of all, we see a higher variation of the precision for the directly geo-referenced data sets, which is in agreement with Fig. 11. For those directly geo-referenced data sets, we see a larger variation for the GNSS data than for the RTS data. Regarding the IQR, GNSS achieves a value of 12 cm and RTS of 8 cm. After performing the multi-sensor adjustment, both distributions are similar with an IQR of 4 cm, showing the large weight of the MBES observations in the adjustment process. Note that the precision does only show the relative agreement between the survey strips, and the similar IQR values of GNSS and RTS after the multi-sensor adjustment does not mean that both data sets have a similar accuracy. However, we observe that the GNSS-based data set shows approximately 50 % worse precision than the RTS-based data set for directly geo-referenced data sets.

4.3 Differences between MBES and bathymetric LiDAR

For comparison between MBES and ALB, we use the final MBES data sets resulting from multi-sensor adjustment based on RTS. Due to the adjustment, the effects of lever arm and boresight misalignment errors are minimized, and, due to the RTS-based geo-referencing of the MBES data and indirect geo-referencing of the ALB data with reference planes, the impact of geo-referencing uncertainty is reduced for both data sets. This approach enables a comparison of both techniques that focusses on the sensors (MBES and ALB) themselves and minimizes the impact of the geo-referencing uncertainty. Due to the lack of reference data in our study, we use this comparison as quality assessment. For our comparison, we use the overlap region of the RTS-based MBES and ALB data (Fig. 1, Patch 1).

It is important to note that, in our study, neither of the techniques can be regarded as reference for the other as we assume both techniques to have similar accuracy values. Consequently, this comparison shows the agreement of both techniques and should serve as motivation for future work where, (i) both techniques can be compared based on reliable reference data or (ii) the integration of MBES and ALB data can be improved by use of the hardware- and software-based approaches presented in our study.

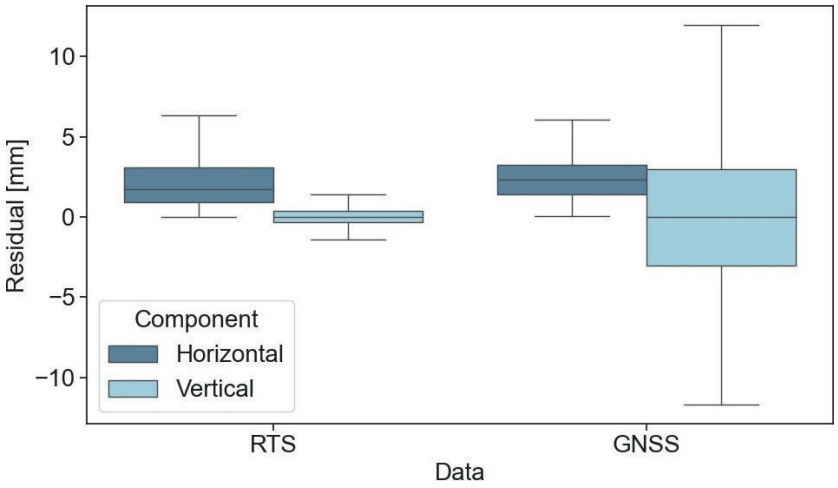


Fig. 13 Residuals of the multi-sensor adjustment combined over all RTS data patches.

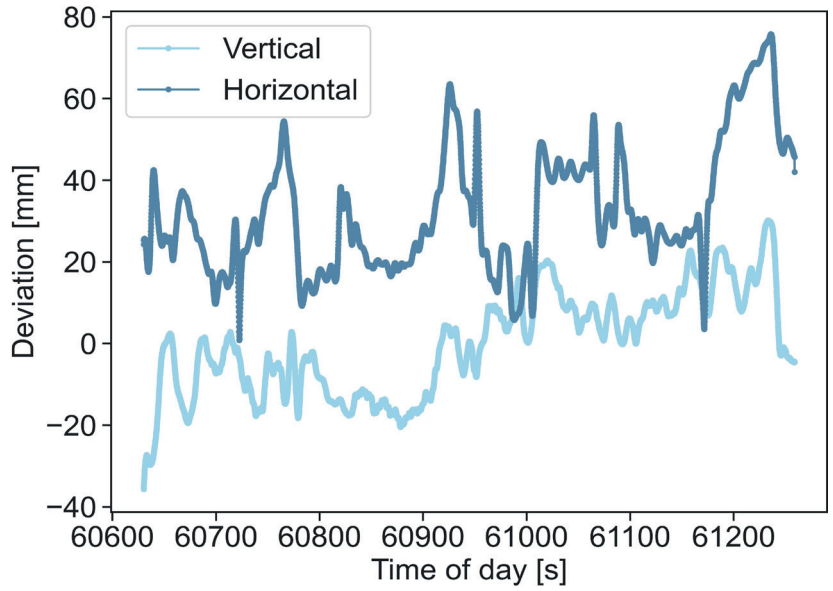


Fig. 14 Discrepancies between RTS- and GNSS-based trajectory estimates.

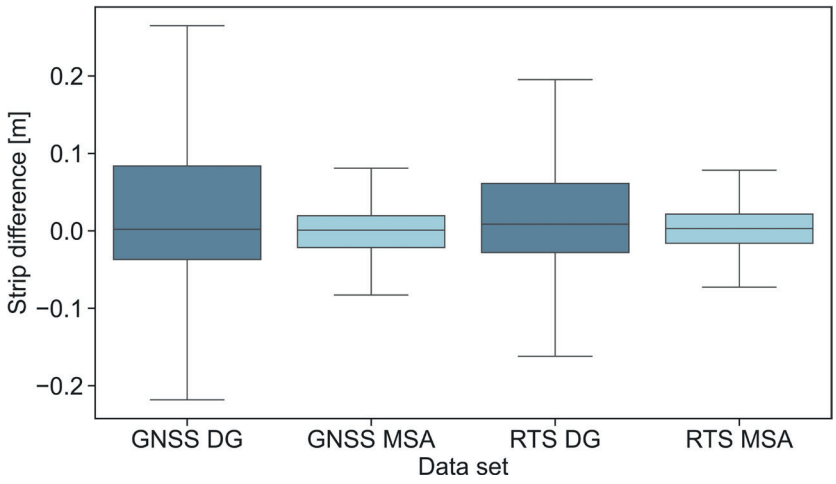


Fig. 15 Precision of all strip pairs for RTS and GNSS data sets, after direct geo-referencing (DG), and after multi-sensor adjustment (MSA).

4.3.1 Quantitative comparison

We compute a DoD grid model for the comparison of both data sets. Both DEMs that serve as input, represent the combined point clouds of the MBES and ALB data, respectively, considering all acquired strips. For the gridding of the point clouds, we use moving planes interpolation and a grid size of 0.5 m. We found the grid size of 0.5 m to allow for robust results that show an acceptable noise level while still giving a high spatial resolution. To allow a reliable comparison of both DEMs, we exclude cells with a point density lower than 15 points per m², which corresponds to the 2.5th percentile of the point density of the ALB data, for the ALB and MBES data. We do this to exclude areas which show incomplete coverage, e.g. because they are too deep for the ALB to penetrate.

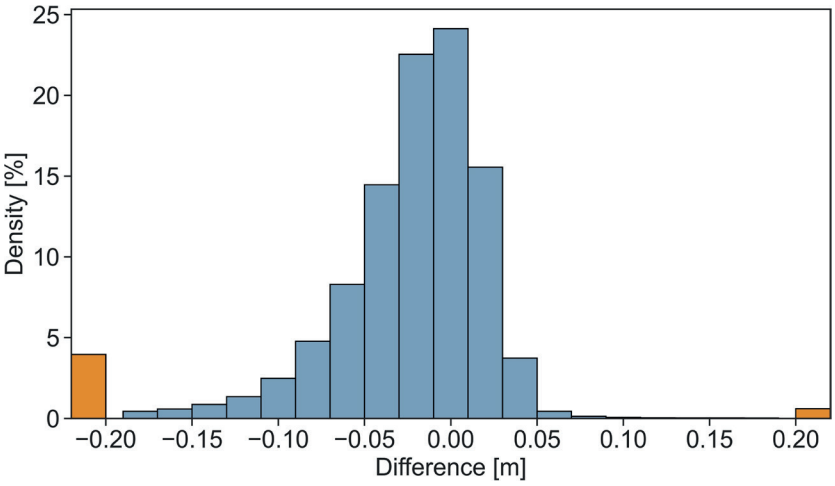


Fig. 16 Histogram of the computed differences between RTS-based MBES data and ALB. Orange bins sum up all values that exceed -0.2 or 0.2 m, respectively.

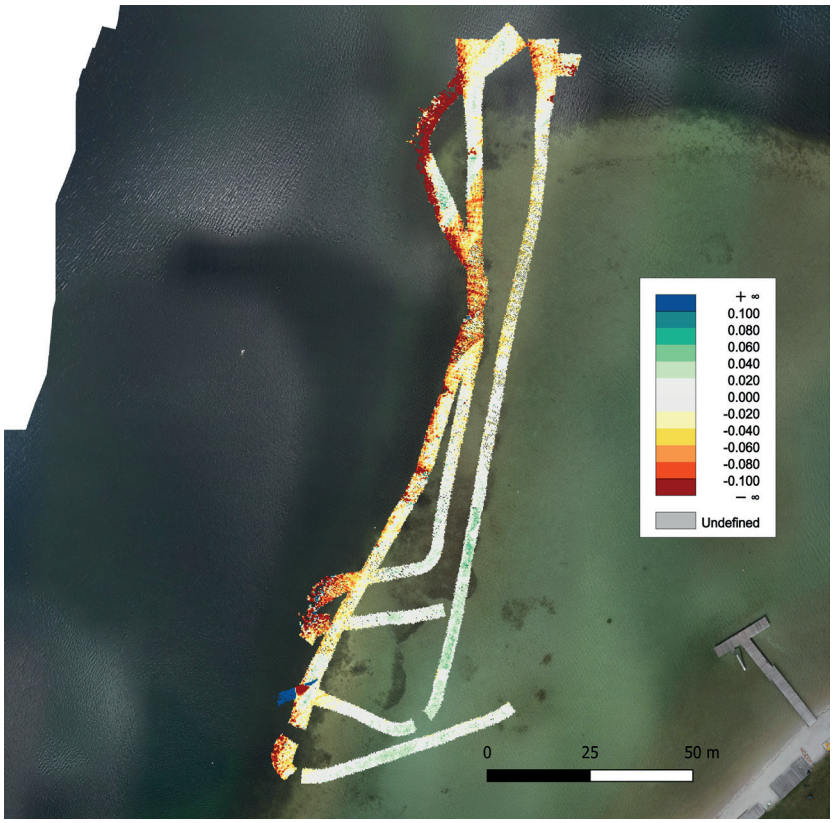


Fig. 17 Map of the differences between RTS-based MBES data and ALB.

Figs. 16 and 17 show the differences between the ALB and the MBES data set as a histogram and as a map visualization. The distribution of the differences shows a slightly asymmetrical shape with a negative centre and a mean value of -2.1 cm. The median value is -1.4 cm and the standard deviation is 4 cm. The asymmetric shape of the histogram is also represented by the percentiles, which show that 75 % of the differences are smaller than 5 mm and 95 % are smaller than 2.5 cm. We clearly see that the ALB measures lower height values than the MBES. The orange bars in the histogram are outlier boxes, which aggregate all values lower or higher than the value range, i.e. -20 cm and 20 cm. Therefore, the boxes show the share of outlier measurements, which is about 3 %. Together with the map visualization (Fig. 17), we see that outliers occur mainly in the deeper areas of the study site, where the extraction of water bottom points from ALB is hardly possible due to signal attenuation. This fact is then seen in the higher measurement noise. In general, the ALB was able to extract bottom points until 10 m water depth. Additionally, in the central part we see an artifact of negative difference, coloured red, which presumably originates from a single ALB strip being slightly lower than the remaining flight block. Finding the reason for the asymmetry of the differences between ALB and MBES is beyond the scope of this article and will be addressed in our future work. However, possible reasons can be the refraction coefficient, signal processing of the ALB waveforms, or an undetected rotation between the ALB and MBES data.

4.3.2 Qualitative comparison

We also take a closer look at the key differences between the MBES and ALB data sets. The MBES has a smaller footprint and a higher point density resulting in a denser point cloud. For example, the MBES footprint is about 8 cm × 14 cm at 10 m water depth (beam divergence of 0.5° × 0.9°) and the ALB footprint is approximately 20 cm × 20 cm (beam divergence of 0.115°). This is visualized in Fig. 18 (left), where the dense swath of the MBES (blue) and the comparably sparse lines of the ALB (red) are visible. In addition, the larger line spacing of the LiDAR can be seen. However, when considering the platform velocities, MBES about 1 ms^{-1} and ALB about 15 ms^{-1}, the ALB actually exhibits temporally closer lines than the MBES. In Fig. 18 (right), the vertical spread of one strip of MBES and ALB data is shown for a vertical section with a width of 2 m. Although the MBES data are much denser than the ALB data, we see that the vertical spread of the ALB is comparable to or even smaller than the spread of the MBES data. However, similar to Fig. 16, we observe a tendency of the ALB data to be lower than the MBES data.

https://doi.org/10.58440/ihr-31-2-a14

5 Discussion

When discussing the use of RTS for trajectory estimation of kinematic multi-sensor systems it is important to keep the limitations in mind. First of all, the RTS relies on an unobscured line-of-sight towards the target. Secondly, the range of the automated target tracking is limited. The threshold value depends on the weather, e.g., rain, mist or certain sunlight conditions reduce the achievable range, and on the prism. In our tests, we found a range of 800 m to be a conservative and reliable estimate for the range threshold when tracking fast moving targets, e.g., airborne drones. In the context of bathymetry, where speeds are often lower than for airborne platforms, the target tracking, at least of the modern RTS models, is very robust. The lower speed also allows to re-establish the target tracking on-the-fly if the target tracking fails, e.g. due to a line-of-sight interruption. In terms of trajectory estimation, those short measurement gaps can be regarded similar to GNSS outages that appear e.g. under bridges. Those short gaps can easily be bridged by the relative position information of the IMU. The limited range of RTS restricts our proposed RTS-based trajectory estimation to inland waters, harbours, and shorelines. However, these are often the areas where highest accuracy is required and GNSS signal obstructions usually occur, e.g. by quay walls.

In general, our contribution shows two separate approaches to improve the overall quality of hydrographic data: (i) the application of RTS for more accurate trajectory measurements, which is a hardware-based approach, and (ii) the multi-sensor adjustment making use of all available information during the trajectory estimation, which is a software-based approach. While (i) is limited to inland and coastal waters that allow the tracking and measurement of the target platform from a shore-based RTS, (ii) is applicable for inland and maritime waters. The main limitations for (i) are thus the limited range of about 800 m and the requirement to be able to set up an RTS. On the other hand, (ii) requires position (RTS or GNSS) and IMU data together with an MBES or LiDAR point cloud and stochastic information for all input data. Thus, it is applicable on most bathymetric data sets. However, (i) allows accurate trajectory information with accuracies in the sub-cm level leading to a potentially very accurate bathymetric point cloud. The multi-sensor adjustment (ii) is limited by its input data. Thus, without accurate trajectory or reference data the resulting point cloud might be precise, i.e. show little discrepancies, but have a lower accuracy. While (i) and (ii) complement each other very well, both approaches can be used independently to improve the quality of bathymetric data.

For our data set, the multi-sensor adjustment excels at creating consistent data. We see a decrease in the strip differences by 33 % when processing our data set with the multi-sensor adjustment, since the point cloud information is used to minimize the discrepancies. The results highlight the importance of integrated, multi-sensor processing strategies in obtaining high-precision data sets. However, such processing strategies are unable to detect systematic shifts of the data, e.g. due to geo-referencing uncertainties, without the use of additional information such as reference geometries. Thus, it works well alongside sensors such as RTS, which are used to determine accurate, absolute trajectories, to obtain a data set with high precision and accuracy.

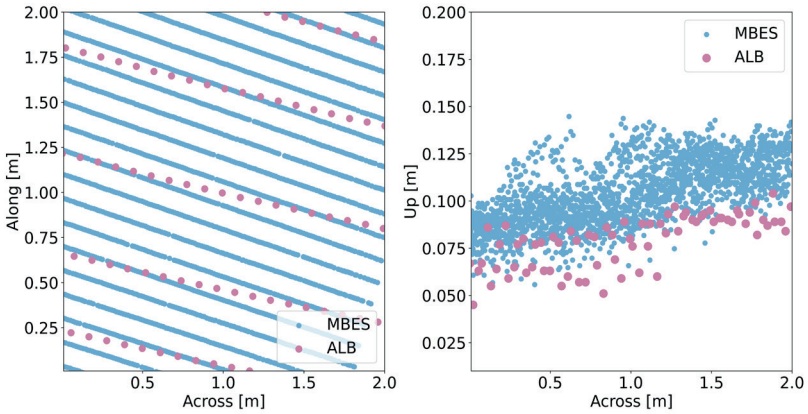


Fig. 18 Characteristics of MBES and ALB: Horizontal plane (left), vertical cross section (right).

However, while for data on dry land, the multi-sensor adjustment leverages the abundance of different exhibitions of man-made features or planar objects in the point cloud, bathymetric point clouds usually show less distinct features. With the correct parametrization, the planes can be fitted to the water bottom. These planes are mostly horizontal, which does not contribute much regarding the horizontal position of the point cloud. Thus, point-cloud-correspondence-driven approaches can be expected to perform worse for bathymetric point clouds than for topographic point clouds due to the less diverse exposition of planar features. This is one of the reasons, why our study shows the large value of employing both, RTS-based trajectory estimation and the multi-sensor adjustment of the entire data, to generate a data set with high precision and accuracy.

For the RTS-based data set, the residuals of the multi-sensor trajectory adjustment show only slightly better values for the horizontal component compared to the GNSS-based data set. In contrast, the vertical residuals are more than 10-times smaller for the RTS data. This shows overall, the superior accuracy of the RTS-based trajectory compared to the GNSS-based trajectory.

However, the residuals only show relative discrepancies between the measurements of RTS or GNSS, IMU, and MBES. The horizontal coordinates of the RTS and GNSS trajectories, on the other hand, show much larger deviations. Although the horizontal residuals of the multi-sensor adjustment suggest only low discrepancies between the RTS and GNSS-based trajectories, the direct comparison of the RTS and GNSS-based trajectories reveal horizontal and vertical discrepancies at the cm-level. However, without

a reliable reference, those discrepancies cannot be attributed to either of the sensor systems. But the known uncertainty information of GNSS and RTS suggests that the main influence comes from GNSS. Thus, the small horizontal residuals of GNSS can be explained by the high temporal correlation of systematic GNSS errors (Luo et al., 2019; Wang et al., 2022) that are not detected in the trajectory estimation but cause a systematic absolute displacement of the point cloud. This systematic displacement can then be seen in comparison with the RTS data. However, for detailed investigations of the accuracy of GNSS and RTS, topographic airborne LiDAR should be preferred (Dammert et al., 2025b) as the uncertainty introduced by the water column is avoided and reliable reference data are easier to acquire. A detailed discussion of those influences is outside the scope of this work. However, it is worth mentioning that the simulated standard deviations for RTS (Section 3.1) fit well with the residuals shown for the multi-sensor adjustment based on RTS.

By analysing the precision of RTS- and GNSS-based data sets, we can see that RTS-based direct geo-referencing leads to better precision of the multi-sensor system. However, in terms of precision, the added value of the RTS is reduced when data of the mapping sensor or correspondences of the point cloud are included in a multi-sensor adjustment. We assume that the strong similarity between both adjusted data sets (RTS- and GNSS-based) is largely due to the range precision of the MBES. With a ranging resolution of 10 mm (Norbit Subsea, 2021), which we treat as standard deviation due to the lack of any information on the systems accuracy, the MBES range measurements receive a high weight in the least-squares adjustment, leading to a large dependence of the trajectory on the MBES data and a comparably lower weight of the RTS or GNSS data. While we generally assume the RTS positions to have a standard deviation of 3–6 mm, the GNSS positions receive estimated standard deviations from the GNSS processing software. For this study these values range between 5–15 mm. We are aware that these values can be very optimistic, but we do not want to change these values by applying an arbitrary factor to it.

The differences between MBES and ALB show a slight underestimation of the bathymetric height by the ALB relative to the MBES data. Due to the asymmetrical shape of the distribution of differences (Fig. 16) and its median value of -1.4 cm, we can state that there is no height bias, that exceeds the measurement noise of either system, between both data sets. However, the systematic overestimation of the water depth by the ALB data set compared to MBES can originate from various sources. Possible reasons include the different sediment penetration characteristics of both systems (Gaida et al., 2020), the signal processing strategy of the ALB software, a poorly determined water surface (Mandlburger et al., 2013), and an imprecise refraction coefficient used for ALB data processing. We used a refraction coefficient of 1.3355 based on the work of Parrish (2020); Mobley (2010); Austin & Halikas (1976) and observations of water parameters on site. However, the differences between ALB and MBES might as well originate from the processing of the MBES data. Nevertheless, we see that, by applying profound (indirect) geo-referencing approaches such as RTS, the standard deviation of the differences between both systems range is about 4 cm. This magnitude motivates further investigation of the uncertainty budget of the sensors (MBES and ALB). Such an investigation also requires adequate ground truth, a topic which we will address in future work. In our future work we also plan to address the seamless integration of MBES and ALB based on RTS, as well as based on a combined multi-sensor adjustment that leverages point cloud correspondences between MBES and ALB data to create a consistent data set that shows minimized discrepancies in the transition zones between MBES and ALB.

6 Conclusion

In our contribution, we present a workflow for RTS-based geo-referencing of a hydrographic multi-sensor system as basis for a multi-sensor-adjustment-based trajectory estimation that leverages correspondences in the bathymetric point cloud. We present a data set acquired at Lake Erlauf consisting of MBES and ALB data. We use this data set to demonstrate our geo-referencing strategy as well as our quality assessment workflow, based on height discrepancies in the point cloud as measure of the precision. We also investigate the impact of varying swath widths on the precision. The dominant decrease in the precision is seen for swath widths of more than 100°, which allows us to use a swath width of 90° and thus make use of a good overlap in our data. However, we assume that this sharp decrease in precision at larger swath widths is mainly caused by the heterogeneous sound velocity at our study site. The quality of the multi-sensor system's trajectory estimation is evaluated by comparing the residuals and differences of the estimated trajectories for RTS- and GNSS-based processing. Additionally, the influence of the presented trajectory estimations based on deviations in the MBES point cloud is analysed. We also compare the resulting MBES point cloud with the ALB data, where we rely on reference planes to precisely register the ALB point cloud data on the RTS measurements and thus the RTS-based MBES data.

The comparison of RTS- and GNSS-based processing show that using RTS enables more accurate geo-referencing, yielding about ten times smaller height residuals in the estimation process. Also, the GNSS-based data show about 50 % worse precision in the resulting point cloud compared to our RTS-based data. However, by leveraging the MBES data in the trajectory estimation in

https://doi.org/10.58440/ihr-31-2-a14

our multi-sensor adjustment, the precision increases to the same level for both geo-referencing sensors. This large improvement can be contributed to the high weight of the MBES observation in the adjustment process. By comparing the resulting point cloud to the ALB data, we can show that the RTS-based data set exhibits a close-to-zero-centred distribution of vertical differences which shows no remaining significant bias.

By introducing accurate geo-referencing of MBES data based on RTS, we lay the basis for improving the integration of MBES and ALB data. The minimization of the geo-referencing errors allows not only the integration but also the comparison of both sensor techniques to one another but also relative to bathymetric reference data. In addition, the accurate registration of both data sets allows the improved combination of both techniques for seamless data transition and connection in shallow water regions.

Acknowledgments

The authors thank BOKU University and VERBUND AG, who performed the MBES data acquisition, *RIEGL* Laser Measurement Systems, who acquired the bathymetric LiDAR data, MacArtney Germany and QPS, who provided a license for QPS Qimera to allow data processing of the MBES data, and lastly Wolfang Sombrowski from MacArtney Germany for counseling during data processing. This research was conducted within the TrackDrone project (Grant No. 895310) funded by the Austrian Research Promotion Agency (FFG).

References

Austin, R. W. and Halikas, G. (1976). *The index of refraction of seawater* [Technical Report]. UC San Diego: Scripps Institution of Oceanography. https://escholarship.org/uc/item/8px2019m (last accessed 20 July 2025).

Dammert, L., Thalmann, T., Monetti, D., Neuner, H. and Mandlburger, G. (2025a). Numerical simulation and sensitivity analysis of UAS trajectory determination with robotic total stations. *Survey Review*, pp. 1–17. https://doi.org/10.1080/00396265.2025.2517540

Dammert, L., Thalmann, T., Pöppl, F., Monetti, D., Neuner, H.-B. and Mandlburger, G. (2025b). High-precision geo-referencing of UAS data with robotic total stations. *ISPRS Annals of the Photogrammetry, Remote Sensing and Spatial Information Sciences, X-G-2025*, pp. 213–220. https://doi.org/10.5194/isprs-annals-X-G-2025-213-2025

Ernstsen, V. B., Noormets, R., Hebbeln, D., Bartholomä, A. and Flemming, B. W. (2006). Precision of high-resolution multibeam echo sounding coupled with high-accuracy positioning in a shallow water coastal environment. *Geo-Marine Letters 26*(3), pp. 141–149. https://doi.org/10.1007/s00367-006-0025-3

Gaida T. C., Mohammadloo T. H., Snellen M. and Simons D. G. (2020). Mapping the Seabed and Shallow Subsurface with Multi-Frequency Multibeam Echosounders. *Remote Sensing 12*(1):52. https://doi.org/10.3390/rs12010052

Gong, X., Zhang, R. and Fang, J. (2013). Application of unscented R-T-S smoothing on INS/GPS integration system post processing for airborne earth observation. *Measurement, 46*(3), pp. 1074–1083. https://doi.org/10.1016/j.measurement.2012.11.028

Groves, P. (2013). *Principles of GNSS, inertial, and multisensor integrated navigation systems*. Artech house. Norwood, MA, USA.

Grzadziel, A. and Waz, M. (2016). Estimation of effective swath width for dual-head MBES. *Annual of Navigation, 23*, pp. 173–183. https://doi.org/10.1515/aon-2016-0012

Gueriot, D., Chedru, J., Daniel, S. and Maillard, E. (2000). The patch test: a comprehensive calibration tool for multibeam echosounders. *Proceedings of OCEANS 2000 MTS/IEEE Conference and Exhibition, Cat. No.00CH37158*, Providence, RI, USA, 3, pp. 1655–1661. https://doi.org/10.1109/OCEANS.2000.882178

Hesse, C., Holste, K., Neumann, I., Esser, R. and Geist, M. (2021). 3D HydroMapper–Ein innovatives Messsystem für die Erfassung, Prüfung und das Management von Wasser-Infrastrukturbauwerken. *ZfV-Zeitschrift für Geodäsie, Geoinformation und Landmanagement. 4*.

IHO (2005). *Manual on Hydrography* (1st ed.). IHO Publication C-13, International Hydrographic Organization, Monaco. https://iho.int/uploads/user/pubs/cb/c-13/english/C-13_Chapter_1_and_contents.pdf (last accessed 19 October 2025).

IHO (2022). *Standards for Hydrographic Surveys* (6th ed.). IHO Special Publication S-44, International Hydrographic Organization, Monaco. https://iho.int/uploads/user/pubs/standards/s-44/S-44_Edition_6.1.0.pdf (last accessed 19 October 2025).

Kerekes, G. & Schwieger, V. (2018). Kinematic positioning in a real time robotic total station network system. *Proceedings of the 6th International Conference on Machine Control & Guidance,* Berlin, Germany, 1–2 October 2018, pp. 35–43.

Kälin, U., Hürzeler, M. and Grimm, D. (2023). Calibration of Kinematic Measuring Systems. I*ngenieurvermessung 23. Beiträge zum 20. Internationalen Ingenieurvermessungskurs Zürich*, pp. 195–207.

Kälin, U., Staffa, L., Grimm, D. E. and Wendt, A. (2022). Highly Accurate Pose Estimation as a Reference for Autonomous Vehicles in Near-Range Scenarios. *Remote Sensing, 14*(1), pp. 90.

Krzyżek, R., Kudrys, J. (2022). Accuracy of GNSS RTK/NRTK height difference measurement. *Appl Geomat, 14*, 491–499. https://doi.org/10.1007/s12518-022-00450-2

Le Deunf, J., Legris, M. and McManus, J. (2020). Automatic Calibration for MBES Offsets. *Hydro International*. https://www.hydro-international.com/content/article/automatic-calibration-for-mbes-offsets (last accessed 15 July 2025).

Lucieer, V., Huang, Z. and Siwabessy, J. (2016). Analyzing uncertainty in multibeam bathymetric data and the impact on derived seafloor attributes. *Marine Geodesy, 39*(1), pp. 32–52. https://doi.org/10.1080/01490419.2015.1121173

Luo, Y., Li, J., Yu, C., Xu, B., Li, Y., Hsu, L.-T. and El-Sheimy, N. (2019). Research on Time-Correlated Errors Using Allan Variance in a Kalman Filter Applicable to Vector-Tracking-Based GNSS Software-Defined Receiver for Autonomous Ground Vehicle Navigation. *Remote Sensing, 11*(9), 1026. https://doi.org/10.3390/rs11091026

Mandlburger, G., Pfennigbauer, M. and Pfeifer, N. (2013). Analyzing near water surface penetration in laser bathymetry – A case study at the River Pielach. *ISPRS Ann. Photogramm. Remote Sens. Spatial Inf. Sci., II-5/W2*, pp. 175-180. https://doi.org/10.5194/isprsannals-II-5-W2-175-2013

Mandlburger, G., Rhomberg-Kauert, J., Gueguen, L.-A., Mulsow, C., Brezovsky, M., Dammert, L., Haines, J., Glas, S., Himmelsbach, T., Schulte, F., Amon, P., Winiwarter, L., Jutzi, B. and Maas, H.-G. (2025). Mapping shallow inland running waters with UAV-borne photo and laser bathymetry. *Journal of Applied Hydrography, 130*, pp. 42–54. https://doi.org/10.23784/HN130-06

Maxim, A., Lerke, O., Prado, M., Dorstelmann, M., Menges, A. and Schwieger, V. (2017). UAV guidance with robotic total station for architectural fabrication processes. *156. DVW-Seminar Unmanned Aerial Vehicles 2017 (UAV 2017)*, Stuttgart, pp. 145–161. Wißner-Verlag Augsburg.

Mobley, C. D. (2010). Optical properties of water. *Handbook of Optics, 4*, pp. 1–1. McGraw-Hill. New York.

Mokhtar, K., Chuah, L. F., Abdullah, M. A., Oloruntobi, O., Ruslan, S. M. M., Albasher, G., Ali, A. and Akhtar, M. S. (2023). Assessing coastal bathymetry and climate change impacts on coastal ecosystems using Landsat 8 and Sentinel-2 satellite imagery. *Environmental Research, 239* (Part 2/2023), p. 117314. https://doi.org/10.1016/j.envres.2023.117314

Möser, M., Hoffmeister, H., Müller, G., Staiger, R. and Wanninger, L. (2012). *Handbuch Ingenieurgeodaesie: Grundlagen* (4 edn). Wichmann. Berlin.

Norbit Subsea (2021). *Norbit Winghead i77h.*

Parrish, C. (2020). Index of refraction for seawater and freshwater as a function of wavelength and temperature. https://research.engr.oregonstate.edu/parrish/indexrefraction-seawater-and-freshwater-function-wavelength-andtemperature (last accessed 20 June 2025).

Pfeifer, N., Mandlburger, G., Otepka, J. and Karel, W. (2014). Opals – a framework for airborne laser scanning data analysis. *Computers, Environment and Urban Systems, 45*, pp. 125–136.

Popielarczyk, D. (2016). Accuracy of vertical trajectory determination of hydrographic survey unit using robotized total station. *International Multidisciplinary Scientific GeoConference: SGEM 2*, Albena, Bulgaria, pp. 39–45.

Pöppl, F., Neuner, H., Mandlburger, G. and Pfeifer, N. (2023). Integrated trajectory estimation for 3D kinematic mapping with GNSS, INS and imaging sensors: A framework and review. *ISPRS Journal of Photogrammetry and Remote Sensing, 196*, pp. 287–305. https://doi.org/10.1016/j.isprsjprs.2022.12.022

Pöppl, F., Ullrich, A., Mandlburger, G. and Pfeifer, N. (2024). A flexible trajectory estimation methodology for kinematic laser scanning. *ISPRS Journal of Photogrammetry and Remote Sensing, 215*, pp. 62–79. https://doi.org/10.1016/j.isprsjprs.2024.06.014

Pöppl, F., Ullrich, A., Mandlburger, G. and Pfeifer, N. (2025). Precise and efficient high-frequency trajectory estimation for LiDAR georeferencing. ISPRS Journal of Photogrammetry and *Remote Sensing, 223*, pp. 344–361. https://doi.org/10.1016/j.isprsjprs.2025.03.007

Ressl, C., Kager, H. and Mandlburger, G. (2008). Quality checking of ALS projects using statistics of strip differences. *International Archives of Photogrammetry and Remote Sensing, 37*(B3b), pp. 253–260.

RIEGL (2021). *RIEGL VQ840-G.* RIEGL Laser Measurement Systems GmbH, Austria.

Skaloud, J. and Lichti, D. (2006). Rigorous approach to bore-sight self-calibration in airborne laser scanning. *ISPRS Journal of Photogrammetry and Remote Sensing, 61*(1), pp. 47–59. https://doi.org/10.1016/j.isprsjprs.2006.07.003

Thalmann, T. and Neuner, H. (2021). Temporal calibration and synchronization of robotic total stations for kinematic multisensor-systems. *Journal of Applied Geodesy, 15*(1), pp. 13–30. https://doi.org/10.1515/jag-2019-0070

Thalmann, T. and Neuner, H. (2024). Sensor fusion of robotic total station and inertial navigation system for 6DoF tracking applications. *Applied Geomatics.* https://doi.org/10.1007/s12518-024-00593-4

Tombrink, G., Dreier, A., Klingbeil, L. and Kuhlmann, H. (2024). Spatio-temporal trajectory alignment for trajectory evaluation. *Journal of Applied Geodesy, 19*(2), pp.321-331. https://doi.org/10.1515/jag-2024-0040

Vaidis, M., Dubois, W., Daum, E., LaRocque, D. and Pomerleau, F. (2023). Uncertainty analysis for accurate ground truth trajectories with robotic total stations. *Proceedings of IEEE/RSJ International Conference on Intelligent Robots and Systems (IROS)*, IEEE, Detroit, MI, USA. https://doi.org/10.48550/arXiv.2308.01553

Wang, J., Yu, X. and Guo, S. (2022). Inversion and characteristics of unmodeled errors in GNSS relative positioning. *Measurement, 195*, pp. 111151. https://doi.org/10.1016/j.measurement.2022.111151.

Zogg, H.-M. and Maar, H. (2020). *Leica Nova MS60.* White Paper, Leica Geosystems AG.

https://doi.org/10.58440/ihr-31-2-a14

Authors' biographies

Lucas Dammert is working as a PhD student at TU Wien on the trajectory estimation of multi-sensor systems (primarily unmanned airborne systems) using robotic total stations in a joint position between the groups of photogrammetry and engineering geodesy. During his B.Sc. and M.Sc. he studied Geodesy and Geoinformation in Dresden and Hamburg with a specialization in hydrography. His research interests lie in the fields of hydrography, photogrammetry and engineering geodesy with a focus on kinematic multi-sensor systems.



Lucas Dammert

Florian Pöppl holds an MSc in Technical Mathematics from TU Wien and wrote his PhD dissertation in Geodesy and Geoinformation on trajectory estimation and integration of satellite and inertial navigation with laser scanning. He is currently heading software development at *RIEGL* Laser Measurement Systems GmbH, where he also continues his work on laser scanning data processing, navigation, sensor orientation and calibration.



Florian Pöppl

Jan Rhomberg-Kauert is a PhD student at TU Wien, working as a research assistant in the Department of Geodesy and Geoinformation. With a broad background in mathematics, computational biology and computer science, Jan currently focuses on developing innovative methodologies to improve hydrographic data classification and LiDAR signal processing. His research aims to enhance the understanding of full waveform bathymetric LiDAR with a focus on aquatic vegetation. There he actively engages with various academic and industry partners, contributing to different projects related to hydrography, photogrammetry and airborne LiDAR.



Jan Rhomberg-Kauert

Tomas Thalmann received his DI in Geodesy from TU Wien in 2015. Since then, he worked in several research projects dealing with inertial navigation, laser scanning and robotic total stations at the research group Engineering Geodesy. Focusing on kinematic multi-sensor-systems and time-synchronization, he currently works on enhancing multi-sensor-systems by fusion of inertial sensors and robotic total stations. Since 2020 he is also employed as a surveying engineer and project manager at Vermessung Thalmann.



Tomas Thalmann

https://doi.org/10.58440/ihr-31-2-a14



David Monetti

David Monetti holds a DI from the TU Vienna. He is currently CEO at Skyability GmbH, a drone service provider based in Austria. He manages daily business and research projects funded by the Austrian national funds. His product development activities focus on lidar systems; using lidar on different platforms like ULS, MLS or TLS have turned it into a tool used daily which now creates the best obtainable digital twin of a target of interest. For more than a year now David is also responsible for implementing lidar-bathymetry at Skyability. His research activities and 5+ years hands-on work have turned him into a true expert in the field.



Hans-Berndt Neuner

Univ. Prof. Dr.-Ing. Hans-Berndt Neuner leads the research group engineering geodes at TU Wien. He wrote his dissertation at the geodetic institute of Leibnitz Universität Hannover in the field of deformation analysis and time series analysis and worked there afterwards as a PostDoc. His expertise lies in geometric modelling and analysis of point-based and space-continuous deformation, filter methods in object space and kinematic measurement systems.



Gottfried Mandlburger

Univ. Prof. Dipl.-Ing. Dr. techn. Gottfried Mandlburger studied geodesy at TU Wien, where he also received his PhD in 2006 and habilitated in photogrammetry with a thesis on "Bathymetry from active and passive photogrammetry" in 2021. In April 2024 he was appointed University Professor for Optical Bathymetry at TU Wien. His main research areas are airborne topographic and bathymetric LiDAR from crewed and uncrewed platforms, multimedia photogrammetry, bathymetry from multispectral images, and scientific software development. Gottfried Mandlburger is chair of the DGPF working group LiDAR and Austrians scientific delegate in EuroSDR. He received best paper awards from ISPRS and ASPRS for recent publications on bathymetry from active and passive photogrammetry.

https://doi.org/10.58440/ihr-31-2-a14

PEER-REVIEWED ARTICLE

Quantifying economic consequences of maritime incidents: a framework for Small Island Developing States

Authors

Shivani Seepersad[1] and Dexter Davis[1]

Abstract

This study develops an economic risk assessment framework for maritime accidents within Trinidad and Tobago's Exclusive Economic Zone, representative of Small Island Developing States. The framework integrates market and contingent valuation methods under the Total Economic Value framework with probabilistic risk modelling of drifting collisions. Consequences, expressed on a five-tier monetary scale adapted from the Simplified IALA Risk Assessment method were combined with probability estimates to quantify annual risk. Results are presented spatially, showing annualised risks of USD 30,000 to 2.48 million, highest in north-western Trinidad. The framework offers a transferable, evidence-based tool for prioritising targeted maritime risk mitigation.

Keywords

maritime risk assessment · economic consequences · market valuation · contingent valuation · willingness to pay · scenarios · probability-consequence integration

Resumé

Cette étude développe un cadre d'évaluation des risques économiques pour les accidents maritimes dans la zone économique exclusive de Trinité-et-Tobago, représentative des petits États insulaires en développement. Ce cadre intègre des méthodes d'évaluation du marché et des contingences dans le cadre de la valeur économique totale, avec une modélisation probabiliste des risques de collisions par dérive. Les conséquences, exprimées sur une échelle monétaire à cinq niveaux adaptée de la méthode d'évaluation des risques simplifiée de l'AISM, ont été combinées avec des estimations de probabilité afin de quantifier le risque annuel. Les résultats sont présentés de manière spatiale, montrant des risques annualisés de 30 000 à 2,48 millions de dollars USD, les plus élevés se situant au nord-ouest de Trinité. Le cadre offre un outil transférable et fondé sur des preuves pour hiérarchiser les mesures d'atténuation de risques maritimes spécifiques

Resumen

Este estudio desarrolla un marco de evaluación de riesgo económico para los accidentes marítimos dentro de la Zona Económica Exclusiva de Trinidad y Tobago, representativa de los Pequeños Estados Insulares en Desarrollo. El marco integra métodos de valoración de mercado y contingente dentro del marco de Valor Económico Total con modelos probabilísticos de riesgo de colisiones a la deriva. Las consecuencias, expresadas en una escala monetaria de cinco niveles adaptada a partir del método de Evaluación Simplificada de Riesgos de IALA, se combinaron con estimaciones de probabilidad para cuantificar el riesgo anual. Los resultados se presentan espacialmente, mostrando riesgos anualizados de 30.000 a 2,48 millones de USD, los más altos en el noroeste de Trinidad. El marco ofrece una herramienta transferible basada en pruebas para priorizar la mitigación de riesgos marítimos específicos.

✉ Shivani Seepersad · dawn@seepersad.org

[1] Department of Geomatics Engineering and Land Management, The University of the West Indies, St. Augustine, The Republic of Trinidad and Tobago

https://doi.org/10.58440/ihr-31-2-a16

1 Introduction

Maritime navigation drives economic and social development in Small Island Developing States (SIDS) such as Trinidad and Tobago (TT). This reliance heightens vulnerability to maritime risks, including vessel collisions, oil spills, and infrastructure damage, which can have severe consequences. Historical and recent accidents in the Caribbean illustrate the impact of such consequences. Notable examples include the 2010 sinking of the Angeln off Saint Lucia, which led to substantial salvage and fuel removal costs (IMO, 2010), and the 1979 collision between the Atlantic Empress and Aegean Captain near Tobago, resulting in fatalities and the largest recorded ship-sourced oil spill of 287,000 tonnes (ITOPF, 2025). More recent events include the 2023 foundering of the Calypso 2 off Anguilla, resulting in the loss of two lives (IMO, 2024), and the 2024 Gulfstream barge spill off Tobago, categorised as a Tier 2 accident requiring regional or national response by the Ministry of Energy and Energy Affairs (MEEA, 2013; TT Guardian, 2024).

Risk assessment combines the probability of maritime accidents with their associated consequences. The Formal Safety Assessment (FSA) guidelines published by the International Maritime Organisation (IMO) defines "risk" as the combination of the frequency/probability and the severity of the consequence (IMO, 2018). "Probability" is defined as the degree of confidence in the occurrence of an event, measured on a scale from 0 to 1, and "consequence" as the outcome of an accident including injuries and/or fatalities to passengers and crew, environmental impact, damage to the ship or port facilities, or commercial impact. Although the terms "likelihood" and "probability" are sometimes used interchangeably in the literature, they differ in application: likelihood is typically used in qualitative risk assessments to express expert judgement about the chance of an event occurring, whereas probability represents the statistical expectation or frequency of occurrence per unit of time (International Organisation of Marine Aids to Navigation (IALA), 2022a). The Safety of Life at Sea (SOLAS) Convention, Chapter V, Regulations 12 and 13 explain that Marine Aids to Navigation (AtoN) should be provided based on the volume of traffic and the degree of risk (IMO, 2020, 2024).

The FSA guidelines suggest quantifying consequences such as fatalities, environmental degradation, and commercial damage. They recommend doing so using observed Willingness-to-Pay (WTP) to avert a fatality, drawing on past decisions and their associated costs, as well as societal indicators such as the Life Quality Index (LQI). These recommended techniques form part of the Total Economic Value (TEV) framework which captures the full economic value of environmental and marine resources by summing both use and non-use components. Use values are benefits from direct or potential use of resources while non-use values reflect intrinsic worth (Bolt et al., 2005). The TEV framework has been widely adopted by institutions including the National Oceanic and Atmospheric Administration (NOAA; Arrow et al., 1993), the World Bank (2025) and the Organisation for Economic Co-operation and Development (OECD, 2012) to estimate the value of resources and therefore potential losses. These institutions have applied the TEV to inform policies concerning the protection of the marine environment.

A bibliometric review by Huang et al. (2023), covering 1,181 publications from 2000 to 2021, found that most maritime risk studies focus on accident probability rather than consequence assessment. Methods that allow consequence assessment typically express results using weighted scores or ranking systems. Moreover, only a few approaches combine probabilities with consequence values or visualise the outcomes through mapping. Expressing the consequences of potential maritime accidents for diverse goods and services in unified monetary terms allows direct integration with budget planning and cost-benefit analyses. Mapping risk spatially then enables clear visual identification of high-risk zones, supporting evidence-based resource allocation and effective communication with decision-makers.

Using the TEV framework, this study develops an adaptable method for the economic assessment of risks to maritime navigation within TT's Exclusive Economic Zone (EEZ), with applicability to other SIDS. TT was selected as the study area because it is representative of the broader maritime landscape of SIDS within the Greater Caribbean Region (GCR), sharing maritime characteristics, governance frameworks, and environmental vulnerabilities (Seepersad & Davis, 2025). This study is guided by the following objectives:

1. To estimate the value of potential consequences that may arise from maritime accidents occurring within the study area.
2. To develop a monetary-based consequence scale specifically tailored for the assessment of maritime risks within the study area.
3. To determine the probable economic consequences associated with maritime accidents, considering both the most likely (ML) and worst credible (WC) scenarios.
4. To estimate and map risk values for the ML and WC scenarios by integrating the consequence and probability metrics.

The probability aspect of the equation "Risk = Probability × Consequence" was examined by Seepersad & Davis (2025), who modelled the drifting collision probability within TT's EEZ. The current study focuses on the consequence component and the combination of probability with consequences. The results of the study present annual maritime navigation risks on maps and provides data that can be used to prioritise risk mitigation resources.

The remainder of this paper is structured as follows: Section 2 reviews the relevant literature on

https://doi.org/10.58440/ihr-31-2-a16

the valuation of resources that can be negatively impacted by maritime accidents. Section 3 outlines the method used to assess economic consequences of maritime accidents. Section 4 presents and discusses the results. Section 5 concludes with policy implications and recommendations for future research.

2 Literature review

2.1 Approaches for assessing the consequences of maritime accidents

Several established approaches are used to assess the negative consequences of maritime accidents. The International Association of Marine Aids to Navigation and Lighthouse (IALA) Guideline G1018 (IALA, 2022a) outlines methods that rely on historical data and expert judgement. For example, the Simplified IALA Risk Assessment (SIRA) method estimates risk using expert judgement and historical data. Scenarios are defined, and likelihood and consequence scores are assigned using assessment scales. IALA provides default assessment scales and recommends local adaptation but offers no specific guidance for doing so. The consequence scale combines monetary values, percentages, and qualitative descriptions, producing a composite risk score that guides whether control measures are needed to reduce risk to a level that is as low as reasonably practicable (ALARP; IALA, 2022c). The Ports and Waterways Safety Assessment (PAWSA) method similarly evaluates risk through weighted likelihood and consequence scores derived via the Delphi consensus technique (IALA, 2022d). The IALA Waterway Risk Assessment Programme (IWRAP) does not consider consequences.

The IMO also provides guidance for evaluating the impacts of maritime accidents (IMO, 2018). This process involves ranking available data and supplementing these rankings with expert judgement to ensure a comprehensive assessment. The FSA also recommends quantifying the potential costs associated with accident consequences through three main strategies: (i) observing the WTP to prevent adverse outcomes, (ii) analysing previous decisions and the financial implications attached to them, and (iii) considering societal indicators such as the LQI. These three strategies form part of the TEV framework.

2.2 Benefits of using the TEV to quantify consequences

Plottu & Plottu (2007) describe the TEV framework as a means of consolidating all categories of value associated with goods and services into a single monetary metric. Pearce & Özdemiroglu (2002) emphasise that assigning monetary values to non-market goods enables more informed decision-making. This aligns with the FSA (IMO, 2018), which notes that applying TEV to accident-related costs allows direct integration into cost-benefit analyses, improving comparability, transparency, and consistency in risk management. However, monetisation, while useful for analysis, may undervalue cultural, social, or intergenerational factors (Plottu & Plottu, 2007).

2.3 Institutions using the TEV framework

Institutions such as the NOAA, OECD, and World Bank apply the TEV framework in policy development, supporting numerous studies that inform cost-benefit analyses and economic decision-making. The NOAA Panel on Contingent Valuation (CV; Arrow et al., 1993), established under the Oil Pollution Act, validated the method for quantifying public WTP for environmental preservation. Carson et al. (2003) applied a dichotomous-choice CV survey following the *Exxon Valdez* oil spill on March 24, 1989, when the tanker ran aground in Prince William Sound, Alaska, releasing 11 million gallons of oil. The study quantified non-market damages and informed the Natural Resource Damage Assessment process. Regional studies, including (Schuhmann & Mahon, 2015), further demonstrate the framework's relevance to SIDS. Despite recognition by the IMO and other international bodies, TEV remains underutilised in maritime risk assessment. Monetary consequences are rarely combined with accident probabilities to generate probability-weighted costs or mapped spatially to guide resource prioritization – an approach essential for meeting SOLAS Chapter V, Regulations 12 and 13.

2.4 TEV in maritime risk assessment

In this study, the TEV framework is applied to quantify the economic value of maritime goods and services that may be damaged or lost due to shipping incidents. The main valuation techniques and their global applications are summarised in Table 1. Because valuation outcomes depend on factors such as national income, demographics, and societal risk perception, results are interpreted as indicative rather than exact.

2.5 Design principles and recommended structure for CV surveys

Mitchell & Carson (1989) describe the CV method as a survey-based approach that asks respondents how much they would be WTP for the preservation or use of an environmental good or service. Implementation involves identifying the good or service being valued, defining the affected population, and selecting a representative sample to ensure the results reflect broader societal preferences.

Next, a questionnaire is developed to elicit WTP, providing respondents with a clear, neutral description of the good or service and the reasons for evaluating the proposed change. Details on changes in quantity, quality, or probability, along with current conditions and responsible agencies, should be clearly stated (Ashford, 2021). The NOAA Panel (Arrow et al., 1993) recommends the use of photos, maps, or illustrations to improve understanding, provided these remain neutral and non-persuasive. Respondents should

https://doi.org/10.58440/ihr-31-2-a16

Table 1 Overview of valuation techniques and supporting global applications.

Technique	Description of the technique	Documented global cases in academic research
Directly applicable market valuation techniques	Market-based valuation estimates the economic value of goods, services, or resources using observed market prices, assuming they reflect real economic worth. Though methodologically simple, these techniques capture substantial portions of ecosystem value through measurable commercial outcomes (Abdullah et al., 2011).	
Market price method	Estimates value using observed prices and quantities in established markets, reflecting actual consumer behaviour. Straightforward to apply where market data exist (EcosystemValuation, 2025).	Applied in forestry, marine fisheries, and agricultural commodity valuation (Khanal, 2001).
Operational cost method	Estimates economic loss by multiplying disruption duration (e.g., delay) by unit operating cost. Effective for quantifying direct financial losses using daily costs, port charges, or lost-revenue rates, though it excludes systemic or reputational costs (EPA, 2017).	Gonyo (2019) identified crew, fuel, and maintenance costs; Nwoloziri et al. (2025) applied it to vessel delays in Apapa terminals; Počuča (2006) calculated ship operating expenses for delay valuation.
Loss-of-hire / replacement cost	Estimates the cost of restoring or replacing assets or environmental functions lost due to accidents or degradation (Abdullah et al., 2011).	Restoration of degraded crayfish streams in France averaged €225,000 over five years; UK peatland loss incurred €1.8–3.6 million in added water treatment costs (Kettunen & ten Brink, 2006).
Insurance claims analysis	Uses insurance data to estimate actual financial losses. Suitable where accident costs are captured through hull, cargo, or liability insurance. The ISO recognises insurance as a formal risk treatment option (ISO, 2018).	Du Plessis et al. (2023) analysed weather-related marine cargo claims in South Africa, showing the method's reliability for quantifying maritime losses.
Non-market valuation techniques		
Used when market data are unavailable. These elicit stated preferences through surveys or hypothetical scenarios to estimate WTP or compensation. They capture non-market ecosystem and social values (Abdullah et al., 2011; Pearce & Özdemiroglu, 2002). WTP represents the "cost averted" by mitigation (IMO, 2018).		
CV such as WTP	Elicits the maximum amount individuals would pay to preserve goods or avoid adverse outcomes; recognised as a robust stated-preference technique (Rozza et al., 2025).	The NOAA Panel on CV, established under the Oil Pollution Act (Arrow et al., 1993), validated its use for environmental damage assessment. Carson et al. (2003) applied it to the Exxon Valdez oil spill using a dichotomous-choice survey. Results informed the Natural Resource Damage Assessment and remain widely used in NOAA, OECD, and World Bank studies.
Value of statistical life (VSL)	Represents aggregated WTP for small reductions in mortality risk, reflecting the value society places on preventing one fatality (Wang & He, 2010). Used by IMO (2018) for monetising loss of life and injury, supporting cost-benefit comparisons of risk control options	Adopted by IMO (2018), DOT (2021), and OECD (2012) for safety-related policy appraisal.
Benefit transfer (BT)	Applies economic values from one location or study to another with similar conditions (Bateman et al., 2002).	OECD (2012) applied meta-analytic BT of VSL across environmental, health, and transport sectors, showing reliability and cost-effectiveness.

also be reminded of budget constraints, trade-offs, and the availability of substitutes or alternative sites.

The next section of the questionnaire introduces the payment vehicle, specifying how contributions would be collected. Common CV payment vehicles include user fees, taxes, voluntary contributions, or price surcharges (Mitchell & Carson, 1989). Carson et al. (2003) selected a tax-based vehicle for the Exxon Valdez study, as volatile oil prices risked biasing responses. The NOAA Panel (Arrow et al., 1993) likewise recommended a referendum-style format with mandatory tax payments. While taxes enhance realism and credibility (Lee & Mjelde, 2007), low public trust can lead to protest responses (Stevens et al., 1991).

The final section of the questionnaire specifies the elicitation format used to measure WTP. Formats are either continuous, where respondents state or select an amount, or dichotomous, where they accept or reject a bid. Continuous formats include the open-ended approach, respondents state their maximum WTP, and the payment card, where they choose from a predefined list. Dichotomous formats include the single-bounded (one yes/no bid) and double-bounded (follow-up higher or lower bid) methods. A hybrid, the multiple-bounded format, presents a range of bid levels with graded certainty responses (e.g., "definitely yes" to "definitely no"), producing interval data (Bateman et al., 2002; Arrow et al., 1993).

Empirical comparisons of contingent valuation formats show mixed findings. The NOAA Panel recommends the dichotomous choice format because it mimics real market decisions and reduces cognitive burden, improving validity and response rates (Arrow et al., 1993). Carson et al. (2001) found that dichotomous formats typically yield higher WTP estimates than open-ended formats, which often generate zero or low bids. Smith (2000) noted that, although WTP

values differ between these approaches, there is no definitive theoretical or empirical reason to prefer one exclusively. Frew et al. (2003) also reported higher WTP values from closed-ended instruments. Vaughan et al. (1999) argued that dichotomous surveys cannot directly elicit true WTP, recommending open-ended pre-tests to set bid ranges and benchmarks. The NOAA Panel's framework remains the benchmark for CV survey design and validity assessment.

The choice of elicitation format affects both respondent behaviour and the econometric models used in analysis (Harris & Roach, 2021). Logistic and probit models are theoretically appropriate for dichotomous dependent variables, where outcomes are binary and relationships with predictors are non-linear (Cleary & Angel, 1984). In contrast, linear regression applies to continuous dependent variables, where outcomes vary across a range and relationships are assumed linear (Schneider et al., 2010).

The survey also captures socio-economic and demographic factors influencing WTP, including age, location, education, income, and marital status (Ashford, 2021). Face-to-face interviews are recommended for more reliable valuations, and surveys should clearly define the target population and sampling frame. Although non-response is common due to the cognitive effort required, well-designed instruments can still yield valid results (Arrow et al., 1993). Minimum sample size is often determined using the Krejcie & Morgan (1970) formula:

$$S = \frac{X^2 \cdot N \cdot P \cdot (1-P)}{d^2 \cdot (N-1) + X^2 \cdot P \cdot (1-P)} \quad (1)$$

In Eq. 1, S is the required sample size, X^2 is chi-square value (3.841 for 95 % confidence) for 1 degree of freedom at the 95 % confidence level (3.841), N is the population size, P is the population proportion, and d is the margin of error.

2.6 Econometric analysis of dichotomous WTP data

In binary logistic regression, the dependent variable is categorical with two outcomes (e.g. yes/no). The model is most theoretically expressed as

$$\ln\left(\frac{P(Y=1)}{1-P(Y=1)}\right) = \beta_0 + \beta_1 X_1 + \cdots + \beta_k X_k \quad (2)$$

which models the log-odds (logit) of the event as a linear function of predictors. Equivalently, this can be transformed into the probability form:

$$P(Y=1) = \frac{1}{1+\mathrm{e}^{-(\beta_0+\beta_1 X_1+\cdots+\beta_k X_k)}} \quad (3)$$

maps this linear predictor onto a 0–1 probability scale. The logit form aids coefficient interpretation, while the probability form supports prediction. These formulations are standard in logistic regression theory (Chua, 2025; Harris, 2021). Analyses were performed in SPSS to test model validity and identify significant predictors.

According to Harris (2021), logistic regression outputs – coefficients, odds ratios (*OR*), and *p*-values – describe both the strength and significance of effects. The coefficient β shows the change in log-odds per unit change in a predictor; $OR > 1$ indicates increased likelihood, $OR < 1$ a reduced likelihood; and the *p*-value confirms statistical significance at $p < 0.05$.

2.7 Scenario analysis in maritime consequence assessment

While valuation and econometric methods quantify the monetary impacts of maritime accidents, they do not show how these impacts vary under different conditions. Scenario analysis complements these methods by evaluating outcomes across plausible situations, typically derived from historical accident data. Two common types are the ML scenario, reflecting expected outcomes under normal conditions, and the WC scenario, representing severe but realistic events while excluding extreme improbabilities (Riding & Rawson, 2015).

Building on Seepersad & Davis (2025), who modelled drifting collision probabilities in TT using Monte Carlo simulation, this study extends the analysis to the consequence dimension. Monetary consequences, estimated within the TEV framework, are combined with probability values to generate integrated, spatially mapped risk estimates. This approach provides policymakers in resource-limited SIDS with an evidence-based tool for prioritising maritime risk mitigation.

3 Method

This study applies the TEV framework to monetise the potential consequences of maritime accidents within TT's EEZ. The approach integrates market and CV techniques with probabilistic risk estimates derived from Seepersad & Davis (2025) to generate spatially explicit risk values that inform evidence-based prioritisation of mitigation measures. The monetisation process followed a structured, multi-step workflow summarised in Fig. 1 and subsequently detailed.

3.1 Step 1 – Identification and valuation of impacted resources

The assessment began with identifying resources most vulnerable to maritime accidents using open-source satellite imagery (Google Earth), literature review, and expert consultation (Step 1, Fig. 1). Key references, including *A Guide to Beaches and Bays of Trinidad and Tobago* (IMA, 2010), validated coastal resource boundaries and classifications. Fourteen experts from government agencies (Maritime Services Division, Environmental Management Authority, Ministries of Agriculture and Energy) and academia (University of the West Indies) contributed through structured interviews.

Vulnerability was determined by exposure to shipping activity, sensitivity to pollution or disturbance, and ecological or economic significance within TT's coastal

https://doi.org/10.58440/ihr-31-2-a16

zone. Suitable valuation techniques were then selected to estimate annual economic contributions, covering both market and non-market values (Step 1, Fig. 1).

3.2 Step 2 – Application of market valuation techniques

Table 2 outlines the key maritime resources, applied valuation methods (see also Table 1), relevant formulas, and data sources. Application of valuation techniques is summarised in Table 2 along with a further explanation of CV in Step 3.

3.3 Step 3 – Application of the contingent valuation technique

To estimate the economic value of environmental resources, a WTP survey was designed following best-practice guidelines from the NOAA Panel and other relevant literature. The objective was to elicit respondents' willingness to reallocate tax payments toward protecting these resources from ship-based accidents.

A mixed-question format combined dichotomous and continuous components. The dichotomous section asked whether respondents were willing to pay (yes/no), capturing general support, while the continuous section quantified the amount, they were willing to pay for aggregation and analysis. The binary format enhanced realism and reduced cognitive effort, and the open-ended question provided finer resolution and cross-validation.

The survey minimised common CV biases, hypothetical, social desirability, anchoring, and framing through neutral wording and fact-based descriptions of resources, hazards, and mitigation actions. Data were collected in person (shopping malls, workplaces, universities) and online via social and professional networks, using snowball sampling to boost participation. The design and collection protocol was validated and approved by the University of the West Indies Ethics Committee. A pilot test refined clarity and flow. The final questionnaire included demographic (income, age, gender, education, occupation) and attitudinal (environmental awareness, prior visits) variables to identify predictors of WTP.

Binary logistic regression was used to model willingness, selected over linear regression due to the dichotomous nature of the dependent variable. Statistical significance was set at $p < 0.05$, and model fit was evaluated using standard diagnostics. Three parameters were interpreted: coefficient β, odds ratio (*OR*), and *p*-value.

3.4 Step 4 – Development of a Monetary-based consequence scale

The SIRA consequence scale (IALA, 2022c) formed the basis for developing the monetary-based consequence scale in this study. The original SIRA scale combines qualitative descriptions, indicative percentage losses, and occasional monetary values, recommending local adaptation but without guidance. This study addressed that gap by tailoring the scale to TT's economic and environmental context. Retaining SIRA's five-tier structure (insignificant to catastrophic), losses were expressed in locally derived monetary terms, providing a consistent and

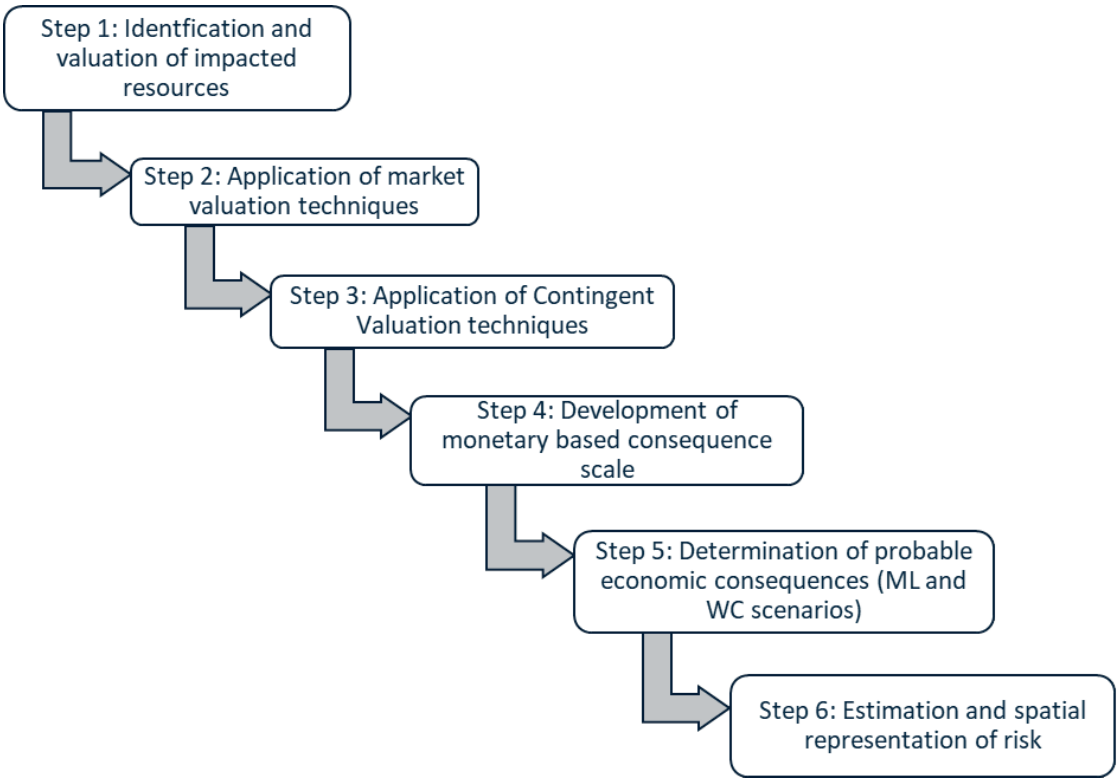


Fig. 1 Method for estimation of maritime risk.

Table 2 Overview of valuation techniques and supporting global applications.

Ressource / potential loss	Description of economic impact	Valuation technique	Formula / quantification basis	Data source
Fisheries	Temporary restrictions or contamination reducing catch volumes and income.	Market price method	$V_f = \Sigma(P_i \times Q_i)$ The mean annual fishery value V_f is derived by multiplying the landed quantity of fish Q_i by the average market price per kilogram P_r.	NAMDEVCO (2025)
Delays	Vessel downtime due to navigational blockage or restricted port access.	Operational cost method	$C_d = C_{op} \times t_d$ The cost of delay C_d equals the daily operating cost of the vessel C_{op} multiplied by the total delay duration t_d. This approach reflects direct financial losses from idle time.	Howard (2019), Bhoncharan (2025)
Infrastructure	Damage to coastal and offshore infrastructure.	Loss-of-Hire or replacement cost	$C_i = R_c \times t_r$ The infrastructure cost C_i equals the daily rental or replacement cost R_c multiplied by the repair or downtime period t_r. This approach is used when direct damage estimates are unavailable.	Cavcic (2022)
Damage to ship	Damage to or loss of the ship.	Insurance claims analysis	$C_s = \Sigma(I_j/n)$ The mean ship damage cost Cs is estimated from insurance claim records Ij averaged over n years to capture the representative annual claim values.	The Swedish Club (2020)
Loss of life	Fatalities, injuries, or long-term health effects from maritime accidents.	VSL, BT	$V_l = \text{VSL} \times N$ The total value of life lost V_l is estimated by multiplying the VSL by the number of affected individuals N, following (IMO, 2018).	IMO (2018)
Beaches recommended for tourism	Temporary restrictions or contamination.	CV WTP	WTP = WTP × P The WTP is calculated as shown in Eqs. 2 and 3. The aggregate WTP equals the mean individual WTP multiplied by the affected population P.	WTP survey, Trinidad and Tobago (2024)
Other beaches				
Swamp				

comparable measure of economic consequences across resources.

Where relevant, percentage losses from the SIRA guideline were multiplied by the estimated annual monetary value of each resource. For instance, a Tier 2 event representing a 10 % fisheries loss was applied to the annual fisheries value to estimate the corresponding economic loss. Because consequence models involve uncertainty, losses were expressed as monetary ranges rather than single values, following FAO/WHO (2006). The adapted scale also extends SIRA by including locally significant resources, such as beaches and swamps, ensuring relevance to the socioeconomic and environmental context of the study area.

3.5 Step 5 – Determination of probable economic consequences (ML and WC scenarios)

Building on the monetary consequence scale in Section 3.2, two scenarios were developed to represent plausible maritime accidents within TT's EEZ. ML scenarios captured frequent, low-severity events identified from Maritime Services Division reports (Rambarran, 2021), newspaper archives

https://doi.org/10.58440/ihr-31-2-a16

(2018–2024), and expert input. Historical incidents and their distribution are detailed in (Seepersad & Davis, 2025). WC scenarios represented severe but credible accidents. Consequences for both scenarios were categorised using the five-tier monetary scale, with mean losses estimated and summed to ensure precision and consistency across resource categories.

3.6 Step 6 – Estimation and spatial representation of risk

For each scenario, the mean estimated loss from the monetary consequence scale was multiplied by the corresponding mean drifting collision probability for the area. Probabilities were derived from (Seepersad & Davis, 2025), who subdivided larger areas into operationally similar segments. The areas were defined by maritime activity, vessel type, and exposure to oceanographic conditions such as currents, winds, and waves, ensuring each zone represented a distinct operational and environmental risk unit. Using mean probability and consequence values produced representative annual risk estimates and maintained consistency across categories, following the standard formulation: Risk = Probability × Consequence.

4 Results

Sections 4.1 and 4.2 present the resources identified as vulnerable to maritime accidents, the valuation techniques applied, and the corresponding estimated economic losses.

4.1 Estimated economic losses for market-valued resources

Fisheries: The annual value of fisheries was calculated by multiplying landed quantities by corresponding market prices per kilogram. Monthly landing data from NAMDEVCO (2025) were analysed for two key sites, Port of Spain and Orange Valley, covering 2019–2021. The mean of the three yearly totals (Table 3) was used as the representative annual value, indicating the potential direct economic loss to the fisheries sector. For broader application, major landing sites should be included, with supplementary data from cooperatives or government agencies when official statistics are unavailable.

Delays: Economic losses from vessel delays were estimated using the operational cost method. The daily operating cost of a Very Large Crude Carrier (VLCC) was taken as USD 25,000, representing break-even levels (Howard, 2019). In Trinidad and Tobago, vessels are typically allocated 72 hours (three days) of laytime; delays beyond this threshold were valued at USD 25,000 per additional day (Bhoncharan, 2025). In other contexts, standard laytime policies and cost structures should be obtained from port or industry sources.

Offshore infrastructure: Losses to offshore installations were estimated using the loss-of-hire or replacement cost method. Public data for the *Noble Jack-up* rig, operational in Trinidad and Tobago since 2013, indicate a daily cost of USD 107,000 (Cavcic, 2022). Where repair data were unavailable, durations from similar incidents were used as proxies. For other contexts, daily operational costs should be sourced from regulators or industry reports.

Ship damage: Costs associated with ship damage were estimated using insurance claims data provided by the Swedish Club (2020). The analysis covered over 600 navigational claims exceeding USD 10,000 between 2014 and 2018, incorporating a mean deductible of USD 100,000. The mean of the annual mean claim costs (Table 4) was adopted as a proxy for expected damage, ensuring deductibles were explicitly considered.

Human life: Valuation of fatalities and injuries followed the FSA (IMO, 2018), which assigns a total value of USD 3 million-USD 1.5 million each for fatalities and injuries or ill health. Ratios based on fatality and injury probabilities were applied to estimate total economic losses. Using the IMO-recommended VSL aligns with OECD (2012) benefit transfer principles, enabling cost-effective adaptation to national contexts.

4.2 Estimated economic values for non-market resources using CV

4.2.1 CV WTP-survey results

A total of 384 surveys were distributed, of which 188 were returned with complete responses, yielding a 49 percent completion rate. Although below the target, this aligns with typical CV studies, where the hypothetical nature of valuation tasks and the cognitive effort required can reduce response rates. The

Table 3 Annual value (USD) of fisheries at Port of Spain and Orange Valley (with rounded values).

2019	$3,100,000
2020	$1,300,000
2021	$4,400,000
Total value of fisheries over 3 years	$8,800,000
The mean annual value of fisheries	$2,900,000

Table 4 Ship damage costs were estimated using data from The Swedish Club (2020) (with rounded values).

Year	Mean claim cost (including a 100,000 USD deductible)
2014	$550,000
2015	$525,000
2016	$650,000
2017	$775,000
2018	$900,000
Mean claim cost	$680,000

https://doi.org/10.58440/ihr-31-2-a16

NOAA Panel notes that lower rates reflect task difficulty rather than disengagement. Dataset adequacy was confirmed using the Events-Per-Predictor (EPP) rule (Riley et al., 2019), which recommends at least 10 positive responses per predictor. With 15 predictors and 188 cases, the dataset met this threshold, ensuring sufficient power for robust binary logistic regression analysis.

4.2.2 Regression findings

The dependent variable represented respondents' WTP (1 = willing, 0 = not willing). The random order of survey responses confirmed independence of observations, satisfying the assumption that data points were not repeated measures from the same individuals. One extreme outlier in the WTP data was replaced with the modal value to minimise distortion of the mean while maintaining the dataset's central tendency. The overall model was statistically significant ($p < 0.005$), indicating that the predictors collectively improved model fit relative to a null model. These conditions confirm that the estimated coefficients and odds ratios are reliable and interpretable.

Income and occupational status emerged as the most significant predictors of WTP. Respondents reporting no income were 95 % less likely to support tax reallocation compared to higher-income groups (*OR* = 0.048, $p = 0.008$), while those earning between USD 5,000 and USD 10,000 annually were 91 % less likely (*OR* = 0.093, $p = 0.026$). Conversely, individuals employed in professional or managerial roles were 7.7 times more likely to support reallocation (*OR* = 7.676, $p = 0.015$), and those in the "other" occupational category were 9.2 times more likely (*OR* = 9.212, $p < 0.001$). An *OR* greater than 1 indicates that the predictor increases the likelihood of willingness to pay, while an *OR* less than 1 indicates a decrease in likelihood. The *p*-value shows the level of statistical significance, with values below 0.05 suggesting that the observed effect is unlikely to have occurred by chance.

Age, education, visit frequency, and environmental awareness did not reach significance, suggesting that willingness to reallocate tax funds is primarily shaped by economic capacity rather than demographic or attitudinal factors. Some of these results displayed numerical instability, a condition where extreme coefficients or odds ratios occur due to sparse data in certain categories (e.g., no respondents in a given age group expressing willingness). While education and environmental awareness showed weak positive trends, the effects were not sufficiently strong to draw firm conclusions. Overall, the regression analysis confirms that economic capacity, as reflected in income and occupational status, is the primary determinant of WTP in this context.

While overall WTP was consistent across marine resources, the amount respondents were prepared to contribute varied by resource type. The mean WTP for the Caroni Swamp was USD 198.89 and mode USD 45. For beaches recommended for tourism the mean was USD 121.27 and median USD 73.50. For non-tourism beaches the mean was USD 102.90 and median USD 45. In all cases, the most frequently stated value (mode) was USD 14.70. The mode is considered a more reliable basis for policy recommendations than the mean, as it reflects the typical respondent's capacity to contribute and avoids inflation from a small number of high-income outliers.

Central Statistical Office data (CSO, 2025) indicate a mean monthly household income of about USD 1,353, so higher thresholds would likely overestimate most taxpayers' capacity. Since the study measures the reallocation of existing taxes rather than new taxation, realistic and equitable values are essential. Using the mode WTP and the national population of 1,368,333, the estimated total contribution for each resource was calculated as:

$$\text{Total Contribution} = \text{Mode WTP} \times \text{Population} \quad (4)$$

Substituting the values, 14.70 × 1,368,333 yields approximately USD 20.1 million.

4.3 Monetary-based consequence scale for the study area

The monetary-based consequence scale adapted from the SIRA Guideline (IALA, 2022c) is presented in Table 5.

4.4 Economic consequences associated with ML and WC scenarios

This section quantifies the economic losses for the ML and WC scenarios. The ML scenario involves a drifting collision between a medium-sized SOLAS vessel and a smaller non-SOLAS craft (e.g., fishing boat) in rough seas within TT's EEZ, causing moderate vessel damage but no major spill or fatalities. Such events occur at an estimated rate of 0.6 per year, mainly due to human error and adverse weather (Seepersad & Davis, 2025). The WC scenario involves a SOLAS-class oil tanker (e.g., the Gulfstream tanker) colliding nearshore, resulting in a major spill, severe environmental damage, and financial and human losses. Mean total losses were approximately USD 0.7 million for ML and USD 6.2 million for WC, dominated by environmental and operational impacts (Table 6).

4.5 Estimated spatial risk values

Fig. 2 presents the spatial distribution of drifting collision probabilities across five focus areas within TT's waters. Each map (Areas one to five) shows grid cells colour-coded from green (low) to red (high) according to the probability that a drifting vessel will collide at that location. Numeric ranges beside the colour bar

https://doi.org/10.58440/ihr-31-2-a16

Table 5 Consequence scale for estimating losses associated with maritime accidents in TT.

Level	Fisheries (USD)	Delays (USD)	Loss of life (USD)	Infrastructure (USD)	Damage to ship	Beaches recommended for tourism	Other beaches	Swamp
1 Insignificant	Insignificant loss or minor disturbance of one or more species in a small area (0–10 % revenue loss). Monetary range: Less than $293,000.	Minor mechanical issues or brief navigational issues; 0–3 days delay. Monetary range: Less than $25,000.	No injury to humans; nuisance level only. Medical/compensation range: $0–$1,000 (check-up).	None or minimal infrastructure cost. Monetary range: Less than $5,000.	Any event with minimal cost Less than $10,000	Minimal disturbance to beach aesthetics due to localized pollution or minor erosion. No impact on tourism revenues. 1.0 % loss ($201,000)	Minor environmental impact, such as a small area of beach contamination. Recreational use remains unaffected. 1.0 % loss ($201,000)	Temporary disruption to swamp-based tourism with negligible long-term effects on biodiversity. 1.0 % loss ($201,000)
2 Minor	Some reduction (<10 %) or noticeable disturbance of species in a small area (10–25 % revenue loss). Monetary range: $293,000–$731,000.	Disruption to traffic for 4–5 days affecting a small number of vessels (e.g., grounded but quickly refloated vessel). Monetary range: $25,000–$350,000.	Minor injury to one or more individuals; may require hospitalization. Medical/compensation range: $1,000–$10,000.	Minor damage to offshore oil & gas installation. Monetary range: $5,000–$10,000.	Minor damages to ship, ships equipment or cargo $10,000 – $50,000 or hull and machine $30,000 – $100,000	Temporary beach closures (1-2 days) due to minor contamination or infrastructure issues. Minimal revenue loss. 2.5 % loss ($503,000)	Local beach closures or degradation affect small visitor numbers, reducing local recreational value. 2.5 % loss ($503,000)	Short-term ecosystem stress leading to reduced bird-watching, fishing, or swamp tours. Recovery expected. 2.5 % loss ($503,000)
3 Severe	Noticeable reduction (>10 %) and/or severe disturbance in a limited area (25–50 % revenue loss). Monetary range: $731,000–$1,462,000.	Six to eight days of disruption affecting a few vessels (e.g., collision causing temporary blockage requiring assistance). Monetary range: $350,000–$750,000.	Injuries to several individuals requiring hospitalization. Medical/compensation range: $10,000–$1,000,000.	Significant damage to offshore oil & gas installation; one day out of use for repair. Monetary range: $5,000–$107,000.	Basic dry docking due to grounding or slight environmental damages Hull and machinery up to $1,000,000 or P&I insurance of up to $300,000	Significant loss of beach quality due to erosion, oil spills, or waste accumulation. Tourism revenue drops. 10.0 % loss ($2,011,000)	Noticeable loss of access to certain beaches, limiting recreational activities. Local businesses experience reduced earnings. 10.0 % loss ($2,011,000)	Severe ecosystem damage causing disruptions to swamp-dependent economies, such as fishing and eco-tourism. Recovery requires intervention. 10.0 % loss ($2,011,000)
4 Major	Over 50 % reduction or extensive disturbance in a limited area (50–75 % revenue loss). Monetary range: $1,462,000–$2,193,000.	Significant disruption with major backlog of vessels (e.g., capsize or collision wedged in waterway for a day). Monetary range: $750,000–$1,500,000.	Severe injuries to many individuals or loss of life. Medical/compensation range: $1,000,000–$6,000,000.	Major damage to offshore oil & gas installation; approx. 5 days of repair. Monetary range: $107,000–$535,000.	Total losses, wreck removals, rescue operations and collisions Hull and machinery up to $120,000,000 or P&I insurance of up to $100,000,000	Widespread degradation of popular tourism beaches, long-term closures, and major impacts on tourism-dependent businesses. 50.0 % loss ($10,057,000)	Permanent damage to key beaches, making large sections unsafe or unusable. Loss of property value. 50.0 % loss ($10,057,000)	Loss of key wetland species, fishery collapse, and water quality deterioration. Economic losses extend to local livelihoods and storm protection. 50.0 % loss ($10,057,000)
5 Catastrophic	Loss of whole population of one or more species in a large area (>75 % revenue loss). Monetary range: $2,193,000 and above.	Long-term waterway closure with supply-chain impacts. Monetary range: Over $1,500,000.	Severe injuries to numerous individuals and/or multiple fatalities. Medical/compensation range: Over $6,000,000.	Catastrophic damage to offshore oil & gas installation. Monetary range: Greater than $535,000.	Examples – Costa Concordia, Prestige and Erika Hull and machinery up to $750,000,000 or Protection and Indemnity (P&I) insurance of up to $100,000,000	Permanent beach degradation, rendering tourism industries unsustainable. Local economies dependent on tourism collapse. 100.0 % loss ($20,114,000)	Complete destruction of beaches, making them unusable for recreation, fishing, or wildlife protection. 100.0 % loss ($20,114,000)	Complete swamp ecosystem collapse, resulting in irreversible loss of biodiversity, carbon storage, and tourism revenue. Severe flooding risks increase. 100.0 % loss ($20,114,000)

https://doi.org/10.58440/ihr-31-2-a16

Table 6 Mean estimated consequences by scenario (expressed in USD with rounded values).

Consequence category	Mean estimated consequence for the ML scenario	Mean estimated consequence for the WC scenario
Fisheries	146,500	1,120,000
Delays	187,500	550,000
Loss of life	750	505,000
Infrastructure	7,500	56,000
Damage to ship	65,000	200,000
Beaches (tourism)	100,500	1,257,000
Other beaches	100,500	1,257,000
Swamp	100,500	1,257,000
Total	709,000	6,202,000

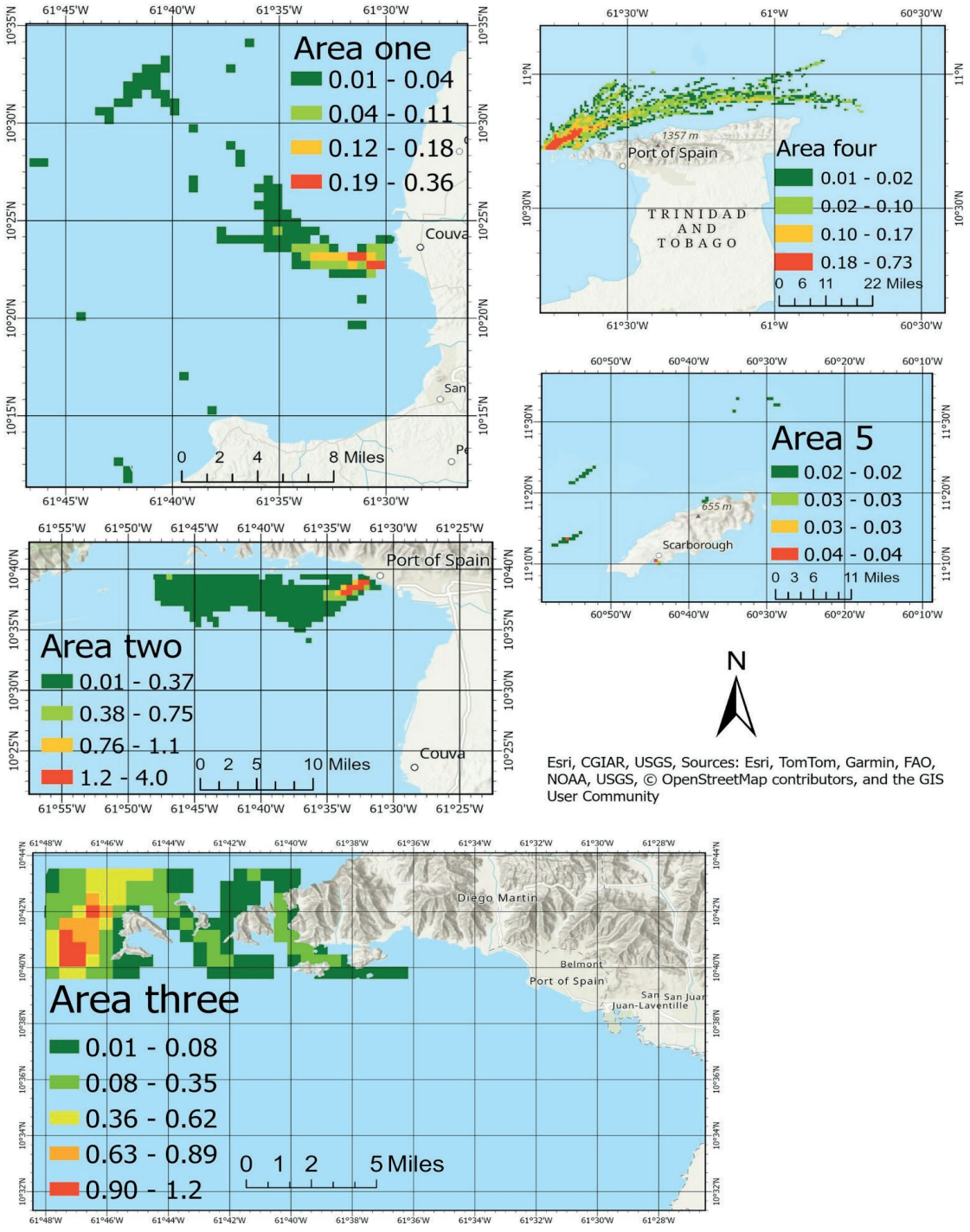


Fig. 2 Spatial distribution of the drifting collision probability (Seepersad & Davis, 2025).

https://doi.org/10.58440/ihr-31-2-a16

Table 7 Mean of the annual probability of drifting collisions per area.

Area	Mean of the annual probability of drifting collisions per area
One	0.04
Two	0.2
Three	0.2
Four	0.06
Five	0.02

Table 8 ML Scenario – estimated annual drifting collision risk by area (USD, rounded).

Consequence category	Area One – ML	Areas Two & Three (combined) – ML	Area Four – ML	Area Five – ML
Fisheries	5,860	58,600	8,790	2,930
Delays	7,500	75,000	11,250	3,750
Loss of life	30	300	45	15
Infrastructure	300	3,000	450	150
Damage to ship	2,600	26,000	3,900	1,300
Beaches (Tourism)	4,020	40,200	6,030	2,010
Other beaches	4,020	40,200	6,030	2,010
Swamp	4,020	40,200	6,030	2,010
Mean risk per area	28,350	283,500	42,525	14,175
Mean risk per area (rounded to nearest $10k)	30,000	280,000	40,000	10,000

Table 9 WC Scenario – estimated annual drifting collision risk by area (USD, rounded).

Consequence category	Area One – ML	Areas Two & Three (combined) – ML	Area Four – ML	Area Five – ML
Fisheries	44,800	448,000	67,200	22,400
Delays	22,000	220,000	33,000	11,000
Loss of life	20,200	202,000	30,300	10,100
Infrastructure	2,240	22,400	3,360	1,120
Damage to ship	8,000	80,000	12,000	4,000
Beaches (Tourism)	50,280	502,800	75,420	25,140
Other beaches	50,280	502,800	75,420	25,140
Swamp	50,280	502,800	75,420	25,140
Mean risk per area	248,080	2,480,800	372,120	124,040
Mean risk per area (rounded to nearest $10k)	250,000	2,480,000	370,000	120,000

indicate model-derived probabilities. Area one shows generally low probabilities with isolated instances of higher risk. Area two reveals the highest variability and overall drifting probability, indicating the need for prioritised risk mitigation strategies. Area three shows stable yet slightly elevated probabilities compared to Area one. Area four shows moderate risks, with distinct pockets of higher probability, while Area five maintains a stable and consistently low-risk profile with minimal variation (Seepersad & Davis, 2025).

The mean of the annual probability of drifting collisions per area is presented in Table 7.

The mean probability of drifting collision per area (Table 7) was combined with the mean economic consequence estimates from Table 6 to calculate the annual risk (USD) for each area and scenario (ML and WC). The results are presented in Tables 8 and 9.

5 Discussion

5.1 Economic implications of potential losses from maritime accidents

Socio-economic status, particularly income and occupation, emerged as the most influential determinants of WTP. Respondents with lower incomes

significantly less likely to support reallocating taxes for marine conservation, reaffirming that financial constraints limit participation even among those expressing environmental concern. In contrast, individuals in higher occupational categories demonstrated greater willingness, reflecting both greater economic capacity and a stronger sense of environmental responsibility. The absence of significant effects for education and environmental awareness suggests that financial capacity exerts a stronger influence on willingness than attitudinal factors. Although stated willingness was generally high, respondents frequently raised concerns about affordability and fairness, indicating that support was conditional, anchored in principle but constrained by household budgets. Any overstatement of willingness may have occurred due to social desirability bias, whereby respondents provide answers aligned with perceived social norms of environmental responsibility.

The regression model exhibited sound performance, consistent with socio-economic theory and statistically significant at the five percent level. Given that the objective of this research was to develop a practical, transferable approach for SIDS, emphasis was placed on achieving a parsimonious model with clear, interpretable results rather than complex statistical optimisation. This reflects the study's focus on ensuring that the analytical framework remains applicable in maritime administrations with limited technical or financial resources. Future applications of this approach could include additional diagnostics, such as pseudo-R^2 statistics and classification accuracy, to further demonstrate model robustness and predictive reliability.

Median WTP amounts varied across resource types, indicating that respondents distinguished between ecosystems based on perceived importance. The Caroni Swamp received the highest valuation, reflecting its ecological rarity and cultural significance, while non-tourism beaches were valued lower, suggesting a preference for resources that provide direct recreational or economic benefits. Survey design effects may also have contributed to this pattern since the swamp appeared first, respondents may have stated higher amounts before experiencing budget fatigue; a recognised response pattern in CV studies. Randomising question order in future surveys would help control for such effects.

These behavioural findings carry clear policy were significantly less likely to support reallocating taxes for marine conservation, reaffirming that financial constraints limit participation even among those expressing environmental concern. In contrast, individuals in higher occupational categories demonstrated greater willingness, reflecting both greater economic capacity and a stronger sense of environmental responsibility. The absence of significant effects for education and environmental awareness suggests that financial capacity exerts a stronger influence on willingness than attitudinal factors. Although stated willingness was generally high, respondents frequently raised concerns about affordability and fairness, indicating that support was conditional, anchored in principle but constrained by household budgets. Any overstatement of willingness may have occurred due to social desirability bias, whereby respondents provide answers aligned with perceived social norms of environmental responsibility.

The regression model exhibited sound performance, consistent with socio-economic theory and statistically significant at the five percent level. Given that the objective of this research was to develop a practical, transferable approach for SIDS, emphasis was placed on achieving a parsimonious model with clear, interpretable results rather than complex statistical optimisation. This reflects the study's focus on ensuring that the analytical framework remains applicable in maritime administrations with limited technical or financial resources. Future applications of this approach could include additional diagnostics, such as pseudo-R^2 statistics and classification accuracy, to further demonstrate model robustness and predictive reliability.

Median WTP amounts varied across resource types, indicating that respondents distinguished between ecosystems based on perceived importance. The Caroni Swamp received the highest valuation, reflecting its ecological rarity and cultural significance, while non-tourism beaches were valued lower, suggesting a preference for resources that provide direct recreational or economic benefits. Survey design effects may also have contributed to this pattern since the swamp appeared first, respondents may have stated higher amounts before experiencing budget fatigue; a recognised response pattern in CV studies. Randomising question order in future surveys would help control for such effects.

These behavioural findings carry clear policy implications. Tiered contribution systems proportional to income could improve fairness and affordability, while allocating a portion of tourism revenue to marine conservation may better align funding with perceived value. Communication campaigns should highlight the long-term and intergenerational benefits of conservation, as these motivations tend to influence willingness. Longitudinal studies could assess whether WTP remains stable under changing economic or environmental conditions, while alternative statistical methods, such as generalised linear or hierarchical models, could refine segmentation and improve predictive accuracy.

Finally, the framework developed in this study integrates accident probability with economic consequence, addressing a key gap in previous maritime risk approaches that emphasised probability alone. By localising consequence categories to the economic and environmental conditions of TT's EEZ, the framework provides a practical and transferable technique for prioritising risk mitigation and resource allocation in SIDS where maritime sectors underpin national economies.

5.2 Applicability and relevance of the consequence scale

The consequence scale classified impacts by severity across key loss categories, using monetary estimates from the valuation framework. This enabled consistent comparison of both ML and WC accidents within a single assessment system. Expressing losses in monetary terms supports cost-benefit and budget planning, strengthening policy relevance. Adaptation to local data and expert input shows that the framework is practical for SIDS, where resources

https://doi.org/10.58440/ihr-31-2-a16

are limited, ensuring methodological rigour and transferability across maritime administrations.

5.3 Estimated economic consequences of the ML and WC scenarios

The results show a pronounced difference in economic magnitude between the ML and WC scenarios. Under the ML scenario, total mean losses were approximately USD 0.7 million, with the largest impacts from delays (USD 187,500) and fisheries (USD 146,500), followed by moderate effects on beaches, swamps, and ship damage. In contrast, the WC scenario produced total losses of USD 6.2 million, dominated by damages to beaches, swamps, and fisheries, each exceeding USD 1.2 million. These findings highlight that while minor incidents cause manageable but recurrent costs, rare severe events could impose substantial, economy-wide losses.

5.4 Integrated risk estimates combining probability and consequence metrics

Risk values were estimated by multiplying mean losses for each scenario by the mean drifting collision probability for each area. Annual drifting-collision risks ranged from USD 10,000 in Area Five to USD 2.48 million along the north-western coastline (Areas Two and Three). These areas show the highest risk due to dense vessel traffic, navigational constraints, and environmental sensitivity, underscoring the need for targeted preventive and mitigation measures (Seepersad & Davis, 2025).

6 Conclusion

This study developed an adaptable economic risk assessment framework grounded in the TEV approach, addressing risks to maritime navigation within TT's EEZ and offering applicability to other SIDS. The framework achieved all four objectives: it quantified potential economic consequences of maritime accidents; constructed a locally relevant, monetary-based consequence scale; estimated losses under both ML and WC scenarios; and integrated these with probability metrics to produce spatially explicit risk maps. The findings revealed that while frequent minor incidents impose modest but recurrent costs, rare high-severity events could generate multi-million-dollar losses. By combining economic valuation with probabilistic risk modelling, the framework provides maritime administrations with a practical, transferable decision-support tool for prioritising mitigation measures and optimising resource allocation in vulnerable maritime regions.

7 Strengths, limitations, and future directions

The strength of this study lies in integrating historical accident data, market valuation, and CV surveys, enhancing reliability through multiple evidence sources. Using locally derived data grounds estimates in real economic conditions, while standardised methods ensure comparability across resource types. The monetary consequence scale marks a major advancement but has limitations. The TEV framework depends on stated preferences, which can introduce uncertainty when respondents are unfamiliar with the resources being valued. The monetary ranges are indicative, providing realistic but generalised estimates rather than precise figures. Percentage losses were adapted from the SIRA scale, offering plausible but simplified relationships. Furthermore, the scale does not fully capture secondary or long-term ecological and socio-economic effects extending beyond the immediate incident timeframe. The scenario-based approach aligns with the FSA (2018) and offers a practical, transferable decision-support tool for maritime administrations. Future work should validate the results of this study against real incident data to refine predictive accuracy and integrate real-time environmental and vessel-traffic parameters. Applying it across other SIDS across the world would further confirm its robustness and generalisability to diverse maritime contexts.

References

Abdullah, S., Markandya, A. and Nunes, P. A. L. D. (2011). Introduction to economic valuation methods. In P. A. L. D. Nunes, P. Kumar, and A. Markandya (Eds.), *Handbook on the Economics of Ecosystem Services and Biodiversity* (pp. 143–187). World Scientific, Singapore. https://doi.org/10.1142/9789814289238_0005

Arrow, K., Solow, R., Portney, P. R., Leamer, E. E., Radner, R. and Schuman, H. (1993). *Report of the NOAA Panel on Contingent Valuation*. National Oceanic and Atmospheric Administration, U.S. Department of Commerce. https://repository.library.noaa.gov/view/noaa/60900 (last accessed 25 October 2025).

Ashford, G. (2021) *Contingent valuation method* [Video]. University of the Sunshine Coast, Queensland, Australia. https://www.youtube.com/watch?v=C7dLbWEmOMY (last accessed 3 October 2025).

Bateman, I. J., Carson, R. T., Day, B., Hanemann, M., Hanley, N., Hett, T., Jones-Lee, M., Loomes, G., Mourato, S., Özdemiroglu, E., Pearce, D. W., Sugden, R. and Swanson, J. (2002). *Economic Valuation with Stated Preference Techniques: A Manual*. Edward Elgar Publishing, Cheltenham, UK.

Bhoncharan, B. (2025). *Interview with Shivani Seepersad*. Phoenix Park Gas Processors Limited, Trinidad.

Bolt, K., Ruta, G. and Sarraf, M. (2005) *Estimating the cost of environmental degradation*. The World Bank Environment Department, Washington, DC, USA.

Carson, R. T., Flores, N. E. and Meade, N. F. (2001). Contingent valuation: Controversies and evidence. *Environmental and Resource Economics, 19*(2), pp. 173–210. https://doi.org/10.1023/A:1011128332243

Carson, R. T., Mitchell, R. C., Hanemann, W. M., Kopp, R. J., Presser, S. and Ruud, P. A. (2003). Contingent valuation and lost passive use: Damages from the Exxon Valdez oil spill. *Environmental and Resource Economics, 25*(3), pp. 257–286. https://doi.org/10.1023/A:1024486702104

Cavcic, M. (2022). *Rig workers evacuated following issue on Noble jack-up*. Offshore Energy, Schiedam, The Netherlands. https://www.offshore-energy.biz/rig-workers-evacuated-following-issue-on-noble-jack-up (last accessed 10 August 2025).

Chua, K. (2025) Binary Logistic Regression. In C. Hua, Y.-J. Choi and Q. Shi, *Companion to BER 642: Advanced Regression Methods*, bookdown – Authoring Books and Technical Documents with R Markdown. https://bookdown.org/chua/ber642_advanced_regression/

binary-logistic-regression.html (last accessed 25 October 2025).

Cleary, P. D. and Angel, R. (1984). The analysis of relationships involving dichotomous dependent variables. *Journal of Health and Social Behavior, 25*(3), pp. 334–348.

CSO (2025). *Household Budgetary Survey (HBS).* Central Statistical Office, Port of Spain, Trinidad and Tobago. https://cso.gov.tt/household-budgetary-survey-hbs/ (last accessed 10 August 2025).

DOT (2021). *Revised Departmental Guidance on Valuation of a Statistical Life in Economic Analysis*. United States Department of Transportation, Washington, DC, USA. https://www.transportation.gov/office-policy/transportation-policy/revised-departmental-guidance-on-valuation-of-a-statistical-life-in-economic-analysis (last accessed 25 October 2025).

Du Plessis, F., Goedhals-Gerber, L., and Van Eeden, J. (2023). Trends in weather-related marine cargo insurance claims: A South African perspective. *Journal of Transport and Supply Chain Management, 17*, https://doi.org/10.4102/jtscm.v17i0.954

EcosystemValuation (2025) *Uses of ecosystem valuation*. https://www.ecosystemvaluation.org/uses.htm (last accessed 1 October 2025).

EPA (2017). Cost Estimation: Concepts and Methodology. In *EPA Air Pollution Control Cost Manual* (7th ed). U.S. Environmental Protection Agency, Washington, DC. https://www.epa.gov/sites/default/files/2017-12/documents/epaccmcostestimationmethodchapter_7thedition_2017.pdf (last accessed 8 October 2025).

FAO/WHO (2006). Risk characterization of microbiological hazards in food: Linking risk assessment and economic analysis. *Microbiological Risk Assessment Series, 17*. Food and Agriculture Organization of the United Nations/World Health Organization, Rome, Italy.

Frew, E. J., Whynes, D. K. and Wolstenholme, J. L. (2003). Eliciting willingness to pay: Comparing closed-ended with open-ended and payment scale formats. *Medical Decision Making*, 23(2), pp. 150–159. https://doi.org/10.1177/0272989X03251245

Gonyo, S. B., Goedeke, T. L., Wolfe, K. E., Jeffrey, C. F. G., Gorstein, M., Poti, M. and Dorfman, D. S. (2019). An economic analysis of shipping costs related to potential changes in vessel operating procedures to manage the co-occurrence of maritime vessel traffic and whales in the Channel Islands region. *Marine Policy, 106*, 103523. https://doi.org/10.1016/j.marpol.2019.103523

Harris, J. K. (2021). Primer on binary logistic regression. *Family Medicine and Community Health, 9*(Suppl 1), p. e001290. https://doi.org/10.1136/fmch-2021-001290

Harris, J. M. and Roach, B. (2021). *Environmental and natural resource economics: A contemporary approach* (5th ed.). Routledge, Abingdon, UK. https://doi.org/10.4324/9781003080640

Howard, M. (2019). *BIMCO: VLCC Freight Rates from Gulf to China Doubles*. MarineLink, Maritime Activity Reports, Inc., Easton, USA. https://www.marinelink.com/news/bimco-vlcc-freight-rates-gulf-china-467582 (last accessed 10 August 2025).

Huang, Y., Wang, C., Zhang, D. and Li, K. (2023) A review on risk assessment methods for maritime transport. *Ocean Engineering, 279*, 114577. https://doi.org/10.1016/j.oceaneng.2023.114577

IALA (2022a). *Risk Management* (G1018, 4 ed.). International Association of Marine Aids to Navigation and Lighthouse, Staint Germain en Laye, France. https://www.iala.int/product/g1018/ (last accessed 9 August 2025).

IALA (2022b). *The Use of IALA Waterway Risk Assessment Programme* (G1123, 2.1 ed.). International Association of Marine Aids to Navigation and Lighthouse, Staint Germain en Laye, France. https://www.iala.int/product/g1123/ (last accessed 20 January 2025).

IALA (2022c). *The Use of the Simplified IALA Risk Assessment Method* (G1138, 2.0 ed.). International Association of Marine Aids to Navigation and Lighthouse, Staint Germain en Laye, France. https://www.iala.int/product/g1138/ (last accessed 20 January 2025).

IALA (2022d). *The Use of Ports and Waterways Safety Assessment* (G1124, 2.1 ed.). International Association of Marine Aids to Navigation and Lighthouse, Staint Germain en Laye, France. https://www.iala.int/product/g1124/ (last accessed 20 January 2025).

IMA (2010). *A Guide to Beaches and Bays of Trinidad and Tobago*. Institute of Marine Affairs, Chaguaramas, Trinidad and Tobago, ISBN 978-976-8194-17-6.

IMO (2010). *Global Integrated Shipping Information System (GISIS)* (Incident record: C0008290). International Maritime Organization, London, United Kingdom. https://gisis.imo.org/Public/MCIR/Occurrence.aspx?Reference=C0008290 (last accessed 30 January 2025).

IMO (2018). *Revised guidelines for Formal Safety Assessment (FSA) for use in the IMO rule-making process* (MSC-MEPC.2/Circ.12/Rev.2). International Maritime Organization, London, United Kingdom.

IMO (2020). *International Convention for the Safety of Life at Sea (SOLAS)* [Consolidated Edition 2020]. International Maritime Organization, London, United Kingdom. https://www.imo.org/en/About/Conventions/Pages/International-Convention-for-the-Safety-of-Life-at-Sea-(SOLAS),-1974.aspx (last accessed 30 January 2025).

IMO (2024). *Global Integrated Shipping Information System (GISIS)* (Incident record: C1000310). International Maritime Organization, London, United Kingdom. https://gisis.imo.org/Public/MCIR/Occurrence.aspx?Reference=C1000310 (last accessed 30 January 2025).

IMO (2024). *IALA Risk Management Toolbox for Aids to Navigation and Vessel Traffic Services*. (SN.1/Circ.296/Rev.1). International Maritime Organization, London, United Kingdom.

ISO (2018). *ISO 31000:2018 – Risk management – Guidelines* (2nd ed.). International Organization for Standardization, Geneva, Switzerland.

ITOPF (2025). *Atlantic Empress, West Indies, 1979*. ITOPF Ltd, London, United Kingdom. https://www.itopf.org/in-action/case-studies/atlantic-empress-west-indies-1979/ (last accessed 30 January 2025).

Kettunen, M., and ten Brink, P. (2006). *Value of biodiversity: Documenting EU examples where biodiversity loss has led to the loss of ecosystem services*. Final report for the European Commission. Institute for European Environmental Policy (IEEP), Brussels.

Khanal, B. R. (2001) *Economic valuation of forest resources*. Institute of Forestry, Tribhuvan University, Kathmandu.

Krejcie, R. V. and Morgan, D. W. (1970). Determining sample size for research activities. *Educational and Psychological Measurement, 30*(3), pp. 607–610. https://doi.org/10.1177/001316447003000308

Lee, C. and Mjelde, J. W. (2007). Valuation of ecotourism resources using a contingent valuation method: The case of the Korean DMZ. *Ecological Economics, 63*(2–3), pp. 511–520. https://doi.org/10.1016/j.ecolecon.2007.01.005

MEEA (2013). *The National Oil Spill Contingency Plan of Trinidad and Tobago*. Ministry of Energy and Energy Affairs, Government of the Republic of Trinidad and Tobago, Port of Spain, Republic of Trinidad and Tobago.

Mitchell, R. C. and Carson, R. T. (1989) *Using surveys to value public goods: the contingent valuation method*. Resources for the Future, Washington, DC, USA.

NAMDEVCO (2025). *Publication*. National Agricultural Marketing and Development Corporation, Debe, Trinidad and Tobago. https://www.namdevco.com/publication (last accessed 12 August 2025).

Nwoloziri, C. N., Nze, I., Hlali, A., Nwachukwu, T. and Nwokedi, T. (2025). Estimation of cost of delays on vessel operations in container terminals of Apapa seaports. *Journal of Maritime Research, 22*(1), pp. 217–223.

OECD (2012). *Mortality Risk Valuation in Environment, Health and*

https://doi.org/10.58440/ihr-31-2-a16

Transport Policies [Report]. Organisation for Economic Co-operation and Development, OECD Publishing, Paris, France. https://doi.org/10.1787/9789264130807-en

Pearce, D. and Özdemiroglu, E. (2002). *Economic Valuation with Stated Preference Techniques: Summary Guide*. Department for Transport, Local Government and the Regions, London, UK. https://assets.publishing.service.gov.uk/media/5a750ff740f0b6397f35d5f5/Economic_valuation_with_stated_preference_techniques.pdf (last accessed 25 October 2025).

Plottu, E. & Plottu, B. (2007). The concept of Total Economic Value of environment: A reconsideration within a hierarchical rationality. *Ecological Economics*, *61*(1), pp. 52–61. https://doi.org/10.1016/j.ecolecon.2006.09.027

Počuča, M. (2006). Methodology of Day-To-Day Ship Costs Assessment. *Promet — Traffic & Transportation, 18*(5), pp. 337–345.

Rambarran, T. (2021). *Correspondence on vessel accidents* [Unpublished]. Maritime Services Division, Trinidad and Tobago.

Riding, J. and Rawson, A. (2015). *LINZ Hydrography Risk Assessment Methodology Update* (report number 15NZ322, issue 03). Land Information New Zealand (LINZ), Wellington, New Zealand. https://iho.int/uploads/user/Inter-Regional%20Coordination/WEND-WG/WENDWG%20Repository/SWPRHP-Hydrography-Risk-Assessment-Methodology.pdf (last accessed 7 April 2025).

Riley, R. D., Snell, K. I. E., Ensor, J., Burke, D. L., Harrell, F. E., Jr, Moons, K. G. M. and Collins, G. S. (2019). Minimum sample size for developing a multivariable prediction model: Part II – binary and time to event outcomes. *Statistics in Medicine, 38*(7), pp. 1276–1296.

Rozza, H. H., Elhoseny, T. A., Abbas, S. H. and Mosallam, R. A. (2025). Patients' willingness to pay for health care quality improvement under universal healthcare coverage in Egypt. *Journal of the Egyptian Public Health Association, 100*(1), p. 15. https://doi.org/10.1186/s42506-025-00195-x

Schneider, A., Hommel, G. and Blettner, M. (2010). Linear regression analysis. *Dtsch Arztebl Int, 107*(44), pp. 776–82. https://doi.org/10.3238/arztebl.2010.0776

Schuhmann, P. W. and Mahon, R. (2015). The valuation of marine ecosystem goods and services in the Caribbean: A literature review and framework for future valuation efforts. *Ecosystem Services, 11*, pp. 56–66.

Seepersad, S. and Davis, D. (2025). Integrating data-limited techniques for maritime risk assessment in Small Island Developing States. *The International Hydrographic Review, 31*(1), pp. 102–118. https://doi.org/10.58440/ihr-31-1-a06

Smith, R. D. (2000). The discrete-choice willingness-to-pay question format in health economics: Should we adopt environmental guidelines? *Medical Decision Making, 20*(2), pp. 194–204. https://doi.org/10.1177/0272989X0002000209

Stevens, T. H., Echeverria, J., Glass, R. J., Hager, T. and More, T. A. (1991). Measuring the existence value of wildlife: What do CVM estimates really show? *Land Economics, 67*(4), pp. 390–400. https://doi.org/10.2307/3146546

The Swedish Club (2020). *Navigational Claims*. The Swedish Club, Gothenburg, Sweden. https://www.swedishclub.com/uploads/2023/12/TSC-Nav-Claims-2020_WEB.pdf (last accessed 10 August 2025).

TT Guardian (2024). PM weighing foreign help if oil spill worsens. https://www.guardian.co.tt/news/pm-weighing-foreign-help-if-oil-spill-worsens-6.2.1923219.50bcf5d956 (last accessed 26 March 2025).

Vaughan, W. J., Russell, C. S. and Rodriguez, D. J. (1999). *Willingness to pay: Referendum contingent valuation and uncertain project benefits*. Sustainable Development Department Technical Papers Series. Inter-American Development Bank, Washington, DC, USA.

Wang, H. and He, J. (2010). *The Value of a Statistical Life: A Contingent Investigation in China*. Policy Research Working Paper 5421. The World Bank, Washington DC, USA.

World Bank (2025) *Search results for "use value" (Research)*. The World Bank, Washington, DC, USA. https://www.worldbank.org/en/search?q=use%20value&Type=Research (last accessed 29 September 2025).

Authors' biographies

Shivani Seepersad is an Advisor to the International Organisation of Marine Aids to Navigation and a PhD candidate in the Department of Geomatics Engineering and Land Management at the University of the West Indies, Trinidad and Tobago. Her doctoral research, titled An Economic Evaluation of Risks due to Maritime Navigation across the Greater Caribbean Region, focuses on maritime safety and risk assessment. She has previously served as a GIS intern at York University, contributing to flood risk modelling for the Greater Toronto Area, and as a GIS technician at Land Information New Zealand on the Niue Hydrographic Risk Assessment. Shivani holds a BSc in Geomatics Engineering (Honours) and an MSc in Geoinformatics (Distinction).



Shivani Seepersad

Dexter Davis is Lecturer in the field of surveying, adjustments and geodetic surveying and is also Coordinator of the B.Sc. Geomatics Engineering Programme in the Department of Geomatics Engineering & Land Management, Faculty of Engineering, The University of the West Indies. He is a member of the Institute of Surveyors of Trinidad and Tobago as well as the ASPRS. His research areas include engineering surveying, digital photogrammetry and digital mapping, GNSS, geodesy and geodetic applications and hydrographic surveying. Some of his recent work includes sea level monitoring, low cost and disaster relief mapping and 3d point cloud applications for engineering and digital twins.



Dexter Davis

PEER-REVIEWED ARTICLE

Nautical depth investigation in fluid mud environment at Santa Catarina Terminal (Port of São Francisco do Sul, Brazil)

Authors

Alberto Pedrassani Costa Neves[1], Augusto Dantas Sampaio[2] and Reginaldo Gonçalves Abreu[2]

Abstract

An apparent dilemma is often presented to port operations as if safety of navigation and port efficiency were opposing forces. Estuaries with heavy loads of sediments pose challenges to both safety and efficiency and they have to be addressed at the same time. The two sides of the same coin. One important matter is the use of low frequency sonars and rheometers, frequently discarded by Hydrographers on the basis that they do not achieve sufficient accuracy for the safety of navigation. However, high frequency sonars are not suitable for areas rich in fluid mud as they can only detect the floating, variable water-mud interface. This work addressed these limitations confronting high frequency multibeam survey with double frequency single beam survey and density measurements to find half a meter of navigable mud below the minimum depth indicated in a high-frequency sonar survey. The work proposes a first step to define a very conservative and safe definition of nautical depth.

Keywords

hydrographic survey · fluid mud · market valuation · nautical depth · safety of navigation · port efficiency

Resumé

Les opérations portuaires sont se heurtent à un dilemme apparent, comme si la sécurité de la navigation et l'efficacité portuaire étaient deux forces opposées. Dans les estuaires fortement chargés en sédiments, les enjeux de sécurité et d'efficacité se posent simultanément et doivent être relevés ensemble : ce sont les deux faces d'une même médaille. Une question importante concerne l'usage des sonars à basse fréquence et des rhéomètres, souvent écartés par les hydrographes au motif qu'ils ne seraient pas suffisamment précis pour garantir la sécurité de la navigation. Pourtant, les sonars à haute fréquence ne sont pas adaptés aux zones riches en vase fluide, car ils ne détectent que l'interface instable et changeante entre l'eau et la vase. Cette étude examine ces limites des levés multifaisceaux à haute fréquence, en les comparant à un levé monofaisceau à double fréquence associé à des mesures de densité. L'objectif est de déterminer si un demi-mètre de vase navigable se trouve sous la profondeur minimale indiquée par un levé sonar à haute fréquence. Elle constitue ainsi une première étape vers une définition plus prudente et sécurisée de la profondeur nautique.

Resumen

A menudo se plantea un dilema aparente en las operaciones portuarias, como si la seguridad de la navegación y la eficiencia portuaria fueran fuerzas opuestas. Los estuarios con grandes cargas de sedimentos plantean desafíos tanto para la seguridad como para la eficiencia, y deben abordarse al mismo tiempo. Son dos caras de la misma moneda. Un tema importante es el uso de sonares de baja frecuencia y reómetros, frecuentemente descartados por los Hidrógrafos por considerar que no alcanzan la precisión suficiente para la seguridad de la navegación. Sin embargo, los sonares de alta frecuencia no son adecuados para zonas ricas en lodo fluido, ya que solo pueden detectar la superficie de contacto flotante y variable entre el agua y el lodo. Este trabajo abordó estas limitaciones a las que se enfrentan los levantamientos multihaz de alta frecuencia con un levantamiento monohaz de doble frecuencia y mediciones de densidad para encontrar medio metro de lodo navegable por debajo de la profundidad mínima indicada en un levantamiento con sonar de alta frecuencia. Este trabajo propone un primer paso para definir una definición muy conservadora y segura de profundidad náutica.

✉ Alberto Pedrassani Costa Neves · alberto@pcn.srv.br

[1] PCN Maritime, Florianópolis, Brazil

[2] Hidrotopo Consultoria e Projetos, Rio de Janeiro, Brazil

https://doi.org/10.58440/ihr-31-2-a15

1 Introduction

In 2018, the operational draft at the Port of Santos was increased by 30 centimeters. The São Paulo State Dock Company (CODESP) estimated a 10 % increase in the company's revenue, in the order of USD 435 million per year. According to CODESP, this increase was made possible by two main factors: dredging services and the technology used for depth monitoring, which includes studies on fluid mud (Carneiro, 2018).

According to the United States National Oceanic and Atmospheric Administration (NOAA), an additional inch of draft allows a ship to gain up to USD 60,000 in additional cargo capacity (NOAA, 2025a). In ports, channels, and waterways where the fluid mud layer reaches significant thickness, this gain goes beyond economic values and represents strategic advantages in market competition and in efforts to reduce the cost of goods reaching the general public.

Chamanmotlagh et al. (2024) report that the Port of Emden (Germany) has areas where the fluid mud layer can reach 4.5 meters. In the Port of Zeebrugge (Belgium), the layer thickness reaches 3 meters in some stretches and 2 meters at the port entrance (Vanlede et al., 2019). In the Europort (Netherlands), up to 2 meters of maximum draft are achieved by conditioning the mud with a water injection process and using the definition of nautical depth (Kiricheck & Rutgers, 2020). The competitive gains of these ports, and many others in Europe, are remarkable.

If mud with the right consistency to be considered navigable is found in a channel, and correctly measured, that channel may require less dredging to maintain operational parameters. Poorly defined nautical depths can lead to unnecessary dredging or to navigation restrictions (PIANC, 2014). There are also other reasons for studying and measuring the fluid mud layer in a port: it can affect ship maneuverability, dynamic draft, buoyancy, and make the bottom harder to detect by navigation echo sounders.

Characterizing and measuring the fluid mud layer is complex due to the large volume of material, the biological, physical, and chemical properties of sediments, and their interaction with the environment – influenced by currents, tides, wind-driven turbulence, temperature variations, mixing of fresh and saltwater, rainfall, among other factors. In addition, human activities such as ship movements, dredging, and the discharge of treated water affect the maintenance and/or changes in the fluid mud layer.

Characterizing fluid mud and using it to define operational port parameters has been a well-established practice in American and European ports and waterways for decades (Kirby et al., 1980; Teeter et al., 1992; Wurpts & Torn, 2005). However, these technologies have often faced resistance from government agencies responsible for permits and authorizations, though they have been adopted gradually. The safety-efficiency dilemma has increasingly been resolved by the integration of both through the use of techniques and technology.

The objective of this study is to review methods in ports with significant amounts of unconsolidated suspended mud, analyze the hydrographic and sedimentological surveys carried out in the Port of São Francisco do Sul (Brazil), and propose a method for defining the fluid mud layer and the nautical bottom, in accordance with PIANC (2014). Defining the nautical bottom is essential to optimize both navigation safety and port operational efficiency.

There are huge challenges to introduce and implement the nautical bottom concept in the Brazilian ports. In the forefront are the lack of government agencies support and the reduced critical mass in ports and universities. Additionally, there is little awareness on the directions to follow, linked to the two challenges above mentioned. Uncertainties in the short and long runs would make it difficult to secure investments to establish the necessary infrastructure (equipment, vessels, laboratories) in a country with an area larger than the European countries (except the Russian part but including Greenland) combined. Brazil is also home to large river systems, with an estimated 42,000 km of navigable inland waterways.

2 Background

According to McAnally et al. (2007), fluid mud is a high concentration of fine sediments in which sedimentation is substantially hindered by the closeness of sediment grains with flocs, and which has not yet formed an interconnected matrix with bonds strong enough to eliminate its potential mobility. Local characteristics can favor the maintenance of sediments in suspension and prevent them from consolidating into a material with high viscosity. However, the definition of fluid mud is not universally established, nor are its measurement methods, since both depend on local characteristics and management needs.

Greiser et al. (2002) point out that an important component of fluid mud is organic matter, which can account for more than 60 % of the *in-situ* mud particle volume, being responsible for particle aggregation and stabilization of the internal structure of the fluid mud. The particles remain suspended for long periods due to their low density and the buoyancy of the flocs (Wurpts & Torn, 2005; Shakeel et al., 2022).

In the United States, fluid mud conditions are more frequent in districts of warmer regions and are more prevalent in estuaries where mineral-rich freshwater mixes with saltwater. In these places, mineralogical flocculation of freshwater sediments is accelerated when the sediment reaches saltwater. These flocculants are very loose aggregates with a water content equal to or greater than 95 % and can remain suspended for long periods (USACE, 2013).

Measuring the thickness of the fluid mud layer is a necessary challenge. When the upper layer of sediment is not well consolidated, the three methods normally used by the U.S. Army Corps of Engineers

https://doi.org/10.58440/ihr-31-2-a15

(USACE) – sounding pole, lead line, and acoustic echo sounder – will generally not correlate with each other and may not even give consistent readings from one moment to the next when using the same instrument or technique (USACE, 2013).

The concentration of sediment in water reduces the propagation speed of sound, which can significantly affect acoustic measurements with echo sounders. USACE (2013) correctly points out that in unconsolidated bottoms – that is, fluid mud – records cannot be reliably interpreted without some form of correlated or corroborative information. The echo sounder alone is not enough to monitor fluid mud, neither for navigation nor for port management.

Various methods and equipment are used to measure the thickness and navigability of fluid mud. The lower limit of navigable mud is defined as the nautical bottom (PIANC, 2014). One technique is to measure the *in-situ* sediment density, and there are different methods to perform this task. According to Claeys (2006), it is possible to distinguish methods as

- remote sensing with echo sounding (acoustic density profile, based on acoustic impedance transitions), and
- profiling with point measurement devices using instruments based on Gamma-ray, tuning fork, and acoustics.

However, a single critical density value cannot always be chosen as the criterion for the nautical bottom (Shakeel et al., 2019). Yield stress is an important discontinuity in the transition between fluid and solid mud, and it can also be a parameter to specify the nautical depth, as used in the Port of Emden (Wurpts & Torn, 2005). Yield stress and density are two essential rheological characteristics for determining nautical depth in the Port of Hamburg (Shakeel et al., 2022). Therefore, multi-criteria approaches – such as combining rheological and echo sounding criteria – can be used to determine nautical depth, depending on the local characteristics.

As fluid mud approaches the consolidation point, its yield stress increases, and its viscosity rises sharply. Beyond the consolidation point, mud can behave like a weak gel or a soft solid. There is no single formula that universally relates all these properties, but rheological tests (e.g., rheometer measurements) help identify the critical yield stress or density that marks the consolidation point. By evaluating rheological properties of fluid mud samples through tuning fork data, Fonseca et al. (2018) describe the functioning of the Densitune, a model similar to the one used in this study.

Carneiro et al. (2017) evaluated strategies for measuring fluid mud layers and their rheological properties in the Port of Santos, where up to 1.4 m of fluid mud was found, with a critical density of 1,200 kg/m^3. The Port of Emden in Germany defined the mud layer with a yield stress of 100 Pa as the navigable depth (Wurpts & Torn, 2005). Adopting 100 Pa as a reference for the Port of Santos, critical densities would range from 1,200 to 1,275 kg/m^3. Using 1,200 kg/m^3 was thus a safer choice for the moment. Carneiro (2018) notes that the critical density of 1,200 kg/m^3 is also used in the ports of Rotterdam and IJmuiden (Netherlands), Bangkok (Thailand), and Nantes-Saint-Nazaire and Bordeaux (France).

An important aspect of fluid mud studies is its impact on ship maneuverability. According to Verwilligen et al. (2014), a full-mission maneuvering simulator study was carried out in the Zeehavenkanaal for access to the Port of Delfzijl (Netherlands) and showed the possibility of working with a nautical bottom located lower than the top of the mud layer. This allowed the port to receive ships with greater draft without additional dredging. To validate the simulator study conclusions, full-scale ship maneuvering tests were performed with a general cargo vessel departing from the port.

In all simulations at Delfzijl, pilots managed to carry out maneuvers acceptably. It was concluded that maneuvers at that port, with vessels navigating with small negative under keel clearance (UKC) relative to the top of a fluid mud layer, were acceptable, provided the pilots had experience with local conditions and were aware of the effects of the mud-water interface on ship handling. It is noteworthy that this channel is about 3.2 nautical miles long.

The above aspects show the possibility and complexity of measuring, mapping, and using the fluid mud layer to improve navigation safety and port operation efficiency. Consequently, the U.S. and many European countries have structures that allow fluid mud navigation to be managed by specialized agencies and ports with competent hydrography services. In the U.S., for example, USACE is responsible for the subject – not the three agencies representing the country at the International Hydrographic Organization (IHO): NOAA's Office of Coast Survey, the National Geospatial-Intelligence Agency, and the Navy's Meteorology and Oceanography Command (IHO, 2025).

In Belgium, France, Germany, Netherlands, and UK, for example, ports and their approaches are the responsibility of port authorities, which carry out surveys and decide on fluid mud navigation, not the hydrographic services represented at the IHO. Austria and Switzerland carry out surveys and nautical charting of their navigable channels and are not IHO Member States. In these countries and in the U.S., agencies and port authorities decide on fluid mud navigation, advised by pilotage services, due to local knowledge and operational needs that cannot be delegated to organizations without such knowledge or vested interest in operations.

These aspects stem from the fact that the IHO does not focus exhaustively on surveys in estuarine regions with high sediment loads. This is due to historical reasons linked to governmental organization in Europe and the U.S., where the IHO headquarters

https://doi.org/10.58440/ihr-31-2-a15

is located. Most IHO Presidents (now Secretary-Generals) and Directors have come from these regions. Currently (2025), the representatives are from Germany, the U.S., and Italy. Furthermore, for most of its existence, the IHO has focused on surveys for nautical charting.

For example, the NOAA Field Procedures Manual and the Hydrographic Survey Specifications and Deliverables (2021, 2025b) do not mention "fluid mud", while this is extensively covered in USACE (2013). Survey specifications in areas with fluid mud depend on the location and are subject to the considerations of each USACE district.

The very creation of the IHO in 1921 was driven by the need to sound and map the oceans in support of international navigation. This began to change when IHO Member States realized the value of Hydrography beyond nautical charting and navigation safety. The publication of S-44 Edition 6.0.0 (IHO, 2020a) marked a new era for survey standardization. But even in this standard, there is no aim to standardize surveys in waters with high sediment loads. However, the IHO Hydrographic Manual (IHO, 2011) presents a broader view, recommending the use of low-frequency echo sounders – though this was not incorporated into current versions of S-44 (IHO, 2024). The reason is that this publication presents survey standards without specifying the technology.

The comments above are not a criticism of the functioning of the IHO and the hydrographic services of its Member States, but simply an observation, since setting universal standards for such heterogeneous environments is often not a tangible goal. Nautical charting is inherently international, and worldwide adoption of standards requires very restrictive approaches. Particularities of each estuarine environment with high sediment loads must be addressed locally, as is the case in Babitonga Bay.

3 Literature review on navigable mud layer measurement

Among the many academic studies, some have been selected for review, particularly due to their connections with the agencies and port authorities involved. References from these articles were used in this study to provide a basis for the analytical method, as well as for the conclusions and recommendations. Not all the references easily apply to the present case. Some of them, like those involving rheological properties, will take time to prove to port authorities and other governmental agencies that they bring value and are worth investments.

3.1 Effects of recirculation dredging on the density, strength, settling, and oxygen concentration of fluid mud in the Port of Emden (Chamanmotlagh et al., 2024)

A bathymetric mapping was carried out using a dual-frequency single-beam echo sounder Kongsberg EA 440. The lutocline (fluid mud–water interface) and the fluid mud-bed interface were detected at 200 kHz and 15 kHz, respectively. According to the EA 440 manual, the accuracy of this dual-frequency echo sounder depends on pulse length, being 0.6 cm for 200 kHz and 4.9 cm for 15 kHz. *In-situ* vertical profiles of density and yield stress were obtained using a Rheotune from Stema. This tool has often been used to quantify strength and density properties of fluid mud for nautical bottom applications (Kirichek & Rutgers, 2020).

In field surveys, density increased significantly with depth, consistent with the natural sedimentation process observed in fluid mud environments. This phenomenon is attributed to the settling of denser particles towards the bottom due to gravity, resulting in a stratified density gradient. From the consolidation point onward, density alone was not considered an adequate criterion for the nautical bottom, as material strength could vary significantly. Using only sediment density as a navigation criterion may overlook the complexity of mud, where similar densities do not guarantee identical yield stresses (Kirichek et al., 2018a; Kirichek & Rutgers, 2020; Shakeel et al., 2021). Consequently, the authors conclude that both density and yield stress are important criteria for defining the nautical bottom.

3.2 Study of fluid mud layers in ports and navigation channels (Carneiro, 2018)

Fluid mud does not behave according to Newton's Law (classical fluid) nor Hooke's Law (classical soil mechanics). Due to high sediment concentrations, it exhibits non-Newtonian rheological properties. While Newtonian fluids have well-defined viscosity, non-Newtonian fluids have viscosity that varies with shear rate. For the Port of Emden, sediments with a yield stress lower than 100 N/m² were defined as navigable. In Itajaí (Brazil), the critical density was adopted as the parameter for navigable fluid mud, defined as 1,300 kg/m³. This density is higher than that used in other ports, which usually ranges between 1,200 and 1,250 kg/m³. According to Plon & Alfredini (2019), the Port of Itajaí has a 50 cm fluid mud layer throughout the area of interest, with some places reaching up to 2.5 m thickness.

The author concludes that combining survey strategies such as acoustic methods, density measurements, and laboratory tests – such as granulometry and rheological properties – is better for navigation purposes when defining the nautical bottom, instead of relying solely on echo sounders. As in solutions already used in major ports worldwide, defining the fluid mud layer can reduce dredging, among other advantages.

A study was conducted in the Port of Santos, the busiest and largest port in Brazil. Due to the extension of the port and its access channel, there is spatial and temporal variability, with the thickness of fluid mud layers increasing towards the inner parts of the port, accompanied by a decrease in sand

https://doi.org/10.58440/ihr-31-2-a15

content. The study was carried out along a 3 km linear transect. During a tidal cycle, the minimum thickness occurred at slack water. The study concluded, among other things, that the critical density for the Port of Santos should be 1,200 kg/m³, allowing up to 1.4 m of navigable fluid mud. It is important that the nautical bottom criterion considers not only rheology and echo sounding but also environmental and port-related parameters and pilot training.

3.3 Fluid mud properties and nautical depth estimation: A case study in navigation channel of Duyen Hai Port, Viet Nam (Nguyen & Le, 2023)

The authors argue that most navigation channels worldwide choose the rheological parameter of fluid mud density to determine nautical depth. This guideline was applied in 18 ports, with the density criterion ranging from 1,150 to 1,300 kg/m³. However, density alone is not a sufficient criterion to predict the rheology of different muds. Therefore, a single critical density value cannot be chosen for the nautical bottom criterion (Shakeel et al., 2019, 2022).

The authors also note that yield stress is an important discontinuity in the transition between fluid, pre-consolidated, and solid mud. In many ports, yield stress is the parameter specifying nautical depth, including in the Port of Emden (Wurpts & Torn, 2005). The combination of density and yield stress are two essential rheological characteristics for determining nautical depth in the Port of Hamburg (Shakeel et al., 2022). The authors conclude that multi-criteria approaches, combining rheology and echo sounding, should be used to determine nautical depth.

3.4 Current surveying strategies in ports with fluid mud layers (Kirichek et al., 2018a)

This article provides an overview of survey strategies that are or can be used in ports and waterways with fluid mud layers. The combination of acoustic methods with others based on density or shear strength measurements is discussed. Typically, fluid mud can be described as a mixture of water, organic matter, and mainly cohesive mineral sediment, generally found in estuaries and rivers with low-intensity currents. Fluid mud is in a transitional state and will eventually settle and consolidate over time, unless disturbed by dredging, currents, or other mechanical processes.

Traditional acoustic bathymetry often fails to detect a sharp interface between fluid mud and consolidated bed. Fluid mud layers can be substantially thick, with small density gradients within the layer. These gradients are often insufficient for detecting acoustic impedance differences. Therefore, other strategies have been developed for surveying ports and waterways with fluid mud layers.

The authors prepared a schematic concept of the nautical bottom (Fig. 1). Applying these definitions requires understanding the physical characteristics of mud and how mud layers affect vessel behavior. Based on experimental research in the Port of Rotterdam in 1974, a density of 1,200 kg/m³ was chosen as the physical characteristic defining the nautical bottom. In other ports, this density value varies from approximately 1,150 to 1,300 kg/m³, or the nautical bottom is defined by echo sounding or rheological criteria.

Kirichek et al. (2018a) gives an overview of different methods for assessing the density and rheological properties of the mud. Due to the non-linear relationship between density and the mud strength, the

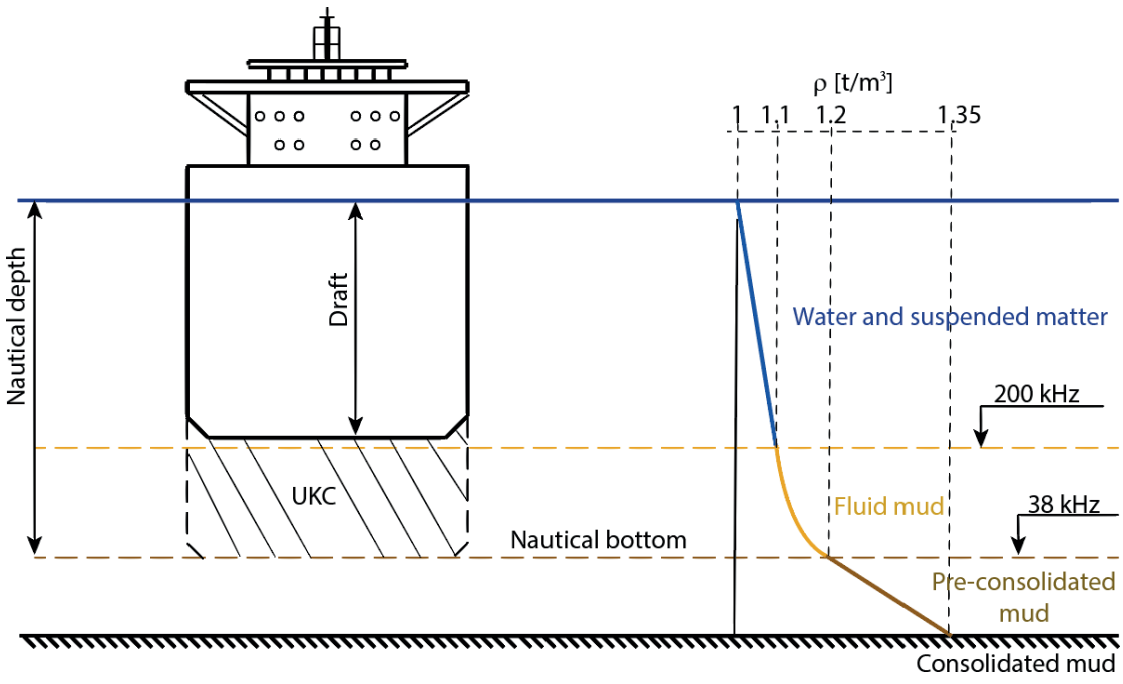


Fig. 1 Nautical depth concept in the Port of Rotterdam for the critical density of 1,200 kg/m³ (Kirichek et. al., 2018b; PIANC, 2014).

https://doi.org/10.58440/ihr-31-2-a15

approach for defining practical criteria for port authorities should be investigated in laboratory in order to assess the best set of parameters. The approach could include the relationship of this set of parameters and acoustic methods.

3.5 Conducting surveys in fluid mud (Buchanan, 2008)

Larry Buchanan, from Teledyne Odom Hydrographic, discusses the challenges of conducting surveys in fluid mud environments. An expert in acoustic propagation and echo sounders, he explains how fluid mud affects acoustic signals, including propagation speed, transmission losses, and reflectivity. He also discusses the dilemmas in selecting the appropriate frequency for an echo sounder in such environments.

USACE (2013) acknowledges this dilemma: *In general, higher-frequency transducers (100 kHz to 1,000 kHz) will provide more accurate depth measurements due to frequency characteristics and narrower beam widths*. A major disadvantage of high-frequency transducers is that there is high signal attenuation with depth, and low-density suspended sediments or bottom vegetation will readily reflect the signal.

High-frequency transducers are not recommended in areas where suspended sediment layers commonly occur. In these areas, frequencies between 20 kHz and 50 kHz are typically used to define dredging volumes. The manual also correctly states that in unconsolidated bottoms – that is, fluid mud – records cannot be reliably interpreted without correlated or corroborative information.

Recognizing that acoustic sensor information alone is not sufficient to establish safe navigation depth in a channel when fluid mud or suspended materials are present in the water column, there has been a search for tools to confirm depths recorded by the echo sounder and for determining nautical depth. When a ship passes through a fluid mud layer, external forces affect its control and maneuverability. The rheology of fluid mud, like that of any real liquid, is defined by its viscosity – its ability to deform and reshape. The direct influence of this property on a vessel's safe navigation makes it an excellent factor to help determine nautical depth.

The difficulty, however, is that the viscosity of the material is not easily obtained in real time. Often, samples must be collected and sent to a laboratory for analysis. The need for real-time, continuous monitoring requires near-immediate results. There are several density-measuring devices capable of determining fluid mud density levels in real time. Once the rheological properties of materials in a specific location are established, appropriate density levels can be determined as safe navigation levels, for determining nautical depth. Generally, these density-measuring devices are directly connected to an existing echo sounder or provide their own specific acoustic signal.

In most cases, calibration is carried out to establish material properties, after which density levels can be determined during hydrographic survey operations. Once established, calibration values for a location change little, if at all. Only periodic confirmation of calibration values is needed. The range of acceptable density levels varies widely from port to port. Studies indicate that the critical nautical bottom density ranges from 1,150 kg/m³ in Zeebrugge (Belgium) to 1,270 kg/m³ in Cayenne (French Guiana)[1]. A typical echo sounder record also allows identification of the fluid mud layer when compared to other bottom types. This makes determining nautical depth simpler and certainly more accurate.

As seen in the above studies, there is a variety of sensors and techniques to address the definition of the nautical bottom and nautical depth. It is also understandable that the local environmental characteristics pose a challenge for port authorities and that they require especial consideration in the selection of the sensors and techniques to assess the parameters that will deliver safety of navigation and efficient port operations.

4 Analysis of standards and guidelines for surveys and projects involving fluid mud

In general, the standards of the IHO, adopted in Brazil by the Directorate of Hydrography and Navigation, are the obvious references for guiding hydrographic surveys in the country. Although the IHO has evolved its standards, as mentioned in Section 2, the focus on hydrographic surveys in areas with high sediment concentration and on defining the nautical bottom has not yet been – and perhaps never will be – incorporated into its objectives, particularly in the Standards for Hydrographic Surveys (IHO, 2024).

In this complex context of surveys in areas with fluid mud and high sediment loads, many other institutions have stood out in terms of standards and guidelines for surveys. The importance of the World Association for Waterborne Transport Infrastructure (PIANC) is noteworthy. The PIANC Report (2014) proposes guidelines and recommendations for the design of ports and their access channels, maneuvering areas, and anchorages. It also defines operational restrictions within a channel and provides guidelines for establishing requirements for depth, width, and other parameters.

One of the pillars of this manual (PIANC, 2014) is the establishment of the nautical bottom concept. It defines the nautical bottom as *the level where physical characteristics of the bottom reach a critical limit beyond which contact with a ship's keel causes either damage or unacceptable effects on controllability and*

[1] Note: currently, the critical nautical bottom density in Zeebrugge is 1,200 kg/m³ (Vanlede, 2019) and in Cayenne, 1,300 kg/m³.

https://doi.org/10.58440/ihr-31-2-a15

maneuverability. Additionally, nautical depth is defined as *the instantaneous and local vertical distance between the nautical bottom and the undisturbed free water surface.*

A first step in this approach is to replace terms such as "bottom" and "depth" with the concepts of nautical bottom and nautical depth, which are more appropriate in fluid mud environments. In fact, in the zone between the water-mud interface and the hard bottom, the physical properties of the mud (density, rheological characteristics) change gradually with increasing depth. Therefore, the definition of the bottom must be based on local circumstances and intended application.

Implementing the nautical bottom approach is recommended in waterways and ports when fluid mud layers cover the bottom. If the water-mud interface is accepted as the bottom level, a reduction in UKC value can be allowed. Even navigation with a negative UKC relative to the interface can be considered, meaning that the ship's keel is permanently in contact with mud. Selecting the water-mud interface as the reference bottom level in fluid mud locations can be questioned, as the bottom is neither clear nor easily defined.

Common bathymetric techniques, such as echo sounding, lead to interpretation problems in muddy areas: high-frequency signals reflect off the water-mud interface, while low-frequency waves penetrate the sediment deposit and may indicate a water depth greater than that actually shown on the nautical chart. Selecting the upper limit for the bottom may be safe, but can cause problems in waterway maintenance, since the water-mud interface level can show significant tidal and seasonal variations and is difficult to maintain using common dredging methods. It is also less efficient both for dredging and for achieving economic efficiency.

In practice, determining the nautical bottom is rarely done based on rheological measurements that require laboratory analysis. Most survey methods are based on the density parameter, which is simpler and easier to measure. Still, care should be taken by using absolute viscosity or yield stress values in addition to density. Anyhow, methods and parameters vary from place to place. Emden (Germany) uses maximum yield stress (100 Pa) as the parameter for defining the nautical bottom, while most ports around the world use density limits for the nautical bottom (Kirichek et al. 2018b). Yield stress is an important component in European countries, but it is rarely used in Brazilian ports, requiring more investigation on the impacts nationwise.

In the United States, the leading institution for conducting surveys and regulating navigation in channels and ports with fluid mud is the U.S. Army Corps of Engineers (USACE), which is responsible for dredging and surveys in coastal navigable channels and inland waterways. Conventional hydrographic surveys in areas with fluid mud can often result in ambiguous depth measurements due to its effects on mechanical (lead line) and acoustic techniques.

USACE recognized these effects as early as 1954 (PIANC, 2014), when it unsuccessfully tried to determine nautical depth by correlating lead line depths with echo sounder measurements. It has also investigated measuring nautical depth with towed devices (Teeter, 1992) and is continuously evaluating other established and emerging technologies for measuring fluid mud, defining nautical depth, and managing projects for a nautical depth policy.

The USACE Hydrographic Surveying Engineer Manual (USACE, 2013) emphasizes that it is unlikely that the nominal accuracy standards recommended in the manual can be achieved in projects containing fluid mud, suspended sediments, extreme tidal ranges, or highly irregular topography and geomorphology. In summary, the accuracy standards and the related performance tests for quality control and assurance described in the manual should be considered only as recommended guidelines.

According to USACE (2013), single beam systems are generally preferred in areas where fluid mud exists. Multibeam systems have bottom detection methods (amplitude, phase, interferometric) that vary with signal strength, automatic signal processing, incidence angle, manufacturer, and other factors. In such areas, depth measurements may not be consistent from one survey to another, between different systems, or even within the same system at different beam angles. The USACE Manual also correctly points out that in unconsolidated bottoms – that is, fluid mud – records cannot be reliably interpreted without correlated or corroborating information (Buchanan, 2008).

The NOAA Office of Coast Survey does not explicitly regulate surveys in fluid mud areas, as seen in its two main publications – the Hydrographic Survey Specifications and Deliverables (NOAA, 2025b) and the Field Procedures Manual (NOAA, 2021). The other U.S. agencies working in Hydrography – the National Geospatial-Intelligence Agency and the Naval Meteorology and Oceanography Command – have their own internal operational regulations.

Some remarks on the IHO are relevant. The IHO Standards for Hydrographic Surveys, Publication S-44 Edition 6.2.0 (IHO, 2024), refer to fluid mud only when discussing acoustic backscatter. Regarding depth determination, it states: *In waters of very high turbidity, such as estuaries, for example, this minimum depth can be determined based on sediment concentrations in the water*. This sediment concentration can be measured through water density using a densimeter. However, there is no specific reference to echo sounder frequency – which is expected, as the publication aims to be technology-independent. Nevertheless, special and exclusive orders can only be achieved with high-frequency multibeam operations (coverage, accuracy, propagated uncertainties), without taking into account surveys in non-Newtonian

https://doi.org/10.58440/ihr-31-2-a15

fluids such as fluid mud.

The IHO Manual on Hydrography, Publication C-13 (IHO, 2011), provides some guidelines on conducting surveys in sediment-rich areas. It specifies that *the frequencies for sediment echo sounders are below 8 kHz* and that the use of dual-frequency echo sounders *allows the separation of the seabed return from the soft surface sediments and the underlying rock due to their different acoustic impedances.* It goes further in recommending the use of dual frequency echo sounder in shallow areas of unconsolidated sediments to differentiate soft sediments from the bed rock.

In Brazil, hydrographic surveys require authorization by the Brazilian Hydrographic Service, operated by the Directorate of Hydrography and Navigation (DHN) of the Brazilian Navy. The IHO S-44 publication is the basis for the Brazilian Maritime Authority Standards for Hydrographic Surveys (NORMAM, 2023a). Reflecting the limitations presented earlier, Brazilian standards do not refer to surveys in fluid mud areas and prohibit the use of single-beam echo sounders for Category "A" surveys (those that will be used to update nautical charts), not taking into account the technical progress of the institutions mentioned in this report. This may seem like criticism, but it is not: the Brazilian Hydrographic Service must regulate surveys on a national scale where there are no significant local particularities. In such locations, local authorities – such as port and waterway authorities – should be responsible for surveying standards considering local characteristics of those areas.

5 Surveys conducted in the Port of São Francisco do Sul (Brazil)

5.1 Characterization of the area of interest

The area of interest for this study comprises Berth 301 of the Terminal Santa Catarina (TESC), located within the port complex of São Francisco do Sul, in the Babitonga Bay. This bay is an estuarine complex located in the northern part of the State of Santa Catarina, between latitudes 26º07' and 26º27' S. It is the largest estuary in the state and contains its most extensive mangrove area. Morphologically, it features a main channel oriented NE/SW, approximately 3.8 km wide, 24 km long and reaching depths of up to 28 m, as well as two elongated axes oriented SE/NW.

The bottom sediments can be grouped into two distinct classes, based on their biodetritic carbonate composition: lithoclastic and lithobioclastic sediments. The bottom sediments range from fine sand (sediments composed of 100 % sand) to various levels of muddy deposits. The climate is temperate (humid mesothermal with hot summers) and is influenced by both polar and tropical Atlantic air masses. Average monthly temperatures range between 15–18 °C in winter and 24–26 °C in summer. Relative humidity, also under maritime influence, reaches an annual average of 80%.

The area is under a microtidal regime (amplitude < 2 m), of a mixed, predominantly semidiurnal type, with unequal high and low tides. The average tidal range is about 0.85 m, reaching a maximum of 1.28 m during spring tides and a minimum of 0.27 m during neap tides. Current measurements showed a peak instantaneous velocity of approximately 1.76 m/s during the ebb tide of a spring tide, aligned with the main channel axis (Vieira & Horn, 2017).

The turbidity in the investigation area, near TESC (Terminal Santa Catarina), is low, despite the presence of a fluid mud layer, due to the high rate of water renewal associated with the bay's proximity to the ocean (Projeto Baías do Brasil, 2018). The salinity intrusion is also relevant near the TESC, which leads the water salinity to seawater levels. Far from the ocean, the bay receives fresh water from a significant drainage basin.

According to information obtained from TESC (2025), the berths have the following characteristics (Table 1). According to the Rules and Procedures of the Santa Catarina Port Captain (NPCP-SC, 2022), not to be confused with the Port Authority, the UKC at these berths ranges from 1.9 to 2.7 m, depending on the type of vessel.

Fig. 2 (nautical chart 1804 crop) shows an overview of the Babitonga Bay region, which contains the

Table 1 Characteristics of TESC Berths (2025).

Berths	Draft	Length
300 + 301	11.5 m	384 m
302	11.5 m	264 m

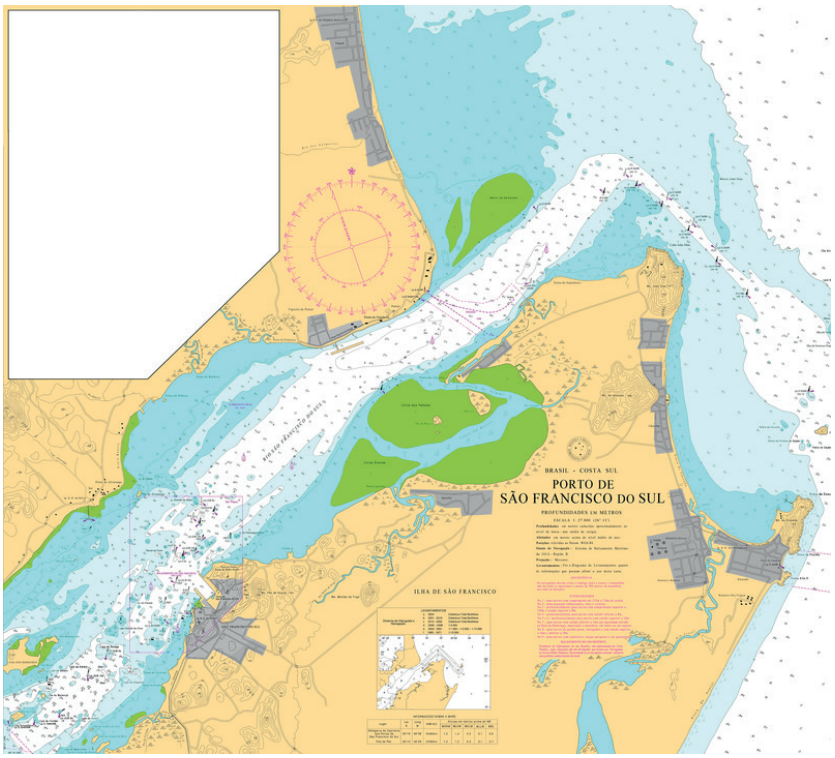


Fig. 2 Crop from nautical chart 1804 (Port of São Francisco do Sul). Source: DHN, Brazilian Navy.

study area covered by this report. Fig. 3 presents the plan of nautical chart 1804, detailing the Port of São Francisco do Sul, with TESC highlighted in red, enclosing the three berths.

The reference depths for the berths in question were obtained from a hydrographic survey conducted by Hidrotopo in February 2025. The survey followed NORMAM (2023a) specifications for Category "A". The minimum depth in the area was 13.5 meters for Berth 301 (Fig. 4). This depth updates the nautical chart for Berth 301. In the vicinity of the berth, the bottom description ("nature of the seabed") is recorded as clay (Arg) and silt (Ld), with no rock (R) identified along Berth 301 (Fig. 3).

This survey represents the depth of the upper limit of the fluid mud layer, since the sharp density gradient from water to fluid mud (lutocline) provides a strong reflector for high-frequency echo sounders – as in the case of the system used at the berths, operating at 200 kHz. This same lutocline is not a strong reflector for frequencies of 24 or 33 kHz, which better detect the transition from fluid to consolidated mud (e.g., Chamanmotlagh et al., 2024; USACE, 2013).

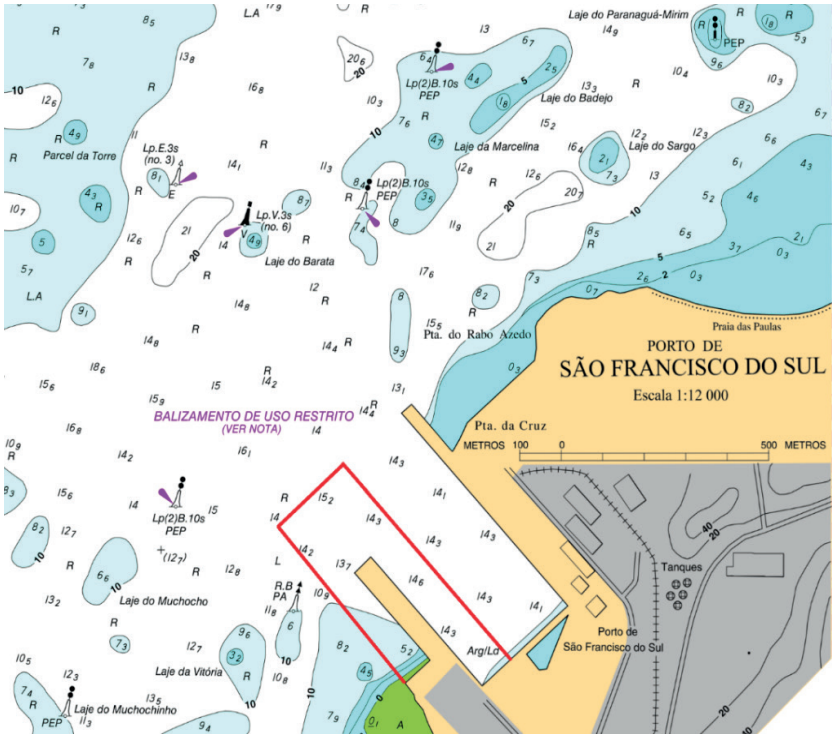


Fig. 3 Crop from nautical chart 1804 plan (Port of São Francisco do Sul). Source: DHN, Brazilian Navy.

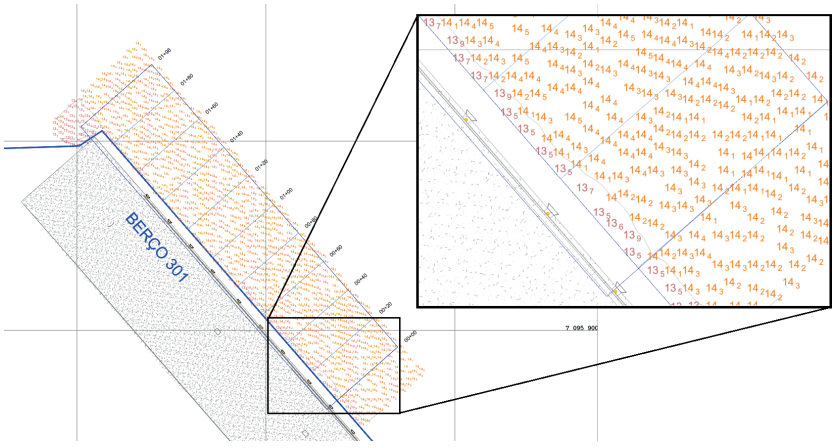


Fig. 4 Minimum depth of 13.5 m at Berth 301, as seen in the inset of the post-dredging survey. Source: Hidrotopo.

5.2 Systems and subsystems used in the hydrographic survey

To assess the fluid mud layer at Berth 301, the deliverables of the hydrographic survey conducted by Hidrotopo during 27–29 April, 30 May – 2 June, and 15 July 2025 were analyzed. This survey was carried out from a manned vessel equipped with the following acquisition and data processing systems:

Positioning: Hemisphere VS330 GNSS receiver, with corrections via the Fugro Marinestar service, achieving horizontal accuracy of less than 10 cm (95 % confidence level; Fugro, 2025).

Motion sensor: TSS DMS-05 motion sensor for roll, pitch, and heave corrections applied to depths measured by the echo sounder, compensating for vessel motion.

Sound velocity profiler: AML-3 LGR sensor, providing sound speed in the water column for correcting echo sounder depth measurements.

Acoustic bathymetry: Teledyne Odom Hydrographic Echotrac CVM dual-frequency single beam echo sounder (200 kHz and 24 kHz) with a OTSBB200/24-4/20 transducer. Fig. 5 and Table 2 summarize the bottom footprint according to beamwidth and typical berth depth.

Direct bathymetry: Hand lead line for depth measurement independently of the echo sounder.

Bottom sampling: Van Veen grab sampler with preliminary onboard analysis of seabed sediment. Characteristics such as texture, granulometry, composition, and color were noted according to IHO (2020b). Samplings were taken both to characterize the bottom and to calibrate the densimeter.

Water level monitoring: Pulsar Measurement dBi-T 6 sensor with Technolog Cello HDT-2 data logger for tidal height monitoring to reduce soundings.

Densitometry: The density and yield stress of the mud, as a function of depth, were assessed using a non-radioactive densimeter, model DensiTune, manufactured by Stema Systems. These mud properties are used to aid in determining nautical depth. The equipment's main technical specifications are summarized in Table 3.

DensiTune uses the tuning fork principle to derive density. The tuning fork probe consists of tines that are designed to vibrate at a specific frequency and amplitude. When a tuning fork is immersed in a fluid, the frequency and amplitude of the vibration changes due to the changes in mass, as it happens in the transition from water to the mud. This change in frequency and amplitude is proportional to the

https://doi.org/10.58440/ihr-31-2-a15

density changes and rheological properties of the substances, allowing the assessment of the mud density.

These frequency and amplitude changes are then correlated with the density of the material through a calibrated algorithm, providing a density measurement. The yield stress of the mud is also derived using this system. However, the focus of this work lays on the density and not the yield stress. Few Brazilian port authorities and research labs that work with fluid mud use density as the main parameter for the definition of the nautical bottom. There is very little critical mass both to produce the necessary knowledge and to consume it at the decision-making level.

As stated in PIANC (2014), fluid mud with low density has a viscosity and yield stress that are not, or only slightly, dependent on density. As a consequence, yield stress will be presented as information only and will be subject to further investigation in future works. Where density was monitored, the DensiTune also provided yield stress profiles for 10 and 100 Pa.

Before probing the bottom, the system has to be calibrated with a local fluid mud sample. This procedure was done at each density location and processed using the DensiCal software.

Yield stress refers to the minimum stress required to initiate flow in cohesive mud. It is a critical parameter for determining when mud begins to behave like a fluid, which is important in seabed assessments for navigational safety. When low resistance to ship motion is required, for example, to allow vessels to navigate safely through fluid mud layers, a low yield stress is desirable. Yield stress is used to define the seabed in some ports, and a limit of 25 Pa is common in international guidelines (PIANC, 2014), although higher values are also used. It is especially relevant for cohesive sediments, such as clay-rich mud, as it helps determine when the mud resists ship motion. This parameter will be further explored in future works.

Data acquisition and processing: Hypack system for bathymetry; Stema DensCal/DensLog for density and yield stress calibration, acquisition, and processing.

5.3 Survey planning and execution

The survey lines were established parallel to the pier housing Berths 300, 301, and 302, in a direction of 138°–218°, as shown in Fig. 3. The lines with the dual-frequency single-beam were planned at 10-m intervals, starting from the pier line. Considering the information shown in Table 2, the bottom coverage for the low-frequency sensor is equivalent to 45 % bottom coverage.

Sampling points for density, yield stress, hand lead depth, and sediment were selected to ensure adequate representation of the information. These points are represented in Fig. 6. These data are relevant to the area of interest (Berth 301), a subset of the data collected for other areas (berths 300 and 302) that may be addressed in future work. No additional points were collected near the pier at berth 301 due to the high occupancy rate of the berth.

The echo sounder was calibrated using bar check to ensure proper operation of the data acquisition system. All collected data was horizontally georeferenced to the WGS-84 system and converted to UTM (Universal Transverse Mercator)

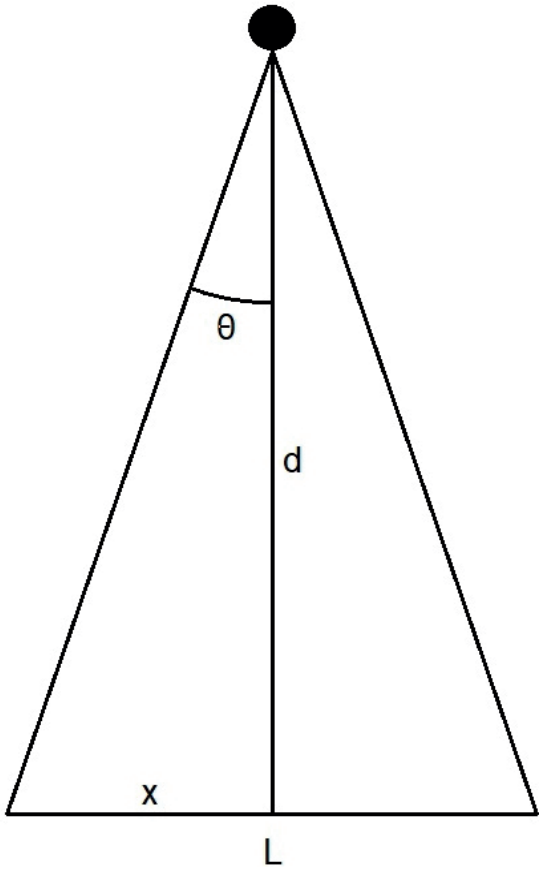


Fig. 5 Schematic drawing of the bottom footprint ($L = 2x$), as a function of depth (d) and beam width (2θ).

Table 2 Echo sounder bottom footprint L.

Frequency	Depth d	Beamwidth 2θ	Footprint L
200 kHz	13.5 m	4°	0.9 m
24 kHz	13.5 m	20°	4.8 m

Table 3 DensiTune technical specifications.

Precision	< 1 % of density of measured density
Range	1,000–1,800 kg/m³
Resolution	1 kg/m³
Temperature range	0–60° C
Depth range	0–60 m
Yield stress range	0–600 Pa.s
Dimensions (max.)	650 mm × 150 mm (diameter)
Weight (dry)	15 kg
Depth precision	< 0.15 % of measured range
Angle measurement	2 inclinometer

Zone 22, Southern Hemisphere, with the central meridian at 51° W.

Vertical coordinates, indicating depth, are all reduced to the chart datum (except in echograms, as discussed in item 6). All information in the survey and this report is referenced to Time Zone Papa, Greenwich Mean Time minus 3 hours (GMT-3).

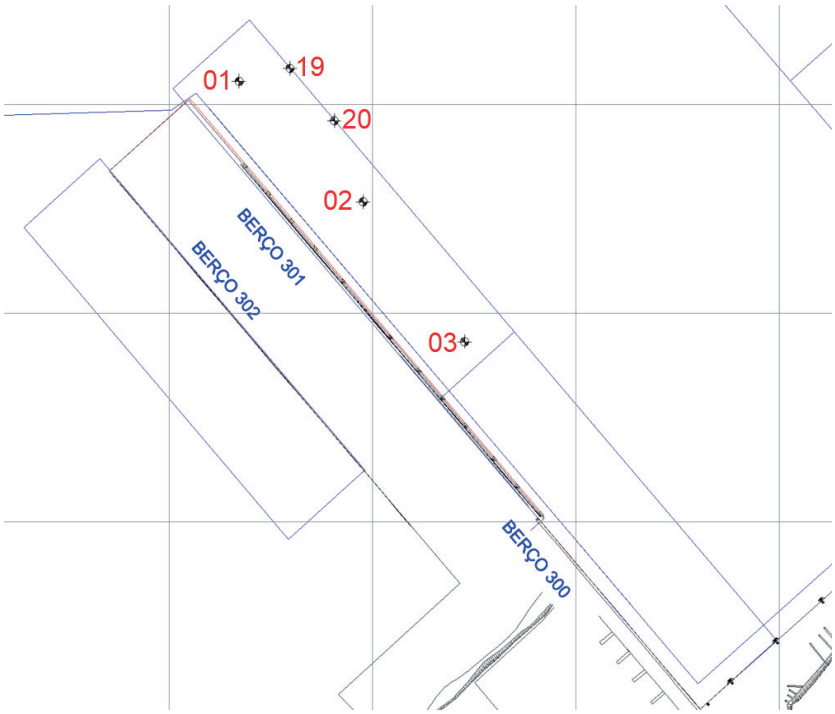


Fig. 6 Sampling points for densimeter (depth, density and yield stress), hand lead line (depth) and Van Veen grab sampler (sediments, only at points 01, 02 and 03). Source: Hidrotopo.

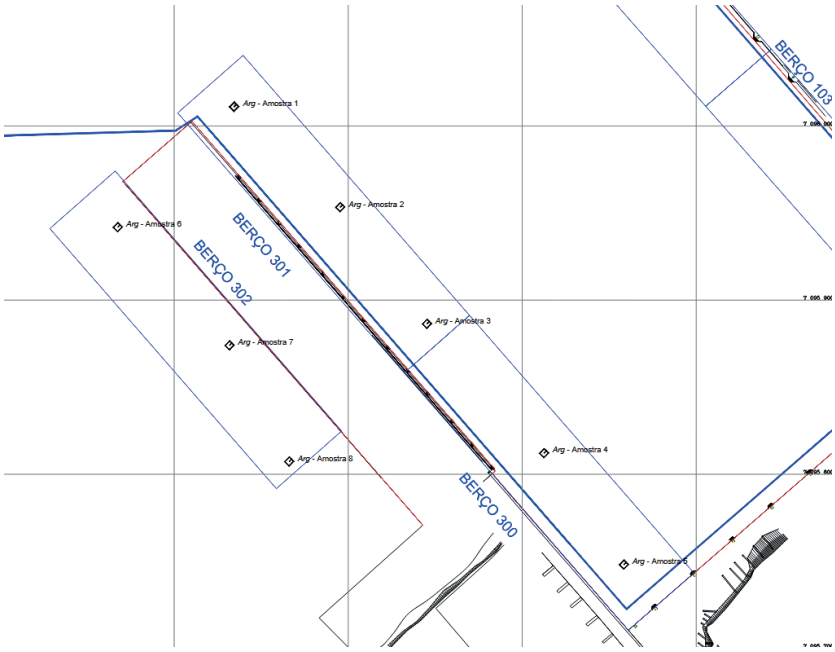


Fig. 7 Bottom samples indicating the presence of clay with low-strength, high-plasticity, soft consistency, brown color. Source: Hidrotopo.

6 Data analyses

6.1 Analysis of information and navigable mud measurements in the Port of São Francisco do Sul

Although this survey is part of a comprehensive campaign commissioned by TESC, this report primarily analyzes data related to Berth 301, as the objective is to evaluate the information needed to define the fluid mud layer and the nautical bottom at this area. These two elements will then used to assess the impact of the bottom on the port's operational parameters and suggest measures to optimize these parameters, benefiting the efficiency of port operations and safety of navigation.

The survey used the chart datum defined in NORMAM (2023a) as a vertical reference. Tide height measurements were taken using the tide gauge installed at the TESC I Tide Gauge Station, located at the western end of Berth 101 of the port of São Francisco do Sul (Latitude 26° 13' 58" S and Longitude 048° 38' 19" W), whose data are recorded in Form F-41-Padrão-TESCI-60312 - version 1/2024.

The three phases of the survey took place from 27–29 April, 30 May – 2 June, and 15 July 2025. On the last day, two additional densimeter and lead line casts were carried out to complement the area of interest (Berth 301), since the area was already covered by a post-dredging multibeam survey in February 2025, and with this dual-frequency (200/24 kHz) single-beam survey. The choice for the 24 kHz frequency was due to its good correlation with density in this type of environment, tested in previous surveys in the Ports of São Francisco do Sul and Itajaí, both in the coast of the State of Santa Catarina.

Bottom samples were collected at points within the area of Berth 301 (points 01, 02 and 03), as well as at Berths 300 (points 04 and 05) and 302 (points 06, 07, 08), indicated in Fig. 7. The samples were described as clay with low-strength, high-plasticity, soft consistency, and brown color, consistent with the classification of nautical chart 1804 (plane) and with estuaries with fluid mud. According to Greer (2008), combinations of clay, silt and organic matter are commonly called mud. The samples were analyzed onboard the survey vessel, in accordance with NORMAM (2023a), and no additional analyses were performed due to the lack of resources and available laboratories. According with IHO (2011), grain size for clay is < 0.002 mm (very fine sediments). These analyses are consistent with the densimeter results for a fluid mud bottom. Future work will contemplate laboratory analysis for bottom samples.

This is consistent with the geotechnical report by CoastalPort Engenharia (CPE) No. CPE048-RL-001 (CPE, 2024). According to the report: *During the geotechnical survey, all points penetrated 44.5 meters (the survey limit), without reaching the bedrock. A layer of compacted plastic sediment was observed, penetrating approximately 10 meters into the seabed.*

The four survey points were located in the extension of the TESC pier, as shown in Fig. 8. These

https://doi.org/10.58440/ihr-31-2-a15

results are consistent with the observations and information collected in the hydrographic survey, that did not find evidence of bedrock.

Fig. 9 presents the digital tide gauge records in analog format for 29 April and 15 July 2025, when density and yield stress data were collected. The vertical bars, labeled 01, 02, 03, 19, and 20, represent the times when density, and hand lead line data were collected, when the tidal current was not significant, barely interfering with the task of lowering and raising the data collection systems. During the density data collection, surveyors noted fair weather with light winds, no rain, low turbidity and insignificant surface currents. Environmental conditions were not expected to pose additional stress in the survey area.

Knowledge of tide times and phases is important for analyzing densimetric and bathymetric profiles, since suspended sediments and the fluid mud layer (unconsolidated sediments) are subject to stress caused by the current associated with the tidal height, along with currents of non-astronomical origin. Both the densimeter and the echo sounder detection can be affected by oscillations in the sediment layers (USACE, 2013). These currents are an important condition for providing dynamic energy to the sediments and reducing the rate of fluid mud consolidation (Carneiro, 2018).

Fig. 10 shows the wind rose for the summer and winter of 2019, a snapshot of the environmental conditions in the region. In the summer, WSW and ENE winds are more frequent, approximately 25 % of the time, with an average intensity of 1.38 m/s and a maximum of 5.9 m/s. In the winter, WSW and SW winds are more frequent, 27 % of the time, with an average intensity of 0.44 m/s and a maximum of 5.1 m/s (Cunha & Abreu, 2023). These data were obtained from the meteorological station of the National Institute of Meteorology (INMET). These winds are an important forcing factor in keeping sediments out of the consolidation zone, allowing the use of unconsolidated (fluid) mud for navigation.

6.2 Density and bathymetry analysis

Although adequate rheological tests can be performed in the laboratory, it is still difficult to generate rheological profiles in situ. Therefore, these properties are generally correlated with more easily measurable properties, such as density and acoustic measurements (Carneiro 2018). Studies on ship maneuverability and empirical models show that fluid mud does not pose an obstacle to navigation when its density is equal to or less than 1,200 kg/m^3 (Michimoto, 2019). Therefore, a densimeter was used to measure the depth where a density of 1,190 kg/m^3 occurs, lower than the limit suggested by the author and other studies, as an initial and safe step.

The data collected at points 01, 02, 03, 19, and 20 (Fig. 6) showed the following depths, as listed in Table 4, for densities of 1,190 kg/m^3 and 1,290 kg/m^3, lead line, and low-frequency echo sounder. These values,

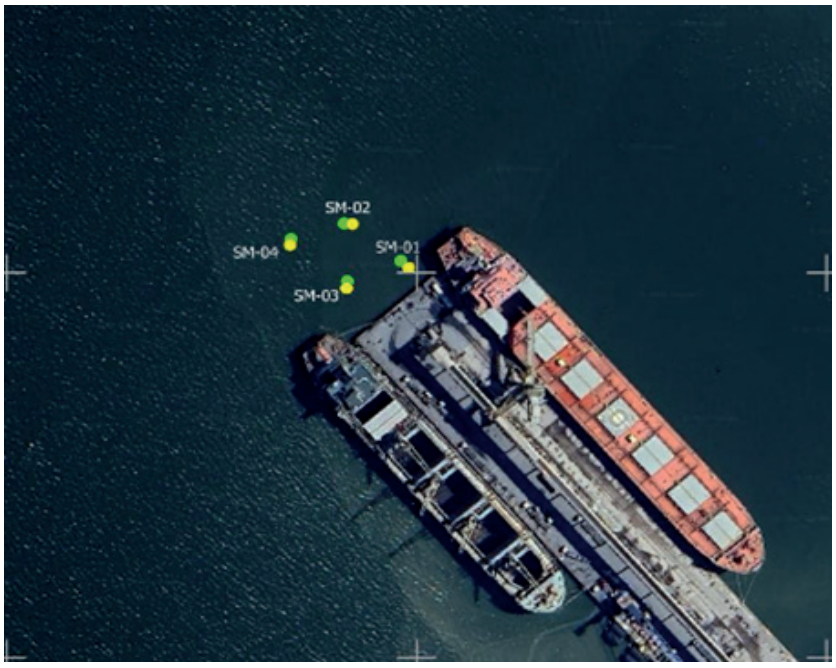


Fig. 8 Location of the four geotechnical survey points carried out by the company CoastalPort Engenharia (CPE), report N. CPE048-RL-001, (CPE, 2024).

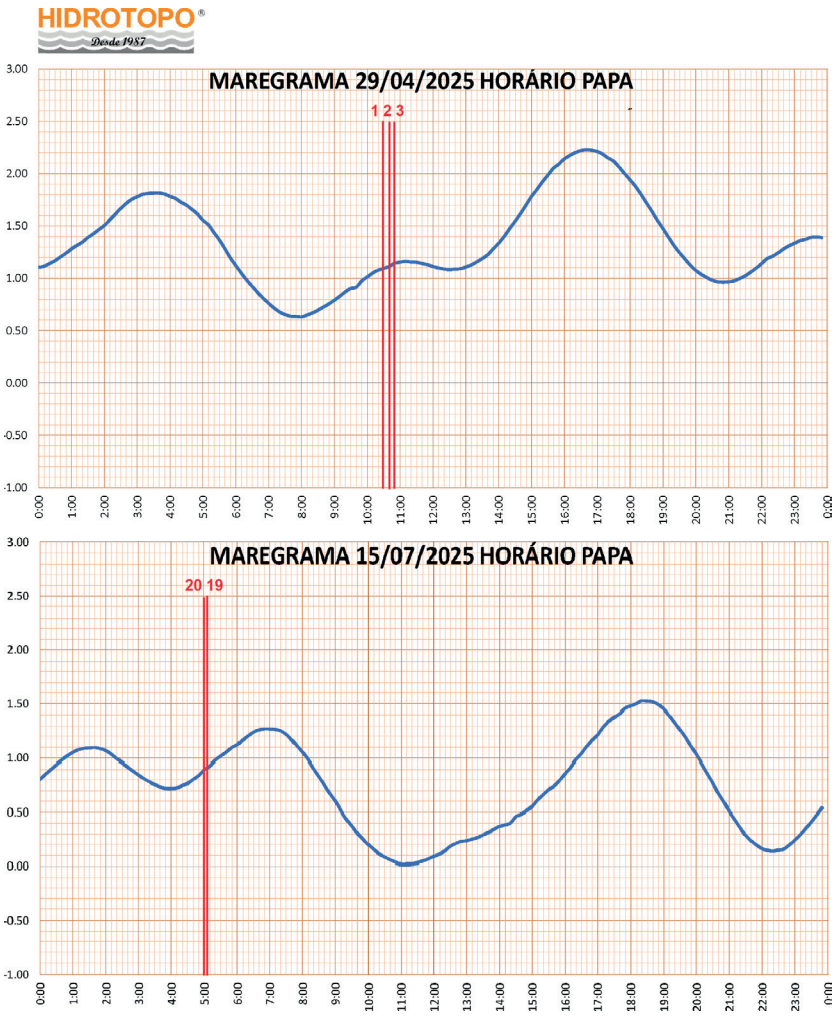


Fig. 9 Tide charts for 29 April and 15 July 2025. The red vertical bars, labeled 01, 02, 03, 19, and 20, represent the collection times for density, yield stress, and lead line. The vertical axis (tide height) is -1–3 meters, and the horizontal axis (time) is 0–24 hours. Source: Hidrotopo.

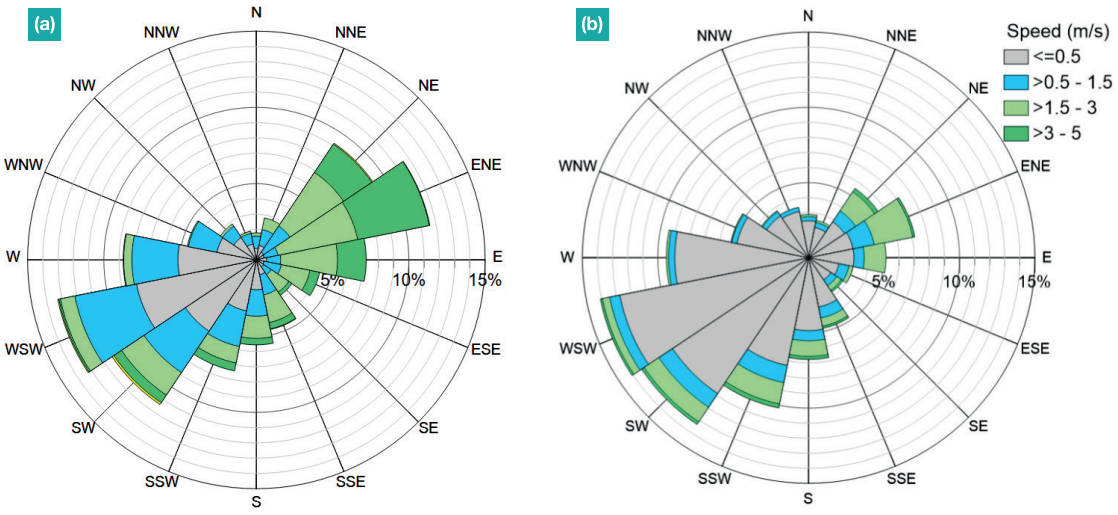


Fig. 10 Distribution of wind direction and intensity in summer (a) and winter (b), at the INMET meteorological station (Cunha & Abreu, 2023).

as expected, indicated greater depths than those obtained with multibeam bathymetry (also shown in the table) and high-frequency single-beam bathymetry. The depth 14.3 m at point 19 stands out when compared to all other depths, being closer to the high-frequency bathymetry. However, a closer look into density changes shows the reason for this discrepancy.

Fig. 11 shows the density (left) and yield stress (right) profiles for point 19. It can be seen that the first density gradient appears at 14.3 m, the depth where the low-frequency echo sounder indicates a depth of 14.3 m (Table 4). Naturally, this is not the bottom, as the densimeter then indicates a depth of 15.26 m, where the density of 1190 kg/m^3 is measured (green line). The yield stress profile for 10 Pa (green line) indicates the bottom at 15,23 m. Density and yield stress values can be seen as useful information to remove ambiguities and used as additional safety factors. This can also potentially be used in future studies to further improve the knowledge of the fluid mud behavior in the area.

In Table 4, the minimum depths were compared with those obtained by the multibeam echo sounder (200 kHz), revealing variable differences that appear to be related to the positions where they were collected and the interpretation of low frequency bottom detection. Points 01 and 02 are in the center of the area occupied by ships, whose movement provides additional energy to keep the sediments in suspension, given the high turnover of ships docking and undocking. Point 03 is on the centerline, but at the extreme of the area, close to the bow of the ships. Points 19 and 20 are farther from the pier, where there is gradually less movement, as the ships are pulled by tugboats toward the channel (parallel to the pier, away from point 03).

As shown in USACE (2013), in estuarine environments with high mud concentrations, the unconsolidated sediment layer varies depending on several environmental parameters, as previously mentioned. In these cases, it is unlikely that the values collected by different sensors will be exactly the same, as one might expect in clear water hard bottom areas. Even measurements from the same instrument can differ from one another in the same location. The variability observed in Table 4 is therefore not surprising. It is important to observe the low frequency echograms carefully.

The single beam echo sounder survey lines in the area of Berth 301 are identified in Fig. 12. Lines A, B, C, and D were planned in conjunction with the collection of points 01, 02, and 03. Lines E and F were established along the previous lines C and D, prior to the collections of points 19 and 20. Finally, line 0 was planned close to the berth 301 pier to improve knowledge in this area, where the shallowest depths were identified in the Category "A" survey conducted in February 2025, using a 200 kHz multibeam.

Because this line is very close to the pier, its true

Table 4 Comparison of minimum depths obtained at the points indicated in Fig. 6, obtained with a densimeter, lead line and low and high frequency echo sounders.

Ponto	Data	Densidade 1,190 kg/m^3	Densidade 1,290 kg/m^3	Prumo de mão	Ecobatímetro SB 24 kHz	Ecobatímetro MB 200 kHz
01	29/04/2025	15.98	15.99	16.10	16.10	14.40
02	29/04/2025	15.56	15.57	15.49	15.70	14.20
03	29/04/2025	14.90	14.91	15.19	15.30	14.10
19	15/07/2025	15.26	15.26	15.47	14.30	14.20
20	15/07/2025	14.78	15.04	15.13	15.30	14.20

https://doi.org/10.58440/ihr-31-2-a15

depth is masked because the beam width of both channels (high and low frequencies) interferes with the pier side wall (Fig. 5). However, the echo sounder recording can provide valuable clues about the thickness of the fluid mud layer. Lines "a" and "b" represent the longitudinal limits of berth 301.

In Fig. 13, two lines coincident in space but separated in time by 34 days (lines D and F) can be seen. These lines were surveyed along the outer edge of berth 301. The echograms show significant variations in the low-frequency channel depth, while maintaining considerable consistency in the high-frequency channel depth. It can also be noted that bottom detection by the high-frequency channel in both lines is not homogeneous, due to bottom and fluid mud layer variability. In the area of interest (Berth 301, delimited by lines "a" and "b"), this variability is relevant, which shows that the nautical bottom can be further deeper than the bottom detected by the low frequency channel, which is not detecting the consolidated bottom but rather the fluid mud plume.

It can be seen that the high-frequency and low-frequency returns are consistent with a sediment bottom (mud and silt), as summarized in Table 5. The returns occur at two main reflectors, with low intensity and penetration. A rocky bottom would present a strong echo at both frequencies, indicating similar depths.

This situation also occurs in the echograms of lines C and E, shown in Fig. 14, parallel to the line in Fig. 13, approximately 10 meters into the area of Berth 301. Point 02 is midway between lines B and C (Fig. 15). The next line toward the pier, line B, is reproduced in Fig. 15, along with the echogram of line C. Line B was established over points 01 and 03. Point 02 is midway between lines B and C (approximately 5 meters from each line). The variability of the mud layer, as represented by the low-frequency sensor, can be observed. Fig. 16 shows lines A and B, both near the pier of Berth 301. Line B passes over density points 01 and 03. Line A is approximately 10 m from the pier.

The analysis of the echograms also provides important clues about the sediment distribution below the first reflector, the one typically detected by high-frequency echo sounders. For this reason, high-frequency echo sounders do not detect suspended sediment below the lutocline. In this case, low-frequency echo sounders are more suitable (USACE, 2013). In Figures 13 to 16, the sediment distribution can be observed between the first reflector, detected by high-frequency sonars, and the lower part of the record, which represents the penetration limit of the low-frequency sonar.

All echograms represent the reduced bathymetry of the tide only, excluding corrections from the sound velocity profile and the motion sensor. This is a characteristic of the processing software, and as a result, the depths are approximately 30 cm off the final depths reduced to the chart datum. In the comparison tables, the final values, after all corrections, are used. This situation is exemplified in Fig. 17, where the echogram does not contain the corrections for

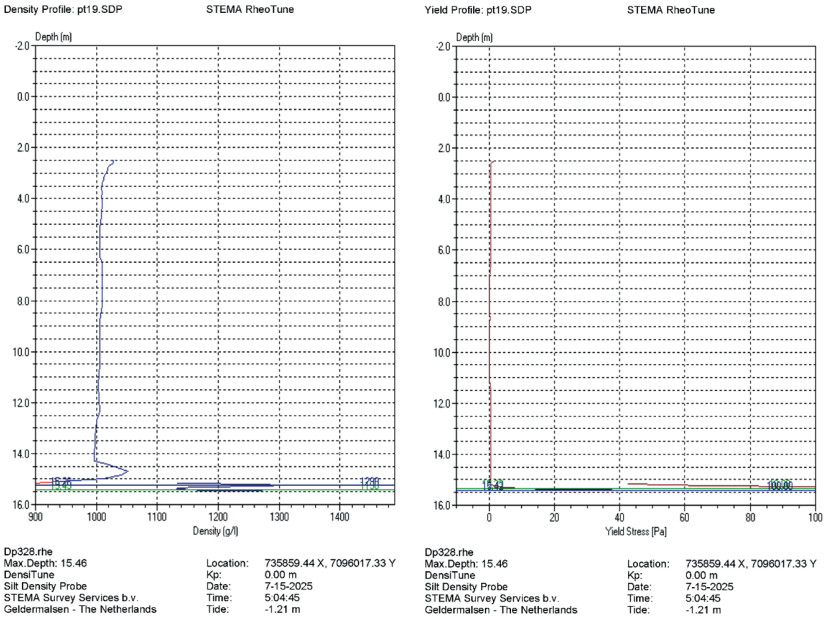


Fig. 11 Density (left) and yield stress (right) profiles for point 19. Vertical axis from -2 m (above water) to 16 m and horizontal axis from 900–1,500 kg/m³ (see text for additional information). Source: Hidrotopo.

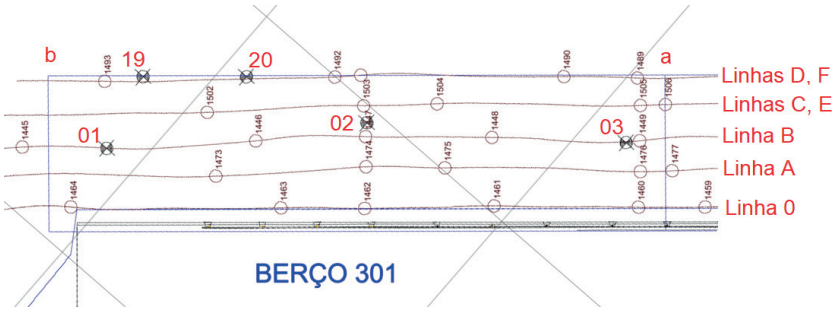


Fig. 12 Planning of the survey lines over the area of Berth 301, parallel to the pier. The densimeter points (01, 02, 03, 19 and 20) are also marked. Lines "a" and "b" represent the longitudinal limits of berth 301. Source: Hidrotopo.

Table 5 Characteristics of hard and soft bottom, when represented on an echogram.

Feature	Hard bottom (rock/gravel)	Soft bottom (mud/silt)
Echo amplitude	High	Low
Echo duration	Short, sharp	Broad, spread
Second return	Often visible	Rare or weak
High-frequency echo	Strong and well-defined	Weak or attenuated
Low-frequency echo	Strong, with penetration	Moderate, better penetration

the sound speed profile and heave at the top. Below, the profile contains all the corrections, which are the information used in plant production and vertical data, reduced to the chart datum.

In Figures 13 to 16, the persistent fluid mud layer can be clearly observed throughout the area of Berth 301, with no indication of a bedrock. In Fig. 18, there is line 0, which ran close to the pier, to measure the mud layer at the shallowest point identified in the post-dredging survey, conducted in February 2025. It can be seen that a fluid mud is persistent in time when comparing survey lines performed at different times. These plumes of fluid mud are also consistent with the bottom samplings (clay) and density monitoring.

The shallower zone in Fig. 18, between points “a”

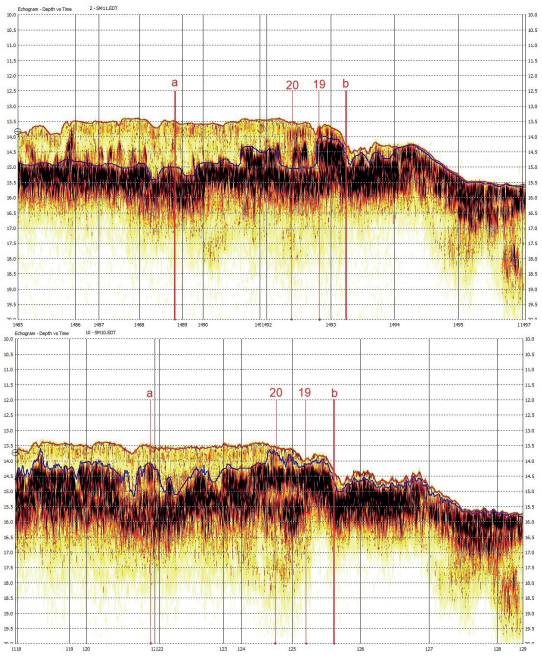


Fig. 13 Echograms of two independent survey lines D (above) and F (below), whose soundings occurred with an interval of 34 days. The vertical lines “a” and “b” indicate the limits of the area of Berth 301, with the densimeter points 19 and 20 also indicated. Source: Hidrotopo.

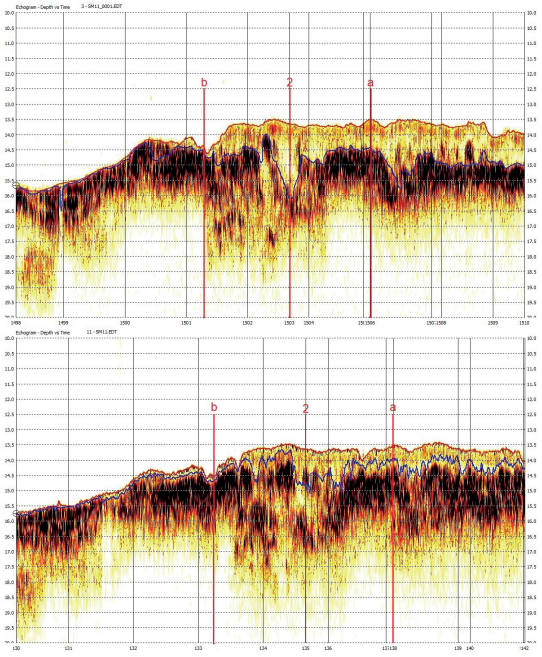


Fig. 14 Echograms of two independent lines C (above) and E (below), whose soundings occurred with an interval of 34 days. Vertical red lines “a” and “b” indicate the limits of the area of berth 301, and densimeter point 02 is also indicated. Source: Hidrotopo.

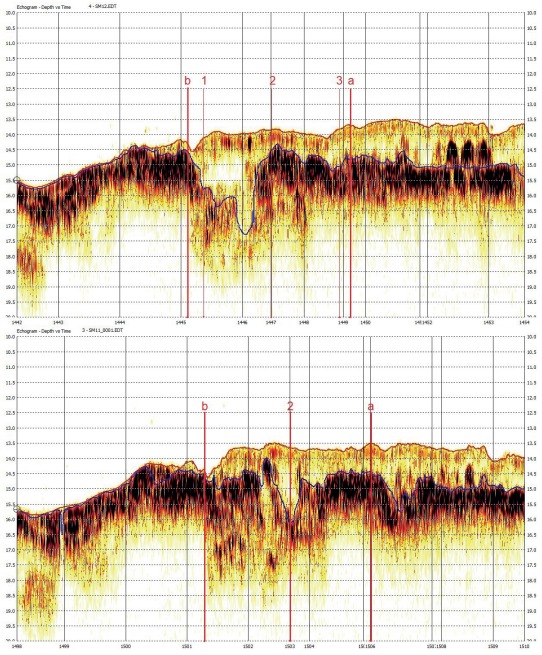


Fig. 15 Echograms of lines B (above) and C (below), where the vertical bars represent the limits of Berth 301 (“a” and “b”) and the points (01, 02 and 03). Source: Hidrotopo.

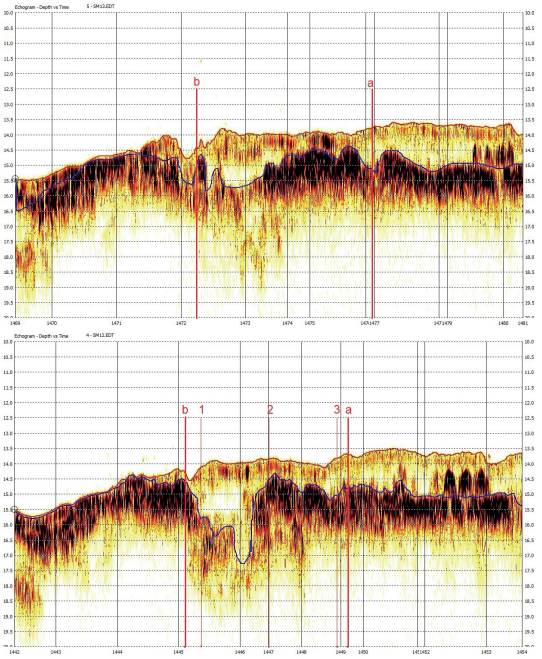


Fig. 16 Echograms of lines A (above) and B (below), where the vertical bars represent the limits of Berth 301 (“a” and “b”) and the points (01, 02 and 03). Source: Hidrotopo.

https://doi.org/10.58440/ihr-31-2-a15

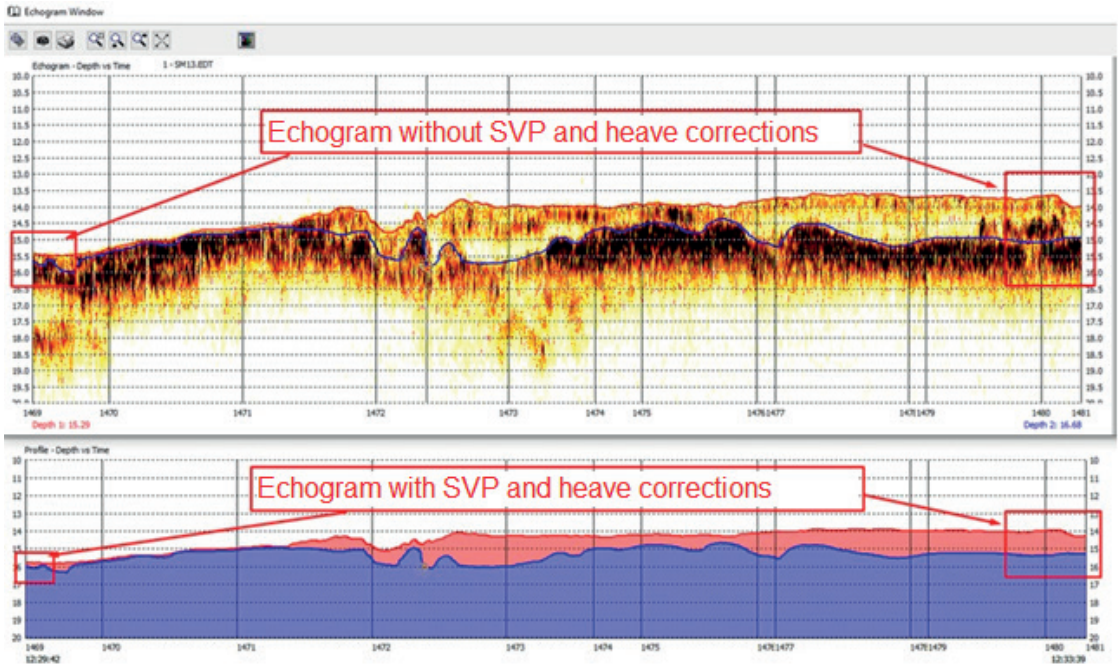


Fig. 17 Example of an echogram, as used in this report, without the sound speed and heave corrections at the top, and below with all corrections. Source: Hidrotopo.

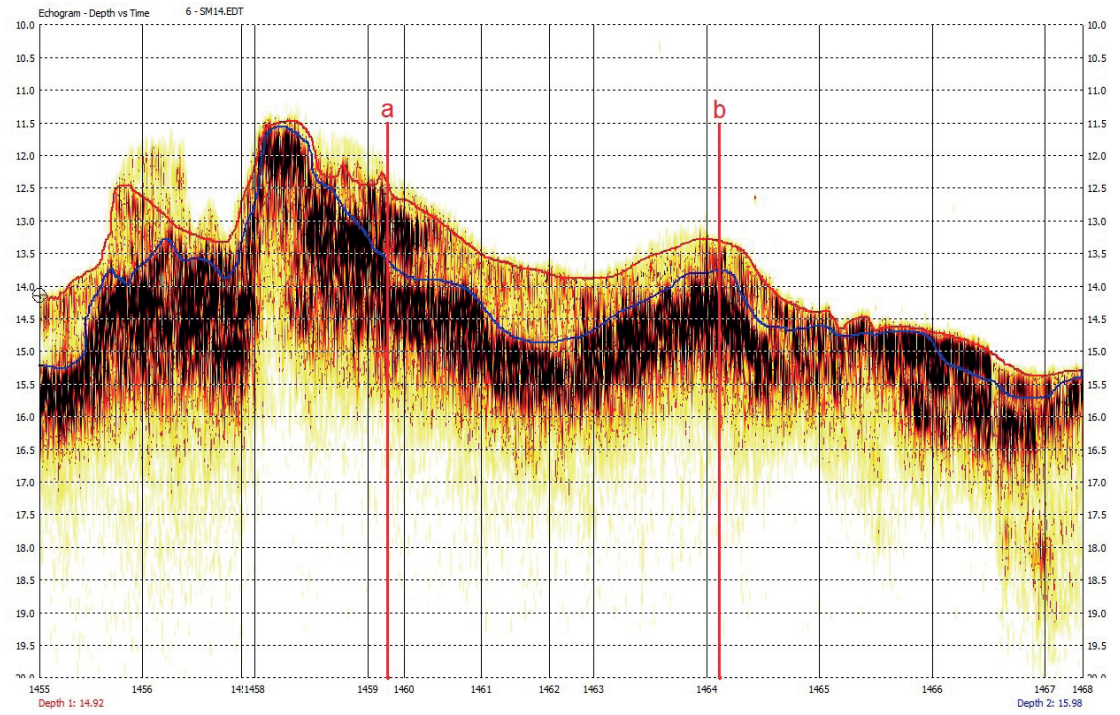


Fig. 18 Line 0, next to the pier of Berth 301, whose longitudinal limits are indicated by vertical bars "a" and "b". Near point "b" is the narrowest zone of the fluid mud layer at the time of the soundings. The blue line indicates the bottom detected by the low-frequency sensor. Source: Hidrotopo.

and "b", has a clear mud layer greater than 0.5 m along the pier, exceeding 1 m in some parts. The blue line indicates the low-frequency echo sounder detection, and the shaded area above it is the suspended mud layer, although fluid mud may occur below this line, as indicated by the densimeter in Table 4. This is the area where the post-dredging survey with high-frequency multibeam indicated the shallowest part (13.5 m).

This situation can be seen in Fig. 19 (viewed from the top), where there is a narrow strip next to the pier, below the fenders, where the minimum depth in the area of Berth 301 is less than 14 m, with the minimum being 13.5 m (upper image). This post-dredging bathymetry was obtained by Hidrotopo in February 2025. In the same figure, lower image, the difference in depths obtained with the high- and low-frequency channels can be observed. The differences between

these frequencies are indicative of fluid mud, whose thickness varies from 0.5 m to 1.2 m.

It can be identified that there is a navigable fluid mud layer with a minimum thickness of 0.5 m along the Berth 301 pier, below the minimum depth established by the post-dredging hydrographic survey of 13.5 m. This means, according to PIANC (2014), that the minimum nautical bottom in the area of Berth 301 can be defined as 14.0 m. The nautical bottom, in this situation, can be used as a reference for the UKC calculation. This is a conservative approach, as density profiles indicate that the nautical bottom is deeper.

Since the UKC ranges from 1.9 to 2.7 m (NPCP-SC, 2022), this does not imply that the ship should sail with its keel in the fluid mud, although this occurs in many ports around the world, which is conventionally referred to as a negative UKC. In this study, we propose that the UKC of 1.9 to 2.7 be calculated relative to the 14 m nautical bottom, rather than the apparent bottom measured by high-frequency sonar (13.5 m).

Some areas of berth 301 have a mud layer, as indicated by the difference between high and low frequencies, that are not significant (from a conservative perspective, without considering density measurements). However, in these areas, the depth is greater than 14 m and does not affect the definition of a minimum nautical bottom that is used throughout the entire area of Berth 301. This occurs in the northernmost part of the Berth.

7 Conclusions and recommendations

7.1 Conclusions

TESC executes a series of environmental programs in Babitonga Bay, in addition to port operations. Efficient dredging management is essential for environmental protection and port efficiency. Performing hydrographic surveys efficiently allows for the definition of the nautical bottom, a non-trivial task in environments with high concentrations of unconsolidated sediments. Knowledge of the nautical bottom allows for accurate measurement of dredging volume and locations, reducing environmental impact. It also increases the efficiency of port operations, helping to ensure products reach the average citizen at more competitive prices (NOAA, 2025a).

This report evaluates a substantial amount of data and information to enable a thorough analysis, optimizing knowledge of the fluid mud layer, its thickness, physical characteristics, and behavior. The final goal is defining the nautical bottom for the UKC calculation. The exit from Berth 301 toward the maneuvering basin and channel is deeper than 14.0 m and is therefore not the subject of investigation at this stage of the work.

The methodology used employs lead line, which, due to the small size of the area of interest and the relatively light currents, allows for this use. Lead line surveys may seem outdated, but it is a consistent tool in cases like this. One difficulty faced was that Berth 301 (the main focus of the report) had nearly 100 % occupation, posing a challenge for the survey given the constant presence of vessels. Another challenge is to demonstrate that the fluid mud thickness exists, and that the horizontal and vertical distribution allows for the definition of nautical depth for the safe navigation of a vessel throughout the entire operating area (Berth 301).

This work adopts a conservative approach, indicating a safe first step, allowing all those involved in the TESC operation (Port Authority, Maritime Authority, Pilotage) to be confident in this step before subsequent progress can be made. One step at a time. There is potential room for improving knowledge of the fluid mud layer and obtaining the nautical depth more accurately,

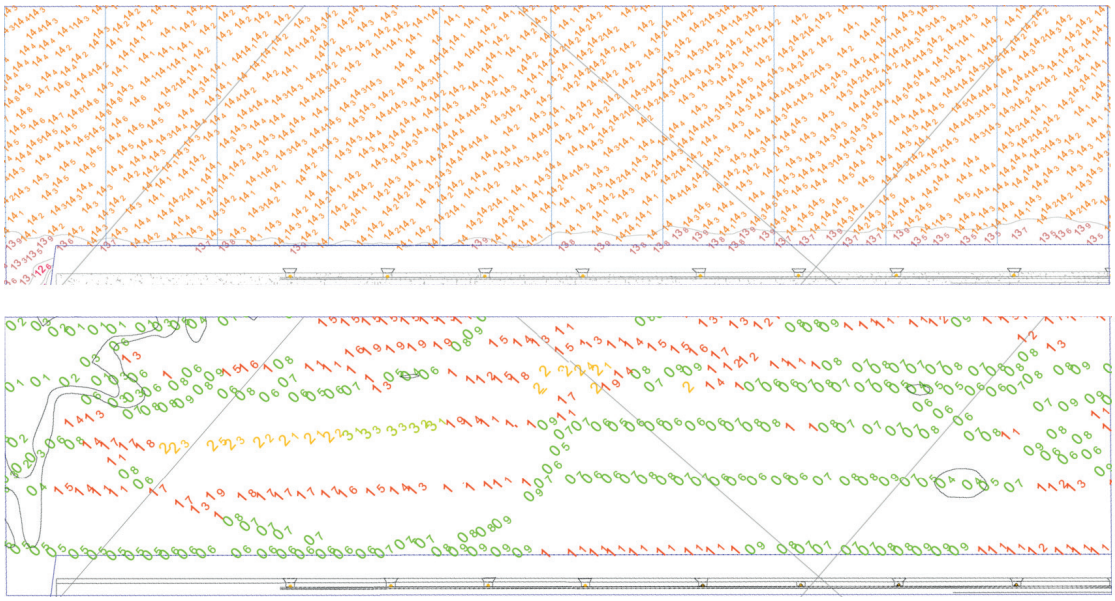


Fig. 19 Post-dredging bathymetry of the Berth 301 area, with a minimum depth of 13.5 m (above) and fluid mud layer thickness (below). The critical area is close to the pier. Source: Hidrotopo.

https://doi.org/10.58440/ihr-31-2-a15

increasing the TESC's operational draft.

It is safe and conservative to conclude that there is a navigable layer of fluid mud with a minimum thickness of 0.5 m along the quay at Berth 301, below the minimum depth established by the post-dredging hydrographic survey of 13.5 m. This means, according to PIANC (2014), that the minimum nautical depth in the area of berth 301 can be defined as 14.0 m. In this situation, the nautical depth can be used as a reference for calculating the UKC. The nautical depth was defined based on the following findings:

- The minimum difference between the low and high frequency channels of echo sounders.
- The confirmation of the density assessments, that indicated even deeper consolidated sediments and thicker fluid mud layer.
- The confirmation of the lead line measurements, also indicating deeper hard bottom (consolidated mud).
- The confirmation of the bottom samples, indicating clay in all sampling points.
- The absence of rocks in the sub-bottom of the area of interest, reported at CPE (2024).
- The local environmental conditions that facilitate the formation and maintenance of fluid mud, similar to those reported at USACE (2013).

Since the UKC ranges from 1.9 to 2.7 m (NPCP-SC, 2022), this does not imply that the vessel must sail with its keel into the fluid mud, although this occurs in many ports around the world, which is conventionally referred to as a negative UKC. In this study, it is proposed that the UKC of 1.9 to 2.7 be calculated in relation to the 14 m nautical bottom, and not to the apparent bottom measured by high frequency sonar (13.5 m). This situation can be seen schematically in Fig. 1.

It is important to note that a central point of the PIANC manual (2014) is the concept of nautical bottom, defined as "the level where the physical characteristics of the bottom reach a critical limit beyond which contact with the keel of a ship causes damage or unacceptable effects on controllability and maneuverability." Due to the conservative approach, the chosen value (14 m) does not precisely define a critical level that would put ships at risk. Further investigation may indicate that the seabed is deeper than 14 m, with more consistent indicators between density and echo bathymetry.

It is possible to observe, from the data provided by the hydrographic survey, that the very dynamics of ship movement contribute to keeping the sediments unconsolidated and in suspension. The movement of ships and tugboats contribute to conditioning the mud to remain fluid and navigable (Fig. 18). Exploring the yield stress can be further considered to define the nautical bottom (PIANC, 2014). It is especially relevant for cohesive sediments, such as clay-rich mud, as it helps determine when the mud resists the ship's movement. This can allow for better characterization of the nautical bottom using the Densitune densimeter.

Vessel behavior, including maneuverability and squat in fluid mud areas, is not expected to be significantly affected, as vessels will be operating at very low speed, under tugboats and with pilots on board, and once they leave the berthing area, they will reach the main channel. According to Michimoto (2019), the impact of fluid mud on ship maneuverability is minimal when the critical density is 1,200 kg/m^3 or less.

From a conservative perspective, it is also important to note that the complexity and risk in the study area are not significant for the following reasons:

- Vessels transit this berth at low speed and with the assistance of tugboats.
- Maneuvers are performed under the supervision of an experienced pilot.
- The bottom is made of fluid mud and there are no indications of bedrock.
- Maneuverability studies indicate that vessels can navigate safely even in contact with the fluid mud.
- The terminal is in a wind and wave sheltered area of Babitonga Bay.

It is worth noting that uncertainties in fluid mud surveys are not accurately estimated or easily measured; this is not a simple method, like that described in IHO (2024) for calculating total propagated uncertainty, also perceived in USACE (2013). Echo sounder measurements in areas with suspended sediments and fluid mud are affected by changes in the sound velocity profile, with absorption, attenuation, scattering, and reverberation occurring at different proportions than in Newtonian fluids.

7.2 Recommendations

a) Adopt the minimum nautical depth in the Berth 301 area as 14.0 m for the purposes of defining the UKC.
b) Establish this nautical depth during a testing period, in coordination with local pilotage. The pilots' data, information, and assessments will be highly relevant to the safe implementation of the nautical depth.
c) Consider using the fluid mud layer definition in the squat formula calculation, due to its potential effect on the ship's squat.
d) Monitor the variability of the fluid mud in the Berth 301 area, in terms of density and depth.
e) Have bottom samples analyzed in laboratory, in addition to the manual analysis performed onboard the survey vessel.
f) Consider in-situ conditioning to improve mud fluidization, potentially increasing the nautical depth in the berthing area.
g) Investigate the adoption of the S-129 Under-Keel Clearance format, currently under development (IHO, 2022).
h) Monitor the work of the Brazilian Hydrographic Society (SBHidro), which recently approved the establishment of a working group to improve hydrography in ports.

https://doi.org/10.58440/ihr-31-2-a15

References

Buchanan, L. (2008). Surveying in Fluid Mud. *Hydro International*, 1 January. https://www.hydro-international.com/content/article/surveying-in-fluid-mud (last accessed 31 October 2025).

Carneiro, J. C. (2018). *Estudo das camadas de lama fluida em portos e canais de navegação* [Doctoral thesis, Universidade Federal do Rio de Janeiro, COPPE]. Pantheon Institutional Repository. http://hdl.handle.net/11422/12564

Carneiro, J. C., Fonseca, D. L., Vinzón, S. B. and Gallo, M. N. (2017). Strategies for measuring fluid mud layers and their rheological properties in ports. *Journal of Waterway, Port, Coastal, and Ocean Engineering, 143*(4), 04017008. https://doi.org/10.1061/(ASCE)WW.1943-5460.0000396

Chamanmotlagh, F., Kirichek, A. and Gebert, J. (2024). Effects of recirculation dredging on density, strength, settling and oxygen concentration of fluid mud in the port of Emden. *Journal of Soils and Sediments, 24*(12), 3887–3897. https://doi.org/10.1007/s11368-024-03891-x

Claeys, S. (2006). Evaluation and combination of techniques used to determine the nautical bottom: A call for rheology-based instruments. In *Proceedings of the 15th International Congress of the International Federation of Hydrographic Societies* (Vol. 55, pp. 141–144). Hydrographic Society Special Publication.

CPE (2024). *Relatório de sondagem N. CPE048-RL-001, Porto de São Francisco do Sul*. CoastalPort Engenharia. Belo Horizonte, MG, Brasil.

Cunha, C. N. and Abreu, A. C. (2023). Mixing process evaluation due to sea level rise in Babitonga Bay, Brazil. *Journal of Integrated Coastal Zone Management (APRH), 23*(2), 135–151. https://doi.org/10.5894/rgci-n521

Fonseca, D. L. (2018). Assessing rheological properties of fluid mud samples through tuning fork data. *Ocean Dynamics, 68*(1), 1–7. https://doi.org/10.1007/s10236-017-1113-3

Fugro (2025). *Fugro Marinestar*. Fugro NV. Leidschendam, Netherlands. https://www.fugro.com/expertise/satellite-positioning/marinestar (last accessed 24 July 2025).

Greer, J. (2008). Not all sediment is created equal. *Chesapeake Quarterly*, 7(3). https://www.chesapeakequarterly.net/V07N03/main/ (last accessed 31 October 2025).

Greiser, N., Gamnitzer, R. and Rupp, J. (2002). Pseudoplasticity of Cohesive Sediments: Causes and Innovative Techniques for Pre-Dredging Surveys. In *Proceedings of the CEDA Dredging Days*, Casablanca, Morocco, pp. 27-33.

IHO (2005). *Manual on Hydrography* (ed. 1.0). IHO Publication C-13, International Hydrographic Organization, Monaco. https://iho.int/uploads/user/pubs/cb/c-13/english/C-13_Chapter_1_and_contents.pdf (last accessed 31 October 2025).

IHO (2020a). *Standards for Hydrographic Surveys* (ed. 6.0). IHO Special Publication S-44, International Hydrographic Organization, Monaco.

IHO (2020b). *INT 1 Symbols and Abbreviations used on Paper Charts* (ed. 8). IHO Special Publication S-4. International Hydrographic Organization, Monaco.

IHO (2022). *Under keel clearance management (UKCM)* [Manuscript in preparation]. IHO Special Publication S-129, International Hydrographic Organization, Monaco.

IHO (2024). *Standards for Hydrographic Surveys* (ed. 6.2.0). IHO Special Publication S-44, International Hydrographic Organization, Monaco. https://iho.int/uploads/user/Services%20and%20Standards/HSSC/HSSC16/S-44_Edition_6.2.0_Proposed.pdf (last accessed 31 October 2025).

IHO (2025). *Yearbook* (Publication P-5). International Hydrographic Organization, Monaco. https://iho.int/uploads/user/pubs/periodical/P5YEARBOOK_ANNUAIRE.pdf (last accessed 31 October 2025).

Kirby, R., Parker, W. R. and van Oostrum, W. H. A. (1980). Definition of the seabed in navigation routes through mud areas. *International Hydrographic Review, LVII*(1), 107–117.

Kirichek, A., Rutgers, R., Nipius, K., Ohle, N., Meijer, H. and Smits, J. (2018a). Current surveying strategies in ports with fluid mud layers. In *Proceedings of the Hydro18 Conference and Trade Exhibition*, 1–10.

Kirichek, A., Chassagne1, C.,Winterwerp, H., Noordijk, A., Rutgers, R., Schot, C., Nipius, K. and Vellinga, T. (2018b). How navigable are fluid mud layers? In *Proceedings of the PIANC World Congress*, Panama City, USA.

Kirichek, A. and Rutgers, R. (2020). Monitoring of settling and consolidation of mud after water injection dredging in the Calandkanaal. *Aqua et Terra, 116*, 12–18.

McAnally, W. H., Friedrichs, C. T., Hamilton, D., Hayter, E. J., Shrestha, P., Sheremet, A. and Teeter, A. M. (2007). Management of fluid mud in estuaries, bays, and lakes: Present state of understanding on character and behavior. *Journal of Hydraulic Engineering, 133*(1), 9–22. https://doi.org/10.1061/(ASCE)0733-9429(2007)133:1(9)

Michimoto, M. (2019). *Aspectos relativos à folga abaixo da quilha de navios com enfoque nos parâmetros operacionais portuários verticais* [Master's thesis, Universidade Federal Fluminense]. UFF Institutional Repository.

Nguyen, V. and Le, V.-A. (2023). Fluid mud properties and nautical depth estimation: A case study in navigation channel of Duyen Hai Port, Vietnam. *Ocean Engineering, 284*, 114833. https://doi.org/10.1016/j.oceaneng.2023.114833

NOAA (2025a). *An inch of water. What's it worth?* National Oceanic and Atmospheric Administration. https://oceanservice.noaa.gov/economy/inch-water (last accessed 30 June 2025).

NOAA (2025b). *Hydrographic surveys specifications and deliverables*. NOAA Office of Coast Survey. Silver Spring, MD, USA.

NORMAM (2023a). *Norma da Autoridade Marítima para Levantamentos Hidrográficos* (NORMAM-501/DHN). Marinha do Brasil. Brasília, DF, Brasil.

NORMAM (2023b). *Norma da Autoridade Marítima para Folga Dinâmica Abaixo da Quilha* (NORMAM-224/DPC). Marinha do Brasil. Brasília, DF, Brasil.

NPCP-SC (2022). *Normas e procedimentos da Capitania dos Portos de Santa Catarina (NPCP-SC)*. Marinha do Brasil. Brasília, DF, Brasil.

PIANC (2014). *Harbour approach channels design guidelines* (Report No. 121). The World Association for Waterborne Transport Infrastructure. Brussels, Belgium.

Pion, L. and Alfredini, P. (2019). Fluid mud and nautical bottom – Concept and application in Itajaí Port Complex (Brazil). *TransNav: International Journal on Marine Navigation and Safety of Sea Transportation, 13*(2), 445–452. https://doi.org/10.12716/1001.13.02.20

Projeto Baías do Brasil (2018). *Baía de Babitonga*. https://www.baiasdobrasil.coppe.ufrj.br/assets/relatorios/rel_baia_babitonga.html (last accessed 10 September 2025).

Shakeel, A., Kirichek, A. and Chassagne, C. (2019). Revising the

https://doi.org/10.58440/ihr-31-2-a15

definition of fluid mud by establishing new protocols for rheological measurements. In *The XVII European Conference on Soil Mechanics and Geotechnical Engineering: Geotechnical Engineering, Foundation of the Future* (pp. 1–8). International Society for Soil Mechanics and Geotechnical Engineering.

Shakeel, A., Kirichek, A. and Chassagne, C. (2021). Rheology of mud: An overview for ports and waterways applications. In Manning, A. J. (Ed.), *Sediment transport – Recent advances*. IntechOpen. https://doi.org/10.5772/intechopen.100123

Shakeel, A., Zander, F., de Klerk, J.-W., Kirichek, A., Gebert, J. and Chassagne, C. (2022). Effect of organic matter degradation in cohesive sediment: A detailed rheological analysis. *Journal of Soils and Sediments, 22*, 2883–2892. https://doi.org/10.1007/s11368-022-03245-3

Teeter, A., Banks, G., Alexander, M. and Salkield, A. (1992). An intrusive fluid mud surveying system. *U.S. Army Engineer Waterways Experiment Station*. Washington, DC, USA.

TESC (2025). *Terminal Portuário de Santa Catarina (TESC), Institucional, Infraestrutura*. https://www.terminalsc.com.br (last accessed 6 July 2025).

USACE (2013). *Hydrographic surveying engineer manual* (Engineer Manual No. 1110-2-1003). United States Army Corps of Engineers. Washington, DC, USA.

Vanlede, J., Dujardin, A., Fettweis, M., Van Hoestenberghe, T. and Martens, C. (2019). Mud dynamics in the Port of Zeebrugge. *Ocean Dynamics, 69*, 1085–1099. https://doi.org/10.1007/s10236-019-01278-9

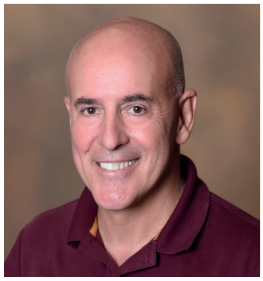
Verwilligen, J., Vantorre, M., Delefortrie, G., Kamphuis, J., Meinsma, R. and van der Made, K.-J. (2014). Manoeuvrability in proximity of nautical bottom in the harbour of Delfzijl. PIANC World Congress, San Francisco, USA.

Vieira, C. and Horn, N. O. (2017). Marine landscape of the Babitonga bay, northeast of Santa Catarina state. *Revista Brasileira de Geografia Física, 10*(5), 1677–1689.

Wurpts, R. and Torn, P. (2005). 15 Years Experience with Fluid Mud: Definition of the Nautical Bottom with Rheological Parameters. *Terra et Aqua, 99*, 22–32.

Authors' biographies

Alberto P. Costa Neves, Capt (Ret), MSc, earned his Hydrography Certificate (with Distinction) from the Brazilian Navy Hydrography School and a MSc degree (with Distinction) in Meteorology and Physical Oceanography from the United States Naval Postgraduate School (NPS). He is based in Portugal and has 40 years of experience in hydrographic surveys and navigation. He is the Director of PCN Maritime, a consultancy company focused on ports, maritime operations, navigation, hydrography, ship maneuver and simulation, aids to navigation, channel design, dredging, and underkeel clearance. In the Navy, he was a survey vessel's captain and Superintendent of Safety of Navigation. Following retirement, he held the position of IHO Assistant Director and Hydrographic Science Program Coordinator at the University of Southern Mississippi (USM).

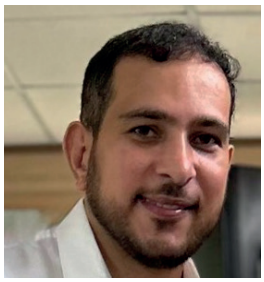


Alberto P. Costa Neves

Augusto Dantas Sampaio, Civil Engineer, is a Port and Waterway Engineer, with over 50 years of experience in the port and waterway sector, with a distinguished career at the Ministry of Transportation and, for the last 38 years, at Hidrotopo Consultoria e Projetos Ltda. He has a solid career in Brazil's main ports and waterways, actively contributing to the development of the sector, always guided by the adoption of new technologies and the promotion of safer and more efficient navigation. Currently, he is the leading technical coordinator and consultant, responsible for developing port projects focused on the implementation, maintenance, and adaptation of infrastructures. He also participates in the supervision of dredging works, nautical support, and hydrographic and geophysical surveys.



Augusto Dantas Sampaio



Reginaldo Gonçalves Abreu

Reginaldo Gonçalves Abreu is a civil engineer with a degree from Estácio de Sá University, with specialization in Environmental Engineering and Port Engineering. Based in Rio de Janeiro, he has worked in hydrography for 23 years, accumulating solid experience in hydrographic and geotechnical surveys, as well as in conducting applied environmental studies. Throughout his career, he has participated in projects of national relevance, including deepening and maintenance dredging, as well as high-precision bathymetric monitoring with multibeam technology. He currently leads the technical team at Hidrotopo Consultoria e Projetos Ltda, coordinating strategic activities focused on maritime infrastructure, including planning and designing navigation channels, monitoring and supervising dredging projects, and implementing technical solutions that ensure operational efficiency and environmental compliance.

https://doi.org/10.58440/ihr-31-2-a15

PEER-REVIEWED ARTICLE

Geostatistical analysis of maritime accidents: identifying contributory factors and risk patterns in maritime navigation

Authors

Amrika Maharaj[1], Keith Miller[1], Dexter Davis[1] and Michael Sutherland[1]

Abstract

Maritime accidents remain a critical concern despite advancements in navigation technology and safety regulations. This paper examines maritime events over a 20-year period (2002–2021) using geostatistical analysis and GIS-based methods to identify key risk factors, trends, and high-risk zones. Analysis of the IMO's Global Integrated Shipping Information System (GISIS) database highlights the influence of vessel type, flag state performance, accident timing, and geographical hotspots on incident frequency. Collisions, groundings, and fires/explosions are the most prevalent events, with aged vessels, open registries and outdated or incomplete hydrographic survey data posing significant risks. Poor flag state oversight, economic constraints, and human factors exacerbate maritime hazards. Although accident rates have declined, high-risk zones persist, necessitating stricter regulatory enforcement, fleet modernization, and improved accident reporting. Strengthening international collaboration and proactive risk management is crucial for ensuring safer global shipping operations, particularly in high-risk regions like the Caribbean Sea.

Keywords

maritime accidents · geographic information system · geographic hotspots · vessel collision · Caribbean Sea · flag state performance · risk factors · shipping

Resumé

En dépit des progrès réalisés dans les domaines de la technologie de navigation et de la réglementation en matière de sécurité, les accidents maritimes restent une préoccupation majeure. Cet article examine les événements maritimes survenus au cours d'une période de 20 ans (2002–2021) à l'aide d'analyses géostatistiques et de méthodes reposant sur les SIG afin d'identifier les principaux facteurs de risque, les tendances et les zones à haut risque. L'analyse de la base de données du Système mondial intégré d'information sur le transport maritime (GISIS) de l'OMI met en évidence l'influence du type de navire, de la performance de l'État du pavillon, du moment de l'accident et des zones géographiques sensibles sur la fréquence des incidents. Les collisions, les échouages et les incendies/explosions sont les événements les plus fréquents, les navires vieillissants, les bases de registres ouvertes et les données hydrographiques obsolètes ou incomplètes présentant des risques importants. La mauvaise surveillance des États du pavillon, les contraintes économiques et les facteurs humains exacerbent les risques maritimes. Bien que les taux d'accidents aient diminué, certaines zones à haut risque persistent, ce qui rend nécessaire un renforcement de l'application de la réglementation, une modernisation de la flotte et une amélioration du signalement des accidents. Le renforcement de la collaboration internationale et la gestion proactive des risques sont essentiels pour garantir la sécurité des opérations maritimes mondiales, en particulier dans les régions à haut risque comme la mer des Caraïbes.

✉ Amrika Maharaj · amrika.maharaj@hotmail.com

[1] Department of Geomatics Engineering and Land Management, The University of the West Indies, St. Augustine, The Republic of Trinidad and Tobago

https://doi.org/10.58440/ihr-31-2-a10

Resumen

Los accidentes marítimos siguen siendo una preocupación crítica a pesar de los avances en la tecnología de navegación y las normas de seguridad. En este artículo se examinan los sucesos marítimos durante un período de 20 años (2002 -2021) usando análisis geoestadísticos y métodos basados en SIG para identificar los principales factores de riesgo, tendencias y zonas de alto riesgo. El análisis de la base de datos del Sistema Mundial Integrado de Información Marítima (GISIS) de la OMI destaca la influencia del tipo de buque, el funcionamiento del estado de abanderamiento, el momento del accidente y los puntos geográficos clave en la frecuencia de los incidentes. Colisiones, tocar fondo e incendios / explosiones son los sucesos más frecuentes, con buques antiguos, registros abiertos y datos de levantamientos hidrográficos anticuados o incompletos suponen riesgos significativos. Una pobre supervisión del estado de abanderamiento, limitaciones económicas y factores humanos agravan los riesgos marítimos. Aunque las tasas de accidentes han disminuido, persisten las zonas de alto riesgo, que necesitan una aplicación más estricta de la normativa, la modernización de la flota y la mejora de los informes de accidentes. El fortalecimiento de la colaboración internacional y la gestión proactiva de los riesgos son cruciales para garantizar unas operaciones marítimas más seguras a nivel global, particularmente en regiones de alto riesgo como el Mar Caribe.

1 Introduction

Maritime transportation is the backbone of global trade, accounting for 90 % of international commerce (IMO, 2025). It underpins economic development by facilitating foreign trade, industrial growth, and market accessibility. As global markets expand, demand for shipping continues to rise, driving advancements in vessel technology, port infrastructure, and navigational safety. While automation and intermodal logistics have improved operational efficiency, growing vessel traffic density has also increased the risks of collisions and congestion, particularly in heavily trafficked waterways. Ensuring safe and efficient maritime operations therefore requires comprehensive risk assessments and stricter regulatory measures. The Caribbean Sea serves as a vital maritime corridor, connecting major international and regional trade routes. Bordered by Venezuela, Colombia, Central America (including Panama), the Greater and Lesser Antilles, and the Atlantic Ocean, it ranks among the world's busiest shipping regions. The Panama Canal enhances its global significance by facilitating interoceanic trade between the Pacific and Atlantic Oceans. The region is also a major hub for passenger vessels, hosting 50 % of the world's cruise ships (Strauch, 2015). Key ports such as Freeport, Colón, and Port of Spain operate as transshipment hubs, supporting both regional and global commerce (Wilmsmeier & Sánchez, 2009). Fig. 1 illustrates the region's high vessel traffic density, with 67,289 vessel tracks recorded in 2016 using Satellite Automatic Identification System (SAIS) data. Traffic is particularly concentrated near the Gulf of Paria and the Panama Canal, underscoring the complexity of maritime operations and associated safety concerns. While AIS coverage is not comprehensive, owing to limited equipment installation across vessel types and the possibility of manual transponder deactivation, it remains a critical tool for mapping vessel movements and delineating key shipping lanes. As maritime activity in the Caribbean increases, rigorous safety assessments and targeted risk mitigation strategies become increasingly significant. This study examines accident trends, vessel risk factors, and

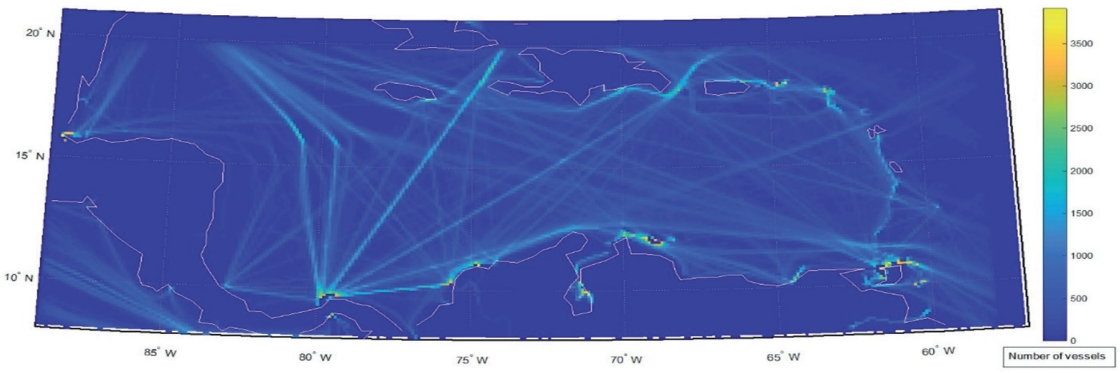


Fig. 1 Vessel traffic density on a 0.1-degree grid across the Caribbean Sea in 2016.

high-risk areas globally and within the Caribbean Sea, offering insights into navigational safety challenges. By analyzing spatial concentrations of maritime events, vessel types with high accident rate, and temporal risk patterns, the research aims to inform interventions that enhance safety and reduce maritime accident risks.

2 The importance of maritime safety and risk management

Maritime transport, while essential for global trade, carries inherent risks, making safety a critical priority. Beyond its economic importance, maritime safety is vital for environmental protection and societal well-being, as marine ecosystems are highly susceptible to pollution from oil spills, chemical leaks, and vessel groundings (Rodrigue, 2017). Ensuring robust safety practices safeguards human lives, marine biodiversity, and coastal communities, reinforcing the need for sustainable and resilient shipping operations. These maritime operations can be affected by a range of adverse events, broadly described as accidents or incidents. In this paper, an accident, also referred to as a marine casualty, denotes any event or sequence of events arising from vessel operations that results in serious consequences, such as loss of life, significant structural damage, grounding, collision, or major environmental harm (UN, EU, & ITF, 2019). An incident refers to an occurrence during vessel operations that does not produce such severe outcomes but poses a credible risk to the vessel, personnel, or the environment if not effectively managed (MAIB, 2019). Accidents ranging from collisions and oil spills to cargo losses can have severe economic, environmental, and human consequences. Beyond financial losses, these events contribute to long-term environmental degradation, biodiversity loss, and disruptions in trade flows (Goerlandt & Kujala, 2011). Notable disasters such as the MV Prestige sinking and the Deepwater Horizon oil spill highlight vulnerabilities in maritime operations and the critical need for stringent safety regulations. The maritime industry operates in an unpredictable environment affected by mechanical failures, human factors, extreme weather, and geopolitical tensions (Montewka et al., 2011). Human factors encompass not only individual actions but also procedural shortcomings, organizational culture, and operational conditions, recognizing that not all human contributions to accidents are the result of errors in the strict sense.

Analyzing maritime accident data is crucial for enhancing safety standards and improving operational protocols. Statistical analysis of past events helps identify patterns, assess risk factors, and develop predictive models to prevent future occurrences (Johansson & Molitor, 2011). Regulatory bodies like the International Maritime Organization (IMO) rely on accident data to enforce safety measures, including mandatory crew training, ship maintenance requirements, and advanced navigation technologies (Baldauf, 2016). Technological advancements, particularly artificial intelligence and data analytics, have further improved maritime traffic monitoring, anomaly detection, and early hazard warnings, enabling more effective risk management strategies (Fratila et al., 2021). A thorough examination of maritime accident databases is essential for uncovering critical causation factors, including human factors, mechanical failure, adverse weather conditions, and navigational hazards. Analyzing vessel records also provides insights into operational history, such as age, maintenance schedules, and compliance with safety regulations. Older vessels are often more prone to structural weaknesses, outdated safety systems, and mechanical breakdowns, increasing their risk of incidents (Maharaj, 2020). By systematically assessing these variables, regulatory bodies, ship operators, and policymakers can implement data-driven strategies to enhance maritime safety, improve vessel design standards, and enforce stricter maintenance protocols.

Long-term analysis of maritime accident trends enables researchers to identify recurring patterns, assess risk levels across shipping routes, and refine international safety regulations. A comprehensive review of accident data over the past two decades provides valuable insights into accident trends, causative factors, and areas for improvement (Smith & Cox, 2007). Understanding these statistical dynamics facilitates the implementation of effective safety regulations, technological innovations, and policy reforms to minimize risks. By prioritizing data-driven accident analysis, the maritime industry can foster a culture of safety, resilience, and sustainability, ensuring the continued growth and reliability of global shipping networks (Williams, 2015).

3 Literature review

Accurate and comprehensive maritime accident data is crucial for effective safety analysis and risk mitigation. The global analysis of maritime accidents reveals a complex landscape of risks influenced by human, technical, environmental, and organizational factors. Studies such as Akyuz & Celik (2023) highlight that cargo vessels are particularly vulnerable to collisions, while tankers face a higher risk of groundings, reinforcing the need for vessel-specific safety measures. Similarly, Zhou et al. (2020) emphasize that accident risks are not uniform across regions, with high-risk hotspots such as the South China Sea and the Gulf of Mexico necessitating tailored safety frameworks. A major challenge in maritime safety is the underreporting of accidents, which limits a comprehensive understanding of risk factors and hinders effective regulation (Psarros et al., 2010). Additionally, Liu et al. (2024) integrate environmental risk factors into maritime accident analysis, showing how severe weather and complex navigational routes significantly influence accident rates. Bowo et al. (2017) further highlight the role of human and organizational factors,

https://doi.org/10.58440/ihr-31-2-a10

identifying management practices, communication breakdowns, and machinery failures as primary contributors to maritime accidents. These findings stress the importance of crew training programs and improved management systems to enhance operational safety.

While global case studies provide essential insights, the Caribbean Sea remains under-researched despite its dense vessel traffic and strategic shipping routes. Existing studies, such as Maharaj (2020), explore AIS data for tracking vessel movements, but lack integration with detailed accident reports and modern analytical techniques, leaving gaps in understanding maritime risks. Historical analyses, such as Gomez Pretel et al. (2023) on the USS Kearsarge grounding, provide valuable perspectives but fail to address contemporary traffic patterns, regulatory changes, or technological advancements, further underscoring the need for updated, data-driven research. The global maritime safety framework is shaped by institutions such as the Marine Accident Investigators' International Forum (MAIIF), Marine Accident Investigation Bureau (MAIB) and the European Maritime Safety Agency (EMSA), which investigate maritime accidents, identify causes, and promote industry-wide safety improvements. However, discrepancies in data collection, reporting criteria, and regulatory enforcement create challenges in developing standardized safety measures, especially in regions like the Caribbean, where multiple coastal and flag states interact.

The IMO plays a central role in maritime safety by promoting international conventions and regulatory frameworks. However, the slow adoption and enforcement of these measures delay critical legislative responses to major accidents. Flag state performance remains a significant factor in vessel safety, with organizations such as the International Chamber of Shipping (ICS), Maritime International Secretariat Services (MARISEC), and the International Transport Workers' Federation (ITF) publishing annual performance indicators on treaty enforcement, maritime security, and seafarers' welfare. These assessments reveal systemic strengths and weaknesses, reinforcing the need for stricter oversight and improved regulatory compliance to enhance global maritime safety.

In the Caribbean, the role of flag states becomes even more critical due to the dominance of open registries, particularly Panama and Liberia, which attract older vessels due to lenient registration policies. This practice compromises safety standards, increasing the likelihood of maritime accidents. The high vessel density and prevalence of open registry vessels place the Caribbean at heightened risk. This issue is further exacerbated by a lack of regional studies that integrate geostatistical methods, AIS data, and detailed accident reports. This study aims to bridge the research gap in the Caribbean Sea by conducting an in-depth geostatistical analysis of maritime accidents over the past two decades. By leveraging comprehensive datasets and advanced analytical methodologies, this research seeks to generate region-specific insights to support policymaking, improve navigational safety, and mitigate accident risks. Furthermore, this study complements global maritime safety efforts by offering data-driven recommendations tailored to the Caribbean's operational challenges. Strengthening flag state oversight, improving data transparency, and integrating modern analytical techniques will be crucial for establishing a robust maritime safety framework in the region. By aligning global safety benchmarks with localized data, this research aims to enhance maritime risk assessments and support regulatory improvements. The findings from global case studies serve as valuable benchmarks, while the localized analysis addresses the specific challenges of the Caribbean. Ultimately, this study contributes to safer maritime operations, more effective accident prevention strategies, and a more sustainable shipping industry in one of the world's most strategic maritime regions.

4 Data and methodology

The Global Integrated Shipping Information System (GISIS), maintained by the International Maritime Organization (IMO), serves as the primary data source for this study. GISIS compiles marine casualty and incident reports from national administrations, containing factual records and detailed investigative findings (IMO, 2012). The database provides key attributes such as incident date, vessel type, flag state, gross tonnage, spatial location, and causation factors, enabling the identification of accident trends and safety concerns. This study analyzed 6,260 maritime events reported globally between January 2002 and December 2021. While GISIS is a critical repository, it is affected by underreporting, resulting in the underestimation of maritime incidents (Psarros et al., 2010). Some records are supplemented by Automatic Identification System (AIS) transmissions, which provide vessel-specific details such as ship type, location, and casualty type. However, SOLAS regulations require AIS transponders only for vessels of 300 Gross Tonnage (GT) and above, excluding smaller vessels from mandatory reporting (IMO, 2012). Additional inconsistencies arise from missing vessel attributes, inaccurate navigational status, and human error in AIS data entry (Calder & Kurt, 2009).

To address these limitations, a comprehensive quality assessment was conducted, and a custom script was developed to retrieve missing static and voyage-related vessel information from online databases such as *MarineTraffic* and *VesselFinder.* By cross-referencing vessel attributes including ship type, gross tonnage, flag state, and year of construction with these sources, dataset completeness and reliability were substantially enhanced, improving the accuracy of maritime accident analyses and supporting evidence-based safety measures. For

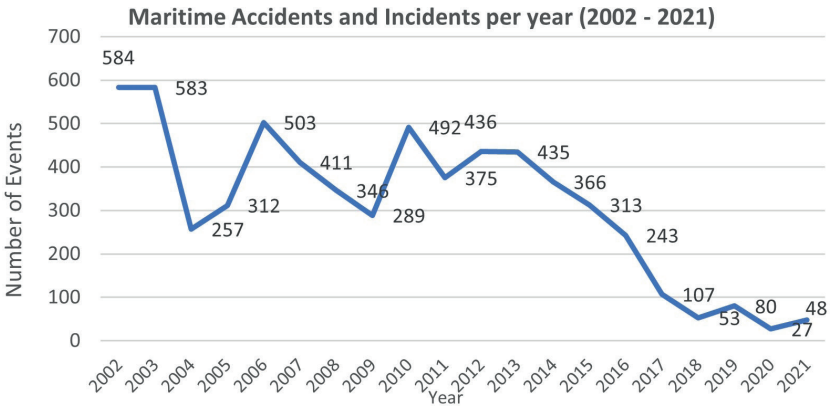


Fig. 2 Maritime accidents and incidents per year.

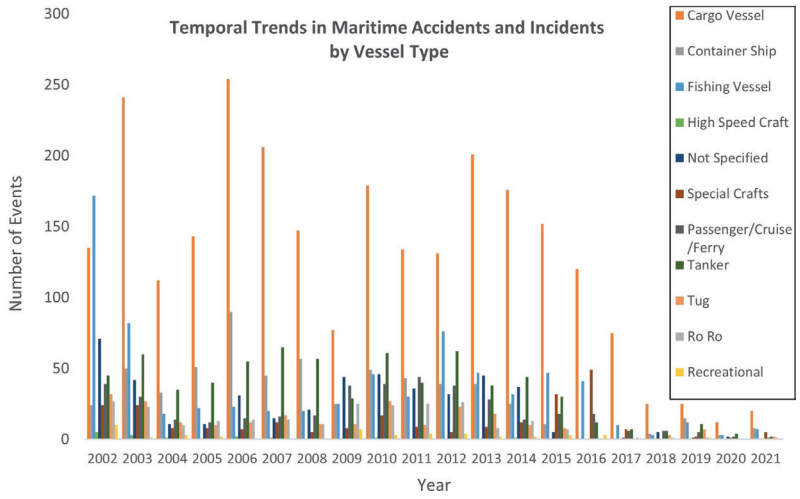


Fig. 3 Number of events per vessel type for each year.

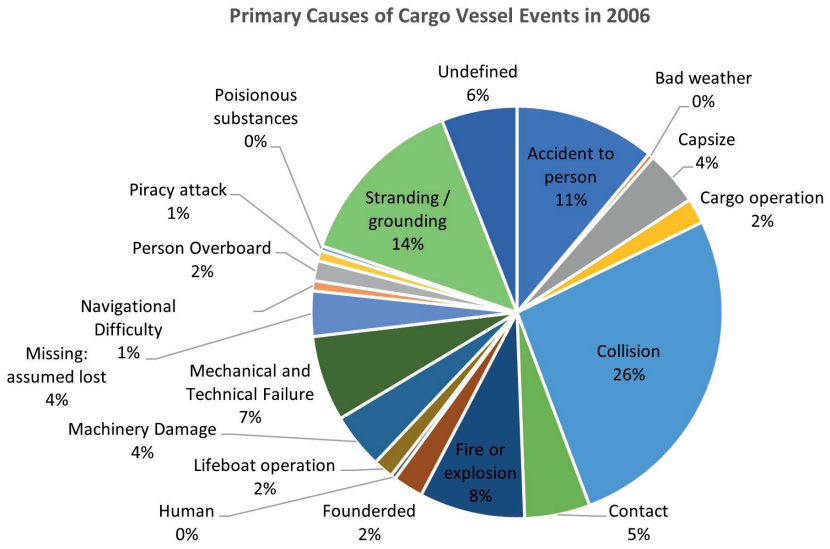


Fig. 4 Number of cargo vessel events for 2006.

analytical clarity, the 145 distinct vessel types recorded in GISIS were reclassified into eleven broader categories, following the approach of Calder & Kurt (2009). This standardization reduced discrepancies between AIS data and supplementary vessel information, provided a structured view of shipping activity and global traffic density, and improved the consistency of maritime safety assessments. The analytical framework employed geostatistical techniques to map accident distribution and identify high-risk zones. Temporal analyses examined seasonal and daily patterns, while causation factor analysis determined the leading causes of events. Flag state performance was also assessed by examining accident frequency. This integrated methodology produced a robust understanding of maritime accident risks, with particular emphasis on the Caribbean region, and informed the development of targeted safety interventions.

5 Results

A comprehensive analysis of global maritime casualty and incident statistics over a 20-year period identified the primary factors contributing to maritime accidents. This timeframe was selected to include significant maritime disasters, such as the *Prestige*, *Deep Water Horizon* and *Costa Concordia* accidents, which catalysed major advancements in maritime safety regulations. The chronological timeline of regulatory changes presented in this study provides insight into the evolving landscape of maritime risk management. The analysis revealed that 2002 recorded the highest number of reported maritime events (584) with cargo vessels, container ships, tankers, fishing vessels, and passenger ships being the most frequently involved. Over time, the overall number of accidents exhibited a substantial decline (Fig. 2). Notably, 2004 and 2009 saw sharp reductions in accident frequency, aligning with the enforcement of the Safety of Life at Sea (SOLAS) Convention. These regulations mandated that all ships of 300 gross tonnage (GT) and above engaged in international voyages, cargo ships of 500 GT and above operating domestically, and all passenger vessels, regardless of size, be equipped with AIS transponders. The AIS regulation, which became fully effective on December 31, 2004, significantly improved vessel tracking and monitoring, enhancing navigational safety (IMO, 2012).

However, periods of increased accident frequency were observed in 2002, 2003, 2006, and 2010, coinciding with global fleet expansions (Gasparotti & Rusu, 2012). This suggests that while regulatory interventions have effectively reduced maritime accidents, fluctuations in fleet numbers and traffic density continue to influence accident trends. Understanding these dynamics is crucial for policymakers and industry stakeholders to further enhance maritime safety and develop adaptive risk management strategies.

5.1 Temporal variation of maritime accidents and incidents by vessel type

An analysis of maritime accidents and incidents by

https://doi.org/10.58440/ihr-31-2-a10

vessel type from 2002 to 2021 reveals notable temporal variations (Fig. 3). Throughout the study period, cargo vessels consistently recorded the highest number of events, reaffirming their status as the most frequently involved vessel type in maritime accidents. The year 2006 (Fig. 4) saw the highest number of cargo vessel events (254 cases). with collisions accounting for 26 %, followed by groundings (14 %) and accidents involving personnel (11%). A significant decline in cargo vessel events was observed after 2013, likely due to the introduction of newer cargo carriers with improved safety measures and technology (Butt et al., 2015). Other vessel types also exhibited distinct peak years, with container ship incidents reaching their highest in 2006 (90 cases) and fishing vessel accidents peaking in 2002 (172 cases). High-speed crafts and recreational vessels had minimal occurrences, whereas other offshore ships recorded their highest number of events in 2016 (49 cases). It is important to note that the decline in reported events from 2018 onward may not reflect an actual reduction in accidents, but rather incomplete records in the GISIS IMO Database for 2018–2021. This pattern is likely due to delayed reporting in the GISIS IMO Database, as earlier years in the dataset also showed artificially low counts until records were updated in subsequent years. This potential underreporting highlights the need for improved data collection mechanisms to ensure a more accurate representation of maritime accident and incident trends.

5.2 Distribution of maritime accident causes

The analysis of maritime events reveals distinct variations in frequency and causation factors across different incident categories. Collisions emerged as the most prevalent accident type, with 1,254 recorded cases, attributed to navigational challenges in congested ports and narrow waterways (Fig. 5). Factors such as restricted visibility, high traffic density, and limited manoeuvring space further increase collision risks, making them a major maritime safety concern.

Stranding/grounding events ranked second, accounting for 16 % of total accidents (832). These events often result from navigational errors, unfavourable currents, wave impacts, or excessive speed (Antão & Guedes Soares, 2006). While groundings pose fewer risks to human life, they increase environmental hazards, such as oil spills and hull damage. Fires and explosions were the third most frequent accident type (15 %, 792 cases), primarily caused by engine failures, electrical malfunctions, or hazardous cargo combustibility (Akten, 2006). These events disproportionately affect tankers and container ships, reinforcing the need for fire prevention measures and advanced firefighting systems. Machinery damage and capsizing events each accounted for 9 %, with 468 and 466 recorded cases, respectively. Machinery failures often stem from structural

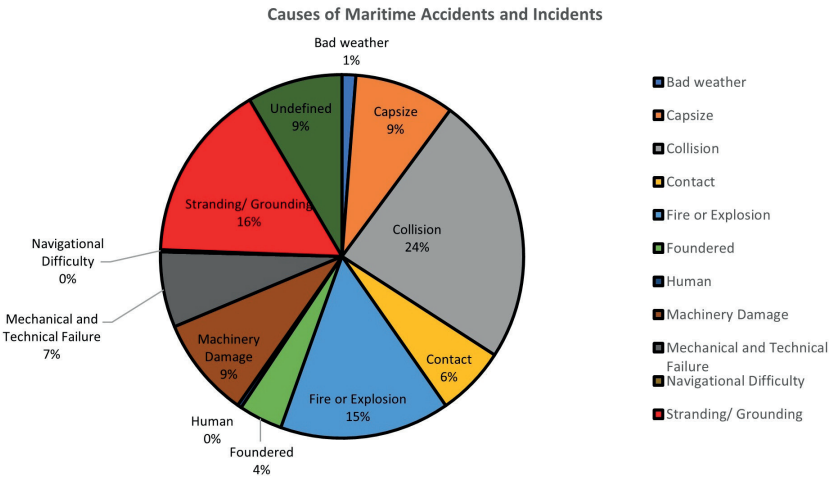


Fig. 5 Percentage distribution of accident types leading to total losses and ship incidents.

weaknesses or mechanical breakdowns, leading to propulsion or steering loss (NTSB, 2017). Capsize events, on the other hand, are frequently linked to improper cargo loading, shifting cargo, progressive rolling, or extreme weather conditions (EMSA, 2014). Other notable causation categories include mechanical and technical failures (7 %, 351 cases), often involving engine malfunctions, GPS failures, or overpressure scenarios (Awal & Hasegawa, 2017). Contact-related events (6 %, 324 cases), occur when vessels collide with submerged objects, offshore platforms, or berths due to adverse weather and navigational miscalculations. Foundering events accounted for 4 % of accidents, occurred primarily in high-risk regions such as the North Sea and Black Sea. These events were typically caused by hull integrity failures, propulsion system breakdowns, and severe storms. The distribution of maritime causation factors highlights the complexity of vessel risks, reinforcing the need for targeted safety interventions that address navigational challenges, human factors, equipment reliability, and environmental conditions. Implementing vessel-specific risk mitigation strategies is essential for enhancing maritime safety and reducing accident rates worldwide.

5.3 Leading cause of maritime events per year

The frequency and nature of maritime events have fluctuated significantly over the study period, with collisions, groundings, and fires or explosions emerging as the most prevalent accident types (Fig. 6). The analysis highlights that certain vessel types are more susceptible to specific accident categories, with cargo vessels, container ships, and tankers most frequently involved in collisions, while cargo vessels and tankers also accounted for a significant share of groundings and fire-related incidents. Between 2011 and 2021, the leading causation factor alternated between collisions and groundings, though collisions remained the dominant accident type for most of the study period. Cargo vessels, tankers, and container ships were consistently the

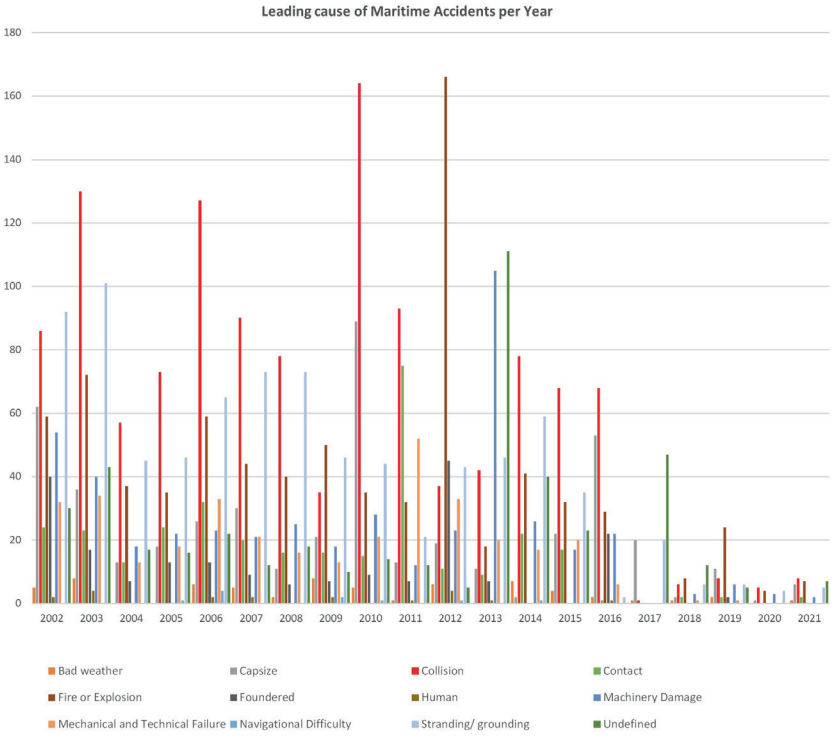


Fig. 6 Leading cause of maritime accidents per year.

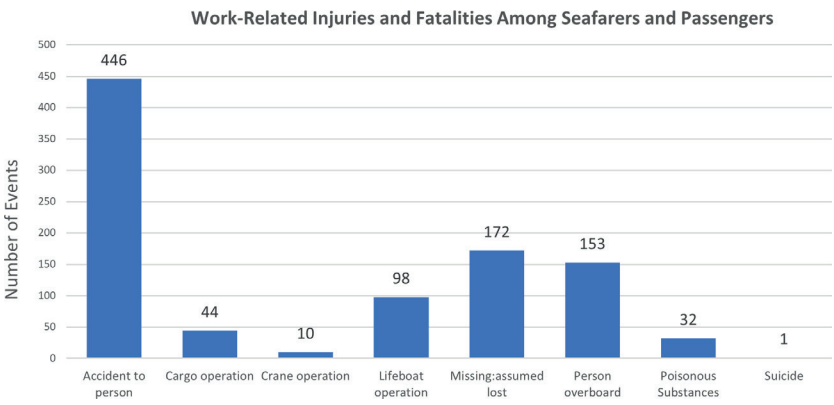


Fig. 7 Work-related injuries and fatalities among seafarers and passengers.

most affected vessel types. Notably, collision events declined significantly in 2017, with only one recorded case. However, this trend reversed over the next three years, with a steady increase in collision occurrences. This fluctuation suggests that while advancements in navigational technologies, safety regulations, and vessel monitoring systems may have temporarily reduced collision rates, dense maritime traffic, congested port operations, and human error continue to be major risk factors.

A closer examination of temporal trends reveals that groundings were the most frequently reported incident in 2002. However, from 2003 to 2008, 2010–2011, and from 2014 onward, collisions overtook groundings as the most common maritime event. Despite this shift, groundings remained notably high in 2002, 2009, 2012, and 2013, which may be associated with shallow-water navigation, adverse weather conditions, and depth miscalculations significantly contributed to accident occurrences during these years. The dominance of collisions and groundings throughout the study period highlights the critical need for enhanced navigational safety measures, stricter traffic separation schemes, and improved situational awareness training for vessel operators. While collisions remain the primary concern due to their high frequency and potential for severe consequences, groundings pose substantial risks, particularly in environmentally sensitive areas, where they can lead to hazardous spills and long-term ecological damage. Addressing the root causes of these accidents through regulatory oversight, technological advancements, and improved vessel traffic management is crucial in reducing future maritime incidents and ensuring safer global shipping operations.

5.4 Analysis of work-related injuries and fatalities among seafarers and passengers

Maritime fatalities and injuries are not solely the result of vessel-related events such as collisions and groundings; many occur due to hazards associated with onboard work processes (Butt et al., 2015). Various sections of a vessel including the deck, cargo area, engine room, and galley pose occupational risks to crew members, often leading to serious injuries or fatalities. The analysis of work-related accidents highlights several dominant categories (Fig. 7). Among these, *Accidents to Persons* emerge as the leading category (446 cases), encompassing trips and falls, fatal medical emergencies such as heart attacks, and structural failures. *Missing: Assumed Lost* refers to crew members who disappeared while on duty and were never recovered, underscoring gaps in monitoring and onboard safety procedures. *Persons Overboard incidents*, where mariners fall into the sea during work-related activities, pose grave risks due to hypothermia, drowning, and delayed rescue responses. Similarly, *lifeboat operations* present notable occupational hazards, with accidents occurring during routine drills, emergency evacuations, and equipment malfunctions.

The high incidence of work-related injuries and fatalities underscores the occupational dangers of maritime professions, emphasizing the need for enhanced safety protocols, improved crew training, and stricter enforcement of onboard risk management measures. Reducing these risks requires advanced safety equipment, standardized emergency response training, and rigorous compliance with international labour safety regulations. Implementing these measures can significantly lower accident rates and improve overall maritime workplace safety.

5.5 Maritime events by time of day: Yearly analysis

A detailed analysis of maritime events from 2002 to 2021 reveals significant variations between morning (AM) and evening (PM) accident frequencies. The findings indicate that most events occurred during

https://doi.org/10.58440/ihr-31-2-a10

morning hours, suggesting a correlation between increased operational activity and heightened accident risks during daytime navigation (Fig. 8). The highest number of AM events was recorded in 2002 and 2003, with 565 reported cases, while PM events remained significantly lower, with only 18 occurrences. This pattern underscores the heightened exposure to maritime risks during peak operational hours, when vessel movements are at their highest. Conversely, in 2010, AM events were the third highest on record (287 events), whereas 2020 had the lowest AM events (19 cases), likely due to reduced maritime activity during the COVID-19 pandemic. For PM events, the highest number of cases occurred in 2006, with 242 events. Apart from the historically low PM accident counts in 2002 and 2003, 2020 also recorded one of the lowest evening incident totals, with only 8 occurrences. These findings highlight the need for heightened vigilance during high-risk operational periods, particularly morning hours when vessel activity peaks. The discrepancy between AM and PM accident frequencies suggests that factors such as crew workload, fatigue, reduced visibility, and port congestion contribute to elevated accident rates during peak hours. Recognizing these temporal patterns is essential for developing strategic interventions, including adjusting operational schedules, implementing fatigue management protocols, and enhancing vessel traffic management systems, to mitigate maritime risks during the most vulnerable periods.

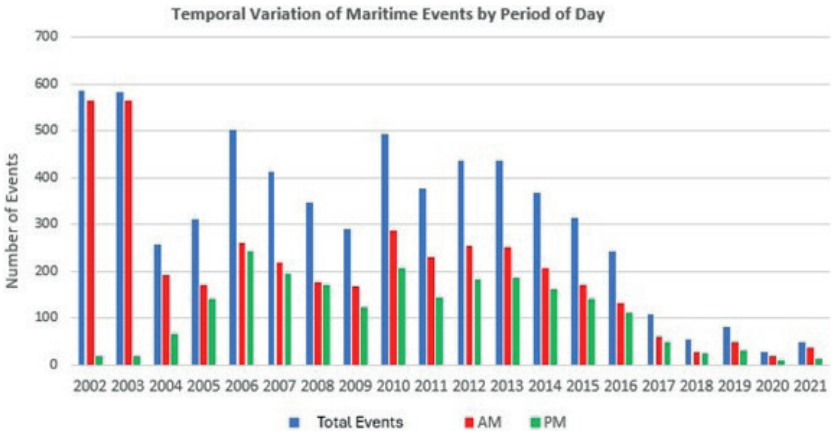


Fig. 8 Temporal variation of maritime accidents by period of day.

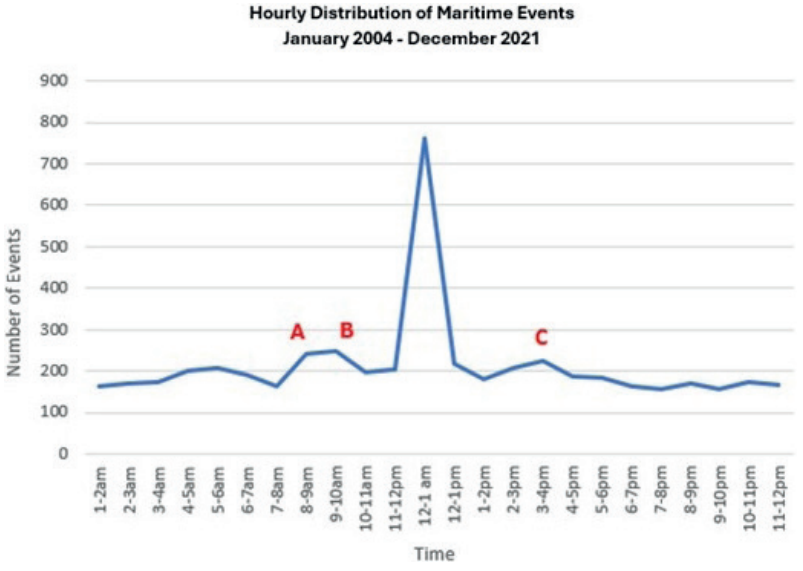


Fig. 9 Hourly distribution of maritime events.

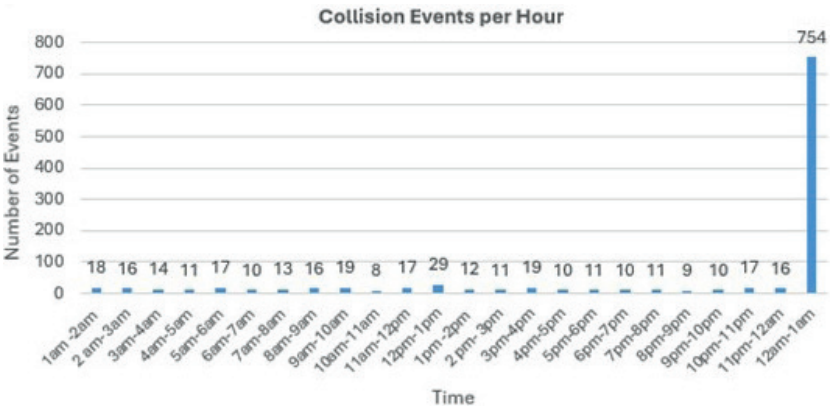


Fig. 10 Collision events per hour.

5.6 Maritime events per hour

An hourly analysis of maritime events revealed notable discrepancies and distinct temporal trends in accident occurrences. A significant anomaly was identified in 2002 and 2003, where all reported events were recorded at 12:00 AM UTC. This systematic error in the GISIS IMO database, likely caused by default time entries or incomplete data submissions, artificially inflated midnight accident statistics. To ensure accurate trend analysis, these two years were excluded from further evaluations. The time interval 12:00 AM – 1:00 AM remained a high-risk, suggesting that restricted nighttime visibility, reduced situational awareness, and crew fatigue significantly contribute to navigational errors and accidents. Daily maritime event patterns exhibited distinct peaks at various times (Fig. 9). Early morning peaks (labelled "A" and "B") align with heightened maritime activity, particularly port arrivals and departures, leading to increased congestion and higher risks of collisions, groundings, and fires. Cargo vessels, tankers, and container ships were the most frequently involved vessel types during these peak hours. Another significant spike occurred between 3:00 PM and 4:00 PM (labelled "C"), where collisions, groundings, and fires were the predominant accident types. The combination of extreme weather conditions, navigational complexities, and human error contributed to elevated risks during this period, especially in high-density port areas where vessels engage in frequent manoeuvring.

A key finding is that collisions, the leading cause of maritime events, peak during nighttime hours, particularly between 12:00 AM and 1:00 AM, with 754



Fig. 11 Contact events per hour.

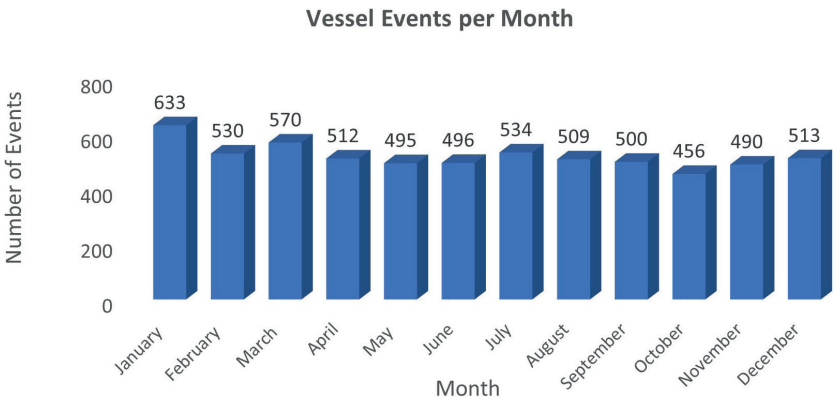


Fig. 12 Seasonal distribution of vessel accidents.

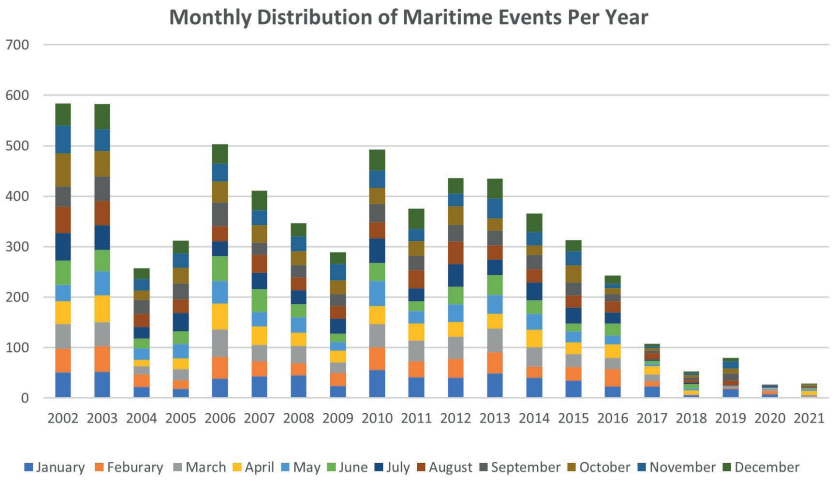


Fig. 13 Yearly incidents per month.

recorded cases (Fig. 10). While this may reflect genuine risk factors such as limited visibility, obstacle detection challenges, and delayed reaction times, it is also possible that the peak is partially influenced by reporting anomalies in the GISIS IMO database. The highest number of vessel contact events with platforms and other fixed objects also occurred during this timeframe, with 26 recorded cases (Fig. 11), reinforcing the risks associated with poor nighttime navigation and inadequate lighting systems. These findings emphasize the need for strategic interventions to mitigate risks during high-incident periods. The high frequency of nighttime accidents underscores the importance of enhanced vessel monitoring, improved lighting and signalling systems, and stricter adherence to nighttime navigational protocols. Additionally, targeted measures such as adjusting port scheduling, enforcing fatigue management regulations, and deploying advanced navigational technologies can significantly reduce accident risks. Understanding these temporal trends is crucial for strengthening maritime safety measures and minimizing casualties at sea.

5.7 Seasonal distribution of maritime events

The analysis of seasonal trends reveals significant fluctuations in frequency throughout the year. As shown in Fig. 12, January recorded the highest number of reported accidents, with 633 occurrences, making it the most hazardous month for maritime operations. March and July followed, with 570 and 534 incidents, respectively, while October recorded the lowest accident count (456 cases), indicating a relative decline in maritime incidents during this period. A 20-year breakdown of monthly accident distribution confirms that January consistently exhibited the highest accident rates (Fig. 13). This seasonal peak was primarily driven by cargo vessel events, which appear more vulnerable to maritime risks during this time. The prevalence of adverse winter weather conditions in the Northern Hemisphere is a significant contributing factor, as vessels face rough seas, strong winds, and reduced visibility, all of which increase accident likelihood. The analysis further reveals that winter months (December to February in the Northern Hemisphere and June to August in the Southern Hemisphere) accounted for approximately 52 % of all maritime events. This aligns with the expected impact of extreme weather phenomena, including storms, high waves, and icy conditions, which pose substantial navigational challenges. However, 17 % of events were recorded between June and July, suggesting that early summer also presents notable risks. While this period follows a mid-year dip in May, the uptick may be influenced by seasonal weather changes, increased maritime traffic, and the intensification of cruise vessel operations during peak tourism months in the Northern Hemisphere. Although the dataset does not isolate cruise ship activity, the timing aligns with known cruise season patterns, warranting further

https://doi.org/10.58440/ihr-31-2-a10

investigation into the role of passenger vessel traffic in summer incident trends. This could be attributed to increased maritime traffic, seasonal weather shifts, and operational adjustments, all of which affect vessel manoeuvrability and accident risk. These findings emphasize the need for seasonally adjusted risk management strategies, particularly during high-risk months such as January and July. Enhanced weather monitoring, seasonal route planning, and stricter navigational safety protocols could help mitigate the impact of seasonal variations on maritime safety. Additionally, cargo vessels, which are disproportionately affected during peak accident months, should be a priority for targeted safety measures, ensuring improved operational preparedness during winter and early summer periods.

5.8 Impact of flag state on maritime accidents and incidents

A vessel's flag state plays a crucial role in maritime safety, influencing maritime accident rates through factors such as regulatory enforcement, vessel age, and operational oversight. While maritime events are often the result of multiple interrelated factors, studies have identified flag state, vessel age, and traffic volume as key contributors to accident probability. Under international maritime law, all merchant ships must be registered with a flag state, which assumes responsibility for ensuring compliance with safety regulations, vessel maintenance, and crew qualifications (Williams, 2015). However, flag state performance varies significantly, as evidenced by accident statistics across different registries. The age of vessels also plays a critical role, as technical standards and crew efficiency tend to deteriorate over time. Many studies have linked a higher probability of accidents to older vessels, often due to corrosion-related structural weaknesses, machinery failures, and reduced manoeuvrability (Görçün & Burak, 2015). While some argue that regular maintenance and repairs can mitigate age-related risks, vessel aging remains a notable concern in accident causation (Butt et al., 2015). Another major factor influencing maritime events is traffic density, with studies confirming that higher vessel activity levels in congested maritime routes correlate with increased accident risks (Stornes, 2015; Houghton & Ulmke, 2014). The review of maritime accidents by flag state reveals significant disparities in safety performance. Panama, which operates the world's largest shipping registry, recorded the highest number of events (1,109 cases) (Table 1). The dominance of Panama-registered vessels in accident statistics can be attributed to its open registry system, which attracts foreign shipowners seeking to circumvent stricter safety regulations imposed by their home countries (Wang, 2017). The flexibility offered by open registries allows operators to reduce operational costs through lenient safety compliance requirements and the employment of lower-cost foreign labour, often at the expense of vessel maintenance and safety oversight. Following Panama, the United Kingdom registered the second-highest number of events (458), followed by Liberia (416) and Malta (274). Notably, 198 events were classified under "Undefined" flag state, representing cases where registry information was missing or unreported in the GISIS database. The high frequency underscores the need for more complete and standardized reporting. These findings highlight that while some flag states maintain relatively stringent safety regulations, others operate under lax enforcement mechanisms, contributing to higher accident frequencies. The persistent high accident rate among Panama-flagged vessels suggests that regulatory oversight remains insufficient, despite international efforts to improve compliance standards. Although normalizing accident counts by fleet size would provide a more precise measure of flag state safety performance, the lack of consistent historical fleet size data across the study period prevents such an adjustment in this analysis.

Within the Caribbean region, similar patterns were observed. The Bahamas recorded the highest number of maritime events among Caribbean flag states, with 209 reported cases, followed by Antigua and Barbuda (171) and Saint Vincent and the Grenadines (81). The high accident rates among these Caribbean registries can be linked to regulatory shortcomings, as weaker enforcement of safety standards and vessel inspections increases the likelihood of operational failures (Butt et al., 2015). These findings emphasize the critical need for stronger regulatory frameworks, enhanced oversight of open registries, and stricter enforcement of vessel maintenance standards. The prevalence of accidents among certain flag states underscores the necessity of global maritime governance reforms to ensure that ship registration policies prioritize safety over cost-cutting measures. Improving flag state accountability, standardizing safety regulations, and enhancing international cooperation will be essential in reducing accident rates and improving overall maritime safety.

5.9 Geographic distribution of maritime events

The analysis of maritime events by geographic area over the 20-year period reveals distinct high-risk zones where events occur more frequently. Variations in accident frequency may partly reflect differences in reporting practices across regions, with some high-risk areas potentially underrepresented in official records. Geographic accident patterns should also be interpreted in relation to vessel traffic density, as high-traffic routes face inherently greater exposure to maritime risks. Fig. 14 presents 3,676 maritime events; however, over 2,500 events recorded in the IMO database lack location details, suggesting that certain high-risk maritime areas may be underrepresented.

The regions with the highest number of maritime events were identified as:

Table 1 Maritime accidents and incidents per flag state (2002–2021).

Flag state	No. of events	Flag state	No. of events	Flag state	No. of events	Flag state	No. of events
Afghanistan	1	Mongolia	10	United Arab Emirates	3	Belize	39
Austria	1	Nigeria	15	Papa New Guinea	4	Saint Vincent and the Grenadines	81
Falkland	1	Poland	10	Qatar	4	Italy	85
Guinea	1	Tuvalu	11	Senegal	4	Norway	88
Taiwan	2	Malaysia	25	Bahrain	4	Sweden	45
Wallis and Futuna	2	Vanuatu	25	Cape Verde	4	Isle of Man	49
Democratic Republic of the Congo	3	Belgium	26	Curacao	4	Ireland	52
French Polynesia	3	Gibraltar	28	Dominica	4	Israel	52
Kenya	3	Spain	28	Guyana	4	Vietam	58
Madagascar	4	Chile	30	Libya	4	Phillippines	66
Mauritius	3	North Korea	33	Mauritania	4	India	71
Romania	3	Lithuania	32	Mayanmar	4	Indonesia	81
Saudi Arabia	4	Austraila	38	Mozambique	4	Denmark	87
Kuwait	1	Bangladesh	14	Argentina	5	Peru	88
Macao	1	Cook Islands	11	Fiji	6	Turkey	95
Micronesia	1	Netherlands Antilles	12	Ghana	5	Singapore	99
Oman	1	Tongo	13	Greenland	6	Cambodia	99
Pakistan	1	Bolivia	13	Iceland	5	France	100
Saint Pierra and Miquelon	1	Luxembourg	13	Lebanon	5	Greece	100
Samoa	1	Ukraine	12	Principe	5	Canada	101
Solomon Islands	1	Comoros	14	Sao Tome	5	Russia	111
Somalia	1	Latvia	14	Uruguay	5	Cypus	122
Tunisia	1	Brazil	15	Azerbaijan	6	Morocco Shall Island	133
Albania	3	Finland	15	Kiribati	6	USA	131
Algeria	2	Moldova	16	Syria	6	Japan	133
Cameroon	2	Thailand	17	Bulgaria	7	Germany	135
Colombia	2	Hong Kong	23	Tanzania	8	China	138
Eritrea	2	Nevis	17	Georgia	8	Netherlands	142
Jamaica	2	Saint Kitts	17	New Zealand	8	South Korea	145
Jordan	2	Barbados	18	South Africa	8	Antigua and Barbuda	171
Namibia	2	Iran	18	Togo	9	Bahamas	209
New Caledonia	2	Portugal	18	Venezuela	8	Undefined	198
Palau	4	Bermuda	20	Faroe Islands	9	Malta	274
Paraguay	2	Honduras	23	Mexico	9	Liberia	416
Seychelles	3	Sierra Leone	25	Egypt	10	United Kingdom	458
Sri Lanka	2	Cayman Island	27	Escuador	12	Panama	1109
Switzerland	2	Croatia	25	Estonia	10		

- Bay of Biscay
- South China Sea (SCS)
- Eastern Mediterranean & Black Sea
- Japan & Korea

These maritime hotspots align with findings from Zhang and Feng (2018) in The Routledge Handbook of Transport in Asia, which analysed maritime accident distribution from 1978 to 2013. Their study highlighted similar high-risk areas, reinforcing that certain maritime regions have persistently high accident rates over multiple decades. A critical observation from these findings is the recurrence of events in densely trafficked waters, particularly in Europe and Asia, where port congestion, complex navigational routes, and high levels of commercial shipping activity contribute to heightened accident risks. Additionally, severe weather conditions, strong currents, and underwater obstructions further exacerbate the likelihood of maritime incidents in these regions.

https://doi.org/10.58440/ihr-31-2-a10

The Bay of Biscay, located along the western European coast, is particularly known for adverse weather conditions, rough seas, and strong Atlantic storms, all of which pose significant navigational challenges for vessels. A breakdown of incident types in the Bay of Biscay reveals that collisions accounted for 126 cases, while groundings totalled 124 incidents. Additionally, fires and explosions were recorded in 64 cases, highlighting the diverse nature of maritime risks in this area. The South China Sea, a critical global shipping corridor, faces dense maritime traffic, geopolitical tensions, and unpredictable monsoon conditions, increasing the risk of collisions and vessel groundings. The South China Sea recorded 577 maritime events over the study period, with collisions accounting for 32 % of all events, followed by groundings (15 %) and fires/explosions (11 %). The high rate of collisions and groundings can be attributed to dense shipping traffic, contested maritime boundaries, and challenging weather conditions, which collectively increase the likelihood of navigational errors and operational hazards.

The geospatial distribution of maritime accidents provides key indicators for where international safety efforts should be focused. Strengthening safety regulations, enforcing navigational protocols, and improving vessel traffic management systems in these high-risk areas could significantly reduce the occurrence of maritime accidents. These findings highlight the dominance of cargo vessels in maritime incidents, emphasizing the need for targeted regional safety measures, including advanced navigational technologies, stricter enforcement of maritime safety laws, and enhanced training for crew members operating in high-risk areas.

5.9.1 Collisions

Collisions are frequently reported within the South China Sea (SCS), one of the world's busiest and most geopolitically sensitive maritime regions (Fig. 15). The dominant vessel types operating in this area include cargo ships, container vessels, and tankers. This is largely due to the SCS serving as a critical maritime corridor linking the Indian Ocean with East Asia. Many of these vessels operate under a tramp trade regime, meaning they lack fixed schedules or designated routes, which contributes to navigational unpredictability and elevated risk. Moreover, the region is characterized by overlapping jurisdictional claims and competing interpretations of freedom of navigation within Exclusive Economic Zones (EEZs), which further intensify the risk of military encounters and accidental collisions. The Bay of Biscay records the second-highest number of maritime collisions globally. The area supports significant cargo, container, and fishing vessel traffic. Severe meteorological conditions are prevalent in this region, particularly during winter months, when the area is routinely affected by strong storms and persistent rainfall. The bay is notorious for the formation of depressions that intensify into thunderstorms, contributing to hazardous sea conditions and numerous reported shipwrecks. These observations highlight the strong influence of environmental conditions and regional geography on maritime incident patterns.

5.9.2 Foundered events

A similar spatial pattern is evident in the distribution of foundered incidents, which are closely tied to specific geographic regions and are often exacerbated by extreme weather conditions. The Bay of Biscay records the highest number of foundered events globally, followed by the South China Sea (Fig. 16). The Caribbean Sea, particularly the area encompassing

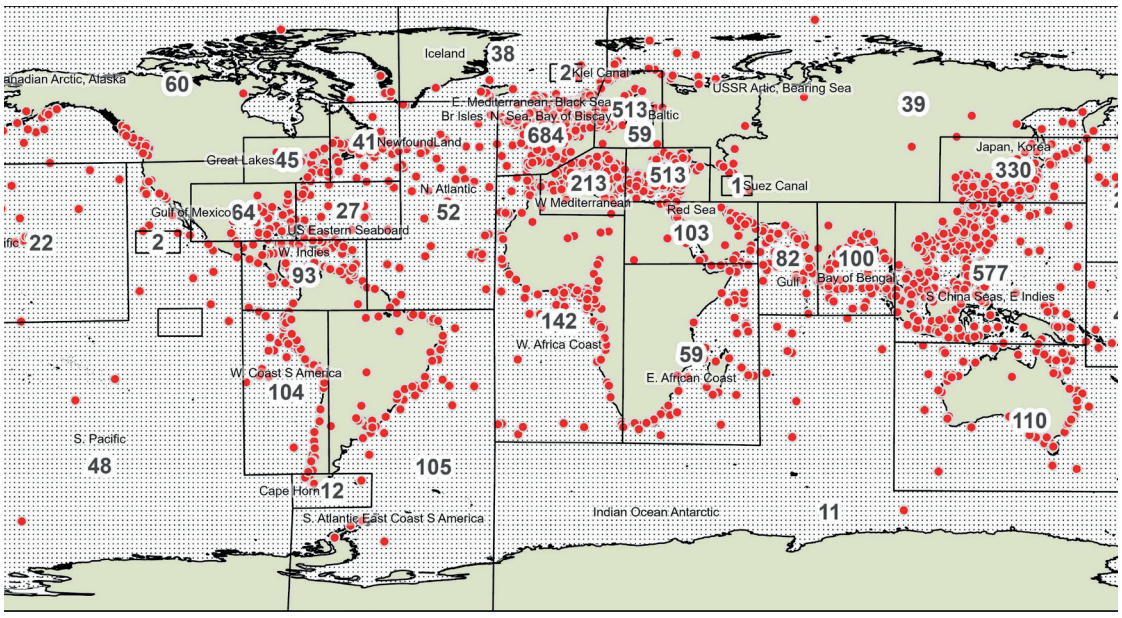


Fig. 14 World map indicating top maritime accident and incident regions (2002–2021).

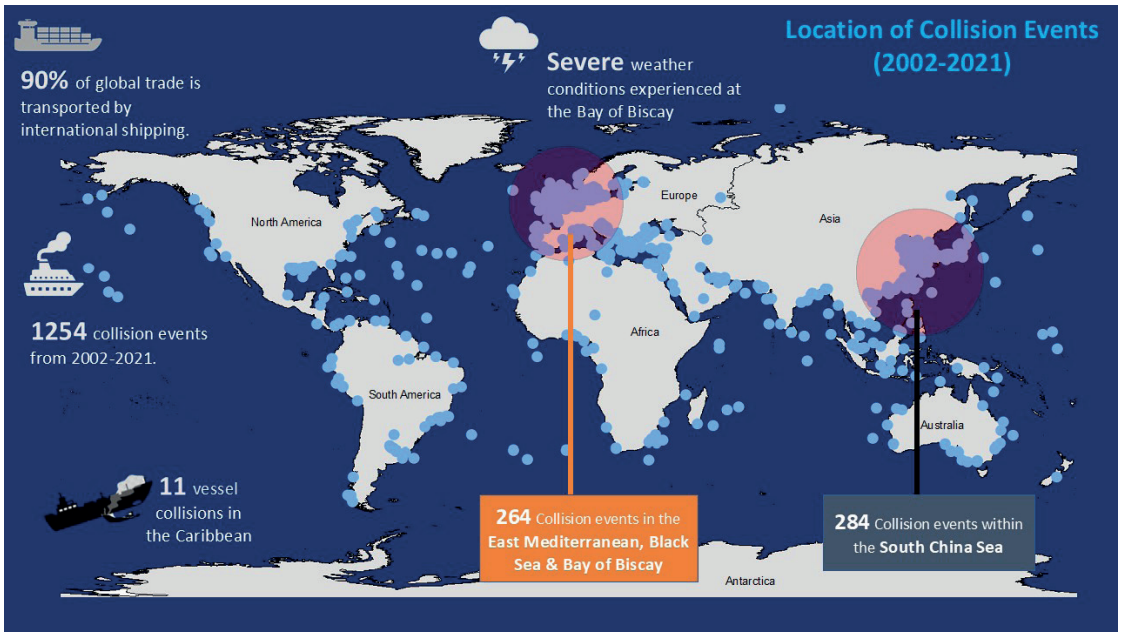


Fig. 15 Location of collision events.

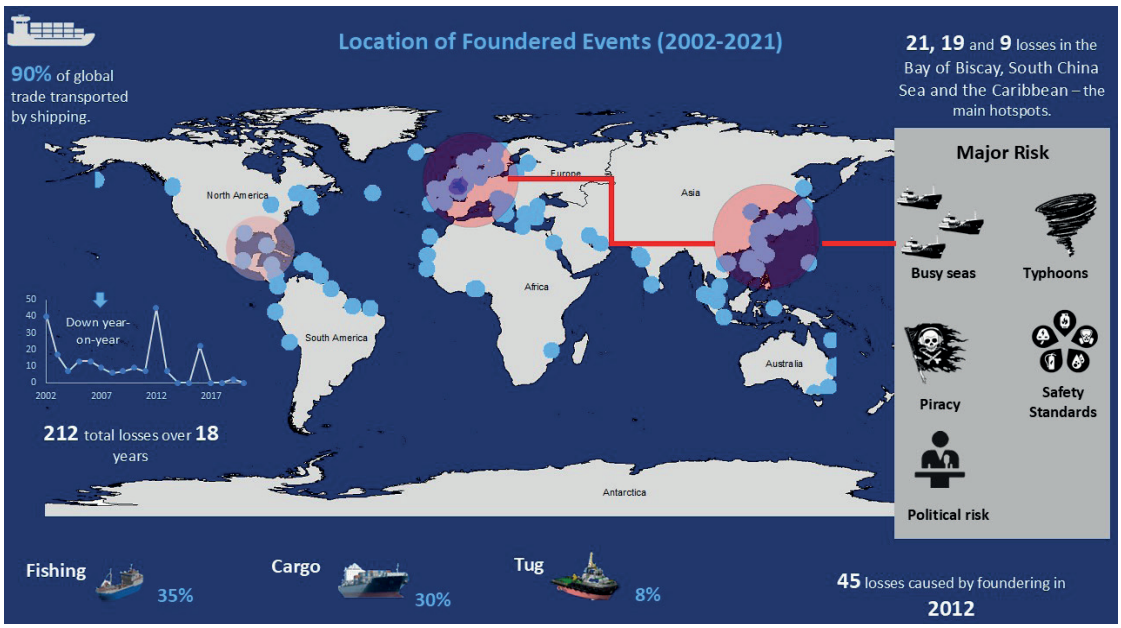


Fig. 16 Location of foundered events.

the Panama Canal, ranks third. Vessels most commonly involved in these incidents include fishing vessels (35 %), cargo ships (30 %), and tugboats (8 %). Foundering is typically initiated by severe meteorological conditions or structural failures such as hull breaches or leaks. These types of incidents are also prevalent in the North Sea, Black Sea, and coastal waters around Japan regions characterized by dense maritime traffic and extensive short sea shipping networks. This distribution underscores the influence of environmental factors, vessel type, and navigational density on the occurrence of foundering.

5.9.3 Heavy weather and grounding events

During the 20-year period under review, 64 maritime events attributed to heavy weather conditions involved a total of 10 different types of vessels (Fig. 17). Analysis reveals that cargo vessels were the most frequently affected, accounting for 27 % of the total, followed by passenger, cruise, and ferry vessels (16 %), and container vessels (15 %). A significant temporal pattern was also observed, with over 73 % of these incidents occurring during the AM period particularly between 12:00 AM and 2:00 AM. While this may partly be attributed to the severe weather conditions sometimes encountered during these hours, coupled with reduced visibility that increases navigational risk, it is also possible that the pattern reflects reporting inconsistencies or default time entries in the GISIS IMO database rather than actual accident timing. Likewise, 832 grounding incidents were recorded globally during the same timeframe,

https://doi.org/10.58440/ihr-31-2-a10

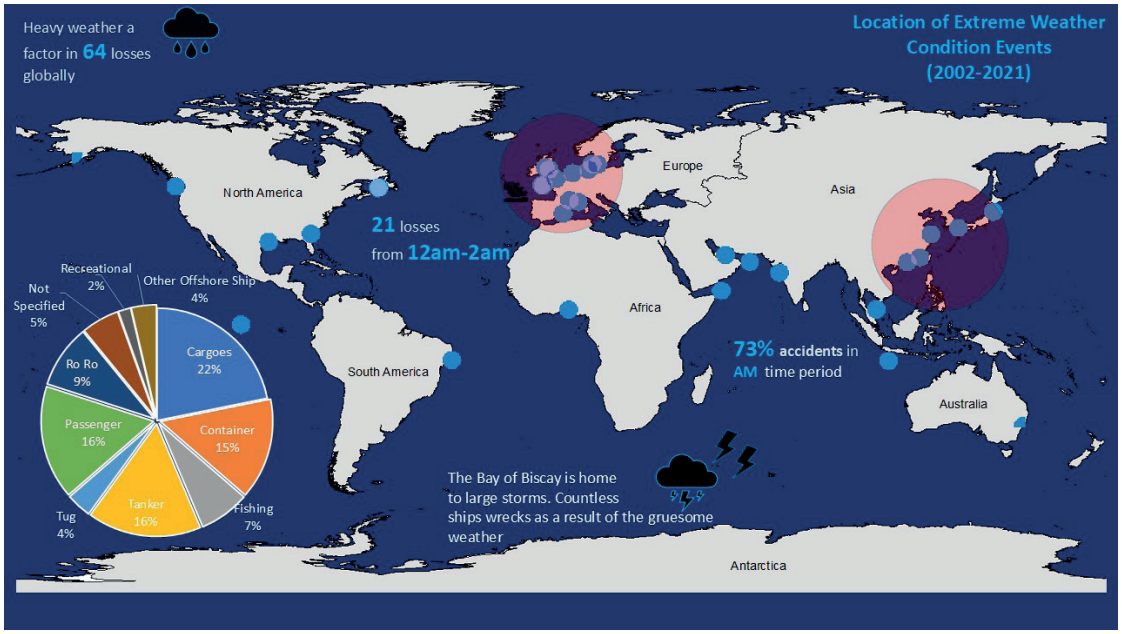


Fig. 17 Location of extreme weather events.

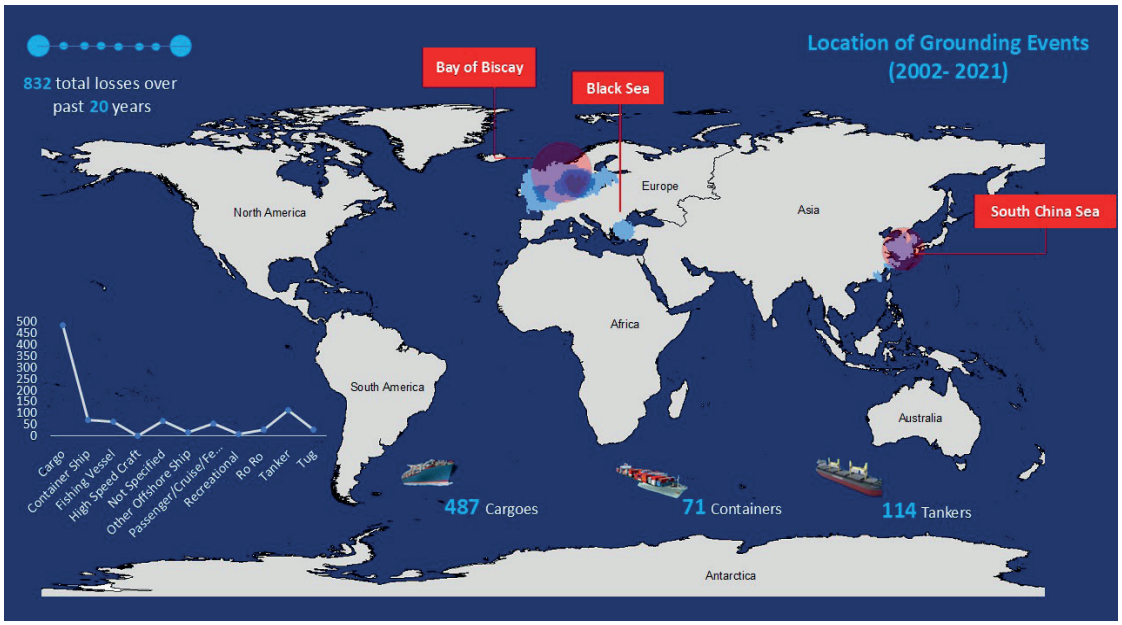


Fig. 18 Location of groundings incidents.

with the distribution also potentially reflecting reporting inconsistencies (Fig. 18). Cargo vessels were again the most frequently involved, accounting for 52 %, followed by tankers (12 %) and container ships (8 %). The East Mediterranean and Black Sea, Bay of Biscay, and the South China Sea emerged as the regions with the highest concentration of grounding events. Notably, 638 of these incidents occurred during AM hours, suggesting that reduced visibility, early-morning operational factors, and potential reporting inconsistencies may also play a role in these types of incidents.

5.10 Impact of vessel age on maritime accidents and incidents

The analysis reveals a strong correlation between vessel age and accident frequency, with older vessels accounting for most maritime events (Fig. 19). Ships over 20 years old face higher risks due to aging structures, mechanical wear, and outdated safety systems. Vessels built in 1997 recorded the highest number of accidents (144), with 10 % registered under Panama and 6 % under Tanzanian and Comorian flags. This trend aligns with open registry policies, allowing older vessels to remain in operation under lenient regulatory frameworks. Similarly, 1985-built vessels recorded 132 events, ranking second, while 2006-built ships had 129 events, reinforcing the link between aging fleets and accident risks. Structural deterioration over time contributes to hull integrity issues, propulsion failures, and navigation system malfunctions, all

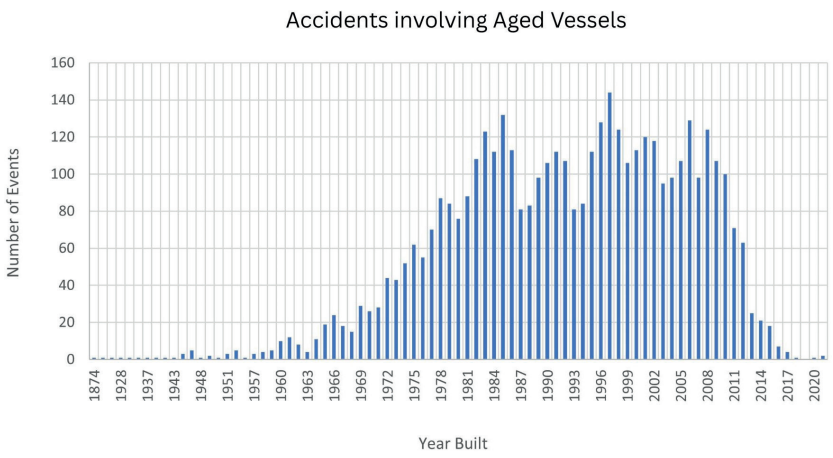


Fig. 19 Aged vessels by year built.

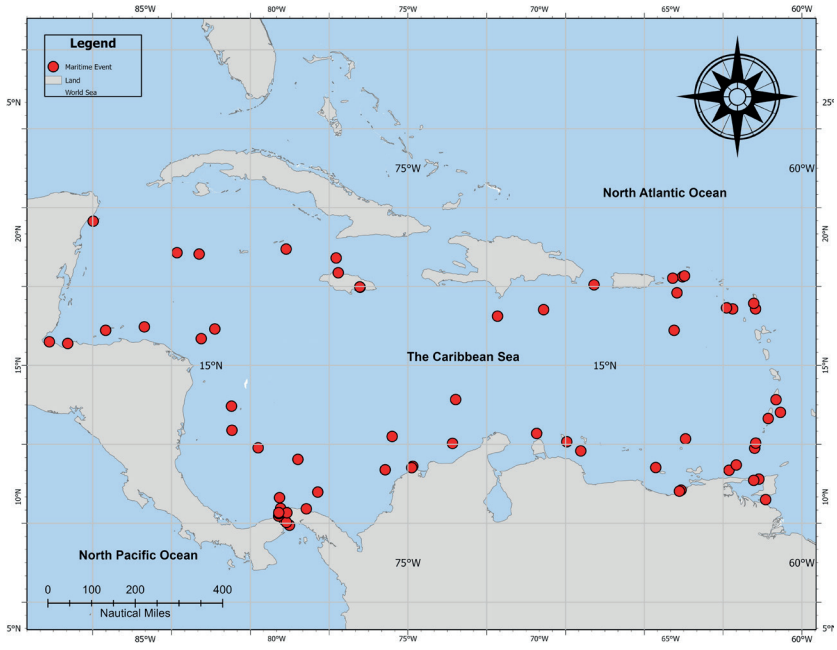


Fig. 20 Location of maritime events in the Caribbean Sea for the period of 2002–2021.

of which increase accident likelihood (Butt et al., 2015). While routine maintenance can mitigate risks, aged vessels require more frequent repairs and stricter oversight. These findings highlight the need for stricter vessel age regulations, particularly for open registry states. Stronger international safety protocols, stricter inspections, and incentives for fleet modernization could significantly reduce accidents tied to aging vessels, improving global maritime safety.

6 Maritime accidents and incidents in the Caribbean Sea: Trends and comparative analysis

The Caribbean Sea, a major global shipping corridor, recorded 69 reported events between 2002 and 2021 (Fig. 20), accounting for just 1.1 % of worldwide maritime incidents. However, the nature and consequences of these events highlight significant regional risks. Fires and explosions were the most common causes, representing 18 % of all accidents, predominantly involving cargo vessels and tankers, followed by groundings (15 %), capsizing (15 %), and collisions (13 %; Fig. 21). This pattern contrasts with global trends, where collisions dominate (24 %), particularly in congested waterways such as the South China Sea, Bay of Biscay, and Black Sea. The high incidence of fires and explosions in the Caribbean aligns with global findings that tankers are especially vulnerable to fire-related events due to transporting flammable materials (Ugurlu et al., 2012). Despite SOLAS fire safety regulations, these incidents persist, underscoring the need for stricter enforcement and improved prevention measures (Molitor, 2012).

Groundings remain a critical concern in both regional and global contexts. In the Caribbean, cargo vessels are particularly at risk, operating along short sea shipping routes and frequently calling at smaller island ports with challenging hydrographic conditions. Contributing factors include navigational errors, adverse weather, submerged obstacles, and hydrographic uncertainties such as outdated charts, insufficient survey coverage, and inaccurate depth soundings. These risks are compounded in areas with dynamic seabed changes, sediment deposition, or uncharted hazards. In the Greater Caribbean Region (GCR), several risk assessments have found that many secondary ports and nearshore approaches still rely on historical survey data, reducing navigational confidence and increasing vulnerability to accidents in restricted waters (Miller, 2015; Seepersad et al., 2021).

6.1 The role of aged vessels in maritime events within the Caribbean Sea

Despite the relatively low number of maritime events (69) in the Caribbean Sea, 41 events involved aged vessels. Analysis indicates that 29 events were recorded by vessels built between 1984 and 2004 and 12 events for vessels built between 1963–1983. This highlights the ongoing issue of older ships operating beyond their economic lifespan. Studies have consistently shown that aged vessels, particularly those over 20 years old, are at greater risk of structural failures, mechanical breakdowns, and compliance deficiencies. All events that occur at midnight (12AM–1AM) involved aged vessels built between 1991 and 1999. Additionally, cargo vessels accounted for 50 % of these events, followed by fishing vessels (17 %) and tankers (11 %). This trend aligns with global studies, indicating that older vessels operating under open registries are more prone to events due to substandard maintenance and safety compliance (Singh & Raju, 2016). A time-based analysis of maritime events in the Caribbean Sea also reveals notable patterns. Approximately 70 % of events occurred during morning hours (AM), with 41 recorded cases (Fig. 22). The highest

https://doi.org/10.58440/ihr-31-2-a10

concentration of events took place between 12 AM and 1 AM, a period associated with reduced visibility, crew fatigue, and navigational errors. Early morning peaks (labelled "A" and "B") correspond to periods of high maritime activity, likely due to vessel arrivals, port calls, and increased traffic density. Evening events also follow distinct patterns, with a notable peak (labelled "C") occurring due to capsizing incidents involving fishing vessels.

6.2 Flag state performance in maritime accidents in the Caribbean Sea

A review of the maritime events by flag state highlights Panama, Liberia, and the Bahamas as the most frequently involved registries within the Caribbean Sea (Table 2). Panama accounted for 12 events, followed by Liberia (6) and the Bahamas (5). Given that Panama operates the world's largest open registry, this trend is expected, as many vessels registered under open registries prioritize cost savings over stringent safety compliance (Gasparotti & Rusu, 2012). Panama's high accident involvement was primarily due to capsizing events, which accounted for 18 % of total regional events, followed by groundings and fires/explosions. Notably, 45 % of Panamanian-registered vessels involved in maritime events were cargo, tankers, or passenger vessels, further reinforcing concerns regarding the operational safety of aging vessels registered under open registries. These findings emphasize the critical need for stricter regulatory frameworks, enhanced oversight of open registries, and stronger enforcement of vessel maintenance standards. The prevalence of accidents among certain flag states underscores the necessity for global maritime governance reforms to ensure ship registration policies prioritize safety over cost-cutting measures.

7 Discussion

This study provides a comprehensive assessment of maritime events over the past 20 years, consolidating key insights into incident trends, vessel characteristics, flag state performance, and regulatory implications. A critical evaluation of maritime accident data underscores the importance of thorough statistical validation before drawing conclusions about accident causes and distributions. Although global accident rates have declined, poorly performing flag states continue to influence maritime risk. Other key determinants that influence a vessel accident includes vessel age, type, navigational environment, limited visibility, and operational timeframes. The study further highlights the need for enhanced regulatory oversight, stricter enforcement of international safety standards, and technological advancements to address persistent maritime risks.

Maritime safety has improved overall, with accident rates declining relative to fleet expansion due to advancements in technology, stricter port state controls, and international safety initiatives.

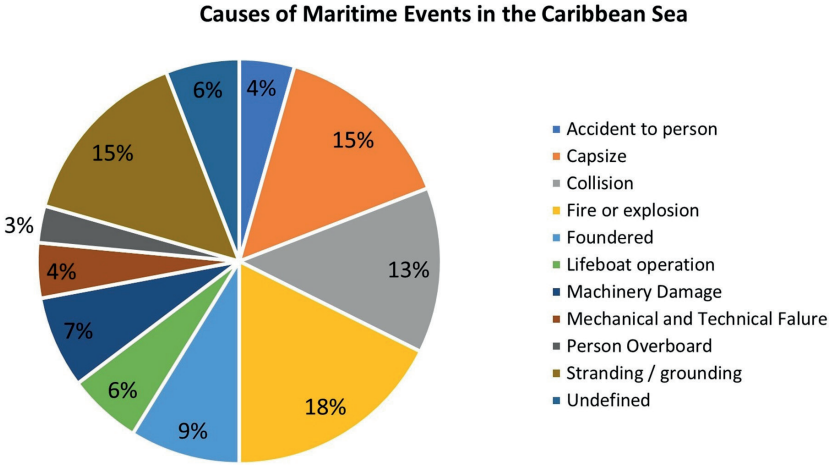


Fig. 21 Causes of maritime events in the Caribbean Sea.

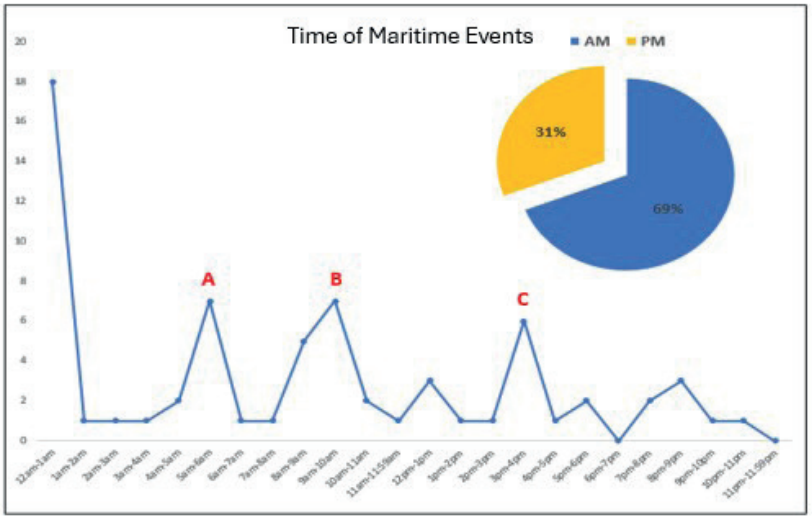


Fig. 22 Time of maritime events in the Caribbean Sea.

However, accidents remain a persistent threat, particularly in high-risk regions and environmentally sensitive areas, where even minor incidents can cause severe ecological and economic damage (NTSB, 2017). Climate change further increases maritime risks, with storm surges, extreme weather, and changing ocean patterns expected to escalate vessel foundering and navigational hazards (Hauser et al., 2018). Smaller vessels, particularly those in coastal waters, remain more vulnerable to accidents than larger ocean-crossing ships. The study also confirms that human fatigue significantly impacts maritime safety, aligning with Project Horizon's findings, which showed that sleep deprivation impairs watchkeepers' cognitive performance, increasing collision and grounding risks (Frith, 2020). Despite safety advancements, poor-performing flag states continue to be a major concern, especially due to inconsistent enforcement of IMO conventions and outdated reporting frameworks, which hinder accurate accident investigations particularly for under-reported fishing vessel and work-related onboard incidents.

Table 2 Flag state of maritime accidents that occurred in the Caribbean Sea.

Flag	Number of incidents	Flag	Number of incidents
Antigua and Barbuda	1	Saint Vincent and the Grenadines	1
Brazil	1	Samoa	1
Canada	1	Sweden	1
China	1	Venezuela	1
Cyprus	1	Vietnam	1
Georgia	1	Greece	2
Germany	1	South Korea	2
Gibraltar	1	Turkey	2
India	1	United Kingdom	2
Ireland	1	Cambodia	3
Isle of Man	1	Chile	3
Italy	1	Hong Kong	3
Malaysia	1	Indonesia	3
North Korea	1	Malta	4
Norway	1	Bahamas	5
Peru	1	Liberia	6
Philippines	1	Panama	12

In the Caribbean Sea, unique challenges such as unregulated Traffic Separation Schemes (TSS), aged vessels, and weak regulatory enforcement further complicate safety efforts. To address these risks, the study recommends:

- Strengthening flag state regulations by enforcing stricter IMO compliance on open registries.
- Implementing TSS to reduce congestion and collision risks.
- Clarifying that TSS issues pertain to inadequate implementation or supervision of existing schemes, rather than the absence of regulation.
- Enhancing fatigue management through better scheduling, improved aids to navigation, and collision avoidance technologies.
- Improving accident reporting systems by establishing a standardized global database, particularly for fishing vessels and onboard work-related incidents.
- Encouraging fleet modernization by phasing out aged vessels and promoting investment in safer ship designs.
- Expanding regional cooperation among Caribbean port authorities and international oversight bodies to enhance enforcement and vessel inspections.
- Strengthening hydrographic surveys, particularly in secondary ports and approaches, to reduce grounding risks linked to chart insufficiencies.
- Encouraging non-IHO member Caribbean states to join the IHO, thereby enhancing hydrographic capacity across the region. Trinidad and Tobago is already a member of the Meso-American and Caribbean Sea Hydrographic Commission (MACHC), while six countries in Central America (Panama, Costa Rica, Nicaragua, Honduras, El Salvador, Belize), and seven islands (Antigua and Barbuda, Barbados, Grenada, Haiti, Saint Kitts and Nevis, Saint Lucia, Saint Vincent and the Grenadines) are not IHO Member States (IHO, 2025).

These measures are essential to improving maritime safety, reducing accident risks, and ensuring sustainable shipping operations worldwide.

8 Conclusion

This study highlights persistent risks and evolving safety challenges within global and Caribbean Sea maritime operations. While technological advancements and regulatory improvements have contributed to a decline in accident rates, key vulnerabilities remain, particularly regarding collisions, nighttime navigation risks, aged vessels, and open registry oversight. In the Caribbean Sea, the absence of Traffic Separation Schemes (TSS) in certain routes, reliance on aged vessels, and open registry policies present significant safety concerns. Panama, Liberia, and the Bahamas continue to dominate accident statistics, largely due to lenient registration policies that attract older and potentially substandard vessels. To improve maritime safety, stricter enforcement of international regulations is necessary, particularly for open registries. Encouraging fleet modernization by phasing out older, high-risk vessels could significantly reduce accident rates. Additionally, implementing fatigue management systems could help mitigate human error risks, particularly during late-night and early-morning navigation periods. Strengthening nighttime navigation safety through improved lighting, automated alert systems, and the establishment of TSS in congested areas could further reduce collision risks. Beyond regulatory and operational measures, the adequacy of hydrographic surveys in the

https://doi.org/10.58440/ihr-31-2-a10

Caribbean Sea plays a vital role in navigational safety. Several areas in the region still rely on outdated or incomplete survey data, which may not accurately reflect current seabed conditions, shifting channels, or newly emerging hazards. Such deficiencies increase the likelihood of grounding incidents, particularly for vessels operating in shallow or poorly charted waters. Updating nautical charts through systematic hydrographic surveys and promoting International Hydrographic Organization (IHO) membership among non-member states, could significantly enhance situational awareness and reduce accident risks. These findings provide critical insights for policymakers, regulatory bodies, and maritime operators. Addressing maritime safety challenges through technological advancements, stricter oversight, and enhanced risk management while prioritizing up-to-date hydrographic data will be crucial for ensuring a safer and more sustainable maritime industry worldwide.

References

Akten, N. (2006). Shipping accidents: A serious threat for marine environment. *Black Sea/Mediterranean Environment, 12*, 269–304. http://www.blackmeditjournal.org/pdf/2006_vol12_no3-5.pdf (last accessed 21 August 2025).

Akyuz, E. and Celik, M. (2014). Utilisation of cognitive map in modelling human error in marine accident analysis and prevention. *The Scientific World Journal*, 1–28. https://doi.org/10.1155/2014/489461

Antão, P. and Guedes Soares, C. (2006). Fault-tree models of accident scenarios of RoPax vessels. *International Journal of Automation and Computing*, 3(2), 107–116. https://doi.org/10.1007/s11633-006-0107-8

Awal, Z. I. and Hasegawa, K. (2017). A study on accident theories and application to maritime accidents. *Procedia Engineering, 194*, 298–306. https://doi.org/10.1016/j.proeng.2017.08.149

Baldauf, M. (2016). Improving and assessing the impact of e-navigation applications. *International Journal of E-Navigation and Maritime Economy, 4*, 1–12. https://doi.org/10.1016/j.enavi.2016.06.001

Bowo, L. P., Mutmainnah, W. and Furusho, M. (2017). The development of marine accidents human reliability assessment approach: HEART methodology and MOP model. *TransNav: The International Journal on Marine Navigation and Safety of Sea Transportation, 11*(2), 249–254. https://doi.org/10.12716/1001.11.02.06

Butt, N., Johnson, D., Pryce-Roberts, N. and Vigar, N. (2015). *15 years of shipping accidents: A review for WWF*. Southampton Solent University, Southampton, UK. http://awsassets.panda.org/downloads/15_years_of_shipping_accidents_a_review_for_wwf_.pdf (last accessed 21 August 2025).

Calder, B. R. and Kurt, S. (2009). Traffic analysis for the assessment of risk assessment methods. *US Hydrographic Conference*. The Hydrographic Society of America, Stamford, USA.

EMSA (2014). *Annual overview of marine casualties and incidents 2014*. European Maritime Safety Agency, Lisboa, Portugal. https://www.emsa.europa.eu/publications/reports/download/3149/2303/23.html (last accessed 3 September 2025).

Fratila, A., Gavril, I. A., Nita, S. C. and Hrebenciuc, A. (2021). The importance of maritime transport for economic growth in the European Union: A panel data analysis. *Sustainability, 13*(14), 7961. https://doi.org/10.3390/su13147961

Frith, J. (2020). *Human error accounts for 75% of marine liability losses*. Maritime Journal, Fareham, UK. https://www.maritimejournal.com/news101/insurance,-legal-and-finance/human-error-accounts-for-75-of-marine-liability-losses

Gasparotti, C. and Rusu, E. (2012). Methods for the risk assessment in maritime transportation in the Black Sea Basin. *Journal of Environmental Protection and Ecology, 13*(3A), 1751–1759.

Gomez Pretel, W., Jeong, M., Rodríguez-Gutiérrez, C. E. and Ortiz, A. J. R. (2023). Preserving sunken military vessels as underwater cultural heritage in Colombia: Legal challenges and prospects for the USS Kearsarge wreck site. *Heritage, 6*(6), 4843–4863. https://doi.org/10.3390/heritage6060250

Goerlandt, F. and Kujala, P. (2011). Traffic simulation-based ship collision probability modeling. *Reliability Engineering & System Safety, 96*(1), 91–107. https://doi.org/10.1016/j.ress.2010.09.003

Görçün, Ö. F. and Burak, S. Z. (2015). Formal safety assessment for ship traffic in the Istanbul Straits. *Procedia - Social and Behavioral Sciences, 207*, 252–261. https://doi.org/10.1016/j.sbspro.2015.10.094

Hauser, D. D. W., Laidre, K. L. and Stern, H. L. (2018). Vulnerability of Arctic marine mammals to vessel traffic in the increasingly ice-free Northwest Passage and Northern Sea Route. *Proceedings of the National Academy of Sciences, 115*(29), 7617–7622. https://doi.org/10.1073/pnas.1803543115

Houghton, K. and Ulmke, M. (2014). Semi-automatic sea lane extraction combining particle filtering and geographic information systems. *Proceedings of GI_Forum 2014: Geospatial innovation for society, 2*, 2–11. https://doi.org/10.1553/giscience2014s2

IHO (2025). *Yearbook 26 August 2025*. IHO Periodic Publication P-5, International Hydrographic Organization, Monaco. https://iho.int/uploads/user/pubs/periodical/P5YEARBOOK_ANNUAIRE.pdf (last accessed 3 September 2025).

IMO (2012). *Implications of the United Nations Convention on the Law of the Sea for the International Maritime Organization*. International Maritime Organization, London, United Kingdom. https://no0ilcanarias.wordpress.com/wp-content/uploads/2012/11/implications-of-unclos-for-imo.pdf (last accessed 3 September 2025).

IMO (2025). *Protecting the environment*. International Maritime Organization, London, United Kingdom. https://www.imo.org/en/OurWork/Environment/Pages/Default.aspx (last accessed 21 August 2025).

Johansson, J. and Molitor, E. (2011). *Risk assessment of the vessel traffic in the Kattegat including effects of traffic separation schemes from the Skaw to the Sound – Oil spill accidents relevant for the coast of Halland*. http://193.183.15.115/PageFiles/27517/

risk-ssessment-of-the-vessel-traffic-in-the-kattegat-eng-tot-21-march-2011.pdf (last accessed 21 August 2025).

Kujala, P. (2012). Influences of variables on ship collision probability in a Bayesian belief network model. *Reliability Engineering and System Safety, 102*, 27–40. https://doi.org/10.1016/j.ress.2012.02.008

Maharaj, A. (2020). *Geostatistical analysis of marine traffic in the Gulf of Paria, Trinidad and Tobago* (Master's thesis). The University of the West Indies, The Republic of Trinidad and Tobago.

MAIB (2019). *MGN 564: Marine casualty and marine incident reporting*. Marine Accident Investigation Branch, Department for Transport, Southampton, UK. https://assets.publishing.service.gov.uk/media/5ca36e19ed915d0c55c71ef1/MGN564-Amendment1.pdf (last accessed 21 August 2025).

Miller, K. (2015). Needs for professional hydrography in the Caribbean towards risk reduction in maritime navigation. *The West Indian Journal of Engineering, 38*(1), 70–78. http://sta.uwi.edu/eng/wije/vol3801_jul2015/documents/M08_v38n1p70-78KMiller-Jul2015.pdf (last accessed 21 August 2025).

Molitor, E. (2012). Feasibility study on LNG fuelled short sea and coastal shipping in the wider Caribbean region. *Caribbean Maritime Journal, 46*(0), 8–31.

Montewka, J., Krata, P., Goerlandt, F., Mazaheri, A. and Kujala, P. (2011). Marine traffic risk modelling – An innovative approach and a case study. *Proceedings of the Institution of Mechanical Engineers, Part O: Journal of Risk and Reliability, 225*(3), 307–322. https://doi.org/10.1177/1748006X11399988

NTSB (2017). *Sinking of US cargo vessel SS El Faro, Atlantic Ocean, Northeast of Acklins and Crooked Island, Bahamas, October 1 2015*. Accident Report, NTSB/MAR-17/01 PB2018-100342, National Transportation Safety Board, Washington, DC, USA. https://www.ntsb.gov/investigations/AccidentReports/Reports/MAR1701.pdf (last accessed 21 August 2025).

Psarros, G., Skjong, R. and Eide, M. S. (2010). Under-reporting of maritime accidents. *Accident Analysis & Prevention, 42*(2), 619–625. https://doi.org/10.1016/j.aap.2009.10.008

Rodrigue, J. P. (2017). The governance of intermediacy: The insertion of Panama in the global liner shipping network. *Research in Transportation Business & Management, 22*, 21–26. https://doi.org/10.1016/j.rtbm.2016.11.005

Seepersad, D., Miller, K., Greenland, A. and Eriksson, O. F. (2020). Benefits of assessing risk in maritime navigation using IALA and LINZ methods. *The International Hydrographic Review, 23*, 7–33. https://ihr.iho.int/articles/benefits-of-assessing-risk-in-maritime-navigation-using-iala-and-linz-methods/ (last accessed 21 August 2025).

Singh, A. and Raju, T. B. (2016). Hazards analysis of routine ship towage operations in Indian coastal waters. *International Journal of E-Navigation and Maritime Economy, 4*, 62–74. https://doi.org/10.1016/j.enavi.2016.06.006

Stornes, P. (2015). *Risk influencing factors in maritime accidents: An exploratory statistical analysis of the Norwegian Maritime Authority incident database*. Studio Apertura, NTNU Social Research, Trondheim, Norway. http://hdl.handle.net/11250/2360509 (last accessed 3 September 2025).

Strauch, B. (2015). Investigating fatigue in marine accident investigations. *Procedia Manufacturing, 3*, 3115–3122. https://doi.org/10.1016/j.promfg.2015.07.859

Smith, K. D. and Cox, G. J. (2007). Improving hydrographic information: Zones of confidence (ZOC) for New Zealand. *Journal of Spatial Science, 52*(1), 121–131. https://doi.org/10.1080/14498596.2007.9635107

Ugurlu, O., Yildirim, U. and Yuksekyildiz, E. (2012). Marine accident analysis with GIS. *Journal of Shipping and Ocean Engineering, 3,* 21–29. (last accessed 3 September 2025).

United Nations, European Union and ITF. (2019). Glossary for transport statistics (5th ed.). https://www.itf-oecd.org/glossary-transport-statistics

Wang, M. (2017). The role of Panama Canal in global shipping. *Maritime Business Review, 2*(3), 247–260. https://doi.org/10.1108/mabr-07-2017-0014

Williams, R. (2015). Potential acoustic impacts of vessel traffic from the Trans Mountain Expansion Project on Southern Resident Killer Whales. *Raincoast Conservation Foundation*.

Wilmsmeier, G. and Sanchez, R. J. (2009). The impact of port characteristics on international maritime transport costs. *Research in Transportation Economics*, 16(1), 117–140. https://doi.org/10.1016/S0739-8859(06)16006-0

Zhang, J. and Feng, C.-M. (Eds.). (2018). *Routledge handbook of transport in Asia* (1st ed.). Routledge. https://doi.org/10.4324/9781315739618

Zhang, L., Wang, H., Meng, Q. and Xie, H. (2019). Ship accident consequences and contributing factors analyses using ship accident investigation reports. *Proceedings of the Institution of Mechanical Engineers, Part O: Journal of Risk and Reliability, 233*(1), 35–47. https://doi.org/10.1177/1748006X18768917

Zhou, X., Cheng, L. and Li, M. (2020). Assessing and mapping maritime transportation risk based on spatial fuzzy multi-criteria decision making: A case study in the South China Sea. *Ocean Engineering, 208*, 107403. https://doi.org/10.1016/j.oceaneng.2020.107403

Authors' biographies

Dr. Amrika Maharaj is a Lecturer in the Department of Geomatics Engineering & Land Management, Faculty of Engineering, The University of the West Indies. Her research focuses on spatial data analysis, geostatistics, and risk assessment, with emphasis on maritime navigation in the Caribbean Sea. Some of her current areas of research expertise include numerical modelling, GIS, remote sensing, hydrography, and maritime navigation studies.



Amrika Maharaj

Dr. Keith Miller is a former lecturer at the University of the West Indies where he specialized in Geodesy and Hydrography, now retired and living in Trinidad and Tobago. He has worked as a lecturer at universities in the UK, Egypt and Australia. In a professional capacity, he was a member of the Chartered Institution of Civil Engineering Surveyors and served for eight years on the IBSC.



Keith Miller

Dr. Dexter Davis is a Lecturer in Geomatics Engineering and Head Department of Geomatics Engineering & Land Management. His research is focused on engineering surveying, digital photogrammetry and digital mapping, geodesy and geodetic applications, as well as GNSS and hydrographic surveying. Some of his current areas of research expertise include sea level monitoring and low cost and disaster relief mapping.



Dexter Davis

Dr. Michael Sutherland is currently an Adjunct Professor at the Department of Geodesy and Geomatics Engineering, University of New Brunswick. He was also a Professor of Land and Marine Administration Systems at the Department of Geomatics Engineering and Land Management, The University of the West Indies, St. Augustine Campus, Trinidad and Tobago. Dr. Sutherland has many years of direct and indirect geomatics-related research experience in the fields of GIS, multidimensional geospatial modelling, land and marine administration systems, climate change, and ocean governance.



Michael Sutherland

https://doi.org/10.58440/ihr-31-2-a10

PEER-REVIEWED ARTICLE

Risk assessment and mitigation measures of maritime navigation in the Caribbean Sea

Authors

Amrika Maharaj[1], Keith Miller[1], Dexter Davis[1] and Michael Sutherland[1]

Abstract

The Caribbean Sea, a vital maritime corridor with high vessel traffic and strategic access to the Panama Canal, faces growing navigational risks. This study develops a probabilistic risk assessment model incorporating vessel and environmental conditions, enhanced by an Artificial Neural Network to estimate incident probability. By leveraging Automatic Identification System (AIS) data and machine learning, mitigation scenarios were evaluated, confirming their effectiveness in reducing risk. The methodology advances traditional models by integrating multiple cause-related factors, offering a more comprehensive understanding of maritime safety. This research highlights the value of AIS and AI-driven approaches in enhancing risk mitigation and navigational resilience in the Caribbean Sea.

Keywords

Caribbean Sea · AIS · probabilistic risk assessment · vessel traffic · artificial neural network · machine learning · maritime accidents

Resumé

La mer des Caraïbes, corridor maritime vital caractérisé par un trafic maritime intense et un accès stratégique au canal de Panama, est confrontée à des risques de navigation croissants. Cette étude développe un modèle probabiliste d'évaluation des risques intégrant les conditions environnementales et celles des navires, amélioré par un réseau neuronal artificiel permettant d'estimer la probabilité d'incidents. En exploitant les données du système d'identification automatique (AIS) et l'apprentissage automatique, des scénarios d'atténuation ont été évalués, confirmant leur efficacité dans la réduction des risques. La méthodologie améliore les modèles traditionnels en intégrant plusieurs facteurs liés aux causes, offrant ainsi une compréhension plus complète de la sécurité maritime. Cette recherche souligne la valeur des approches basées sur l'AIS et l'IA pour améliorer l'atténuation des risques et la résilience de la navigation dans la mer des Caraïbes.

Resumen

El Mar Caribe, un corredor marítimo vital con un alto tráfico de buques y un acceso estratégico al Canal de Panamá, afronta crecientes riesgos a la navegación. Este estudio desarrolla un modelo probabilístico de evaluación de riesgos que incorpora las condiciones de los buques y del medio ambiente, mejorado por una Red Neuronal Artificial para estimar la probabilidad de incidentes. Aprovechando los datos del Sistema de Identificación Automática (AIS) y el aprendizaje automático, se evaluaron escenarios de mitigación, confirmando su eficacia para reducir el riesgo. La metodología mejora los modelos tradicionales al integrar múltiples factores relacionados con las causas, ofreciendo una comprensión más completa de la seguridad marítima. Esta investigación resalta el valor de los enfoques basados en AIS e IA para mejorar la mitigación de riesgos y la resiliencia de la navegación en el Mar Caribe.

✉ Amrika Maharaj · amrika.maharaj@hotmail.com

[1] Department of Geomatics Engineering and Land Management, The University of the West Indies, St. Augustine, The Republic of Trinidad and Tobago

https://doi.org/10.58440/ihr-31-2-a11

1 Introduction

Global maritime trade is facilitated by an intricate web of shipping routes shaped by geographic constraints, chokepoints, and strategic trade corridors (UNCTAD, 2019). Maritime transportation accounts for over 90 % of international commerce and is a critical driver of economic development, particularly in developing regions such as the Caribbean (IMO, 1972). Strategically positioned along East–West and North–South trade flows and adjacent to the Panama Canal, the Caribbean Sea functions as a major hub for global transhipment activities. Growing vessel traffic, offshore operations, and energy exploration further heighten its economic importance (Rodrigue, 2019; Sabonge, 2014). Transhipment activity has expanded into a triangular configuration linking the key ports of Freeport, Colon, and Port of Spain (Fig. 1), which anchor the region's integration into the global maritime network and support hinterland development (Wilmsmeier & Sánchez, 2009). Despite the geographic dispersion of the Caribbean Community and Common Market (CARICOM) member states, maritime navigation unites the region economically, facilitating trade in energy, agriculture, manufactured products, and consumer goods (Wilmsmeier & Sánchez, 2009).

Nevertheless, increasing maritime activity heightens navigational risks, particularly in confined waterways and heavily trafficked shipping lanes (Styliadis & Koliousis, 2012). Despite significant advances in navigation and communication technologies, the maritime industry remains vulnerable. Operational complexity, unpredictable environmental conditions, and the continued lack of surveys for over 80 % of the Caribbean Sea leave the region exposed to collisions, groundings, and environmental disasters (MarineMarico, 2013). Despite advancements, maritime accidents continue to occur, underscoring the importance of understanding incident causation and developing proactive risk mitigation strategies (Kristiansen, 2005). Given the region's reliance on maritime transport and its growing role in international trade, there is an urgent need to assess and manage the risks associated with increased vessel traffic. This includes examining the parameters that influence maritime accidents and understanding the consequences of accidents on the marine environment, human safety, and economic stability (Calder & Kurt, 2009). The designation of the Caribbean Sea as an International Convention for the Prevention of Pollution from Ships (MARPOL) Special Area underscores the urgency of improving maritime safety standards (IMO, 2012). Modern navigation technologies, particularly the Automatic Identification System (AIS), have revolutionized maritime monitoring by enabling real-time tracking and analysis of vessel behaviour (Eriksen et al., 2006). However, existing risk models for the Caribbean often remain limited to restricted waters or omit key environmental and vessel-specific factors. To address this gap, this study leverages one year of Satellite Automatic Identification System (S-AIS) data and applies an Artificial Neural Network (ANN) to develop a probabilistic risk assessment model integrating vessel, environmental, and charting conditions for the Caribbean Sea. The model quantifies incident probability, evaluates targeted mitigation strategies, and supports data-driven decision-making to enhance navigational safety and resilience across the region's complex maritime domain.

2 S-AIS data and vessel traffic analysis in the Caribbean Sea

S-AIS data offers continuous global tracking of vessel location, course, and speed, revolutionizing maritime surveillance (Eriksen et al., 2006). In this study, S-AIS data purchased from ORBCOMM was used to determine vessel traffic density in the Caribbean Sea by extracting vessel positions, mapping high-traffic zones, and generating track lines for analysis. However, several limitations were encountered. Errors in Maritime Mobile Service Identity (MMSI) values were common, including duplicate identifiers and inconsistent formatting. Type 5 AIS messages, containing static and voyage-related vessel data, were often missing or miscatalogued. Additionally, AIS units were sometimes reset or switched off, leading to positional gaps particularly among smaller, locally operating vessels, as also documented by Maharaj (2020). Signal interruptions from reliance on low Earth orbit satellites caused fragmented tracks (Jelavić et al., 2008), while both satellite and terrestrial AIS suffered from asynchronous transmissions and limited bandwidth, leading to message collisions and data loss (Pedersen, 2002; Carson-Jackson, 2012). To address these issues, a custom MATLAB script retrieved missing Type 5 data from *MarineTraffic* and *VesselFinder* using MMSI queries to obtain International Maritime Organization (IMO) number, tonnage, dimensions, and flag. This information was then linked to the reconstructed vessel tracks, and misplaced routes caused by coverage gaps were corrected with verified *MarineTraffic* navigational data. In total, 67,289 vessel tracks were reconstructed for 2016, providing a detailed picture of vessel movements and maritime corridors sufficient for developing the regional risk assessment model (Fig. 2).

2.1 Port to port activity in the Caribbean Sea

To better understand the flow and concentration of vessel movements within the Caribbean Sea, a detailed port-to-port analysis was performed using the refined S-AIS data. This analysis leveraged spatially referenced vessel track lines entering and exiting designated port areas, represented by geofenced rectangular zones, to identify the start and end of voyages. These geofences included both regional ports and boundary points at the edges of the Caribbean Sea, which allowed for the classification of local, regional, and international traffic patterns.

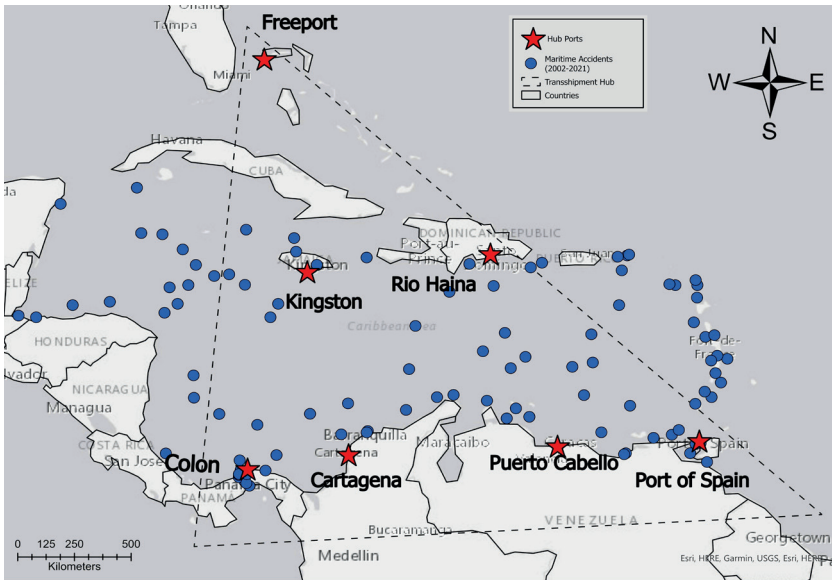


Fig. 1 Caribbean transshipment triangle with hub ports and maritime events (2002–2021).

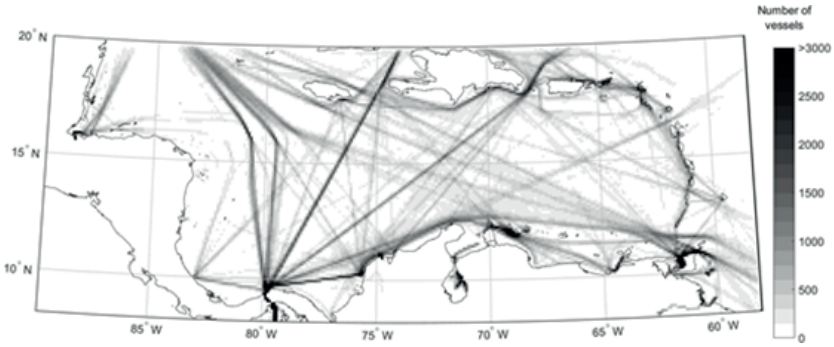


Fig. 2 Number of vessels passing through 0.1° cells in 2016.

2.1.1 Cargo port calls

The cargo port call analysis revealed over 2,000 cargo transits in the Caribbean Sea for the year 2016, with dense inter-island and international cargo routes represented in varying intensities (Fig. 3). For this study, "cargo" includes container ships, general cargo vessels, bulk carriers, roll-on/roll-off (Ro-Ro) vessels, refrigerated cargo ships, heavy load carriers, livestock carriers, and other specialized dry cargo ships as classified in the S-AIS dataset. Lighter passages indicated regular regional trading, while heavier transit lines particularly between the Panama Canal and the Mexico-Cuba and Cuba-Haiti borders reflected high-frequency movements associated with major global trade lanes. Ports such as Mariel in Cuba, Cristobal in Panama, and Cartagena in Colombia emerged as key cargo hubs due to their proximity to the Panama Canal and investments in deep-water and transhipment infrastructure. Table 1 highlights the busiest cargo ports, with the Cuba-Haiti and Mexico-Cuba border regions registering over 10,000 port calls each. These ports benefit from their strategic positioning near global trade lanes and strong bilateral trade relationships. High volumes were also noted between the Lesser Antilles and the eastern maritime boundary, indicating significant regional connectivity.

2.1.2 Passenger port calls

For this analysis, passenger vessels included both dedicated passenger ships (e.g., cruise ships, ferries) and mixed-use passenger vessels, reflecting the operational realities of Caribbean maritime transport. Passenger traffic, vital to the tourism-dependent economies of the Caribbean, was found to be densely concentrated in areas such as Puerto Rico, the U.S. and British Virgin Islands, and the Lesser Antilles (Fig. 4). Notably, the Port of Fajardo in Puerto Rico recorded the highest number of passenger journeys 7,416 in total due to frequent sea bridges to nearby islands such as Vieques and Culebra. Passenger routes also showed intense clustering around Charlotte Amalie, Guadeloupe, and Turks and Caicos (Table 2). These ports facilitate inter-island cruise operations and ferry services, reflecting the regional importance of tourism-related maritime transport. The concentration of these movements reinforces the critical role of port infrastructure in supporting tourism, employment, and local development.

2.1.3 Tanker port calls

Tankers were classified to include vessels transporting liquid bulk cargo such as oil, chemicals, liquefied gas, asphalt, and other specialized liquid products. Categories included Asphalt Tanker, Chemical Tanker, Crude Oil Tanker, LPG/LNG Tanker, Products Tanker, Oil/Chemical Tanker, and other related liquid-cargo vessel types. The Caribbean's role in the global oil and gas trade was evident with over 19,000 tanker transits recorded in 2016 (Fig. 5). Traffic was dominated by routes connecting Venezuela, Panama, Mexico, and Trinidad and Tobago. The Mexico-Cuba Northwest to East Border route recorded over 7,000 tanker journeys, underscoring the region's use as a passage for crude oil and gas to North America. Ports such as Punta Cardon and Caicara in Venezuela, as well as Curacao's Port of Willemstad, were identified as key tanker hubs (Table 3). Trinidad's Point Fortin also demonstrated significant regional tanker traffic. These ports serve as vital nodes for both export and transhipment of oil and gas products. Notably, intra-Venezuelan movements between Maracaibo, Punta Cardon, and Caicara illustrated high national-level oil distribution.

The port-to-port analysis provides critical insight into the volume, type, and pattern of vessel activity within the Caribbean Sea. It confirms the region's status as a central corridor for global and regional maritime flows, connecting numerous systems of circulation. The concentration of cargo, passenger, and tanker operations within confined geographic spaces underscores the need for robust safety protocols, modernized port infrastructure, and environmental protection strategies. With increasing vessel sizes, rising trade volumes, and growing cruise tourism, the

https://doi.org/10.58440/ihr-31-2-a11

risks of collision, congestion, and pollution are heightened. Regional ports vary in capacity and efficiency, which can affect their ability to safely accommodate rising traffic. Given the Caribbean's economic dependence on maritime transport and its designation as a MARPOL Special Area, targeted efforts are essential to enhance navigational safety, enforce international regulations, and invest in risk mitigation and monitoring systems. This data-driven overview not only maps critical maritime gateways but also serves as a foundation for assessing vulnerabilities and prioritizing future infrastructure and policy interventions across the region.

3 Risk assessment strategies in maritime navigation

Accurately assessing the risk of maritime navigation has become increasingly complex due to the dynamic nature of the marine environment and the intensity of vessel traffic. Traditionally, maritime risk assessment models have relied on statistical and geometric methodologies to evaluate navigational hazards, particularly within confined waterways such as ports and straits (Macduff, 1974; Fujii, 1974; Kristiansen, 2005). These models often provide a static or simplified view of vessel movement, focusing largely on linear traffic flows and spatial proximity calculations. While foundational to the discipline, such approaches fall short of capturing the multifactorial risks present in open seas and broader maritime domains (Mazaheri et al., 2014). With the advent of AIS data and enhanced computational capabilities, maritime risk assessment has shifted toward more dynamic, data-driven methodologies (IALA, 2019; Goerlandt & Montewka, 2015). AIS enables the capture of real-time vessel movements, producing rich datasets that reflect the spatial–temporal complexities of modern maritime traffic. This has paved the way for simulations and probabilistic models capable of representing vessel interactions and predicting collision scenarios under varied conditions (Chen et al., 2019; Montewka et al., 2011).

Among early foundational models, Blackwell's ship domain theory served as a cornerstone for collision risk evaluation, focusing on the spatial interaction zones of navigating vessels (Blackwell, 1989). However, many traditional models, while incorporating AIS data, remain limited in scope, primarily addressing risk within restricted waters and neglecting broader risk-inducing variables such as vessel age, flag state, navigational equipment, sea conditions, bathymetry, Aids to Navigation (AtoN), and regional hazards (Kristiansen, 2009; Montewka et al., 2010). Approaches by Macduff (1974), Fujii (1974), Pedersen (2002), Kaneko (2002), and COWI (2008) typically employ geometric probabilities, historical data, and simplified assumptions about vessel behaviour. These have provided valuable insights in confined waterways but perform poorly in open-sea contexts, where they often assume uniform traffic density, overlook external factors such as weather

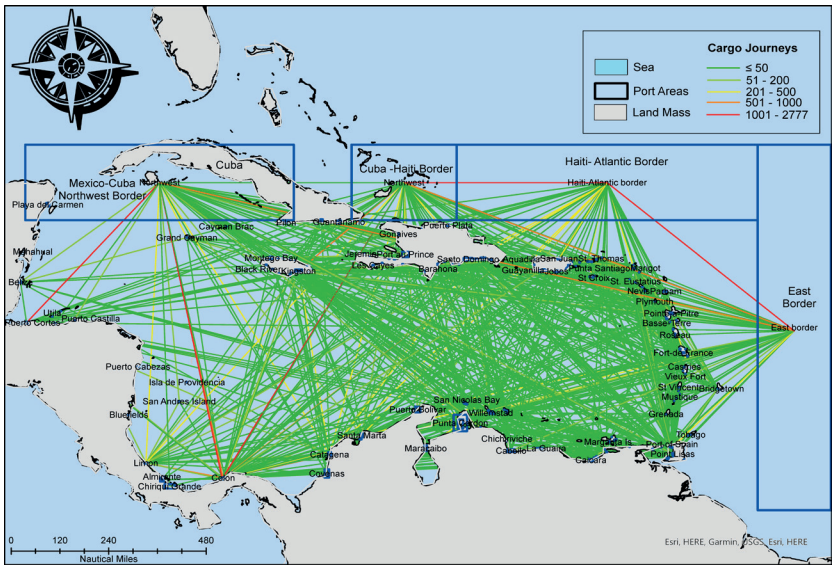


Fig. 3 Cargo Vessel Port Call and Track Density Patterns in the Caribbean Sea, 2016.

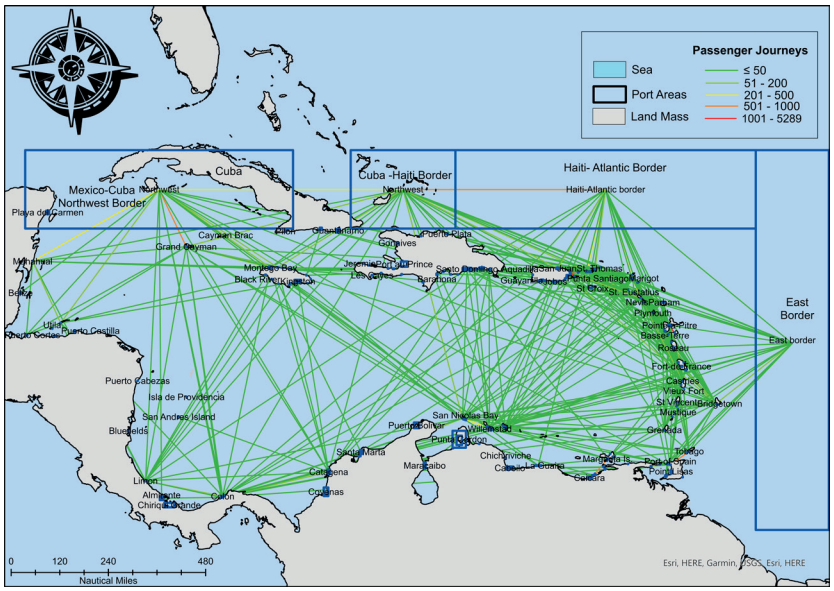


Fig. 4 Passenger Vessel Port Call and Track Density Patterns in the Caribbean Sea, 2016.

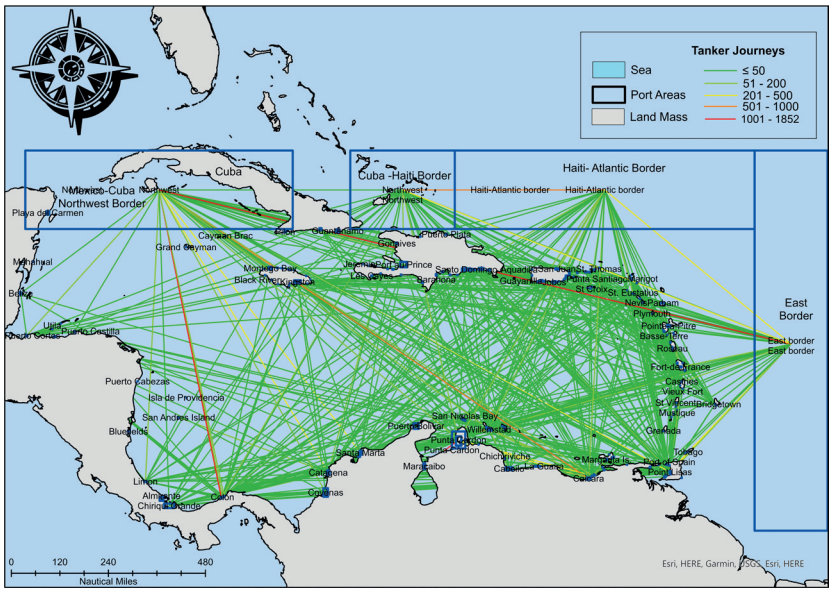


Fig. 5 Tanker Vessel Port Call and Track Density Patterns in the Caribbean Sea, 2016.

Table 1 Cargo journeys within the Caribbean Sea, 2016.

Country	Port	Number of journeys
Cuba-Haiti border	Northwest	10682
Mexico-Cuba border	Northwest	10502
Panama	Canal	7614
Panama	Cristobal	6962
Haiti-Atlantic border	Haiti-Atlantic border	6738
East border	East border	5990
Columbia	Cartagena	5013
Jamaica	Port of Kingston/Port Royal	4181
Dominican Republic	Santo Domingo	2858
United States of America	San Juan	2783

Table 2 Passenger journeys within the Caribbean Sea, 2016.

Country	Port	Number of journeys
United States of America	Port of Fajardo	7416
American Virgin Islands	Port of Cruz Bay	5474
American Virgin Islands	Redhook Bay	5345
United States of America	Ensenada Honda Harbour	3769
United States of America	Port of Vieques	3750
American Virgin Islands	Charlotte Amalie	2399
British Virgin Islands	Road Harbour	1891
Guadeloupe	Port of Pointe-a-Pitre	1709
Guadeloupe	Port of Grand-Bourg	1494
Haiti-Atlantic Border	Haiti-Atlantic Border	1469

Table 3 Tanker journeys within the Caribbean Sea, 2016.

Country	Port	Number of journeys
Mexico-Cuba Border	Northwest	7124
East Border	East Border	3615
Venezuela	Port of Punta Cardon	2913
Panama	Canal	2628
Haiti-Atlantic Border	Haiti-Atlantic Border	2247
Cuba-Haiti Border	Northwest	2238
Venezuela	Port of Caicara	1689
Netherlands Antilles	Port of Willemstad	1495
Venezuela	Los Boqueticos	992
Columbia	Cartagena	940

and human error, and fail to account for dynamic vessel interactions (Goerlandt & Montewka, 2015; Chen et al. 2019).

Contemporary AIS-based models have improved understanding of vessel movement patterns and collision probabilities. Case studies employing Monte Carlo simulations (Miller et al., n.d.), Cellular Automata (Qu & Meng, 2012), and Convolutional Neural Networks (Georlandt et al., 2020) demonstrate considerable potential, yet still frequently omit critical variables such as vessel flag, age, and weather. They also often rely on static causation probabilities, suffer from incomplete databases, and rarely undergo real-world validation (Ylitalo, 2010; Mazaheri et al., 2014). Many are geographically specific, such as the Land Information New Zealand (LINZ) strategy for the South Pacific and cannot

https://doi.org/10.58440/ihr-31-2-a11

be applied elsewhere without modification (Riding & Rawson, 2015). International Association of Marine Aids to Navigation and Lighthouse Authorities (IALA) based models like IALA Waterway Risk Assessment Program (IWRAP) also assume narrow, fixed traffic corridors and do not scale well to open seas where vessel paths are highly variable and multidirectional.

Recent comprehensive reviews on maritime risk analysis methods have further broadened the field. Li et al. (2012) provide an overview of quantitative risk assessment models; Kulkarni et al. (2020) assess prevention-oriented waterway risk management strategies and outlines methods for detecting near-miss events using AIS. Collectively, these works span traditional quantitative models through to AI-based and non-accident event detection techniques, setting the stage for recent research integrating artificial intelligence and spatial analytical approaches. For example, Chen et al. (2019) reviewed probabilistic risk-analysis methods for ship–ship collisions, highlighting persistent difficulties in modelling causation due to limited human and organizational factor data. Yang et al. (2023) developed a hybrid Bayesian network and systems-theoretic process analysis (STAMP/STPA) model, exemplifying multi-method integration in maritime risk modelling. Rawson and Brito (2022) expanded the AI perspective with a review of supervised machine learning for maritime accident prediction, severity estimation, ship detentions, and collision risk modelling, identifying challenges in data representativeness, model transparency, and validation issues highly relevant to open-sea contexts. Complementing these approaches, Feng et al. (2025) demonstrated the value of global spatial accident hotspot mapping using kernel density estimation and K-means clustering, revealing marked spatial heterogeneity in risk across chokepoints, traffic hubs, vessel types, and time periods.

Despite these advances, few studies have applied such integrated approaches to the Caribbean Sea or incorporated the full range of vessel-specific, environmental, and charting parameters needed for regional-scale, open-sea risk analysis. To address this gap, this research develops a holistic risk model that moves beyond traditional traffic simulations. ANNs are particularly well-suited to this task, as they can recognise nonlinear patterns and adapt to evolving maritime conditions while processing large datasets with multiple input variables (Supomo & Nugroho, 2021). This study therefore employs an ANN-based approach that combines AIS data with vessel characteristics, environmental data, and navigational parameters to estimate maritime incident probabilities. The model supports robust, data-driven decision-making for targeted risk mitigation in the Caribbean Sea and other complex maritime domains.

4 Method

To construct an accurate and robust maritime risk assessment model, a comprehensive review of global maritime events was conducted using data from the Global Integrated Shipping Information System (GISIS), maintained by the IMO. This dataset contained 6,260 marine casualties and incidents reported globally between January 2002 and December 2021. Combined with prior literature, this 20-year analysis was instrumental in identifying recurring causal patterns and confirming the most significant and recurrent risk factors in the Caribbean context (Maharaj et al., 2025). The selected variables were chosen to reflect both navigational hazards and the region's unique data availability. Several key causal factors were identified: velocity of ocean currents, availability and reliability of AtoN, Category Zone of Confidence (CATZOC) from hydrographic surveys, known navigational hazards, bathymetric characteristics, vessel nationality (flag), and vessel age. Vessel movement data from S-AIS for 2016 was used to analyse traffic density within the Caribbean Sea, representing a stable period in regional traffic patterns. Vessel density is a fundamental indicator of collision risk and was treated as a core modelling variable. Supporting spatial datasets, including bathymetry and CATZOC classifications, were sourced from the United Kingdom Hydrographic Office (UKHO, 2019) in GIS-compatible formats. Each variable was processed into a 1 km² grid within the Caribbean Maritime Exclusive Economic Zone (EEZ) and prepared for integration into the ANN model. Detailed derivations included:

- Vessel traffic density: Number of vessel transits per 1 km² from 2016 S-AIS data (ORBCOMM).
- Bathymetry: Average sounding depth per grid cell (UKHO, 2019).
- Proximity to navigational hazards: Density of reefs, wrecks, shoals, pipelines, and other hazards (UKHO, 2019).
- Proximity to AtoN: Density of AtoN per grid cell (UKHO, 2019).
- Current velocity: Long-term hydrodynamic averages interpolated using kriging (UKHO).
- CATZOC quality: Hydrographic survey accuracy and seafloor coverage (UKHO, 2019).
- Chart age: Years since last survey based on UKHO metadata.
- Vessel age: Percentage distribution of vessel ages aggregated from GISIS data, calculated only for grid cells with reported accidents.
- Flag state: Percentage distribution of vessel flags aggregated from GISIS data, calculated only for grid cells with reported accidents.

4.1 Comparison with earlier work

This selection of navigational risk factors builds on, yet diverges from, earlier maritime risk assessment methods. Classic models, such as those by Macduff (1974), Fujii (1974), Pedersen (2002), and the IALA Waterway Risk Assessment Program (IWRAP), have primarily emphasised traffic geometry, vessel encounter rates, and collision probabilities in restricted

waters. While effective in ports and channels, these models are less suited to the open-sea conditions of the Caribbean, where vessel movements are multidirectional, traffic density is uneven, and environmental conditions are highly variable. Some variables in this study such as traffic density and flag state are common to previous approaches (Montewka et al., 2011; Goerlandt & Montewka, 2015). Others, such as CATZOC, chart age, AtoN density, and current velocity, are rarely integrated into probabilistic models but are particularly relevant in this study. CATZOC and chart age address hydrographic uncertainty, which is critical in a region where over 80 % of waters remain un-surveyed to modern standards (MarineMarico, 2013). Similarly, current velocity, although noted in navigation literature (Kristiansen, 2005), has seldom been operationalised in ANN-based maritime risk modelling.

4.2 Approach to risk assessment

The primary objective of this study was to develop a comprehensive risk assessment model to estimate the probability of maritime events based on contributory factors. This was achieved by integrating domain knowledge, historical accident data, and spatial risk variables within an ANN implemented in an R Studio environment. The methodological process involved the analysis of twenty years of archived maritime accident reports to identify and quantify the primary causal factors associated with vessel incidents. Spatial and aspatial datasets, including S-AIS vessel traffic density and multiple risk factor layers, were prepared and integrated. Each accident record was matched to the spatial values of these variables such as bathymetry, current velocity, CATZOC quality, and AtoN density, within its grid cell, thereby ensuring consistency in the model inputs. A predictive probability model was developed using a Multi-Layer Perceptron (MLP) ANN to simulate the relationships between the identified risk factors and the likelihood of maritime events. The model was applied across the Caribbean Sea to evaluate risk levels and identify potential hotspots for maritime eventss. Mitigation strategies were assessed by modifying the input variables to reflect the implementation of measures such as increasing AtoN, improving CATZOC quality, and reducing navigational hazards in high-risk zones. The ANN was retrained with the modified inputs, and the resulting predicted probabilities were compared to the baseline scenario to estimate reductions in incident risk.

4.3 Model development using ANN

Following the global comprehensive analysis of maritime accidents, 69 events occurred in the Caribbean Sea (Fig. 6), all involving vessels equipped with AIS at the time of the event. These events included 9 foundered events, 17 collisions, 13 contacts, 15 groundings, 8 fires/explosion, and 7 capsize events. To ensure accurate and unbiased predictions, the dataset was split into two subsets: 70 % for training and 30 % for testing. The training set was used to identify patterns and model the spatial structure of risk, while the testing set validated predictive accuracy. Each event location was spatially linked to the corresponding values of the identified risk factors using GIS-derived raster. The ANN was developed in R using the neuralnet package, adopting a Multi-Layer Perceptron (MLP) architecture configured as 9-5-1, nine input nodes for the explanatory variables identified in Section 4.0 (vessel density, bathymetry, hazard proximity, AtoN density, current velocity, CATZOC quality, chart age, vessel age, and flag state), five hidden neurons, and one output neuron. Five hidden neurons were selected after iterative testing of multiple configurations (3–7 neurons) and yielded the optimal balance between predictive accuracy and avoidance of overfitting. The chosen 1 km^2 spatial resolution provided sufficient granularity for regional-scale analysis without excessive computational load or AIS noise sensitivity.

A logistic activation function was applied to the hidden and output layers to enable nonlinear pattern detection while constraining outputs between 0 and 1, consistent with probabilistic risk estimation. The learning rate and weight initialization were tuned experimentally to minimize mean squared error during training, and all variables were normalized to a [0,1] scale to improve convergence stability. Training used forward–backward propagation. In the forward pass, input data moved through weighted connections and activation functions, producing increasingly abstract feature representations in the hidden layer before yielding a probability estimate in the output layer. Backpropagation then calculated prediction errors and propagated them backward through the network, adjusting weights according to error gradients. This process iterated over multiple epochs until predefined accuracy thresholds were met. By prioritising relatively stable variables (e.g., bathymetry, hazards, long-term traffic patterns) over short-term dynamic parameters, the model produces a baseline probabilistic risk surface for strategic planning rather than near-miss or real-time collision prediction. This differentiates it from operational timescale models and enhances its relevance for long-term maritime safety management in the Caribbean. The novelty of this work lies in synthesising underutilised hydrographic, environmental, and regulatory variables into a single probabilistic framework, yielding region-specific, actionable insights into navigational risk.

4.4 Model evaluation

A robust evaluation framework was employed to assess the ANN model's performance. Pairwise scatter plots were first used to visually examine relationships between each explanatory variable and the response variable. Generalized Weight Plots (GWP) were then generated to evaluate the independent contribution of each covariate, where high weight variance indicated

https://doi.org/10.58440/ihr-31-2-a11

nonlinearity. Sensitivity analysis using the Lek-profile method was applied to explore how changes in individual inputs affected predicted probabilities, verifying that the ANN was capturing real-world patterns. To further interpret model behavior, a Neural Interpretation Diagram (NID) and Garson's algorithm (1991) quantified and visualized the relative influence of each variable, revealing both direct and interactive effects. This combination of predictive modelling and interpretability techniques provided a transparent, objective, and rigorous approach to maritime risk assessment. By overcoming the limitations of traditional statistical models and removing subjective weighting, the ANN framework delivered data-driven probability estimates for open-sea incidents, supporting targeted mitigation strategies in the Caribbean Sea. The methodological framework for the probability model outlines the sequential process used to integrate data preparation, ANN model development, and evaluation procedures (Fig. 7).

5 Results

A hybrid evaluation and interpretability framework was implemented to rigorously assess the ANN and to elucidate the contribution of each predictor variable to maritime incident probability modelling. The framework integrates complementary statistical, graphical, and model decomposition techniques to address common challenges in neural network interpretability, including black-box opacity, nonlinear dependencies, and variable interaction effects. By combining correlation analysis, weight-based diagnostics, connection topology inspection, and perturbation-based sensitivity testing, the approach provides both global variable importance rankings and local behavioural insights.

The pairwise scatterplots and correlation coefficients, visualized in the heatmap (Fig. 8), provided an initial diagnostic of linear dependencies between predictors and the response variable, revealing relationships consistent with established maritime risk mechanisms. Strong positive correlations were observed between bathymetry and traffic density, AtoN density, and hazard proximity, indicating that shallow or constrained waters tend to concentrate vessel movements, require more navigational aids, and coincide with mapped hazards conditions commonly associated with grounding risk. AtoN density and hazard proximity were also strongly correlated, reflecting the clustering of navigational aids in hazardous zones, where their absence or malfunction could significantly increase risk. Similarly, CATZOC and survey age showed strong correlations with hazard proximity, underscoring the role of outdated or poor-quality charting as a latent risk factor. These patterns confirm that empirical variable relationships align closely with the ANN-predicted incident hotspots, reinforcing the model's grounding in real-world maritime safety dynamics.

NIDs further illuminated the ANN's decision-making process by visualizing the magnitude and polarity of connections from each input through the hidden layer to the output neuron. Thick positive-weight connections were identified for traffic density, vessel age, CATZOC, and hazard proximity, whereas less influential variables showed thinner or negative connections, indicating their comparatively smaller role in shaping predictions (Fig. 9).

Garson's algorithm decomposed network weights into normalized relative importance scores, producing a global ranking of predictor influence. Traffic density emerged as the most dominant factor, followed by navigational hazards, vessel age, current velocity, and chart quality. Minimal contributors, such as current

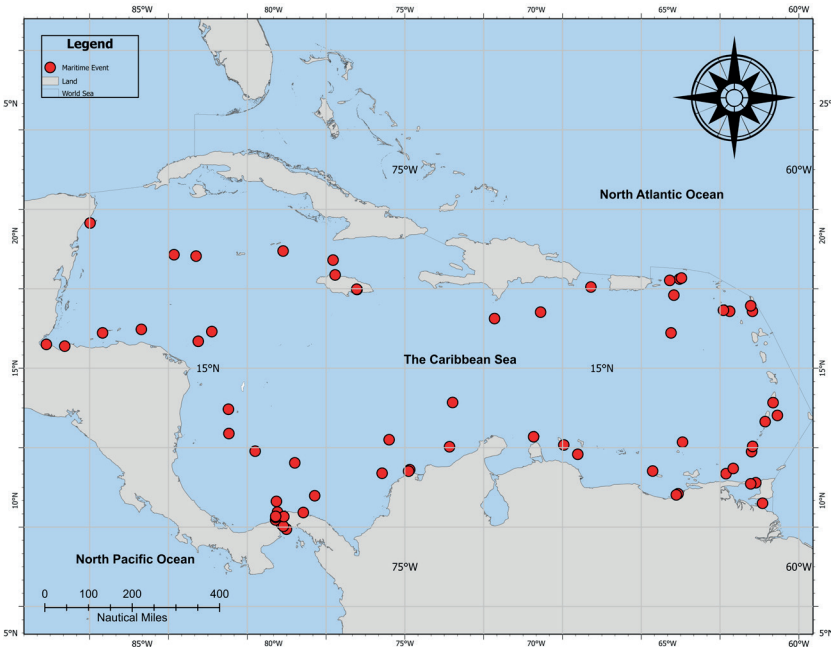


Fig. 6 Location of maritime events in the Caribbean Sea for the period of 2002–2021.

Preparation of Data
- RStudio Environment Setting
- Preparation of Train and Testing Data

Compute Neural Net with Training Data
- Plotting of NN function network
- Pairwise NN model results of Explanatory and

Variable Importance using NNET Package
- Compute NNET functon
- Plot NNET function network
- Variables Importance using NNET
- Sensitivity Analysis of Expanatories and Response Data

Compute Neural Net fuunction for Prediction with Validation Data
- Prediction Validation results with AUC Value and ROC plots

Produce prediction map using Raster data
- Import and process thematic maps
- Compute prediction function
- Export final prediction map as raster.tif

Fig. 7 Methodological framework for probability model.

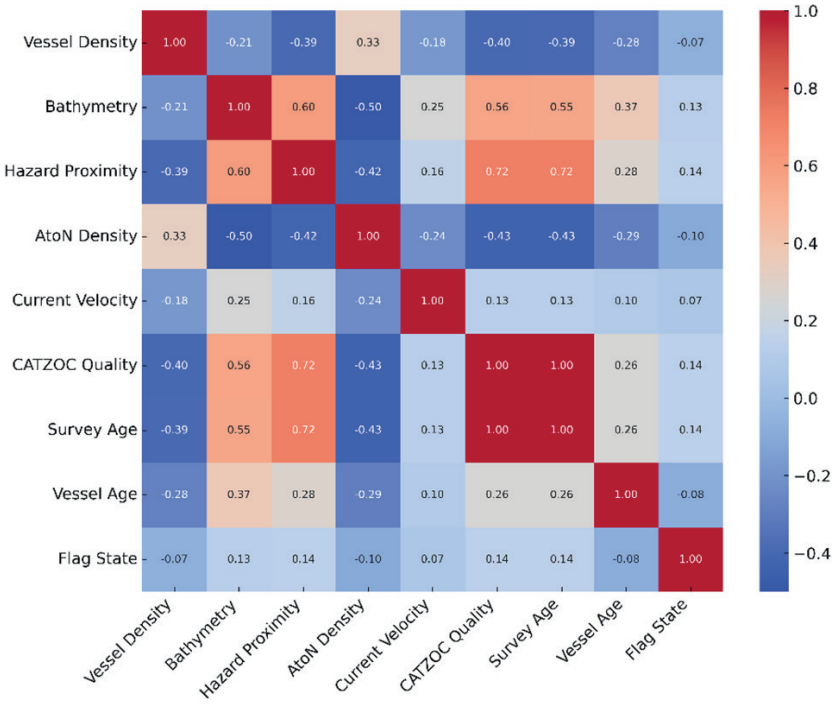


Fig. 8 Correlation heatmap of maritime risk factors and response variable.

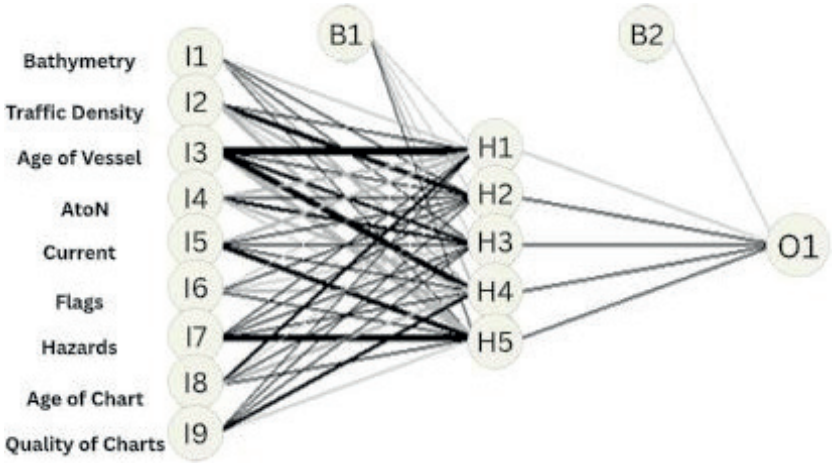


Fig. 9 NID showing variable influence pathways in ANN model.

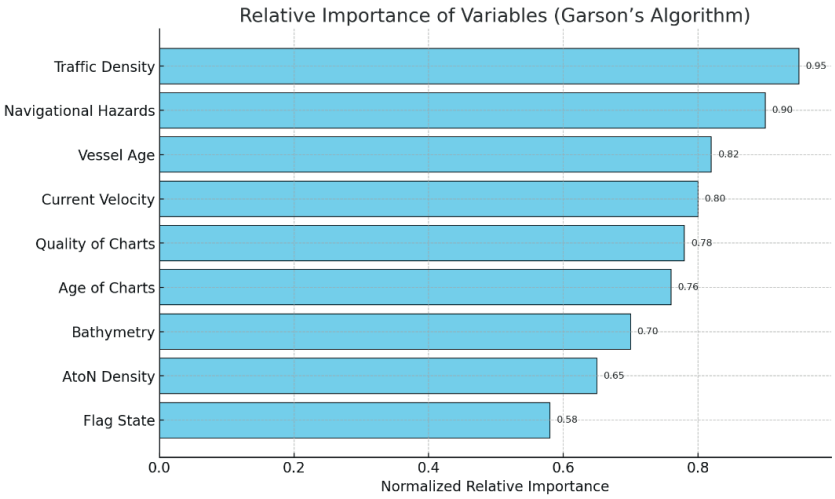


Fig. 10 Relative importance of risk factors derived using Garson's algorithm.

velocity and AtoN density, were retained in the model due to their potential interaction effects, as later confirmed through sensitivity testing (Figure 10).

Finally, model performance was assessed using Receiver Operating Characteristic (ROC) curves and Area Under the Curve (AUC) metrics. The ANN achieved perfect classification on the training dataset (AUC = 1.00) and 91 % accuracy on the independent test dataset (AUC = 0.91), demonstrating strong predictive skill and generalization with only a minor reduction in performance on unseen data (Fig. 11). The integration of these evaluation techniques provided a transparent, data-driven, and technically rigorous understanding of the ANN's predictive behavior, directly informing the prioritization of maritime risk factors for navigation safety planning in the Caribbean Sea.

5.1 Spatial analysis of predictive surface

The ANN model generated a raster-based probability surface highlighting spatial variation in maritime incident risk across the Caribbean Sea. The map revealed a range of prediction probabilities from low (0.0–0.3) to moderate (0.4–0.6) and high (0.6–1.0) with high-risk zones concentrated near busy port approaches, congested shipping corridors, and constrained areas (Fig. 12).

High-probability areas were pronounced in the approaches to major ports such as George Town (Cayman Islands), Belize City, Kingston (Jamaica), and the Panama Canal, reflecting the influence of vessel traffic density, outdated or poor-quality charting, navigational hazards, and high-risk flag states. For instance, Cuba's southern coast and port *Cienfuegos* and *Jucaro* showed very high predicted probabilities due to narrow channels, dense traffic, and charting deficiencies. Similarly, Belize's shallow docking limitations and high density of navigational hazards contributed to frequent groundings, confirming elevated risk levels in the ANN output. In the Gulf of Honduras, Puerto Cortes and Coxen Hole Island also emerged as risk-prone zones, reinforced by historical incidents, cargo volumes, and offshore supply traffic. The Panama Canal, a major global transhipment bottleneck, had the highest predicted probabilities, aligning with its global accident rate and concentration of Panamanian-flagged vessels often associated with poor safety oversight. Notably, open sea regions also exhibited high probabilities, suggesting that risk is not exclusive to coastal or port-adjacent waters. Events in these areas were primarily associated with collisions and onboard safety failures, indicating the need for increased navigational awareness even in deep-water zones. The Lesser Antilles showed extensive high-risk zones, especially near Port of Spain, Dominica, and Castries. This was attributed to dense cruise and cargo vessel activity, bathymetric constraints, and the presence of over 6,000 documented navigational hazards. The ANN model reinforced that vessel congestion, traffic type, and uncharted waters amplify the likelihood of accidents.

https://doi.org/10.58440/ihr-31-2-a11

Together, the ANN-derived probability surface offers a robust spatial representation of maritime risk across the Caribbean Sea. It validates key patterns observed in the historical accident database and confirms the role of multiple converging risk factors, such as traffic density, navigational hazards, port congestion, vessel flag and vessel type in shaping where future incidents are most likely to occur. The model's insights are vital for informing regional risk mitigation strategies and improving navigational safety.

5.2 Mitigation strategies for maritime navigation

To evaluate the effectiveness of risk mitigation strategies, specific improvements were applied to key causation factors within the ANN model. These included enhancements to Admiralty chart data (improving both quality and survey age), reduction of navigational hazards, ensuring proximity to functional AtoN, improvements in vessel registry safety (flag state), and replacement of older vessels with newer ones. For each variable, the improvement was implemented by modifying the corresponding raster layer used as ANN input: chart quality and survey age were adjusted to improved CATZOC categories; hazard density values were reduced; AtoN density was increased near major routes; flag state risk scores were reassigned to reflect higher safety compliance; and vessel age distributions were shifted toward newer vessels. These modifications were applied across the study area on a randomized but spatially consistent basis to simulate feasible, real-world improvements. The updated variables were reintroduced into the trained ANN model to predict new incident probabilities, allowing for direct comparison with the baseline scenario and quantification of the reduction in navigational risk.

The ANN was retrained using the improved datasets, and the resulting prediction surfaces were compared against the original model output. By subtracting the improved surfaces from the baseline probability map, the analysis quantified reductions in maritime risk as a function of each mitigation measure. This approach allowed for a spatially explicit assessment of how individual changes such as improved charting or an increase in AtoN could reduce the likelihood of maritime events. Unlike traditional assessments limited to confined waterways, this study addressed navigational risk at a regional scale, accounting for international waters across the Caribbean Sea. The findings underscore the importance of proactive mitigation strategies and their measurable impact on reducing risk, supporting informed decision-making for regional maritime safety enhancement.

5.2.1 Improvements to CATZOC

The CATZOC, which reflects the accuracy and reliability of Admiralty chart data, plays a critical role in maritime navigation safety. Most areas across the Caribbean Sea fall within lower-confidence categories (D and U), indicating inadequate or outdated surveys, particularly in open sea areas. In contrast, high confidence zones (A1 and A2) are typically limited to frequently dredged and surveyed port approaches. To assess the impact of improved hydrographic data, CATZOC categories were improved at random locations across the region, and the ANN model was retrained with these modified inputs. The results revealed a notable reduction in predicted maritime incident risk, particularly in high-traffic zones such as the Lesser Antilles, the Panama Canal, the southern coast of Cuba, and parts of Belize and Honduras. In several areas, predicted

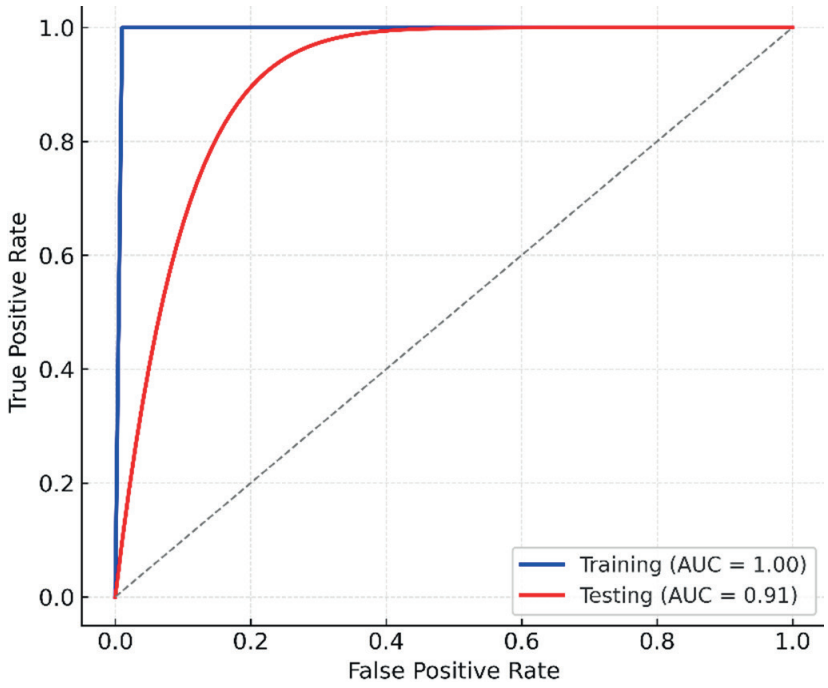


Fig. 11 ROC curve for ANN model performance.

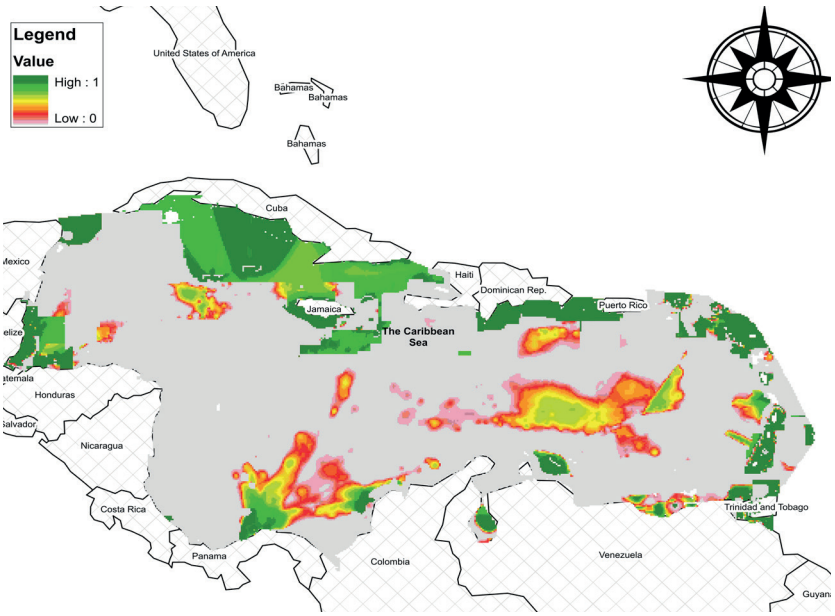


Fig. 12 Probability surface of the Caribbean Sea.

incident probabilities decreased from 0.8–1.0 to as low as 0.3–0.5, confirming that enhancing CATZOC data significantly reduces navigational risk (Fig. 13). This analysis highlights the importance of modern, accurate seabed surveys in improving maritime safety and supports prioritizing hydrographic efforts in poorly charted regions.

5.2.2 Improvements to navigational hazards

Outdated hydrographic surveys and sediment shifts on the seafloor have contributed to the accumulation of numerous navigational hazards in the Caribbean Sea, including reefs, wrecks, rocks, pipelines, and foul grounds. These hazards pose significant threats to maritime safety, especially when located near key shipping lanes or densely trafficked port approaches. It is important to note that while the ANN model was trained and tested using 69 maritime events from the Caribbean Sea. The navigational hazard layer used as one of the input variables was sourced from UKHO data, which contains 9,404 documented hazard locations across the entire study area. To evaluate the potential impact of hazard reduction, approximately 2,000 of these hazard points were randomly removed from the hazard layer, and the modified dataset was used to retrain the ANN model. The retrained model was re-evaluated using ROC, AUC, and classification accuracy metrics, which confirmed performance levels comparable to the baseline model, indicating that the scenario modification did not compromise predictive capability. The updated prediction surface showed a substantial reduction in maritime incident probability, particularly across high-traffic regions such as the Lesser and Greater Antilles, Jamaica, the Panama Canal entrances, northern Honduras, and northeast Venezuela. In some open sea areas west of the Lesser Antilles, predicted risk values decreased between 0.1 and 0.3 (Fig. 14). This result demonstrates that decreasing the density of navigational hazards either through improved charting, hazard removal, or better hazard management can meaningfully reduce the probability of maritime incidents in high-risk zones.

5.2.3 Improvements to AtoN

AtoN including buoys, beacons, lighthouses, and lights are vital for guiding vessels safely through confined channels, port approaches, and offshore areas. These systems assist mariners in avoiding hazards and maintaining accurate bearings, especially where natural landmarks are absent. However, their effectiveness can diminish due to environmental conditions, poor maintenance, or drifting, which poses significant risks to maritime safety. Despite global oversight from the IALA, several limitations remain, including limited regional coverage, resource constraints, and a lack of regional enforcement power. As a result, mariners often rely on multiple navigation methods alongside AtoN, particularly in high-risk or poorly monitored areas. To assess risk reduction, the number of AtoN was increased across the Caribbean Sea by adding more locations along channels, port approaches,

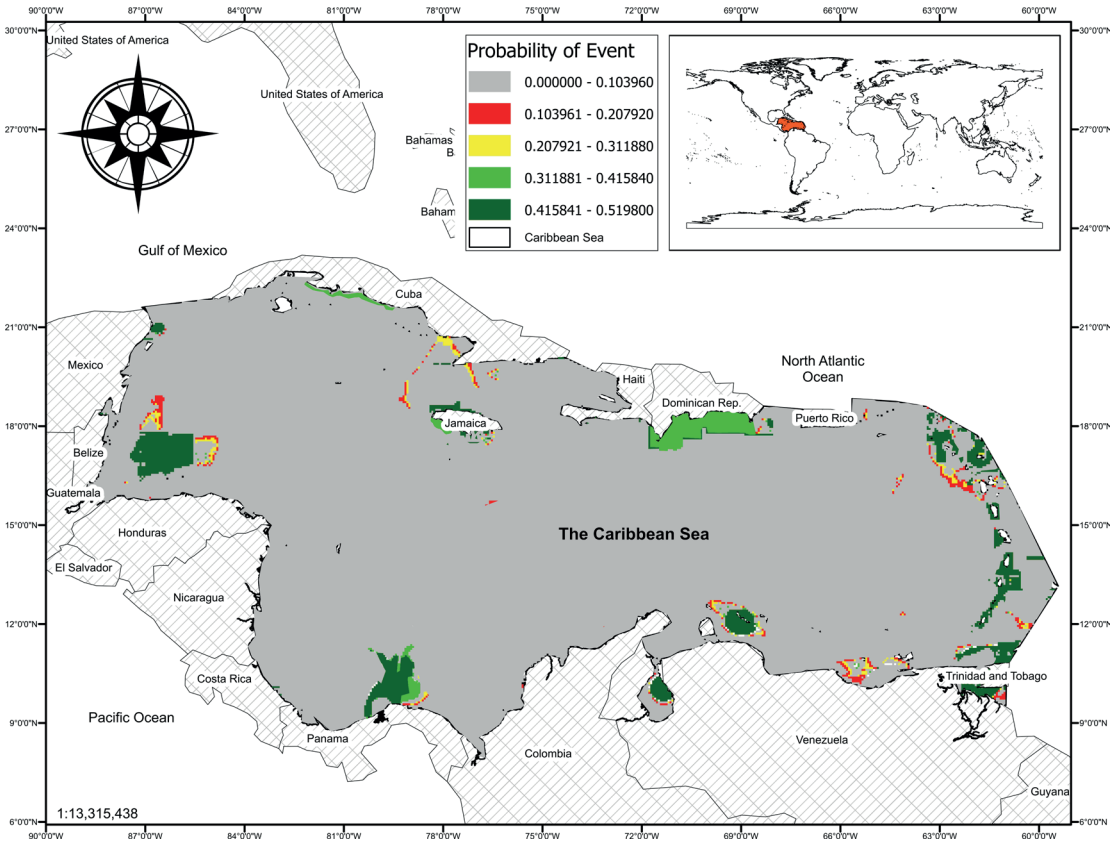


Fig. 13 Improvements due to CATZOC probability surface.

https://doi.org/10.58440/ihr-31-2-a11

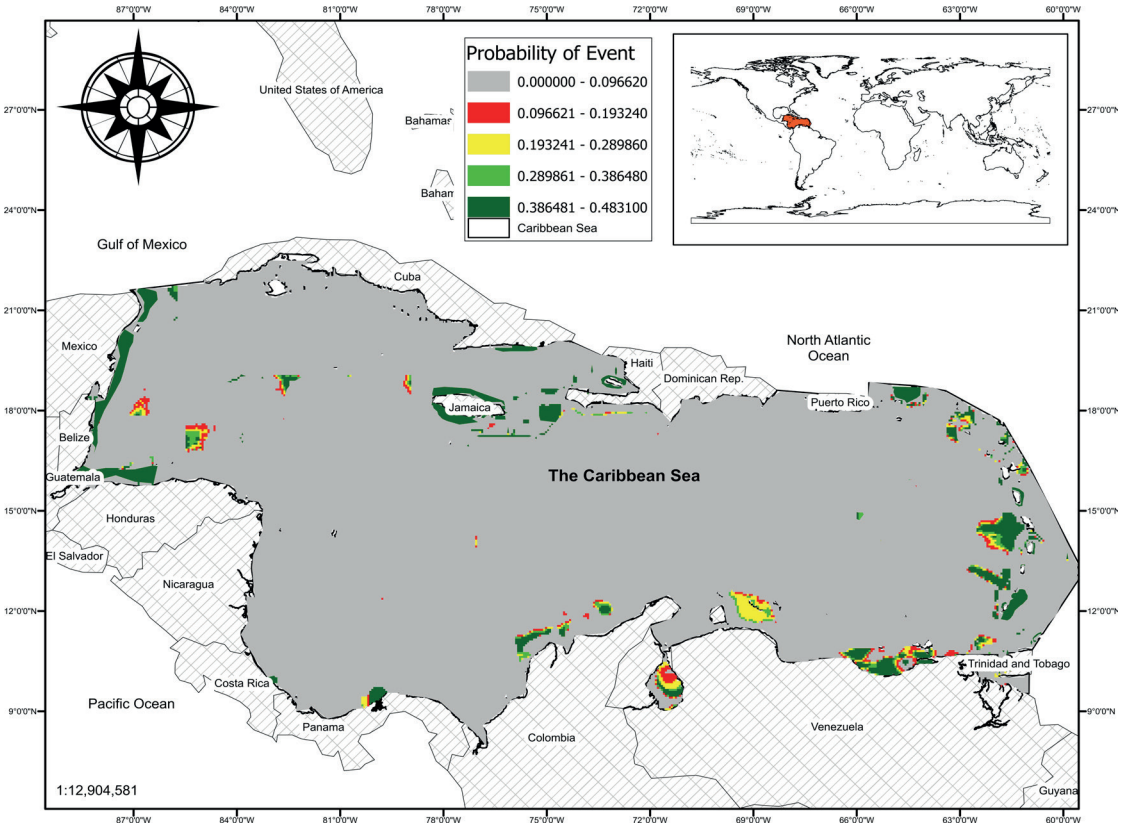


Fig. 14 Improvements due to navigational hazards probability surface.

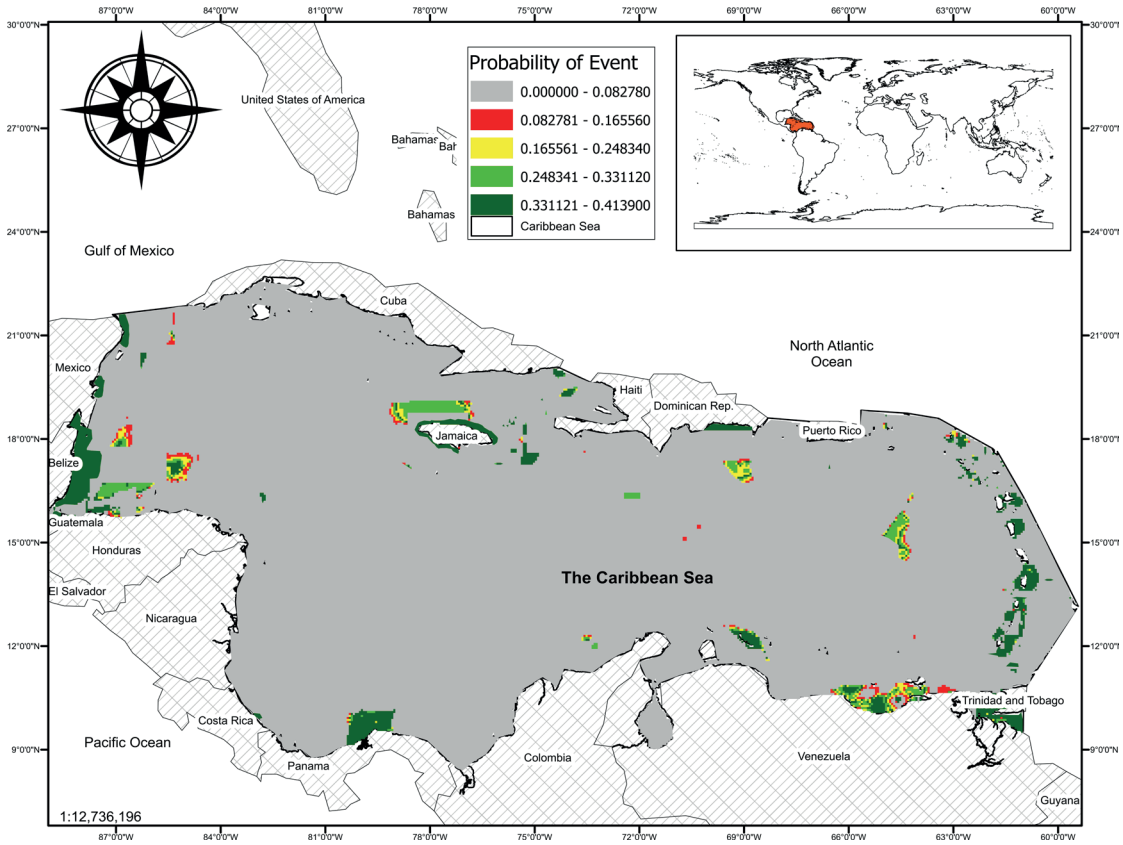


Fig. 15 Improvements to AtoN probability surface.

and high-traffic offshore areas. The ANN model was then retrained with the updated AtoN dataset. This improvement led to a notable reduction in accident probability, particularly within the port approaches of the Greater and Lesser Antilles, Southern Cuba, the Dominican Republic, Panama Canal entrances, and coastal waters near Belize and Honduras. In many of these areas, predicted accident probabilities decreased from 0.8 to as low as 0.2 (Fig. 15). These results underscore the importance of maintaining and expanding AtoN infrastructure as a practical and impactful mitigation strategy for improving maritime safety in the region.

5.3 Evaluation of mitigation strategies

The effectiveness of the proposed mitigation strategies was evaluated through a detailed examination of historical maritime accident reports. This assessment involved comparing the spatial and causal characteristics of past incidents with the areas and variables targeted for improvement within the risk model. By aligning reductions in predicted risk with documented causes of accidents such as outdated charting, insufficient AtoN, and navigational hazards the study validated that the improvements addressed real-world vulnerabilities within the Caribbean Sea maritime domain. This comparative analysis helped to determine the associated long-term benefits of each mitigation strategy. Key outcomes included the potential to significantly reduce pollution events, loss of life, and vessel damage through proactive interventions such as updated bathymetric data, enhanced AtoN, and modernization of vessel fleets. The reductions in risk observed across port approaches and open sea areas especially where historical events had occurred provided strong evidence of the accuracy and practical value of the mitigation strategies adopted. These findings support their application in broader maritime safety planning and underscore their role in fostering a safer and more resilient navigation environment throughout the Caribbean Sea.

5.3.1 Evaluation of CATZOC and survey age risk reduction measures

To assess the effectiveness of improvements made to the CATZOC and survey age, three main types of maritime events; collisions, contacts, and groundings were analysed in relation to the improved risk surface. The findings revealed that a majority of these events occurred in poorly surveyed areas (CATZOC D and U), particularly at night when visibility is limited, and vessel manoeuvrability is reduced. Collision and contact events were concentrated near the entrances of the Panama Canal and the Lesser Antilles, often compounded by ineffective or missing AtoN. Grounding events, primarily involving cargoes, tankers, and container vessels, were found in high-traffic zones like Jamaica's northern coast, the Panama Canal approaches, and east of Belize regions previously identified as high risk due to inadequate survey coverage. Following improvements to CATZOC in these critical areas, the risk probability significantly decreased, with model outputs showing a reduction in likelihood to approximately 0.4 (Fig. 16). These results validate the CATZOC improvement as an effective mitigation strategy, particularly for reducing risk in port approaches and high-density navigational corridors across the Caribbean Sea.

5.3.2 Evaluation of mechanical failure due to aged vessels

The analysis found that vessels between 17 and 37 years of age were significantly more prone to mechanical failure, contributing to a high number of maritime events. Globally, vessels built between 1984 and 2004 contributed to most accidents, with similar patterns observed in the Caribbean Sea, where 29 incidents involved aged ships. Specifically, seven mechanical failure incidents attributed to the aging of a vessel occurred in high-risk areas such as the entrances to the Panama Canal, the northern coast of Venezuela, and open sea regions. These seven cases consisted of 2 collisions, 2 groundings, 1 fire/explosion, and 2 contact events. This distribution highlights that mechanical failures in aged vessels can manifest in multiple accident types, reinforcing their role as a critical underlying risk factor. Following targeted improvements to reduce the presence of aged vessels in the maritime domain, the ANN model was retrained with the modified dataset. The results showed a significant decrease in incident probability in these zones (Fig. 17). The risk map depicts a reduced likelihood of occurrence to 0.2, confirming that replacing or upgrading older vessels is an effective mitigation strategy for enhancing maritime safety.

5.3.3 Evaluation of collision and groundings with improved AtoN

Over the 20-year period, 69 maritime events occurred in the Caribbean Sea, with 11 collisions and 16 groundings being the most common, primarily involving cargo, tanker, fishing, and container vessels. These events often occurred at night due to limited visibility and manoeuvrability, particularly in areas without effective AtoN. To evaluate the potential benefits of enhancing navigational aids, a modified AtoN layer in which the number of AtoN was increased, particularly near port approaches across the Greater and Lesser Antilles and is assumed to be fully operational. This modified layer replaced the original AtoN input in the ANN model, which was then used to generate a new prediction surface. The resulting output (Fig. 18) shows the simulated reduction in incident probability compared to the baseline, with risk in previously high-incident areas decreasing to approximately 0.4. This indicates that strategic increases in functional AtoN could substantially improve navigational safety, especially in collision- and grounding-prone zones.

This section evaluated a series of mitigation measures aimed at reducing maritime navigation risk

https://doi.org/10.58440/ihr-31-2-a11

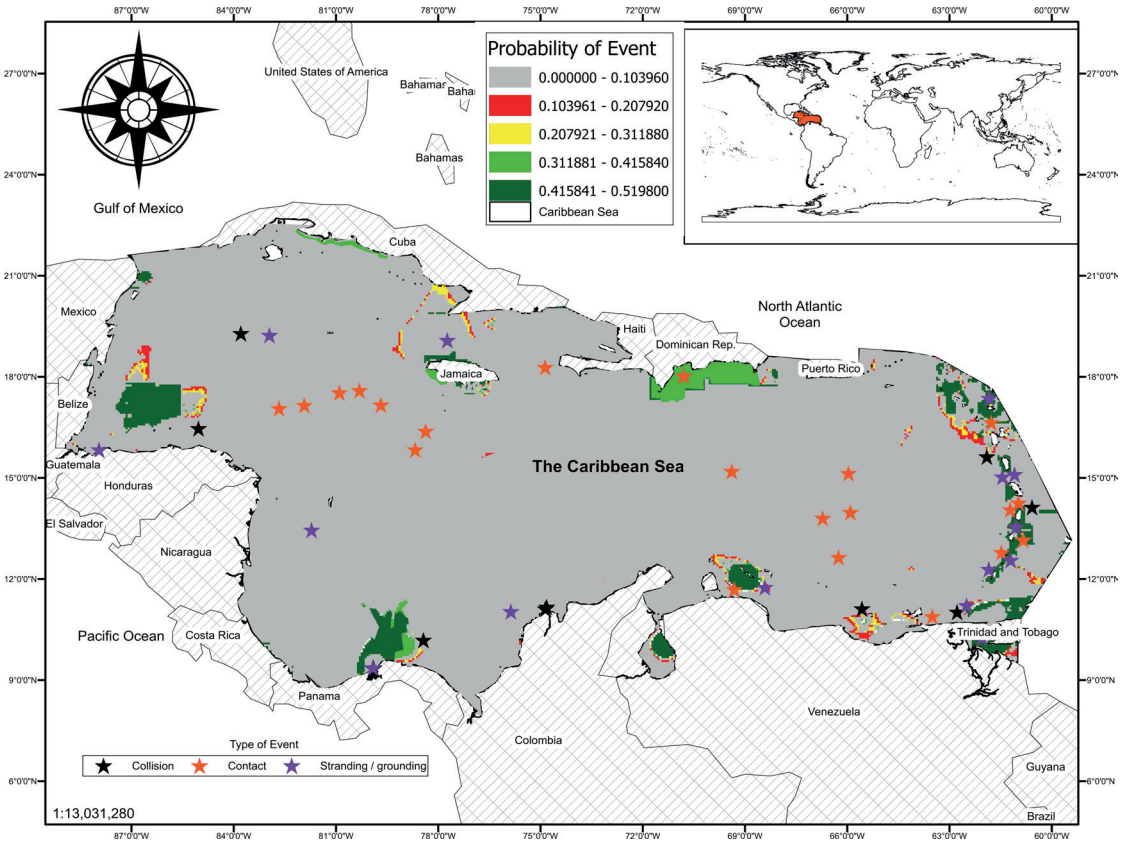


Fig. 16 Maritime accidents with CATZOC improvements probability surface.

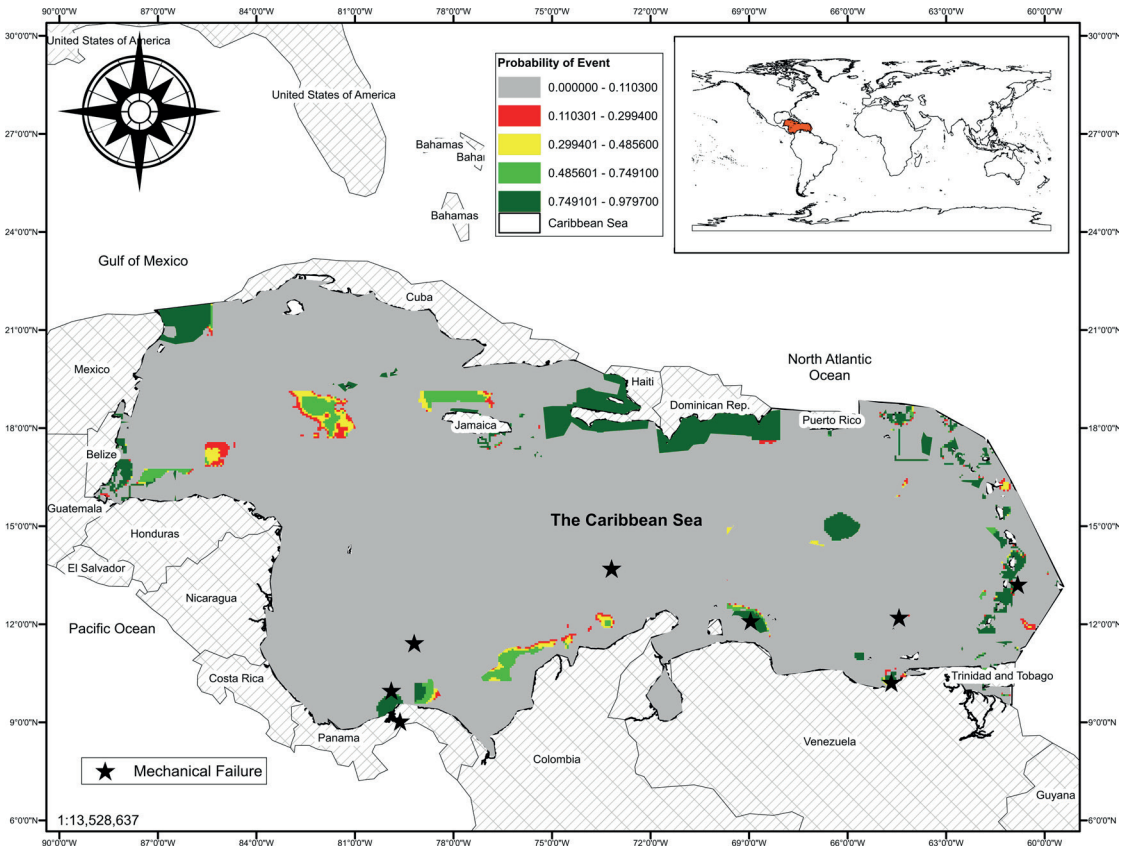


Fig. 17 Location of mechanical failure events superimposed on improved aged vessels probability surface.

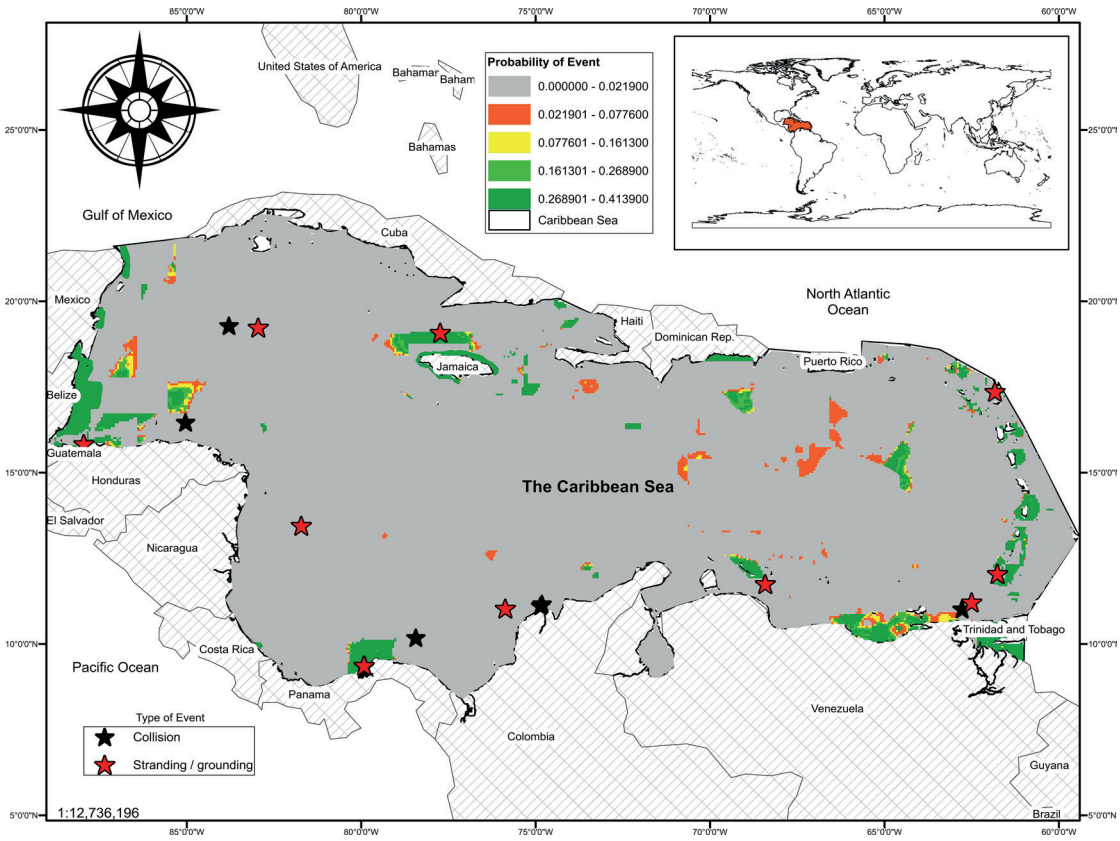


Fig. 18 Collision and groundings events with improved AtoN probability surface.

across the Caribbean Sea. Improvements to key causation factors such as updated charting, AtoN, navigational hazard reduction, vessel flag, vessel age, CATZOC classification were applied as part of a comprehensive traffic management strategy. Using ANN and consistent vessel traffic data derived from AIS, simulated testing demonstrated the effectiveness of these measures. The analysis revealed significant risk reductions across the region, with notable improvements in high-risk areas. Overall, the findings underscore the value of targeted mitigation strategies in improving navigational safety and support the continued use of data-driven approaches to guide maritime risk management in the Caribbean.

6 Conclusion

This study introduced a novel, data-driven risk assessment strategy for maritime navigation in the Caribbean Sea, leveraging ANN and a wide array of contributory variables. Unlike traditional hydrographic risk assessments that are typically confined to specific waterways, this research expanded the scope to open seas and regional contexts. It integrated geospatial data, historical maritime accident records, and satellite AIS data to develop a probability model capable of predicting high-risk locations for maritime events. The research began by identifying key causal factors influencing maritime accidents, including traffic density, bathymetry, velocity of current, vessel age, flag state, navigational hazards, chart quality and age and AtoN. Using ANN, the model was trained and validated with over 20 years of accident data, achieving a high prediction accuracy of 91 %. The ANN model not only predicted accident likelihood but also provided interpretability through techniques such as generalized weight plots, sensitivity analysis, and Garson's algorithm. The probability surface revealed key high-risk regions, including the entrances to the Panama Canal, port approaches of Jamaica and the Lesser Antilles, and open sea areas driven by dense traffic, outdated surveys, poor chart quality, and aged vessels. Mitigation strategies were tested by improving individual causation factors, such as updating charting data, reducing navigational hazards, increasing AtoN, and enhancing vessel safety by flag state and vessel age. Simulation of these mitigation scenarios showed significant risk reductions, particularly near major ports and transhipment corridors. The CATZOC improvements alone halved the probability of events in several high-risk areas. Evaluations of events such as collisions, groundings, and mechanical failures validated these reductions, confirming the effectiveness of the mitigation strategies. Importantly, this paper demonstrated the applicability of ANN for maritime risk assessment at a regional scale. The methodology enables prioritization of hydrographic surveys, supports decision-making for maritime authorities, and provides a foundation for future Vessel Traffic Services (VTS) or Traffic Separation Schemes (TSS) across the Caribbean Sea. The study offers actionable insights for enhancing maritime safety, reducing environmental impacts, and informing regional marine traffic

https://doi.org/10.58440/ihr-31-2-a11

management in support of sustainable development.

While this study demonstrates the potential of ANNs for regional maritime risk assessment, it is not without limitations. The integration of datasets compiled across different time periods, the reliance on a standard 70:30 training-to-test data ratio, and the use of simulated adjustments in mitigation scenarios all reflect necessary assumptions. These assumptions, though common in data driven modelling, may introduce uncertainties when applied to real-world operations. Nonetheless, the framework developed here provides a transparent and adaptable foundation for prioritizing hydrographic surveys, guiding maritime authorities, and evaluating future safety interventions as more harmonized and comprehensive datasets become available.

References

Acejo, I., Sampson, H., Turgo, N., Ellis, N. and Tang, L. (2019). *Seafarers and transnationalism in the twenty-first century.* Manchester: Manchester University Press.

Beaton, K., Cebotari, A., Ding, X. and Komaromi, A. (2017). Trade Integration in Latin America: A Network Perspective. *IMF Working Papers, 2017*(148). https://doi.org/10.5089/9781484303665.001

Blackwell, D. (1989). *The geometric domain model for maritime collision risk* (11), p.2092. https://doi.org/10.3390/jmse11152092

Calder, B. R. and Kurt, S. (2009). Traffic Analysis for the Assessment of Risk Assessment Methods. *US Hydrographic Conference, 22*, The Hydrographic Society of America.

Carson-Jackson, J. (2012). Satellite AIS – Developing Technology or Existing Capability? *The Journal of Navigation, 65*(2), pp. 303–321. https://doi.org/10.1017/S0373463311000684

Chen, P., Huang, Y., Mou, J. and van Gelder, P. H. A. J. M. (2019). Probabilistic risk analysis for ship-ship collision: State-of-the-art. *Safety Science, 117*, pp. 108–122.

COWI (2008). *Risk Analysis of Sea Traffic in the Area around Bornholm, 2008—VTT*. https://www.yumpu.com/en/document/read/35601367/risk-analysis-of-sea-traffic-in-the-area-around-bornholm-2008-vtt (last accessed 28 November 2020).

Eriksen, T., Høye, G., Narheim, B. and Meland, B. J. (2006). Maritime Traffic Monitoring Using a Space-Based AIS Receiver. *Acta Astronautica, 58*, pp. 537–549.

Feng, Y., Huang, D., Hong, X., Wang, H., Loughney, S. and Wang, J. (2025). Spatial-temporal evolution of maritime accident hot spots in the East China Sea: A space-time cube representation. *Journal of Marine Science and Engineering, 13*(2), 233. https://doi.org/10.3390/jmse13020233

Fujii, Y., Yamanouchi, H. and Mizuki, N. (1974). Some Factors Affecting the Frequency of Accidents in Marine Traffic. *Journal of Navigation, 27*, pp. 235–252.

Garson, G. D. (1991). Interpreting neural-network connection weights. *AI Expert, 6*(4), pp. 46–51.

Goerlandt, F. and Montewka, J. (2015). Maritime transportation risk analysis: Review and analysis in light of some foundational issues. *Reliability Engineering and System Safety, 138*, pp. 115–134.

IALA (2019). *Predicting Collision Frequencies.* International Association of Marine Aids to Navigation and Lighthouse Authorities, Staint Germain en Laye, France.

IMO (1972). *Convention on the International Regulations for Preventing Collisions at Sea (COLREGS).* International Maritime Organization, London, United Kingdom.

IMO (2012). *Convention on the International Maritime Organization, Part I – Purposes of the Organization, 1(c)*. International Maritime Organization, London, United Kingdom.

Jelavić, V., Brajović, M. and Tomaš, I. D. (2008). Analyses of State and Density of Traffic in the Port of Dubrovnik – Gruž. *Promet – Traffic – Traffico, 20*(3), pp. 189–193. https://doi.org/10.7307/ptt.v21i3.1001

Kaneko, F. (2002). Methods for probabilistic safety assessments of ships. *Journal of Marine Science and Technology, 7*, pp. 1–16.

Kristiansen, S. (2004). *Maritime Transportation Safety Management and Risk Analysis*. Oxford: Elsevier.

Kulkarni, K., Goerlandt, F., Li, J., Valdez Banda, O. and Kujala, P. (2020). Preventing shipping accidents: Past, present, and future of waterway risk management with Baltic Sea focus. *Safety Science, 129*, 104798. https://doi.org/10.1016/j.ssci.2020.104798

Langard, S. (2013). Human and Organisational Factors in Maritime Accidents: Analysis of Collisions at Sea Using the HFACS. *Accident Analysis and Prevention, 59*(May), pp. 26–37. https://doi.org/10.1016/j.aap.2013.05.006

Macduff, T. (1974). The Probability of Vessel Collisions. *Ocean Industry, 9*(9), pp. 144–148.

Maharaj, A. (2020). *Geo-statistical Analysis of Vessel Traffic in the Caribbean Sea* [MSc thesis, The University of the West Indies].

Maharaj, A. Miller, K. Davis, D. and Sutherland M. (2025). *Geostatistical analysis of maritime accidents: Identifying contributory factors and risk patterns in maritime navigation.* The International Hydrographic Review, 31(2), pp. 102–121. https://doi.org/10.58440/ihr-31-2-a10

MarineMarico (2013). *South-West Pacific Regional Hydrography Programme: LINZ Hydrography Risk Assessment.*

Mazaheri, A., Montewka, J. and Kujala, P. (2014). Modeling the Risk of Ship Grounding—a Literature Review from a Risk Management Perspective. *WMU Journal of Maritime Affairs, 13*(2), pp. 269–297. https://doi.org/10.1007/s13437-013-0056-3

Miller, K., Maharaj, A. and Seepersad, D. (n.d.). Computing the likelihood of collision of ships at sea from AIS data [Manuscript in preparation].

Montewka, J., Krata, P., Goerlandt, F., Mazaheri, A. and Kujala, P. (2011). Marine Traffic Risk Modelling: An Innovative Approach and a Case Study. *Proceedings of the Institution of Mechanical Engineers, Part O: Journal of Risk and Reliability, 225*(3), pp. 307–322. https://doi.org/10.1177/1748006X11399988

Pedersen, P. T. (2002). Traffic Simulation Based Ship Collision Probability Modeling. *Reliability Engineering and System Safety,*

96(1), pp. 91–107. https://doi.org/10.1016/j.ress.2010.09.003

Qu, X. and Meng, Q. (2012). Development and applications of a simulation model for vessels in the Singapore Straits. *Expert Systems with Applications, 39*, pp. 8430–8438.

Rawson, A. and Brito, M. P. (2022). A review of supervised machine learning for maritime risk and safety applications. *Transport Reviews, 42*(4), pp. 457–481. https://doi.org/10.1080/01441647.2022.2036864

Riding, J. and Rawson, A. (2015). *South-West Pacific Regional Hydrography Program: LINZ Hydrography Risk Assessment Methodology*. Report No: 15NZ322, Issue 03. Land Information New Zealand: Wellington, New Zealand.

Rodrigue, J. P. (2019). *The Expanded Panama Canal: Initial Impacts on North American Ports*. https://doi.org/10.13140/RG.2.2.13963.85281

Sabonge, R. (2014). *The Panama Canal Expansion: A Driver of Change for Global Trade Flows*. Documentos de Proyectos 37039, Naciones Unidas Comisión Económica para América Latina y el Caribe (CEPAL). http://repositorio.cepal.org/handle/11362/37039 (last accessed 21 September 2025).

Styliadis, T. and Koliousis, I. (2012). *Shipping accidents, damage assessment & accident consequences*. http://www.onthemosway.eu/wp-content/uploads/2015/06/ship-accidents-1final.pdf (last accessed 12 April 2017).

Supomo, H. and Nugroho, S. (2021). Cause of Ship Accident: A Literature Review. *IOP Conference Series: Earth and Environmental Science, 716*(1), 012007.

UNCTAD (2019). *Review of Maritime Transport 2019*. Geneva: United Nations.

Wilmsmeier, G. and Sánchez, R. J. (2009). *Maritime Sector and Ports in the Caribbean: The Case of CARICOM Countries*. https://www.cepal.org/es/node/22670 (last accessed 21 September 2025).

Yang, X., Zhu, Y., Zhou, T., Xu, S., Zhang, W., Zhou, X. and Meng, X. (2023). Integrating software FMEA and STPA to develop a Bayesian network-based software risk model for autonomous ships. *Journal of Marine Science and Engineering, 12*(1), 4. https://doi.org/10.3390/jmse12010004

Ylitalo, J. (2010). *Modelling Marine Accident Frequency* [MSc Thesis, Aalto University, Espoo, Finland].

Zhang, M., Teixeira, A. P., Guedes Soares, C. and Yan, X. (2021). Spatial pattern analysis of global ship accidents using AIS and GISIS data. *Reliability Engineering & System Safety, 210*, 107310. https://doi.org/10.1016/j.ress.2020.107310

Authors' biographies



Amrika Maharaj

Dr. Amrika Maharaj is a Lecturer in the Department of Geomatics Engineering & Land Management, Faculty of Engineering, The University of the West Indies. Her research focuses on spatial data analysis, geostatistics, and risk assessment, with emphasis on maritime navigation in the Caribbean Sea. Some of her current areas of research expertise include numerical modelling, GIS, remote sensing, hydrography, and maritime navigation studies.



Keith Miller

Dr. Keith Miller is a former lecturer at the University of the West Indies where he specialized in Geodesy and Hydrography, now retired and living in Trinidad and Tobago. He has worked as a lecturer at universities in the UK, Egypt and Australia. In a professional capacity, he was a member of the Chartered Institution of Civil Engineering Surveyors and served for eight years on the IBSC.

https://doi.org/10.58440/ihr-31-2-a11

Dr. Dexter Davis is a Lecturer in Geomatics Engineering and Head Department of Geomatics Engineering & Land Management. His research is focused on engineering surveying, digital photogrammetry and digital mapping, geodesy and geodetic applications, as well as GNSS and hydrographic surveying. Some of his current areas of research expertise include sea level monitoring and low cost and disaster relief mapping.



Dexter Davis

Dr. Michael Sutherland is currently an Adjunct Professor at the Department of Geodesy and Geomatics Engineering, University of New Brunswick. He was also a Professor of Land and Marine Administration Systems at the Department of Geomatics Engineering and Land Management, The University of the West Indies, St. Augustine Campus, Trinidad and Tobago. Dr. Sutherland has many years of direct and indirect geomatics-related research experience in the fields of GIS, multidimensional geospatial modelling, land and marine administration systems, climate change, and ocean governance.



Michael Sutherland

https://doi.org/10.58440/ihr-31-2-a11

PEER-REVIEWED ARTICLE

A comparative assessment of spatial regression methods for predicting maritime events in the Caribbean Sea

Authors

Amrika Maharaj[1], Keith Miller[1], Dexter Davis[1] and Michael Sutherland[1]

Abstract

Predicting maritime events requires spatially aware techniques that account for complex geographic and operational dynamics. By applying Geographic Weighted Regression, Generalized Linear Regression, Forest-Based Classification and Regression, and Empirical Bayesian Kriging, this research models the spatial distribution of vessel events across the Caribbean Sea. Key influencing variables include vessel traffic density, charted zone confidence, flag state, and vessel age. Results highlight regional hotspots such as the Panama Canal and Gulf of Paria. Comparative analysis demonstrates the strengths and limitations of each technique, informing the development of adaptive, location-specific maritime risk mitigation strategies.

Keywords

maritime accidents · geographic information systems · Caribbean Sea · regression techniques · vessel traffic density · automatic identification system

Resumé

La prévision des événements maritimes nécessite des techniques sensibles à la dimension spatiale, capables de prendre en compte la complexité des dynamiques géographiques et opérationnelles. En appliquant la régression pondérée géographique, la régression linéaire généralisée, la classification et la régression basées sur les forêts et le krigeage bayésien empirique, cette recherche modélise la diffusion spatiale des événements maritimes dans la mer des Caraïbes. Les principales variables influentes comprennent la densité du trafic maritime, la fiabilité des zones cartographiées, l'État du pavillon et l'âge des navires. Les résultats mettent en évidence des zones sensibles telles que le canal de Panama et le golfe de Paria. L'analyse comparative révèle les forces et les limites de chaque technique, contribuant à l'élaboration de stratégies adaptatives de réduction des risques maritimes, spécifiques à chaque localisation.

Resumen

La predicción de eventos marítimos requiere técnicas de conciencia espacial que tengan en cuenta las complejas dinámicas geográficas y operativas. Aplicando la Regresión Ponderada Geográficamente, la Regresión Lineal Generalizada, la Clasificación y Regresión Basadas en Bosques y el Kriging Bayesiano Empírico, esta investigación modela la distribución espacial de los eventos relacionados con buques en el Mar Caribe. Las variables clave que influyen incluyen la densidad del tráfico marítimo, la confianza en la zona cartografiada, el estado de abanderamiento y la edad del buque. Los resultados destacan puntos críticos regionales como el Canal de Panamá y el Golfo de Paria. El análisis comparativo demuestra las fortalezas y limitaciones de cada técnica, contribuyendo al desarrollo de estrategias adaptativas para mitigar los riesgos marítimos de cada localización específica.

✉ Amrika Maharaj · amrika.maharaj@hotmail.com

[1] Department of Geomatics Engineering and Land Management, The University of the West Indies, St. Augustine, The Republic of Trinidad and Tobago

https://doi.org/10.58440/ihr-31-2-a12

1 Introduction

The Caribbean Sea, a major corridor for international shipping and regional trade, faces persistent challenges related to maritime safety. With increasing vessel traffic, outdated navigational charts, and limited Aids to Navigation (AtoNs), the region is particularly vulnerable to navigation related accidents. Over the past two decades, maritime incident reports have highlighted recurring patterns influenced by spatial and operational risk factors, including high vessel density, inadequate AtoNs, and poorly charted areas (Maharaj et al., 2025). Understanding where and why maritime accidents occur is essential for effective risk mitigation and maritime domain awareness. Given the inherently spatial nature of these events, conventional analytical tools fall short of capturing the complex relationships between vessel traffic patterns, operational practices, and environmental hazards. Spatial statistical techniques, on the other hand, allow researchers and maritime authorities to quantify these relationships, identify incident-prone zones, and develop predictive insights that can inform proactive safety measures (Waller & Gotway, 2004; Pfeiffer, 1996; Fotheringham et al., 2002).

Despite the importance of maritime safety in the Caribbean, there remains a clear research gap: limited studies have systematically compared multiple spatial regression and machine learning approaches for predicting maritime events in this region. Much of the existing literature has focused on either global maritime accident trends or localized port-level analyses, leaving a lack of comparative, region wide evaluations of model performance and predictive capacity. This absence constrains the ability of decision makers to identify the most suitable modelling techniques for operational use in complex, heterogeneous maritime environments.

To address this gap, this paper analyses various regression methods that best capture spatial heterogeneity in maritime events across the Caribbean Sea, and how consistent hotspot patterns are across different modelling techniques. This is central for determining both the explanatory and predictive strengths of different approaches, and to guiding their practical application in regional maritime risk management. Accordingly, the objective of this study is to undertake a comparative assessment of four spatial prediction techniques, Geographically Weighted Regression (GWR), Generalized Linear Regression (GLR), Forest-Based Classification and Regression (FBCR), and Empirical Bayesian Kriging (EBK). By applying these methods to a database of maritime events and associated spatial covariates including traffic density, AtoNs, current velocity, navigational hazards, bathymetry, chart confidence (CATZOC), survey age, vessel flag state, and vessel age, this research evaluates their ability to identify high-risk zones and to explain underlying causal factors.

By benchmarking the performance of statistical, spatial, and machine learning approaches, this paper provides new insights into the suitability of different modelling frameworks for maritime accident prediction in geographically heterogeneous environments. The contribution of the study is threefold: (i) it advances understanding of how different spatial modelling techniques perform when applied to real-world maritime accident data; (ii) it highlights consistent and divergent hotspot patterns, thereby informing risk-based prioritization of maritime safety interventions; and (iii) it proposes a framework that can guide adaptive, geographically targeted strategies for enhancing navigational safety and reducing future maritime accidents. Ultimately, this work supports the development of evidence-based tools for maritime authorities to better anticipate, prepare for, and mitigate navigational risks in the Caribbean Sea.

2 Literature review: Spatial approaches to maritime incident modelling

Understanding maritime risk requires methods that go beyond simple attribute analysis. Spatial statistical models incorporate location and context, enabling the identification of incident clusters and causal relationships. These models handle both spatial and aspatial data, allowing for localized exploration of how risk factors vary geographically. The prediction and analysis of maritime incidents require modelling techniques that can capture both the spatial structure of data and the complex interactions between geographic and operational risk factors. Traditional statistical models often assume independence among observations and disregard the influence of location, rendering them insufficient for spatially dependent phenomena such as vessel incidents (Fotheringham et al., 2002). As a result, spatial statistical methods have emerged as essential tools for understanding maritime risk, particularly in geographically heterogeneous environments like the Caribbean Sea.

Spatial statistical techniques focus on identifying patterns, relationships, and dependencies among spatially distributed events and their associated attributes. These methods assume that "location matters" that the spatial distribution of events is not random but influenced by underlying environmental and operational conditions (Waller & Gotway, 2004). Maritime incidents, by their nature, are spatial events influenced by locational factors such as depth (bathymetry), traffic density, charting accuracy, proximity to AtoNs, proximity to navigational hazards and current velocity. Therefore, spatial analysis becomes a critical component in determining where incidents are more likely to occur and why. Spatial data consist of two components: geometry (location) and attributes (characteristics or measurements at that location). In contrast, aspatial data include only the latter (Pfeiffer, 1996). Methods developed for aspatial data analysis often fail when applied to spatial data due to spatial autocorrelation and non-stationarity the tendency for relationships between variables to vary across space

(Fotheringham et al., 2002).

To explore and quantify these relationships, a series of regression and machine learning techniques have been developed and applied to real world maritime accident data. The following subsections review the theoretical foundations and prior applications of four key methods used in this study: GWR, GLR, FBCR, and EBK. Collectively, these approaches provide the methodological backbone for our comparative analysis of maritime accident prediction, demonstrating effectiveness in revealing hidden spatial patterns, identifying high-risk zones, and generating actionable insights for navigation safety and risk mitigation strategies.

2.1 Regression techniques

To explore and quantify the relationship between maritime events and their contributing factors, a series of spatial and non-spatial regression techniques were employed. These methods are essential for understanding how risk variables such as traffic density, chart accuracy, vessel characteristics, and environmental conditions influence the likelihood of vessel events across the Caribbean Sea. Each technique offers a unique analytical lens: some allow for localized parameter estimation, while others emphasize statistical robustness or predictive accuracy. This section explains the theoretical foundations, assumptions, and implementation procedures of each technique as applied to the maritime accident dataset.

2.1.1 Geographic weighted regression

GWR is a spatial statistical technique designed to explore and model spatially varying relationships between a dependent variable and a set of independent variables (Charlton & Fotheringham, 2009). Unlike global regression models that assume a uniform relationship across an entire study area, GWR estimates local models at each spatial location, thereby capturing the heterogeneity in relationships that may exist across geographic space. In GWR, each local model is calibrated using a subset of data points that are geographically proximate to the location of interest. Observations closer to the target location are assigned higher weights in the regression analysis, typically using a spatial weighting function based on distance decay (Lin & Wen, 2011). This allows for the production of spatially adaptive regression coefficients that can reveal how explanatory variables influence the dependent variable differently from one location to another. For this study, GWR was applied to investigate the relationship between maritime incidents and their contributing factors across the Caribbean Sea. Given the region's diverse maritime geography and operational contexts, GWR provided an initial exploratory framework to assess whether these relationships varied spatially. This was particularly important in understanding how localized features such as traffic density, AtoNs, bathymetry, and charting accuracy contribute to the likelihood of maritime incidents (Weisent et al., 2012).

Mathematically, GWR extends the standard linear regression model by allowing the coefficients to vary at each spatial location. The GWR equation is expressed as:

$$y_i = \beta_0(u_i, vi) + \sum_k \beta_k(u_i, v_i)x_{ik} + \varepsilon_i \quad (1)$$

where:

- y_i is the dependent variable at location i (e.g., maritime incident occurrence),
- $\beta_k(u_i,v_i)$ are the location-specific coefficients for the k^{th} explanatory variable,
- (u_i,v_i) are the spatial coordinates of location i,
- x_{ik} are the values of the independent variables at location i, and
- ε_i is the residual or random error term at location i.

The estimated β coefficients describe how each explanatory factor influences the dependent variable at a specific location. The intercept term β_0 represents the expected value of y_i when all explanatory variables are zero, while the residual ε_i captures the portion of variation not explained by the model either due to unmeasured factors or random variation. By generating a distinct regression equation for each location within the study area, GWR reveals spatial variations in model structure and predictive relationships that global models often obscure. This makes it particularly effective for identifying regional maritime risk patterns and informing location-specific interventions. In the context of this research, GWR results were instrumental in mapping incident-prone areas and highlighting the spatial variability in how different covariates, such as vessel flag state or survey age of charts, contribute to risk.

2.1.2 Generalized linear regression

GLR is a flexible extension of classical linear regression designed to model relationships where the assumptions of normality and linearity do not hold. In the context of maritime risk assessment where the dependent variable (e.g., incident occurrence) is often non-normally distributed GLR offers a robust statistical framework for capturing complex, non-linear associations between maritime incidents and their causal factors (Awal & Hasegawa, 2017). At its core, GLR links the expected value (mean) of the dependent variable to a linear combination of independent variables through a *link function*. This function governs how the mean of the response variable relates to the linear predictor, allowing the model to accommodate a wide range of data types, including binary outcomes, count data, and skewed continuous variables (Jetz et al., 2005). The model is estimated using maximum likelihood estimation, which identifies the parameter values that best fit the observed data under the assumed probability distribution (Gao & Li, 2011). The GLR model assumes that the dependent variable follows a probability distribution from the exponential family, such as the normal,

https://doi.org/10.58440/ihr-31-2-a12

Poisson, or binomial distribution. The appropriate distribution is selected based on the characteristics of the response variable. For example, Poisson distribution is often used for count data, while binomial distribution applies to binary outcomes (e.g., incident occurred vs. did not occur). Once the link function and distribution are specified, GLR can be used to make predictions for new observations, interpret the strength and direction of predictor variables, and test hypotheses regarding statistical significance.

In this study, GLR was implemented to assess the global relationships between maritime accidents across the Caribbean Sea and a set of explanatory variables, including traffic density, navigational hazards, CATZOC, survey age, vessel flag, and vessel age. The technique proved particularly useful given the sparsity and variability of the incident data. It allowed for robust statistical inference by estimating coefficients, odds ratios, and confidence intervals enabling a clearer understanding of how each factor influences incident likelihood. Although GLR does not account for spatial heterogeneity treating the relationships as constant across the entire study area, its interpretability and adaptability make it a valuable component of the analytical framework. In this research, it provided a complementary perspective to localized models such as GWR and informed the identification of dominant risk factors at a global scale.

2.1.3 Forest-based classification and regression

FBCR is a supervised machine learning technique designed to model complex relationships between a set of explanatory variables and a dependent variable. Based on Leo Breiman's Random Forest algorithm, FBCR combines two approaches: Random Forest (RF) for classification problems and Regression Forest for regression problems (Scott & Bennett, 2012). In both cases, the method builds an ensemble of decision trees each trained on a randomly selected subset of the input data and variables and aggregates their outputs to produce a final prediction (ESRI, 2016). For classification tasks, the final prediction is typically derived through majority voting, whereas for regression problems, the predictions from all trees are averaged (Wilmsmeier et al., 2006). This ensemble approach allows FBCR to capture non-linear and high-dimensional relationships that traditional regression techniques may overlook. Moreover, the method is robust to outliers and missing data, making it particularly useful for working with real-world maritime datasets where data completeness and distribution may vary (Zhang et al., 2011). In this study, FBCR was implemented to generate predictive surfaces for maritime incidents across the Caribbean Sea. The training phase involved constructing a forest that models the relationship between the dependent variable (incident occurrence) and the independent variables, which included maritime traffic density, AtoNs, bathymetry, current velocity, navigational hazards, CATZOC, vessel flag, vessel age, and survey age of navigational charts (Jetz et al., 2005). During this phase, the model automatically excluded 10 % of the training data for validation purposes. Predictions generated for this excluded portion were then compared against observed values to assess model accuracy. A key output of the FBCR analysis was the Variable Importance table, which ranks explanatory variables based on their contribution to the model's predictive power. This importance is calculated using Gini coefficients, a measure reflecting how often a variable is used to split decision nodes and the relative impact of those splits across all trees in the forest (Su et al., 2012). Variables that appear more frequently in high-impact splits are considered more influential in predicting the outcome. FBCR's ability to handle complex interactions, high-dimensional data, and missing values while also producing interpretable outputs such as variable importance makes it a powerful tool for maritime risk modelling. Despite its advantages, however, the technique may be susceptible to overfitting, particularly in cases with sparse or highly imbalanced data. Therefore, model tuning and validation remain critical to ensuring reliable predictions. In this research, FBCR provided not only spatial predictions of incident likelihood but also insights into which factors contributed most significantly to those predictions, enhancing our understanding of maritime risk dynamics across the Caribbean Sea.

2.1.4 Empirical Bayesian Kriging

EBK is a geostatistical interpolation method designed to estimate values at unsampled locations by incorporating spatial autocorrelation and uncertainty into its predictions. It is an enhancement of traditional kriging, which estimates unknown values as weighted averages of observed data points. EBK improves upon this by automatically accounting for spatial heterogeneity and uncertainty in the model parameters through a Bayesian framework (Mainuri & Owino, 2017; Scott & Bennett, 2012). The core innovation of EBK lies in its use of Bayesian simulation to repeatedly estimate semivariogram models from subsets of the observed data. These simulated models reflect different plausible spatial structures and are averaged to produce a final predictive surface. This approach allows EBK to incorporate prior knowledge about spatial patterns and produce more robust predictions, especially in areas where the spatial structure varies significantly across the study region. In EBK, predictions at unsampled locations are based on observed data within a specified local neighborhood. Weights are assigned based on both geographic distance and the strength of spatial autocorrelation derived from the local semivariogram (Wang et al., 2013). Unlike traditional kriging, which typically fits a single global semivariogram for the entire dataset, EBK fits a unique local semivariogram for each neighborhood, making it highly responsive to spatial

heterogeneity. In the context of this study, EBK was applied to generate predictive surfaces of maritime incident likelihood across the Caribbean Sea. Its capacity to model local variation made it particularly well suited for interpolating across regions with sparse data, variable maritime infrastructure, and diverse navigational conditions. While EBK does not produce explicit regression coefficients or quantify the impact of individual variables, its strength lies in producing highly localized, accurate predictions that complement the explanatory power of other models such as GWR, GLR, and FBCR. As part of the broader modelling framework, EBK offered a valuable spatial perspective, especially in identifying incident-prone areas that may be underrepresented in the observed dataset. Its minimal reliance on user defined parameters and robust handling of nonstationary data further supports its application in maritime risk modelling.

3 Approach to spatial prediction

For the purpose of this study, the dependent variable was defined as the spatial occurrence of maritime events across the Caribbean Sea. The independent variables were identified through a quantitative analysis of maritime accident records from 2002 to 2021 obtained from the GISIS IMO database (Maharaj et al., 2025). Each accident report was examined to determine contributing causes, which informed the selection of the risk factors most relevant to navigation safety. These variables, vessel traffic density (transits), current velocity, proximity to navigational hazards, bathymetry, the location of AtoNs, and the quality and survey age of Admiralty nautical charts provided by the UK Hydrographic Office (UKHO), along with vessel flag state and vessel age represent a comprehensive set of physical, environmental, and operational elements influencing the likelihood of maritime events. The study area was delineated using the Caribbean Maritime Boundary Exclusive Economic Zone (EEZ), which provided a legally recognized and geographically bounded framework for analysis. Within this EEZ, a spatial grid was developed in ArcGIS Pro at a 1-kilometre resolution. This grid served as the foundational spatial unit for storing both the dependent and independent variable data in a standardized format. The choice of 1 km as the grid dimension was informed by an initial investigation into the distribution of maritime accident data. Given the relatively low number of recorded events in certain areas of the Caribbean Sea, a finer resolution was avoided to prevent sparse data issues and minimize the risk of multicollinearity among the explanatory variables.

The final dataset consisted of 302 grid cells, each representing a unique spatial unit across the Caribbean Sea (Fig. 1). These grid cells aggregated the aspatial attributes of the explanatory variables, enabling consistent input for all subsequent modelling techniques. Prior to model calibration, a multicollinearity diagnostic was conducted to assess the interdependencies among the explanatory variables. Multicollinearity, a condition in which two or more independent variables are highly correlated, can significantly inflate the standard errors of regression coefficients, leading to unreliable parameter estimates (Callaghan & Chen, 2008). Following established guidelines (Wheeler & Tiefelsdorf, 2005), variables were evaluated and transformed as necessary to ensure all predictor fields were numeric, continuous, and exhibited acceptable levels of variance. Binary variables, which typically exhibit weak collinearity, were retained where applicable, while highly collinear continuous variables were excluded or restructured. Given that some regression techniques used in this study, such as GWR, are not suited for binary outcome prediction, care was taken to ensure that the dependent variable remained continuous and appropriately distributed for the chosen modelling approaches. This rigorous data preparation process ensured the analytical integrity and statistical robustness of all subsequent regression and machine learning models.

4 Results of regression techniques

The results of the GWR model provided spatial insights into where maritime incidents are most likely to occur across the Caribbean Sea. Fig. 2 illustrates the spatial distribution of predicted incident probabilities, highlighting key maritime zones with statistically significant co-movements between the dependent and independent variables. The fitted values derived from the regression equation are presented as p-values, with darker shades indicating areas of high incident likelihood.

The model revealed that strong correlations both positive and negative exist across different regions. Notably, areas with the highest probability of incident occurrence included:

- The Panama Canal region
- Waters north of Trinidad
- The vicinity of Grenada, St. Lucia, the British Virgin Islands, and Jamaica

These regions are characterized by “under-predictions” locations where actual incident counts exceed model estimates. Conversely, lighter shaded areas represent “over-predictions”, where the model estimates exceed the observed incident volumes.

The GWR model produces several spatial diagnostics to evaluate the performance and reliability of the regression results. The diagnostics derived from the GWR model provide valuable insights into the reliability and performance of the regression analysis. The condition number values indicated that multicollinearity was not present in the model, as all values remained below the threshold commonly associated with unstable estimates. This suggests that the explanatory variables were sufficiently independent to produce robust parameter estimates. The local R^2 values, which quantify how well the model explains

https://doi.org/10.58440/ihr-31-2-a12

variation in the dependent variable across space, varied throughout the study area. Higher values were observed in key maritime zones, indicating strong model performance and good predictive fit in these regions, while lower values in other areas suggest reduced explanatory power. Standardized residuals, representing the difference between observed and predicted values, were generally low in regions with a high local R^2, indicating accurate model predictions. However, isolated areas showed higher residuals, reflecting local deviations that the model could not fully explain. Finally, the spatial variation in regression coefficients highlighted the heterogeneity in the strength and direction of relationships between the explanatory variables and the occurrence of maritime incidents. These locally varying coefficients underscore the importance of accounting for geographic context when assessing maritime risk, as the influence of specific variables changes significantly across the Caribbean Sea.

The GWR model yielded significant parameter estimates for nine explanatory variables, each characterized by a direction (sign) and strength (magnitude). A positive coefficient indicates that an increase in the respective variable is associated with a corresponding increase in the likelihood of a maritime incident, while a negative coefficient suggests a mitigating effect. The magnitude of the parameter reflects the degree of influence that a one-unit change in the variable has on the dependent outcome (Chang et al., 2008). Among the most influential factors, the analysis revealed that regions surrounding the Panama Canal exhibited the strongest associations, particularly for vessel flag state, survey age of nautical charts (CATZOC), and vessel traffic density (Table 1). These same variables were also prominent in other high-risk locations such as northwest Trinidad and Jamaica. Interestingly, current velocity and CATZOC values in the Panama Canal area contributed less to incident prediction relative to other factors. GWR produces a surface of parameter estimates, allowing the model to capture spatial changes in the magnitude of influence for each covariate. This ability to reflect the locally varying strength of relationships is central to the concept of spatial heterogeneity. In some locations, certain variables exert a much stronger influence on the dependent variable than in others. Conversely, parameter estimates close to zero are often spatially clustered, indicating that in those regions, changes in the respective variables have little to no effect on incident likelihood. These clusters may result from uniform local conditions, weak variable variance, or the absence of relevant interactions. Such spatial dynamics invite deeper exploration into the processes shaping maritime risk and underscore the importance of localized modelling in revealing nuanced patterns that global models may obscure. Together, these findings enrich the understanding of the region's risk



Fig. 1 302 grid cells within the Caribbean Sea EEZ.

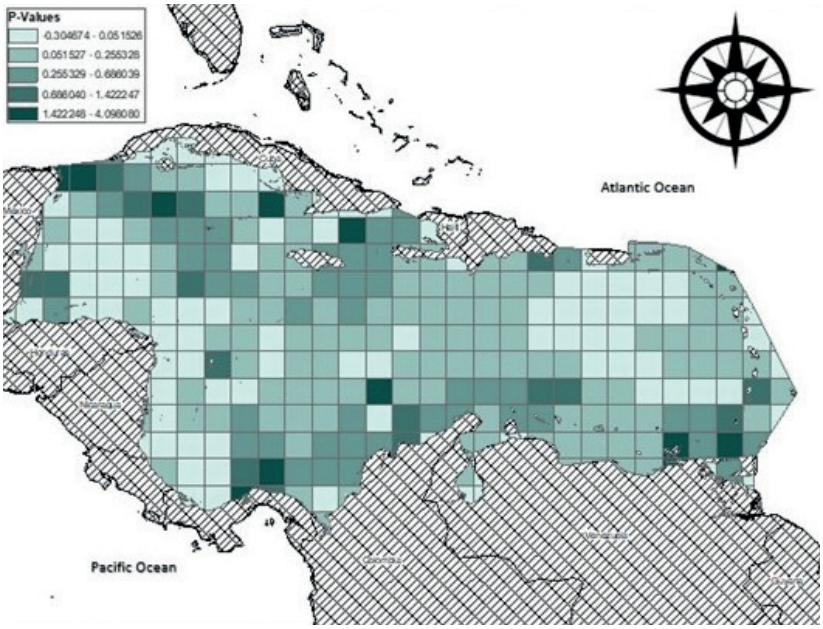


Fig. 2 GWR P-values.

Table 1 Parameter estimates of hotspot locations.

Coefficients current velocity	Coefficients traffic density	Coefficients CATZOC	Coefficients survey age	Coefficients flag state	Location
-0.089040303	0.0000839	-0.030459982	0.02242219	0.644299132	Panama Canal
-0.115263682	0.0000818	-0.037947247	0.022592015	0.630958731	NW, Trinidad
-0.092792259	0.0000860	-0.031691154	0.02369738	0.649360068	Jamaica
-0.136586501	0.0000819	-0.044245746	0.024081995	0.625691053	British Virgin Islands
-0.154913036	0.0000913	-0.04870322	0.03102929	0.653840374	Grenada

landscape and highlight the practical utility of GWR in informing maritime safety interventions across diverse operational environments.

The GLR approach provided a global view of the relationships between the dependent variable and its predictors, offering valuable insights into which factors most strongly influence the likelihood of incidents across the Caribbean Sea. Among the variables assessed, vessel flag state, vessel age, and the CATZOC emerged as the most influential contributors to the dependent variable. Notably, traffic density was found to be statistically significant, indicating a robust and direct association with incident likelihood. The model also generated odds ratios to interpret the strength of association for each variable. An odds ratio greater than one suggests that increased exposure to a given variable elevates the probability of an incident occurring. In this study, variables such as traffic density, AtoNs, current velocity, CATZOC, vessel age, and flag state exhibited odds ratios above one, underscoring their importance in predicting risk (Table 2). Conversely, variables with odds ratios close to or below one, such as survey age and bathymetry, were associated with either minimal or inverse effects. Further diagnostics were used to assess model reliability. The Wald's Chi-Squared test confirmed the statistical significance of the explanatory variables included, validating their relevance within the GLR framework. Additionally, the Variance Inflation Factor (VIF) was calculated to evaluate multicollinearity among predictors. All VIF values were well below the threshold of 10, indicating that collinearity did not undermine the model's stability. For example, the survey age variable showed a VIF of approximately 1.8, suggesting moderate inflation but not to a degree that would compromise the results. The spatial prediction output of the GLR model revealed high-risk areas across the Caribbean, with particular concentration around maritime corridors such as the Panama Canal, the Gulf of Paria (Trinidad), Grenada, St. Vincent and the Grenadines, St. Lucia, Antigua, Montserrat, the British Virgin Islands, Jamaica, and Belize (Fig. 3). These locations were identified as zones with a high probability of incident occurrence based on the values of the explanatory variables. In contrast, areas classified with low, or zero probability were primarily situated in open sea regions, where maritime activity and associated risk factors are comparatively minimal.

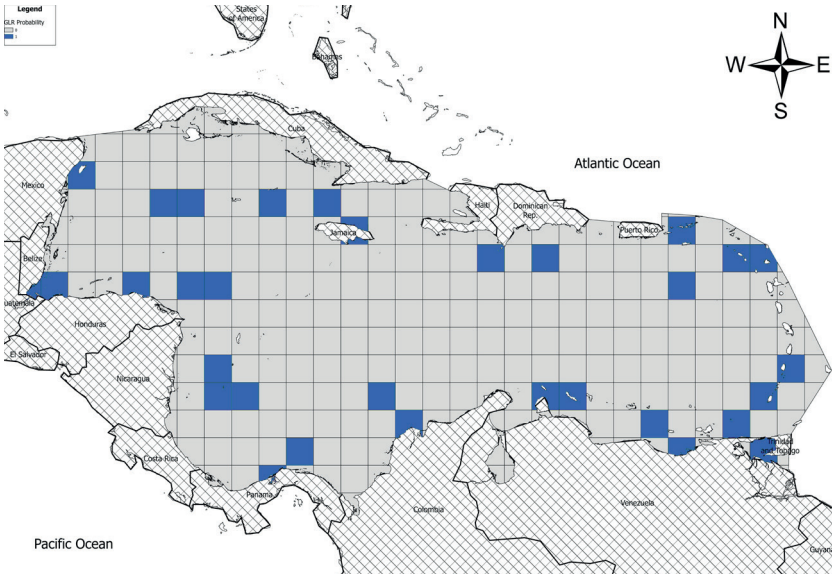


Fig. 3 Prediction surface generated using GLR.

The FBCR model provided critical insight into the relative influence of each explanatory variable in predicting maritime incident risk across the Caribbean Sea. Variable importance was determined using the sum of Gini coefficients generated from all decision trees in the model. These values indicate how frequently and effectively each variable contributed to data splits within the forest, offering a robust diagnostic for understanding which inputs drive the model's predictions. According to the analysis, traffic density was identified as the most influential variable, accounting for 15 % of the model's total predictive power. This was followed closely by the location of Aids to Navigation (13 %), navigational hazards (12 %), and CATZOC (12 %). It is important to note that variable importance measures do not reflect model accuracy unlike metrics such as R^2 used in regression analysis but rather indicate the contribution of each variable to the predictive decision-making process. The FBCR model's prediction results aligned closely with the outputs of GWR and GLR, identifying a consistent set of high-risk locations. These included the Panama Canal, Gulf of Paria, Trinidad, Grenada, St. Vincent and the Grenadines, St. Lucia, Montserrat, Antigua, British Virgin Islands, Jamaica, and Belize. The similarity in prediction trends across models strengthens the reliability of the identified hotspots and highlights the spatial coherence of incident-prone areas in the region (Fig. 4). FBCR thus reinforces the value of ensemble decision-tree approaches in revealing dominant maritime risk factors and supporting targeted mitigation efforts across the Caribbean Sea.

The EBK model produced a predictive surface that highlights spatial variations in the likelihood of maritime incidents across the Caribbean Sea. The model identified several high-risk areas, characterized by a higher probability of incident occurrence, particularly in regions surrounding the Panama Canal, Gulf of Paria, Trinidad, Grenada, St. Vincent and the Grenadines, St. Lucia, Montserrat, Antigua, British Virgin Islands, Jamaica, and Belize (Fig. 5). These areas exhibited elevated prediction values compared to surrounding open sea regions, which were associated with lower risk levels. The EBK output demonstrated strong alignment with the prediction patterns generated by the other regression techniques applied in this study, namely GWR, GLR, and FBCR. This consistency reinforces the validity of the identified hotspots and confirms the robustness of spatial interpolation methods in capturing underlying spatial patterns of maritime risk. EBK's ability to model local

https://doi.org/10.58440/ihr-31-2-a12

Table 2 GLR coefficient diagnostic.

Variable	Coefficient [a]	StdError	Z-statistic	Probability [b]	Odds ratio [c]	Wald's low (95 %) [d]	Wald's high (95 %) [d]	VIF [e]
Intercept	-2.302016	3.670614	-0.627147	0.530563	0.100057	0.000075	133.271415	-
Survey age	-0.914001	0.732144	-1.24839	0.211888	0.400917	0.095464	1.683713	1.867827
Navigational hazards	-0.004042	0.006317	-0.639797	0.522305	0.995967	0.983711	1.008375	1.78854
Bathymetry	-0.000004	0.000276	-0.013114	0.989537	0.999996	0.999456	1.000537	1.145088
Traffic density	0.000348	0.000129	2.695553	0.007027*	1.000348	1.000095	1.000602	1.077603
Atons	0.021859	0.029867	0.731878	0.464243	1.022099	0.963985	1.083717	1.740065
Current velocity	0.090804	0.882044	0.102947	0.918005	1.095055	0.194368	6.169459	1.347341
CATZOC	0.593922	0.530677	1.119178	0.263064	1.811077	0.640053	5.124575	1.046801
Age of vessel	13.825304	4075.428641	0.003392	0.997293	1009841.863	0.941245	1.000602	1.502486
Flag of vessel	25.26346	5005.806328	0.005047	0.995973	93708958281	0.847512	1.002513	1.509231

variations in spatial autocorrelation allowed for a nuanced depiction of incident-prone zones, particularly in areas where observed incident data were sparse or unevenly distributed. As a result, the model effectively contributes to a more comprehensive understanding of regional maritime safety dynamics and supports the development of targeted risk mitigation strategies.

6 Discussion

Maritime accidents, regardless of their nature, remain one of the most significant threats to seafarers and shipping operations (Maharaj, 2017). Whether occurring in confined or open waters, the risks are heightened in regions characterized by dense vessel traffic, poorly charted waters, inadequate AtoNs, and the presence of navigational hazards. Despite advancements in satellite-based navigation and precision technology, maritime casualties continue to occur (Calle & Alves, 2015). As such, the ability to model and predict areas vulnerable to vessel incidents is essential to reducing risk and improving maritime safety. This research demonstrated that specific causal factors when concentrated geographically can significantly increase the probability of incidents, thereby creating identifiable hotspots across the Caribbean Sea. To assess these relationships and predict incident-prone areas, four spatial modelling techniques were applied: GWR, GLR, FBCR, and EBK. GWR, GLR, and FBCR produced localized parameter estimates, enabling the capture of spatial heterogeneity and revealing complex relationships between maritime incidents and their explanatory variables (Gao & Li, 2011). Key variables such as traffic density, flag state, vessel age, CATZOC, and survey age emerged as dominant contributors across all models. GWR highlighted the influence of current velocity, GLR identified flag state as the most significant statistical contributor, and FBCR emphasized traffic density as the most impactful variable. Although EBK did not produce explicit parameter estimates, it delivered reliable spatial predictions that closely mirrored the outputs of the other models.

All four techniques identified high-risk zones, particularly around the Panama Canal, Gulf of Paria, Trinidad, Grenada, St. Lucia, Jamaica, and the British Virgin Islands. While GWR, GLR, and FBCR were effective in revealing variable-specific contributions

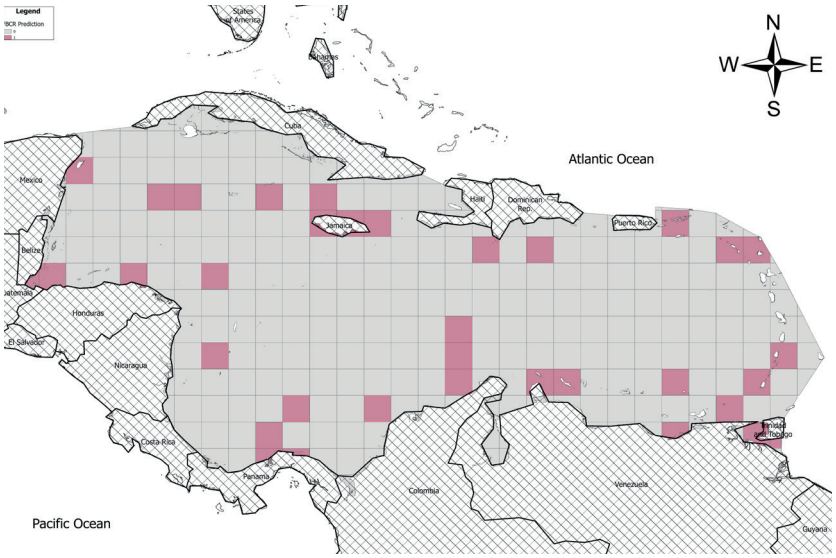


Fig. 4 Prediction surface generated using FBCR regression.

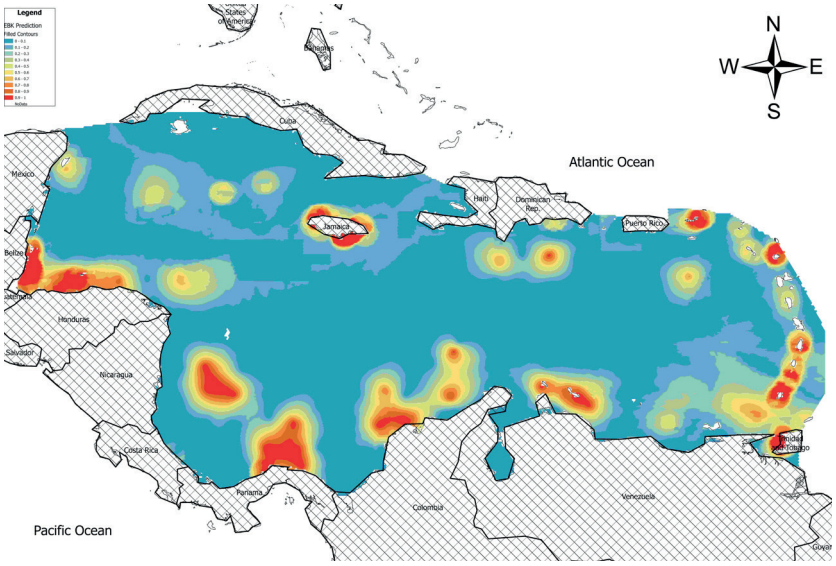


Fig. 5 Prediction surface generated using EBK regression.

and spatial trends, their ability to account for highly localized dynamics was limited. EBK, on the other hand, excelled in generating spatially adaptive predictions without requiring complex model configurations, making it especially useful when incident data are sparse or exhibit moderate nonstationarity. However, each method showed notable limitations. GLR assumes a linear relationship and a normally distributed dependent variable assumptions not satisfied by the maritime incident data. While FBCR was more suited to non-linear relationships, its performance can be hindered by data sparsity and overfitting. EBK, although spatially flexible, does not estimate the strength or direction of explanatory variable effects and therefore lacks interpretability for causal analysis. GWR, while spatially explicit, is sensitive to multicollinearity and may produce unstable coefficients in areas with limited data. The analysis further revealed that conventional regression models face challenges when applied to real-world maritime risk data. These models often require the aggregation of point-based incident data into spatial units, which can reduce precision. Moreover, their statistical assumptions and sensitivity to data quality can limit their applicability in operational decision-making. It was also observed that regression-based approaches are not well suited for complex, spatially variable phenomena, such as maritime incidents influenced by interacting environmental and operational factors.

More critically, the study confirmed several key limitations of the regression techniques:

1. The GIS-derived covariates, though essential for spatial modelling, were not always suitable for statistically robust regression outcomes.
2. Spatial heterogeneity was evident but poorly captured by traditional methods.
3. The models lacked capacity to make causal inferences or to identify interactions between variables.
4. Spatial autocorrelation introduced bias in traditional models, leading to potential overcounting effects.
5. Improvements in data quality, frequency, and granularity are needed to support more accurate spatial modelling of maritime incidents.

The findings of this research underscore the limitations of traditional regression models in capturing the full complexity of maritime incident risk. While techniques such as GWR, GLR, FBCR, and EBK are valuable for exploratory spatial analysis and identifying general trends, they fall short when it comes to modelling the intricate, non-linear, and multi-dimensional interactions that characterize real-world maritime environments. These methods are constrained by assumptions of linearity, normality, and spatial stationarity assumptions rarely satisfied in dynamic coastal and open-sea environment. As such, they should be regarded as supportive analytical tools rather than definitive predictors of risk. To address these shortcomings, more sophisticated approaches and advanced modelling techniques can offer a powerful alternative (Maharaj et al., 2025). These alternative techniques are not bound by rigid statistical assumptions and are capable of learning complex, hidden relationships within the data. Their ability to model non-linear behaviours and adapt to spatial and operational variability makes them especially well-suited for risk prediction in heterogeneous maritime regions like the Caribbean Sea. Potential techniques include artificial intelligence and machine learning approaches such as gradient boosted trees, support vector machines, deep neural networks, and ensemble learning; spatio-temporal models such as Bayesian hierarchical frameworks and spatial panel regression; and hybrid approaches that combine AIS trajectory mining with environmental and operational data. Incorporating such advanced methods allows for a more robust, data-driven modelling framework, one that aligns more closely with the realities of maritime navigation and safety planning.

7 Conclusion

Understanding where and why maritime incidents occur is essential to improving navigational safety and risk mitigation across the Caribbean Sea. The application of spatial regression techniques, GWR, GLR, FBCR, and EBK offered valuable insights into the geographic distribution of risk and the influence of key operational and environmental variables. Factors such as traffic density, vessel flag state, age of navigational charts, and proximity to hazards consistently emerged as significant across the models. However, while these methods proved useful for exploratory spatial analysis and surface-level prediction, they fell short in capturing the deeper, non-linear, and interactive dynamics that characterize real-world maritime risk. Their reliance on assumptions of normality, linearity, and fixed spatial relationships limits their effectiveness, especially in complex and data-sparse environments like the Caribbean. The inability to model variable interactions or adapt to rapidly changing maritime conditions further constrains their operational utility. These findings highlight the importance of adopting more advanced modelling frameworks that go beyond traditional regression. Unlike regression models, advance modelling techniques can accommodate non-linear, high dimensional relationships and uncover latent patterns within data, offering a more robust and adaptive tool for maritime risk prediction. In moving toward a hybrid spatial modelling approach one that combines the interpretability of regression techniques with the predictive capabilities of machine learning researchers and maritime authorities can develop more precise, targeted, and data informed strategies to enhance safety at sea. The lessons learned from this comparative analysis serve as a stepping stone for advancing predictive analytics in the maritime domain, with the ultimate goal of fostering safer, smarter navigation throughout the region.

https://doi.org/10.58440/ihr-31-2-a12

References

Awal, Z. I. and Hasegawa, K. (2017). A study on accident theories and application to maritime accidents. *Procedia Engineering, 194*, pp.298–306. https://doi.org/10.1016/j.proeng.2017.08.149

Callaghan, K. and Chen, J. (2008). Revisiting the collinear data problem: An assessment of estimator 'ill-conditioning' in linear regression. *Practical Assessment, Research and Evaluation, 13*(5), pp. 1–6.

Calle, M. A. G. and Alves, M. (2015). A review-analysis on material failure modeling in ship collision. *Ocean Engineering, 106*, pp.20–38. https://doi.org/10.1016/j.oceaneng.2015.06.032

Charlton, M. and Fotheringham, A. S. (2009). Geographically weighted regression: White paper. *White Paper,* pp. 1–17. https://doi.org/10.1111/1467-9884.00145

ESRI (2016). Esri Training – Getting started with ArcGIS Pro. http://training.esri.com/gateway/index.cfm?fa=catalog.webCourseDetail&courseid=2889 (last accessed 26 March 2025).

Fotheringham, A. S., Brunsdon, C. and Charlton, M. (2002). *Geographically weighted regression: The analysis of spatially varying relationships.* Chichester: John Wiley & Sons.

Gao, J. and Li, S. (2011). Detecting spatially non-stationary and scale-dependent relationships between urban landscape fragmentation and related factors using geographically weighted regression. *Applied Geography, 31(*1), pp. 292–302. https://doi.org/10.1016/j.apgeog.2010.06.003

Jetz, W., Rahbek, C. and Lichstein, J. W. (2005). Local and global approaches to spatial data analysis in ecology. *Global Ecology and Biogeography, 14*(1), pp. 97–98. https://doi.org/10.1111/j.1466-822X.2004.00129.x

Lin, C. H. and Wen, T. H. (2011). Using geographically weighted regression (GWR) to explore spatial varying relationships of immature mosquitoes and human densities with the incidence of dengue. *International Journal of Environmental Research and Public Health, 8*(7), pp. 2798–2815. https://doi.org/10.3390/ijerph8072798

Mainuri, G. and Owino, J. O. (2017). Spatial variability of soil aggregate stability in a disturbed river watershed. *European Journal of Economics and Business Studies, 3*(3), pp. 278–290.

Maharaj, A. (2017). *Geo-statistical analysis of marine traffic in the Gulf of Paria* [MSc thesis, Department of Geomatics Engineering and Land Management, The University of the West Indies].

Maharaj, A., Miller, K., Davis, D. and Sutherland, M. (2025). Geostatistical analysis of maritime accidents: Identifying contributory factors and risk patterns in maritime navigation. *The International Hydrographic Review, 31*(2), pp. 102–121, https://doi.org/10.58440/ihr-31-2-a10

Pfeiffer, D. U. (1996). Issues related to handling of spatial data. *Proceedings of the Epidemiology and State Veterinary Programmes, New Zealand Veterinary Association / Australian Veterinary Association Second Pan-Pacific Veterinary Conference.* Christchurch, New Zealand. ftp://131.252.97.79/Transfer/ES_Pubs/ESVal/spatial_statistics/issues_related_to_spatial_data.pdf (last accessed 10 November 2015).

Scott, L. M. and Bennett, L. R. (2012). Modeling spatial relationships using regression analysis. *ESRI International User Conference.*

Su, C. M., Chang, K. Y. and Cheng, C. Y. (2012). Fuzzy decision on optimal collision avoidance measures for ships in vessel traffic service. *Journal of Marine Science and Technology, 20*(1), pp. 38–48.

Waller, L. A. and Gotway, C. A. (2004). *Applied spatial statistics for public health data.* New Jersey, NY: Wiley & Sons.

Wang, H., Jiang, H. and Yin, L. (2013). Cause mechanism study to human factors in maritime accidents: Towards a complex system brittleness analysis approach. *Procedia - Social and Behavioral Sciences, 96*, pp. 723–727. https://doi.org/10.1016/j.sbspro.2013.08.083

Weisent, J., Rohrbach, B. and Dunn, J. R. (2012. Socioeconomic determinants of geographic disparities in campylobacteriosis risk: A comparison of global and local modeling approaches. *International Journal of Health Geographics, 11*(1), p. 45.

Wilmsmeier, G., Hoffmann, J. and Sanchez, R. J. (2006). The impact of port characteristics on international maritime transport costs. *Research in Transportation Economics, 16*, pp. 117–140. https://doi.org/10.1016/S0739-8859(06)16006-0

Zhang, C., Tang, Y., Xu, X. and Kiely, G. (2011). Towards spatial geochemical modelling: Use of geographically weighted regression for mapping soil organic carbon contents in Ireland. *Applied Geochemistry, 26*(7), pp. 1239–1248. https://doi.org/10.1016/j.apgeochem.2011.04.014

Authors' biographies

Dr. Amrika Maharaj is a Lecturer in the Department of Geomatics Engineering & Land Management, Faculty of Engineering, The University of the West Indies. Her research focuses on spatial data analysis, geostatistics, and risk assessment, with emphasis on maritime navigation in the Caribbean Sea. Some of her current areas of research expertise include numerical modelling, GIS, remote sensing, hydrography, and maritime navigation studies.



Amrika Maharaj



Keith Miller

Dr. Keith Miller is a former lecturer at the University of the West Indies where he specialized in Geodesy and Hydrography, now retired and living in Trinidad and Tobago. He has worked as a lecturer at universities in the UK, Egypt and Australia. In a professional capacity, he was a member of the Chartered Institution of Civil Engineering Surveyors and served for eight years on the IBSC.



Dexter Davis

Dr. Dexter Davis is a Lecturer in Geomatics Engineering and Head Department of Geomatics Engineering & Land Management. His research is focused on engineering surveying, digital photogrammetry and digital mapping, geodesy and geodetic applications, as well as GNSS and hydrographic surveying. Some of his current areas of research expertise include sea level monitoring and low cost and disaster relief mapping.



Michael Sutherland

Dr. Michael Sutherland is currently an Adjunct Professor at the Department of Geodesy and Geomatics Engineering, University of New Brunswick. He was also a Professor of Land and Marine Administration Systems at the Department of Geomatics Engineering and Land Management, The University of the West Indies, St. Augustine Campus, Trinidad and Tobago. Dr. Sutherland has many years of direct and indirect geomatics-related research experience in the fields of GIS, multidimensional geospatial modelling, land and marine administration systems, climate change, and ocean governance.

https://doi.org/10.58440/ihr-31-2-a12

NOTE / TECHNICAL REPORT

Bathymetry in caves

Authors
Guy Van Rentergem[1] and Sofie de Volder[2]

1 Introduction

The global water cycle is of vital importance to life on Earth (Poeter et al., 2020). It is the process by which freshwater continuously moves through the oceans, atmosphere and land. The oceans contain an astonishing 97.5 % of the planet's water. However, due to its high salinity, this vast quantity of seawater cannot be used directly as freshwater. Natural desalination of seawater is powered by the sun's energy and happens through evaporation. The water enters the atmosphere as vapour, leaving the salts behind. The water then condenses into clouds, which release rain or snow onto the land, replenishing rivers and lakes with fresh water.

Only 2.5 % of the planet's water reserves are freshwater. A large proportion of this, 69 %, is locked in glaciers and the polar regions as ice. It is estimated that only 1.2 % of this freshwater is found in rivers, lakes and swamps. So where is the remainder? Around 30 % of the world's freshwater reserves are stored beneath the Earth's surface as groundwater. If we ignore the ice, an impressive 99 % of all liquid freshwater is groundwater. Therefore, of all the water on Earth, both seawater and freshwater, only a tiny fraction, less than 1 %, is accessible liquid freshwater. This groundwater flows through aquifers. These are permeable geological layers of sand, gravel or fractured rock. Flowing through these porous materials is considered slow, and finer materials, such as sand, act as natural filters for contaminants.

2 Karst aquifers

Karst landscapes are home to a particular type of aquifer. This type of landscape forms in regions with soluble rock, such as limestone, dolomite and gypsum. One of the defining features of karst is the absence of surface rivers. The dissolution of these rocks allows water to infiltrate into vast underground drainage systems. Around 20 % of the Earth's total land surface is covered by karst, and karst aquifers supply water to over 25 % of the global population. Karst aquifers can transport large quantities of water very quickly. Unlike other types of aquifers, such as those found in sand and gravel, karst aquifers do not have filtering capacities. Consequently, pollution can spread quickly. This makes the careful study and management of karst aquifers particularly important. The presence of caves can sometimes allow access to these important aquifers.

Working in caves is demanding on both people and equipment due to its peculiarities. Therefore, an unsinkable, remote-controlled, portable boat (Fig. 1) was built to map difficult-to-reach underground drainage systems. It is equipped with a single-beam echo sounder (SBES), the Ping2 from Blue Robotics and two Blue Robotics T200 thrusters.

3 No GPS in caves

Ocean survey vessels use GPS to determine their exact location. This data, combined with sonar depth readings, is used to create seafloor maps. However, GPS does not work in caves, so an alternative localisation system must be used. We use a two-way ranging (TWR) real-time location system (RTLS) based on the ultra-wideband (UWB) transceiver module DWM1001C from Qorvo. These devices exchange ultra-short 6.5 GHz (channel 5) pulses and calculate round-trip times to determine distances. Our setup includes six fixed UWB anchors and a UWB tag mounted on the boat. The exact positions of the anchors must be known and are measured using a LiDAR scanner. The distances between the anchors and the tag are recorded several times per second and saved together with the sonar data on an SD card. Back in the office, we use our own software, which uses multilateration and Kalman filtering, to calculate the boat's position in relation to the fixed anchors. With this setup, we can cover a 100-metre stretch of water. This is significant in caves. The ranging accuracy falls to within 20 cm.

✉ Guy Van Rentergem · guy.van.rentergem@skynet.be
[1] GVR 3D Tech, Deinze, Belgium
[2] TRAQUA SA, Namur, Belgium

https://doi.org/10.58440/ihr-31-2-n10

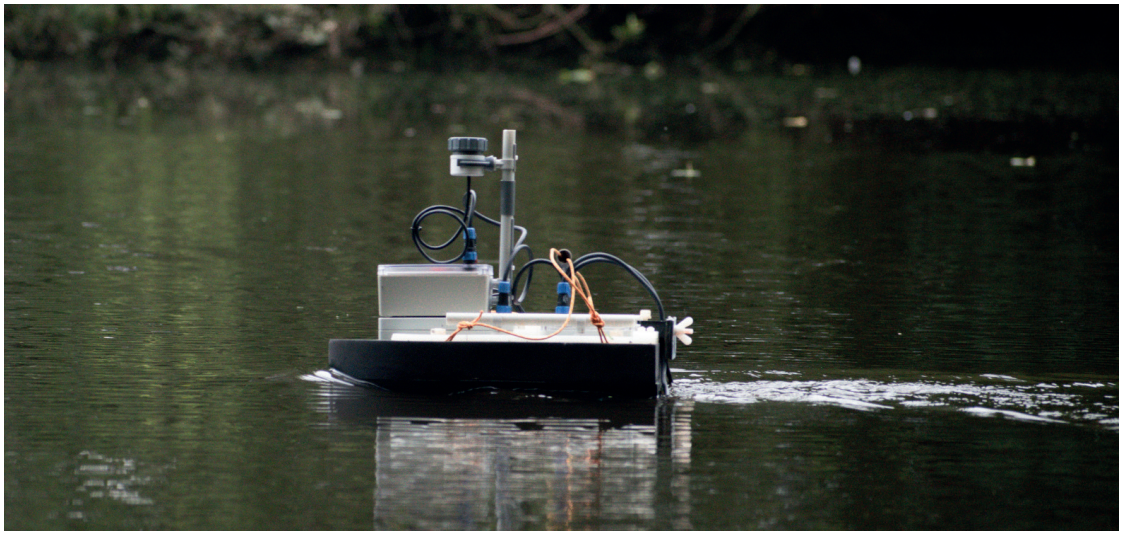


Fig. 1 This is a side view of the small sonar EVA boat measuring only 540 mm × 380 mm × 220 mm. The pod on the mast houses the UWB receiver.

4 A cave-proof construction

Since cave passages can be very narrow, the boat must be small. Measuring just 540 mm × 380 mm × 220 mm and weighing only 7 kg, it can easily be stowed in an airline suitcase or backpack (Fig. 2). It is also built to withstand serious wear and tear when being dragged through caves. After considering materials such as acrylonitrile butadiene styrene (ABS) and polyester plastics for the hull, the rather unusual material Ethylene-vinyl acetate (EVA) foam was chosen. This closed-cell material is lightweight, flexible, chemically resistant, highly durable and easy to work with. It is the same material used in running shoes, for example.

Another basic requirement was that the construction should be simple and use readily available parts, to make assembly and repair in the field easier. The boat's hull is made of two 50 mm-thick, low-density EVA foam blocks (EVA-45 kg) sandwiched between two 10 mm-thick polyethylene (HDPE) boards. The construction is held together with four 10 mm threaded nylon rods. Two compartments cut into the EVA foam tightly fit two water-resistant boxes that house the batteries and electronics. These enclosures are made of polycarbonate or a similar plastic, with a minimum ingress protection class of IPX5. IPX5 provides protection against water jets. Higher protection ratings, such as IPX7 or IPX8, are unnecessary as this is not a submarine. The boat only needs to be protected against the occasional splash of water, which makes it cheaper to build.

5 Power supply

Batteries are another important component of a boat. Due to their weight and size, they significantly impact the boat's stability and usability. Nickel-metal hydride (NiMH) batteries are used for power. Although lithium polymer (LiPo) or lithium-ion batteries have a higher energy density and are much lighter, they have one major drawback. They are classified as dangerous goods by airlines due to a potential fire risk, so size, number and packaging limits are imposed. We aren't as concerned about weight with a boat as we would be with a drone or an RC airplane. In fact, a boat can benefit from some extra weight to go deeper into the water and become more stable. The system has two separate battery circuits. One delivers higher voltage and more power for propulsion, while the other, with lower voltage, powers the sonar and other electronics. This separation prevents brownouts. If all circuits were on the same power rail, a sudden high current demand from the motors could cause a voltage dip and reset of the built-in controllers, which would ruin the measurements.

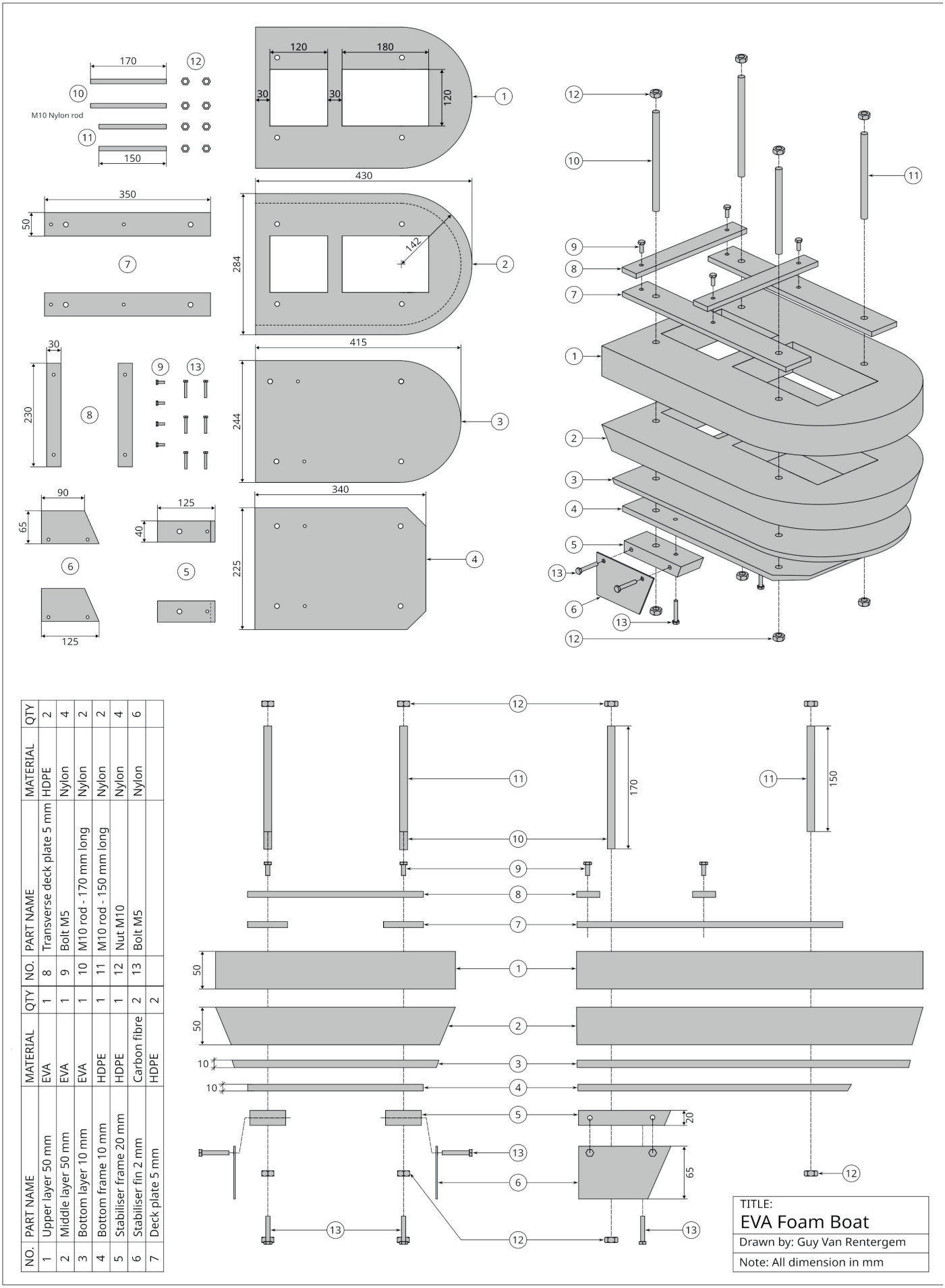
6 Conclusion

A sturdy and versatile small survey platform that works very well in caves and other extreme or remote locations can be built using simple materials. For example, this mini sonar boat has been deployed in 'Laguna Caliente', the hyperacidic (pH 0.5) and hot (55 °C) crater lake of the Poás Volcano in Costa Rica. As we did not want to use our thrusters in such an extreme environment, we equipped the boat with an air propeller mounted on a steerable mast. The boat's design is highly versatile, and new modules can easily be added to provide additional functionality.

7 Projects

As part of his doctoral research, Romain Deleu surveyed several segments of the subterranean course of the Lesse River in Belgium using a mini-sonar boat, under the supervision of Professor Vincent Hallet at the University of Namur.

Upon reaching the Grottes de Han limestone massif, the river disappears into a 45-metre-deep siphon known as the Gouffre de Belvaux. To bypass this, a narrow tunnel was excavated by dedicated cavers over eight years. On the other side, the now underground Lesse can be explored for more than



NO.	PART NAME	MATERIAL	QTY
1	Upper layer 50 mm	EVA	1
2	Middle layer 50 mm	EVA	1
3	Bottom layer 10 mm	EVA	1
4	Bottom frame 10 mm	HDPE	1
5	Stabiliser frame 20 mm	HDPE	1
6	Stabiliser fin 2 mm	Carbon fibre	2
7	Deck plate 5 mm	HDPE	2

NO.	PART NAME	MATERIAL	QTY
8	Transverse deck plate 5 mm	HDPE	2
9	Bolt M5	Nylon	4
10	M10 rod - 170 mm long	Nylon	2
11	M10 rod - 150 mm long	Nylon	2
12	Nut M10	Nylon	4
13	Bolt M5	Nylon	6

Fig. 2 Technical drawing of the portable sonar boat made from EVA.

https://doi.org/10.58440/ihr-31-2-n10

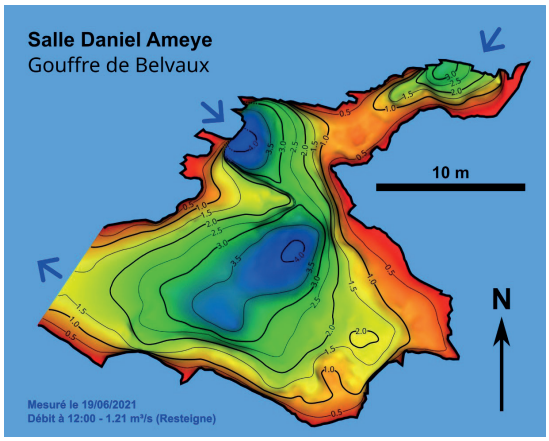


Fig. 3 Bathymetric map of the underground river La Lesse in the Salle Daniel Ameye (Belgium).

900 metres before it disappears again in an area called Au-delà. A bathymetric survey was conducted in the Salle Daniel Ameyer (Fig. 3). The sonar scan revealed an unknown large sump, which was identified as the main inlet through which the river enters the chamber.

After disappearing into the Au-Delà, the water re-emerges in the Salle d'Armes, a chamber within the famous Grotte de Han tourist cave. The exact location of this siphon was not well known, and it was assumed that the water came from a passageway on the right when looking upstream. This opening can be explored for some distance until it ends in a sump. However, the sonar boat revealed the true position and depth of the siphon (Fig. 4).

Once the Lesse enters the Grotte de Han, it passes through several more sumps before flowing into the Salle d'Embarquement. From there, it travels through a large external tunnel via the Trou de Han. A survey was conducted of this navigable section of the river, from the Salle d'Embarquement to the barrage outside (Fig. 5). As this distance is rather long for UWB technology, the measurements have been divided into eight sections.

In this project, the geometry of the riverbed was mapped and correlated with multipoint fluorescent dye tracing tests (Deleu, 2024). Dye tracing is a valuable technique that is often used in karst systems due to their complex and heterogeneous hydrogeology. It involves injecting a fluorescent dye into the water and tracking its movement using optical or manual monitoring tools, providing insights into groundwater flows and networks. For this project, TRAQUA's STREAM fluorometers were used. These optical sensors detect fluorescent dye. Tracer tests involved placing multiple fluorometers at various locations, revealing significant heterogeneity in the results. This is due to the cave's complex geometry, which induces variability in underground river hydrodynamics. The hydrogeological information obtained through the tracer tests provides a clear insights into the behaviour of underground rivers in karst systems. This extensive research will improve our understanding of karst aquifers and consequently help to preserve this vital resource.

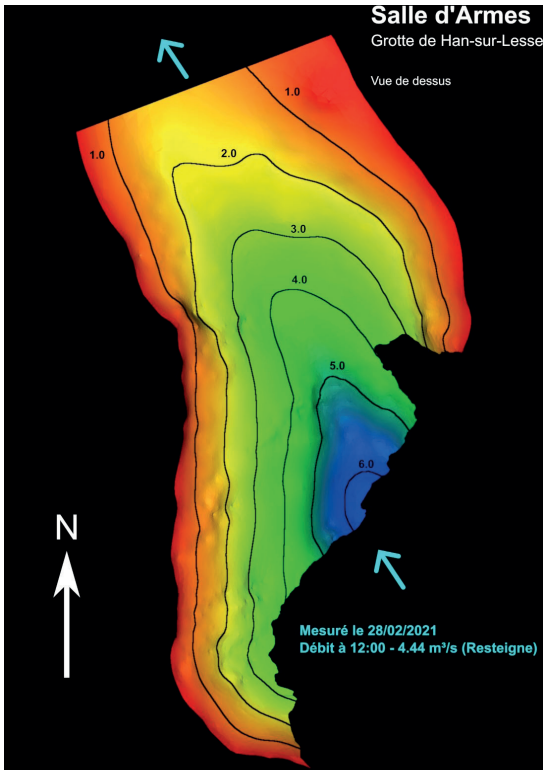


Fig. 4 Bathymetric map showing the underground river La Lesse re-emerging in the Salle d'Armes of the Grotte de Han. The location of the siphon can easily identified as the deepest part of the survey.

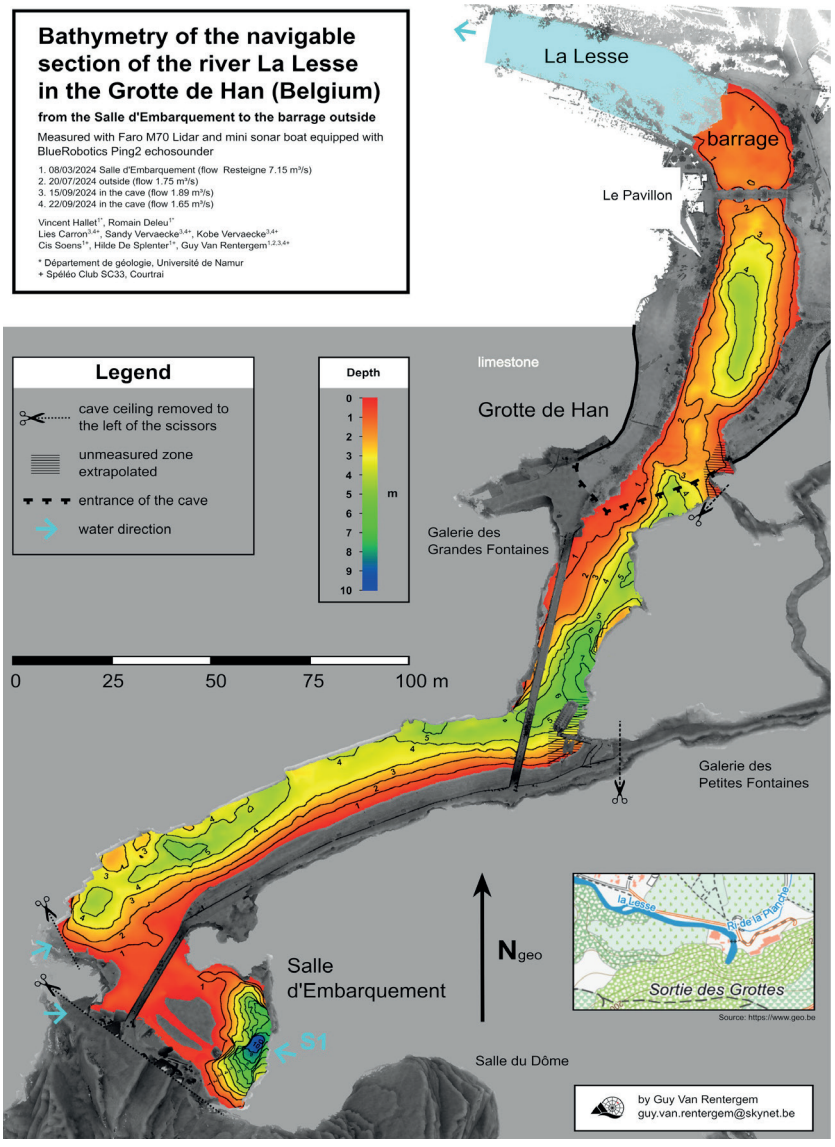


Fig. 5 Bathymetric map of the navigable section of the La Lesse river, which emerges from the Trou de Han in Belgium.

https://doi.org/10.58440/ihr-31-2-n10

References

Deleu, R. (2024). *Hydrodynamics of solute transport in karst conduits: Assessment by multi-point dye tracing and numerical modelling* [Doctoral dissertation, Université de Namur].

Poeter, E., Fan, Y., Cherry, J., Wood, W., Mackay, D. (2020). *Groundwater in our water cycle – getting to know Earth's most important fresh water source.* The Groundwater Project, Guelph, Ontario, Canada. https://doi.org/10.21083/978-1-7770541-1-3

https://doi.org/10.58440/ihr-31-2-n10

NOTE / TECHNICAL REPORT

Survey systems verification and calibration in the hydrospatial domain

Authors

Chandana Rathnayake[1] and Huibert-Jan Lekkerkerk[2]

Abstract

Calibration, alignment, and verification represent the essential foundations of accuracy in hydrospatial surveys, underpinning the reliability of data used in navigation safety, environmental monitoring, and subsea critical infrastructure planning. This technical report consolidates professional practices, IHO standards for safe navigation and other industrial standards, and real-world operational experience to present a structured framework for survey system calibration and verification. This is an essential knowledge particularly for people aspiring to become Certified Hydrographers Level 1, as it strengthens their understanding of professional standards and practices. The methodologies outlined address critical hydrospatial technologies including GNSS positioning, IMU alignment and gyro verification, MBES patch testing, and USBL calibration, with practical emphasis on accuracy control, system integration, and compliance with IHO S-44 standards and industrial standards for offshore surveying. Drawing upon both theoretical knowledge and daily operational experience, the report highlights systematic approaches that minimize errors, validate sensor integrity, and optimize survey efficiency. The practices detailed herein are not only procedural requirements but professional obligations for hydrographic surveyors, ensuring data integrity, client acceptance, and operational success. This report provides a reference guide for hydrospatial practitioners particularly junior professionals, and explicitly cross-references the IHO Manual of Hydrography (C13) alongside S-44 and industry handbooks. Bridging theoretical frameworks with applied methodologies in order to advance consistent, high-quality hydrospatial survey operations.

Keywords

hydrospatial surveys · hydrographic surveying · calibration · verification · MBES patch test · USBL calibration · data integrity

1 Introduction

In the hydrospatial domain (Hains et al., 2022), where accuracy underpins success, calibration and verification stand as the foundations of accurate and actionable data. Hydrospatial surveys provide critical insights into “all the blue of our blue planet and its contiguous zones” (Hains et al., 2022), the marine environments, facilitating marine exploration, environmental assessment, and subsea infrastructure development. Achieving these objectives depends heavily on the meticulous calibration and verification of advanced technologies such as Global Navigation Satellite Systems (GNSS) including Inertial Measurement Units (IMU), Multi-Beam Echo Sounders (MBES), and underwater positioning systems (LBL and USBL) and other related sensors deployed in the surveys. These sophisticated systems, commonly complemented by tools like Side-Scan Sonar (SSS), Magnetometers (MAG), Sub-Bottom Profilers (SBP), and Ultra-High Resolution Seismic (UHRS), demand rigorous calibration to minimize systematic errors and maintain data integrity (Lekkerkerk, 2024). Precision in Hydrospatial data is not just an aspiration; it is a professional mandate for Hydrospatial and even more specifically for certified hydrographic surveyors Level 0, 1 and 2, ensuring compliance with standards such as the International Hydrographic Organization (IHO) S-44 or project specific industrial standards.

✉ Chandana Rathnayake · chandu.ckr44@gmail.com

[1] EGS International Ltd, Bordon, United Kingdom

[2] Maritiem Instituut Willem Barentsz, NHL Stenden University of Applied Sciences, Leeuwarden, The Netherlands

https://doi.org/10.58440/ihr-31-2-n09

Calibration and verification are indispensable for reducing systematic errors, ensuring system integrity, and meeting industry standards such as IHO S-44 (IHO, 2020).

For hydrographic professionals, calibration and verification practices are more than procedural necessities they are an essential discipline. They validate system performance under real-world conditions, safeguard data reliability, and align outputs with contractual benchmarks and industry standards. The results enable informed decision-making, whether mapping complex seabed topographies, monitoring environmental changes, or planning subsea infrastructure in the Hydrospatial domain. Today in many modern hydrospatial surveys, the mobilisation of the vessel will be completed and signed off by the respective clients only after completion of successful calibration and verifications of the survey systems that are ready to be deployed. Hence this also mandate the calibration and verification for the survey industry.

- Calibration and verification processes are crucial for achieving:
- Data accuracy and uncertainty: Calibration minimizes systematic errors and aligns sensors for optimal performance (IHO, 2020).
- System integrity: Verification confirms that systems operate as expected under real-world conditions.
- Standards compliance: Adherence to established industry standards, along with relevant national and international regulations, enhances the credibility and acceptance of survey results.
- Operational efficiency: Early identification and resolution of issues prevent expensive re-surveys and delays (Lekkerkerk & Theijs, 2013).
- Seamless integration: Ensures compatibility and alignment among GNSS, IMU, MBES, USBL, and other systems for comprehensive data acquisition (Schnare, 2014).

This article draws from the authors' extensive experience in calibration projects, integrating standards and materials from IHO publications including Manual of Hydrography, Category 'A' and 'B' Hydrographic courses (S-5A and S-5B; IHO, 2018), and real-world surveying operations. It provides a concise overview of the importance of calibration and verification, equipping surveyors, especially junior professionals, with a robust framework to approach these critical processes.

The practices and principles outlined here are not exhaustive but are carefully organised to underscore the key technical depth and best practices that underpin successful all types of hydrospatial surveys. Having understand that there are many approaches for calibration and verification for the survey systems this guide reflects the dynamic interplay between theoretical knowledge and practical application, with an emphasis on fostering precision and reliability. As we navigate the complexities of marine surveying, this preamble sets the stage for a comprehensive exploration of calibration and verification methodologies, offering professionals a structured approach to mastering the tools and techniques that define excellence in the field.

Scope and contribution: This article focuses on the verification and calibration for positioning, attitude swath bathymetry and USBL as used in hydrospatial surveys. It does not attempt to reproduce all general practice material already documented in the IHO Manual on Hydrography (C-13; IHO, 2005); instead, it consolidates offshore procedures and error-control techniques and then links each step to the relevant C-13 clauses where applicable.

2 Positioning systems: verification and geodetic integrity

2.1 GNSS position verification in geophysical surveys: techniques and best practices

GNSS form the backbone of positioning in any hydrospatial including geophysical surveys, ensuring both horizontal and often also vertical accuracy for data acquisition (IHO, 2005). Accurate dimensional control and comparison of GNSS systems is critical to aligning survey systems with geodetic references and ensuring positional integrity across various survey operations. Although you cannot really calibrate a GNSS; this chapter explores the techniques, methodologies, and challenges associated with GNSS position verification, emphasizing its role in calibration and integration with other survey systems such as MBES and USBL. GNSS systems ensure that positional data is accurate and reliable, forming the basis for spatially consistent datasets. Verification of GNSS systems includes:

- Validating real-time positioning accuracy against reference standards.
- Ensuring offsets and lever arms are correctly accounted for.
- Cross-verifying primary and secondary systems using independent methods such as Real-Time Kinematic (RTK), Precise Point Positioning (PPP), or Post-Processed Kinematic (PPK).
- Validating final product positioning accuracies to meet the specific standards.

Primary and secondary GNSS systems. Position validation begins with a comparison between primary and secondary GNSS systems if available. These systems, typically integrated into the survey setup, operate using RTK or PPP corrections. The comparison ensures spatial consistency and accuracy in positioning, providing redundancy in case of primary system failures. The positions should be checked against project coordinates through the survey software to include any geodetic settings made in the survey software. Lever arms must be entered into the survey software with precision, as errors in these parameters can propagate through the system, affecting positional accuracy (IHO, 2005, Appendix 1 Part I).

https://doi.org/10.58440/ihr-31-2-n09

Independent verification using standalone GNSS systems. Standalone RTK GNSS systems or total station checks, provide an independent layer of validation. These systems offer precise positioning unaffected by biases in the primary setup, serve as an additional verification method, particularly in challenging environments or where the primary GNSS system's data quality is questioned. On smaller vessels an (extra) antenna can also be placed directly over a benchmark to check the position output against the benchmark coordinates. Standalone GNSS systems or total station checks are often employed to validate positional accuracy independently. Setting up RTK receivers illustrate in Figs. 1 and 2. Further, different way of raw data and processed data representations can be found in Figs. 3 and 4.

2.2 Key considerations in positioning verification: limitations of numerical averaging

Numerical averaging, while a simple method for position determination, is not recommended for high-precision applications such as geophysical surveys.

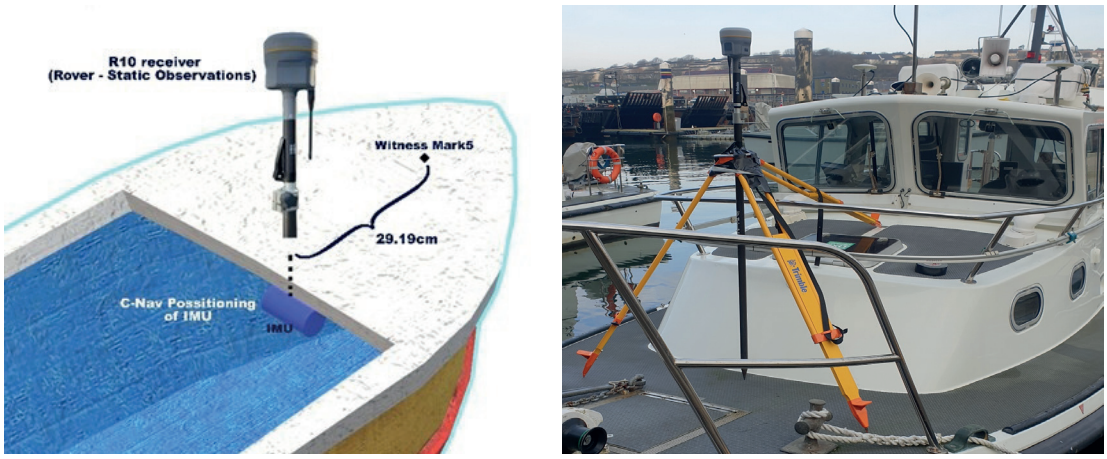


Fig. 1 Schematic of setting up RTK receiver on a vessel (left) and real-world setting up Trimble RTK receiver for alongside validation (right).



Fig. 2 Setting up RTK receiver close as possible to the primary GNSS receiver on-board (left) and measuring offset to the RTK Receiver from

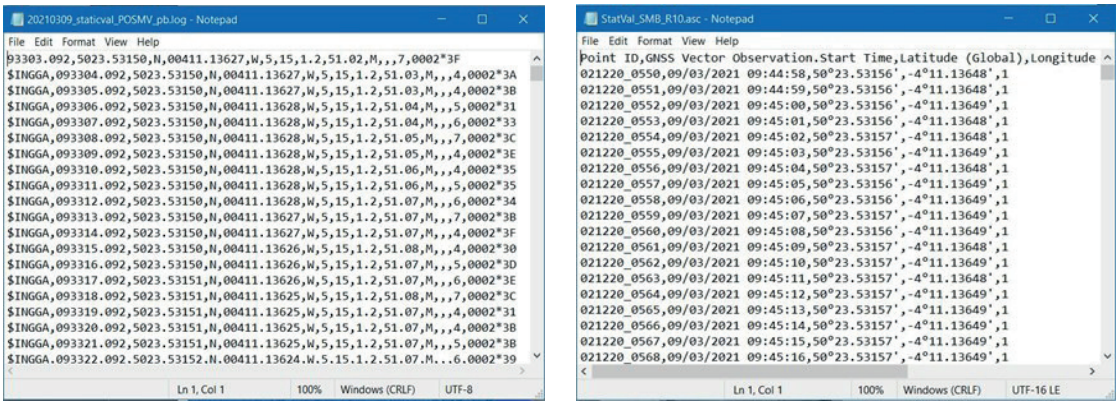
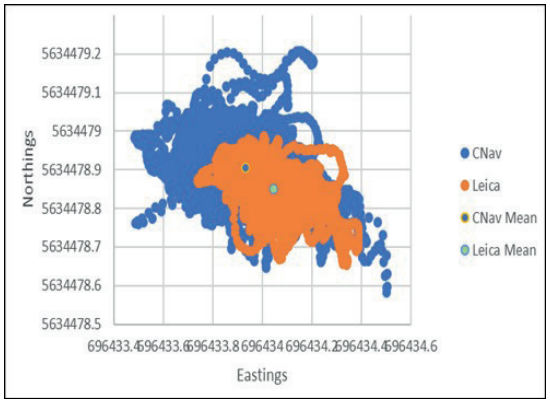


Fig. 3 Raw data recorded from primary (POSMV) GNSS system (left) and independent RTK (Trimble R10) receiver (right).

https://doi.org/10.58440/ihr-31-2-n09



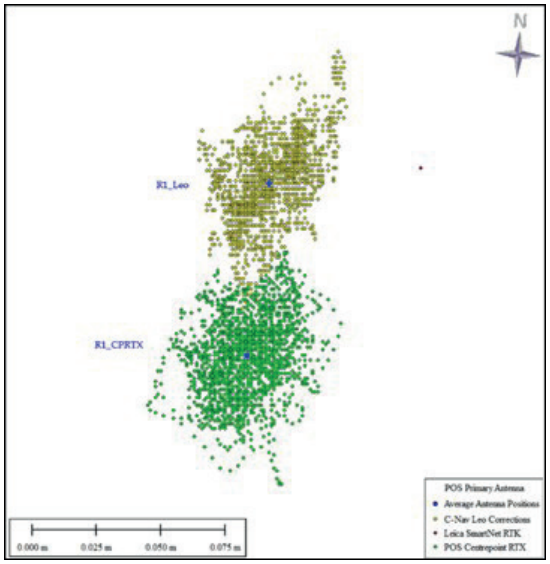


Fig. 4 Raw data recorded from primary (POSMV) GNSS system (left) and independent RTK (Trimble R10) receiver (right).

Oversimplification: Numerical averaging of horizontal coordinates (X, Y) ignores the full 3D error ellipsoid inherent in GNSS data. This can lead to biased results, especially in cases where vertical uncertainty (Z) or correlated errors between axes are significant.

Error distribution: GNSS errors are not evenly distributed; atmospheric effects, satellite geometry, and multipath can introduce systematic biases.

Loss of covariance information: Numerical averages do not account for covariance between positional components, which is critical for understanding true positional uncertainty.

Hence the referred methods for positioning calculations are GNSS processing software, dedicated GNSS processing software offers advanced tools for deriving accurate positions:

- Weighted averaging: Observations are weighted by their estimated accuracy, ensuring that higher-quality data contributes more significantly to the final position.
- Error ellipsoid consideration: The software incorporates the 3D error ellipsoid, capturing positional uncertainties comprehensively.
- Residual analysis: By evaluating the residuals (differences between observed and modelled positions), the software identifies and excludes outliers, enhancing data reliability.
- Time-based integration: Longer observation times reduce the impact of random noise, a method particularly effective in static surveys.

These capabilities make GNSS processing software indispensable for high-precision applications, such as control point establishment and baseline verification.

2.3 Absolute position validation

Validate lever arms by comparing GNSS-derived positions with those calculated from IMU measurements during static and dynamic tests. This could be done by using a separate (RTK) GNSS unit placed on corners of the vessel and comparing the obtained coordinates with those produced from the vessel main GNSS through the ship reference frame (SRF) and IMU / gyro towards the node on which the separate GNSS is placed. By placing the separate GNSS on the extremities any errors in alignment can be noted. Document this as a pre-survey verification in line with C-13 checklists (IHO, 2005, Appendix 1 Part I).

3 Motion reference systems: alignment, calibration, and performance

3.1 Gyro / heading sensor alignment against the SRF

Accurate heading data is indispensable in hydrographic surveys, ensuring precise alignment of positioning and survey lines with real-world coordinates. Errors in gyro compass readings can result in inaccuracies in bathymetric geophysical data and any hydrospatial data, making calibration a critical component of survey preparations (Royal Navy, 2019). A gyro compass with a recent manufacturer calibration report serves as the baseline for surveys (calibrated gyro). However, verifying the alignment of the gyro with the SRF is essential.

Modern surveys increasingly rely on GNSS-aided heading systems and Fibre Optic or Ring Laser gyros. Integrating an aligned gyro compass with other survey systems, such as MBES and USBL, ensures heading discrepancies remain within acceptable. This integration is essential for maintaining alignment between survey lines and geodetic coordinates. Verifying the alignment of heading systems and cross-referencing with transits or established heading references such as light lines or sun azimuth checks enhances the overall reliability of the survey data. Such practices not only meet industry standards but also build redundancy and resilience into the survey workflow, ensuring high data integrity in hydrographic operations.

Heading alignment ensures the correct alignment of the vessel or survey platform. It is used to

determine any alignment errors between the gyro and the SRF.

Methodology: Two positions along the centreline of the vessel (bow-stern SRF axis) at known, fixed locations on the vessel or platform. These positions can be determined using two GNSS receivers but also using a total station or through (tape) measurements from a reference heading such as a quay of which the heading was determined using a topographic survey. The true heading of the vessel is computed and at the same time the output from the gyro is observed. The difference between the two gives the computed-observed (C – O) correction. Care should be taken when grid headings are compared with calculated values, incorporating projection corrections to account for grid convergence. Fig. 5 illustrate schematic of vessel reference frame and GNSS aided heading. For combined gyro-IMU instruments, the gyro C – O must be implemented in the instrument (not only in the acquisition software) before IMU alignment, to eliminate roll- pitch cross talk at the source.

Grid convergence (γ) is the angle between the projection or chart north and true north. It varies across

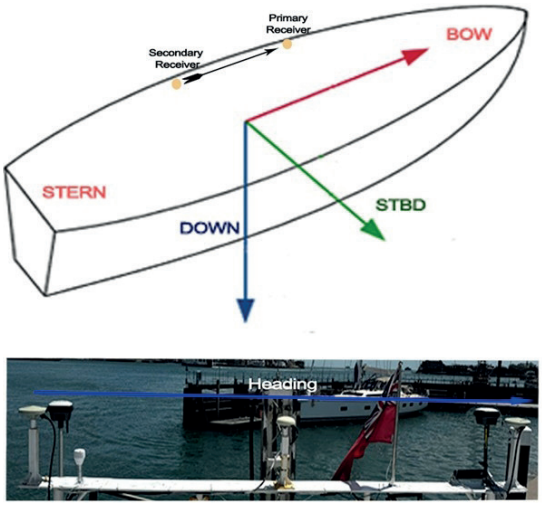


Fig. 5 Schematic of vessel reference frame and GNSS aided heading (top), real world orientation of GNSS receivers (leaver arms) and RTK receivers for heading verification (bottom).

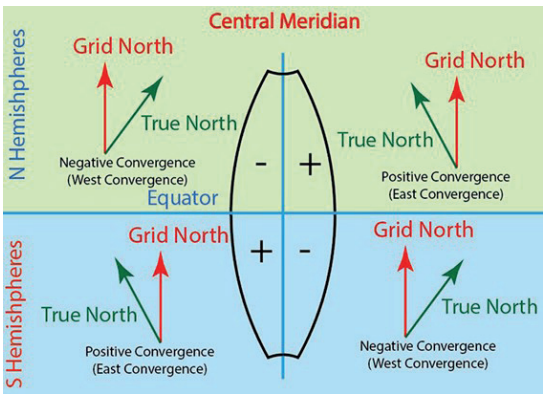


Fig. 6 Relation of grid north and true north in different quadrants (DrillingFormulas, 2016).

the projection, depending on the point's position relative to the origin of the projection. In a UTM projection the origin is the central meridian of the UTM zone but in other projections this may be a central point or parallel. Fig. 6 indicate the relation of grid north and true north. Grid convergence conventions vary from projection to projection and may also differ depending on the formula used.

Software tools like CARIS, QGIS, or Trimble GNSS software can compute grid convergence automatically. However, it should always be ensured that the C-O correction of the gyro compass is entered as a true north correction, free of any convergence.

3.2 Inertial measurement unit and gyro against SRF

This alignment must be performed only after the gyro/heading alignment has been completed and the gyro C – O applied in the instrument for integrated units. In the context of hydrospatial surveys, the Inertial Measurement Unit (IMU) plays a pivotal role in ensuring accurate motion compensation by measuring accelerations and angular velocities. This is especially critical in marine environments, where vessel dynamics introduce complex motion patterns. Proper alignment of the IMU against the SRF ensures seamless integration with other systems, such as GNSS and MBES, and enhances the overall quality of survey data. This chapter provides a comprehensive guide to the alignment of IMU systems on board survey vessels, focusing on industry best practices, methods, and tools for precise alignment and validation (IHO, 2005, Chapter 7).

The IMU measures the vessel's motion in six degrees of freedom: three linear accelerations (surge, sway, and heave) and three angular rotations (roll, pitch, and yaw). Aligning the IMU (often erroneously called calibration) ensures that the IMU data aligns with the SRF. Lever arms and offsets between the IMU, GNSS antennas, and other on-board sensors are accurately accounted for and Integration errors are minimized. There are mainly two types of 'calibration' for IMU system: factory Calibration and Onboard alignment. Factory calibration is performed by the manufacturer and focuses on ensuring that the IMU output is correct with regard to the internal reference frame of the sensor itself. This includes:

- Sensor biases: Correcting systematic measurement errors.
- Scale factors: Adjusting the sensitivity of each sensor.
- Alignment: Aligning IMU sensors with its internal reference frame.

Factory calibration ensures the IMU operates within specified tolerances under ideal conditions but does not account for vessel-specific installation factors. Periodic factory calibrations are recommended per manufacturer's standards and needs. Alignment focuses on aligning the IMU with the vessel's coordinate system (SRF). This includes:

- Accounting for lever arms (offsets between the

https://doi.org/10.58440/ihr-31-2-n09

IMU, GNSS antennas, and other sensors).
- Correcting installation angular misalignments.
- Validating dynamic performance under survey conditions.

Dimensional Control (DIMCON) survey is a fundamental procedure in hydrographic surveying, ensuring precise spatial measurements of offsets between key survey equipment components. This process involves advanced accurate land survey techniques, such as the use of total stations, laser scanners or photogrammetry, to determine the lever arms and spatial relationships between GNSS antennas, MBES systems, USBL transducers, and IMUs within the SRF. Regular updates to DIMCON surveys are essential, especially after any equipment modifications or changes to sensor mountings and locations, as these trigger the need for redetermination. While there is no specific validation period for DIMCON, ongoing node verifications can provide valuable insights into any potential changes in DIMCON values. However, it is considered good practice to conduct a DIMCON survey roughly every few years, even if no modifications have been made, as advancements in methodologies and survey accuracies may result in updated and more precise offset measurements. This procedure not only mitigates alignment errors but also optimizes data reliability for both dynamic and static survey operations. It is very important to understand different conventions for the offset by different manufacturers. Fig. 7 illustrates the different approach by few industrial standard software and system for the offset and rotation conventions.

The optimal IMU on a survey vessel is not solely determined by its proximity to the vessel's centre of gravity (COG) but rather by a strategic balance between minimizing lever arms and reducing motion-induced errors. While manufacturers often recommend installing the IMU near the COG, a more precise approach considers the vessel's pivoting centre to minimize accelerations and mitigate 'false heave' effects. In modern survey configurations utilizing RTK or PPP corrections for height, false heave is significantly reduced, making rotational accuracy a more critical factor. Consequently, a few installation strategies exist: one prioritizes the reduction of lever arms to minimize rotational errors, while the other places the IMU at the vessel's centre of rotation to limit accelerations. For "all-on-the-pole" setups, an optimal position is near the waterline, between the GNSS and MBES, ensuring better alignment and data consistency. Given these considerations, the best placement is survey-specific, requiring an evaluation of vessel dynamics, system integration, and operational requirements (Lekkerkerk & Theijs, 2013) When initially installiing the IMU onboard ensure the mounting is rigid to prevent relative movement between the IMU and the vessel. Then enter approximate lever arms into the system software based on DIMCON survey results. Align the IMU with the vessel's reference frame (fore-aft, athwart ship, and vertical axes).

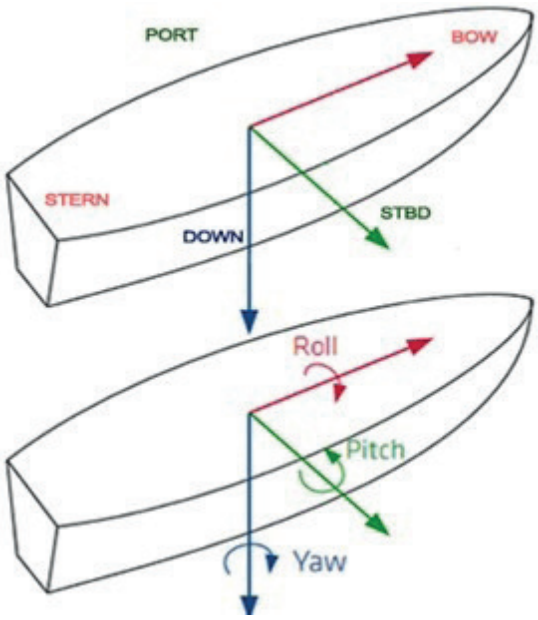


Fig. 7 Rotation conventions.

Ensure that the unit is aligned with the SRF in all three dimensions to prevent 'cross-talk', i.e. for example a pitch motion inducing a false roll motion due to a yaw offset of the IMU. Perform Lever arm calibration which determines the offsets between the IMU, GNSS antennas, and other reference points.

Alignment calibration addresses misalignments between the IMU's internal axes and the vessel's reference frame. Vertical axis misalignments of the MRU are particularly problematic, as they introduce cross-talk between pitch and roll angles. This is especially critical for outer beams of wide swaths (e.g., 120°), where even a minor yaw misalignment (e.g., 2°) can result in seabed "wobble" errors of up to ±10 cm in 20 m water depths. This wobble, primarily roll induced by pitch, is difficult to eliminate due to the challenge of aligning the MRU with the SRF at its mounting location (de Hilster, 2009). Nicolàs de Hilster explain in his article series on Hydro International (The MRU and SRF Aligned) the principles of the Dutch method for MRU alignment, developed by the Survey Department of Rijkswaterstaat (the Directorate-General for Public Works and Water Management of the Netherlands). The method addresses both vertical axis alignment with the SRF and the correction of pitch and roll angles. For this article, only the vertical axis alignment is considered (de Hilster, 2009); readers are referred to the articles for a detailed explanation.

Some GNSS aided IMUs, and INS (such as POSMV systems) require an alignment against the SRF followed by an alignment between the GNSS antenna's and the IMU (heading alignment). As this is difficult to do under stationary conditions this is done using a dynamic alignment. Dynamic alignment involves executing specific manoeuvres and leveraging GNSS data to detect and correct misalignments in pitch, roll, and yaw, as well as synchronizing data

streams to eliminate latency discrepancies. Straight-line runs at constant speeds identify fore-aft misalignments, while controlled turns assess heading (yaw) and athwartship (roll) errors by comparing angular velocity data from the IMU with GNSS-derived headings. GAMS (GNSS Azimuth Measurement Subsystem) calibration further refines the alignment of GNSS antennas, reinforcing and validating DIMCON results for optimal IMU performance in geophysical surveys. In integrated units, perform gyro alignment first, apply the gyro C – O in the instrument, and then carry out dynamic alignment and subsequent checks.

Analyse roll, pitch, and yaw data for unexpected variations or noise.

Best practices for onboard IMU calibration:

- Verify all hardware and software are functioning correctly.
- Verify sign conventions in both unit and software
- Conduct a DIMCON survey before mobilization to measure lever arms.
- Align regularly: Perform alignment at the start of every project or when equipment configurations change.
- Document results: Maintain detailed records of calibration parameters and verification results. Include reports generated by software aids.
- Train survey teams: Ensure team members are familiar with calibration procedures and equipment.
- Produce a short alignment verification note and attach plots to the pre-survey file, following the structure suggested in C-13 Appendix 1 (IHO, 2005).

IMU alignment is an essential process in marine surveys, ensuring accurate motion compensation and seamless integration with GNSS and MBES systems. By adhering to structured calibration procedures and leveraging advanced tools, surveyors can minimize errors, enhance data quality, and meet industry standards. Regular calibration and verification not only ensure compliance but also build confidence in the reliability of survey data, making it indispensable for professional hydrographic operations.

3.3 Integrated INS (Gyro_IMU) alignment workflow and GAMS

For the modern integrated units (gyro + IMU/ INS), perform gyro/ heading alignment first and apply the gyro C – O in the instrument to suppress roll – pitch cross talk before any IMU alignment. Then execute an INS dynamic alignment (straight runs and controlled turns) to solve installation angles and confirm timing, followed by GAMS/dual antenna heading calibrations, which is technically a separate GNSS azimuth subsystem integrated to refine heading and validate DIMCON.

4 Swath Systems: Calibration and Quality Assurance

4.1 Alignment and verification of MBES systems

Sound Velocity Profile (SVP) verification is a critical step in ensuring the accuracy of survey data, particularly for systems reliant on sound velocity for calculations, such as MBES), USBL positioning systems, and data acquisition platforms like QINSy and SIS. Using tools like the SVP or Moving Vessel Profiler (MVP), surveyors can capture updated and precise sound velocity data at varying depths to mitigate refraction errors and ensure accurate beam steering. Regularly updated SVP data is essential for calibrations, as deviations in sound velocity can introduce significant errors in depth, positioning, and acoustic data processing. By integrating real-time or recently measured SVP data into survey operations, professionals ensure optimal system performance and adherence to industry standards such as IHO S-44. Most modern MBES systems require not only a separate SVP, MVP or CTD to measure the sound velocity profile but also require a separate sound velocity measurement near the transducer to properly compute the direction of the receives acoustic information. The values from this sensor should be cross referenced to those from comparable depths using the SVP / MVP or CTD.

Alignment is a critical step in ensuring the accuracy and reliability of MBES systems, particularly for dual-head setups. These systems, widely used in Hydrospatial surveys, require precise adjustments to account for offsets in pitch, roll and yaw. Accurate alignment determines the transducers axes with the SRF, reduces systematic errors, and enhances data integrity, enabling compliance with standards like the IHO S-44 for safety of navigation. This chapter delves into the essential calibration processes, with a focus on dual-head systems, while emphasizing best practices and practical considerations for effective alignment and verification.

For the purposes of estimating the resultant beam vector (the intersection of transmit and received steered cones) in the local level coordinate systems, the patch test is adequate as it solves for the sonar to SRF misalignments as well as the latency (or lack thereof when precise time stamping is used) between the GNSS and MBES. But without a proper alignment of either (and thus by inference both as they are only relatively aligned) sensor with respect to the SRF, the lever arm offsets cannot be applied correctly (Clarke, 2003).

4.2 Patch test calibration

The patch test is designed to address angular offsets in the MBES system. For dual-head MBES setups as illustrated in Fig. 8, each transducer head must be calibrated independently to ensure cohesive data output. The calibration process includes adjustments for pitch, roll, yaw, and latency, conducted through carefully planned survey lines.

https://doi.org/10.58440/ihr-31-2-n09

4.3 General conditions for patch testing

- Conduct tests in calm weather and low current conditions to minimize noise and motion artifacts.
- Use a flat seabed at a depth at least equal or deeper to those encountered in surveying or distinct sloping terrain (preferably slope between 1:2 and 1:5), depending on the specific calibration parameter.
- Maintain steady vessel speeds, with variations for latency calibration.
- Perform all previously described tests, alignments and verifications.
- Obtain a recent sound velocity profile and enter it into the software
- Ensure sufficient overlap of beams for both heads during calibration.

Most software packages have automated routines for the patch test. While there is nothing against these routines the prudent surveyor should always visually check the results by applying the suggested values and inspecting the resulting bottom for any remaining discrepancies.

4.4 Roll calibration

Roll calibration addresses angular misalignment along the vessel's port-starboard axis; roll offset illustrate in Fig. 9, typically the most sensitive offset to correct.

Line Plan: For a single head, sail the same (theoretical) line in opposite direction over a flat bottom. For dual head, use three parallel lines over a flat seabed one central and two with lateral offsets. Ensure these lines provide overlapping beams from each transducer head.

Procedure: Analyze the outer beams from overlapping data to isolate roll offsets. A flat seabed ensures that observed discrepancies are due solely to roll misalignment.

Dual-Head consideration Fig. 10: Treat port and starboard heads individually. Roll errors in one head may not align with those in the other, necessitating separate corrections.

Record conditions, line plans, and results as part of the C-13 Appendix 1 pre-survey / survey records, including Annex E SVP entries (IHO, 2005).

4.5 Pitch calibration

Pitch calibration corrects fore-aft angular misalignment of the transducers relative to the vessel's longitudinal axis.

Line Plan: Run two lines as indicated in Fig. 11, over a sloping seabed in opposite directions (uphill and downhill). Ensure overlapping coverage for port and starboard heads. Avoid lateral offsets in the lines to maintain data consistency.

Procedure: Compare the profiles from the two lines. Any pitch error will visible as a growing discrepancy in depth as distance increases.

Dual-Head Consideration: Each head must be treated as a separate entity. Overlap data from individual transducers to isolate pitch offsets effectively. Fig. 12 illustrate patch test interface of Caris HIPS & SIPS processing software. Survey line plan recommendation for pitch calibration illustrate in Fig. 13.

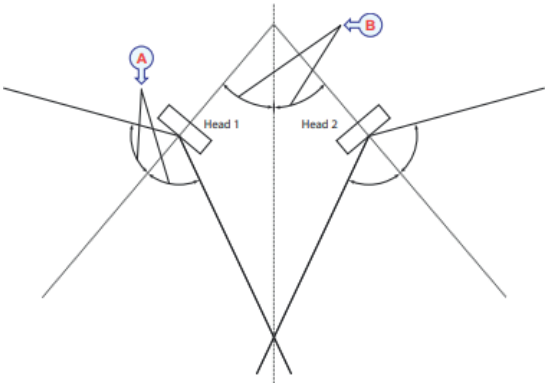


Fig. 8 Head1 (Port) and Head2 (Stbd) arrangement of dual head MBES system (SIS, 2024).

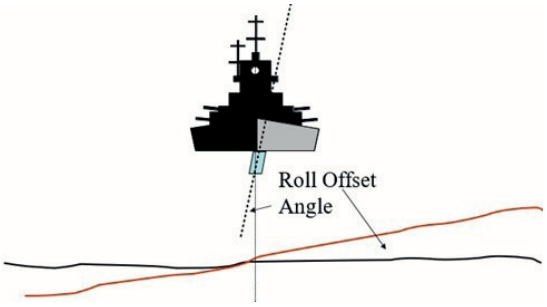


Fig. 9 Roll offset angle (SIS, 2024).

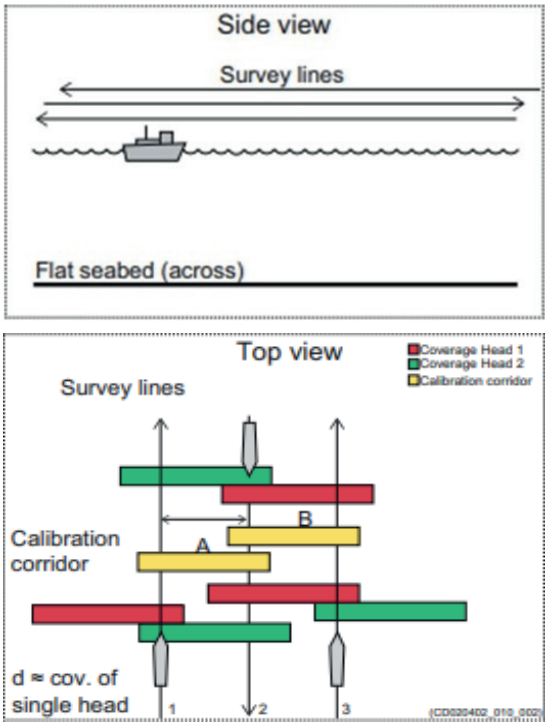


Fig. 10 Survey lines for patch test: Roll calibration and calibration corridor for roll calibration for SIS calibration (SIS, 2024).

4.6 Yaw (heading) calibration

Yaw calibration corrects rotational misalignment between the transducers and the vessel's heading.

Line Plan: Single head: run two lines across a distinct target or slope with the two lines overlapping each other. Dual head illustrate in Fig. 14: Run three lines across a distinct target (e.g., a wreck) or slope with the second line crossing the target at 90 degrees.

Ensure lateral spacing of 1.5x the water depth between lines for optimal sensitivity. Heading calibration of a dual head system will need careful planning. Run 3 lines as indicated below with the 2nd Line crossing a distinct object STB Head: Select line 1 and 2, make a calibration corridor along the centre beam of line 2.

PORT Head: Select line 2 and 3, make a calibration corridor along the center beam of line 2.

Procedure: Compare the central beams from overlapping data. Any heading misalignment will cause the target positions to deviate. Adjust offsets in the software to align targets.

Dual-Head Consideration Fig. 15: Perform separate yaw calibration for each head. For the starboard head, use lines 1 and 2; for the port head, use lines 2 and 3. Create calibration corridors along the central beams for precise analysis.

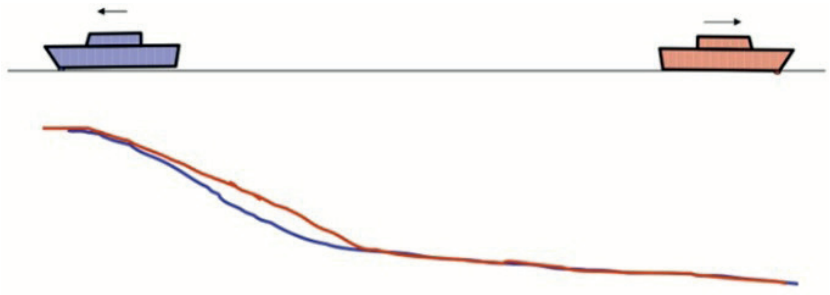


Fig. 11 Line plan for pitch calibration (SIS, 2024).

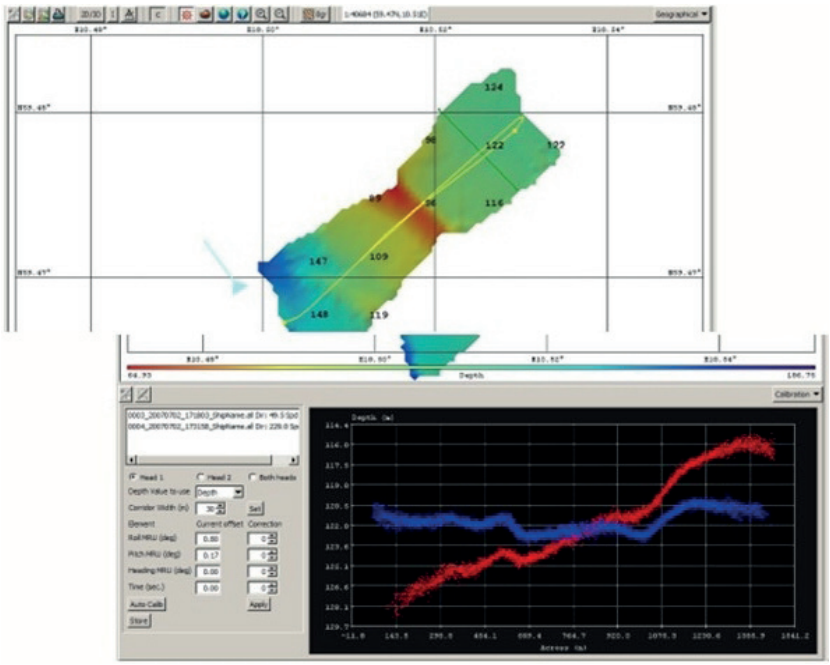


Fig. 12 Calibration in Caris HIPS and SIPS for single head system.

4.7 Latency calibration

Latency calibration ensures synchronization between positional data and acoustic measurements. Yaw calibration is performed using crossing lines over distinct features, while latency calibration overlays lines at varying speeds to detect timing discrepancies (Lekkerkerk & Theijs, 2019).

Line Plan: Run two lines over a distinct feature at distinctly different speeds as illustrated in Fig. 16 (e.g., 3.5 knots and 7 knots).

Procedure: Overlay the data from the two lines. Any latency offset will cause positional discrepancies, which can be corrected in the system settings.

Best Practice: Use PPS (Pulse Per Second) timing where available, as it minimizes latency issues.

4.8 Post-calibration verification

Verification ensures that the calibration process has effectively addressed all offsets and that the MBES system meets required accuracy standards. This involves repeatability tests, noise analysis, and cross-track error assessments. Repeatability is surveying a known feature (e.g., a wreck or underwater structure) in opposite directions. Compare overlapping data for depth consistency and accuracy.

MBES Integration; Use MBES data to verify motion compensation accuracy by analysing beam footprints and depth consistency. For example, roll the vessel in a heavy sea and check if a flat bottom remains flat in the recorded data.

Cross-Track Error Assessment: Validate positional accuracy using cross-track and along-track error metrics and confirm compliance with project-specific tolerances.

4.9 Best practices for dual-head systems

Efficient line pattern for dual head system recommended in Fig. 17. The alignment of MBES systems, particularly dual-head configurations, is a meticulous process that requires careful planning, execution, and verification. By addressing angular offsets through patch testing, surveyors can achieve high-precision bathymetric data.

4.10 Absolute depth check

After the calibration and verification of the MBES as outlined above a further check should be made to verify that the depths as measured are correct with regard to the chosen vertical datum. This can be accomplished by checking the obtained depths against an independent reference. This could be a topographically surveyed sill of a set of locks, a bottom with known depth or even against a lead and line (and tidal) measurement near the nadir of the MBES. Care should be taken that the depths taken independently are compared against the

https://doi.org/10.58440/ihr-31-2-n09

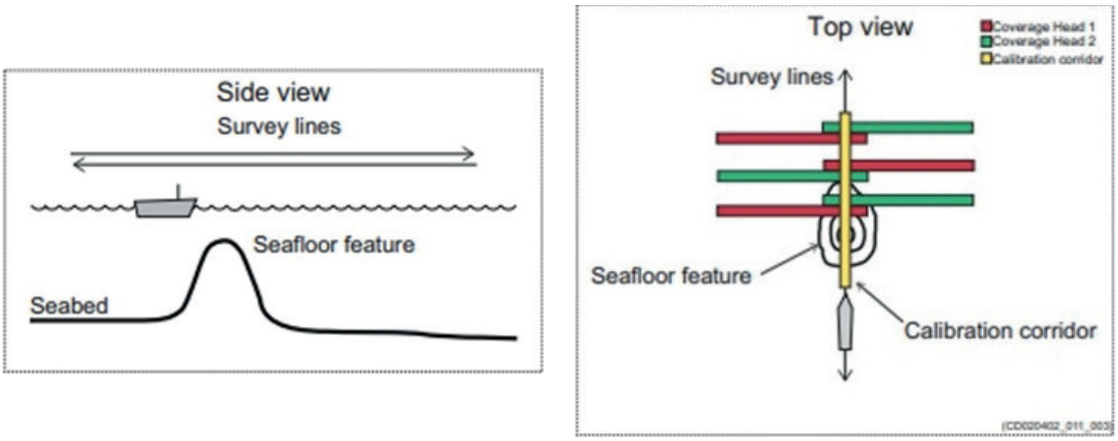


Fig. 13 Survey lines for patch test: Pitch calibration (left) and calibration corridor for pitch calibration (right) for SIS calibration (SIS, 2024).

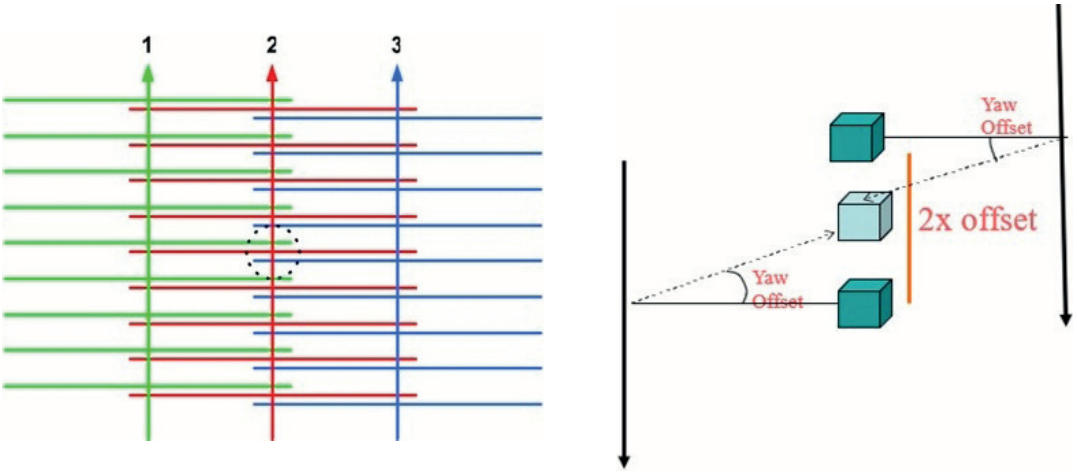


Fig. 14 Line pattern for yaw calibration (left) and maintaining line spacing for the calibration (right) (SIS, 2024).

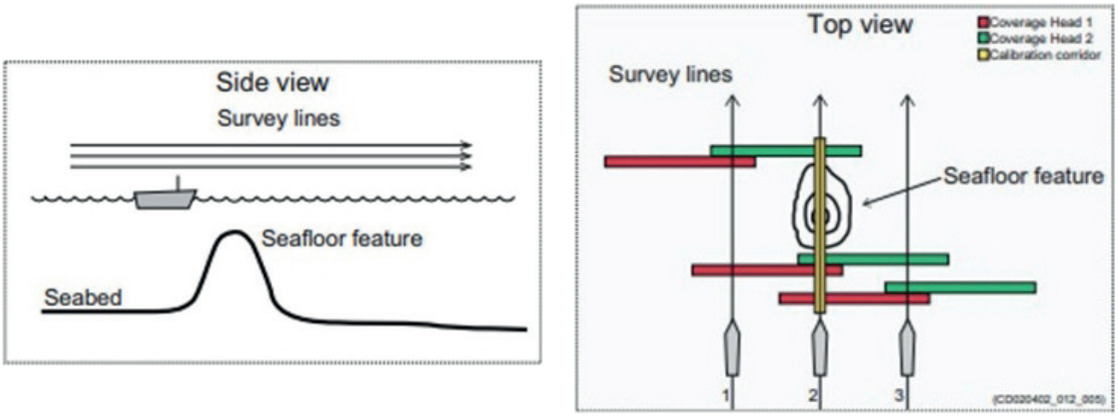


Fig. 15 Survey lines for patch test: Yaw calibration (left) and calibration corridor for yaw calibration (right) for SIS calibration (SIS, 2024).

depths as processed in the proper vertical datum through the survey software to verify all alignments and settings in the software.

5 Underwater positioning and system calibration

5.1 Calibration of USBL systems: a technical guide

Ultra-Short Baseline (USBL) systems are pivotal in subsea positioning, particularly for the accurate deployment and tracking of remotely operated vehicles (ROVs), towed equipment, and underwater sensors. A USBL Calibration is essential to ensure correct electronic alignment of the vessel's USBL acoustic, GNSS and attitude sensor offsets. This chapter outlines a professional and structured approach to USBL calibration, focusing on the widely preferred box-in calibration method, along with considerations for verification and best practices.

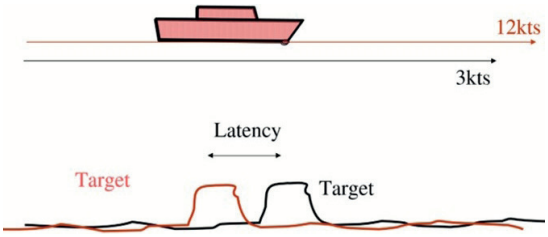


Fig. 16 Survey lines for patch test: Latency calibration (SIS, 2024).

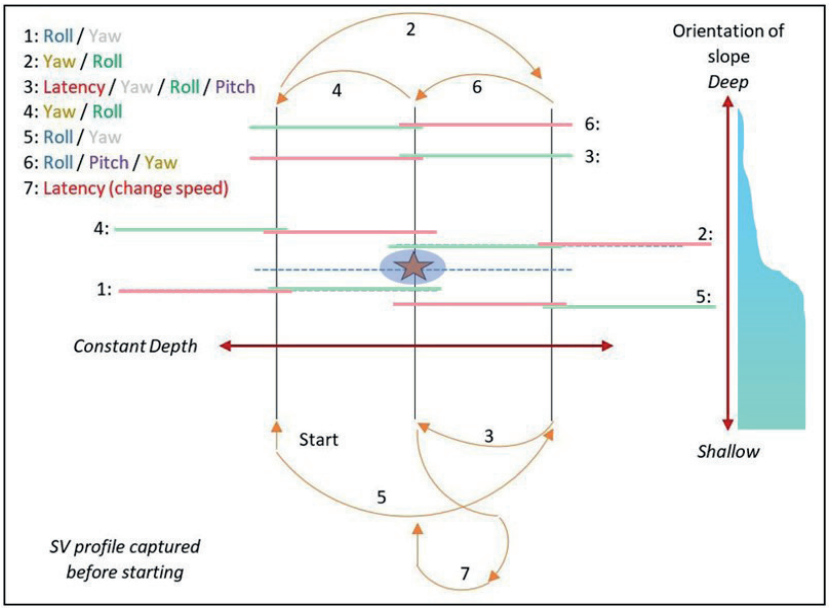


Fig. 17 Best and efficient line pattern to run for dual head system patch test.

Verification involves comparing observed beacon positions with theoretical coordinates, ensuring compliance with project-specific tolerances and industry benchmarks. Some USBL systems include a built-in motion reference unit. These systems are calibrated in the factory and the electronic offsets are known and set prior to delivery. These systems usually require no calibration, but a verification test is recommended upon installation to correct any physical heading, pitch and roll errors, and to check the GNSS offsets for absolute positions of USBL contacts.

USBL Calibration: Box-In Method; Box-in calibration is the most commonly used method for USBL systems, ensuring precise alignment and correcting for latency. This approach uses predefined survey lines around a beacon to collect data for detailed analysis. While box-in calibration is preferred for its accuracy and flexibility, vessels equipped with dynamic positioning (DP) systems can opt for static calibration in certain scenarios. Fig. 18 shows the radius of the offset at ⅓ water depth; however, this is only for deep water (1000m+) calibrations where the DP vessels tend to operate.

5.2 Calibration procedure

Calibration procedure describes here specify for the shallow water USBL calibration approach as the context for the document is more focus on survey using MBES (usually shallow water operations). Hence, include only the techniques and associated diagrams for shallow water calibrations are used below.

offshore vessels using USBL for the purposes you described above will conduct USBL Calibrations at significantly greater depths. Arguably the optimum depth for a USBL Calibrations is over between 300 m and 1000 m. The technique you describe for the USBL calibrations will produce good results at these depths, but not so good at 35–50m depths due to refraction errors and thruster wash experienced at the high angles of attack for acoustic ranges.

Beacon Deployment: Position the beacon at a fixed and known depth, typically between 35–50 m (Depending on the project and general depth of the area or as per the manufacture guidelines for the specific system), ensuring that it is free from obstructions or significant underwater noise. Beacon can deploy in floating (3–5 m above the seabed with help of Float collar) or in a fix frame on the seabed. Document beacon deployment depth, mooring type, and environmental conditions in (IHO, 2005, C-13 Appendix 1, survey log).

For the shallow water depths (30–50 m) it is recommended that only a fixed frame is used, or a very short tether of less than 0.5 m. This is to reduce errors in the beacon position introducing errors into the vessel calibration result. A 3–5 m tether in 35–50 m of water will be subject to significant sway caused by current, and the beacon position may move by up to 3 m (up to 10 % of the water depth) during the calibration invalidating the results by introducing large systematic errors. In deep water the sway offset of a tethered is a far smaller percentage of the overall systematic errors (0.03 %), and therefore more acceptable. However, with some USBL systems delivering accuracies of 0.01 % of water depth, fixed frames are still best for a Box-in style calibration.

Remember you are calibrating against a fixed known reference. The pre-calibrated beacon position results for each run will see differences in the calculated result. (2D before plot). The CASIUS or QINSY software will then make/suggest changes to sensor offsets to align the position results into one point (2D after plot). The operator can QC the data, make informed changes to other settings such as sound speed, and error rejection filters to fine tune the results for the best calibration result. Sonardyne CASIUS (Calibration of Attitude Sensors in a USBL System) software, when run directly from Ranger 2 will apply the final changes to system and produce a calibration report. Operators using QINSY or other USBL systems apply the changes manually. The results can then be verified post calibration.

Survey Line Design (Deep water line pattern): Run 12 lines around the beacon: Four lines in

https://doi.org/10.58440/ihr-31-2-n09

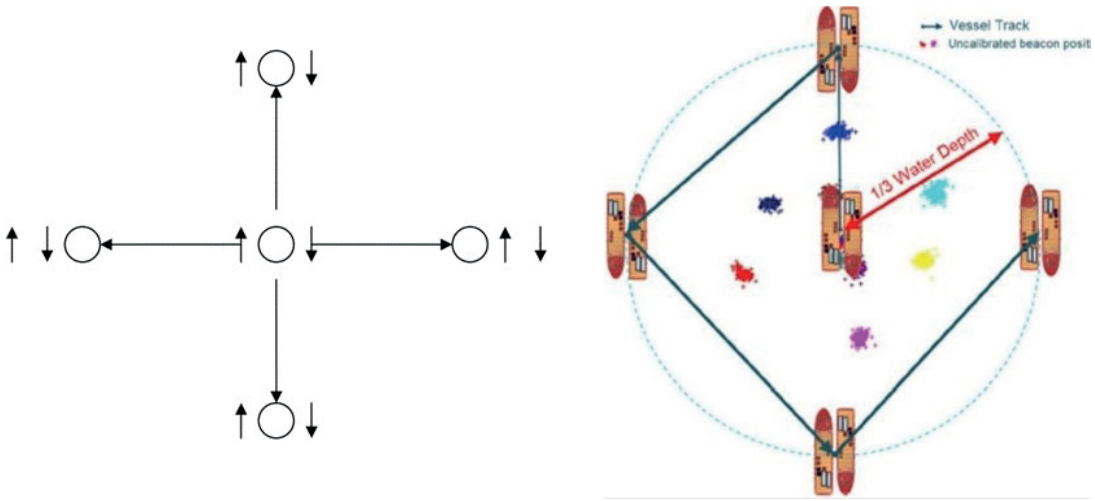


Fig. 18 Schematic of vessel position in static USBL validation for deep water calibration (left) and illustration of vessel and USBL calibration beacon (right).

cardinal directions: North (N), South (S), East (E), and West (W). Two diagonal crossings to enhance data density and improve angular accuracy.

Data Processing: Process the acquired data using specialized software such as CASIUS, QINSy, or equivalent. Store before/after calibration plots and software reports with (IHO, 2005, C-13 Appendix 1, calibration record). The software computes alignment and latency corrections, ensuring the USBL system aligns seamlessly with the vessel's reference frame. These are profiles sailed for deep water USBL calibration of 1000 m + water depths. It would be very challenging to sail this profile at ⅓ water depth with a beacon deployed at 30 m. Hence for shallow water survey the vessel sailing a four-leaf clover profile extending to 50 m from beacon position are recommended as illustrated in Figs. 19 and 20. Recommended deployment of USBL calibration procedures for shallow water shown in Fig. 21.

Example report of a CASIUS and data representation within the Ranger2 software interface illustrated in Fig. 22. While performing a real world USBL calibration, a screen capture for QINSy Navigation screen taken by author in Fig. 23.

Key considerations for box-in calibration:

- Lateral offsets: Maintain lateral offsets proportional to 33–50 % of the water depth (max. offset 500 m) for optimal coverage and accuracy.
- Vessel speed and stability: Ensure a steady course and maintain a survey speed of 3.5 knots throughout the calibration process.
- Environment: Select a calibration area with minimal underwater noise and interference to improve data clarity.
- Data Verification: Validate processed results against industry benchmarks to ensure alignment and latency corrections meet project requirements.

5.3 Verification of USBL systems

Purpose and Importance; Verification ensures that the USBL system's calibration has been executed correctly and that its accuracy aligns with project-specific tolerances. Verification is critical to confirm that positional deviations are within acceptable limits.

Spin Test: A spin test in Fig. 24 involves rotating the vessel around the deployed beacon at a steady rate. This evaluates the system's pitch and roll offsets, and GNSS offsets for absolute positioning errors and its ability to maintain accurate positioning during rotational movements.

Walk-Away Test: Move the vessel away from the beacon at a steady speed Fig. 25, observing and recording positional data to confirm heading offset alignment and the calibration's reliability over varying distances.

Ensure deviations fall within acceptable tolerances as outlined in project specifications or industry standards. Spin checks and walk-away tests further validate the calibration's stability and accuracy under operational conditions.

Mobilisation remains one of the most demanding and critical phases of any hydrographic survey, regardless of its scope. While this article has focused on the GNSS, MBES, and USBL systems, it is important to recognise the broader array of sensors within the hydrospatial domain such as magnetometers, SSS, SBP, and SVP, including MVP and many other sensors. Each of these instruments requires specific calibration and verification procedures such as spanner tests and positional verifications for SSS, surrogate item tests (SIT) for MAG, and SVP comparisons to ensure optimal performance and many other test, calibrations and verifications for individual system. Completing these checks is essential for formally signing off the mobilisation phase and authorising the commencement of survey operations. As hydrographic surveyors, it is imperative

not only to perform these procedures but to understand the theory behind them, ensuring confidence, reliability, and accuracy throughout the survey lifecycle.

6 Discussion: error propagation, verification value, and limits of guidance

Calibration reduces systematic components of error, while verification demonstrates fitness-for-purpose under operating conditions. Errors propagate through lever arms, timing, refraction, and heading alignment; their combined impact is most visible in outer-beam depth bias, seafloor "wobble," and target positional spread. Offshore practice often extends beyond general guidance in C-13 (IHO, 2005), which treats such topics across positioning, depth, and practice chapters and in Annex E rather than in a single "calibration" chapter. The framework presented here therefore complements C-13 by linking everyday offshore procedures (patch tests, INS dynamic alignment, USBL box-ins) to S-44's uncertainty outcomes and to traceable records in (IHO, 2005, Appendix 1), offering a practical bridge between standards and operations.

7 Conclusion

Calibration and verification are not supplementary tasks but the cornerstones of hydrospatial survey integrity. The technical frameworks described in this report covering GNSS verification, IMU alignment, gyro calibration, MBES patch testing, and USBL calibrations demonstrate that systematic validation directly safeguards data quality, reduces operational risk, and ensures compliance with international standards such as IHO S-44 for safety of navigation and other industrial standards. Mobilisation phases now routinely require formal calibration sign-off before survey commencement, underscoring their role as contractual and professional imperatives. By tying each procedure to C-13 record-keeping and S-44 uncertainty criteria, the workflow becomes both defendable and repeatable (IHO, 2005).

Beyond compliance, rigorous calibration fosters confidence in the results, enhances the

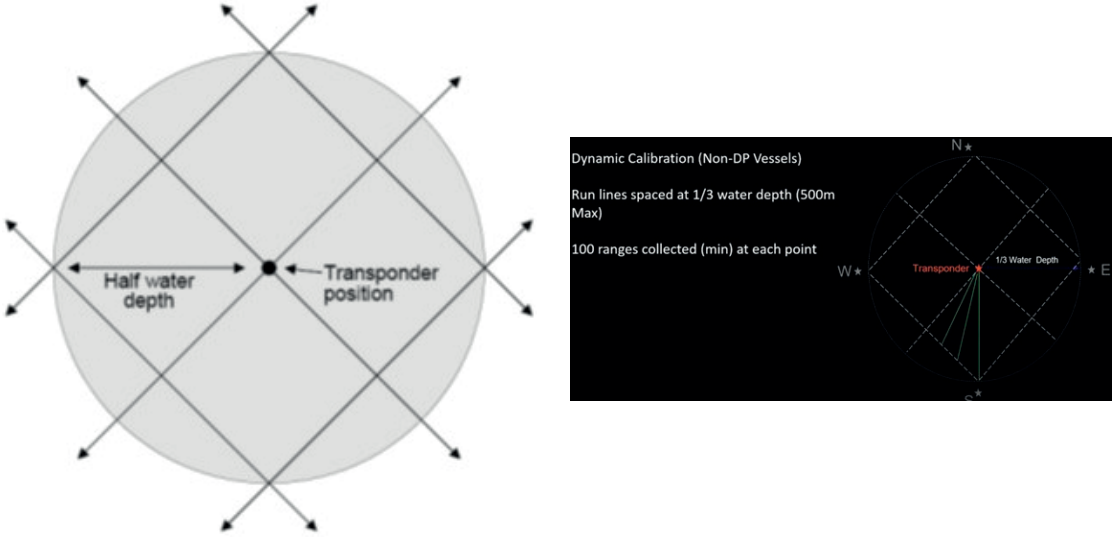


Fig. 19 Dynamic USBL calibration line pattern: Deep water (left) and standard stipulated by Sonardyne for Ranger2 system (right) (Sonardyne, 2020).

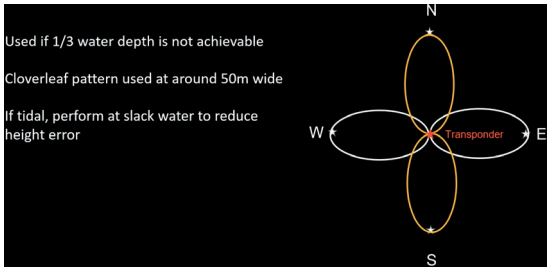


Fig. 20 Dynamic USBL calibration line pattern for shallow water (Sonardyne, 2020).

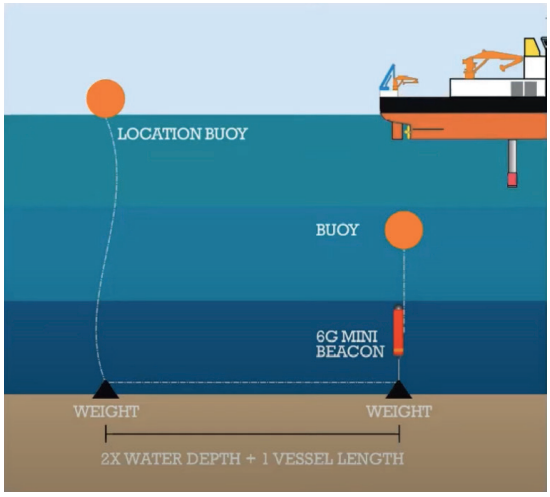


Fig. 21 Deployment in USBL calibration procedures for shallow water (Sonardyne, 2020).

https://doi.org/10.58440/ihr-31-2-n09

CASIUS Calibration Report

Sonardyne SOUND IN DEPTH

Vessel: Ship 1 **Date/Time:** 12 February 2019 15:12:38

Transceiver Settings:

Name	Device No	X/Y Offset Error	Depth Offset Error
Transceiver 1	001234	1.0m	0.5m

GNSS Settings:

Name	Forward Offset	Starboard Offset	Height Offset
GNSS 1	0.000m	0.000m	20.000m

Pitch, Roll & Heading Settings:

Name	Usage	Pitch Offset	Roll Offset	Heading Offset
PitchRoll 1	Pitch, Roll & Heading	0.00°	0.00°	0.00°

Beacon Settings:

Name	Received Signal	X/Y Error	Depth Error
2401	IRS 2401	30.0m	5.0m

Sound Speed:

	Surface	Average (Initial)	Average (Computed)
Sound Speed	1490.0m/s	1490.0m/s	1490.0m/s
Error	15.0m/s	0.0m/s	0.0m/s

Beacon 2401 Result:

	Beacon Latitude	Beacon Longitude	Beacon Depth	Beacon Eastings	Beacon Northings
Before	51.999999879°	-2.999999643°	499.998m	500000.039m	5761038.198m
Calculated	52.000000059°	-3.000000049°	499.992m	499999.997m	5761038.218m
Calculated Accuracy			0.004m	0.033m	0.034m

	Before CASIUS (distance)	After CASIUS (distance)	Before CASIUS (% depth)	After CASIUS (% depth)
39.4% Beacon Positions (1 sigma)	82.19m	0.48m	16.44	0.10
50.0% Beacon Positions (CEP)	83.66m	0.57m	16.73	0.11
63.2% Beacon Positions (1 Drms)	85.89m	0.67m	17.18	0.13
86.5% Beacon Positions (2 sigma)	88.45m	0.92m	17.69	0.18
95.0% Beacon Positions	89.03m	1.10m	17.81	0.22

Transceiver 'Transceiver 1' Result:

	Transceiver Starboard Offset	Transceiver Forward Offset	Transceiver Depth Offset	Transceiver Pitch Offset	Transceiver Roll Offset	Transceiver Heading Offset
Before	1.000m	2.000m	0.000m	0.10°	0.20°	50.30°
Calculated	0.114m	0.228m	0.000m	0.03°	-0.01°	0.01°
Calculated Accuracy	0.031m	0.032m	0.000m	0.00°	0.00°	0.01°

Summary Stats:

	Range RMS	Direction Cosine RMS	Observations	Excluded	Iterations
Box-in	0.032m		507	0	3

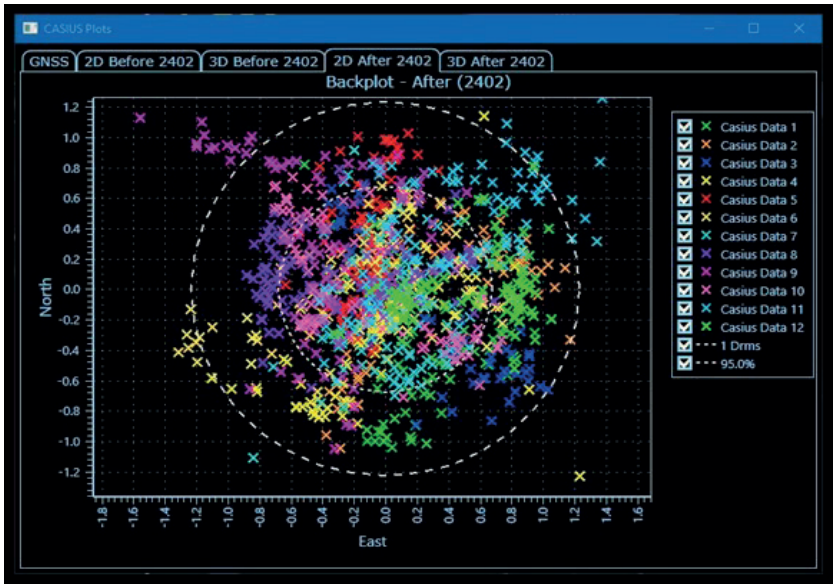


Fig. 22 Example of CASIUS report after Ranger2 USBL calibration (left) and 2D Backplot from CASIUS plots (right).

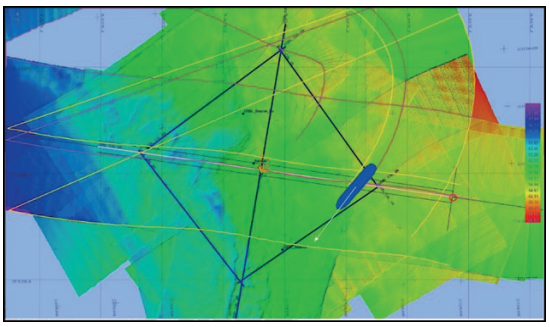


Fig. 23 Navigation display of QINSy acquisition software while the vessel performing CASUIS from Ranger2.

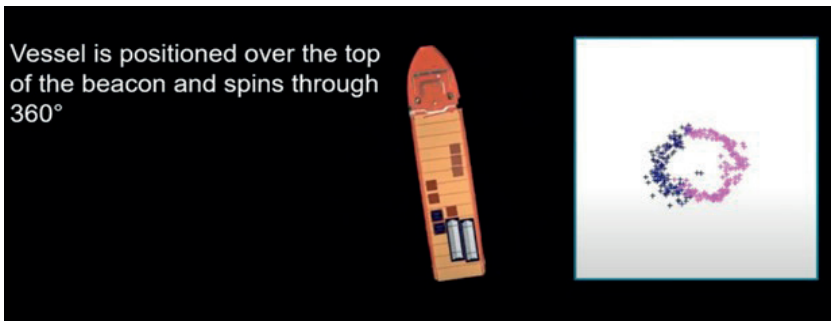


Fig. 24 Spin check for USBL verification on completion of the calibration (Sonardyne, 2020).

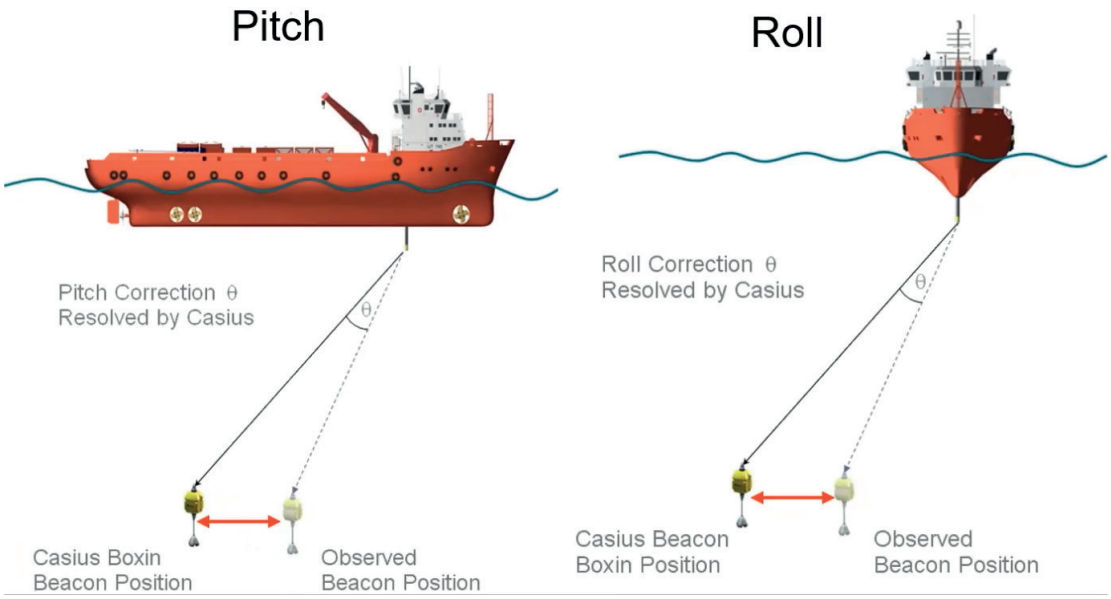


Fig. 25 Walk-away test for USBL verification on completion of the calibration (Sonardyne, 2020).

interoperability of complex sensor suites, and prevents costly re-surveys or project delays. Importantly, these practices also serve as a training foundation for the next generation of hydrographic professionals, instilling precision, accountability, and a structured approach to system verification. As hydrospatial operations expand in scope and complexity driven by offshore energy, environmental stewardship, and subsea infrastructure the ability to execute reliable calibrations will remain a defining standard of excellence. Continuous peer collaboration, analysis of recurring calibration issues, and adherence to best practices will not only uphold operational quality but also contribute to the evolution of hydrospatial standards. Ultimately, calibration and verification are not just technical necessities, but professional disciplines that underpin the trust, safety, and credibility of hydrographic survey operations worldwide.

References

Clarke, J. (2003). A reassessment of vessel coordinate systems: what is it that we are really aligning? *Proceedings of the US Hydrographic Conference*. pp. 1–12. https://api.semanticscholar.org/CorpusID:111076905 (last accessed 1 November 2025).

de Hilster, N. (2009). The MRU and SRF Aligned. *Hydro International*. https://www.hydro-international.com/content/article/the-mru-and-srf-aligned-ii-and-iii (last accessed 1 November 2025).

DrillingFormulas (2016). *Magnetic Declination and Grid Convergent and Their Applications in Directional Drilling*. Drilling Formulas and Drilling Calculations, Grapevine, USA. https://www.drillingformulas.com/magnetic-declination-and-grid-convergent-and-their-applications-in-directional-drilling/ (last accessed 1 November 2025).

Hains, D., Schiller, L., Ponce, R., Bergmann, M., Cawthra, H. C., Cove, K., Echeverry, P., Gaunavou, L., Kim, S.-P., Lavagnino, A. C., Maschke, J., Mihailov, M. E., Obura, V., Oei, P., Pang, P. Y., Njanaseelan, G. P., Sharma, S. L. (2022). Hydrospatial – Update and progress in the definition of this term. *The International Hydrographic Review, 28*, pp. 221–225. https://doi.org/10.58440/ihr-28-n14

IHO (2005). *Manual on Hydrography* (1st ed.). IHO Publication C-13, International Hydrographic Organization, Monaco. https://iho.int/uploads/user/pubs/cb/c-13/english/C-13_Chapter_1_and_contents.pdf (last accessed 1 November 2025).

IHO (2018). *Standards of Competence for Category 'A' Hydrographic Surveyors* (ed. 1.0.2). IHO Publication S-5A, International Hydrographic Organization, Monaco. https://iho.int/iho_pubs/standard/S-5/S-5A_Ed1.0.2.pdf (last accessed 1 November 2025).

IHO (2020). *Standards for Hydrographic Surveys* (ed. 6.0). IHO Special Publication S-44, International Hydrographic Organization, Monaco.

Lekkerkerk, H.-J. and Theijs, M. J. (2013). *Handbook of Offshore Surveying* (Volume III). Skilltrade, London, UK.

Lekkerkerk, H.-J. and Theijs, M. J. (2019). *Handbook of Offshore Surveying* (Volume I). Skilltrade, London, UK.

Lekkerkerk, H.-J. (2024). S-44 and the systematic error. *Hydro International*. https://www.hydro-international.com/content/article/s-44-and-the-systematic-error (last accessed 1 November 2025).

Royal Navy (2019). *The Admiralty manual of navigation: Vol. 1: Principles of navigation* (11th ed.). The Nautical Institute. ISBN 9781906915643.

Schnare, T. (2014). *Caris HIPS & SIPS 8.0 Manual for Hydrography & Survey Use*. MGEO 2014.

SIS (2024). *Seafloor Information System Reference Manual* (ed. 5.12).K ongsberg Discovery AS, Norway.

Sonardyne (2020). *Sonardyne Training Webinar 7 – CASIUS* [Video]. YouTube. https://www.youtube.com/watch?v=yulHh-linMh4 (last accessed 1 November 2025).

https://doi.org/10.58440/ihr-31-2-n09

NOTE / TECHNICAL REPORT

Submarine geographical names – a review of the recent incorporation of seabed features submitted by Chile to the GEBCO gazetteer

Author
Jacob Inostroza Torres[1]

Abstract

Between 2021 and 2024, Chile discovery and naming of six submarine features has been recognized internationally through the Sub-Committee on Undersea Feature Names of the General Bathymetric Chart of the Oceans, within the framework of the International Hydrographic Organization. Thanks to advancements in multibeam technology, a range of seafloor features located in surrounding oceanic areas have been identified and proposed for naming. This note outlines the approved denominations and their relevance as contributions to ocean knowledge within the framework of the United Nations Decade of Ocean Science for Sustainable Development.

Keywords
Atacama Deep · Chilean seamounts · GEBCO gazetteer · guyot · multibeam echosounders · SCUFN · submarine geomorphology · submarine toponymy

1 Chile and the naming of submarine features: An ongoing commitment to international hydrography

The seafloor remains one of the least explored and understood geographical domains, despite its scientific, environmental, and strategic significance. In recent decades, the development and refinement of bathymetric survey technologies – particularly multibeam echosounders – have enabled Chile to make significant progress in mapping its seabed. This has facilitated the identification and characterization of important submarine features.

In this context, SCUFN is the Sub-Committee on Undersea Feature Names (SCUFN) of the General Bathymetric Chart of the Oceans (GEBCO), within the framework of the International Hydrographic Organization (IHO) and the Intergovernmental Oceanographic Commission (IOC), responsible for reviewing, evaluating, and approving proposals for naming undersea features worldwide. Its mandate is to ensure consistency in toponymy and to ensure the standardized use of official names in maps, nautical charts, scientific research, and international publications.

The Hydrographic and Oceanographic Service of the Chilean Navy (SHOA) is the State's permanent technical agency responsible for hydrography, oceanography, and the unification of nautical toponymy, among other matters (SHOA, 2023). In this regard, it chairs and leads the National Committee on Antarctic Geographic Names, which brings together the country's official cartographic institutions and seeks to achieve concordance and standardization of geographic names for use on charts and related publications. For this reason, the SHOA has also taken an active role in proposing and submitting names to the SCUFN through oceanographic cruises

✉ Jacob Inostroza Torres · jactorres@gmail.com
[1] Hydrographic and Oceanographic Service of the Chilean Navy (SHOA), Chile

https://doi.org/10.58440/ihr-31-2-n11

and hydrographic surveys, primarily conducted by the Chilean Navy's research vessel *AGS Cabo de Hornos* (Fig. 1). These efforts seek to contribute to the international progress of toponymic standardization and provide high-resolution bathymetric data on the seafloor.

2 The importance of submarine toponymy

Submarine toponymy is a key tool in the advancement of scientific research, marine geospatial data management, and international hydrographic cooperation. The standardized naming of seafloor features enables precise identification of structures relevant to oceanography, marine geology, benthic biology, and ocean engineering, ensuring consistent reference across scientific and technical domains.

The assignment of geographic names to seafloor features contributes to the orderly and internationally recognized representation of underwater entities in oceanic spaces. This fosters data interoperability between nautical charts, databases, and marine monitoring platforms, which supports oceanographic research initiatives. In this regard, it is important to emphasize the availability of the bathymetric data from the proposals submitted to SCUFN, to contribute to GEBCO's seafloor mapping.

This SCUFN-regulated methodology, highlights the technical commitment of States to generating high-resolution bathymetric data and to the systematic characterization of the ocean floor.

As multibeam hydrographic surveys expand, the need to update and increase undersea toponymy grows, in accordance with IHO principles and standards and those of the broader ocean science community. These efforts contribute to Seabed 2030 – a global initiative aimed at mapping the entire ocean floor by 2030 – and reinforce international collaboration for the UN Decade of Ocean Science for Sustainable Development (2021–2030). The Decade seeks to advance scientific research and knowledge of the oceans to promote their health and sustainable use.

To this end, proposals submitted to the SCUFN undergo an exhaustive review process by its members, who possess advanced knowledge in bathymetry, submarine geomorphology, among other topics, where, among other variables, they must verify the appropriateness of the proposed name, the morphometric characterization of the entity and its delimitation, also reviewing compliance in the proposals with the formats and indications established in IHO-IOC Publication B-6: Standardization of Undersea Feature Names.

The approved names were incorporated into the GEBCO Gazetteer of Undersea Feature Names[1], which serves as the international reference database for submarine toponymy.

3 Chilean proposals approved (2021–2024)

Since 2021, Chile has contributed six undersea feature names. Their main characteristics are briefly outlined below.



Fig. 1 Vessel *AGS Cabo de Hornos*.

[1] https://www.ngdc.noaa.gov/gazetteer (last accessed 5 August 2025).

3.1 Piloto Pardo Seamount (2021)

The Piloto Pardo Seamount is a prominent feature with a vertical relief of over 1,700 meters (Table 1), located on the seafloor of the Drake Passage. The name *Piloto Pardo Seamount* (Fig. 3) honors Second Pilot Luis Pardo Villalón (Fig. 2), a renowned officer of the Chilean Navy who, in 1916, led the schooner *Yelcho* during the heroic rescue of the crew of Ernest Shackleton's ship *Endurance* on Elephant Island in Antarctica (Cárcamo, n.d.).

The name was officially accepted at SCUFN's 34th meeting in 2021 and is now recognized for use in the international ocean science community and represented in charts and related publications.

3.2 O'Higgins Seamount and O'Higgins Guyot (2023)

The O'Higgins Seamount and O'Higgins Guyot are large-scale submarine features located west of Valparaíso and east of the Juan Fernández Archipelago (Fig. 4; Valenzuela & Vergara, 1982). Classified based on their geomorphological characteristics, the guyot is the largest feature, with a relief exceeding 2,700 m. These features (Tables 2 and 3), named *O'Higgins Seamount* and *O'Higgins Guyot,* commemorate Chilean independence leader General Bernardo O'Higgins Riquelme (Fig. 5). These names had already been widely used informally in marine scientific literature prior to their official approval. These names were officially accepted at the 36th SCUFN meeting in 2023.

3.3 Atacama Deep (2024)

The Atacama Deep is a located west of the Mejillones Peninsula in northern Chile (Fig. 6), this is the deepest point (8,087 m) in the Peru-Chile Trench (Table 4). The name *Atacama Deep* references its proximity to the Atacama Desert, one of the driest regions on Earth. The area is of high interest to the international scientific community for studies of deep-sea ecosystems. The name was officially accepted at SCUFN's 37th meeting in 2024.

3.4 Morales Seamount (2024)

The Morales Seamount located east of Alejandro Selkirk Island in the Juan Fernández Archipelago (Table 5). This feature was submitted at SCUFN's 37th meeting in 2024. Morales Seamount (Fig. 7) honors Chilean geographer Dr. Esteban G. Morales (Fig. 8), a pioneer in Chile's scientific exploration of the seafloor (Morales, 2007).

3.5 Vidal Gormaz Seamount (2024)

The Vidal Gormaz Seamount is a prominent seamount with over 1,200 meters of relief (Fig. 9), located in the Drake Passage, approximately 37 miles southwest of Piloto Pardo Seamount. The name Vidal Gormaz Seamount commemorates Captain Francisco Vidal Gormaz (Fig. 10; Maldonado, 2016), regarded as the Father of Hydrography in Chile and the first director of the Chilean Hydrographic Office. The name was officially accepted at SCUFN's 37th meeting in 2024.

Table 1 Piloto Pardo Seamount – Technical sheet.

Location	59°01.40' S, 65°46.38' W
Minimum depth	586 m
Maximum depth	2,300 m
Relief	1,714 m
Dimensions	21 km × 11 km

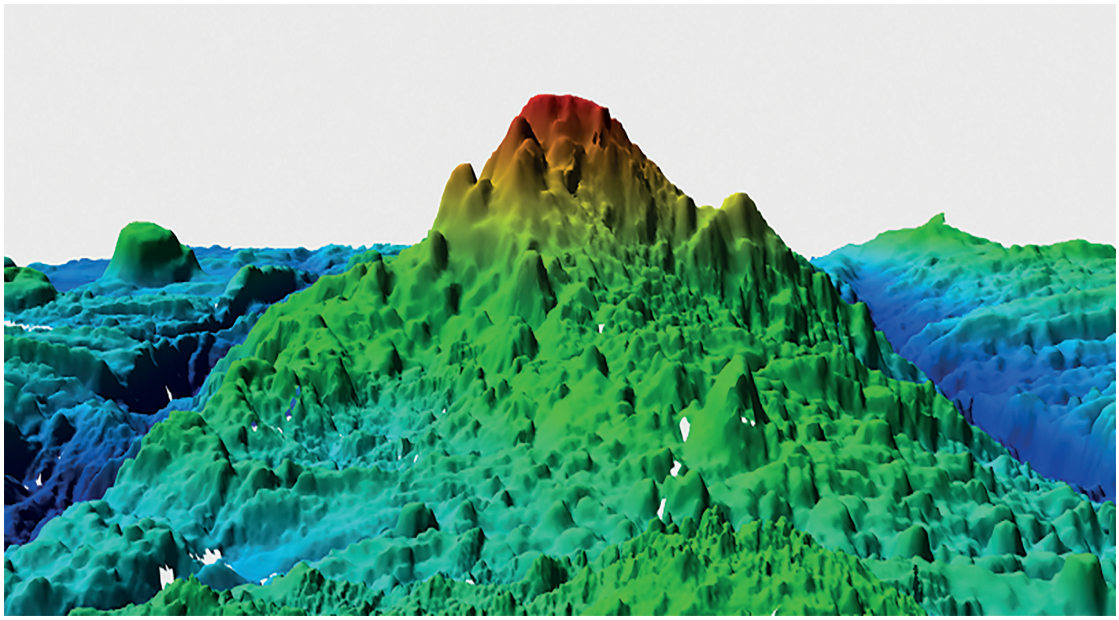


Fig. 2 3D image of the Piloto Pardo Seamount.

https://doi.org/10.58440/ihr-31-2-n11



Fig. 3 Pilot 2nd Luis Pardo Villalón, commander of the auxiliary vessel *Yelcho*.

Table 2 Technical sheet of O'Higgins Seamount.

Location	32°50.3' S, 73°37.5' W
Minimum depth	712 m
Maximum depth	3,174 m
Relief	2,462 m
Dimensions	17 km × 12 km

Table 3 Technical sheet of O'Higgins Guyot.

Location	32°54.4' S, 73°53.1' W
Minimum depth	345 m
Maximum depth	3,128 m
Relief	2,783 m
Dimensions	36 km × 27 km

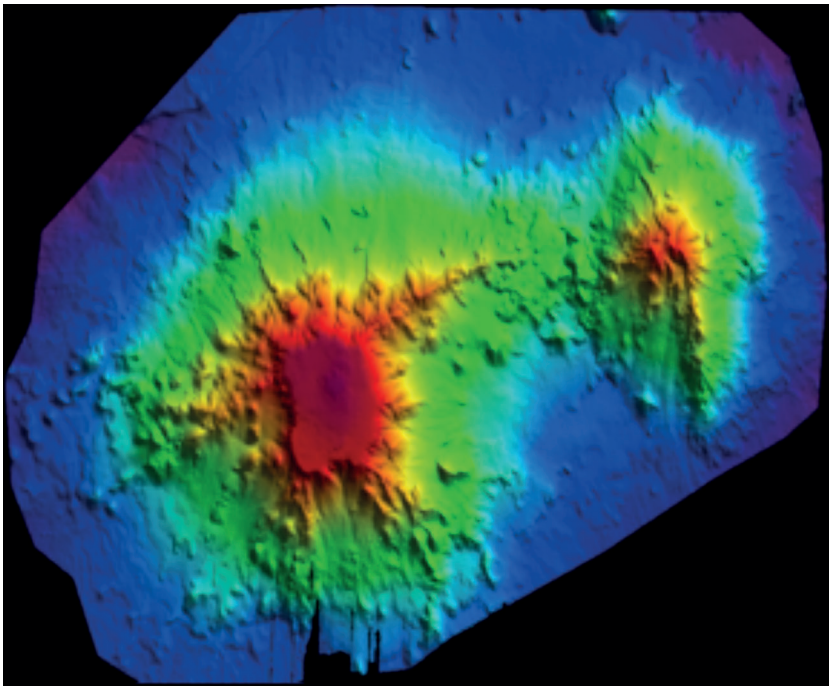


Fig. 4 Bathymetric surface of the O'Higgins seamount and guyot.



Fig. 5 Portrait of Bernardo O'Higgins Riquelme (Author: José Gil de Castro, 1820).

https://doi.org/10.58440/ihr-31-2-n11

Table 4 Technical sheet of Atacama Deep.

Location	23°24.56' S, 71°20.56' W
Minimum depth	6,898 m
Maximum depth	8,087 m
Dimensions	24 km × 5 km

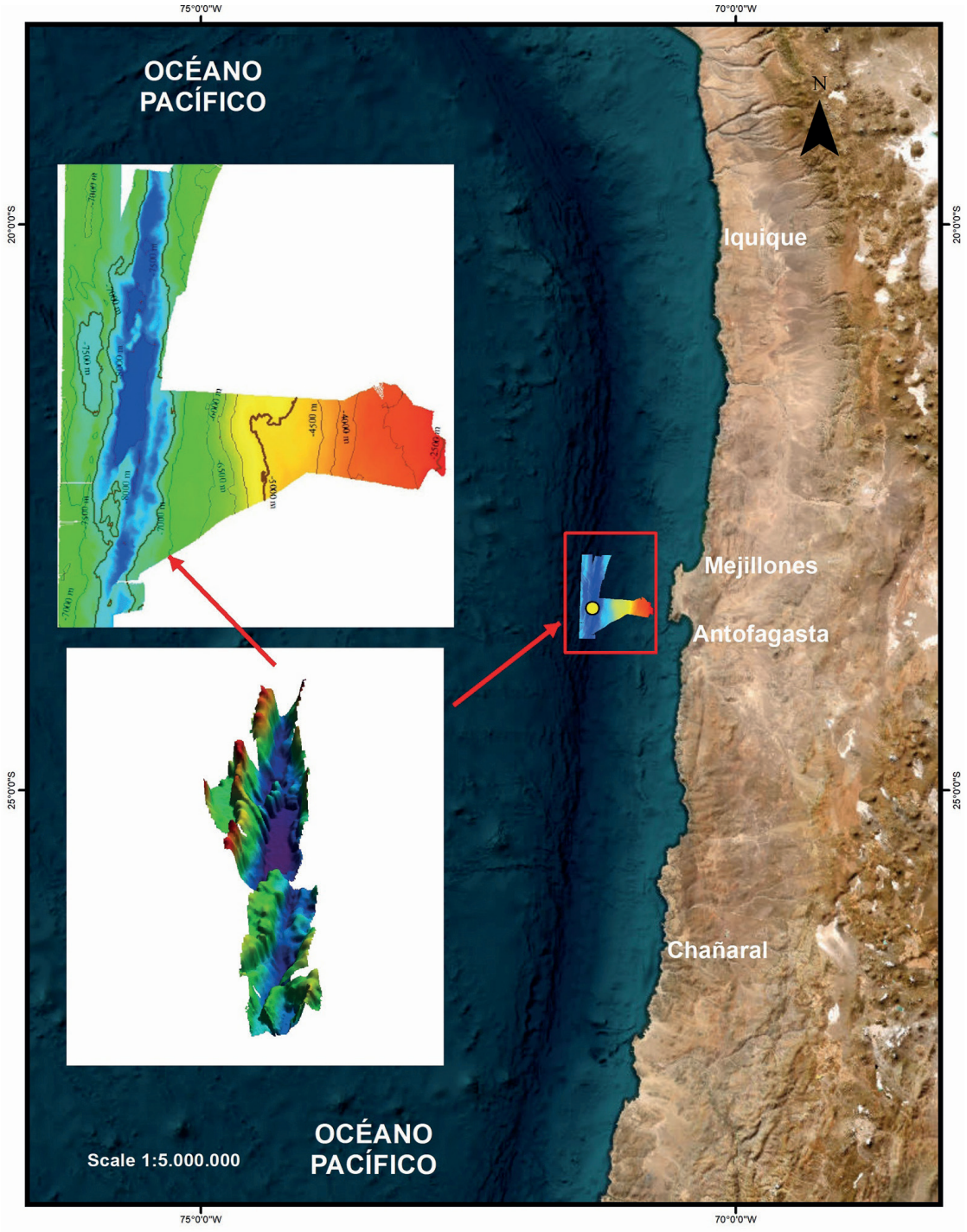


Fig. 6 Geographic context of the Atacama Deep.

https://doi.org/10.58440/ihr-31-2-n11

Table 5 Technical sheet of Morales Seamount.

Location	33°48.04' S, 80°21.89' W
Minimum depth	717 m
Maximum depth	3,193 m
Relief	2,476 m
Dimensions	27 km × 25 km

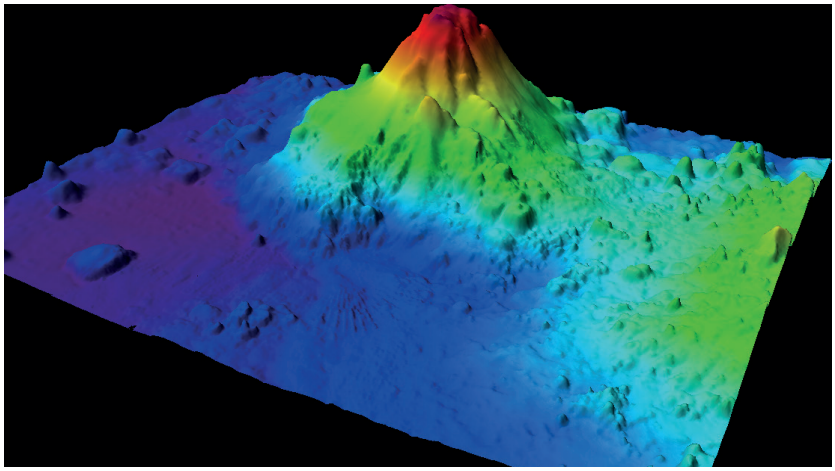


Fig. 7 3D image of the Morales Seamount.



Fig. 8 Dr. Esteban G. Morales (1942–2022).

Table 6 Technical sheet of Vidal Gormaz Seamount.

Location	58°58.99' S, 64°34.83' W
Minimum depth	2,556 m
Maximum depth	3,779 m
Relief	1,223 m
Dimensions	18 km × 15 km

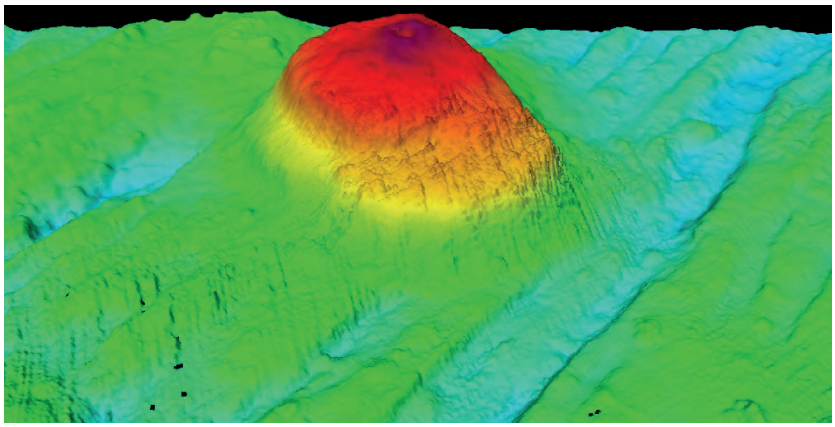


Fig. 9 3D image of the Vidal Gormaz Seamount.



Fig. 10 Captain Francisco Vidal-Gormaz (1837–1907).

4 Conclusion

The approval of toponymic proposals by SCUFN marks a significant step forward in the global effort to enhance the knowledge and representation of undersea features. Chile's contribution reflects its commitment to the marine scientific community by incorporating these names into the GEBCO Gazetteer and promoting the standardized use of submarine toponymy across cartographic products, geospatial databases, and scientific publications. Also important is the contribution of bathymetric data made available with these proposals, which directly benefits the effort to achieve complete coverage of the ocean floor.

The process of identifying, characterizing, and officially naming these features has been supported by high-resolution bathymetric surveys using

multibeam technologies, conducted in accordance with IHO standards and methodologies. Therefore, we are grateful for the enormous contribution of SCUFN in receiving and reviewing the proposals to nominate underwater geoforms that contribute to the dissemination and knowledge of the seabed. The inclusion of these names strengthens the principle of interoperability in marine geospatial data and enhances the accuracy and consistency of international hydrographic information.

As bathymetric data becomes increasingly available and global interest in ocean floor exploration grows, this contribution aligns with the broader efforts in standardized seafloor cartography, international scientific cooperation, and reliable geospatial information to support ocean governance.

References

Cárcamo, V. E. (n.d.). *La gran hazaña del Piloto Pardo y su tripulación en la escampavía Yelcho: Rescate de la expedición británica en la Antártica en 1916*. Academia de Historia Naval y Marítima de Chile.

Morales, E. (2007). *Historia de la exploración submarina.* Ediciones Universitarias de Valparaíso, PUCV.

Maldonado, Z. S. (2016). Francisco Vidal Gormaz: Hidrógrafo olvidado del Chile decimonónico. *Revista de Marina, 6,* pp. 34–39. https://revistamarina.cl/revistas/2016/6/zsaldiviam.pdf (last accessed 30 September 2025).

SHOA (2023). *Hydrographic Instructions No. 3: Geographic Naming Determination* (3rd ed.). Publication No. 3103, Hydrographic and Oceanographic Service of the Chilean Navy, Valparaíso, Chile.

Valenzuela, E. and Vergara, H. (1982). Morfología submarina del Guyot O´Higgins, extremo oriental del cordón asísmico Juan Fernández. *III Congreso Chileno de Geología*, Concepción, Chile.

https://doi.org/10.58440/ihr-31-2-n11

NOTE / TECHNICAL REPORT

The Directorate of Hydrography and Navigation inaugurates the new LA-RENC training center of IC-ENC in favor of navigation safety

Authors

Nickolás Roscher[1], Ana Mileze[1], Isaias Brito[1], Bruna Pinheiro[1] and Igor Justino[1]

As part of the celebrations for World Hydrography Day, June 21st, and the 9th Anniversary of LA-RENC, the Directorate of Hydrography and Navigation inaugurated the LA-RENC training center (Figs. 1–4).

The Latin American training center has been realized with the support of the International Centre for Electronic Navigational Charts (IC-ENC) Steering Committee and DHN, and it will play a crucial role in both the LA-RENC and IC-ENC. The LA-RENC training center is the first regional training center, not only of the IC-ENC but also recommended by the IHO, and represents an important milestone for technical training in Latin America. The creation of this center reinforces IC-ENC's commitment to developing regional skills and disseminating best practices in the area of hydrography and nautical cartography.

It was developed to transform relevant hydrographic data and information into electronic charts and services as a creative and well-considered teaching tool for the IC-ENC community. Its first goal is to provide training for the new vector electronic chart series of the S-100 standard. The main objective of this center is to offer specialized courses not only in the validation of Electronic Nautical Charts (ENCs) in the S-57 format, but also in supporting the transition and production of ENCs in the new international S-101 standard.

Based on the aptitude and commitment of each student, the training center's primary goal is to offer the best training possible to the IC-ENC Member States, especially the Iberophone countries. DHN believes that education is the foundation for building a better and more just future, and this training center provides a welcoming, stimulating, and quality environment for all 54 IC-ENC members (Fig. 4).

As part of the inauguration activities, the first training session at the new facilities was held from the 23rd to the 27th June 2025: "Quality Training for S-57 Electronic Navigation Charts, S-57 to S-101 Conversion, and S-101 Validation" (Fig. 5). The training was led by two IC-ENC validators from the UK, and was attended by representatives from several countries: Argentina, Brazil, Chile, Colombia, Cuba, Panama, Uruguay, and Venezuela.

The training allowed participants to familiarize themselves with the entire validation process performed by IC-ENC, from ENC submission to the validation report. A wide range of topics were highlighted, including the standards used in the production of S-57 and S-101 ENCs and the IHO S-58 validation standard. The various software tools used for validation (Dkart and ENC Analyzer) were also discussed. ENCs in S-57 format were converted to S-101 format and validated according to the criteria established for the S-101 product.

During the interactive sessions, participants were able to deepen their technical knowledge about cartographic data validation, as well as discuss the challenges associated with the transition to the new S-101 standard.

Complementing the technical training was a workshop led by LtCdr Mileze. This session provided a forum for participants to share experiences and clarify questions, addressing topics such as the operational impacts of adopting the S-101 standard, the implementation strategies planned in each country, and the specific needs for technological and institutional adaptation.

✉ Nickolás de Andrade Roscher · nickolas.roscher@marinha.mil.br

[1] Directorate of Hydrography and Navigation, Brazilian Navy, Brazil

https://doi.org/10.58440/ihr-31-2-n08



Fig. 1 Training center opening.



Fig. 2 Course opening.

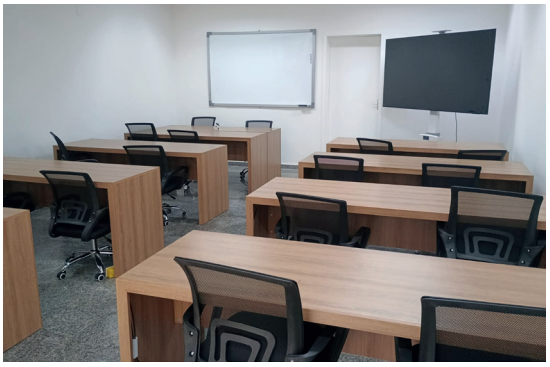


Fig. 3 LA-RENC training center.



Fig. 4 IC-ENC training.



Fig. 5 Official photo S-57 ENC quality training.

The success of this first initiative is already driving the planning of new training courses for 2026 and 2027, which will follow the same collaborative and multilingual format (Fig. 6), bringing even more updated content aligned with international trends in the area of electronic nautical cartography.

The future is bright and the LA-RENC is committed to staying ahead of the curve, offering ongoing and strategic support to IC-ENC member countries. Our goal is to ensure that the production of ENCs is carried out with excellence, aligned with the highest international standards of quality, innovation, and accuracy. Through technical training, regional cooperation, and continuous education, IC-ENC seeks to strengthen the capacity of member states to meet the present and future challenges of nautical cartography.

LA-RENC, located at the Navy Hydrographic Base in Niterói (BHMN; Figs. 7–9), began its validation processes in June 2016. Since then, the office has completed a total of 15,703 validations, including updates, new editions, and new cells. In addition to these activities, the LA-RENC also plays an important role as the IC-ENC's primary point of contact for member states in the Latin American region, providing guidance and support on issues related to S-57 ENCs and, in the future, supporting production in S-101.

The LA-RENC team of validators has expertise in



Fig. 6 IC-ENC training instructors from UK and Brazil.



Fig. 7 LA-RENC office.



Fig. 8 LA-RENC building.

validation processes. It uses various software tools to analyze each ENC according to the coding rules and practices defined in the S-57, S-58, and future S-101 and S-158 standards, as well as the IC-ENC policies, based on real and practical user experience.

The standards and reports generated by software tools, due to different concepts, can be ambiguous and complex, so the expertise of validators in interpreting these reports is crucial. This ensures our members receive reports with clear and objective explanations, making it easier for member countries to correct potential errors. Consistency across the entire data set and the overall security and usability of the products are also assessed.

The detailed feedback report for each validation includes possible consistency improvements, providing an overview of the quality and suitability of each ENC for release, as well as offering guidance on how to correct any identified issues and recommending improvement actions.

To ensure the quality, consistency, and reliability of ENCs, IC-ENC and all offices of regional authorities adopt practices based on the standard ISO 9000, focused on quality management systems. In July 2025, the LA-RENC successfully passed its audit, thus maintaining its ISO 9000 certification. Certifying that the IC-ENC and Regional offices are aligned with international standards, especially those of the IHO, are a fundamental requirement for global cooperation.

Regional ENC Coordinating Centres (RENCs) are centers responsible for the validation, maintenance, and distribution of ENCs, ensuring that the data meets the international standards and specifications established by the IHO.

ENCs are designed to ensure the safety and accuracy of navigation routes, facilitating vessel movement in maritime areas, with constant updates to reflect changes in sea conditions and signaling infrastructure. For ENCs to be distributed to the market and used safely, they must be validated by a competent authority, such as a RENC.

https://doi.org/10.58440/ihr-31-2-n08

One of the RENCs available to the international hydrographic community is the IC-ENC, whose mission is to assist Hydrographic Offices in the production, harmonization, and distribution of high-quality ENCs. This helps ensure that ENCs comply with international standards and with the International Convention for the Safety of Life at Sea (SOLAS).

Currently, IC-ENC has approximately 54 member hydrographic offices who contribute towards the objective, through "global collaboration, with a regional focus". This is achieved through carrying out the validation of approximately 10,000 cells per year in the IC-ENC Regional Offices located in Australia, Brazil (LA-RENC), the United States, and in the future also in Nigeria.



Fig. 9 Brazilian navy staff.

NOTE / TECHNICAL REPORT

Leadership in regional hydrography: vision, capacity building and integration

Author
Mohammad Musa[1]

1 Introduction

In an era of growing maritime significance and ever-increasing emphasis on sustainable use of ocean resources, Hydrography has emerged as a cornerstone of maritime safety, economic development, and environmental stewardship. For a nation like Bangladesh, with a vast maritime zone in the Bay of Bengal, hydrographic leadership is not only a strategic imperative but also a national responsibility. Under the leadership of the Bangladesh Navy, the country's hydrographic journey has undergone a transformative evolution-marked by advanced capability development, international collaboration, and regional leadership.

The nomination of Bangladesh as Chair of the North Indian Ocean Hydrographic Commission (NIOHC) for the term of 2025–2027, marks a significant milestone in its maritime diplomacy and regional influence. This leadership position reflects the growing recognition of Bangladesh Navy's technical expertise, operational readiness, and institutional vision in the field of Hydrography and Oceanography. Through initiatives like Electronic Navigational Chart (ENC) production, seabed mapping, capacity building, and collaboration with the International Hydrographic Organization (IHO), Bangladesh has positioned itself as a central actor in promoting safe navigation, regional data sharing, and sustainable Blue Economy activities. The participation by the Chairman of National Hydrographic Committee (NHC) in global hydrographic forums, such as the Capacity Building Sub-Committee (CBSC) and Inter-Regional Coordination Committee (IRCC) meetings held in Monaco, further underscores Bangladesh's growing integration into the global hydrographic framework.

This paper aims to explore the vision of Bangladesh Navy's leadership in Hydrography, the institutional and operational roles it plays through regional bodies and national committee, and the ways in which regional cooperation, capacity enhancement, and technological innovation are being prioritized. It delves into how the leadership of Bangladesh is bridging gaps between national and regional interests, aligning Hydrography with broader strategic goals, and positioning the country as a key contributor to regional maritime safety and sustainable development.

2 Aim

This paper aims to explore the leadership of Bangladesh in regional Hydrography through its active roles in the NIOHC and NHC. It will also highlight the Navy's vision, capacity building efforts, and strategic integration to promote maritime safety, regional collaboration, and sustainable blue economy activities.

3 North Indian Ocean Hydrographic Commission

The NIOHC is a Regional Hydrographic Commission (RHC) under the IHO. It aims to promote regional cooperation in Hydrography, nautical charting, and marine geospatial data among member states bordering the North Indian Ocean (Fig. 1). The commission facilitates the exchange of technical expertise, capacity building, and implementation of international hydrographic standards such as S-100 (Universal Hydrographic Data Model) developed by the IHO as a framework for digital maritime data. By supporting safe navigation, maritime trade, and environmental protection, NIOHC plays a vital role in strengthening maritime governance in the region. Bangladesh Navy has taken over the chairmanship of NIOHC from Thailand for next two years (i.e. 2025–2027; Figs. 2 and 3; IHO, 2025).

✉ Mohammad Musa · mmusa67@gmail.com
[1] Bangladesh Navy, Office of the Assistant Chief of Naval Staff (Operations), Dhaka, Bangladesh

https://doi.org/10.58440/ihr-31-2-n12

4 Role of Bangladesh Navy as Chair of NIOHC with the vision

As the Chair of the NIOHC for the term of 2025–2027, Bangladesh holds a leadership position of strategic importance in advancing regional co-operation in Hydrography. With growing maritime activities in the North Indian Ocean, the need for accurate nautical information and coordinated hydrographic efforts has become increasingly critical. Bangladesh is committed to fostering collaborative frameworks among member states to enhance navigational safety, protect the marine environment, and ensure efficient maritime trade. As Chair, Bangladesh promotes a comprehensive and forward-looking agenda that strengthens the collective capacity of the region's hydrographic services.

A key priority under Bangladesh's chairmanship is capacity building across the NIOHC member states. By facilitating training programs, technical workshops, and knowledge exchanges, Bangladesh is working to uplift the technical competencies of hydrographic offices, especially among developing countries in the region. The focus includes strengthening national hydrographic capabilities, modernizing data collection techniques, and enhancing access to contemporary tools and technologies. These efforts are aligned with the broader goals of the IHO, ensuring that all members can effectively contribute to and benefit from a harmonized regional hydrographic infrastructure.

Moreover, Bangladesh is placing strong emphasis on the transition towards the S-100 framework, the next generation of hydrographic standards developed by the IHO. This transition is vital for supporting emerging needs such as e-navigation, marine spatial planning, disaster risk reduction, and blue economy initiatives. Through its leadership, Bangladesh is encouraging interoperability, standardization, and data-centric services across the region, facilitating the production of advanced hydrographic products and services. These initiatives not only strengthen maritime safety but also contribute to sustainable ocean governance and the long-term development goals of the NIOHC member states (IHO, 2023).

In light of the above, the Chairman's vision extends to the sustainable development of the blue economy. Recognizing the critical role of modern Hydrography and maritime geospatial data in unlocking economic potential, the focus will be on establishing a robust data infrastructure that supports marine resource management, coastal planning, disaster preparedness, and climate resilience. Through strategic leadership, Bangladesh seeks to ensure that Hydrography not only serves the needs of the maritime industry but also becomes a catalyst for environmental stewardship and long-term economic growth throughout the North Indian Ocean region (Sarker & Islam, 2018).

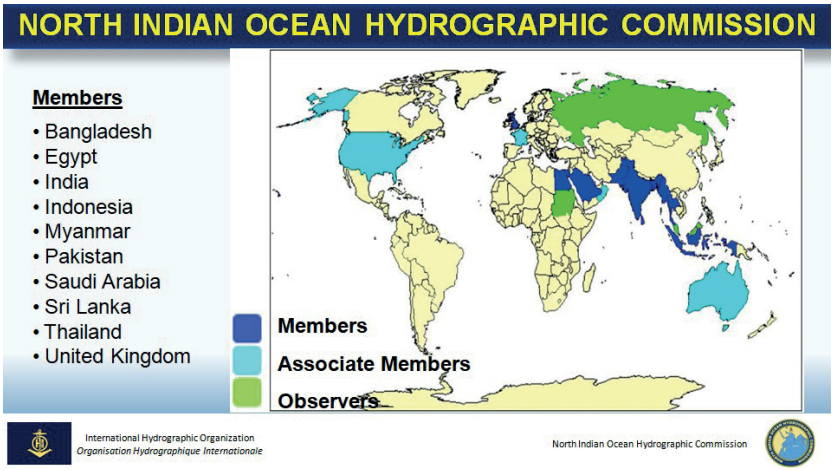


Fig. 1 NIOHC Member States map (IHO, 2025).



Fig. 2 Bangladesh Navy is taking over the chairmanship of NIOHC from Thailand during 24th NIOHC conference at Bangkok (ISPR, 2025).



Fig. 3 Bangladesh Navy is taking over the chairmanship of NIOHC from Thailand during 24th NIOHC conference at Bangkok (ISPR, 2025).

5 Capacity building in the NIOHC region

Capacity building remains a cornerstone priority in the NIOHC region, particularly for enhancing the capabilities of developing member states. Many of these nations face significant limitations in resources, infrastructure, and trained personnel, which hinder their ability to contribute effectively to regional

https://doi.org/10.58440/ihr-31-2-n12

hydrographic initiatives. Under the dynamic leadership of Bangladesh and with continued support from the IHO, capacity development has been prioritized to bridge these gaps and promote equitable participation. These efforts aim to build a more capable and collaborative regional hydrographic community, capable of responding to the demands of modern maritime safety, coastal management, and economic development (Fig. 4; IHO, 2025).

To this end, a range of practical initiatives have been implemented, including the organization of technical workshops, seminars, and collaborative exercises focused on current and emerging hydrographic needs. Bangladesh Navy, through its Hydrographic School, has taken the initiative by offering specialized training such as Category 'B' Hydrography course, supporting the professional development of Hydrographers from across the region. These training programs are further complemented by initiatives such as equipment-sharing arrangements, survey planning support, and technical guidance on ENC production and S-57 implementation. These programs not only enhance operational readiness but also promote regional interoperability and adherence to IHO standards.

Through these sustained efforts, Bangladesh is playing a transformative role in advancing regional hydrographic capacity. By focusing on human resource development and technology transfer, Bangladesh Navy is enabling member states to produce their own navigational charts, conduct reliable hydrographic surveys, and support marine spatial data infrastructure. As the region moves toward a digital and data-centric future, capacity building also supports the broader goals of maritime safety, environmental stewardship, and blue economy growth. Ultimately, this vision reinforces sustainable ocean governance and ensures that all NIOHC nations, regardless of size or capacity, have a voice and a role in shaping the maritime future of the North Indian Ocean.

6 National Hydrographic Committee of Bangladesh

The NHC of Bangladesh serves as the apex body responsible for overseeing and coordinating hydrographic efforts across the nation. Established to foster a unified national approach to Hydrography, the NHC is chaired by Assistant Chief of Naval Staff (Operations) of the Bangladesh Navy and comprises representatives from major maritime and coastal stakeholders. These include government departments and agencies associated with ports, shipping, fisheries, energy, the environment, disaster management etc. (Table 1). The committee provides a structured platform for inter-agency collaboration and ensures that the hydrographic needs of various sectors are addressed coherently and effectively. The Chairman NHC is responsible to the Ministry of Defense (MOD) to the Government of Bangladesh.

A key mandate of the NHC is to align national hydrographic initiatives with the standards and strategic directions set by the IHO. This involves the promotion of modern hydrographic practices, adherence to international charting norms, and the integration of emerging technologies such as S-57 and S-100 based products. The committee also facilitates the sharing of hydrographic data among stakeholders to eliminate duplication of efforts and promote efficient



Fig. 4 Capacity building in the NIOHC region. Source: Gerd Altmann/geralt, Pixabay.

https://doi.org/10.58440/ihr-31-2-n12

Table 1 Members of NHC. Source: Bangladesh Government Gazette.

Organizations name	Remarks
Chairman, Assistant Chief of Naval Staff (Operations)	ACNS (O)
Bangladesh Navy	BN
Secretary, Maritime Affairs Unit, Ministry of Foreign Affairs	MOFA
Secretary, Law and Justice Division, Ministry of Law, Justice and Parliamentary Affairs	Law & Justice Division
Secretary, Ministry of Defense	MoD
Secretary, Ministry of Shipping	MoS
Secretary, Ministry of Fisheries and Livestock	MoF&L
Surveyor General, Survey of Bangladesh	SoB
Chairman, Bangladesh Water Development Board	BWDB
Head of Department, Hydrographic Department, BIWTA	BIWTA
Chairman, Chittagong Port Authority	CPA
Chairman, Mongla Port Authority	MPA
Director General, Geological Survey of Bangladesh.	GSB
Director General, Department of Shipping	DoS
Chairman, Bangladesh Space Research and Remote Sensing Organization	SPARSO
Chairman, Center for Environmental and Geographic Information Services	CEGIS
Executive Director, Institute of Water Modeling	IWM
River Research Institute, Harukandi, Faridpur	RRI
Director General, Coast Guard Headquarters	BCG
Army Headquarters, GS Branch	AHQ, GS Br
Bangladesh Oceanographic Research Institute	BORI
Chairman, Payra Port Authority	PPA
Bangladesh Maritime University	BMU

resource utilization. Such coordination supports the development of critical infrastructure, improves navigational safety, and enhances national capabilities in marine spatial data management.

The NHC plays a pivotal role in capitalizing Hydrography for broader national interests such as the sustainable use of marine resources, coastal resilience, and the growth of the blue economy. By guiding hydrographic support for marine spatial planning, offshore energy exploration, port development, and environmental monitoring, the committee ensures that Hydrography remains central to Bangladesh's maritime governance. It is strategic leadership and policy integration help for building national capacity, improve compliance with international obligations, and promote safer, smarter, and more sustainable maritime operations.

7 Resource sharing via NIOHC and NHC

Both the NIOHC and NHC function as key platforms for collaborative resource sharing among regional and national stakeholders. They facilitate the exchange of hydrographic assets such as survey equipment, data repositories, training materials, and skilled personnel. By pooling resources, these bodies enhance operational efficiency and build collective capacity, especially for developing nations with limited infrastructure or technical expertise.

For example, as an active member of NIOHC, BNHOC actively engages in regional resource sharing and collaboration, benefiting from access to modern survey equipment, hydrographic data, and specialized training from partner nations and organizations like the UKHO and IHO. At the national level, BNHOC shares hydrographic information and expertise with agencies such as the various port authorities, Department of Shipping, and BIWTA to ensure consistent and accurate charting. This cooperative approach enhances Bangladesh's hydrographic capacity, reduces duplication of effort, and promotes standardized practices, ultimately strengthening maritime safety and supporting sustainable marine resource management in the region.

This shared approach to hydrographic development not only reduces redundancy but also promotes standardization and interoperability across national and regional initiatives. Through coordinated training programs, joint survey missions, and mutual access to hydrographic data, NIOHC and NHC help optimize the quality and reach of hydrographic services. Ultimately, such cooperation strengthens maritime safety, supports sustainable marine resource management, and advances the broader goals of integrated ocean governance.

8 Landward role of the NHC Chairman

Beyond traditional maritime responsibilities, the Chairman of the NHC plays a vital role in fostering inter-ministerial cooperation on projects that address the land-sea interface. These initiatives include coastal erosion mapping, port infrastructure development, shoreline management, and disaster risk reduction planning. By bridging the gap between maritime and terrestrial sectors, the NHC ensures that hydrographic data and expertise are effectively integrated into national development strategies.

This dual land-sea function highlights hydrography's broader relevance beyond navigation, emphasizing its importance in environmental monitoring, climate resilience, and sustainable coastal development. Under the Chairman's leadership, the NHC advocates for the inclusion of hydrographic considerations in national policy and planning processes, enabling better-informed decisions across ministries and agencies. This integrated approach strengthens the country's ability to manage its coastal and marine zones holistically and sustainably.

For example, Bangladesh's exposure to flooding, storm surges, and coastal inundation makes hydrographic planning essential for resilience and infrastructure protection. Chairman NHC, coordinates data-driven mapping of priority coastal areas such as the Sundarbans, Meghna estuary, Cox's Bazar, Teknaf, and St Martin's Islands etc. Collaboration with the NIOHC further strengthens data sharing and technical cooperation, enhancing national capacity to safeguard communities and critical assets.

9 Bangladesh Navy Hydrographic and Oceanographic Centre

The Bangladesh Navy Hydrographic and Oceanographic Centre (BNHOC; BNHOC, 2024b) serves as the central hub for all hydrographic and oceanographic activities of the Bangladesh Navy. Its core responsibility lies in the production, procurement, and distribution of navigational charts and maritime publications to meet the operational requirements of Bangladesh Navy ships, submarines, and shore-based establishments under the supervision of BN Chief Hydrographer. These products are critical for ensuring navigational safety, supporting maritime patrols, and enabling precise route planning for both national and international waters.

Beyond the chart production, BNHOC plays an instrumental role in the maintenance, calibration, and management of a wide array of specialized equipment. This includes Hydrographic and oceanographic survey instruments, cartographic systems, meteorological tools, and advanced data processing units. The center ensures that all deployed systems are functioning optimally to support accurate data acquisition, which is essential for mission planning, maritime situational awareness, and environmental analysis. Regular servicing and upgrades of instruments ensure operational readiness and compliance with international standards.

Furthermore, BNHOC contributes significantly to national and regional maritime knowledge through data management, technical support, processed hydrographic and oceanographic data aid in producing reliable nautical charts, ENCs (Tables 2 and 3), tide tables, and ocean current models (Fig. 5). These outputs not only support naval operations but also benefit civilian sectors such as port management, coastal development, disaster preparedness, and scientific research. By maintaining a high standard of technical capability, BNHOC upholds Bangladesh Navy's commitment to safe navigation, marine resource management, and integrated maritime governance (BNHOC, 2024a)

10 BN's capacity in producing paper charts and S-57 ENCs

The Bangladesh Navy has demonstrated significant capability in modern hydrographic charting by producing 11 in number S-57 ENCs as shown in Fig 6, which are regularly supplied to the International Centre for ENCs (IC-ENC) and all BN ships. These charts meet international standards set by the IHO and are crucial for ensuring safe, digital navigation in Bangladesh's waters. By contributing to the global ENC database, the Navy supports both national maritime safety and international shipping operations, reinforcing its role as a reliable chart producer in the region.

In addition to digital products, the Navy has produced 54 national series paper charts and 9 international series charts to date as shown in Fig 7. The national charts enhance coastal and inland waterway navigation, while the international charts align with global charting schemes to support safe passage through the Bay of Bengal. These efforts reflect the Bangladesh Navy's growing technical expertise and its commitment to maintaining navigational safety, supporting maritime trade, and contributing to regional and global hydrographic initiatives.

11 Transition from paper chart to S-100 ENC (IHO directives)

BN is at the forefront of the global transition from traditional paper charts to ENC usage, aligned with the IHO's goal to discontinue paper charts on or after 2029 as shown in Table 4. The conversion from S-57 to S-100 standards is ongoing, ensuring compliance with next-generation hydrographic and maritime information models (IHO, 2023).

https://doi.org/10.58440/ihr-31-2-n12



Fig. 5 Various hydrographic activities at sea under the supervision of BNHOC.

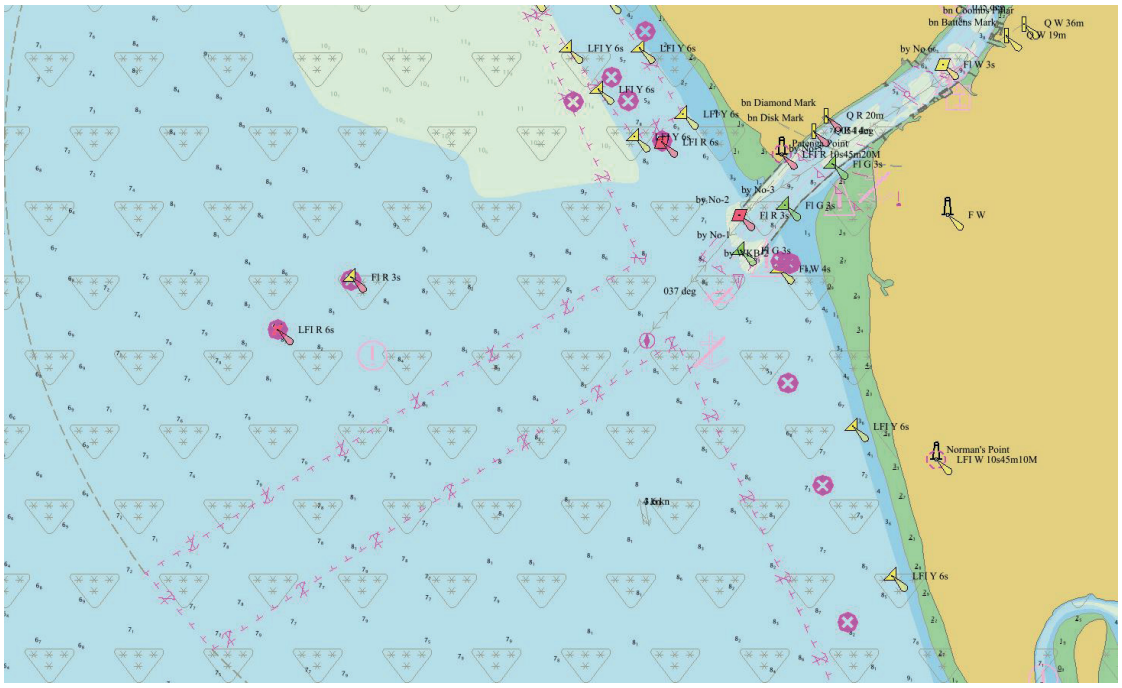


Fig. 6 ENC of BN Chart 3001, INT 7427 Chattogram harbour (BNHOC, 2024a).

12 Actions to be taken for the transition from S-57 to S-100 standards

BN is undertaking the transition from the S-57 to the S-100 standard to align with the IHO future framework for marine data. This transition requires the formulation of a comprehensive national roadmap, coordinated through the NHC. The roadmap defines priorities, such as the development of S-101 (ENC), S-102 (bathymetry), and S-104 (tides) products, while ensuring policy alignment across national maritime stakeholders. A phased implementation plan with clear milestones will help manage the shift smoothly while maintaining existing services.

To support this transition, BN must enhance capacity through targeted training, workshops, and technical support. Personnel need to be trained in

S-100 data models, production tools, and quality control techniques. Upgrading hydrographic software and equipment systems is also essential to ensure compatibility with new standards. Pilot projects on S-101 ENC production should be launched by BNHOC to test workflows and validate data handling. Close collaboration with regional partners under the NIOHC and engagement with IHO working groups will be vital for knowledge sharing and technical support.

Furthermore, BN must focus on building robust data governance and quality assurance frameworks to ensure reliable and standardized S-100 product outputs. At the same time, awareness programs for end users such as port authorities, pilots, and mariners which will help prepare stakeholders for the new products and interfaces. Through a coordinated

Table 2 International series paper chart published by Bangladesh Navy (BNHOC, 2024a).

Chart No.	Title	Publication date
INT7425 (BD35001)	Malancha River to St. Martin's Island	26 Aug 2010
INT7454 (BD7504)	Approaches to Payra Harbour	02 Feb 2017
INT7428 (BD7510)	Approaches to Chattogram	02 Feb 2017
INT7429 (BD7511)	Elephant Point to Matarbari Island	29 Jun 2009
INT7426 (BD5001)	Approaches to Hiran Point	06 Dec 2017
INT7427 (BD3001)	Chattogram Harbour	02 Feb 2017
INT7453 (BD3002)	Payra Harbour	02 Feb 2017
INT7452 (BD3004)	Trikona Island to Monkey Point	04 Jun 2017
INT7451 (BD2508)	Pussur River - Monkey Point to Mongla Port	04 Jun 2017

Table 3 ENCs published by Bangladesh Navy (BNHOC, 2024).

ENC Cell No.	INT No.	BD No.	Title	Remarks
BD307425	INT7425	35001	Malancha River to St. Martin's Island	International Series ENC
BD407426	INT7426	5001	Approaches to Hiran Point	
BD507427	INT7427	3001	Chattogram Harbour	
BD407428	INT7428	7510	Approaches to Chattogram	
BD407429	INT7429	7511	Elephant Point to Matarbari Island	
BD57451A	INT7451	2508	Pussur River- Monkey Point to Joyman Reach	
BD57451B			Pussur River-Joyman Reach to Mongla Port	
BD57452A	INT7452	3004	Pussur River-Trikona Island to Ghusaingari Khal	
BD57452B			Pussur River-Ghusaingari Khal to Monkey Point	
BD507453	INT7453	3002	Payra Harbour	
BD407454	INT7454	7504	Approaches to Payra Harbour	
BD503501	-	3501	St.Martin's Island and Adjoining Area	National Series ENC
BD503506	-	3506	Kutubdia Channel and Adjoining Area	
BD270001	-	70001	Bangladesh and Adjoining Area	
BD503003	-	3003	Matarbari Harbour	
BD330001	-	30001	Hariabhanga River to Char Fasson	
BD330002		30002	Char Fasson to St. Martin's Island	
BD407512	-	7512	St. Martin's Island to Teknaf	

Table 4 Timeline and transition status of hydrographic products toward S-100 compliance.

Hydrographic product	Current status	Target year for S-100
S-57 ENC Coverage	18 (National + Intl)	Transition ongoing
Paper Charts	63 (National + Intl)	Phase out by 2029
S-101 (Vector ENCs)	Initial stage	Full coverage by 2029
S-102 (Bathymetry Surfaces)	In preparation	Coverage by 2029
S-104 (Tidal Data)	In preparation	Coverage by 2029

https://doi.org/10.58440/ihr-31-2-n12

approach involving policy, people, and technology, Bangladesh Navy can successfully lead the national implementation of S-100 standards and enhance its role in regional hydrography.

13 Bangladesh Navy Hydrographic School: A national platform for hydrography

Bangladesh Navy Hydrographic School (BNHS; Fig 8), established in 1983, stands as a cornerstone institution in the maritime education and training infrastructure of Bangladesh. Dedicated to producing skilled Hydrographer capable of supporting national, regional, and international maritime initiatives, BNHS has consistently evolved to meet the growing demands of the hydrographic community under the supervision of BN Chief Hydrographer. In 2005, the school achieved a significant milestone when it was formally recognized by the International Board on Standards of Competence for Hydrographic Surveyors and Nautical Cartographers (IBSC), operating under the joint auspices of the International Federation of Surveyors (FIG), the IHO, and the International Cartographic Association (ICA), to deliver a Category 'B' basic hydrography course. It was again recognized in 2010, 2015 and 2020, as a Category B programme, reaffirming the institution's compliance with international standards and its continued commitment to excellence in hydrographic education. This recognition is valid for the year 2025, and the renewal process for the period 2026 to 2030 is currently underway.

Over the past two decades, BNHS has conducted a total of 18 Category 'B' hydrography courses between 2005 and 2025. These training programs have successfully qualified 136 professionals, including 81 officers from the Bangladesh Navy, 27 personnel from Bangladesh Inland Water Transport Authority (BIWTA) and various port authorities, as well as 28 international participants from friendly foreign nations. This diverse participation reflects BNHS's growing reputation as a regional hub for hydrographic training and its role in fostering international cooperation and capacity building in the maritime domain.

In addition to its success in delivering Category 'B' training, BNHS has also contributed significantly to the professional development of hydrographic experts (Fig 9). A total of 33 Bangladesh Navy officers, after obtaining their Category 'B' qualification from the school, have progressed further to successfully complete the more advanced Category 'A' Hydrography Course from internationally accredited institutions. This progression not only strengthens the Bangladesh Navy's own hydrographic capabilities but also enhances its ability to lead and support complex hydrographic and oceanographic missions both at home and abroad.

Today, BNHS remains committed to advancing hydrographic education in line with emerging global

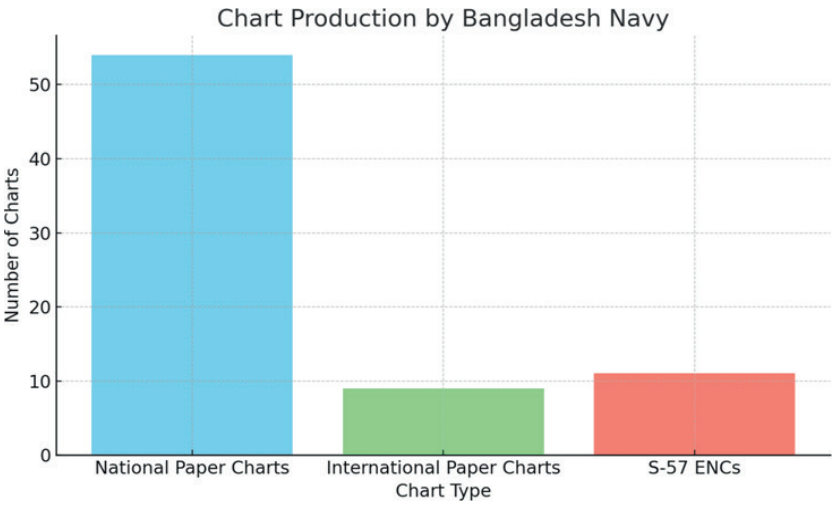


Fig. 7 Chart production overview by Bangladesh Navy, including national series paper charts, international series, and S-57 ENCs. Source: Bangladesh Navy Annual Hydrographic Report (2024).



Fig. 8 BN training complex located at Chattogram.

standards, including the adoption of S-100-based training frameworks and integration of modern technologies such as GNSS positioning, LiDAR, Multibeam Echo Sounders, and Marine Spatial Data Infrastructure (MSDI). Through continuous professional development, international collaboration, and quality assurance, the school plays a pivotal role in supporting Bangladesh's maritime ambitions, including the sustainable development of the blue economy and regional maritime safety and security.

As Bangladesh assumes greater leadership roles within the international hydrographic community including chairing the NIOHC, institutions like BNHS will be instrumental in shaping the future of hydrography in the region. Recently, BNHS has received confirmation that the Category 'A' long hydrography course has been recognized. BNHS will conduct the said course from 2026.

14 Integration of maritime stakeholders

Bangladesh is successfully integrating a wide range of maritime stakeholders including the BN, Bangladesh Coast Guard (BCG), Bangladesh Oceanographic Research Institute (BORI), port authorities, universities (i.e. Bangladesh Maritime University), fisheries, environment, energy, and disaster management sectors

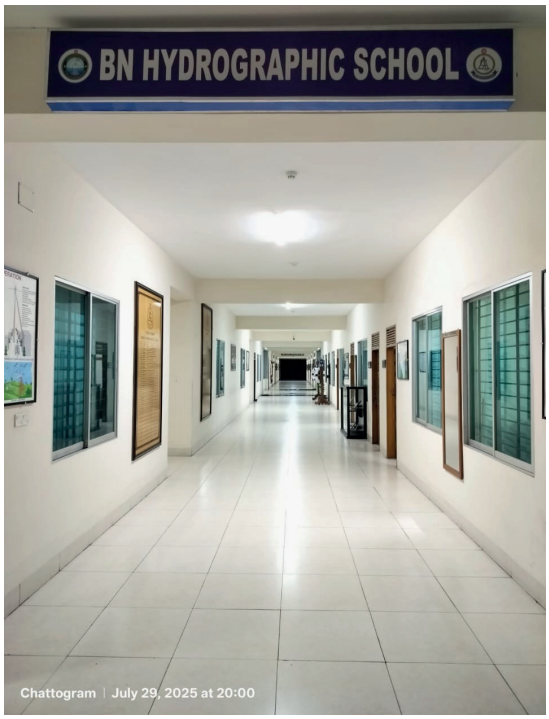








Fig. 9 Training activities of BNHS during Category 'B' hydrography course.

(Fig 10) under a unified hydrographic framework and supervision of the Chairman NHC. This strategic alignment enables coordinated planning, data sharing, and efficient use of resources, ensuring that hydrographic activities support the broader goals of maritime governance. By bringing together civil and military agencies, the NHC promotes a whole-of-government approach to managing marine and coastal affairs.

This integration fosters the development of a cohesive maritime policy framework that is essential for addressing key national priorities. It strengthens maritime security by improving situational awareness and navigation safety, supports economic growth through better port planning and marine infrastructure, and contributes to environmental protection and marine conservation by facilitating informed decision-making. Through this collaborative model, the NHC ensures that hydrography remains a foundational element in sustainable ocean governance and national development.

15 Challenges ahead

Despite its rapid advancement in Hydrography and charting capacity, Bangladesh continues to face several challenges that may affect the pace and scope of its progress in the coming years. These challenges are multidimensional and require coordinated efforts both at the national and regional levels.

15.1 Transition from S-57 to S-100 ENC

The transition from S-57 to S-100 Standards ENC poses several challenges. Firstly, it requires significant technical upgrades in chart production systems, software, and hardware to support the new standard. Capacity building is another key challenge, as specialized training and expertise are needed for Hydrographers and navigators to efficiently manage S-100 products. Financial constraints may also impact timely procurement of modern infrastructure and tools required for the transition. Additionally, ensuring data interoperability and integration with regional and global hydrographic systems demands strong coordination and compliance with IHO guidelines. For the Bangladesh Navy, the challenge extends to upgrading onboard navigation and combat management systems across its fleet to be fully compatible with S-100 ENCs, while maintaining operational readiness during the transition period.

15.2 Climate change and coastal dynamics

As one of the most climate-vulnerable countries in the world, Bangladesh's dynamic coastline presents an ongoing hydrographic challenge. Rising sea levels, coastal erosion, siltation, and sediment deposition in riverine areas require frequent re-surveying and chart updates. The pace of environmental change in the Bay of Bengal demands adaptive survey techniques, predictive modeling, and near real-time data

https://doi.org/10.58440/ihr-31-2-n12

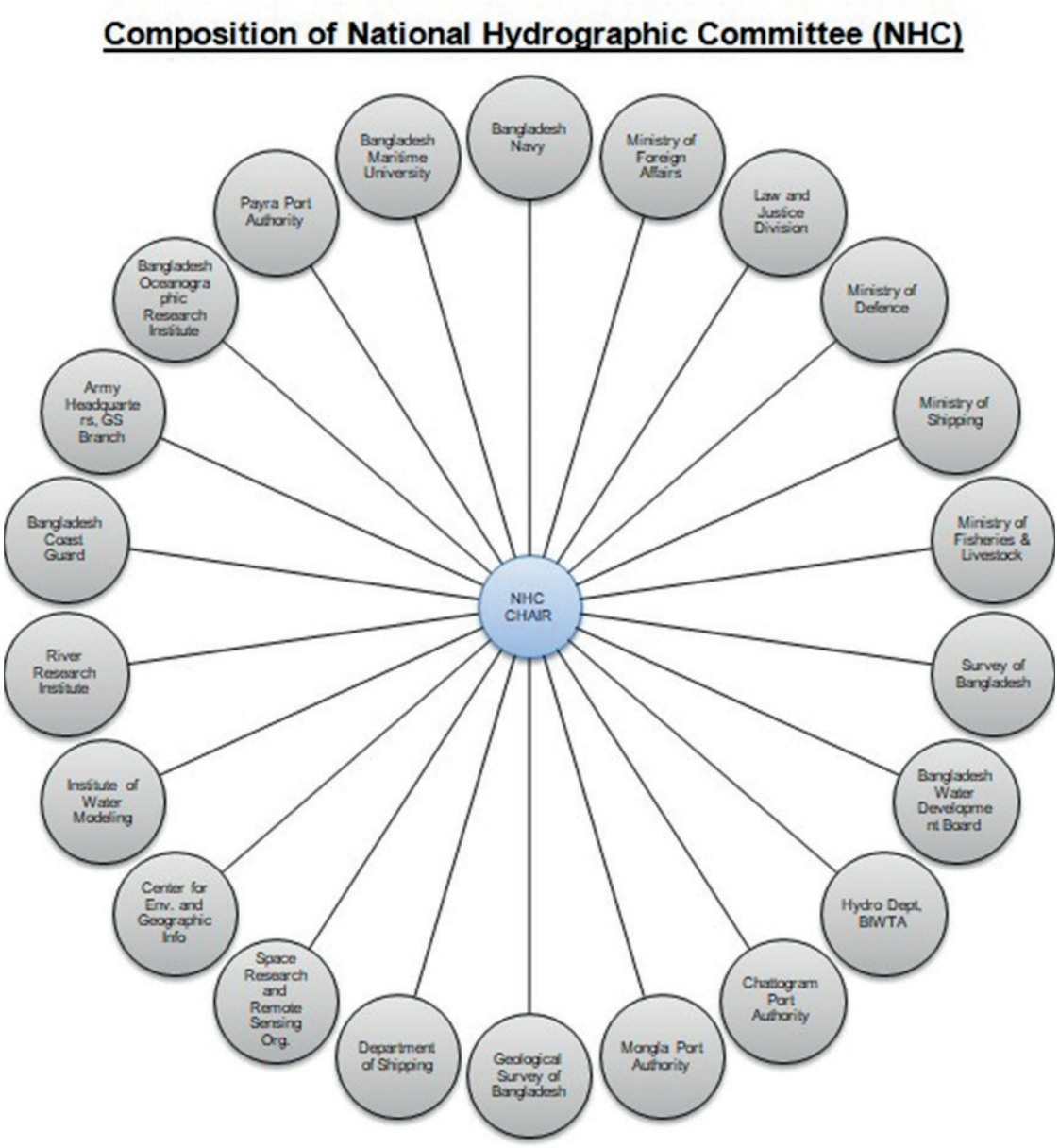


Fig. 10 Members of NHC as per Bangladesh government official notification. Source: Bangladesh Govt. Official Notification No 275/23 of September 2001 and 555/05 of October 2016.

integration – all of which require technical readiness and adequate resources.

15.3 Technological and digital infrastructure gaps

Although Bangladesh Navy has made significant strides in digital Hydrography, the broader national infrastructure still faces gaps. Bandwidth limitations, cyber security vulnerabilities, and lack of seamless inter-agency data-sharing protocols pose risks to building an integrated MSDI. Additionally, real-time data transmission from remote survey platforms and offshore locations remains an area that needs technological reinforcement.

15.4 Skilled human resource development

BNHS has been providing the Basic Hydrography Category B course since 2005 whilst the demand for Hydrographers, oceanographers, and geospatial analysts continues to rise. Recently the same institution has gained Recognized by IBSC for its Category 'A' long Hydrography course. BN will conduct the Category 'A' course in the 2026. Retaining trained professionals, adapting to evolving standards like S-100, and providing continuing education opportunities are ongoing challenges, particularly as global hydrographic competencies are becoming more complex and data-driven.

15.5 Budgetary constraints

Hydrographic operations, especially in transitioning from traditional charting methods to digital platforms such as S-100, require significant financial investment. From acquiring survey vessels like the HMS Enterprise to procuring advanced equipment such as Multibeam Echo Sounders, Side Scan Sonar, AUVs etc., the cost burden on a developing nation like Bangladesh remains high. While support from development partners and international agencies partially

offsets this burden, sustained investment from the national treasury is critical to meet long-term goals.

16 Future plans beyond 2025

Looking beyond the 2025–2027 chairmanship of NIOHC, Bangladesh envisions a broader and more strategic role in the global hydrographic community. The roadmap for the post-2027 period is guided by a commitment to innovation, regional leadership, and maritime sustainability.

16.1 Becoming a regional S-100 charting hub

By 2028, Bangladesh aims to position itself as a regional charting center for S-100 (Universal Hydrographic Data Model) data products, offering services not only to domestic stakeholders but also to NIOHC member states with limited ENC production capacity. This would include generating and maintaining S-101 ENCs, S-102 (Bathymetric Surfaces) and S-104 (Tidal Data Products) using high-resolution data from its upgraded fleet and hydrographic labs.

16.2 Establishment of a national marine data repository

Plans are underway to build a centralized marine geospatial data repository under the NHC framework. This repository will integrate data from hydrographic surveys, oceanographic research, port operations, and environmental studies. It will serve as the national backbone for Marine Spatial Planning (MSP), maritime research, disaster preparedness, and blue economy development.

16.3 Expansion of international collaboration

Beyond the Indian Ocean, Bangladesh seeks deeper engagement with global hydrographic communities such as the East Asia Hydrographic Commission (EAHC) and the Intergovernmental Oceanographic Commission (IOC). Participation in international research expeditions, co-hosting of workshops, and staff exchanges are part of this forward-looking agenda.

16.4 Full ENC coverage and S-100 integration by 2029

In alignment with the IHO's global initiative, Bangladesh is targeting complete national ENC coverage under the S-101 standard by 2029, in preparation for the global phase-out of paper charts. This will involve automated chart update systems, improved metadata services, and direct integration with navigational systems onboard domestic and foreign vessels.

16.5 Creating a blue economy Decision Support System

Hydrography will play a central role in the development of a blue economy Decision Support System (DSS), a GIS-based platform that integrates economic, environmental, and navigational data to support decision-making by government agencies, investors, and planners. It is envisioned as a live dashboard powered by real-time hydrographic and oceanographic feeds.

16.6 Upgrade to National Hydrographer

The role of the BN Chief Hydrographer has expanded well beyond Naval boundaries, supporting national maritime governance and international obligations. With Bangladesh's vision to become a regional S-100 charting hub, establish a National Marine Data Repository, and achieve full ENC coverage by 2029, Hydrography has become central to the nation's maritime strategy. To reflect this elevated scope and ensure effective coordination with ministries, port authorities, research institutions, and global bodies, it is planned to upgrade the position from BN Chief Hydrographer to the National Hydrographer to the Government of Bangladesh. This up gradation would align the country with international best practices and strengthen Bangladesh's leadership in the global hydrographic community.

17 Recommendations

Foster regional cooperation: Strengthen collaboration with all the members of NIOHC to enhance data sharing, joint surveys, and technical assistance.

Advance S-100 implementation: Develop a national and regional roadmap for a smooth transition to S-100 based products and services.

Expand capacity building efforts: Enhance training programs (Cat A and Cat B), and seminar through BN Hydrographic School and conduct regional workshops.

Integrate national stakeholders: Strengthen the National Hydrographic Committee (NHC) to coordinate hydrographic efforts across agencies and sectors.

Support the blue economy and MSDI: Utilize hydrographic data for sustainable marine development and accelerate the establishment of MSDI.

Upgrade to National Hydrographer: Upgrade the BN Chief Hydrographer to National Hydrographer under the Government of Bangladesh to effectively address expanded national and international hydrographic responsibilities.

18 Conclusion

Bangladesh Navy's leadership in regional Hydrography, through the chairmanship of the NIOHC and proactive role in the NHC, marks a significant milestone in the maritime journey of the country. This leadership reflects Bangladesh's strategic commitment to enhancing maritime safety, economic development, and regional cooperation. As the custodian of national hydrographic responsibilities, the Navy has not only advanced domestic charting and survey capabilities but also emerged as a key contributor to the international hydrographic region.

The vision articulated by the current NIOHC Chair,

https://doi.org/10.58440/ihr-31-2-n12

aligned with IHO's strategic goals, emphasizes innovation, capacity building, and data integration, particularly in transitioning towards S-100 standards. Bangladesh Navy's focus on multilateral partnerships, technology driven solutions, and sustainable use of marine resources reflects a broader regional vision where Hydrography becomes a cornerstone of safe navigation, climate resilience, and blue economy initiatives. Through collaboration with regional stakeholders and technical bodies, Bangladesh is fostering an inclusive approach that supports both national priorities and international hydrographic development.

Looking ahead, the Bangladesh Navy is well-positioned to lead the hydrographic domain through emerging challenges and opportunities. Also, the NIOHC has given an opportunity to lead the hydrographic field. With strengthened institutional mechanisms, increasing technical competence, and a clear strategic direction, the Navy is advancing not only its own capabilities but also contributing to collective regional resilience. The path forward involves deepening integration, addressing digital and environmental challenges, and preparing for future roles such as becoming a regional S-100 data service hub and thereby ensuring Bangladesh retains a lead role in shaping the hydrographic future of the Indian Ocean region.

References

BNHOC (2024a). *CHARTS*. Bangladesh Navy, New Mooring, Chattogram-4218, Bangladesh. http://bnhoc.navy.mil.bd/charts (last accessed 19 July 2025).

BNHOC (2024b). *Hydrographic & Oceanographic Center (BNHOC)*. Bangladesh Navy, New Mooring, Chattogram-4218, Bangladesh. http://bnhoc.navy.mil.bd/: http://bnhoc.navy.mil.bd/ (last accessed 22 August 2025).

IHO (2020). *Strategic Plan for 2021–2026*. International Hydrographic Organization, Monaco. https://iho.int/uploads/user/About%20IHO/Strategic%20Plan/IHOSP2021_2026_final.pdf (last accessed 31 October 2025).

IHO (2023). *Report of the IHO Hydrographic Services and Standards Committee to the 7th Meeting of the IHO Council*. International Hydrographic Organization, Monaco. https://iho.int/uploads/user/About%20IHO/Council/council7/C7_2023_04.1A_EN_HSSC_Report_to_C7_ver1.0.pdf (last accessed 31 October 2025).

IHO (2025). *North Indian Ocean HC*. International Hydrographic Organization, Monaco. https://iho.int/en/north-indian-ocean-hc (last accessed 27 June 2025).

ISPR (2025). *Bangladesh Navy Taken Over the Chairmanship Of North Indian Ocean Hydrographic Commission (NIOHC)*. Inter Services Public Relation Directorate (ISPR), Dhaka, Republic of Bangladesh. https://ispr.gov.bd/en/bangladesh-navy-taken-over-the-chairmanship-of-north-indian-ocean-hydrographic-commission-niohc/ (last accessed 2 November 2025).

Sarker, S. and Islam, M. A. (2018). From science to action: Exploring the potentials of Blue Economy for enhancing economic sustainability in Bangladesh. *Ocean & Coastal Management, 157*, 180–192. https://doi.org/10.1016/j.ocecoaman.2018.03.001

NOTE / TECHNICAL REPORT

Evaluation of SDB data for near shore mapping around Agatti Island, India: a comparative study with echo sounder survey

Author
Varun Jai[1]

Abstract

Bathymetric data acquisition in shallow nearshore waters is often constrained by safety risks and limited access for conventional survey vessels. Satellite-derived bathymetry (SDB) offers a non-intrusive, wide-coverage alternative, particularly effective in coral reef environments. This study evaluates the accuracy of physics-based SDB, processed by EOMAP GmbH & Co. KG using Sentinel-2 imagery, over Agatti Island in the Lakshadweep archipelago. Ground-truth validation was carried out using single beam echo sounder data collected from shallow water crafts and multibeam echo sounder data acquired from survey motorboats and a hydrographic ship. The analysis showed that while SDB provided reliable depth patterns across all zones, vertical uncertainties scaled to the 95% confidence level (LE95 = 1.96 σ) exceeded the IHO S-44 Order 1a TVU limits in all depth bands. These findings, consistent with guidance in IHO B-13 (IHO, 2024), highlight the operational value of SDB for reconnaissance and coastal planning, while underscoring the need for careful statistical treatment of uncertainties when evaluating SDB against hydrographic standards.

Keywords
satellite derived bathymetry · hydrographic surveying · single beam echo sounder · multibeam echosounder · nautical charting · Agatti Island · Lakshadweep

1 Introduction

Bathymetric surveys are time consuming and resource-intensive, potentially involving multiple platforms and inherent risks. The field surveyor must anticipate and manage operational challenges and envisage the solutions to timely complete a project survey. Hydrographic surveys for the production of navigational charts are critical, as mariners remain dependent on the data collected by the surveyor until subsequent surveys of the area are conducted. A trade-off between accuracy and risk is often unavoidable and achieving the set standards ensuring safety has been paramount for all the surveyors. A remote survey solution for nearshore treacherous areas with coral reefs and underwater rocks would be a sigh of relief, provided it meets the set standards of the International Hydrographic Organization (IHO). Existing systems for bathymetric measurements such as multibeam echo sounder (MBES), single beam echo sounder (SBES) and light detection and ranging (LiDAR), are accurate depth measurement sensors. The challenges in a survey are cost, time, access to remote areas and environmental constraints. Earth observation (EO) satellites monitor the earth round the clock and provide new datasets for every single pass over targeted areas. Some of these datasets can be processed to derive bathymetric data. Hence, satellite-derived bathymetry (SDB) is as derived data

✉ Varun Jai · jaivarun4195@gmail.com
[1] Indian Naval Hydrographic Department, India

https://doi.org/10.58440/ihr-31-2-n07

as compared to an in-situ measurement. SDB is increasingly viewed as a faster, cost-effective alternative to shallow water sounding. The paper aims at exploring SDB's utilisation and comparing it with traditional methods.

Each of the data sets (images) which are collected in every pass of satellite is put through a rigorous processing applying multiple corrections. Multispectral imagery from satellites is used for depth estimation. Due to the turbidity and suspended particles present in water nearshore area, the area for study was selected in Agatti island of Lakshadweep in India which has clear and pristine waters. The SDB data utilised in the study were provided by EOMAP GmbH & Co. KG. The dataset was generated using Sentinel-2 (ESA, 2015, 2025) satellite at 10 m pixel resolution, which is equipped with multispectral sensors capable of capturing eight visible to near infrared bands. The sensors used by the satellites for SDB are CAVIS, Panchromatic, Multispectral and Shortwave Infrared (EOMAP, 2025).

The IHO's Satellite-Derived Bathymetry Best Practice Guide (IHO, 2024) provides a comprehensive global framework for the classification, processing, and quality assessment of SDB data. It identifies major challenges such as the influence of turbidity, substrate variability, and spectral limitations on bathymetric retrieval, and categorizes commonly used models into empirical, physics-based, and machine learning methods. This study focuses on evaluating SDB performance around Agatti Island, integrating MBES/SBES data to quantify accuracy, and aligning results with IHO S-44 uncertainty thresholds (IHO, 2022) to assess its applicability for hydrographic charting. Updation of Nautical chart is a cyclic process which continues as a need for new chart is projected or done after a certain time frame depending on the relevance of the area. SDB is a tool in identifying critical shallow areas which require update. It can also be handy in mapping hazardous and ecologically sensitive areas (Gunathilaka et al., 2024). Areas such as Polar Regions (as the ice melts) or archipelagos with limited access by ships may also be mapped remotely. As many Hydrographic Offices (UKHO published BA 2066 in October 2015) have integrated SDB in their charts and ENCs, the data is being utilised for nautical charting. SDB data helps in reconnaissance of an area prior to commencement of survey and helps in prioritising the areas depending on the surf and breakers and approximate depth profile. A case study on use of SDB for tsunami modelling report is also relevant (EAHC, 2015).

2 Data source and methodology

The data for SDB was acquired by EOMAP GmbH & Co. KG on various dates from November 2022 to March 2024 under different turbidity, wave height and sunlight conditions. The data was derived using physics-based inversion approach based on the radiative transfer equation (RTE; IHO, 2024), which models the complete light pathway through the atmosphere, water surface, water column and seafloor. The RTE based approach enables sensor independent processing and reduces reliance on in-situ calibration data (Hartmann et al., 2023).

The data processing for SDB was carried out by EOMAP GmbH & Co. KG. They also compared the SDB data with satellite-lidar bathymetry for quality control and fine tuning. The data was compared with ICESat satellite lidar bathymetry and results were provided as metadata.

The SDB data is referenced to lowest astronomical tide (LAT) as each single image is referenced to LAT separately and combined to reduce the effects. Tides were modelled as per FES 2014 tidal model. Table 1 lists the tide values applied to each image.

The bathymetric data in field was collected by shallow water crafts for reef areas, survey motor boats for shallow depths and by ship for deeper areas. The data collected was referenced to LAT as tidal monitoring using tide pole was done simultaneously at Agatti jetty. The shallow water crafts used Deso 30 SBES, the survey motor boat a Seabeam 3180 MBES and the ship a Hydro Sweep DS MBES. The data acquired was processed in Teledyne CARIS HIPS and SIPS version 11.3. The SDB data was referenced and bathymetric surface of each line of data was compared in the processing software. The surface resolution of each line was kept the same as the SDB data to achieve an actual comparison.

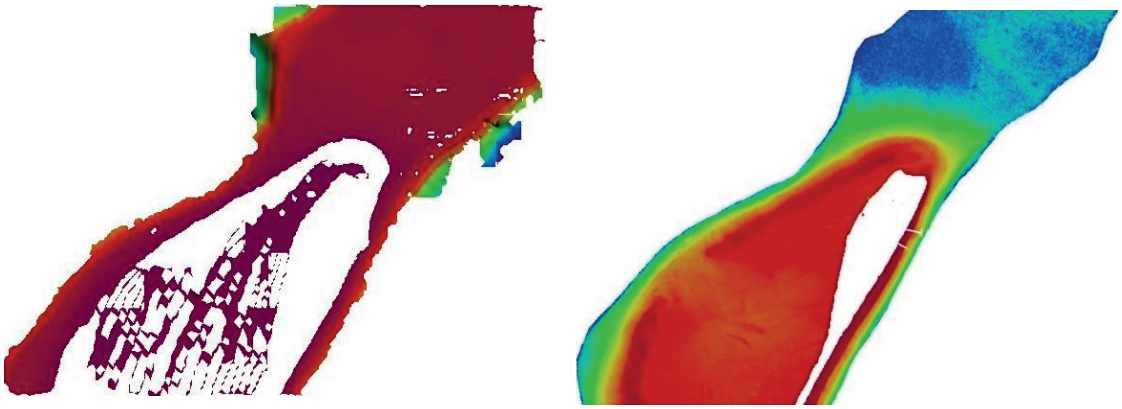


Fig. 1 MBES and SBES data of Agatti (left) and SDB data of Agatti (right).

https://doi.org/10.58440/ihr-31-2-n07

Table 1 Tidal values applied to each capture as per date and time (data courtesy of EOMAP GmbH & Co. KG).

Ser	Date	Time (UTC)	Tide correction (m)
(a)	2024/02/23	05:28:31	1.18
(b)	2024/01/29	05:30:59	1.06
(c)	2023/06/03	05:26:49	1.52
(d)	2023/01/19	05:31:41	0.76
(e)	2023/02/23	05:28:29	1.07
(f)	2024/03/09	05:26:39	1.28
(g)	2023/02/18	05:29:01	0.97
(h)	2024/01/24	05:31:11	1.10
(j)	2024/03/29	05:26:49	0.98
(k)	2022/12/20	05:32:31	0.80
(l)	2022/11/20	05:31:21	1.01
(m)	2023/05/24	05:26:49	0.84
(n)	2023/01/29	05:31:01	0.46

3 Result and analysis

To assess the accuracy and reliability of SDB data, a structured quality control process was implemented. SDB depths were compared against in-situ measurements acquired from MBES and SBES surveys. Statistical analyses included the calculation of mean bias, standard deviation σ, and root mean square error (RMSE) across depth intervals of 0–3 m, 3–5 m, 5–10 m, and >10 m. For each depth interval, three survey lines were analyzed to increase the number of evaluation points. This stratification enabled a detailed examination of SDB performance relative to depth. Acceptance criteria were based on the IHO S-44 standards (IHO, 2022), where vertical uncertainty is expressed at the 95 % confidence level (LE95). Accordingly, compliance was judged by comparing 1.96 σ with the allowable total vertical uncertainty (TVU) for Order 1a, while mean bias and RMSE were reported as supplementary indicators of overall accuracy (Athmaram et al., 2017).

The accuracy of SDB against reference acoustic data was quantified using a combination of statistical measures. RMSE was initially computed as a descriptive metric since it accounts for both systematic bias and random variability, providing a useful indication of the total magnitude of depth deviation. However, for compliance with IHO S-44 standards (IHO, 2022), which define TVU at the 95 % confidence level (LE95), the standard deviation σ of the residuals was scaled by 1.96 (i.e., LE95 = 1.96 σ). This approach is consistent with the IHO guidelines for the use of SDB in hydrography (IHO, 2024) and avoids conflating systematic offsets with random uncertainty. Thus, while RMSE was reported for completeness, the determination of compliance with IHO Order 1a limits was made strictly using LE95 = 1.96 σ.

$$\text{Mean Error} = \frac{1}{N}\sum_{i=1}^{N}(SDB_i - MBES_i) \quad (1)$$

where

N: Total number of points

SDB_i: Depth from satellite-derived bathymetry at point i

$MBES_i$: Depth from multibeam or single beam echo sounder at point i

$$\text{Standard Deviation} = \sqrt{\frac{1}{N-1}\sum_{i=1}^{N}(d_i - \text{Mean Error})^2} \quad (2)$$

where

$d_i = SDB_i - MBES_i$: difference at point i

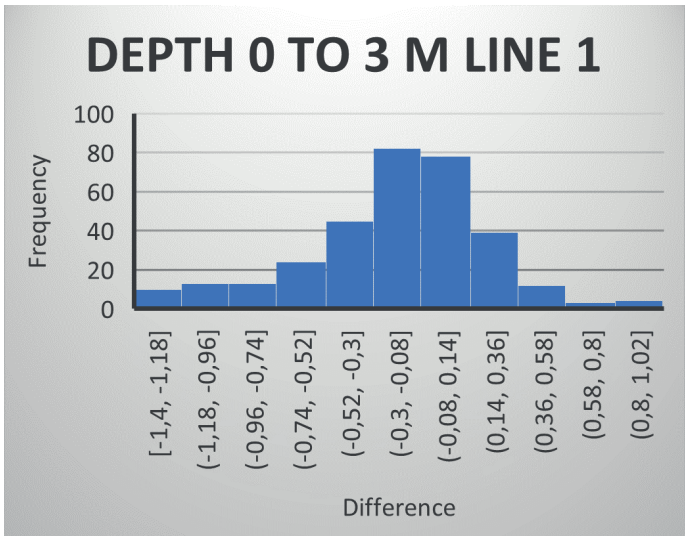
$$\text{RMS error} = \sqrt{\frac{1}{N}\sum_{i=1}^{N}(d_i)^2} \quad (3)$$

Figs. 2–13 showing the lines run on ground on top of SDB data (on the right) and an error histogram for each line in mentioned depth range (on left). Tables 2–13 displaying basic statistics of each line. All the errors and values in meter.

4 Discussion

The summary of all the comparison is as follows. Table 14 below presents a detailed statistical comparison of SDB against ground-truth acoustic data (MBES/SBES) for each of the three survey lines within the defined depth intervals. The metrics include mean error, standard deviation, and RMSE for each line, along with the number of comparison points. The line-wise breakdown provides granularity to the performance assessment and underscores the need for selective application of SDB products based on local depth and optical conditions.

https://doi.org/10.58440/ihr-31-2-n07



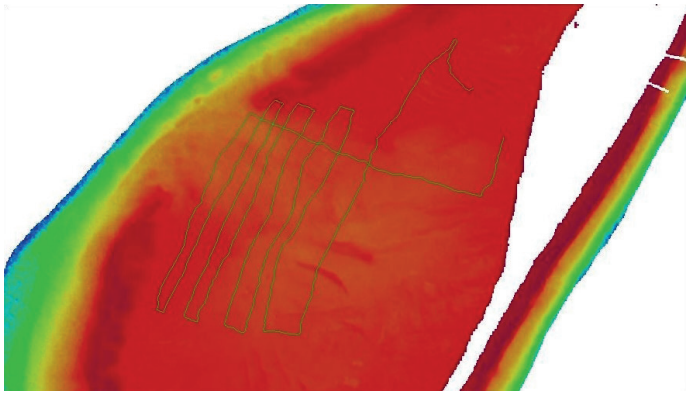
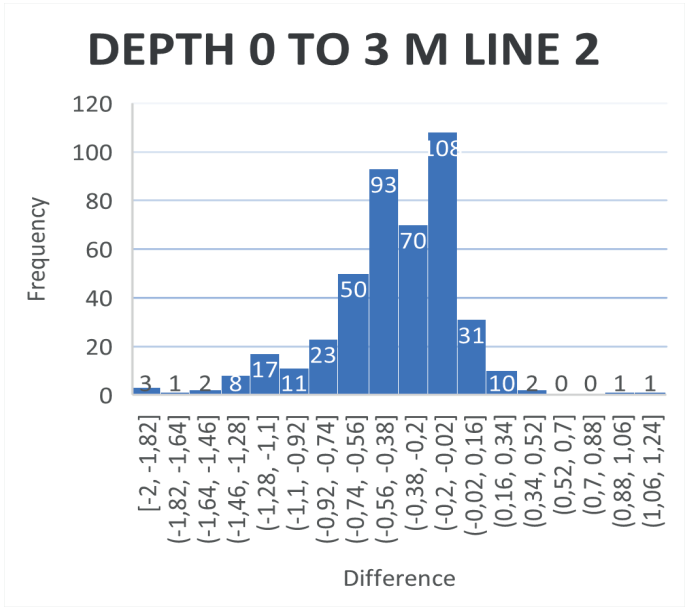


Fig. 2 Line 1 of depth 0–3 m of SBES compared with SDB in reef area and the difference histogram.

Table 2 Line 1 of depth 0–3 m.

Mean error (m)	Std. dev. (m)	RMSE (m)	Min. error (m)	Max. error (m)
-0.1838509	0.42446971	0.4620	-1.4	1.0



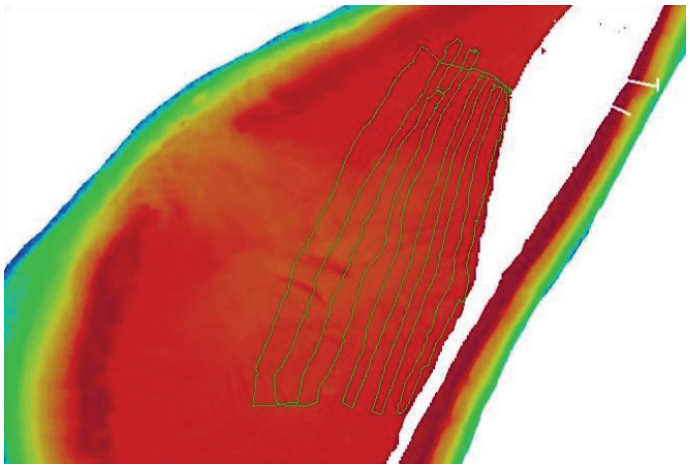
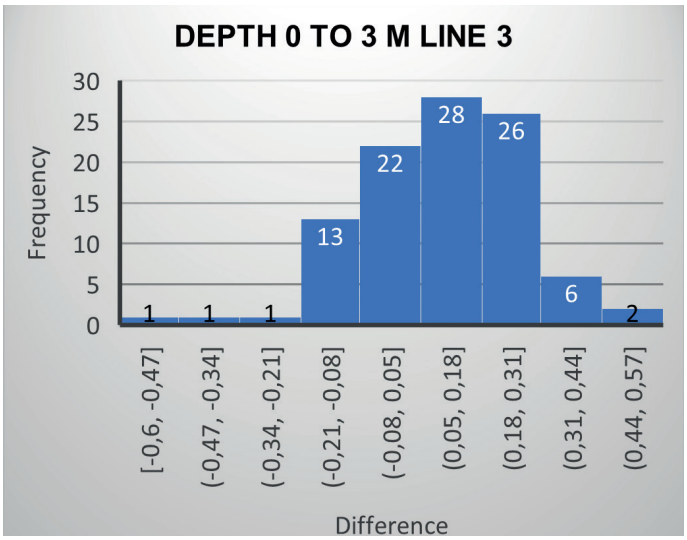


Fig. 3 Line 2 of depth 0–3 m of SBES compared with SDB in reef area and the difference histogram.

Table 3 Line 2 of depth 0–3 m.

Mean error (m)	Std. dev. (m)	RMSE (m)	Min. error (m)	Max. error (m)
-0.4095	0.3838	0.5610	-2.0	1.2



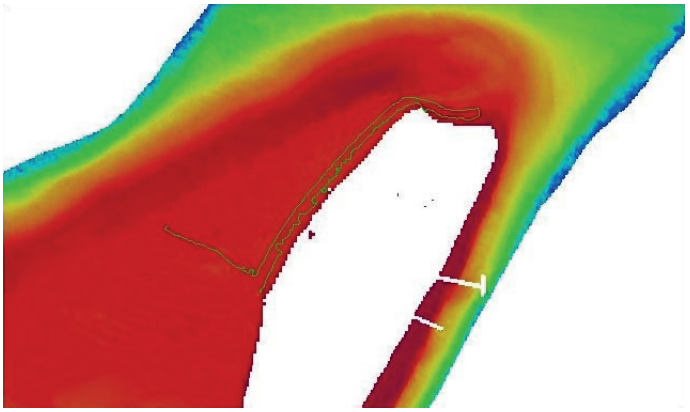
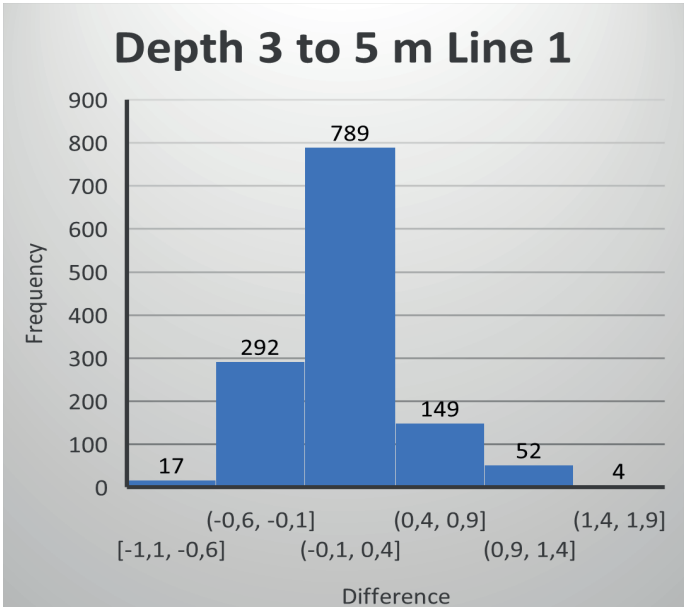


Fig. 4 Line 3 of depth 0–3 m of SBES compared with SDB in reef area and the difference histogram.

Table 4 Line 3 of depth 0–3 m.

Mean error (m)	Std. dev. (m)	RMSE (m)	Min. error (m)	Max. error (m)
0.0899	0.1753	0.1962	-0.6	0.5



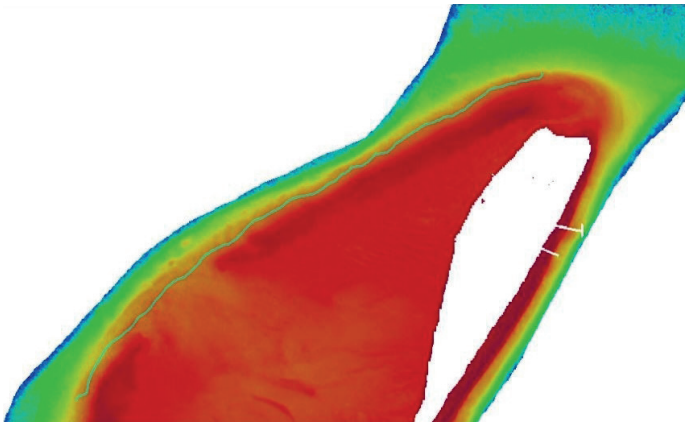
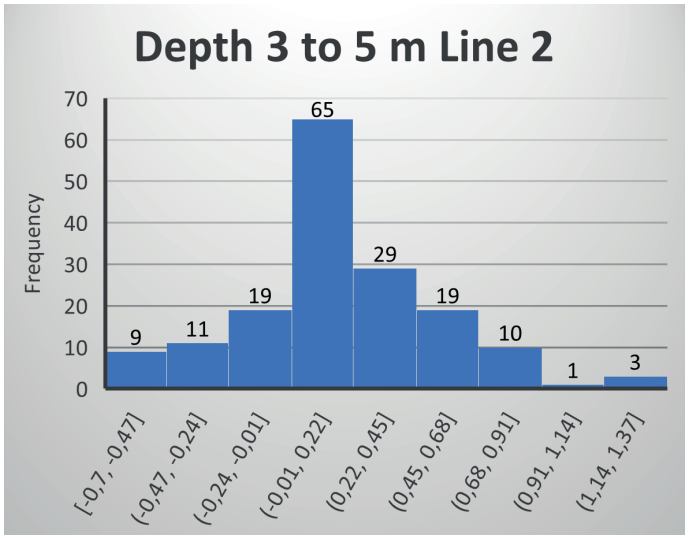


Fig. 5 Line 1 of depth 3–5 m of SBES compared with SDB in reef area and the difference histogram.

Table 5 Line 1 of depth 3–5 m.

Mean error (m)	Std. dev. (m)	RMSE (m)	Min. error (m)	Max. error (m)
0.059600614	0.36648	0.3712	-1.1	1.9

https://doi.org/10.58440/ihr-31-2-n07



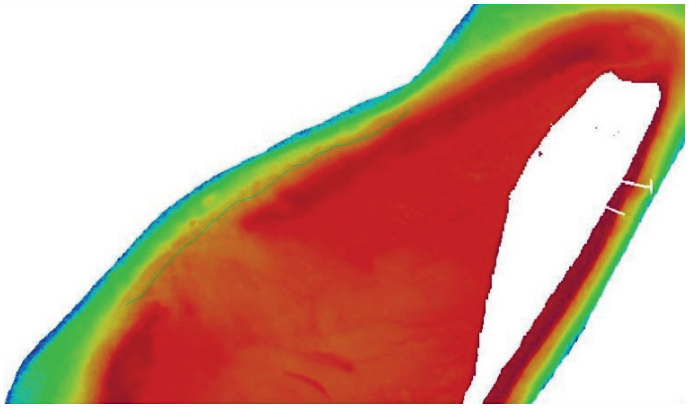
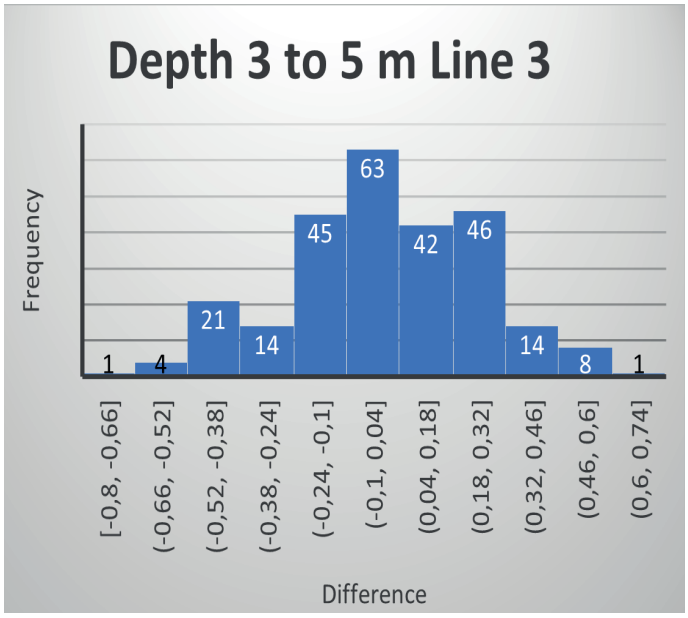


Fig. 6 Line 2 of depth 3–5 m of SBES compared with SDB in reef area and the difference histogram.

Table 6 Line 2 of depth 3–5 m.

Mean error (m)	Std. dev. (m)	RMSE (m)	Min. error (m)	Max. error (m)
0.16446	0.36548	0.3998	-0.7	1.3



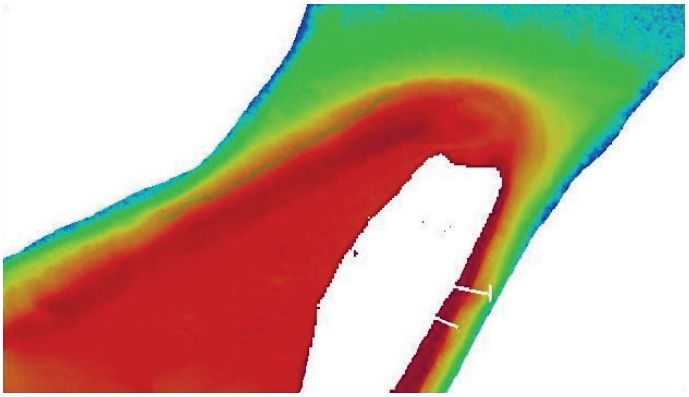


Fig. 7 Line 3 of depth 3–5 m of SBES compared with SDB in reef area and the difference histogram.

Table 7 Line 3 of depth 3–5 m.

Mean error (m)	Std. dev. (m)	RMSE (m)	Min. error (m)	Max. error (m)
0.01351	0.25137	0.2513	-0.8	0.7

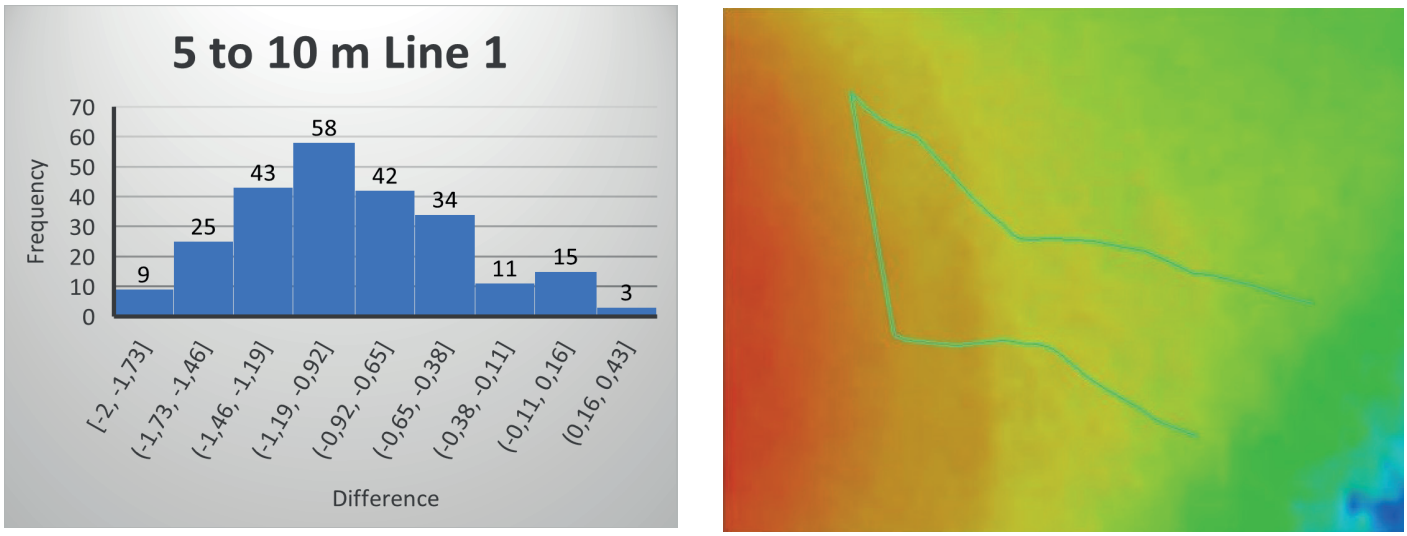


Fig. 8 Line 1 of depth 5–10 m of SBES compared with SDB and the difference histogram.

Table 8 Line 1 of depth 5–10 m.

Mean error (m)	Std. dev. (m)	RMSE (m)	Min. error (m)	Max. error (m)
-0.9462	0.47347	1.0577	-2.0	0.2

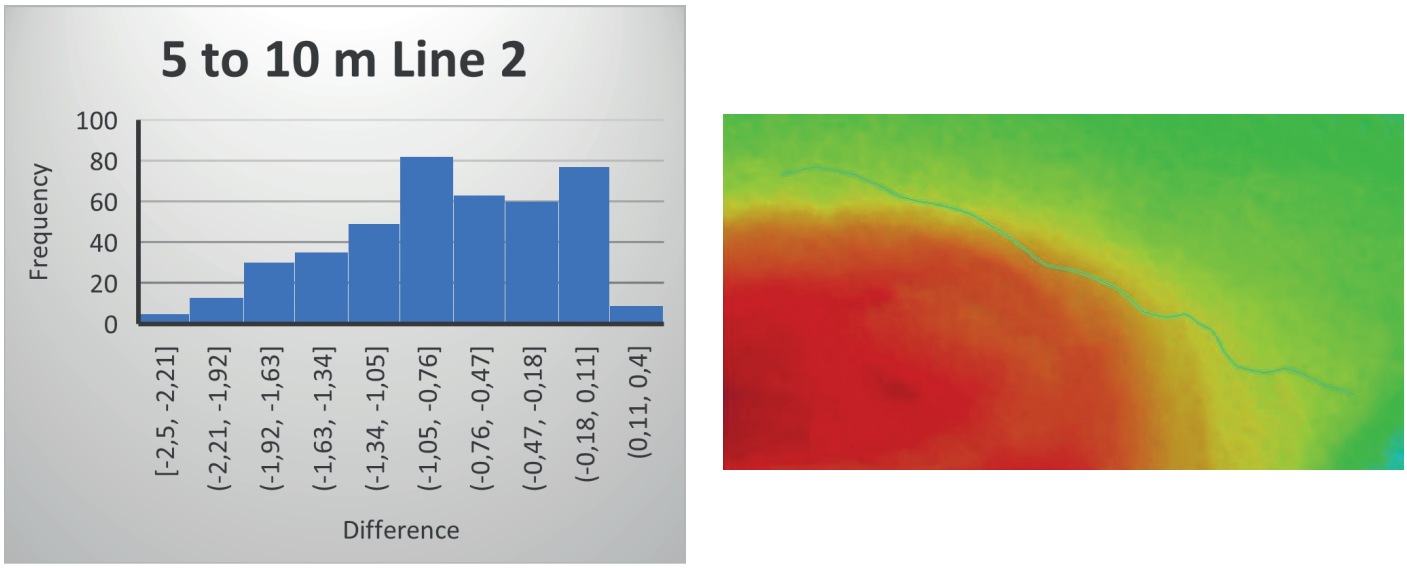


Fig. 9 Line 2 of depth 5–10 m of SBES compared with SDB and the difference histogram.

Table 9 Line 2 of depth 5–10 m.

Mean error (m)	Std. dev. (m)	RMSE (m)	Min. error (m)	Max. error (m)
-0.7842	0.62293	1.0010	-2.5	0.4

https://doi.org/10.58440/ihr-31-2-n07

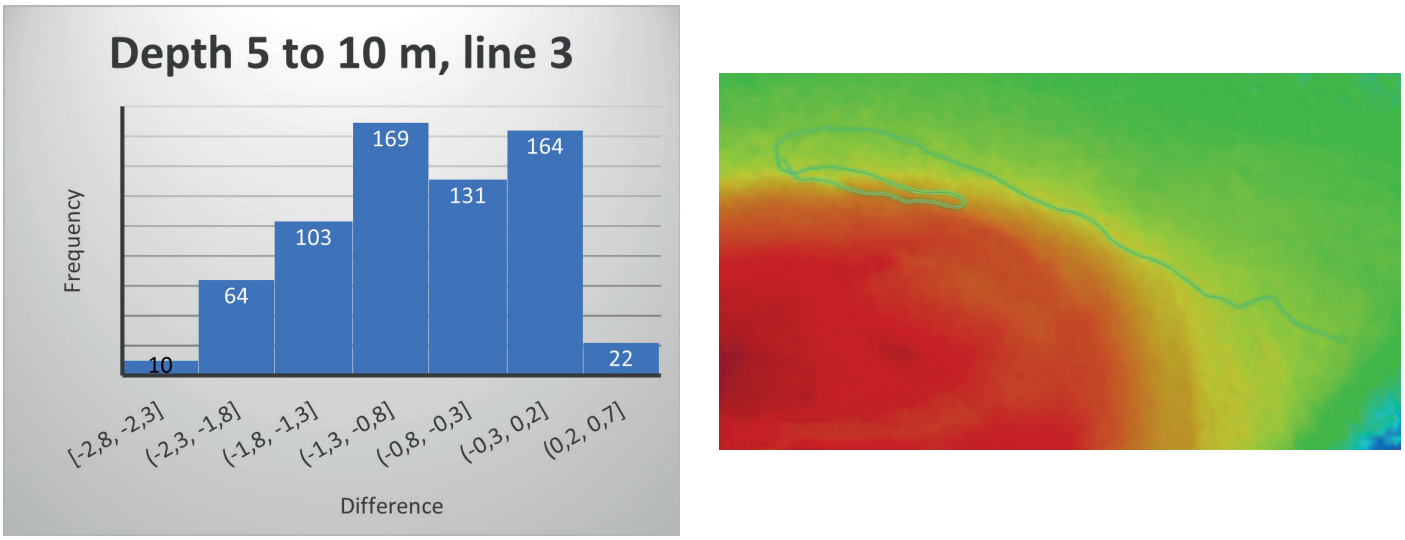


Fig. 10 Line 3 of depth 5–10 m of SBES compared with SDB and the difference histogram.

Table 10 Line 3 of depth 5–10 m.

Mean error (m)	Std. dev. (m)	RMSE (m)	Min. error (m)	Max. error (m)
-0.8029	0.69583	1.0621	-2.8	0.6

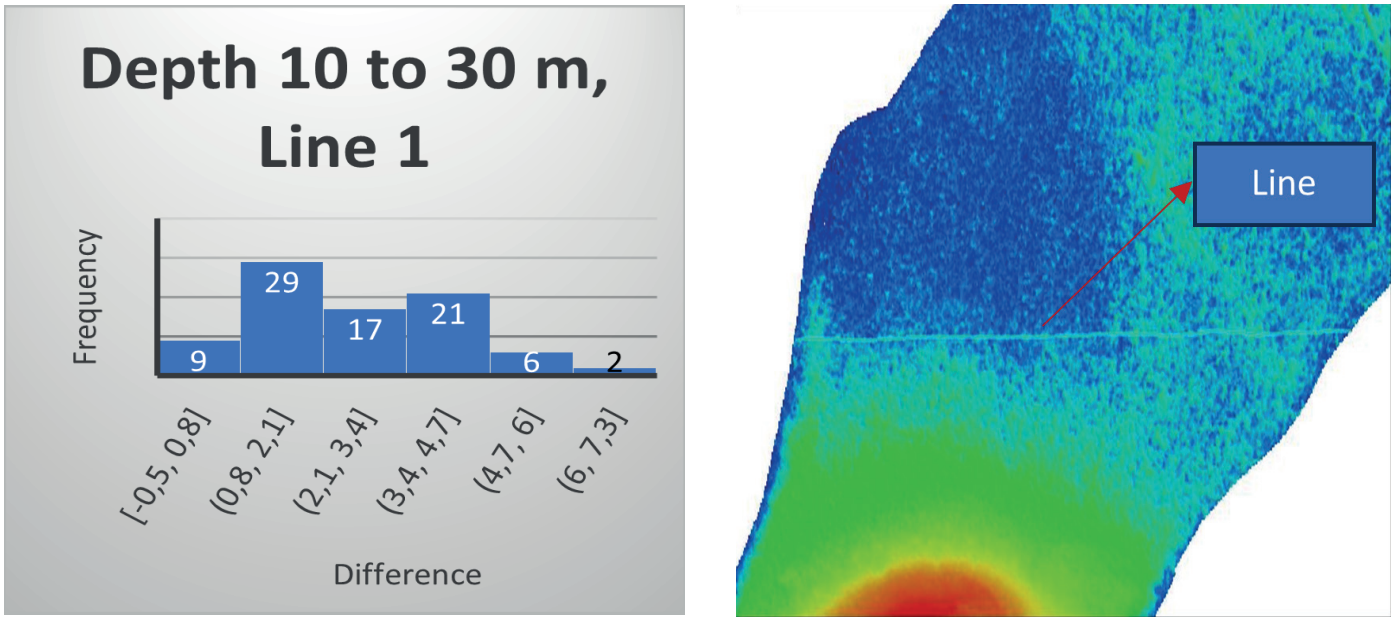
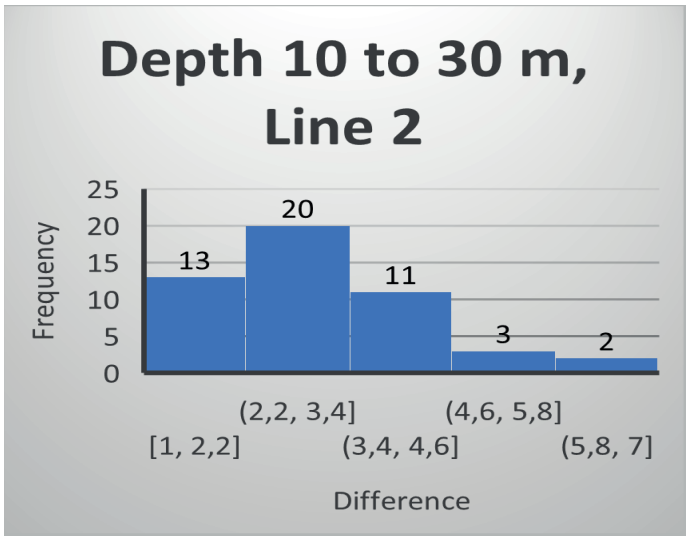


Fig. 11 Line 1 of depth 10–30 m of SBES compared with SDB and the difference histogram.

Table 11 Line 1 of depth 10–30 m.

Mean error (m)	Std. dev. (m)	RMSE (m)	Min. error (m)	Max. error (m)
2.7072	1.553	3.1164	-0.5	6.9



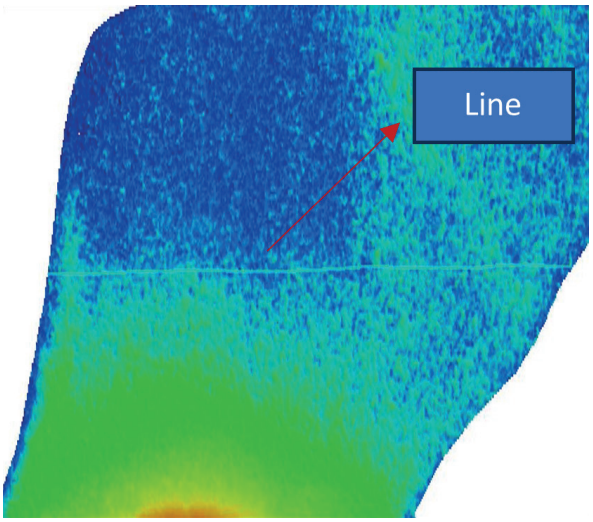
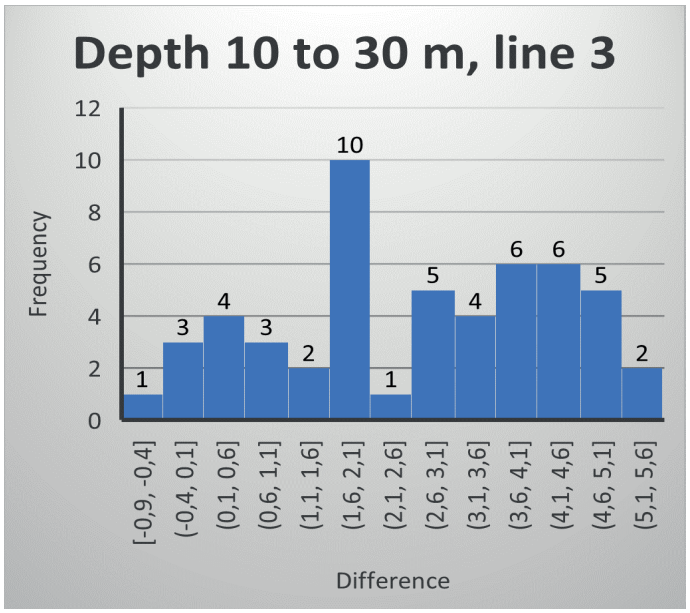


Fig. 12 Line 1 of depth 0–3 m of SBES compared with SDB in reef area and the difference histogram.

Table 12 Line 2 of depth 10–30 m.

Mean error (m)	Std. dev. (m)	RMSE (m)	Min. error (m)	Max. error (m)
3.0265	1.2868	3.2836	1	7



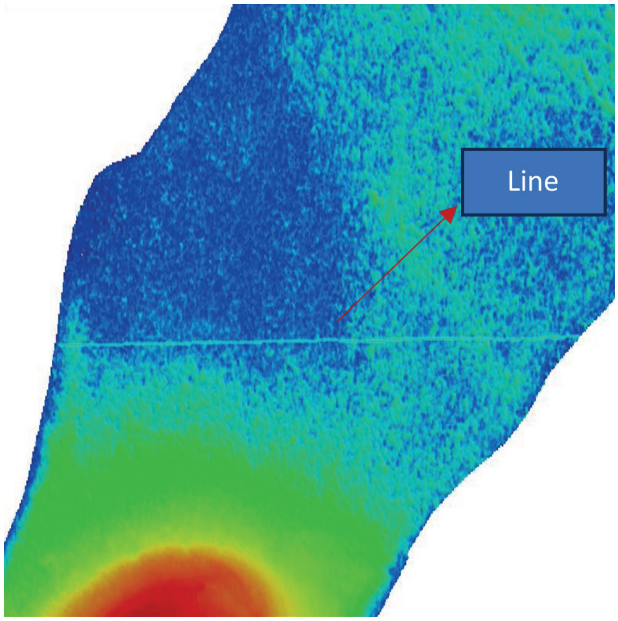


Fig. 13 Line 3 of depth 10–30 m of SBES compared with SDB and the difference histogram.

Table 13 Line 3 of depth 10–30 m.

Mean error (m)	Std. dev. (m)	RMSE (m)	Min. error (m)	Max. error (m)
2.7314	1.6375	3.1764	-0.9	5.6

https://doi.org/10.58440/ihr-31-2-n07

Fig. 14 presents the comparison of SDB vertical uncertainties, expressed as LE95 (1.96 σ), with IHO S-44 Order 1a TVU limits at the midpoints of each depth range. The results clearly show that while the LE95 values capture the general trend of increasing uncertainty with depth, they exceed the Order 1a limits across all bands, including the shallowest 0–3 m zone. This indicates that, although SDB reproduces the bathymetric pattern consistently, its uncertainties are above the stringent IHO thresholds when evaluated at the 95 % confidence level. These findings reinforce the suitability of SDB for reconnaissance-level mapping and coastal monitoring, while underscoring the importance of cautious interpretation when comparing to hydrographic survey standards.

In Table 15, in order to evaluate compliance with IHO S-44 standards (IHO, 2022), it is important to note that the TVU limits are expressed at the 95 % confidence level (LE95). Statistically, this corresponds to 1.96 times the standard deviation σ of normally distributed residuals. While RMS error values are often reported as a summary metric of accuracy, RMS includes both the random scatter (σ) and any systematic bias. Since TVU thresholds are intended to constrain random uncertainty rather than systematic offset, the appropriate measure for comparison is 1.96 σ, with bias reported separately. Accordingly, the compliance analysis presented here is based on 1.96 σ, ensuring consistency with the IHO S-44 LE95 definiton. The RMSE values computed in this study were compared against these limits under the assumption of a normal distribution of residuals. As per the results none of the depth criteria meet the requirements of order 1a.

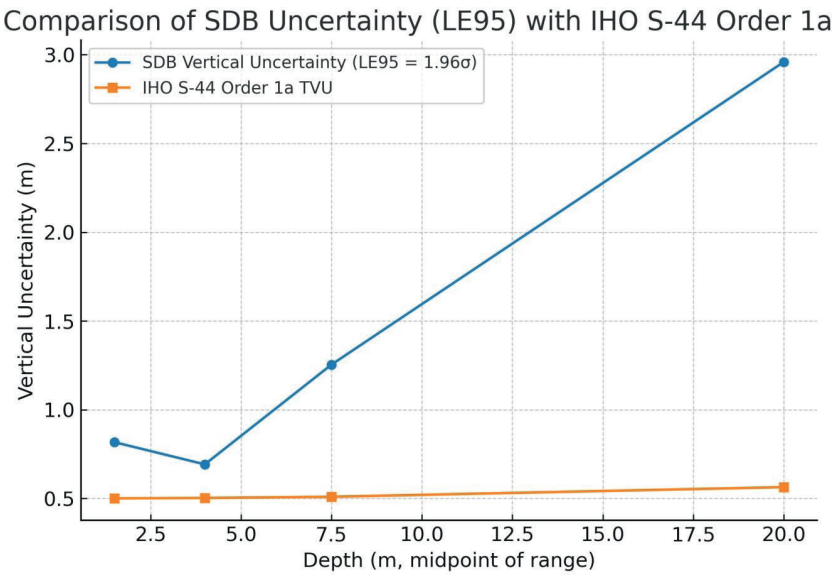


Fig. 14 Comparison of SDB vertical uncertainty (LE95 = 1.96 σ) with IHO S-44 Order 1a TVU limits.

Table 14 Detailed statistical comparison of SDB against ground-truth acoustic data (MBES/SBES).

Depth range (m)	Line	Mean error (m)	Std. dev. (m)	RMSE (m)	Point count
0–3	1	-0.1839	0.4245	0.4620	322
	2	-0.4095	0.3838	0.5610	430
	3	+0.0899	0.1753	0.1962	99
3–5	1	+0.0596	0.3665	0.3712	1,302
	2	+0.1645	0.3655	0.3998	166
	3	+0.0135	0.2514	0.2513	259
5–10	1	-0.9463	0.4735	1.0577	240
	2	-0.7842	0.6229	1.0010	424
	3	-0.8029	0.6958	1.0621	662
10–30	1	+2.7072	1.5530	3.1164	83
	2	+3.0265	1.2868	3.2836	49
	3	+2.7314	1.6375	3.1764	51

Table 15 SDB LE95 error against IHO S-44 Order 1a vertical uncertainty limits.

Depth range (m)	Mean error (m)	Std. dev. (m)	RMSE (m)	Point count	1.96 σ (m) LE95	IHO TVU (Order 1a)	Compliance
0–3	–0.2660	0.417	0.4942	851	0.817	0.52	No
3–5	+0.0628	0.353	0.3587	1,727	0.692	0.55	No
5–10	–0.8229	0.640	1.0421	1,326	1.254	0.62	No
10–30	+2.7995	1.510	3.1786	183	2.959	0.95	No

5 Conclusions

This study assessed the applicability of physics-based SDB over the reef-fringed waters of Agatti Island using Sentinel-2 imagery processed by EOMAP GmbH & Co. KG. Validation against echo sounder data collected from shallow-water crafts (SBES) and survey vessels (MBES) demonstrated that while SDB provided reliable depth trends across all zones, the statistical comparison revealed limitations when benchmarked against IHO S-44 standards (IHO, 2022). Specifically, when residuals were assumed normally distributed and scaled to the 95 % confidence level (LE95 = 1.96 σ), SDB vertical uncertainties exceeded the Order 1a TVU limits across all depth bands. This indicates that, although the SDB performed within RMS magnitudes close to IHO thresholds in shallow waters, strict compliance was not achieved once LE95 criteria were applied.

Nevertheless, the results confirm the operational value of SDB as a reconnaissance tool, especially in logistically challenging or environmentally sensitive areas where conventional hydrographic surveys are constrained. The findings also highlight the importance of explicitly accounting for statistical definitions of uncertainty when comparing SDB results to hydrographic standards. With ongoing improvements in satellite sensor resolution, atmospheric correction, and water column modelling, SDB is expected to become an increasingly important complement to traditional surveys, particularly for coastal planning and monitoring in remote island regions.

While SDB alone cannot currently replace traditional surveys for safety-of-navigation charting in deeper waters, it holds considerable promise as a force multiplier – enabling prioritization, survey planning, and ecological monitoring in compliance with internationally accepted hydrographic standards. Future efforts may benefit from integrating optically active substance (OAS) data and machine learning enhancements, as explored in recent Indian studies (Ashphaq et al., 2025), to improve SDB depth retrieval in complex coastal waters.

Acknowledgement

The author expresses sincere gratitude to the Indian Naval Hydrographic Department (INHD) for the opportunity to undertake this study on an emerging and operationally relevant topic, and for the valuable guidance and support extended by senior officers and colleagues throughout the course of this work. Special thanks are also due to EOMAP GmbH & Co. KG for providing the SDB dataset, for the analysis presented in the paper. Special mention of Cdr Ashsish G Srinivasan (Ret.) for the valuable insights and guidance.

References

Ashphaq, M., Srivatsav, P. K. and Mitra, D. (2025). Optimizing satellite-derived bathymetry in coastal turbid waters through integration of optically active substances: Insights from the SATCORE project. *Journal of Coastal Research, 86*, 104208. https://doi.org/10.1016/j.rsma.2025.104208

Athmaram, J. and Srinivasan, A. G. (2017). Acquisition of satellite-derived bathymetry data for offshore engineering projects: Island case study. *Abu Dhabi International Petroleum Exhibition & Conference*, Abu Dhabi, UAE. doi: https://doi.org/10.2118/188714-MS

EAHC (2015). *Report on International Workshop on Tsunami Inundation Mapping.* East Asia Hydrographic Commission, Tokyo, Japan. http://home.eahc.asia/tsunami/(Final)_Full_Report_on_Tsunami_Workshop.pdf (last accessed 9 Otober 2025).

EOMAP (2025). *Key insights from Earth Observation*. EOMAP GmbH & Co. KG, Seelfeld, Germany. https://www.eomap.com (last accessed 1 April 2025).

ESA (2015) *Sentinel-2 User Handbook* (Issue 1, Rev. 2). European Space Agency, Paris, France. https://sentinels.copernicus.eu/documents/247904/685211/Sentinel-2_User_Handbook.pdf (last accessed 9 Otober 2025).

ESA (2025). *Earth Online.* European Space Agency, Paris, France. https://earth.esa.int (last accessed 1 April 2025).

Gunathilaka, M. D. E. K., Wishwajith, K. L. K. K. and Rathnayake, R. M. D. I. Satellite derived bathymetry for rapid investigation for possible navigational channel design for coastal wind farm installation: a case study at Silavathurai, Sri Lanka. *Discov Appl Sci, 6*(54). https://doi.org/10.1007/s42452-024-05689-5

Hartmann, K., Reithmeier, M., Knauer, K., Wenzel, J., Kleih, C., Heege, T. (2022). Satellite-derived bathymetry online. *The International Hydrographic Review, 28*, pp. 53–75. https://doi.org/10.58440/ihr-28-a14

IHO (2022). *Standards for Hydrographic Surveys* (ed. 6.1). IHO Special Publication S-44, International Hydrographic Organization, Monaco. https://iho.int/uploads/user/pubs/standards/s-44/S-44_Edition_6.1.0.pdf (last accessed 9 October 2025).

IHO (2024). *Guidance to Satellite-derived Bathymetry* (1st ed.). IHO Publication B-13, International Hydrographic Organization, Monaco. https://iho.int/uploads/user/pubs/bathy/B_13_Ed100_032024.pdf (last accessed 9 October 2025).

https://doi.org/10.58440/ihr-31-2-n07

GENERAL INFORMATION

Acknowledgement to peer-reviewers

The International Hydrographic Review (IHR) would like to express its gratitude to the following individuals for their invaluable contribution to the peer review process, having reviewed one or more scientific manuscripts in 2025.

Musa Animashaun
Bismarck Jigena Antelo
Björn Baschek
Daniel Basil
Michael Bleier
Julia Bräker
Stephan O'Brien
Thomas Brüggemann
Pengfei Chen
Ian Church
Olagoke Daramola
Yordan Denev
Tanja Dufek
Dennis Edler
Melanie Elias
Merv Fingas
Floris Goerlandt
Stephan Große
Emre Gülher
Christopher O. Ilori
Alex Kirichek
Huibert-Jan Lekkerkerk
Derek Lichti
David Mader
Ferdinand Maiwald
Wojciech Maleika
Arthur Ayres Neto
Alberto Pedrassani Costa Neves
Nino Ohle
Marko Perkovič
Rafael A. Ponce
Jan Rhomberg-Kauert
Annette Scheider
Thierry Schmitt
Luigi Sinapi
Thomas Thies
Arkadiusz Tomczak
Yuzui Tomohiro
Jesús Valle
Dagoberto Uriel David Viteri
Daniel Wright
Luca Zamparini

https://doi.org/10.58440/ihr-31-2-i01


IHO
International
Hydrographic
Organization